# PARTICLES AT FLUID INTERFACES

EDITED BY: Erica Wanless, Grant Webber and Syuji Fujii
PUBLISHED IN: Frontiers in Chemistry

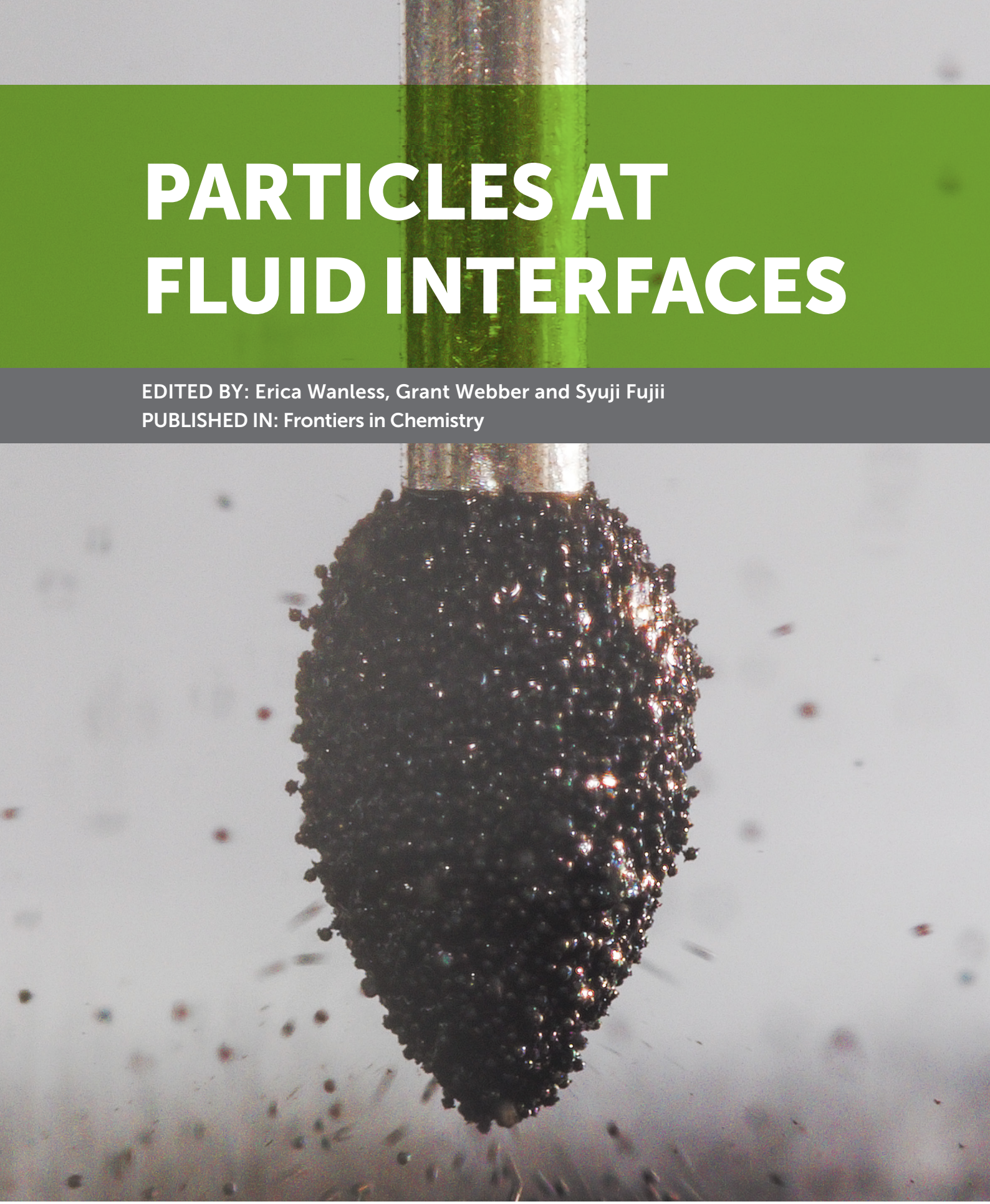

frontiers Research Topics

# frontiers



ISSN 1664-8714
ISBN 978-2-88945-808-0
DOI 10.3389/978-2-88945-808-0

## About Frontiers

Frontiers is more than just an open-access publisher of scholarly articles: it is a pioneering approach to the world of academia, radically improving the way scholarly research is managed. The grand vision of Frontiers is a world where all people have an equal opportunity to seek, share and generate knowledge. Frontiers provides immediate and permanent online open access to all its publications, but this alone is not enough to realize our grand goals.

## Frontiers Journal Series

The Frontiers Journal Series is a multi-tier and interdisciplinary set of open-access, online journals, promising a paradigm shift from the current review, selection and dissemination processes in academic publishing. All Frontiers journals are driven by researchers for researchers; therefore, they constitute a service to the scholarly community. At the same time, the Frontiers Journal Series operates on a revolutionary invention, the tiered publishing system, initially addressing specific communities of scholars, and gradually climbing up to broader public understanding, thus serving the interests of the lay society, too.

## Dedication to Quality

Each Frontiers article is a landmark of the highest quality, thanks to genuinely collaborative interactions between authors and review editors, who include some of the world's best academicians. Research must be certified by peers before entering a stream of knowledge that may eventually reach the public - and shape society; therefore, Frontiers only applies the most rigorous and unbiased reviews.
Frontiers revolutionizes research publishing by freely delivering the most outstanding research, evaluated with no bias from both the academic and social point of view. By applying the most advanced information technologies, Frontiers is catapulting scholarly publishing into a new generation.

## What are Frontiers Research Topics?

Frontiers Research Topics are very popular trademarks of the Frontiers Journals Series: they are collections of at least ten articles, all centered on a particular subject. With their unique mix of varied contributions from Original Research to Review Articles, Frontiers Research Topics unify the most influential researchers, the latest key findings and historical advances in a hot research area! Find out more on how to host your own Frontiers Research Topic or contribute to one as an author by contacting the Frontiers Editorial Office: researchtopics@frontiersin.org

# PARTICLES AT FLUID INTERFACES

Topic Editors:
**Erica Wanless,** University of Newcastle, Australia
**Grant Webber,** University of Newcastle, Australia
**Syuji Fujii,** Osaka Institute of Technology, Japan



Particles at Fluid Interfaces encompasses the processes and formulations that involve the stabilisation of fluid interfaces by adsorbed particles. The prevalence of these multiphase materials underpins their use in a broad range of industries from personal care and food technology to oil and mineral processing. The stabilisation conferred by the adsorbed particles can be transient as found in froth flotation or long-lived as occurs within Pickering Emulsions. The particles can range in size from nanoparticles to millimetre-sized particles, and cover a spectrum from collapsed proteins, polymeric colloids of controlled size and shape to high dispersity mineral particles.

**Citation:** Wanless, E., Webber, G., Fujii, S., eds. (2019). Particles at Fluid Interfaces. Lausanne: Frontiers Media. doi: 10.3389/978-2-88945-808-0

# Table of Contents


*05* ***Editorial: Particles at Fluid Interfaces***
Erica J. Wanless, Grant B. Webber and Syuji Fujii

## FUNDAMENTAL STUDIES

*07* ***Experimental Technique to Study the Interaction Between a Bubble and the Particle-Laden Interface***
Xingshi Yang, Alexander Mayer, Ghislain Bournival, Robert Pugh and Seher Ata

*22* ***Anisotropic Polymer Adsorption on Molybdenite Basal and Edge Surfaces and Interaction Mechanism With Air Bubbles***
Lei Xie, Jingyi Wang, Jun Huang, Xin Cui, Xiaogang Wang, Qingxia Liu, Hao Zhang, Qi Liu and Hongbo Zeng

*33* ***Rice Starch Particle Interactions at Air/Aqueous Interfaces—Effect of Particle Hydrophobicity and Solution Ionic Strength***
Cathy E. McNamee, Yu Sato, Berthold Wiege, Ippei Furikado, Ali Marefati, Tommy Nylander, Michael Kappl and Marilyn Rayner

*48* ***Dynamic Surface Wetting and Heat Transfer in a Droplet-Particle System of Less Than Unity Size Ratio***
Subhasish Mitra and Geoffrey Evans

## PARTICLE STABILISED FOAMS

*67* ***Effects of Contact Angle and Flocculation of Particles of Oligomer of Tetrafluoroethylene on Oil Foaming***
Ryo Murakami, Syuji Kobayashi, Manami Okazaki, Alexander Bismarck and Masahiro Yamamoto

*75* ***pH-Responsive Aqueous Bubbles Stabilized With Polymer Particles Carrying Poly(4-vinylpyridine) Colloidal Stabilizer***
Masaya Ito, Koki Takano, Haruka Hanochi, Yuta Asaumi, Shin-ichi Yusa, Yoshinobu Nakamura and Syuji Fujii

*85* ***Influence of Shell Thickness on the Colloidal Stability of Magnetic Core-Shell Particle Suspensions***
Frances Neville and Roberto Moreno-Atanasio

## PARTICLE STABILISED OIL-WATER INTERFACES

*96* ***Tailoring the Wettability of Colloidal Particles for Pickering Emulsions via Surface Modification and Roughness***
Meina Xiao, Anli Xu, Tongtong Zhang and Liangzhi Hong

*110* ***Pickering Emulsions Electrostatically Stabilized by Cellulose Nanocrystals***
Swambabu Varanasi, Leeav Henzel, Llyza Mendoza, Ragesh Prathapan, Warren Batchelor, Rico Tabor and Gil Garnier

*119* ***Influence of pH-Responsive Monomer Content on the Behavior of Di-Block Copolymers in Solution and as Stabilizers of Pickering Latex Particle Emulsifiers***
Mohamed S. Manga, Olivier J. Cayre, Simon Biggs and Timothy N. Hunter

132 ***Comparing the Relative Interfacial Affinity of Soft Colloids With Different Crosslinking Densities in Pickering Emulsions***
Man-hin Kwok and To Ngai

144 ***Mixing Time, Inversion and Multiple Emulsion Formation in a Limonene and Water Pickering Emulsion***
Laura Sawiak, Katherine Bailes, David Harbottle and Paul S. Clegg

153 ***Particle-Stabilized Fluid-Fluid Interfaces: The Impact of Core Composition on Interfacial Structure***
Alison Tasker, Frank Sainsbury and Simon Puttick

160 ***Metal Coated Colloidosomes as Carriers for an Antibiotic***
Qian Sun, Ziyan Zhao, Elizabeth A. H. Hall and Alexander F. Routh

## MULTICOMPONENT SYSTEMS

168 ***Droplet Fusion in Oil-in-Water Pickering Emulsions***
Catherine P. Whitby and Floriane Bahuon

174 ***Ultrafine Particle Recovery Using Thin Permeable Films***
Daniel J. Borrow, Kim van Netten and Kevin P. Galvin

## LIQUID MARBLES & AGGREGATES

182 ***An Electrostatic Method for Manufacturing Liquid Marbles and Particle-Stabilized Aggregates***
Peter M. Ireland, Casey A. Thomas, Benjamin T. Lobel, Grant B. Webber, Syuji Fujii and Erica J. Wanless

188 ***pH-Responsive Particle-Liquid Aggregates—Electrostatic Formation Kinetics***
Peter M. Ireland, Kohei Kido, Grant B. Webber, Syuji Fujii and Erica J. Wanless

frontiers in Chemistry

EDITORIAL
published: 07 February 2019
doi: 10.3389/fchem.2019.00052

# Editorial: Particles at Fluid Interfaces

*Erica J. Wanless*[1]*, *Grant B. Webber*[1] *and Syuji Fujii*[2,3]

[1] Priority Research Centre for Advanced Particle Processing and Transport, University of Newcastle, Callaghan, NSW, Australia, [2] Department of Applied Chemistry, Faculty of Engineering, Osaka Institute of Technology, Osaka, Japan, [3] Nanomaterials Microdevices Research Center, Osaka Institute of Technology, Osaka, Japan

**Keywords: particle, colloid, interface, Pickering emulsion, foam, liquid marble**

## Editorial on the Research Topic

## Particles at Fluid Interfaces

The research topic Particles at Fluid Interfaces encompasses the industrial processes and product formulations that involve the stabilization of fluid interfaces by adsorbed particles. The prevalence of these multiphase materials underpins their use in a broad range of industries from personal care and food technology to oil and mineral processing. The stabilization conferred by the adsorbed particles can be transient as found in froth flotation or long-lived as occurs within Pickering Emulsions. The particles can range in size from nanoparticles to millimeter-sized particles, and cover a spectrum from collapsed proteins, polymeric colloids of controlled size and shape to high dispersity mineral particles. In this Research Topic we present an important collection of reviews and original research articles that illustrate the pertinence of this interfacial activity in a breadth of applications backed up by fundamental investigations.

Fundamental studies provide an avenue to deepen our understanding of high interfacial area multiphase systems. In this issue a modified Langmuir trough is deployed by Yang et al. to study single air bubble interactions with a particle coated air-water interface. Atomic force microscopy is used by Xie et al. to investigate the interaction of single bubbles with the basal plane of molybdenite. McNamee et al. explore the interfacial behavior of approved food additive starch particles using their Monolayer Interaction Particle Apparatus. Meanwhile Mitra and Evans probe the influence of temperature on dynamic contact angles of a single water droplet on a stationary brass particle backed up by computational fluid dynamics modeling. Oil foams stabilized by tetrafluoroethylene oligomer particles (Murakami et al.) and pH-responsive aqueous foams (Ito et al.) are examples of harnessing particle contact angle to control the foam stability. Controlled particle flocculation using magnetic particles as could be found in a layer of adsorbed particles on a fluid interface is modeled using Discrete Element Analysis by Neville and Moreno-Atanasio.

Particle stabilized oil-water interfaces as found in Pickering emulsions are another interface of intense current research interest and are highlighted in this special Research Topic. Xiao et al. present a review of the use of nanoparticles to stabilize such systems. A specific example of this stability is the use of nanocrystalline cellulose as reported by Varanasi et al. Pickering emulsion stability can be controlled through the use of pH-responsive latex stabilizers as demonstrated by Manga et al. Pickering stabilization using soft microgel particles is reported by Kwok and Ngai. Moreover, the transformation from an oil continuous to a water continuous phase Pickering emulsion stabilized by fumed silica upon prolonged mixing is shown by Sawiak et al. Pickering emulsions are currently favored for their prospects as delivery vehicles for therapeutics as reviewed by Tasker et al. A well-documented limitation of this encapsulation approach is the undesired leakage of the small active agents. Sun et al. chose to minimize this issue via metal coating of their cross-linked Pickering emulsion, or colloidosome for antibiotic encapsulation and delivery.

This issue also includes novel multicomponent systems that offer exciting future prospects for the deployment of particle-stabilized interfaces in formulations that frequently also contain

OPEN ACCESS

***Edited by:***
*Gil Garnier,*
*Bioresource Processing Institute of Australia (BioPRIA), Australia*

***Reviewed by:***
*Olivier Cayre,*
*University of Leeds, United Kingdom*

****Correspondence:***
*Erica J. Wanless*
*erica.wanless@newcastle.edu.au*

***Specialty section:***
*This article was submitted to Chemical Engineering, a section of the journal Frontiers in Chemistry*

***Received:*** *06 September 2018*
***Accepted:*** *21 January 2019*
***Published:*** *07 February 2019*

***Citation:***
*Wanless EJ, Webber GB and Fujii S (2019) Editorial: Particles at Fluid Interfaces. Front. Chem. 7:52. doi: 10.3389/fchem.2019.00052*

surfactant.Whitby and Bahuon took advantage of transient droplet coalescence events to form compound droplets made of two or more drops of immiscible oils by temporarily destabilizing Pickering oil-in-water emulsions. While Borrow et al. use a high internal phase water-in-oil emulsion to selectively agglomerate fine mineral particles as a route to enhance their recovery via their adsorption to the oil-water interface. Finally, Ireland et al.; Ireland et al. outline a contactless route to liquid marble formation using electrostatic transfer of particles to pendent water droplets with a view to enhanced control in formation and prospects for scaling up production.

We believe that the Particles at Fluid Interfaces Research Topic explores the latest particle-stabilized fluid interfaces research including fundamental theory and experiments together with articles focusing on more applied research. More efficient production processes and formulations with improved control over the lifetime of product stability are two current goals in the pursuit of greater understanding. Furthermore, particle-stabilized soft dispersed systems are expected to function as a development platform for smart soft materials, and a wide range of academic and industrial future applications are anticipated. Interdisciplinary research is crucial to the continued improved utilization of particles at fluid interfaces for the development of multiphase science and engineering, as highlighted by the contributing authors to this special Research Topic who span such fields as chemistry, chemical engineering, nanotechnology, and bioresource processing and bioengineering. This Research Topic has the objective of stimulating discussion and cross-fertilization of ideas between the industries dependent upon these multiphase systems.

## AUTHOR CONTRIBUTIONS

All authors listed have made a substantial, direct and intellectual contribution to the work, and approved it for publication.

**Conflict of Interest Statement:** The authors declare that the research was conducted in the absence of any commercial or financial relationships that could be construed as a potential conflict of interest.

frontiers in Chemistry

ORIGINAL RESEARCH
published: 14 August 2018
doi: 10.3389/fchem.2018.00348

# Experimental Technique to Study the Interaction Between a Bubble and the Particle-Laden Interface

*Xingshi Yang[1], Alexander Mayer[1], Ghislain Bournival[1], Robert Pugh[2] and Seher Ata[1]**

[1] School of Mining Engineering, University of New South Wales, Sydney, NSW, Australia, [2] Department of Physics and Mathematics, Nottingham Trent University, Nottingham, United Kingdom

An experimental apparatus was developed based on the Langmuir-Blodgett trough design to investigate the compression of monolayers of micron size spherical glass particles at the air-water interface and the interaction of an air bubble with the monolayers. The setup modifies the regular Langmuir-Blodgett trough by using a deep and clear glass cell. The cell allowed both the optical observation of the particle monolayer and the insertion of a capillary to produce a bubble under the layer of particles. Surface pressure-area (Π-A) isotherms were measured while the particles rearranged at the interface during compression and expansion for different pH values and particle wettability. We also analyzed the motion of particles in the monolayer by the surface pressure and packing factor to gain further insights into the behavior of particles during the coalescence process. The results suggested that the coalescence of a bubble was dependent on the formation of a defect in the particle layer and the defect size was both strongly influenced by particle hydrophobicity and the pH of the subphase.

**Keywords: particle monolayer, packing factor, particle tracking, surface pressure, bubble coalescence**

OPEN ACCESS

***Edited by:***
*Grant Bruce Webber, University of Newcastle, Australia*

***Reviewed by:***
*Cathy Elizabeth McNamee, Shinshu University, Japan*
*Michael Kappl, Max-Planck-Institut für Polymerforschung, Germany*
*Olivier Cayre, University of Leeds, United Kingdom*

***Correspondence:**
*Seher Ata*
*s.ata@unsw.edu.au*

***Specialty section:***
*This article was submitted to Chemical Engineering, a section of the journal Frontiers in Chemistry*

***Received:*** *28 March 2018*
***Accepted:*** *25 July 2018*
***Published:*** *14 August 2018*

***Citation:***
*Yang X, Mayer A, Bournival G, Pugh R and Ata S (2018) Experimental Technique to Study the Interaction Between a Bubble and the Particle-Laden Interface. Front. Chem. 6:348. doi: 10.3389/fchem.2018.00348*

## INTRODUCTION

Langmuir monolayers and Langmuir–Blodgett (LB) films are widely used to investigate the morphology and dynamics of particle monolayers at air-water interfaces. Most studies focus on insoluble surfactant layers and nanoparticles owing to their wide range of applications, but there have been several investigations of visible micron size particles with different surface wettabilities (Santini et al., 2011; Kralchevsky et al., 2016; Petkov et al., 2016). Hórvölgyi et al. (1996) investigated the behavior of a monolayer consisting of artificially hydrophobized glass beads of 75 μm at the air-water interface in a Langmuir film balance and found that the reorganization occurring in the particle-laden interface was strongly correlated to the particle hydrophobicity and surface packing density. Upon mechanical compression of the interface, particle layers of high density were found to buckle into bilayer structures and/or collapse. It was also found that the energy required to compress the most strongly hydrophobic particles into a close-packed layer was significantly greater than that required for the compression of the less hydrophobic particles. Onoda (1985) studied the assembly of polystyrene particles in the size range of 2–15 μm at a flat air-water interface and found that particle clustering was strongly dependent on the particle size. For 2 μm particles, the particle rafts appeared to be well ordered while the clusters formed from large particles displayed less stable and loose agglomerates with branched structures.

The formation and ordering of particles at an interface are complex phenomena and the physics governing the process are controlled by various factors such as particle size and shape, nature of the phases forming the interface and hydrophobicity of particle material. In recent years, several studies have combined the Langmuir trough technique with surface-specific analysis techniques to provide further insights into the complex behavior of particles at liquid interfaces. Some examples of such techniques include x-ray diffraction (Yun and Bloch, 1989; Fujii et al., 2017), grazing incidence x-ray diffraction (Reitzel et al., 2000), ellipsometry (Hunter et al., 2009), Brewster angle microscopy measurements (Safouane et al., 2007), vibrational sum frequency generation spectroscopy (Ma and Allen, 2006), atomic force microscopy (Reitzel et al., 2000) and imaging techniques such as microscopy and high speed camera (Cote et al., 2009; McNamee et al., 2011). There have also been studies where the Langmuir-Blodgett trough was modified to examine the orientational order, packing, and morphology in monolayers or the behavior of the monolayer as a whole. Krägel et al. (1996) used a modified Langmuir-Blodgett trough with an oscillating barrier to generate periodic dilation and compression to measure the dilational elastic modulus as a function of surface area. The method permitted a direct measurement of the amplitude of surface pressure oscillation and the phase angle between the generated area oscillation and the resulting pressure oscillations. A similar technique was used by Planchette et al. (2013) where the air-water interfaces coated with monodispersed hydrophobic silica particles with diameters ranging from 35 to 159 μm were oscillated with a vertical oscillating glass plate coupled to a vibrating pot and frequency generator. The mechanical properties of particle-laden interfaces were investigated by studying capillary wave propagation along the interface.

Langmuir monolayers provide an excellent model for studying the properties of the surface layers in response to compression and shear. Such studies are important in understanding the behavior of particles at an air-bubble surface in a turbulent environment. Particle coated bubbles are found in a number of processes and applications, such as froth flotation. In mineral flotation, air bubbles in the range of 1 mm are introduced into water containing suspended solid particles with various surface hydrophobicities in a suitable flotation vessel. Hydrophobic particles attach to the surface of bubbles and rise to the surface of the liquid where they form a froth layer, which overflows the lip of the vessel. For a particle to attach to a bubble, both must first be brought together, generally in a highly turbulent environment. Particle coated bubbles trapped in turbulent flow undergo intensive surface deformation with large amplitude shape oscillation (Schulze, 1984) leading to compression and expansion of the particle layer in response to the shear applied. Similarly, bubbles in the froth layer undergo surface deformation as a result of continuous rearrangement and morphological changes caused by bubble coalescence within the froth (e.g., Pugh, 1996; Bournival et al., 2015a), bubble bursting on the top layer (Barbian et al., 2003), and drainage of water (Pugh, 1996). Understanding the behavior of the particle layer at bubble surfaces is important for the fine tuning of bubble stability and for optimizing the efficiency of froth flotation as well as other processes that include particle coated bubbles and foams.

The aim of this study is to introduce an experimental method based on the Langmuir-Blodgett trough. It consists of a trough modified with a transparent deep glass cell, which made it possible to produce an air bubble through a capillary tube beneath the particle monolayer. As demonstrated in this study, the setup allowed direct observation of interaction between a bare bubble and a particle-laden interface, while also being capable of controlling the particle coverage at the interface. By analyzing the recordings during the interaction of the bubble and the particles, the changes in the particle packing and particle movement could be quantified and related to the stability of the interface. Two-dimensional particle networks were studied in order to investigate their ability to stabilize bubbles. This paper shows the different analyses, which can be conducted with the experimental setup. It is part of a larger body of work, which will examine the interaction of surfactants and particles with bubbles.

# EXPERIMENTAL PROCEDURE

## Materials

Soda-lime glass beads with a density of 2.5 g/cm$^3$ were purchased from Potters Industries Pty Ltd. (Melbourne, Australia). The particles had a volume-surface equivalent diameter (Sauter diameter, $D_{32}$) of 64 μm while the 90% passing diameter ($D_{90}$) was $D_{90} = 92\,\mu m$. While most of the particles were nearly spherical in shape, some irregularly shaped particles were also found. The glass particles were cleaned in a mixture of ammonia (Ajax Finechem Pty Ltd., 28%) and hydrogen peroxide (Chem-Supply, 30% w/w) and hydrophobized with 1-octanol (Sigma-Aldrich, 99%) or 1-butanol (Chem-Supply, 99%) as described below. Dichlorodimethylsilane (DCDMS) (Sigma-Aldrich, ≥99.5%) and hydrochloric acid (HCl) (Chem-Supply, 32% w/w) were employed in the hydrophobization of glass plates making up the trough. All glassware was cleaned in a mixture of ethanol and sodium hydroxide (Sigma-Aldrich, ≥97.0%).

During the experiments, the pH of the aqueous phase was adjusted with hydrochloric acid or sodium hydroxide and the ionic strength of solution was kept at 0.01 M with sodium chloride (Ajax Finechem Pty Ltd., analytical grade). The spreading solvent for particle dispersion was spectroscopic grade toluene (Chem-Supply, ≥99.5%). All water used throughout was Milli-Q water from a Millipore system. The water had a resistivity of 18.2 MΩ cm and a surface tension of 72.8 mN/m. All experiments were conducted in a temperature controlled room ($22 \pm 1.5^{\circ}C$).

## Cleaning and Hydrophobization Methods

Glass beads used in the experiments were cleaned in an alkaline solution to remove any organic surface films through an oxidative breakdown of the contaminants following the procedure of Ata (2009). A solution of 50 mL of ammonia in 250 mL of water was heated to 80°C. A total of 50 g of particles was added to the hot solution with 50 mL of hydrogen peroxide. The mixture was stirred for 5 min and left to cool down to room temperature. The particles were decanted and rinsed with Milli-Q water until the

pH reached that of Milli-Q water. The particles were oven-dried at 60°C, then transferred to a desiccator to minimize contact with moisture.

Particles were hydrophobized by esterification following the method of Bournival et al. (2015b). A total weight of 130 g of 1-octanol or 1-butanol was refluxed in a conical flask with 50 g particles for 7 h to produce a surface of intermediate hydrophobicity. The equilibrium contact angles in the water phase (i.e., at natural pH) were 75°For the 1-octanol treated particles and 43°For the 1-butanol treated particles (Bournival et al., 2014). The particles are referred to as more hydrophobic (75°) or less hydrophobic (43°) throughout. The particle-alcohol mixture was then cooled down to room temperature and the alcohol decanted. The particles were twice suspended in acetone and ethanol to remove the excess alcohol. The particles were dried in the oven at 40°C and stored in a desiccator. It should be noted that the contact angle is expected to slightly change with the pH of the subphase, with a decrease in the contact angle at elevated pH (i.e., about 9) as demonstrated by Laskowski and Kitchener (1969). However, more work is needed to determine the effect of the contact of the spreading solvent with the hydrophobized surface on the contact angle. The values of the contact angles were assumed to be equivalent to that reported in the literature.

Glass plates, which made up the trough, were first placed in an ethanol-sodium hydroxide solution following the procedure described by Bournival et al. (2015b) and then dried in an oven at 40°C. Once dried, the plates were protonated by soaking in a 5% (v/v) HCl solution and rinsed with Milli-Q water prior to drying in an oven at 90°C for 30 min. The protonation helps the silanation process by forming head groups which are important for the reaction of the DCDMS with the surface. Once the plates cooled down to 35°C, they were placed in a desiccator along with a small beaker containing 3 mL of DCDMS for 3 h to expose the glass surface to silane vapor. The glass substrates were then baked in the oven at 125°C for 30 min, cooled down to room temperature, and sonicated in toluene to remove any residual (unbound) molecules and polymer. The hydrophobized glass plates had a contact angle of 90 ± 5° in water as measured by the static sessile drop method.

## Experimental Setup

An experimental setup was built to study the interaction between individual particles positioned at an air-water interface while subjecting the interface to compressive, expansive, and oscillatory (i.e., bubble coalescence induced) forces. The surface is considered representative of the air-water interface found at a bubble's boundary. The setup was modified from the Langmuir-Blodgett trough as shown in **Figure 1**. The cell (75 × 25 × 25 mm) was made of hydrophobized glass plates. The projected area (area of the particle-laden interface under compression) ranged from 500 to 1,750 $mm^2$. A motor (Uxcell, DC 6 V) rotated the screw that drove the rail carriage block (HIWIN, HGW15CC) to move linearly along the track. A hydrophobized glass plate (25 × 40 mm) was used as a barrier which was driven by the rail carriage block. The area of the particle-laden interface was controlled by the moving barrier at a rate of 11.25 $mm^2$/s with a barrier moving speed of 0.45 mm/s or a rate of 20 $mm^2$/s for a moving speed of 0.8 mm/s for some experiments (section The Effect of Particle Shape and Size on Particle Displacement During Compression). The Wilhelmy plate, made of a mica sheet (TED PELLA, grade V1, 5 × 25 mm), was hung on a loadcell perpendicular to the moving barrier. The loadcell used for the force measurement was made from four micro strain gauges (#CEA-06-500UW-120) in full bridge configuration (one gauge per leg) and had the precision of 0.1 mg. The instrument was connected to a National Instrument system and recorded the data in Labview every 10 ms. A hook-shaped stainless steel capillary (inner diamater = 0.69 mm, outer diameter = 1.04 mm) was connected to a syringe mounted on an Aladdin® Syringe Pump in order to create an air bubble just beneath the air-water interface. The distance between the capillary tip and the interface was maintained at 2 mm in all experiments. The whole setup sat on a vibration-free table to eliminate unwanted surface vibrations.

The images of the bubble and its interection with particle monolayers were captured on a high-speed camera (Photron FASTCAM APX RS, Photron USA) from both the top and side views. The top view, for which results are presented in this study, used a long distance lens (DistaMax, Infinity Photo-Optical) covering an area of 3.4 × 4.5 mm. The compression and expansion of the particle layers were recorded at a capture rate of 50 frames per second (fps) while the oscillation of the interface following the coalescence of a bubble with the interface was captured at 3000 fps.

The dispersion of particles at the air-water interface was similar to that of Máté et al. (1996) who also used micron-sized particles. In a typical experiment the glass container was filled with water to a depth of 20 mm and 3 mL of spreading solvent was poured on the surface of the aqueous phase. Approximately 0.25 g of hydrophobized particles were evenly sprinkled with a spatula onto the spreading solvent, which was left to evaporate for at least 15 min. After complete evaporation of the solvent, the particle monolayer was subjected to compression by movement of the mobile barrier and the surface pressure was recorded as a function of the area per particle in the film. To assess the interaction of a bubble with the interface, a capillary was placed in the subphase at a depth such that a bubble of 2 mm in diameter was just in contact with the interface. The high-speed camera was used to capture the interaction of the bubble with the particle-laden interface. The movement of the particles was tracked during the coalescence of the bubble and during the compression and expansion of the particle layer.

Previous studies have related the surface pressure change in the particle-laden interface to the mean area of each particle in the monolayer (Aveyard et al., 2000). The packing factor was used to describe the coverage of particles on the bubble surface in studies of controlled bubble coalescence (Bournival and Ata, 2010). It is defined as the ratio of the surface area covered by particles to the total surface area (i.e., surface area covered by

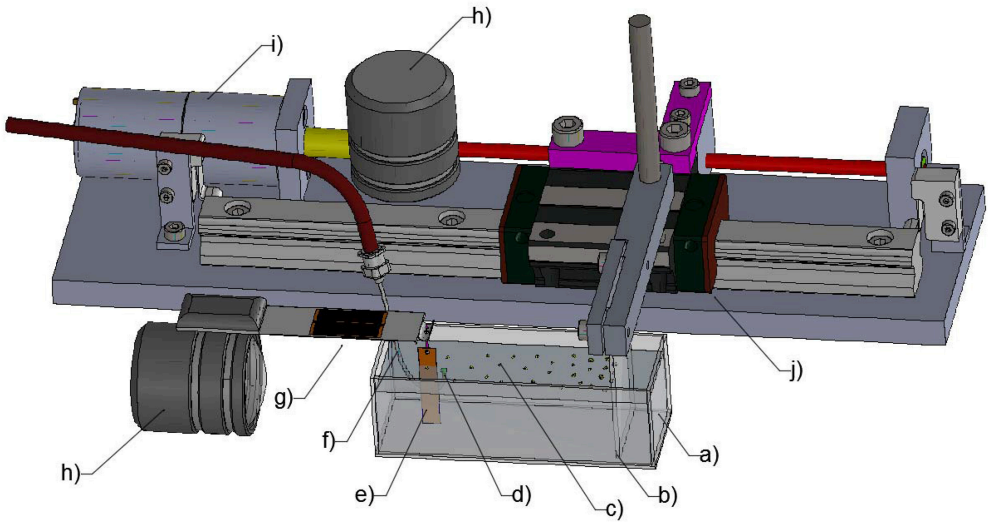


**FIGURE 1 |** Schematic of the modified Langmuir-Blodgett trough: **(a)** transparent glass cell; **(b)** barrier; **(c)** particle-laden interface; **(d)** bubble; **(e)** Wilhelmy plate; **(f)** the capillary; **(g)** the loadcell; **(h)** high-speed camera; **(i)** motor; **(j)** rail carriage block.

particles and the voids). To relate the particle packing to the properties of the interface, both the surface pressure and particle packing were measured and analyzed by assessing the top view of the recordings captured by the high-speed camera.

## Analysis of Surface Pressure Isotherms

The surface pressure was measured by a Wilhelmy plate in conjunction with an electronic balance as previously described. The data stream was corrected using cubic spline to remove the noise in the surface pressure measurements. The data was fitted using Spyder (Spyder IDE, version 3.1.4). The software is an open source IDE (integrated development environment) based on Python programming language. The code used is given in the **Supporting Information**.

## Image Analysis and Particle Tracking

The monolayer and individual particles were imaged using a high-speed camera. Using the recorded video frames as an input the packing factor, defined as the percentage of area covered by particles, was calculated using the ImageJ2 software (NIH). ImageJ2 allowed the frames to be transformed into a binary image by applying a threshold turning particles into black objects and leaving voids as white objects. A summation of these black areas was calculated from each frame and then used to calculate the packing factor by dividing it by the total surface area. Considering the small surface area observed it is important to note that the packing factor may be viewed as a local property rather than the overall packing factor. It was taken in the vicinity of the Wilhelmy plate.

Particle movement across the air-water interface was tracked using Tracker (version 4.97, Open Source Physics Project). Tracker is capable of gathering data from video recordings on the basis of a time and a coordinate system (Brown and Christian, 2011). The program allowed the particles to be tracked both with an autotracker function and a manual tracking function.

Video files that were imported into Tracker required the scale to be calibrated, for which a point of interest within the video with known measurements was identified. For experiments involving the coalescence of a bubble, the capillary tube, which is easily distinguishable and has a known outer diameter of 1.04 mm, was used. Compression and expansion videos were calibrated using the largest particles where the sizes were afterwards crosschecked with other particles. The largest particles were defined as having a size of 92.5 μm (corresponding to the $D_{90}$). Occurrence where two of these particles were found adjacent was then defined as twice the $D_{90}$. Coordinates were established and defined within the Tracker software to understand how particles moved through the video frames. For tracking the motion of particles following the coalescence of a bubble with the interface, the origin of the coordinate system was defined as the center of the capillary tube. As all compression and expansion videos had the same orientation the origin was defined in all experiments as the top right corner, ensuring continuity during analysis of the different videos. All y-axes were vertically orientated while all x-axes were horizontally orientated when compared with the video orientation.

The primary method used to track particles within Tracker was autotracker due to the quantity of frames requiring analysis. The manual approach was used when the defined automark level was higher than the matching score as calculated by the software. Particles identified for tracking had their center point identified within the software. The autotracker function subsequently defined both a template [characterizing the red, blue, and green (RGB) pixels inside] and a search area within which the particle was searched for in the following frame. The sum of squares of the RGB differences between the template and

the search area is inversely proportional to the match score. The speed of the particles was calculated by the software according to the positions of the particles in each frame.

# RESULTS AND DISCUSSION

## Relationship Between the Normalized Area and the Packing Factor

The influence of the pH of the subphase on the surface pressure for the more hydrophobic particles ($\theta_{eq} = 75°$) is shown in **Figure 2A** while the effect of particle hydrophobicity, at pH 9, is presented in **Figure 2B**. The solid lines indicate the compression cycles and dashed lines correspond to the subsequent expansion cycles [the second cycle is used since it is more consistent due to the breakdown of long-range and short-range structure (Hórvölgyi et al., 1996)]. The surface pressure is defined as $\Pi = \gamma_0 - \gamma$, where $\gamma_0$ is the surface tension of pure water and $\gamma$ is the surface tension of the interface, representing a difference in interfacial tension. The figures show that the surface pressure increased under compression and decreased under expansion. As the movable barrier compressed the particles into a densely packed film, the surface pressure rose relatively slowly in more dense area but began to rise more steeply with further reduction in the area. The surface pressure eventually reached a maximum value, which ranged from 9.9 to 11.8 mN/m for all conditions studied. It should be noted that the monolayers were not compressed beyond the limiting value as the layers appeared to be unstable beyond the collapse point (i.e., the particles started to detach from the interface). For the three pH values tested, the surface pressure started to increase at a higher normalized surface area upon compression with increases in the pH. A similar behavior was found in the hydrophobicity of the particles with the more hydrophobic particles causing an increase in the surface pressure at a larger normalized surface area as found by others such as Hórvölgyi et al. (1996), Safouane et al. (2007). Changing the pH for the less hydrophobic particles did not have a pronounced effect on the pressure isotherm compared with the more hydrophobic particles. The effect of the change in hydrophobicity is thus discussed only at pH 9.

The packing of particles at an interface can vary widely for any packed layer depending on whether the particles are monodispersed or polydispersed (Bournival and Ata, 2010; Grishaev et al., 2017). As the layer is compressed the structure of the array of particles, assuming they are spherical and monodispersed, should theoretically reach a coverage density of $\sqrt{3}\pi/6$ if surface forces are overcome (further discussed in the following section). As such it is well known that the average separation distance between the particles tends to increase with increases in the pH for glass beyond the isoelectric point (i.e., pH 2–3) (Hórvölgyi et al., 1996; Sastry et al., 1997; Blute et al., 2009). However this concept needs to be discussed in terms of the packing factor and surface forces.

### Packing of Particles at the Air-Water Interface Under a Compression Force

**Figure 2** demonstrated that a different normalized area (i.e., inter-particle average distance) was produced for a similar surface pressure. The average separation distance was then explored in terms of the packing of the particles. **Figure 3** shows the packing factor at different pH values during the compression cycles shown in **Figure 2**. As the surface pressure increased and the average separation distance decreased, the percentage of voids in the particle network decreased resulting in a higher packing factor. Similarly to the work of Huang et al. (2004) with nanoparticles, the micron-sized particles formed rafts at the interface which became more compact and rearranged as the surface pressure increased. As such the average separation distance between the particles was not uniform. However, it provides an average over the entire surface of the trough. On the other hand, the packing factor was a localized measurement. Consequently it can be observed that the more hydrophilic particles and the less densely charged particles (pH 3) produced rafts with more closely packed particles. This discrepancy between the two measurements decreased at higher surface pressures as a result of the gaps between the rafts closing in. It should also be noted that the packing factor was a local packing factor determined in the vicinity of the Wilhelmy plate while the normalized area considered the entire area of the monolayer. Such distinction may explain that the packing factor for particles with a contact angle of 75° at pH 5.8 and 9 are similar. However,

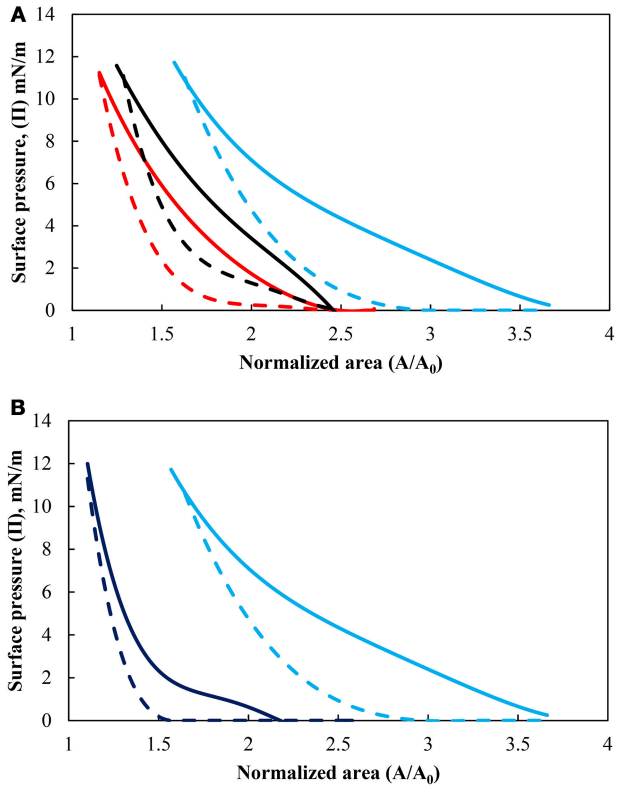


**FIGURE 2 | (A)** Surface pressure isotherms of hydrophobized particles ($\theta_{eq} = 75°$) at pH values of 3 (red), 5.8 (black), and 9 (light blue) and **(B)** surface pressure isotherms for particles hydrophobized with contact angle of 43° (dark blue) and 75° at pH 9 (light blue). Solid lines are the compression cycle while dashed lines correspond to the expansion cycle.

the minimum normalized area before the detachment of particles occurred was larger when the pH of the subphase was higher.

## Particle Interaction Force

The behavior of the particles under compression and expansion and the packing factors presented in **Figures 2**, **3** may be explained in terms of the interaction force between the particles. A variety of theoretical models have been developed to calculate the interaction energy between two particles at an interface. In its simplest form the particles may be considered to be fully submerged (Clint and Taylor, 1992) which may lead to a satisfactory correlation of the force with the surface pressure isotherm. However, differences in force resulting from the particle being exposed to a different phase, such as air or oil, can limit such simplification (Kralchevsky et al., 2001; Danov et al., 2004).

The calculation of the interaction forces was made assuming two identical particles partially submerged at the air-water interface. Due to the number of assumptions made and the limited number of forces considered the calculations represent a semi-quantitative assessment of the interaction force between particles. The interaction forces included the van der Waals force ($F_{vdW}$), the electrostatic force ($F_{el}$), and the capillary force ($F_l$). The equations for these three forces are given as (Bournival et al., 2016):

$$F_{vdW} = -\frac{A_{eff} r_p}{12h^2} f(p) \quad (1)$$

$$F_{el} = \frac{6\varepsilon_{air} q_{water}^2}{4\pi\varepsilon_0 \varepsilon_{water}^2 \kappa^2 h^4} \quad (2)$$

$$F_l = -2\pi\gamma r_p B^{\frac{5}{2}} S^2 K_l(\lambda_c l) \quad (3)$$

where $A_{eff}$ is the effective Hamaker constant, $r_p$ is the radius of the particles, $h$ is the separation distance, $f(p)$ is a function which corrects the van der Waals force for retardation effects and takes the form:

$$f(p) = (1 + 3.54p)/(1 + 1.77p)^2;\ p < 1$$
$$f(p) = 0.98/p - 0.434/p^2 + 0.067/p^3;\ p > 1 \quad (4)$$

where $p = \frac{2\pi h}{\lambda}$ and $\lambda$ is the retardation length scale. The effective Hamaker constant was given as

$$A_{eff} = A_{12} + f^2(3 - 2f)(A_{13} - A_{12}) \quad (5)$$

in which $f$ is the linear fractional immersion height of the particles and $A_{12}$ and $A_{13}$ are the Hamaker constants in the gas and the water phase, respectively. In Equation (2), $\varepsilon_0$, $\varepsilon_{air}$, and $\varepsilon_{water}$ are the permittivity of vacuum, the relative permittivity of air, and of water, respectively. $\kappa$ is the Debye-Hückel parameter and $q_{water}$ is the charge of the immersed section of the particles, which follows

$$q_{water} = 2\pi r_p \kappa^{-1} \sigma \tau_{water} \sin\theta \quad (6)$$

where $\sigma$ is the surface charge density, $\tau_{\text{water}}$ is the degree of surface group dissociation on the particle and $\theta$ is the contact angle of the particles. The zeta potential was used as a substitute for the surface potential in the calculation of the surface charge. The zeta potential were assumed to be −5, −40, and −70 mV at pH 3, 5.8, and 9, respectively (Bergna and Roberts, 2006). The degree of surface group dissociation of a particle in water was assumed to be 0.02 as it is expected to be much lower than 0.53, the maximum value obtained in polysilicic acids (Shchipalov, 1999; Bournival et al., 2016). The capillary force (Equation 3) is a function of $\gamma$, the surface tension, $B$, the Bond number, $S$, a sphere constant, and $K_l$, a modified Bessel function, which was approximated $1/(\lambda_c l)$ *where* $\lambda_c = \sqrt{(\rho_l - \rho_g) g/\gamma}$ is an inverse capillary number with $\rho_l$, and $\rho_g$ representing the densities of the liquid phase and gas, $g$ is the gravitional acceleration, and $l$ is the separation distance of the particles from the center of mass as previously reported (Chan et al., 1981; Ata, 2008; Bournival et al., 2016).

**Figure 4** shows the total interaction force, which is a summation of Equations (1)–(3), for particles of 64 μm in size and a contact angle of 75° at pH 3, 5.8 and 9 as well as a contact

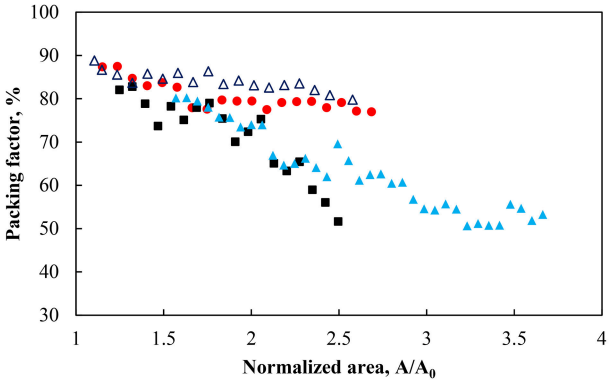


**FIGURE 3 |** Packing factor during compression for particles hydrophobized with a contact angle of 75° at pH 3 (red solid circle), pH 5.8 (black solid square), pH 9 (light blue solid triangle), and 43° at pH 9 (dark blue triangle).

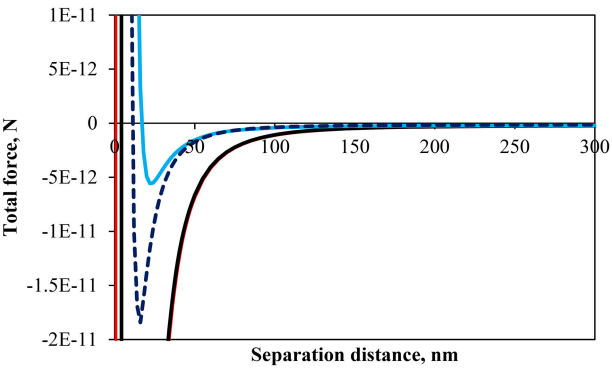


**FIGURE 4 |** Calculated total interaction force between two identical particles with a contact angle of 75° at an air-water interface at pH 3 (red), pH 5.8 (black), pH 9 (light blue), and particles with a contact angle of 43° at pH 9 (dark blue dashed line).

angle of 43° at pH 9. In all cases the interaction force appears to be slightly negative at large separation distances (see **Figure 4** for separation distances >150 nm). An individual evaluation of the three forces shows that the capillary pressure is acting at larger separation distances due to the strong effect of gravity on these large particles. At a closer separation distance the particles are, theoretically, increasingly attractive as the pH decreases. The calculations are consistent with the fact that the isoelectric point for glass lies approximately between 2 and 3, which, implies that the repulsive force should become increasingly important as the pH increased due to increases in the density of negative surface charges (Behrens and Grier, 2001). It should be noted that the zeta-potential used in the calculation of the repulsive force was assumed to be the same as non-esterified glass beads as in the work of Hórvölgyi et al. (1991) and Laskowski and Kitchener (1969) for methylated silica. This assumption stems from the fact that the number of silanol groups on a silica surface is in the order of 5.2 per nm$^2$ (Zhuravlev, 2006). The esterification of silica produces a coating with an average density of 1.57 ester groups per nm$^2$ (Ossenkamp et al., 2001). Since the ester is formed through the reaction of a silanol group it was expected that the number of silanol groups would be well above 0.5 per nm$^2$, which is the limit under which electrophoretic mobility of particles is affected according to Blake and Ralston (1985). The calculations of the interaction force, although semi-quantitative, corroborate the results shown in **Figures 2A**, **3** where the surface pressure and the packing factor differed for the different pH at any given normalized surface area. Noteworthy is the fact that the minimum normalized area, in **Figure 3**, before the removing of particles from the interface decreased with the pH. It indicates that the detachment of particles occurred when particles were more loosely arrayed and the total force was less attractive.

**Figure 4** also includes the calculation for a less hydrophobic particle ($\theta = 43°$) at pH 9. The interaction force curves are relatively close to one another although the difference in fractional immersion would slightly affect all forces indirectly (cf. *f*, *q*, and *S*). However, it should be noted previous studies have shown that a reduction in surface wettability increased the repulsive force between particles (Hórvölgyi et al., 1991; Horozov et al., 2005; Safouane et al., 2007; Blute et al., 2009), which is consistent with the results of **Figure 2B**. Although the portion of the particle immersed in water is larger for the less hydrophobic particles the charge of the water immersed section is larger for the more hydrophobic particles due to the screening of charge for $\kappa a >> 1$ (Aveyard et al., 2002). Moreover, the length of the alkyl coating (similar to flocculation by neutral polymers) (van de Ven, 1989), which imparts the hydrophobicity to the particles, and hydrophobic forces (e.g., Wang and Yoon, 2004) were not taken into account in the calculations and could explain the similar pressure isotherms between the less hydrophobic particles and the more hydrophobic particles at pH 3, unlike the calculated interaction forces.

Furthermore, a model may be fitted to correlate the packing factor with the surface pressure (Horvölgyi et al., 1999). The expression, which was developed by Fainerman et al. (2006), applies to both molecules and particle monolayers as follows:

$$\Pi = -\frac{kT}{\omega_0}\left[\ln\left(1-\frac{\omega}{A}\right)+\left(\frac{\omega}{A}\right)\right]-\Pi_{coh} \quad (7)$$

where $\Pi$ is the surface pressure, $k$ is the Boltzmann constant, $T$ is the temperature, $\omega_0$ is the molecular area of a solvent molecule (taken as 0.18 nm$^2$ for water Fainerman et al., 2006), $\omega/A$ is the packing factor in which $\omega$ is the average area of a particle, $A$ is the surface area occupied by each particle, and $\Pi_{coh}$ is the cohesion pressure (i.e., the pressure arising from the interaction of the components of the monolayer). The cohesion pressure may be expressed as $kT/\omega_0 \ln f_0^H$ with $f_0^H$ being the activity coefficient. The cohesion pressure can be estimated from the approximation given by Fainerman et al. (2003) as $f_0^H = a(\omega/A)^2$ in which $a$ is the Frumkin interaction parameter for non-ideality. However, to simplify the calculations the cohesion pressure was assumed to be constant (Fainerman and Vollhardt, 1999) and fitted for each system, i.e., a constant affected by the hydrophobicity of the particles and the pH of the subphase.

The packing factor as a function of the surface pressure is shown in **Figure 5** for the hydrophobic ($\theta = 75°$) and less hydrophobic ($\theta = 43°$) particles at different pH along with the fitted model. As expected an increase in the surface pressure produced an increase in the packing factor albeit at a different rate. For the same change in the surface pressure, the packing factor at pH 9 increased approximately from 50% to more than 75%, while at pH 3 the overall increase in the packing density was around 15%. The smallest change in the packing factor was observed for the less hydrophobic particles at pH 9. It appears that the different systems had different total pressure ($\Pi+\Pi_{coh}$). As seen in **Table 1** the values of the cohesion pressure increased with the decrease in the pH value and would explain the lower packing factors for particles in more acidic suspensions and for particles of lower hydrophobicity.

The cohesion pressure is related to the interaction energy (or force) between the particles (Hórvölgyi et al., 1994) and should be consistent with the calculations of **Figure 4** in terms of

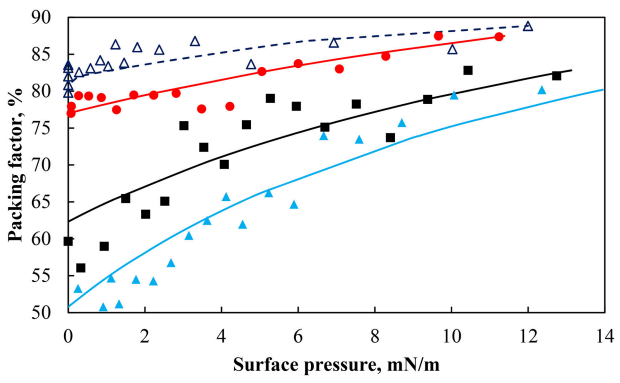


**FIGURE 5 |** Particle packing factor as a function of surface pressure for particles of contact angle 75° at pH 3 (red solid circle), pH 5.8 (black solid square), pH 9 (light blue solid triangle), and a contact angle of 43° at pH 9 (dark blue triangle). Lines are lines of best fit of Equation (7).

the minimum force. The cohesion pressures seem in agreement with the interaction force curves since the more attractive the interaction force, the larger is the cohesion pressure. The effect of particle hydrophobicity on the cohesion pressure has been studied by Fainerman et al. (2006) who found that less hydrophobic particles had a higher cohesion pressure, which is consistent with the result presented in **Table 1**. However, the difference was not as marked in the surface force calculations. It should be noted that the calculations did not take into account the hydrophobization method, which may have affected the actual interaction forces of the particles.

## Particle Movement During Compression

### Particle Movement Under Different Compressing Speeds

Video recordings of the particle layer in the vicinity of the Wilhelmy plate were taken to study the re-organization of particles under different compression speeds. Particles were seen to move across the field of view of the camera as they moved toward the Wilhelmy plate.

**TABLE 1 |** Cohesion pressure for the packing of glass particles of different hydrophobicity partially submerged in water at different pH.

| Particle contact angle (°) | Subphase pH | Cohesion pressure ($\Pi_{coh}$) (mN/m) |
|---|---|---|
| 75 | 3 | 15.6 (0.3) |
| 75 | 5.8 | 8.0 (0.5) |
| 75 | 9 | 4.7 (0.4) |
| 43 | 9 | 22.9 (0.7) |

*The standard error of the estimate on the cohesion pressure is in brackets.*

**Figure 6** shows the particle speed and the packing factor as a function of the barrier displacement from its initial position at two different barrier compressing speeds: 0.45 and 0.8 mm/s. The packing factor started at ∼55% and reached 85% after a 35 mm displacement of the barrier irrespective of the barrier speed. The average speed of particles (circles in **Figure 6**) was averaged over 5 particles. In each case the particles momentarily reached a speed that was close to the barrier speed but much of the movement of the particles (around the Wilhelmy plate) was much slower due to the restriction of other particles (Jeng et al., 2002). The speed of the particles was further reduced as the packing factor reached its maximum value, which corresponded to the removal of particles from the interface. In general the particles traveled at speeds below the compression speed and the traveling speed decreased as the particles get close packed.

### The Effect of Particle Shape and Size on Particle Displacement During Compression

After the initial spreading of the particles and the evaporation of the spreading solvent, small rafts of particles with high stability moved uniformly. During compression, the small rafts came into contact with each other. For particles at a low pH the repulsive force between particles was weaker and the small rafts, under the force supplied by the barrier, rearranged to form a single raft (discussed in section The Motion of Particles Raft During Compression). **Figure 7** shows a frame from a video on the compression of the more hydrophobic particles at pH 3. Particles of different shapes were selected to study the effect of particle shape in the motion of particles with a monolayer. The particles were characterized by their equivalent diameter ($d_e$):

$$d_e = \sqrt{\frac{particle\ area}{\pi}} \tag{8}$$

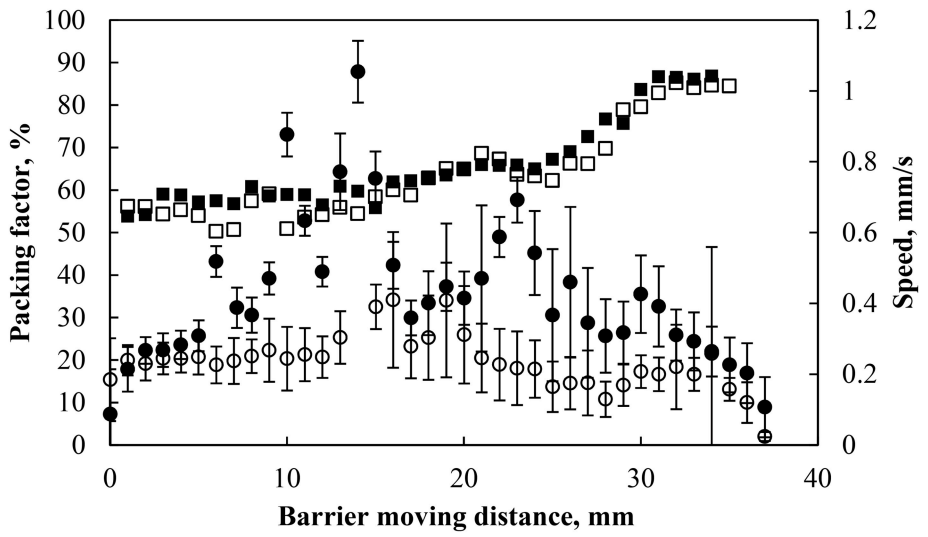


**FIGURE 6 |** Packing factor (black solid square) and particle speed during compression (black solid circle) of particles hydrophobized at 75° and pH 5.8 with a barrier speed of 0.8 mm/s and packing factor (black square) and particle speed (black circle) under the same conditions with a barrier speed of 0.45 mm/s. The particle speed was averaged over 5 particles and the error bars represent one standard deviation of the averaged 54 and 40 data points at 0.8 (black solid circle) and 0.45 (black circle) mm/s, respectively.

and their aspect ratio ($r$) (Barreiros et al., 1996):

$$r = \frac{minimum\ Feret\ diameter}{maximum\ Feret\ diameter} \quad (9)$$

The particles did not move independently but instead moved coherently with the surrounding particles forming the raft. As a whole the particle layer behaved uniformly during the compression. The correlations between the speeds of four particles found within the same video frame over a period of 15 s were relatively high. During that time period, the local packing factor increased from 77 to 79%.

A correlation factor was used to quantify the strength of the association between the speeds of each pair of particles. The correlation was calculated using the Pearson product-moment correlation coefficient ($c$) between the speed of one particle ($v_1$) and that of another ($v_2$) through:

$$c = \frac{\sum (v_1 - \overline{v_1})(v_2 - \overline{v_2})}{\sqrt{\sum (v_1 - \overline{v_1})^2 \sum (v_2 - \overline{v_2})^2}} \quad (10)$$

where $\overline{v_1}$ and $\overline{v_2}$ are averages of $v_1$ and $v_2$ respectively. The correlation was higher than 0.98 in all cases, which indicates a strong correlation between speeds of the different particles (value close to 1) and that they are moving in the same direction (positive correlation coefficient). Differences in the shape and size of particles did not result in different behavior of particles at the air-water interface during compression under the test conditions.

## The Motion of Particles Raft During Compression

In addition to examining the compression and expansion behavior of particle monolayers in relation to pH, it is also of great interest to understand the motion of individual particles in the monolayer undergoing compression. The correlation coefficient was used during analysis of compression experiments to measure how particles moved in relation to one another, since they could rotate or fill voids as discussed later.

The average correlation coefficient during compression at different pH as a function of total surface pressure is shown in **Figure 8**. At pH 9, the correlation coefficient is high around 1, suggesting that the particles move at the same speed and in the same direction. The surface forces exerted between the particles seem to prevent the particles from undergoing substantial rearrangement within the monolayer. The correlation coefficients of the differences in relative speed of two particles obtained at pH 5.8 and 3 at various total surface pressures are quite scattered. The data shows that the difference in the relative speed of the particles moving through the layer is largest in the less dense particle layer for a total surface pressure ranging between ~2–6 mN/m corresponding to a packing factor of 50–70% while more variation at a total surface pressure >6 mN/m was found at pH 3 for a packing factor of ~85–88%. It is worthwhile to mention that the monolayer rearrangement at pH 3 could only be activated under a sufficient compressive loading. The ease at which particle rearrangement takes place follows the order of the interaction force with the conditions creating the less repulsive environment being more conducive

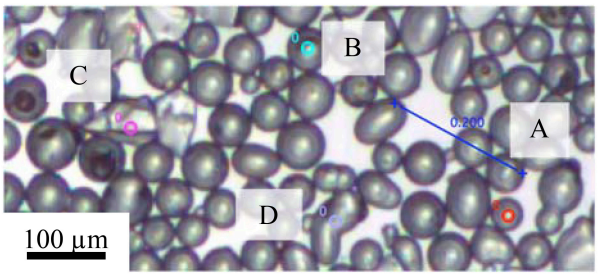


**FIGURE 7 |** Selected particles in the calculation of correlation between particle speed with size and shape: **(A)** ($d_e = 44.9\,\mu m$, $r = 1$); **(B)** ($d_e = 60.4\,\mu m$, $r = 1$); **(C)** ($d_e = 81.0\,\mu m$, $r = 0.6$), and **(D)** ($d_e = 80.7\,\mu m$, $r = 0.6$). The measurements were conducted on particles with a contact angle of 75° and at pH of 3.

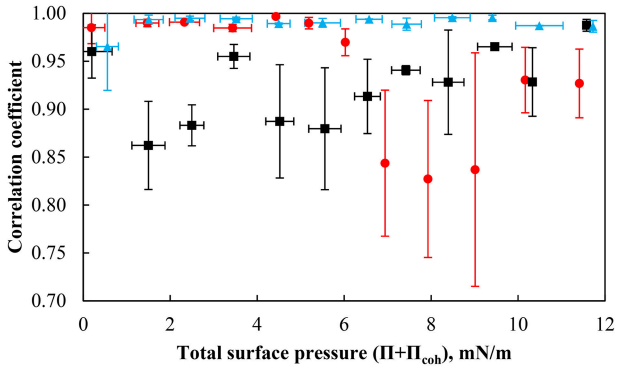


**FIGURE 8 |** Correlation coefficient of the particles with a contact angle of 75° at pH 3 (red solid circle), pH 5.8 (black solid square), and pH 9 (light blue solid triangle) as a function of the total surface pressure. The error bars represent one standard deviation obtained from evaluating the correlation coefficient between 10 particle pairs.

to the rearrangement of particles at higher packing factors (i.e., smaller average separation distances) and may be related to the concept a yield stress resulting in building a monolayer network as indicated by the pressure isotherms and the interaction force. Finally, although particle rearrangement occurs, the correlation coefficient is still relatively high, which is consistent with the particles moving nearly uniformly at the interface.

Two distinct particle behaviors were observed to cause a reduction of the correlation coefficient. **Figure 9** shows the particle rearrangement under compression at the natural pH (pH 5.8) for particles with a contact angle of 75°. As the layer is compressed, individual particle rafts approached each other to form larger agglomerates. In some cases, (**Figure 9a**), individual clusters were observed to rotate as a whole in such a way that they fitted into the big interstitial voids between the particles. This phenomenon was commonly observed in the layers with lower packing densities where small particle rafts float relatively freely at the air-water interface. A drop in the correlation coefficient here is caused by a difference in the direction in which the particles travel. In contrast, at relatively higher packing factors, voids collapsed as highlighted by the change in the shaded area

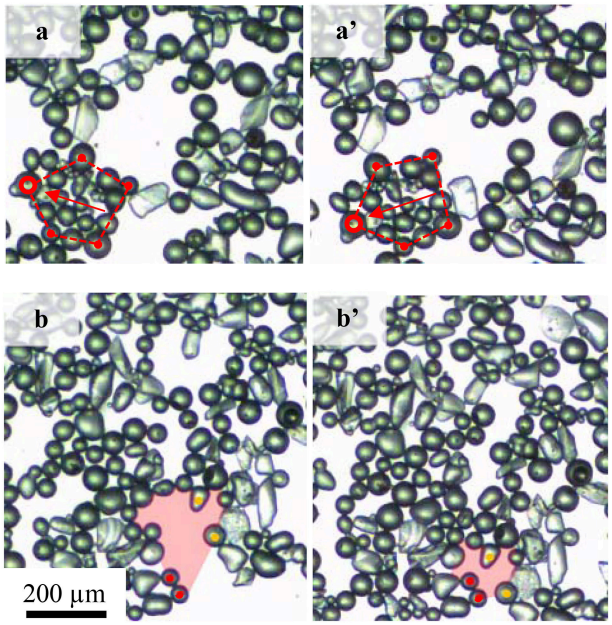


**FIGURE 9 |** Two particle arrangements causing the correlation coefficient drop: **(a,a')** rotation of a group of particles and **(b,b')** void collapse. **Videos** are available as supporting document.

for **Figure 9b**. The change in the correlation coefficient is the result of variations in the traveling speed between particles as illustrated in **Figure 9b** where particles marked in red remained almost stationary and particles marked in orange traveled as a result of the void collapse. Rotation of particle groups caused the correlation to drop more than the collapse of bare areas.

## Interaction Between a Bubble and Particle-Laden Interface

### Coalescence of Bubbles With a Particle-Laden Interface

Several investigations (Ata, 2009; Bournival et al., 2016) have studied experimentally the effect of the physicochemical properties of particles on the stability and coalescence behavior of air bubbles in water. While in the mentioned studies the bubble coating process reflects real conditions, it was not possible to manipulate the packing of the particles on the surface. The present experimental setup allows fine control of particle monolayer formation at the air-water interface, making it possible to study the role of surface pressure and the packing factor in bubble coalescence and the behavior of the interface after the rupture coalescence.

**Figure 10** shows the interaction of a single bubble with the air-water interface sparsely (a,a') and heavily (b,b') laden with particles of contact angle 75° at natural pH. In **Figure 10** the left (a,b) and right (a',b') images present the bubble just reaching the interface and before coalescence, respectively. Both layers contained the same number of particles, but compressed to different surface pressures, 2.1 and 6 mN/m corresponding to packing factors of 69 and 81%, respectively. An air bubble was introduced beneath the layer and allowed to grow slowly. The bubble approached the interface and started to push the surface upward due to the buoyancy force of the bubble and the gradual increase in the bubble volume. The deformation of the interface led to the formation of a bare region at the top with the displaced particles thickly accumulating at the lower part of the convex interface. Eventually, the film ruptured due to the local particle packing defect (Pugh, 1996; Wasan et al., 2005; Planchette et al., 2013; Bournival et al., 2016). It appears that the initial packing factor significantly affected the formation of the bare region. Compared to the more densely packed interface, the bubble easily pushed the particles from the contact region forming a larger void in the low density film. For lower particle packing densities the lateral mobility of particles was much greater than that of higher density particle packing, which might have allowed the formation of a larger particle-barren area.

**Figure 11** shows the equivalent diameter of the bare region formed at the interface just before coalescence as a function of the total surface pressure for strongly hydrophobic particles ($\theta_{eq} = 75°$) at various pH values and the less hydrophobic particles at pH 9. Measurements were repeated a number of times under nearly similar conditions and averaged. As mentioned previously, the particles were densely packed at the interface at pH 3, and therefore measurements could only have been performed at high surface coverages. As seen in the figure, there appears to be a low variation in the size of the particle-free region for a total surface pressure below ∼12 mN/m. Above a total surface pressure of 12 mN/m, which corresponds to a packing factor of ∼80%, the size of the defect is dependent on the hydrophobicity of the particles and the pH of the subphase with a low pH value necessitating a larger bare region for coalescence. Thus at higher surface coverages, a higher capillary pressure, as presented by Kaptay (2006), is needed for coalescence to occur. Since the bubble diameter is constant (i.e., the capillary pressure is not changed), a greater defect is needed for coalescence, which resulted in longer bubble coalescence times.

The formation of a defect is important to initiate bubble coalescence. As the bubble approached the interface, a thin liquid film between the bubble and the free surface must have developed (e.g., Wasan et al., 1992). The liquid in the film drained out gradually and the film ruptured once it reached a critical thickness. In the presence of particles, a three phase contact line between the bubble and particle may be established leading to particles forming a bridge in the thin liquid film (Kaptay, 2004; Morris et al., 2011), which may be influenced by the hydrophobicity of the particles and the pH of the liquid phase. The bridging of the particles may result in a significant delay in bubble coalescence time. The effect of particle bridging on bubble stabilization is well established (Dippenaar, 1982). Moreover, particles in the periphery of the bare region can influence the drainage of liquid and particles (Cain and Lee, 1985; Baets and Stein, 1993).

**Figure 12** shows the coalescence time as a function of total surface pressure for an air bubble beneath the particle monolayer compressed at various packing factors. The coalescence time was

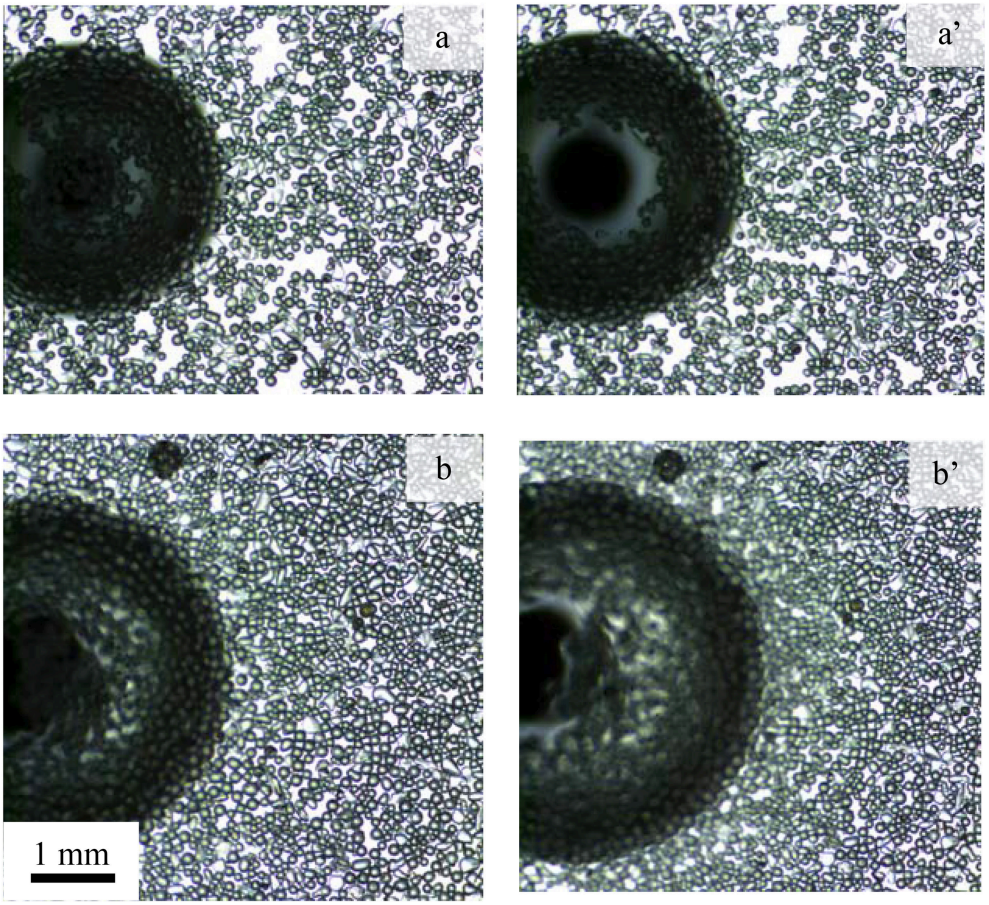


**FIGURE 10 |** Particle layer under the influence of a bubble forming a bare contact region. Photographs show **(a,b)** the contact of the bubble with the interface and **(a',b')** the interface prior to coalescence for initial packing factor of **(a,a')** 69% and **(b,b')** 81% in an experiment using hydrophobic particles (contact angle of 75°) at natural pH.

defined as the time measured from the first contact of the bubble with the interface and the rupture of the thin liquid film. The coalescence time is generally small at low total surface pressures with times below 5 s. However as the total surface pressure increased above ∼12 mN/m the coalescence times started to vary. There was no clear correlation between the coalescence time and the total surface pressure of the combined systems. However, the total pressure within a given system (i.e., pH of the subphase and the contact angle of the particles) affected the coalescence time.

## Wave Propagation and Layer Healing

Upon the rupture of the thin film separating the bubble and the particle-laden interface, a ripple spreads out from the contact region of the bubble and the interface during which the particles undergo significant rearrangement at the interface. **Figure 13** shows the evolution of the ripple diameter with time for a bare air-water interface and a particle-laden interface with similar packing factors produced by the coalescence of a 2 mm bubble. It is clear from the figure that compared to water, the speed of the ripple was considerably reduced by the presence of particles, indicating that particles play an important role in the control of the response of particle-laden interfaces against surface deformations. The figure also suggests that the subphase pH may have a negligible effect on the wave propagation due to slight variations in the initial packing factor and in the size of the bubble. It is yet to be investigated how the size of the bare region (i.e., the number of particles displaced) affects the propagation of the ripple.

**Figure 14** shows the packing factor variation for strongly hydrophobic particles (75°) at natural pH after coalescence. The region of interest was divided into four sections numbered 1–4, starting at the center of the contact area of the bubble with the interface. The width of each section was set to 0.7 mm (note the capillary appears smaller in **Figure 14** due to the deformation of the interface by the bubble). The results indirectly quantified the movement of the particles at the interface and the healing of the particle-free region. After the bubble coalesced, the particle packing in region 2 immediately decreased followed by regions 3 and 4. The videos also revealed that particles from regions 3 and 4 moved inward because of the surface

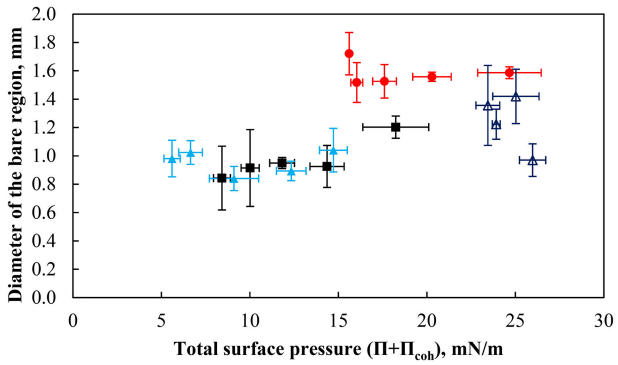


**FIGURE 11 |** The equivalent diameter of bare contact region prior to coalescence for bubbles of 2.00 ± 0.12 mm under the interface as a function of the total surface pressure of particles with a contact angle of 75° at pH 3 (red solid circle), pH 5.8 (black solid square), and pH 9 (light blue solid triangle) as well as particles with a contact angle of 43° and at pH 9 (dark blue triangle). The error bars show the standard deviation calculated from at least 6 measurements, which were performed under similar conditions.

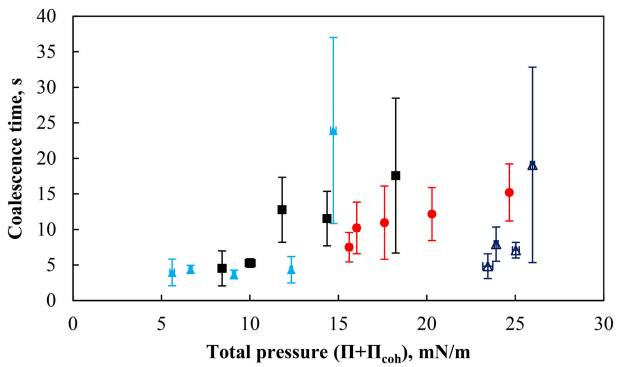


**FIGURE 12 |** Coalescence time for 2.00 ±0.12 mm bubble as a function of particle packing factor for more hydrophobic particles (75°) at pH 3 (red solid circle), pH 5.8 (black solid square), pH 9 (light blue solid triangle), and weakly hydrophobic particles (43°) at pH 9 (dark blue triangle). The error bars show standard deviation of 6 measurements, which were performed under similar conditions.

pressure difference. According to **Figure 5**, the region with a high packing factor has a higher local surface pressure, which results in a surface pressure gradient. This surface pressure gradient can cause particles to spread toward the low surface pressure bare region (La Mer and Robbins, 1958; Robbins and La Mer, 1960). The coalescence caused the waves to spread out from the contact region providing kinematic energy to the particles. After the reduction in packing factor, particles from a more distant region moved back to the inner region as a result of wave propagation (Denissenko et al., 2006). As a result, region 2, which was close to the bare region, had a net decrease in the amount of particles while region 1 had a net gain of particles over the timeframe of 15 ms as indicated by the packing factor. The energy of the wave further away from the capillary was reduced because of the viscoelastic property of the interface (Vignati et al., 2003; Cichocki et al., 2004). As a result, the change in the packing factor in regions 2–4 gradually diminished.

## CONCLUSIONS

A series of experiments were conducted using a modified Langmuir-Blodgett trough which had a transparent deep glass cell beneath the interface. The aim was to explore the use of such a system to study the interaction of an air bubble with a particle-laden interface, which characteristics could be controlled. The technique enabled the interaction between a particle stabilized air bubble (generated through a capillary in the aqueous phase below the Langmuir-Blodgett thin film) and Langmuir-Blodgett film coated with particles to be studied using a high-speed video together with image analysis. Spherical glass particles (92 μm) with different degrees of hydrophobicity (contact angle with water 75 and 43°) were used in the experiments which were carried out at three different subphase pH values. From the use of the conventional Langmuir-Blodgett technique, the surface pressure isotherms, the rearrangement of the particles at the air-solution interphase under compressed and expansion, were quantified. In addition, the movement of particles in the monolayer at a range of surface pressures was measured and the packing factor of the interfacial particles was determined. The particles were observed to initially form rafts which closed up and rearranged as the surface pressure increased and more hydrophobic particles (less densely charged) produced more closely packed rafts. It was also found that as the surface pressure on the film increased, the average separation between rafts decreased and the percentage of voids in the network decreased resulting in a higher packing factor. The interaction forces, the cohesive pressure and the capillary force interactions were calculated for two particle submerged particles and related to the experimental data.

From the modified Langmuir-Blodgett trough, the influence of the particle flow under different rates of compression and on the packing factor as the bubble approached the Langmuir-Blodgett film was studied, together with the influence of pH and hydrophobicity on particle displacement during compression. Two distinct types of behavior occurred involving the rotation and the clustering of particles which caused the filling of interfacial voids. As the surface pressure on the film increased, the average separation distance decreased and the percentage of voids in the network decreased, resulting in a higher packing factor. The correlation coefficient data could be used to explain the differences in the direction in which the particles flow and also the collapse of the voids. Video recording showed that the packing factor significantly affected the movement of particles in the less densely packed regions. Finally, the kinetics of coalescence of the bubble with the Langmuir-Blodgett film was studied by recording the velocity of the ripples which spread out from the contact region. In addition, the healing of the interfacial layer was measured. It was found that the speed of the ripple was considerably reduced by the presence of

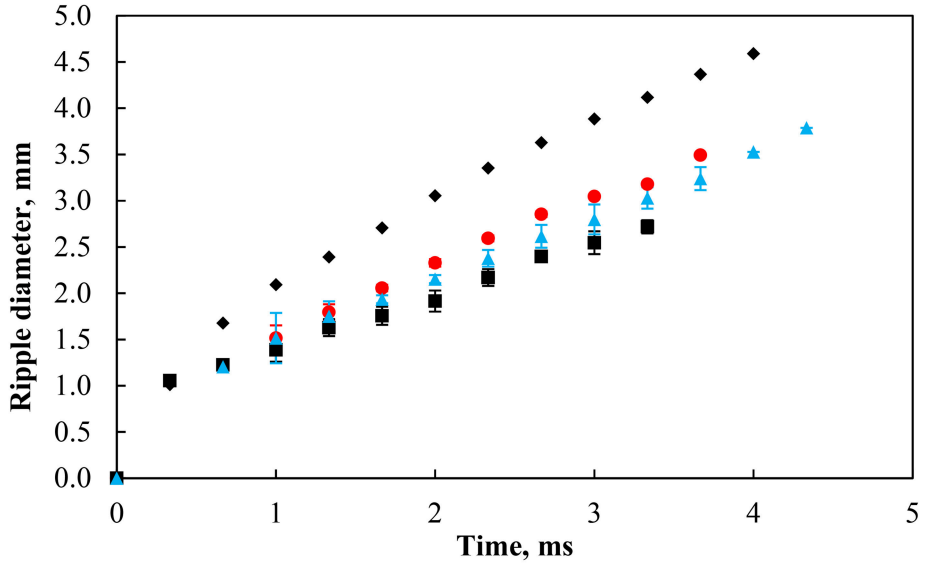


**FIGURE 13 |** Ripple diameter in pure water (black solid diamond) and with particles at contact angle of 75° with a similar packing factor at pH 3 (red solid circle, 77%), 5.8 (black solid square, 79%), and 9 (blue solid triangle, 79%). The bubble size was 2.00 ±0.12 mm.

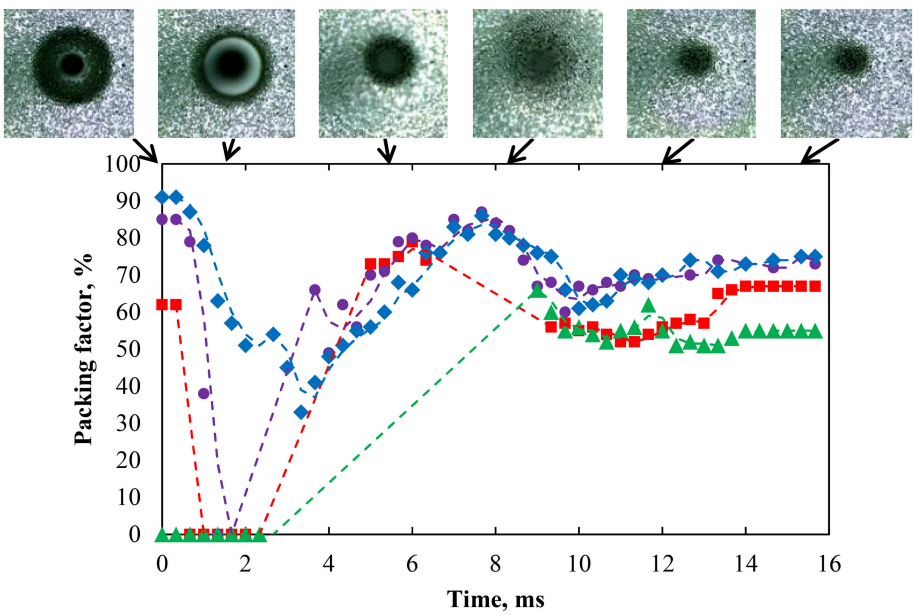


**FIGURE 14 |** Packing factor of four regions from innermost to outermost—region 1 (green solid triangle), region 2 (red solid square), region 3 (purple solid circle), and region 4 (blue solid diamond)—after coalescence of a bubble with an interface laden with hydrophobized particles (75°) with a packing factor of 82% at natural pH. Region 1 has a radius of 0.76 mm corresponding to most of the bare region while the other regions were at constant surface area. The coalescence time was 2.54 s.

particles in the film indicating the particles play an important role in controlling the response of the interface to surface perturbations.

## SUPPORTING DOCUMENT

The re-arranging of particles at the interface—rotation of a particle group (AVI), The re-arranging of particles at the interface—void collapse (AVI), The spreading ripple on a particle-laden interface (AVI). The code for fitting data with Cubic Spline method (DOC) **Supplementary Data Sheet 1**.

## AUTHOR CONTRIBUTIONS

XY data collection, data analysis and interpretation and drafting the article. AM data collection regarding the particle

tracking. RP helped to evaluate and edit the manuscript. GB and SA conception or design of the work; critical revision of the article and final approval of the version to be published.

## ACKNOWLEDGMENTS

The HDR Student Support Grant from UNSW is acknowledged for financial support of the lab equipment. The authors wish to thank Mr. Mark Whelan (UNSW) for his help in developing the experimental setup.

## SUPPLEMENTARY MATERIAL

The Supplementary Material for this article can be found online at: https://www.frontiersin.org/articles/10.3389/fchem.2018.00348/full#supplementary-material

**Movie S1 |** The re-arranging of particles at the interface.

**Movie S2 |** The re-arranging of particles at the interface-void collapse.

**Movie S3 |** The spreading ripple on a particle-laden interface.

**Supplementary Data Sheet 1 |** The code for fitting data with Cubic Spline method (DOC).

## REFERENCES


Ata, S. (2008). Coalescence of bubbles covered by particles. *Langmuir* 24, 6085–6091. doi: 10.1021/la800466x

Ata, S. (2009). The detachment of particles from coalescing bubble pairs. *J. Colloid Interface Sci.* 338, 558–565. doi: 10.1016/j.jcis.2009.07.003

Aveyard, R., Binks, B. P., Clint, J. H., Fletcher, P. D., Horozov, T. S., Neumann, B., et al. (2002). Measurement of long-range repulsive forces between charged particles at an oil-water interface. *Phys. Rev. Lett.* 88:246102. doi: 10.1103/PhysRevLett.88.246102

Aveyard, R., Clint, J. H., Nees, D., and Quirke, N. (2000). Structure and collapse of particle monolayers under lateral pressure at the octane/aqueous surfactant solution interface. *Langmuir* 16, 8820–8828. doi: 10.1021/la000060i

Baets, P. J. M., and Stein, H. N. (1993). Drainage of CTAB films containing solid particles. *Chem. Eng. Sci.* 48, 351–365. doi: 10.1016/0009-2509(93)80022-I

Barbian, N., Ventura-Medina, E., and Cilliers, J. J. (2003). Dynamic froth stability in froth flotation. *Miner. Eng.* 16, 1111–1116. doi: 10.1016/j.mineng.2003.06.010

Barreiros, F. M., Ferreira, P. J., and Figueiredo, M. M. (1996). Calculating shape factors from particle sizing data. *Part. Part. Syst. Characterization* 13, 368–373. doi: 10.1002/ppsc.19960130607

Behrens, S. H., and Grier, D. G. (2001). The charge of glass and silica surfaces. *J. Chem. Phys.* 115, 6716–6721. doi: 10.1063/1.1404988

Bergna, H. E., and Roberts, W. O. (eds). (2006). *Colloidal Silica: Fundamentals and Applications*. New York, NY: Taylor & Francis Group.

Blake, P., and Ralston, J. R. (1985). Controlled methylation of quartz particles. *Colloids Surf.* 15, 101–118. doi: 10.1016/0166-6622(85)80059-7

Blute, I., Pugh, R. J., van de Pas, J., and Callaghan, I. (2009). Industrial manufactured silica nanoparticle sols. 2: surface tension, particle concentration, foam generation and stability. *Colloids Surf. A* 337, 127–135. doi: 10.1016/j.colsurfa.2008.12.009

Bournival, G., and Ata, S. (2010). Packing of particles on the surface of bubbles. *Miner. Eng.* 23, 111–116. doi: 10.1016/j.mineng.2009.10.012

Bournival, G., Ata, S., and Jameson, G. J. (2014). The influence of submicron particles and salt on the recovery of coarse particles. *Miner. Eng.* 69, 146–153. doi: 10.1016/j.mineng.2014.07.003

Bournival, G., Ata, S., and Wanless, E. J. (2015a). The roles of particles in multiphase processes: particles on bubble surfaces. *Adv. Colloid Interface Sci.* 225, 114–133. doi: 10.1016/j.cis.2015.08.008

Bournival, G., Ata, S., and Wanless, E. J. (2016). The behavior of bubble interfaces stabilized by particles of different densities. *Langmuir* 32, 6226–6238. doi: 10.1021/acs.langmuir.6b00656

Bournival, G., de Oliveira e Souza, L., Ata, S., and Wanless, E. J. (2015b). Effect of alcohol frothing agents on the coalescence of bubbles coated with hydrophobized silica particles. *Chem. Eng. Sci.* 131, 1–11. doi: 10.1016/j.ces.2015.03.036

Brown, D., and Christian, W. (2011). "Simulating what you see: combining computer modeling with video analysis," in *8th International Conference on Hands-on Science* (Ljubljana).

Cain, F. W., and Lee, J. C. (1985). A technique for studying the drainage and rupture of unstable liquid films formed between two captive bubbles: measurements on KCl solutions. *J. Colloid Interface Sci.* 106, 70–85. doi: 10.1016/0021-9797(85)90382-0

Chan, D. Y. C., Henry, J. D. Jr., and White, L. R. (1981). The interaction of colloidal particles collected at fluid interfaces. *J. Colloid Interface Sci.* 79, 410–418. doi: 10.1016/0021-9797(81)90092-8

Cichocki, B., Ekiel-Jezewska, M. L., Nägele, G., and Wajnryb, E. (2004). Motion of spheres along a fluid-gas interface. *J. Chem. Phys.* 121, 2305–2316. doi: 10.1063/1.1766016

Clint, J. H., and Taylor, S. E. (1992). Particle size and interparticle forces of overbased detergents: a Langmuir trough study. *Colloids Surf.* 65, 61–67. doi: 10.1016/0166-6622(92)80175-2

Cote, L. J., Kim, F., and Huang, J. (2009). Langmuir-Blodgett assembly of graphite oxide single layers. *J. Am. Chem. Soc.* 131, 1043–1049. doi: 10.1021/ja806262m

Danov, K. D., Kralchevsky, P. A., and Boneva, M. P. (2004). Electrodipping force acting on solid particles at a fluid interface. *Langmuir* 20, 6139–6151. doi: 10.1021/la0497090

Denissenko, P., Falkovich, G., and Lukaschuk, S. (2006). How waves affect the distribution of particles that float on a liquid surface. *Phys. Rev. Lett.* 97:244501. doi: 10.1103/PhysRevLett.97.244501

Dippenaar, A. (1982). The destabilization of froth by solids. I. The mechanism of film rupture. *Int. J. Miner. Process.* 9, 1–14. doi: 10.1016/0301-7516(82)90002-3

Fainerman, V. B., Kovalchuk, V. I., Lucassen-Reynders, E. H., Grigoriev, D. O., Ferri, J. K., Leser, M. E., et al. (2006). Surface-pressure isotherms of monolayers formed by microsize and nanosize particles. *Langmuir* 22, 1701–1705. doi: 10.1021/la052407t

Fainerman, V. B., Lucassen-Reynders, E. H., and Miller, R. (2003). Description of the adsorption behaviour of proteins at water/fluid interfaces in the framework of a two-dimensional solution model. *Adv. Colloid Interface Sci.* 106, 237–259. doi: 10.1016/S0001-8686(03)00112-X

Fainerman, V. B., and Vollhardt, D. (1999). Equations of state for Langmuir monolayers with two-dimensional phase transitions. *J. Phys. Chem. B* 103, 145–150. doi: 10.1021/jp983109q

Fujii, S., Mouri, E., Akiyama, K., Nakayama, S., Uda, K., Nakamura, Y., et al. (2017). pH-sensitive adsorption behavior of polymer particles at the air-water interface. *Langmuir* 33, 1451–1459. doi: 10.1021/acs.langmuir.6b03895

Grishaev, V., Saverio Iorio, C., Dubois, F., and Amirfazli, A. (2017). Impact of particle-laden drops: particle distribution on the substrate. *J. Colloid Interface Sci.* 490, 108–118. doi: 10.1016/j.jcis.2016.11.038

Horozov, T. S., Aveyard, R., Binks, B. P., and Clint, J. H. (2005). Structure and stability of silica particle monolayers at horizontal and vertical octane-water interfaces. *Langmuir* 21, 7405–7412. doi: 10.1021/la050923d

Horvölgyi, Z., Máté, M., Dániel, A., and Szalma, J. (1999). Wetting behaviour of silanized glass microspheres at water-air interface: a Wilhelmy film balance study. *Colloids Surf. A* 156, 501–508. doi: 10.1016/S0927-7757(99)00107-7

Hórvölgyi, Z., Máté, M., and Zrínti, M. (1994). On the universal growth of two-dimensional aggregates of hydrophobed glass beads formed at the (aqueous solution of electrolyte)-air interfaces. *Colloids Surf.A* 84, 207–216. doi: 10.1016/0927-7757(93)02725-T

Hórvölgyi, Z., Medveczky, G., and Zrínti, M. (1991). Experimental study of the aggregate structures formed in the boundary layer of water-air phases. *Colloids Surf.* 60, 79–95. doi: 10.1016/0166-6622(91)80270-X

Hórvölgyi, Z., Németh, S., and Fendler, J. H. (1996). Monoparticulate layers of silanized glass spheres at the water-air interface: particle-particle and particle-subsurface interactions. *Langmuir* 12, 997–1004. doi: 10.1021/la940658o

Huang, S., Minami, K., Sakaue, H., Shingubara, S., and Takahagi, T. (2004). Effects of surface pressure on the formation of Langmuir-Blodgett monolayer of nanoparticles. *Langmuir* 20, 2274–2276. doi: 10.1021/la0302293

Hunter, T. N., Jameson, G. J., Wanless, E. J., Dupin, D., and Armes, S. P. (2009). Adsorption of submicrometer-sized cationic sterically stabilized polystyrene latex at the air-water interface: contact angle determination by ellipsometry. *Langmuir* 25, 3440–3449. doi: 10.1021/la803879p

Jeng, F. S., Lin, M. L., Lai, Y. C., and Teng, M. H. (2002). Influence of strain rate on buckle folding of an elasto-viscous single layer. *J. Struc. Geol.* 24, 501–516. doi: 10.1016/S0191-8141(01)00073-6

Kaptay, G. (2004). Interfacial criteria for stabilization of liquid foams by solid particles. *Colloids Surf. A* 230, 67–80. doi: 10.1016/j.colsurfa.2003.09.016

Kaptay, G. (2006). On the equation of the maximum capillary pressure induced by solid particles to stabilize emulsions and foams and on the emulsion stability diagrams. *Colloids Surf. A* 282–283, 387–401. doi: 10.1016/j.colsurfa.2005.12.021

Krägel, J., Li, J. B., Miller, R., Bree, M., Kretzschmar, G., and Möhwald, H. (1996). Surface viscoelasticity of phospholipid monolayers at the air/water interface. *Colloid Poly. Sci.* 274, 1183–1187. doi: 10.1007/BF00655690

Kralchevsky, P. A., Danov, K. D., and Petkov, P. V. (2016). Soft electrostatic repulsion in particle monolayers at liquid interfaces: surafce pressure and effect of aggregation. *Philos. Trans. R. Soc. A* 374:20150130. doi: 10.1098/rsta.2015.0130

Kralchevsky, P. A., Denkov, N. D., and Danov, K. D. (2001). Particles with an undulated contact line at a fluid interface: interaction between capillary quadrupoles and rheology or particulate monolayers. *Langmuir* 17, 7694–7705. doi: 10.1021/la0109359

La Mer, V. K., and Robbins, M. L. (1958). The effect of the spreading solvent on the properties of monolayers. *J. Phys. Chem.* 62, 1291–1295. doi: 10.1021/j150568a029

Laskowski, J., and Kitchener, J. A. (1969). The hydrophilic-hydrophobic transition on silica. *J. Colloid Interface Sci.* 29, 670–679. doi: 10.1016/0021-9797(69)90219-7

Ma, G., and Allen, H. C. (2006). DPPC langmuir monolayer at the air-water interface: probing the tail and head groups by vibrational sum frequency generation spectroscopy. *Langmuir* 22, 5341–5349. doi: 10.1021/la0535227

Máté, M., Zrínyi, M., and Horvölgyi, Z. (1996). Structure formation and interaction of silanized glass beads at water-fluid interfaces: a redispersability study. *Colloids Surf. A* 108, 147–157. doi: 10.1016/0927-7757(95)03417-X

McNamee, C. E., Kappl, M., Butt, H.-J., Ally, J., Shigenobu, H., Iwafuji, Y., et al. (2011). Forces between a monolayer at an air/water interface and a particles in solution: influence of the sign of the surface charge and the subphase salt concentration. *Soft Matter* 7, 10182–10192. doi: 10.1039/c1sm06247f

Morris, G. D. M., Neethling, S. J., and Cilliers, J. J. (2011). A model for the stability of films stabilized by randomly packed spherical particles. *Langmuir* 27, 11475–11480. doi: 10.1021/la202028p

Onoda, G. Y. (1985). Direct observation of two-dimensional, dynamical clustering and ordering with colloids. *Phys. Rev. Lett.* 55, 226–229. doi: 10.1103/PhysRevLett.55.226

Ossenkamp, G. C., Kemmitt, T., and Johnson, J. H. (2001). New approach to surface-alkoxylated silica with increased hydrolytic stability. *Chem. Mater.* 13, 3975–3980. doi: 10.1021/cm000883t

Petkov, P. V., Danov, K. D., and Kralchevsky, P. A. (2016). Monolayers of charged particles in a Langmuir trough: could particle aggregation increase the surface pressure? *J. Colloid Interface Sci.* 462, 223–234. doi: 10.1016/j.jcis.2015.09.075

Planchette, C., Biance, A.-L., Pitois, O., and Lorenceau, E. (2013). Coalescence of armored interface under impact. *Phys. Fluids* 25, 1–11. doi: 10.1063/1.4801320

Pugh, R. J. (1996). Foaming, foam films, antifoaming and defoaming. *Adv. Colloid Interface Sci.* 64, 67–142. doi: 10.1016/0001-8686(95)00280-4

Reitzel, N., Greve, D. R., Kjaer, K., Howes, P. B., Jayaraman, M., Savoy, S., et al. (2000). Self-assembly of conjugated polymers at the air/water interface. Structure and properties of Langmuir and angmuir-Blodgett films of ampliplilic regioregular polythiophenes. *J. Am. Chem. Soc.* 122, 5788–5800. doi: 10.1021/ja9924501

Robbins, M. L., and La Mer, V. K. (1960). The effect of the spreading solvent on the properties of monolayers. *J. Colloid Sci.* 15, 123–154. doi: 10.1016/0095-8522(60)90013-1

Safouane, M., Langevin, D., and Binks, B. P. (2007). Effect of particle hydrophobicity on the properties of silica particle layers at the air-water interface. *Langmuir* 23, 11546–11553. doi: 10.1021/la700800a

Santini, E., Krägel, J., Ravera, F., Liggieri, L., and Miller, R. (2011). Study of the monolayer structure and wettability properties of silica nanoparticles and CTAB using the Langmuir trough technique. *Colloids Surf. A* 382, 186–191. doi: 10.1016/j.colsurfa.2010.11.042

Sastry, M., Mayya, K. S., Patil, V., Paranjape, D. V., and Hegde, S. G. (1997). Langmuir-Blodgett films of carboxylic acid derivatized silver colloidal particles: role of subphase pH on degree of cluster incorporation. *J. Phys. Chem. B* 101, 4954–4958. doi: 10.1021/jp964087f

Schulze, H. J. (1984). *Physico-Chemical Elementary Processes in Flotation: An Analysis from the Point of View of Colloid Science Including Process Engineering Considerations* New York, NY: Elsevier.

Shchipalov, Y. K. (1999). Evaluation of electrical surface properties of hydrated quartz-glass particles based on the ζ-potential value. *Glass Ceram.* 56, 335–338. doi: 10.1007/BF02681336

van de Ven, T. G. M. (1989). *Colloidal Hydrodynamics*. London: Academic Press.

Vignati, E., Piazza, R., and Lockhart, T. P. (2003). Pickering emulsions: interfacial tension, colloidal layer morphology, and trapped-particle motion. *Langmuir* 19, 6650–6656. doi: 10.1021/la034264l

Wang, L., and Yoon, R. H. (2004). Hydrophobic forces in the foam films stabilized by sodium dodecyl sulfate: effect of electrolyte. *Langmuir* 20, 11457–11464. doi: 10.1021/la048672g

Wasan, D. T., Nikolov, A. D., Lobo, L. A., Koczo, K., and Edwards, D. A. (1992). Foams, thin films and surface rheological properties. *Prog. Surf. Sci.* 39, 119–154. doi: 10.1016/0079-6816(92)90021-9

Wasan, D. T., Nikolov, A. D., and Moudgil, B. (2005). Colloidal dispersions: structure, stability and geometric confinement. *Powder Technol.* 153, 135–141. doi: 10.1016/j.powtec.2004.12.005

Yun, W. B., and Bloch, J. M. (1989). Langmuir trough dedicated for x-ray study of monolayer systems. *Rev. Sci. Instrum.* 60, 214–218. doi: 10.1063/1.1140463

Zhuravlev, L. T. (2006). "The surface chemistry of silica - the Zhuravlev model," in *Colloidal Silica: Fundamentals and Applications*, eds H. E. Bergna and W. O. Roberts (New York, NY: Taylor & Francis Group), 261–266.

**Conflict of Interest Statement:** The handling editor declared a past co-authorship with one of the authors SA.

The remaining authors declare that the research was conducted in the absence of any commercial or financial relationships that could be construed as a potential conflict of interest.

frontiers in Chemistry

ORIGINAL RESEARCH
published: 20 August 2018
doi: 10.3389/fchem.2018.00361

# Anisotropic Polymer Adsorption on Molybdenite Basal and Edge Surfaces and Interaction Mechanism With Air Bubbles

*Lei Xie[1], Jingyi Wang[1], Jun Huang[1], Xin Cui[1], Xiaogang Wang[2], Qingxia Liu[1], Hao Zhang[1], Qi Liu[1] and Hongbo Zeng[1]**

[1] Department of Chemical and Materials Engineering, University of Alberta, Edmonton, AB, Canada, [2] College of Material Science and Engineering, Heavy Machinery Engineering Research Center of Education Ministry, Taiyuan University of Science and Technology, Taiyuan, China

The anisotropic surface characteristics and interaction mechanisms of molybdenite ($MoS_2$) basal and edge planes have attracted much research interest in many interfacial processes such as froth flotation. In this work, the adsorption of a polymer depressant [i.e., carboxymethyl cellulose (CMC)] on both $MoS_2$ basal and edge surfaces as well as their interaction mechanisms with air bubbles have been characterized by atomic force microscope (AFM) imaging and quantitative force measurements. AFM imaging showed that the polymer coverage on the basal plane increased with elevating polymer concentration, with the formation of a compact polymer layer at 100 ppm CMC; however, the polymer adsorption was much weaker on the edge plane. The anisotropy in polymer adsorption on $MoS_2$ basal and edge surfaces coincided with water contact angle results. Direct force measurements using CMC functionalized AFM tips revealed that the adhesion on the basal plane was about an order of magnitude higher than that on the edge plane, supporting the anisotropic CMC adsorption behaviors. Such adhesion difference could be attributed to their difference in surface hydrophobicity and surface charge, with weakened hydrophobic attraction and strengthened electrostatic repulsion between the polymers and edge plane. Force measurements using a bubble probe AFM showed that air bubble could attach to the basal plane during approach, which could be effectively inhibited after polymer adsorption. The edge surface, due to the negligible polymer adsorption, showed similar interaction behaviors with air bubbles before and after polymer treatment. This work provides useful information on the adsorption of polymers on $MoS_2$ basal/edge surfaces as well as their interaction mechanism with air bubbles at the nanoscale, with implications for the design and development of effective polymer additives to mediate the bubble attachment on solid particles with anisotropic surface properties in mineral flotation and other engineering processes.

**Keywords: polymer depressant, molybdenite ($MoS_2$) basal/edge, anisotropic adsorption, froth flotation, atomic force microscope (AFM), adhesion, bubble probe AFM**

OPEN ACCESS

***Edited by:***
*Erica Wanless,*
*University of Newcastle, Australia*

***Reviewed by:***
*David Harbottle,*
*University of Leeds, United Kingdom*
*George Vincent Franks,*
*University of Melbourne, Australia*

***Correspondence:**
*Hongbo Zeng*
*hongbo.zeng@ualberta.ca*

***Specialty section:***
*This article was submitted to Chemical Engineering, a section of the journal Frontiers in Chemistry*

***Received:*** *12 March 2018*
***Accepted:*** *30 July 2018*
***Published:*** *20 August 2018*

***Citation:***
*Xie L, Wang J, Huang J, Cui X, Wang X, Liu Q, Zhang H, Liu Q and Zeng H (2018) Anisotropic Polymer Adsorption on Molybdenite Basal and Edge Surfaces and Interaction Mechanism With Air Bubbles. Front. Chem. 6:361. doi: 10.3389/fchem.2018.00361*

## INTRODUCTION

Molybdenite ($MoS_2$), the most important mineral source of molybdenum, has exhibited excellent characteristics and functionality in a broad range of biomedical and engineering applications, such as hydrogen evolution catalysis (Jaramillo et al., 2007; Karunadasa et al., 2012; Li et al., 2016; Liu et al., 2016), friction and lubrication (Chhowalla and Amaratunga, 2000; Lee et al., 2010; Sheehan and Lieber, 2017), and clinical devices (Liu et al., 2014; Yin et al., 2014). The consecutive S-Mo-S layers held by weak van der Waals (vdW) interaction can be readily exfoliated, generating the basal plane that is inherently hydrophobic in nature with ultra-low friction (Chhowalla and Amaratunga, 2000; Lee et al., 2010; Sheehan and Lieber, 2017). On the other hand, $MoS_2$ edge generated by breaking Mo-S covalent bonds is relatively hydrophilic, with great potential as an alternative electrocatalyst for hydrogen evolution reaction (Jaramillo et al., 2007; Karunadasa et al., 2012; Li et al., 2016). The anisotropic surface properties of $MoS_2$ basal and edge planes can significantly influence their interaction behaviors at air-water-solid interfaces. In froth flotation, $MoS_2$ minerals are selectively separated from other mineral particles (e.g., chalcopyrite, talc). The basal to edge ratio of $MoS_2$ minerals greatly impacts their flotation performance, depending on the attachment propensity of air bubbles to both the basal and edge planes (Fuerstenau et al., 2007; Rao, 2013). Therefore, understanding the anisotropic surface properties and interaction mechanisms of $MoS_2$ basal and edge planes with air bubbles is of both fundamental and practical importance.

Over the last several decades, the anisotropy in $MoS_2$ basal and edge surfaces has attracted much research interest (Okuhara and Tanaka, 1978; Roxlo et al., 1986; Zhang et al., 2004; Gaur et al., 2014; Jin et al., 2014; Lu et al., 2015; Tan et al., 2015; Govind Rajan et al., 2016; Bentley et al., 2017). The molecular dynamics simulations showed the water contact angle of 54° for the armchair-edge and 24° for the zigzag-edge of $MoS_2$, much lower than that of 83° for $MoS_2$ basal plane (Jin et al., 2014). The edge plane was found to exhibit more negative surface potential than the basal plane in neutral and alkaline pH conditions, and the hydrophobic interaction was only detected on the basal plane (Lu et al., 2015). In molybdenum-containing ores, water-soluble polymers are widely used as the depressants to alter the surface characteristics of $MoS_2$ basal planes (Pugh, 1989; Liu et al., 2000; Pearse, 2005; Bulatovic, 2007; Beaussart et al., 2009; Kor et al., 2014; Castro et al., 2016). The adsorption of polymer depressants [e.g., dextrin, carboxymethyl cellulose (CMC)] on $MoS_2$ basal plane was reported to depend on the solution condition and polymer charge density. The adsorption of these polymers could lead to a reduced surface hydrophobicity and slower rate of dewetting process during the single bubble collision study (Beaussart et al., 2009; Kor et al., 2014). To date, no report is available to distinguish the adsorption mechanisms of polymer depressants on the $MoS_2$ basal planes from the $MoS_2$ edge planes, nor are there quantitative measurements of their interaction forces with air bubbles.

Atomic force microscope (AFM) and surface forces apparatus (SFA) have been widely employed to measure the surface forces and interaction mechanisms of various solid material systems in vapor and liquid media at the nanoscale (Ducker et al., 1991; Butt et al., 2005; Israelachvili et al., 2010; Greene et al., 2011; Huang et al., 2014; Kristiansen et al., 2014; Yang et al., 2014; Wang et al., 2016, 2017; Xie et al., 2016, 2017c; Zhang et al., 2016; Gao et al., 2018). The force-distance profiles and the adhesion magnitude are closely correlated to a variety of interfacial phenomena, including adsorption, aggregation and deposition. The adsorption of protein on polymer surfaces has been investigated by measuring the interaction and adhesion between the protein coated probe and polymer surfaces (Chen et al., 1997; Taylor et al., 2008). Recently, a polydopamine (PDA) coated AFM probe has been employed to investigate the interaction between PDA and solid surfaces of varied hydrophobicity, aiming to understand the adsorption, deposition and adhesion of PDA on solids (Zhang et al., 2017). Thus, force measurements using a polymer coated probe could be used to study the interaction of polymers with mineral surfaces, which is highly relevant to the polymer adsorption on minerals. The limitation of force measurements using the polymer coated probe is that the polymers adsorbed on the AFM probe would perform differently from polymers in aqueous solution. Apparently, the exploit of polymer coated AFM probe can provide the comparable information on the polymer adsorption on different surfaces, but the adsorption capability of polymers cannot be directly and quantitatively provided. The bubble/drop probe AFM technique has also been developed and applied to study the interaction mechanisms involving deformable gas bubbles and emulsion drops, enabling the precise quantification of surface forces at air/water and oil/water interfaces with sub-nN resolution (Manor et al., 2008; Chan et al., 2011; Tabor et al., 2011; Shi et al., 2014a,b, 2016a,b, 2017; Xie et al., 2015, 2017a,b,d; Cui et al., 2016, 2017; Rocha et al., 2016). Very recently, the effect of aqueous conditions (e.g., pH, salinity and salts) on the interaction forces between air bubble and bitumen surface was quantitatively measured, and the evolution of confined thin water film drainage process was successfully analyzed using the theoretical model based on the Reynolds lubrication theory and augmented Young-Laplace equation (Xie et al., 2017d). It was found that the complex aqueous media effectively affected the bubble-surface attachment behaviors by mediating the electrical double layer (EDL) repulsion and hydrophobic attraction (Xie et al., 2017a). The bubble probe AFM technique coupled with other complementary surface analytic tools enables the investigation of the anisotropic adsorption and associated interaction mechanisms on $MoS_2$ basal and edge planes.

In this work, the thin edge plane of $MoS_2$ with relatively large surface area ($15 \times 5$ mm$^2$) and low root-mean-square (rms) roughness (~1.6 nm) was prepared by carefully polishing the edge sample (see Materials and Methods) (Wang et al., 2013), which could be used for AFM imaging and force measurements in a fluid cell. The effect of adsorbed polymer (i.e., CMC) on the wettability and morphology of $MoS_2$ basal and edge surfaces was compared using contact angle measurement and *in-situ* AFM imaging. The adsorption mechanism of polymer depressants was investigated by measuring their intermolecular forces and adhesion on both $MoS_2$ basal and edge surfaces

using CMC functionalized AFM tips. In addition, the bubble probe AFM technique was employed to quantitatively measure the interaction forces between an air bubble and $MoS_2$ basal or edge surfaces in aqueous solution with or without the influence of polymer adsorption. This work provides valuable information regarding the polymer adsorption and bubble interaction mechanism on the anisotropic basal and edge planes of $MoS_2$ at the nanoscale. The results show useful implications for the design and development of effective polymer additives to mediate the bubble attachment on solid particles with anisotropic surface properties in froth flotation and many other interfacial processes.

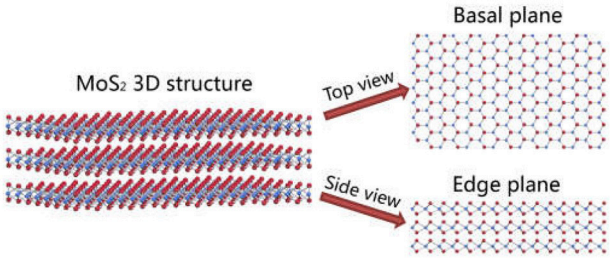


**FIGURE 1 |** Illustration of $MoS_2$ crystal structure: 3D structure, top view (basal plane) and side view (edge plane) (Color red: sulfur atom and color blue: molybdenum atom).

## MATERIALS AND METHODS

### Materials

Sodium chloride (NaCl, ACS reagent grade), hydrochloric acid (HCl, ACS reagent grade) and sodium hydroxide (NaOH, ACS reagent grade) were purchased from Fisher Scientific Canada and used as received without further purification. (3-Aminopropyl)triethoxysilane (APTES) and sodium carboxymethyl cellulose (CMC, molecular weight $M_W$ ~2.5 × $10^5$ g/mol, degree of substitution DS ~1.2) were purchased from Sigma Aldrich. All aqueous solutions were prepared using Milli-Q water (Millipore deionized, 18.2 MΩ·cm resistivity), and the pH was adjusted and fixed at 9 in this work.

### Preparation of $MoS_2$ Basal and Edge Planes

The $MoS_2$ bulk minerals (Ward's Science, Rochester, NY) were embedded in epoxy resin for preparing the edge surface. After curing overnight, the epoxy samples were polished by hand with wet silicon carbide paper of 60 grit to expose the edge plane. The smooth edge surface was obtained by polishing with wet silicon carbide paper of 60, 240, 320, 400, 600, 800, and 1200 grit, and then polishing with 5, 1, and 0.3 μm alumina powder suspension, respectively (Wang et al., 2013). The freshly polished edge samples were ultrasonically washed in Milli-Q water, ethanol and Milli-Q water for 5 min, respectively. The natural cleavage surface of the basal plane (1 × 1 $cm^2$) was obtained by peeling off the top layers using a sticky tape. Specifically, the thin $MoS_2$ sample was fixed on a glass slide using double sided adhesive tape, and Scotch tape was then applied to remove the top layers of $MoS_2$ sample. After repeating the peeling for over three times to avoid the contamination, the prepared basal plane was observed using the microscopy until a desired surface was detected. The freshly prepared $MoS_2$ basal and edge surfaces were immediately used for surface characterizations and polymer adsorption tests. **Figure 1** shows the illustration of the 3D structure, top view (basal plane) and side view (edge plane) of a typical $MoS_2$ crystal.

The polymer stock solution (~100 ppm) was prepared by dissolving a desired amount of CMC in Milli-Q water under stirring overnight to ensure complete hydration. By diluting the stock solution in Milli-Q water and adjusting the pH to 9, solutions of desired concentration (i.e., 5 and 10 ppm) were obtained. Thereafter, the freshly prepared $MoS_2$ basal and edge planes were conditioned in the desired polymer solutions for further surface characterization.

### Surface Characterization

A contact angle goniometer (ramé-hart instrument Co., NJ, USA) was used to measure the static water contact angle on $MoS_2$ basal and edge planes using a sessile drop method. For the same type of sample, at least two different surfaces and three different locations on each surface were tested, and the average water contact angle was reported. The topographic images of $MoS_2$ basal and edge planes were obtained using the tapping mode of an AFM.

### Adsorption Mechanism of CMC

The interaction between a CMC functionalized AFM tip and a $MoS_2$ basal or edge plane was measured in 1 mM NaCl at pH 9 using a MFP-3D AFM (Asylum Research, Santa Barbara, CA, USA). Prior to force measurements, AFM silicon probes were cleaned by UV/ozone treatment for 30 min and coated with APTES through a vapor deposition process for 4 h (Lu et al., 2011). The APTES coated AFM probes were immersed in 100 ppm CMC solution overnight, after which the prepared AFM probes were washed with Milli-Q water and positioned over the mineral surface for force measurements. The spring constant of the probe was determined to be 0.1–0.2 N/m using the Hutter and Bechhoefer method (Hutter and Bechhoefer, 1993). The schematic of typical experiment setup for measuring the interaction forces between the CMC functionalized AFM tip and $MoS_2$ surface is shown in **Figure 2A**.

### Bubble-$MoS_2$ Interaction

The interaction between an air bubble and a $MoS_2$ basal or edge plane was measured in 500 mM NaCl at pH 9 using the bubble probe AFM. Prior to force measurements, the glass disk of a fluid cell was mildly hydrophobized by immersing in 10 mM octadecyltrichlorosilane (OTS) in toluene for ~10 s for bubble immobilization; while custom-made rectangular AFM cantilevers (400 × 70 × 2 μm) with a circular gold patch (diameter ~65 μm, thickness ~30 nm) were strongly hydrophobized by immersing in 10 mM dodecanethiol in absolute ethanol overnight to provide higher hydrophobicity than the glass disk for bubble anchoring (Shi et al., 2014b). Air bubbles were generated and immobilized on the glass disk by

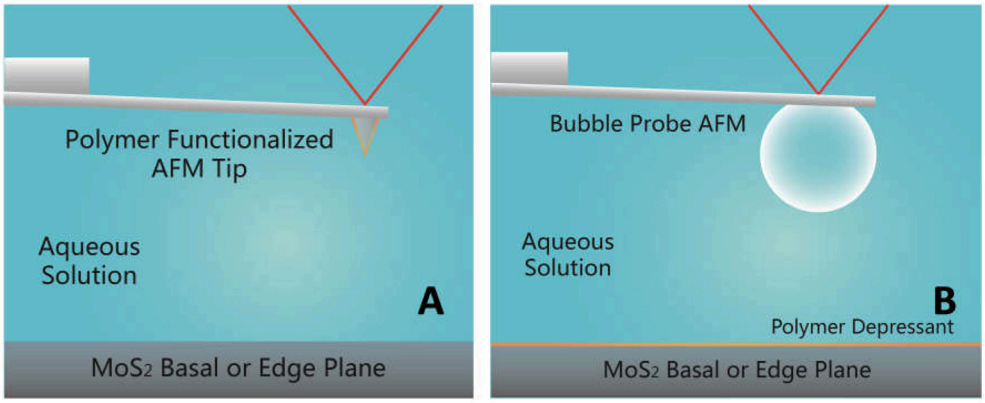


**FIGURE 2 |** Schematic of force measurements **(A)** between polymer functionalized AFM tip and $MoS_2$ basal or edge plane, and **(B)** between air bubble and $MoS_2$ basal or edge plane using the bubble probe AFM.

carefully purging air through a custom-made ultra-sharp glass pipette into the aqueous solution. The bubble probe was then prepared by picking up an air bubble of suitable size (typically 50–90 μm radius) with the AFM cantilever. The cantilever-anchored air bubble was positioned over the mineral surface and then driven to approach the substrate surface until a fixed deflection of the cantilever was reached or bubble attachment occurred. The spring constant of the cantilever was determined to be 0.3–0.4 N/m (Hutter and Bechhoefer, 1993). The force measurements were performed at a driving velocity of 1 μm/s, under which the effect of hydrodynamic interaction was negligible as compared to surface forces. The movement of the cantilever (anchored with air bubble) and the corresponding interaction forces were recorded as a function of time by AFM software. The schematic of typical experiment setup for force measurements on $MoS_2$ surface using the bubble probe AFM is shown in **Figure 2B**.

## Theoretical Model

A theoretical model based on the Reynolds lubrication theory coupled with augmented Young-Laplace equation was applied to analyze the experimentally measured forces between air bubbles and mineral surfaces.

The bubble deformation under the combined influence of hydrodynamic interaction and disjoining pressure is given by the augmented Young-Laplace equation (Shi et al., 2014a,b; Xie et al., 2015).

$$\frac{\gamma}{r}\frac{\partial}{\partial r}\left(r\frac{\partial h}{\partial r}\right) = \frac{2\gamma}{R} - p - \prod \tag{1}$$

where $\gamma$ is the surface tension of water, $h(r, t)$ is the thickness of confined thin water film, $R$ is the bubble radius, $p(r, t)$ is the excess hydrodynamic pressure in the water film relative to the bulk solution, and $\Pi(r, t)$ is the overall disjoining pressure arising from surface forces such as vdW, EDL, and hydrophobic interactions.

The Reynolds lubrication theory describes the drainage process of thin water films confined between air bubbles and mineral surfaces (Shi et al., 2014a,b; Xie et al., 2015).

$$\frac{\partial h}{\partial t} = \frac{1}{12\mu r}\frac{\partial}{\partial r}\left(rh^3\frac{\partial p}{\partial r}\right) \tag{2}$$

where $\mu$ is the dynamic viscosity of water. Consistent with recent reports, immobile boundary condition was assumed at air-water and water-mineral interfaces (Shi et al., 2014a,b; Xie et al., 2015).

In this work, high salinity condition (i.e., 500 mM NaCl) was chosen to suppress the EDL interaction, with a Debye length less than 1 nm. The contributions of vdW and hydrophobic interactions to the disjoining pressure $\Pi_{vdW}$ and $\Pi_{HB}$ are described by equations 3 and 4, respectively, where $A$ is the Hamaker constant for air-water-$MoS_2$ ($A = -2.68 \times 10^{-20}$ J), $D_0$ is the decay length of hydrophobic interaction and $C$ is a constant (N/m) related to the static water contact angle $\theta$ on the substrate and surface tension of water $\gamma$ (Israelachvili, 2011; Xie et al., 2015).

$$\prod_{vdW} = -\frac{A}{6\pi h^3} \tag{3}$$

$$\prod_{HB} = -\frac{C}{2\pi D_0}e^{-h/D_0} = -\frac{\gamma(1-\cos\theta)}{D_0}e^{-h/D_0} \tag{4}$$

The overall interaction force $F(t)$ between an air bubble and a mineral surface is theoretically calculated by integrating $p(r, t)$ and $\Pi(r, t)$ based on the Derjaguin approximation in equation 5 (Shi et al., 2014a,b; Xie et al., 2015).

$$F(t) = 2\pi\int_0^\infty (p(r,t) + \prod(h(r,t)))rdr \tag{5}$$

# RESULTS AND DISCUSSION

## Surface Morphology

**Figure 3** shows the AFM images of $MoS_2$ basal planes conditioned at different CMC concentrations at pH 9 for 30 min. **Figure 3A** demonstrated that the basal plane generated

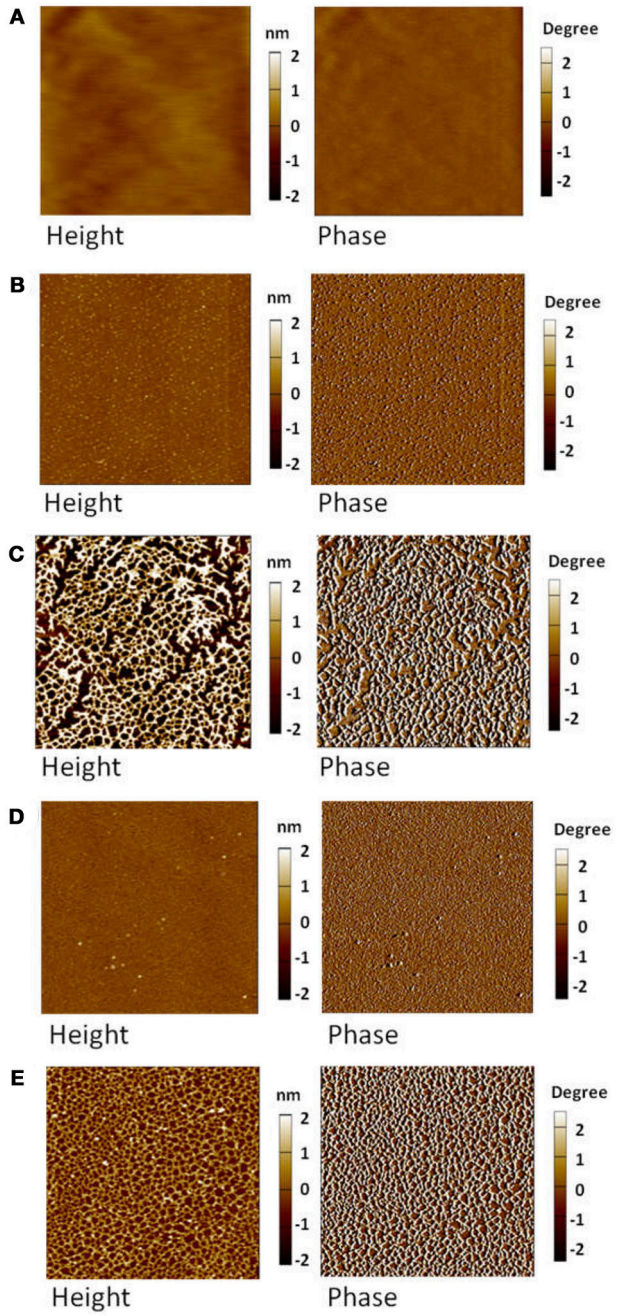


**FIGURE 3 |** AFM height (**Left**) and phase (**Right**) images of $MoS_2$ basal plane conditioned at different CMC concentrations in Milli-Q water at pH 9 for 30 min: **(A)** 0 ppm (5 × 5 $\mu m^2$), **(B)** 5 ppm (5 × 5 $\mu m^2$), **(C)** 10 ppm (5 × 5 $\mu m^2$), **(D)** 100 ppm (5 × 5 $\mu m^2$), and **(E)** 100 ppm (2 × 2 $\mu m^2$).

by exfoliation along the vdW gap is molecularly smooth with the rms roughness of ∼0.20 nm, which is consistent with our previous result (Xie et al., 2017d). After polymer adsorption for 30 min, evident variations in the morphology of the basal planes (5 × 5 $\mu m^2$) conditioned in CMC solutions of different concentrations could be detected from both the height and phase images in **Figures 3B–D**. The basal plane conditioned in 5 ppm CMC solution in **Figure 3B** showed randomly and sparsely distributed aggregates (bright spots) that exhibited apparent phase difference with surrounding areas. Thus, the formed aggregates were attributed to the adsorbed polymers, which covered ∼14.8% of the basal plane. With CMC concentration increasing to 10 ppm, an interconnected polymer network formed on the basal plane with the surface coverage achieving ∼47.1% in **Figure 3C**. After conditioned in 100 ppm CMC solution, **Figure 3D** showed the formation of a smooth polymer film on the basal plane. The magnified image (2 × 2 $\mu m^2$) of the polymer film formed in 100 ppm CMC solution showed the interconnected polymer network (**Figure 3E**), which was more closely compact than the 10 ppm case in **Figure 3C**, indicating that the full polymer coverage was not be achieved even at the CMC concentration as high as 100 ppm. Overall, the polymer concentration plays a significant role in the polymer adsorption on $MoS_2$ basal plane. In our previous study, the adsorption of guar gum on $MoS_2$ basal plane was found to lead to the formation of interconnected polymer network at 5 ppm and a fully covered polymer film at 10 ppm (Xie et al., 2017d). It is evident that the adsorption of CMC is more difficult than guar gum most likely due to the negatively charged carboxyl groups of CMC that could induce stronger electrostatic repulsion with the negatively charged $MoS_2$ basal plane (surface potential at pH 9: −55 mV in 1 mM NaCl and −44 mV in 10 mM NaCl) (Lu et al., 2015; Xie et al., 2017d).

The adsorption of CMC on $MoS_2$ edge plane was also investigated using AFM imaging. On the topographic AFM image of freshly polished edge plane shown in **Figure 4A**, the dark regions were polishing defects that could not be totally avoided, while the bright regions were the aggregates possibly arising from the edge crystal structure. The rms roughness of the polished edge plane was measured to be 1.61 nm, which was smoother than the $MoS_2$ edge plane obtained by the ultramicrotome cutting technique (1.6–3.3 nm) reported previously (Lu et al., 2015, 2016). Since the edge plane was not as molecularly smooth as the basal plane, the polishing defects and aggregates pre-existed on the edge plane might affect the determination of adsorbed polymer. To better monitor the evolution of polymer adsorption on the edge plane, **Figure 4** shows the *in-situ* topographic AFM images scanned over the same 5 × 5 $\mu m^2$ region in 100 ppm CMC solution at pH 9. **Figures 4B–F** showed that slight variation in the surface morphology could be observed during the polymer treatment at different times. Certain aggregates were detected after polymer adsorption and the size of aggregation domains (circled in different colors) increased with longer adsorption time. As the adsorption time increased from 30 min to 60, 90, 120, and 180 min, the rms roughness increased from 1.70 nm to 1.78, 1.85, 1.86, and 1.91 nm, respectively. Both the *in-situ* evolution of aggregation domains and increased rms roughness obtained from AFM imaging indicate that CMC can only slightly adsorb on $MoS_2$ edge surface, although it would be difficult to differentiate if CMC might preferentially adsorb on the polishing defects. As compared to the formation of a smooth polymer film on the basal plane (**Figure 3D**), the polymer adsorption on the edge plane (**Figure 4B**) at the same polymer concentration (i.e., 100

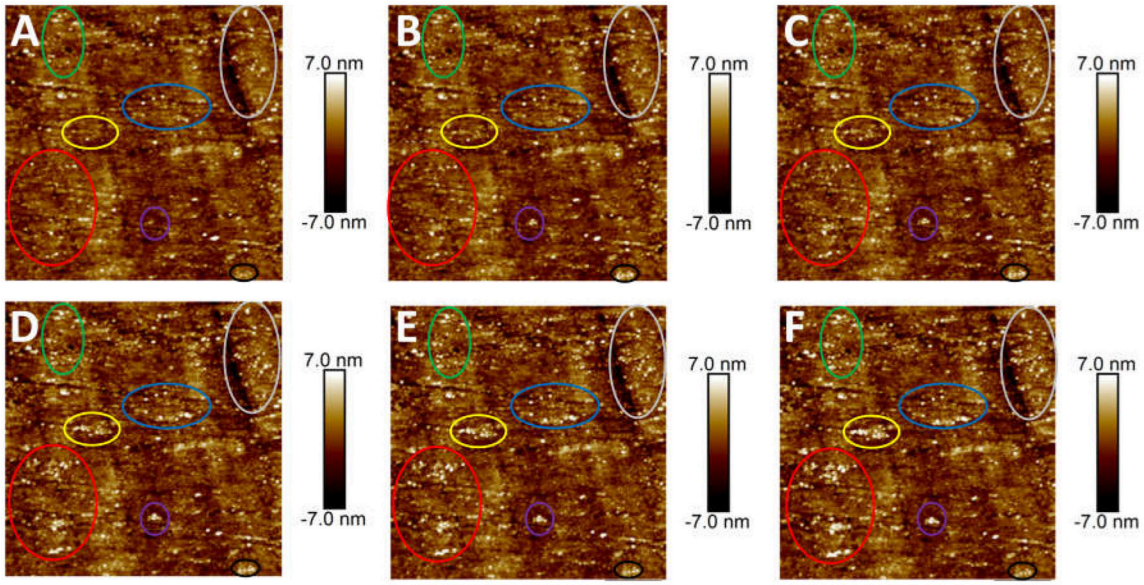


**FIGURE 4 |** AFM height images (5 × 5 $\mu m^2$) of $MoS_2$ edge plane conditioned in 100 ppm CMC solution in Milli-Q water at pH 9 for different adsorption times: **(A)** 0 min, **(B)** 30 min, **(C)** 60 min, **(D)** 90 min, **(E)** 120 min, and **(F)** 180 min.

pm) for the same adsorption time (i.e., 30 min) seemed almost negligible.

## Surface Wettability

**Figure 5** shows the typical microscope images of water contact angle on $MoS_2$ basal and edge surfaces before and after conditioning in 100 ppm CMC solution at pH 9 for 30 min. The freshly exfoliated basal plane exhibited inherent hydrophobicity with a static water contact angle of 76° (**Figure 5A**), which decreased to 54° after polymer adsorption (**Figure 5B**), indicating that CMC is an efficient polymer depressant to reduce the hydrophobicity of $MoS_2$ basal surface. On the other hand, the freshly polished edge plane is relatively hydrophilic with a static water contact angle of 48° (**Figure 5C**), and the water contact angle almost remained unchanged after polymer adsorption (**Figure 5D**), suggesting the negligible CMC adsorption on $MoS_2$ edge surface. The anisotropy in water contact angle of $MoS_2$ basal and edge planes agreed well with AFM imaging results on the effect of polymer adsorption (**Figures 3**, **4**).

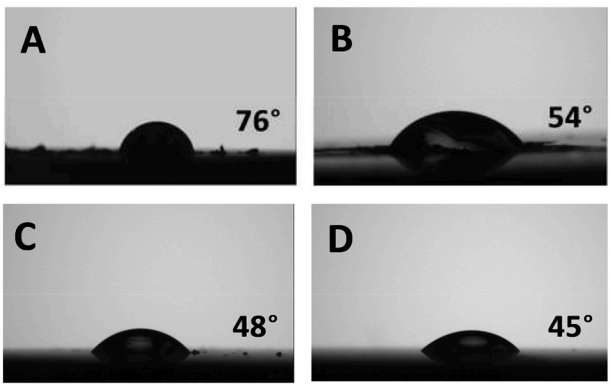


**FIGURE 5 |** Water contact angle of $MoS_2$ basal plane **(A)** before and **(B)** after polymer adsorption, and $MoS_2$ edge plane **(C)** before and **(D)** after polymer adsorption, in 100 ppm CMC solution at pH 9 for 30 min.

## Adsorption Mechanism of CMC

To investigate the adsorption mechanism of CMC on $MoS_2$ basal and edge surfaces, the CMC functionalized AFM tip was used to measure the interaction with the basal and edge surfaces. The CMC functionalized AFM tips were prepared by coating AFM silicon probes with APTES that enabled the adsorption of CMC through both chemical and physical interactions (e.g., amide bond, electrostatic attraction, hydrophobic attraction). The APTES coating and the follow-up CMC coating were examined by measuring the water contact angle and imaging the topography on silicon wafers that were treated using the same procedure as AFM silicon probes. The fresh silicon wafer, APTES coating and CMC coating showed the water contact angle of 9.5°, 58.4°, and 33.1°, respectively, indicating the successful coating of APTES on the silicon wafer and the adsorption of CMC on the APTES coating. **Figure 6** shows the AFM images of APTES coating and CMC coating. The prepared APTES coating was molecularly smooth with a rms roughness of ∼0.34 nm. After polymer adsorption overnight, the surface became rougher and the measured rms roughness increased to ∼0.54 nm. The difference in surface morphology further demonstrated the successful and uniform adsorption of CMC on APTES coating.

**Figure 7** shows the interaction forces measured between CMC functionalized AFM tip and $MoS_2$ basal or edge plane in 1 mM NaCl at pH 9. The typical force-separation curves

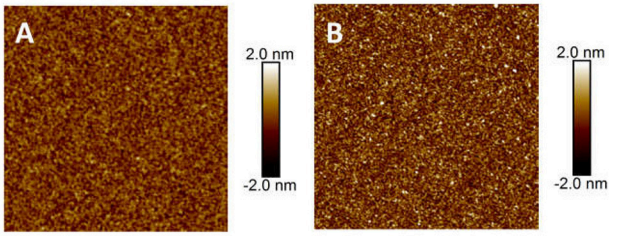


**FIGURE 6 |** AFM height images (5 × 5 $\mu m^2$) of **(A)** APTES coated silicon and **(B)** adsorbed CMC on APTES coating.

in **Figures 7A,C** show very strong repulsion during approach for both the basal and edge surfaces, attributed to the EDL repulsion and steric repulsion between the negatively charged CMC and $MoS_2$. When the CMC functionalized AFM tip was retracted from the basal plane (**Figure 7A**), a strong jump-out behavior was detected, indicating strong adhesion between CMC and the basal plane. In contrast, as illustrated in **Figure 7C**, the adhesion on the edge plane was about one order of magnitude weaker. The histograms of measured adhesion $F_{adh}$ and the fitted Gaussian distribution (red curve) in **Figures 7C,D** show that the adhesion distribution on the basal plane falls in a range of 1.0 to 6.0 nN with the fitted peak centered at 3.85 nN, much larger than that on the edge plane (centered at 0.13 nN), which supported the anisotropic adsorption of CMC on $MoS_2$ basal and edge planes in **Figures 3**, **4**. The observed adhesion might be originated from hydrogen bonding and other interactions (e.g., vdW and hydrophobic interactions). The exposed layer of $MoS_2$ basal plane is composed of S atoms, while the polished edge plane is composed of both Mo and S atoms. The negligible polymer adsorption and very weak adhesion on the edge plane suggest that the formation of either chemical bond (with S or Mo atom) or hydrogen bond (with S atom) is not the main cause of CMC adsorption on $MoS_2$. Since the vdW interaction between polymer and basal or edge surface is similar due to the same $MoS_2$ bulk composition, the polymer adsorption would be most likely due to the hydrophobic attraction between the mineral surface and hydrophobic moieties of polymer chains. Such adhesion difference on the basal and edge surfaces could be attributed to their difference in surface hydrophobicity (water contact angle: 76° for the basal and 54° for the edge) and surface charge (surface potential in 10 mM NaCl at pH 9: −44 mV for the basal and −69 mV for the edge) (Lu et al., 2015), with weakened hydrophobic attraction and strengthened electrostatic repulsion between the polymer and edge plane leading to much weaker adhesion. Ab-initio modeling can provide useful information on the interaction between CMC and $MoS_2$ basal/edge surface to supplement the force measurements in this work, which will be further studied and reported in a separate work.

## Bubble-$MoS_2$ Interaction

**Figure 8A** shows the interaction between air bubble and $MoS_2$ basal plane in 500 mM NaCl at $v = 1$ μm/s. The measured force profile (open symbols) shows a sudden "jump-in" behavior at some critical separation during approach, revealing that the bubble was attached to the basal plane, which was also confirmed by the optical microscope. It is noted that the EDL interaction is significantly suppressed in 500 mM NaCl and the vdW interaction is repulsive at any separation for the air-water-$MoS_2$ system (Xie et al., 2017d). Thus, the observed bubble attachment must be induced by the attractive hydrophobic interaction that has been incorporated into the aforementioned theoretical model. The fitted results showed the decay length of hydrophobic interaction $D_0 = 1.2 \pm 0.1$ nm, which was the same as our previously reported $D_0$ value at lower salinity (i.e., 1 and 100 mM NaCl) (Xie et al., 2017d), suggesting that the salt concentration plays a negligible role in the hydrophobic effect here. The calculated thin water film profiles at different times in **Figure 8B** shows that the bubble gradually approached the basal plane until the attachment occurred at the critical central separation of 11.5 nm (the red curve at 0.70 s), where the overall disjoining pressure just exceeded the Laplace pressure of the bubble (**Figure 8C**) and a pimple was formed at the central portion of bubble surface. The calculated disjoining pressure profiles in **Figure 8C** also indicate the hydrophobic attraction is much stronger than the vdW repulsion, which is the driving force for the bubble attachment on $MoS_2$ basal plane.

The interaction forces measured between air bubble and $MoS_2$ edge plane in 500 mM NaCl at $v = 1$ μm/s under the influence of maximum force load $F_{max}$ and contact time $t_{contact}$ (under $F_{max}$) are shown in **Figure 9**. Evidently no "jump-in" behavior was observed during the approach-retraction cycle at $F_{max} = 18$–72 nN and $t_{contact} = 0$–10 s. The measured force results could not be fully interpreted by the aforementioned theoretical model (equations 1 and 2), indicating that other parameters, such as surface roughness of the edge plane due to polishing defects and aggregates, had an influence on the bubble-surface interaction. When the cantilever-anchored bubble approached the edge plane, a strong repulsion was detected. During retraction of the cantilever, the repulsion gradually decreased and a strong adhesion was detected, which was most likely due to the interaction of the hydrophobic domains (i.e., polishing defects/aggregates) of $MoS_2$ edge plane with the bubble surface in contact during approach. With $F_{max}$ increasing from 18 nN to 36, 54, and 72 nN in **Figures 9A,C**, the measured adhesion increased from 0.14 mN/m to 0.65, 0.76 and 0.95 mN/m due to the enlarged contact area between the bubble surface and the edge plane. When the bubble probe approached the edge plane and remained in contact for $t_{contact} = 1$ s at $F_{max} \sim 18$ nN (**Figures 9B,D**), the adhesion measured significantly increased to 1.08 mN/m since the polishing defects and aggregates on the edge plane could have more time to interact with the bubble surface. As shown in **Figures 9B,D**, continuously increasing $t_{contact}$ to 3, 5 and 10 s only resulted in the slight rise of adhesion to 1.19, 1.31, and 1.37 mN/m, respectively, revealing that a few seconds of contact could be sufficient to ensure strong contact and adhesion between the bubble surface and the polishing defects/aggregates on $MoS_2$ edge plane.

After conditioned in 100 ppm CMC solution at pH 9 for 30 min, the treated $MoS_2$ basal and edge planes were used for

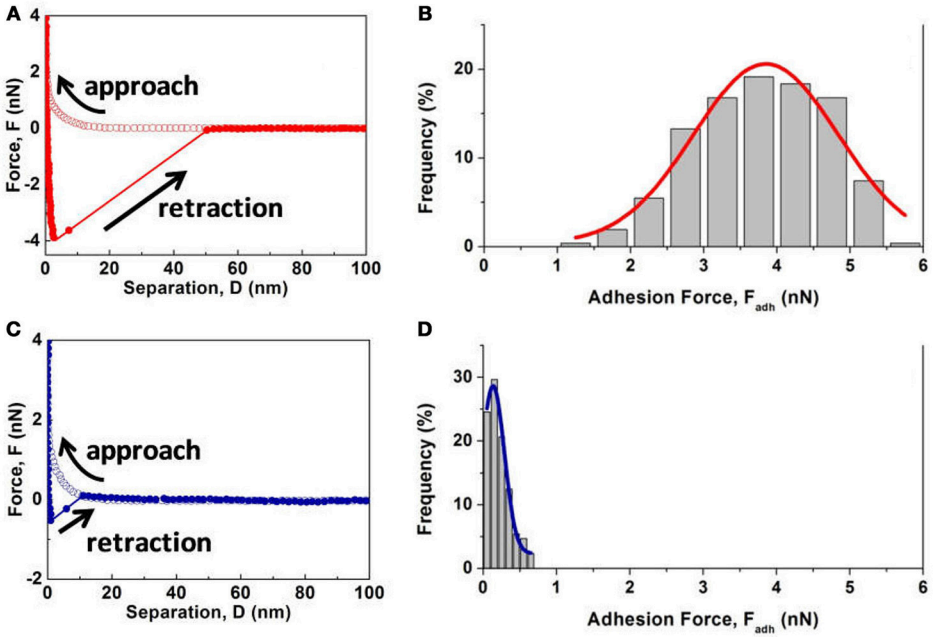


**FIGURE 7 | (A,C)** Typical force-separation curves and **(B,D)** histograms of measured adhesion $F_{adh}$ between CMC functionalized AFM tip and **(A,B)** $MoS_2$ basal plane or **(C,D)** edge plane in 1 mM NaCl at pH 9.

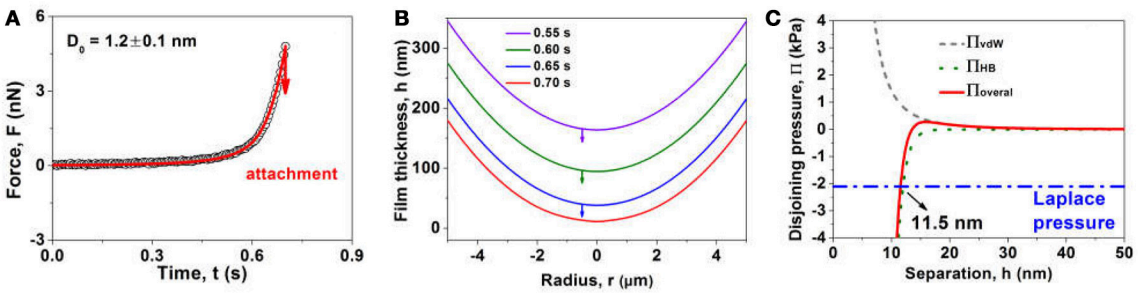


**FIGURE 8 | (A)** Interaction forces (open symbols: experiment results, solid curve: theoretical calculations), **(B)** calculated thin water film profiles at different times, and **(C)** calculated disjoining pressure profiles due to vdW, hydrophobic (HB) and their overall interactions, between an air bubble ($R =$ 69 μm) and a $MoS_2$ basal plane in 500 mM NaCl at $v = 1$ μm/s.

force measurements with air bubbles in 500 mM NaCl at $v = 1$ μm/s. For both the basal and edge planes, no obvious "jump in" behavior of the air bubbles was observed during the approach process, while adhesion could be detected during the surface separation. The interaction between air bubble and treated $MoS_2$ basal plane is illustrated in **Figure S1**. The normalized interfacial adhesion $F_{adh}/R$ measured between air bubble and treated $MoS_2$ basal or edge plane is shown in **Figure 10**. The treated edge plane after polymer adsorption showed similar interfacial adhesion as that without polymer adsorption (**Figures 9C,D**), which was attributed to the negligible adsorption of CMC on the edge plane. On the other hand, the polymer film formed on the basal plane could effectively inhibit the attraction and jump-in attachment behavior of the bubble-basal plane; while the measured interfacial adhesion during separation was about 10-fold weaker than the edge case, which was most likely due to the presence of hydrated CMC chains adsorbed on the basal plane.

Based on the bubble-$MoS_2$ force results, it is revealed that the size of molybdenite particles could affect the bubble-mineral attachment and flotation performance due to different basal/edge ratios. The bubble-mineral attachment is governed by the combined influence of hydrodynamic and surface interactions (Xie et al., 2015, 2017a). The particle size can affect the hydrodynamic force, which will influence the bubble-mineral attachment. Moreover, molybdenite sheets of different sizes exhibit different basal/edge ratios, with larger basal/edge ratio and more hydrophobic properties for larger particles (Lu et al., 2015). The change of surface characteristics will also influence the bubble-mineral attachment. It is of both fundamental and practical importance to establish the correlation between the flotation behavior and the surface interaction mechanism at the

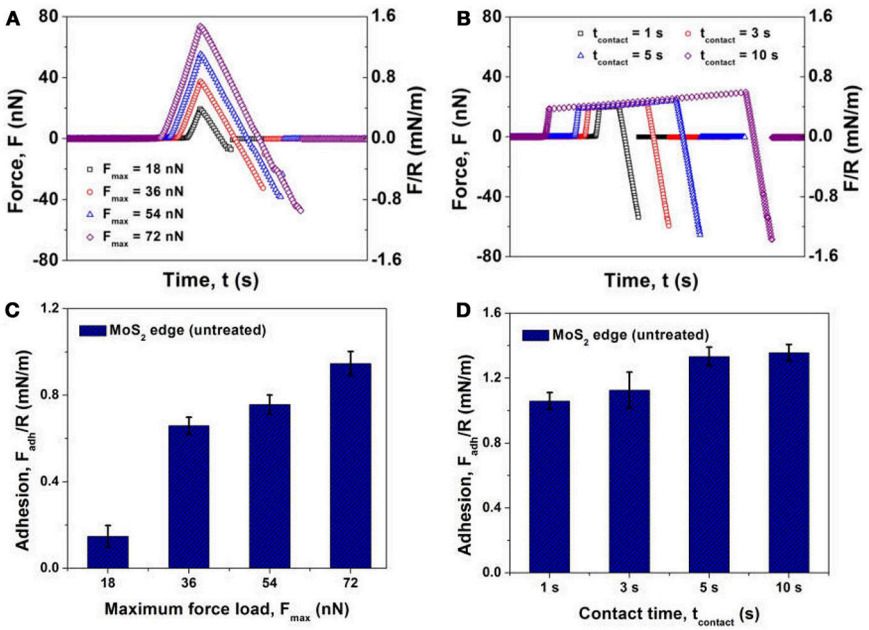


**FIGURE 9 |** Interaction force $F$ and normalized interaction $F/R$ between an air bubble ($R = 50\ \mu m$) and an untreated $MoS_2$ edge plane in 500 mM NaCl at $v = 1\ \mu m/s$ under the influence of **(A)** maximum force load $F_{max}$ and **(B)** contact time $t_{contact}$ at a $F_{max}$ ~18 nN. Normalized interfacial adhesion $F_{adh}/R$ measured between an air bubble and an untreated $MoS_2$ edge plane in 500 mM NaCl at $v = 1\ \mu m/s$ under the influence of **(C)** maximum force load $F_{max}$ and **(D)** contact time $t_{contact}$ at a $F_{max}$ ~18 nN.

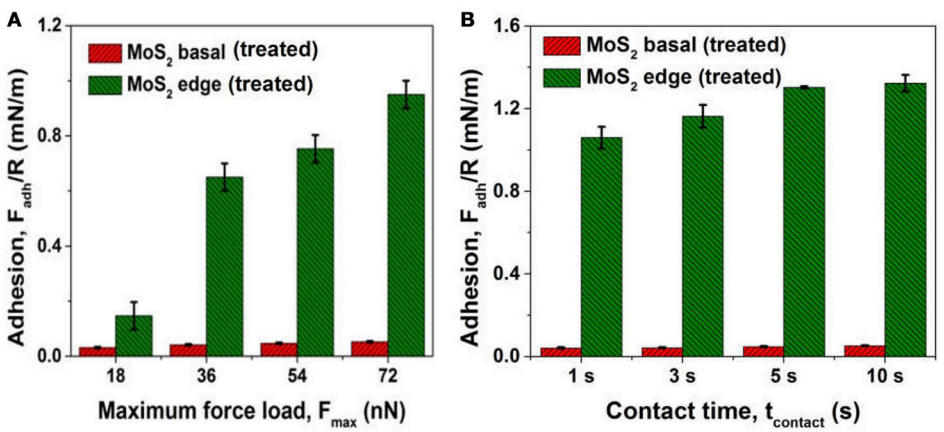


**FIGURE 10 |** Normalized interfacial adhesion $F_{adh}/R$ measured between an air bubble and a treated $MoS_2$ basal or edge plane conditioned in 100 ppm CMC solution in 500 mM NaCl at $v = 1\ \mu m/s$ under the influence of **(A)** maximum force load $F_{max}$ and **(B)** contact time $t_{contact}$ at a $F_{max}$ ~18 nN.

nanoscale, which could provide useful information to better modulate the related process at macro-scale.

## CONCLUSIONS

In this work, AFM imaging and force measurements were employed to directly probe the adsorption of a polymer (i.e., CMC) on both $MoS_2$ basal and edge surfaces as well as their interaction mechanism with air bubbles. AFM imaging showed the increased polymer coverage on the basal plane with elevating polymer concentration. As compared to the formation of a compact polymer layer on the basal plane at 100 ppm CMC, the polymer adsorption on the edge plane at the same concentration was almost negligible, which coincided with water contact angle results. Direct force measurements between CMC functionalized AFM tip and $MoS_2$ showed about one order of magnitude higher adhesion on the basal plane than on the edge surface, which could be attributed to their difference in surface hydrophobicity and surface charge. For the bubble-$MoS_2$ interaction, it was found that the polymer treatment could significantly influence the surface forces between air bubbles and basal plane while it had almost negligible

impact on the bubble-edge interaction. The adsorbed polymers on the basal plane led to a strong repulsion during the bubble approaching process, as compared to the "jump-in" behavior and bubble attachment observed for the untreated basal plane case. This study provides quantitative information on the interactions of a model polymer depressant (i.e., CMC) and $MoS_2$ basal/edge surfaces as well as how the polymer treatment on $MoS_2$ basal/edge surfaces influences their anisotropic interaction mechanism with air bubbles at the nanoscale. Our results have implications for the fundamental understanding of bubble-mineral-additive interaction mechanisms in froth flotation and other related interfacial processes.

## AUTHOR CONTRIBUTIONS

LX and JW conducted the experiments. LX, JW, JH, XC, and HoZ conducted the data analysis. HoZ conceived the project and supervised the research. All authors contributed to the writing of the manuscript.

## ACKNOWLEDGMENTS

We gratefully acknowledge the financial support from the Natural Sciences and Engineering Research Council of Canada (NSERC), the Canada Foundation for Innovation (CFI), the Alberta Advanced Education and Technology Small Equipment Grants Program (AET/SEGP) and the Canada Research Chairs Program (HoZ).

## SUPPLEMENTARY MATERIAL

The Supplementary Material for this article can be found online at: https://www.frontiersin.org/articles/10.3389/fchem.2018.00361/full#supplementary-material

## REFERENCES

Beaussart, A., Mierczynska-Vasilev, A., and Beattie, D. A. (2009). Adsorption of dextrin on hydrophobic minerals. *Langmuir* 25, 9913–9921. doi: 10.1021/la9010778

Bentley, C. L., Kang, M., Maddar, F. M., Li, F., Walker, M., Zhang, J., et al. (2017). Electrochemical maps and movies of the hydrogen evolution reaction on natural crystals of molybdenite (MoS 2): basal vs. edge plane activity. *Chem. Sci.* 8, 6583–6593. doi: 10.1039/C7SC02545A

Bulatovic, S. M. (2007). *Handbook of Flotation Reagents: Chemistry, Theory and Practice: Flotation of Sulfide Ores. Vol. 1*. Oxford, UK: Elsevier.

Butt, H.-J., Cappella, B., and Kappl, M. (2005). Force measurements with the atomic force microscope: technique, interpretation and applications. *Surf. Sci. Rep.* 59, 1–152. doi: 10.1016/j.surfrep.2005.08.003

Castro, S., Lopez-Valdivieso, A., and Laskowski, J. (2016). Review of the flotation of molybdenite. Part I: surface properties and floatability. *Int. J. Miner. Process.* 148, 48–58.doi: 10.1016/j.minpro.2016.01.003

Chan, D. Y., Klaseboer, E., and Manica, R. (2011). Theory of non-equilibrium force measurements involving deformable drops and bubbles. *Adv. Colloid Interface Sci.* 165, 70–90. doi: 10.1016/j.cis.2010.12.001

Chen, X., Davies, M. C., Roberts, C. J., Tendler, S. J. B., Williams, P. M., Davies, J., et al. (1997). Recognition of protein adsorption onto polymer surfaces by scanning force microscopy and probe-surface adhesion measurements with protein-coated probes. *Langmuir* 13, 4106–4111.

Chhowalla, M., and Amaratunga, G. A. (2000). Thin films of fullerene-like MoS2 nanoparticles with ultra-low friction and wear. *Nature* 407, 164–167. doi: 10.1038/35025020

Cui, X., Shi, C., Xie, L., Liu, J., and Zeng, H. (2016). Probing interactions between air bubble and hydrophobic polymer surface: impact of solution salinity and interfacial nanobubbles. *Langmuir* 32, 11236–11244. doi: 10.1021/acs.langmuir.6b01674

Cui, X., Shi, C., Zhang, S., Xie, L., Liu, J., Jiang, D., et al. (2017). Probing the effect of salinity and pH on surface interactions between air bubbles and hydrophobic solids: implications for colloidal assembly at air/water interfaces. *Chem. Asian J.* 12, 1568–1577. doi: 10.1002/asia.201700388

Ducker, W. A., Senden, T. J., and Pashley, R. M. (1991). Direct measurement of colloidal forces using an atomic force microscope. *Nature* 353, 239–241. doi: 10.1038/353239a0

Fuerstenau, M. C., Jameson, G. J., and Yoon, R.-H. (2007). *Froth Flotation: A Century of Innovation*. Littleton, CO: SME.

Gao, Z., Xie, L., Cui, X., Hu, Y., Sun, W., and Zeng, H. (2018). Probing anisotropic surface properties and surface forces of fluorite crystals. *Langmuir* 34, 2511–2521. doi: 10.1021/acs.langmuir.7b04165

Gaur, A. P., Sahoo, S., Ahmadi, M., Dash, S. P., Guinel, M. J. F., and Katiyar, R. S. (2014). Surface energy engineering for tunable wettability through controlled synthesis of MoS2. *Nano Lett.* 14, 4314–4321. doi: 10.1021/nl501106v

Govind Rajan, A., Sresht, V., Pádua, A. A., Strano, M. S., and Blankschtein, D. (2016). Dominance of dispersion interactions and entropy over electrostatics in determining the wettability and friction of two-dimensional MoS2 surfaces. *ACS Nano* 10, 9145–9155. doi: 10.1021/acsnano.6b04276

Greene, G. W., Banquy, X., Lee, D. W., Lowrey, D. D., Yu, J., and Israelachvili, J. N. (2011). Adaptive mechanically controlled lubrication mechanism found in articular joints. *Proc. Natl. Acad. Sci. U.S.A.* 108, 5255–5259. doi: 10.1073/pnas.1101002108

Huang, J., Yan, B., Faghihnejad, A., Xu, H., and Zeng, H. (2014). Understanding nanorheology and surface forces of confined thin films. *Korea Aust. Rheol. J.* 26, 3–14. doi: 10.1007/s13367-014-0002-8

Hutter, J. L., and Bechhoefer, J. (1993). Calibration of atomic-force microscope tips. *Rev. Sci. Instrum.* 64, 1868–1873. doi: 10.1063/1.1143970

Israelachvili, J., Min, Y., Akbulut, M., Alig, A., Carver, G., Greene, W., et al. (2010). Recent advances in the surface forces apparatus (SFA) technique. *Rep. Prog. Phys.* 73:036601. doi: 10.1088/0034-4885/73/3/036601

Israelachvili, J. N. (2011). *Intermolecular and Surface* Forces: *Revised 3rd Edn*. Oxford, UK: Academic press.

Jaramillo, T. F., Jørgensen, K. P., Bonde, J., Nielsen, J. H., Horch, S., and Chorkendorff, I. (2007). Identification of active edge sites for electrochemical H2 evolution from MoS2 nanocatalysts. *Science* 317, 100–102. doi: 10.1126/science.1141483

Jin, J., Miller, J. D., and Dang, L. X. (2014). Molecular dynamics simulation and analysis of interfacial water at selected sulfide mineral surfaces under anaerobic conditions. *Int. J. Miner. Process.* 128, 55–67. doi: 10.1016/j.minpro.2014.03.001

Karunadasa, H. I., Montalvo, E., Sun, Y., Majda, M., Long, J. R., and Chang, C. J. (2012). A molecular MoS2 edge site mimic for catalytic hydrogen generation. *Science* 335, 698–702. doi: 10.1126/science.1215868

Kor, M., Korczyk, P. M., Addai-Mensah, J., Krasowska, M., and Beattie, D. A. (2014). Carboxymethylcellulose adsorption on molybdenite: the effect of electrolyte composition on adsorption, bubble–surface collisions, and flotation. *Langmuir* 30, 11975–11984. doi: 10.1021/la503248e

Kristiansen, K., Stock, P., Baimpos, T., Raman, S., Harada, J. K., Israelachvili, J. N., et al. (2014). Influence of molecular dipole orientations on long-range exponential interaction forces at hydrophobic contacts in aqueous solutions. *ACS Nano* 8, 10870–10877. doi: 10.1021/nn504687b

Lee, C., Li, Q., Kalb, W., Liu, X. Z., Berger, H., Carpick, R. W., et al. (2010). Frictional characteristics of atomically thin sheets. *Science* 328, 76–80. doi: 10.1126/science.1184167

Li, H., Tsai, C., Koh, A. L., Cai, L., Contryman, A. W., Fragapane, A. H., et al. (2016). Activating and optimizing MoS2 basal planes for hydrogen evolution through the formation of strained sulphur vacancies. *Nat. Mater.* 15, 48–53.doi: 10.1038/nmat4465

Liu, H., Hu, H., Wang, J., Niehoff, P., He, X., Paillard, E., et al. (2016). Hierarchical ternary MoO2/MoS2/heteroatom-doped carbon hybrid materials for high-performance lithium-ion storage. *ChemElectroChem* 3, 922–932. doi: 10.1002/celc.201600062

Liu, Q., Zhang, Y., and Laskowski, J. (2000). The adsorption of polysaccharides onto mineral surfaces: an acid/base interaction. *Int. J. Miner. Process.* 60, 229–245. doi: 10.1016/S0301-7516(00)00018-1

Liu, T., Wang, C., Gu, X., Gong, H., Cheng, L., Shi, X., et al. (2014). Drug delivery with PEGylated MoS2 nano-sheets for combined photothermal and chemotherapy of cancer. *Adv. Mater.* 26, 3433–3440. doi: 10.1002/adma.201305256

Lu, Q., Wang, J., Faghihnejad, A., Zeng, H., and Liu, Y. (2011). Understanding the molecular interactions of lipopolysaccharides during *E. coli* initial adhesion with a surface forces apparatus. *Soft Matter* 7, 9366–9379. doi: 10.1039/c1sm05554b

Lu, Z., Liu, Q., Xu, Z., and Zeng, H. (2015). Probing anisotropic surface properties of molybdenite by direct force measurements. *Langmuir* 31, 11409–11418. doi: 10.1021/acs.langmuir.5b02678

Lu, Z., Lu, Z., Peng, S., Zhang, X., and Liu, Q. (2016). Microwetting of pH-sensitive surface and anisotropic MoS2 surfaces revealed by femtoliter sessile droplets. *Langmuir* 32, 11273–11279. doi: 10.1021/acs.langmuir.6b02224

Manor, O., Vakarelski, I. U., Tang, X., O'shea, S. J., Stevens, G. W., Grieser, F., et al. (2008). Hydrodynamic boundary conditions and dynamic forces between bubbles and surfaces. *Phy. Rev. Lett.* 101:024501.doi: 10.1103/PhysRevLett.101.024501

Okuhara, T., and Tanaka, K. (1978). Anisotropic properties of molybdenum disulfide single crystals in catalysis. *J. Phys. Chem.* 82, 1953–1954.

Pearse, M. (2005). An overview of the use of chemical reagents in mineral processing. *Miner. Eng.* 18, 139–149. doi: 10.1016/j.mineng.2004.09.015

Pugh, R. (1989). Macromolecular organic depressants in sulphide flotation—a review, 1. Principles, types and applications. *Int. J. Miner. Process.* 25, 101–130. doi: 10.1016/0301-7516(89)90059-8

Rao, S. R. (2013). *Surface Chemistry of Froth Flotation, Vol. 1. Fundamentals*. New York, NY: Springer Science and Business Media.

Rocha, J., Baydak, E., Yarranton, H., Sztukowski, D., Ali-Marcano, V., Gong, L., et al. (2016). Role of aqueous phase chemistry, interfacial film properties, and surface coverage in stabilizing water-in-bitumen emulsions. *Energy Fuels* 30, 5240–5252. doi: 10.1021/acs.energyfuels.6b00114

Roxlo, C. B., Daage, M., Leta, D. P., Liang, K. S., Rice, S., Ruppert, A. F., et al. (1986). Catalytic defects at molybdenum disulfide "edge" planes. *Solid State Ionics* 22, 97–104.

Sheehan, P. E., and Lieber, C. M. (2017). Friction between van der Waals solids during lattice directed sliding. *Nano Lett.* 17, 4116–4121. doi: 10.1021/acs.nanolett.7b00871

Shi, C., Chan, D. Y., Liu, Q., and Zeng, H. (2014a). Probing the hydrophobic interaction between air bubbles and partially hydrophobic surfaces using atomic force microscopy. *J. Phys. Chem. C* 118, 25000–25008. doi: 10.1021/jp507164c

Shi, C., Cui, X., Xie, L., Liu, Q., Chan, D. Y., Israelachvili, J. N., et al. (2014b). Measuring forces and spatiotemporal evolution of thin water films between an air bubble and solid surfaces of different hydrophobicity. *ACS Nano* 9, 95–104. doi: 10.1021/nn506601j

Shi, C., Yan, B., Xie, L., Zhang, L., Wang, J., Takahara, A., et al. (2016a). Long-range hydrophilic attraction between water and polyelectrolyte surfaces in oil. *Angew. Chem. Int. Edn. Engl.* 55, 15017–15021. doi: 10.1002/anie.201608219

Shi, C., Zhang, L., Xie, L., Lu, X., Liu, Q., He, J., et al. (2017). Surface interaction of water-in-oil emulsion droplets with interfacially active asphaltenes. *Langmuir* 33, 1265–1274. doi: 10.1021/acs.langmuir.6b04265

Shi, C., Zhang, L., Xie, L., Lu, X., Liu, Q., Mantilla, C. A., et al. (2016b). Interaction mechanism of oil-in-water emulsions with asphaltenes determined using droplet probe, AFM. *Langmuir* 32, 2302–2310.doi: 10.1021/acs.langmuir.5b04392

Tabor, R. F., Manica, R., Chan, D. Y., Grieser, F., and Dagastine, R. R. (2011). Repulsive van der Waals forces in soft matter: why bubbles do not stick to walls. *Phy. Rev. Lett.* 106:064501. doi: 10.1103/PhysRevLett.106.064501

Tan, S. M., Ambrosi, A., Sofer, Z., Huber, Š., Sedmidubský, D., and Pumera, M. (2015). pristine basal-and edge-plane-oriented molybdenite MoS2 exhibiting highly anisotropic properties. *Chem. A Eur. J.* 21, 7170–7178. doi: 10.1002/chem.201500435

Taylor, M., Urquhart, A. J., Anderson, D. G., Williams, P. M., Langer, R., Alexander, M. R., et al. (2008). A methodology for investigating protein adhesion and adsorption to microarrayed combinatorial polymers. *Macromol. Rapid Commun.* 29, 1298–1302. doi: 10.1002/marc.200800171

Wang, J., Li, J., Xie, L., Shi, C., Liu, Q., and Zeng, H. (2016). Interactions between elemental selenium and hydrophilic/hydrophobic surfaces: direct force measurements using AFM. *Chem. Eng. J.* 303, 646–654. doi: 10.1016/j.cej.2016.06.039

Wang, J., Liu, Q., and Zeng, H. (2013). Understanding copper activation and xanthate adsorption on sphalerite by time-of-flight secondary ion mass spectrometry, X-ray photoelectron spectroscopy, and *in situ* scanning electrochemical microscopy. *J. Phys. Chem. C* 117, 20089–20097. doi: 10.1021/jp407795k

Wang, J., Xie, L., Zhang, H., Liu, Q., Liu, Q., and Zeng, H. (2017). Probing interactions between sphalerite and hydrophobic/hydrophilic surfaces: effect of water chemistry. *Powder Technol.* 320, 511–518. doi: 10.1016/j.powtec.2017.07.084

Xie, L., Shi, C., Cui, X., Huang, J., Wang, J., Liu, Q., et al. (2017a). Probing the interaction mechanism between air bubbles and bitumen surfaces in aqueous media using bubble probe, AFM. *Langmuir* 34, 729–738. doi: 10.1021/acs.langmuir.7b02693

Xie, L., Shi, C., Cui, X., and Zeng, H. (2017b). Surface forces and interaction mechanisms of emulsion drops and gas bubbles in complex fluids. *Langmuir* 33, 3911–3925. doi: 10.1021/acs.langmuir.6b04669

Xie, L., Shi, C., Wang, J., Huang, J., Lu, Q., Liu, Q., et al. (2015). Probing the interaction between air bubble and sphalerite mineral surface using atomic force microscope. *Langmuir* 31, 2438–2446. doi: 10.1021/la5048084

Xie, L., Wang, J., Shi, C., Cui, X., Huang, J., Zhang, H., et al. (2017c). Mapping the nanoscale heterogeneity of surface hydrophobicity on the sphalerite mineral. *J. Phys. Chem. C* 121, 5620–5628. doi: 10.1021/acs.jpcc.6b12909

Xie, L., Wang, J., Shi, C., Huang, J., Zhang, H., Liu, Q., et al. (2016). Probing surface interactions of electrochemically active galena mineral surface using atomic force microscopy. *J. Phys. Chem. C* 120, 22433–22442. doi: 10.1021/acs.jpcc.6b07204

Xie, L., Wang, J., Yuan, D., Shi, C., Cui, X., Zhang, H., et al. (2017d). Interaction mechanisms between air bubble and molybdenite surface: impact of solution salinity and polymer adsorption. *Langmuir* 33, 2353–2361. doi: 10.1021/acs.langmuir.6b04611

Yang, D., Xie, L., Bobicki, E., Xu, Z., Liu, Q., and Zeng, H. (2014). Probing anisotropic surface properties and interaction forces of chrysotile rods by atomic force microscopy and rheology. *Langmuir* 30, 10809–10817. doi: 10.1021/la5019373

Yin, W., Yan, L., Yu, J., Tian, G., Zhou, L., Zheng, X., et al. (2014). High-throughput synthesis of single-layer MoS2 nanosheets as a near-infrared photothermal-triggered drug delivery for effective cancer therapy. *ACS Nano* 8, 6922–6933. doi: 10.1021/nn501647j

Zhang, C., Gong, L., Xiang, L., Du, Y., Hu, W., Zeng, H., et al. (2017). Deposition and adhesion of polydopamine on the surfaces of varying wettability. *ACS Appl. Mater. Interfaces* 9, 30943–30950. doi: 10.1021/acsami.7b09774

Zhang, H., Loh, K. P., Sow, C. H., Gu, H., Su, X., Huang, C., et al. (2004). Surface modification studies of edge-oriented molybdenum sulfide nanosheets. *Langmuir* 20, 6914–6920. doi: 10.1021/la049887t

Zhang, L., Xie, L., Shi, C., Huang, J., Liu, Q., and Zeng, H. (2016). Mechanistic understanding of asphaltene surface interactions in aqueous media. *Energy Fuels* 31, 3348–3357. doi: 10.1021/acs.energyfuels.6b02092

**Conflict of Interest Statement:** The authors declare that the research was conducted in the absence of any commercial or financial relationships that could be construed as a potential conflict of interest.

frontiers in Chemistry

ORIGINAL RESEARCH
published: 15 May 2018
doi: 10.3389/fchem.2018.00139

# Rice Starch Particle Interactions at Air/Aqueous Interfaces—Effect of Particle Hydrophobicity and Solution Ionic Strength

*Cathy E. McNamee[1]*, Yu Sato[1], Berthold Wiege[2], Ippei Furikado[3], Ali Marefati[4], Tommy Nylander[3], Michael Kappl[5] and Marilyn Rayner[4]*

*[1] Faculty of Textile Science and Technology, Shinshu University, Ueda, Japan, [2] Max Rubner-Institut, Detmold, Germany, [3] Physical Chemistry, Lund University, Lund, Sweden, [4] Department of Food Technology, Engineering and Nutrition, Lund University, Lund, Sweden, [5] Max Planck Institute for Polymer Research, Mainz, Germany*

Starch particles modified by esterification with dicarboxylic acids to give octenyl succinic anhydride (OSA) starch is an approved food additive that can be used to stabilize oil in water emulsions used in foods and drinks. However, the effects of the OSA modification of the starch particle on the interfacial interactions are not fully understood. Here, we directly measured the packing of films of rice starch granules, i.e., the natural particle found inside the plant, at air/aqueous interfaces, and the interaction forces in that system as a function of the particle hydrophobicity and ionic strength, in order to gain insight on how starch particles can stabilize emulsions. This was achieved by using a combined Langmuir trough and optical microscope system, and the Monolayer Interaction Particle Apparatus. Native rice starch particles were seen to form large aggregates at air/water interfaces, causing films with large voids to be formed at the interface. The OSA modification of the rice starches particles decreased this aggregation. Increasing the degree of modification improved the particle packing within the film of particles at the air/water interface, due to the introduction of inter-particle electrostatic interactions within the film. The introduction of salt to the water phase caused the particles to aggregate and form holes within the film, due to the screening of the charged groups on the starch particles by the salt. The presence of these holes in the film decreased the stiffness of the films. The effect of the OSA modification was concluded to decrease the aggregation of the particles at an air/water interface. The presence of salts, however, caused the particles to aggregate, thereby reducing the strength of the interfacial film.

**Keywords: octenyl succinic anhydride (OSA), starch granules, NaCl, Lagmuir films, optical microscopy, surface forces**

OPEN ACCESS

***Edited by:***
*Erica Wanless,*
*University of Newcastle, Australia*

***Reviewed by:***
*Timothy Nie Hunter,*
*University of Leeds, United Kingdom*
*Adelina Voutchkova-Kostal,*
*George Washington University,*
*United States*

****Correspondence:***
*Cathy E. McNamee*
*mcnamee@shinshu-u.ac.jp*

***Specialty section:***
*This article was submitted to Chemical Engineering, a section of the journal Frontiers in Chemistry*

***Received:*** *09 February 2018*
***Accepted:*** *12 April 2018*
***Published:*** *15 May 2018*

***Citation:***
*McNamee CE, Sato Y, Wiege B, Furikado I, Marefati A, Nylander T, Kappl M and Rayner M (2018) Rice Starch Particle Interactions at Air/Aqueous Interfaces—Effect of Particle Hydrophobicity and Solution Ionic Strength. Front. Chem. 6:139. doi: 10.3389/fchem.2018.00139*

## INTRODUCTION

Oil in water (O/W) emulsions can be stabilized by adsorbing particles at the oil/water interfaces, i.e., the so-called Pickering type emulsions (Pickering, 1907). Particles can also stabilize foams without the use of surfactants by adsorbing to the air/liquid interfaces of the gas bubbles that are suspended in a liquid continuous phase (Chevalier and Bolzinger, 2013). Other systems where an air/liquid

interface is stabilized by particles are liquid marbles (Aussillous and Quéré, 2001; Bormashenko, 2011) and colloidosomes (Dinsmore et al., 2002; Thompson et al., 2015). In particle stabilized systems, the interactions between particles at and with the hydrophobic (e.g., oil or air)/aqueous interfaces are crucial. The attachment of particles to these interfaces has been shown to be affected by the surface chemistry, charge, size, and shape of the particle (Aveyard et al., 2000; Kralchevsky and Nagayama, 2000; Schultz et al., 2006; Min et al., 2008; Bleibel et al., 2013). The surface chemistry controls the stability of the particles at the interface and their tendency to aggregate at the interface. A particle that is too hydrophilic will readily detach from the interface into the aqueous phase, causing the emulsion to become instable. A particle that is too hydrophobic will cause the particles to aggregate together and clump at the interface, causing defects such as holes in the film at the interface. Areas of the bare oil/aqueous interface generally result in a less stable emulsion. The surface groups on the particles and their degree of dissociation will contribute to the charge on the particles. An increased charge increases the inter-surface electrostatic repulsions at the interface, which acts to reduce the aggregating and clumping of the particles at the interface. Increasing the particle size increases the magnitude of the inter-surface van der Waals attractive force and the inter-surface attractive capillary force. These forces may cause the particles to aggregate and clump, causing holes in the film of particles at the interface.

Starch is a carbohydrate produced by most green plants to store energy. It consists of a large number of glucose units joined by glycosidic bonds. The resulting polysaccharides (linear amylose and branched amylopectin) are efficiently packed in the plant cells into semi-crystalline starch granules. Starch granules (referred to as "starch particles" from here on) can be isolated from a variety of plants, mainly from tubers and cereals. They have a considerable natural variation with respect to granule size (0.5 to 100 $\mu$m), shape (round, oblong, sharp edged polyhedral, etc.) and composition (the ratio between the two constituent polymers of the starches, i.e., amylopectin and amylose) depending on its botanical origin (Jane et al., 1994). Starch particles have been used to stabilize O/W food emulsions (Li et al., 2013; Song et al., 2014; Marefati et al., 2017). This is because starch is a naturally occurring polysaccharide that is safe to use in foods (Sweedman et al., 2013) and because it is abundant, biodegradable, and inexpensive (Hui et al., 2009). Native (non-modified) starch, however, has limitations in its applications, due to its hydrophilic surface properties, which makes it less suitable as a stabilizer. Chemical or physical modifications of the starch particles to change the physical and chemical properties of the starch are common, as this improves the applicability of starch in the food industry as well as for other applications like those used in pharmaceutical technologies.

The emulsifying capacities of native starch particles can be improved by increasing the hydrophobicity of the starch particles via chemically modifying the starch. Octenyl succinic anhydride (OSA) modified starch (OSA starch) is obtained from the esterification reaction between the hydroxyl (OH) groups on starch and octenylsuccinic anhydride, see **Figure 1A** (Sweedman et al., 2013). An increase in the number of OH groups substituted by OSA has been reported to increase the hydrophobicity of the otherwise hydrophilic native starch (Miao et al., 2014). As the hydrophilicity of the starch backbone is retained (Ovando-Martinez et al., 2017), this reaction can create amphiphilic particles with unique properties. The most widely described synthesis pathway is a reaction in aqueous medium under mild alkaline conditions with the starch in its granular form (Trubiano, 1986). The level of OSA modification is commonly reported by the percentage of OSA used based on the dry weight of starch or the degree of substitution (DS), which is the average number of octenyl succinate (OS) derivatives per glucose unit. The substitution with OSA can occur at carbon 2, 3, and 6 in the glucose molecule of starch (**Figure 1A**) (Nilsson and Bergenståhl, 2007b; Sweedman et al., 2013). The OH-group at carbon 6 is esterified preferably because of the steric hindrance of the other two OH-groups. A degree of substitution (i.e., the average number of esterified hydroxyl groups per monosaccharide unit) of ∼0.02 is typical for commercial OSA starches (Shogren et al., 2000). OSA groups are thought to be mostly present in the amorphous parts of the amylopectin molecule in the interior of the starch. However, they may also exist on the exterior of the granule (Shogren et al., 2000). Starches modified with octenyl succinic anhydride (OSA) have been used in a range of formulations, particularly as a food additive, over the past 50 years. OSA modified starch (E1450) is approved for food applications with a degree of modification up to 3% based on the dry weight of starch (Tesch et al., 2002; Rayner et al., 2012b). For this reason, OSA is generally studied at intervals less than 3%. Rice, corn, tapioca, potato, amaranth, and wheat starch particles have been successfully modified using OSA (Saari et al., 2016; Whitney et al., 2016; Marefati et al., 2017; Ovando-Martinez et al., 2017). There are also reports that show such OSA modified starch particles can be used to stabilize O/W emulsions (Saari et al., 2016; Marefati et al., 2017).

The physical properties of OSA modified starch particles affect their ability to effectively stabilize O/W emulsions. The effect of the OSA modification on the physical properties of starch particles has been studied. The hydrophobicity of a starch particle is reported to increase after the OSA modification. This modification not only increases the amphiphilicity of the starch particle, but also weakens the internal hydrogen bonding of the starch particle (Ovando-Martinez et al., 2017). These effects cause the physical properties of the starch particles to change. For example, the OSA modification of a starch particle has been reported to disrupt the crystalline structure of the starches, causing the OSA starches to have a lower gelatinization temperature than their native starches (Sweedman et al., 2013). In general, OSA starch gels have also been found to be softer than the native starch gels (Ovando-Martinez et al., 2017). The OSA modified rice starch particles have also been shown to aggregate less than the native rice starch (Ovando-Martinez et al., 2017).

The properties of starch particles affecting their behavior at and with a hydrophobic (oil)/hydrophilic (aqueous) interface and the effect of the OSA modification of starch particles is less understood. Studies have shown that the degree of modification of the starch particle, the weight percent of particles used in the system, and the size of the starch particles can affect the

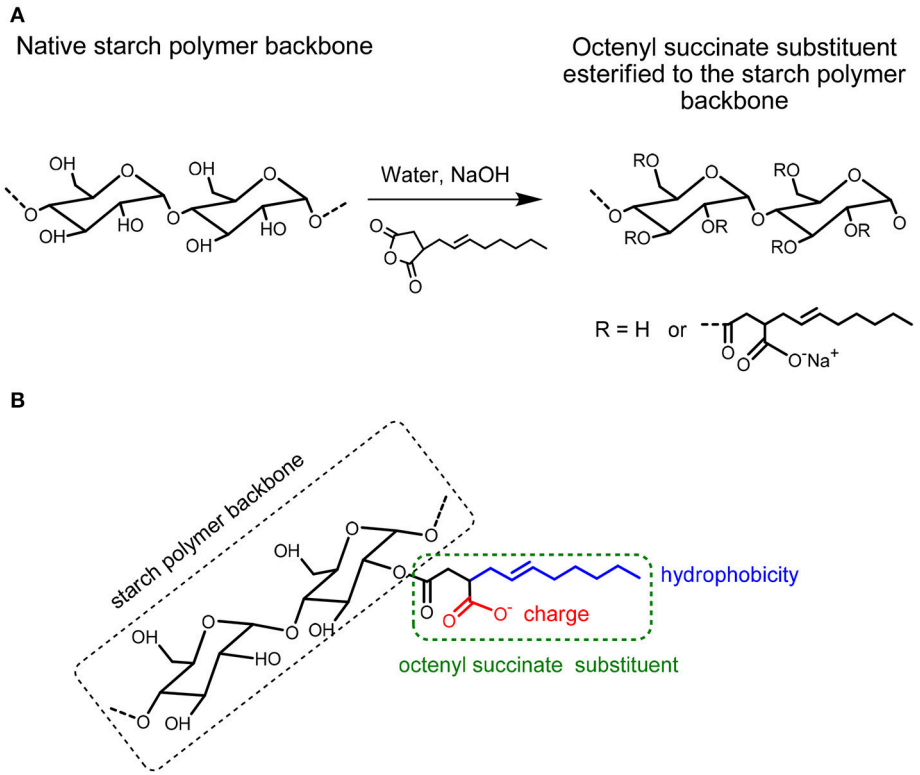


**FIGURE 1 | (A)** Modification of starch by Octenylsuccinic Anhydride (OSA) modification. **(B)** Hydrophobicity (blue color) and possible charge (red color) in the octenyl succinate substituent esterified to the starch polymer backbone.

surface coverage of the oil/water interface by the particles and the stability of the droplet (Yusoff and Murray, 2011; Li et al., 2013; Marefati et al., 2017). The stability of the droplet with adsorbed particles generally increases as the coverage of the droplet by the particles increases. This is due to the electrostatic interactions that act between two particle stabilized droplets, whose adsorbed particles are charged, and also due to the steric repulsions resulting from the finite size of the particles at the oil/water interface. The OSA modification has been reported to change the charge of starch (Nilsson and Bergenståhl, 2007a; Miao et al., 2014). Thus, the interactions between the particles at the hydrophobic/hydrophilic interface is expected to change with the OSA modification of the starch particles. Additionally, the ionic strength of the aqueous phase is also expected to affect the magnitude of the attractions between charged starch particles in the interfacial layer. This is because the electrostatic repulsions between two charged surfaces in aqueous solutions are screened by salts (Israelachvili, 2011), causing the inter-surface force to be more attractive in solutions of high ionic strength. The addition of salt can therefore potentially be used to increase the particle packing density at the oil/water interface and to improve the packing of the particles at the interface.

In spite of the numerous studies into the physical properties of starch particles modified by OSA and their interactions at and with hydrophobic/hydrophilic interfaces, the effects of the OSA modification of the starch particles and the addition of salt to the aqueous phase on these interactions are still not well-understood. For this purpose, we have systematically studied here the effect of OSA modification of starch particles on the colloidal interactions in films of starch particles deposited at hydrophobic/aqueous interfaces in the absence and presence of salt. This was achieved by modeling the hydrophobic/aqueous interface with an air/aqueous interface. The advantage of using an air/aqueous interface is that the effect of the particle type, particle packing density, and the presence of salts in the aqueous phase on the physical properties (inter-particle interactions, particle aggregations, interfacial stiffness, etc.) of the air/aqueous interface can be systematically studied. Here, we used a combined Langmuir trough and optical microscope system, and the Monolayer Interaction Particle Apparatus (MPIA) (McNamee et al., 2015; McNamee and Kappl, 2016; Azakami et al., 2017), which allows the interactions between the particles to be studied at the same time as the particle packing density and bulk phase properties are varied. In this study, we compared native rice starch particles (NRS) and rice starch particles that were modified with OSA to different degrees. This starch type was chosen, as the size of the rice starch particles (diameter $= 6.92 \pm 0.17\,\mu m$) was large enough to allow their visualization at the air/aqueous interface with an optical microscope. As many food applications of the starch particles also include salt, the effect of salt on the physical properties of the air/aqueous interface in the presence of OSA modified starch particles was also determined. This also

allowed us to reveal the impact of electrostatic forces on the particle interactions. The results of this study will help reveal the effect of OSA modification of starch particles on the physical properties of hydrophobic/hydrophilic interfaces in the presence of starch particles. This information is envisioned to improve the use of the starch particles in food applications.

# EXPERIMENTAL

## Materials

The materials in this experiment were chloroform ($CHCl_3$, 99.0% purity, Wako Pure Chemical Industries, Japan), sodium chloride (NaCl, JIS Special Grade, Wako Pure Chemical Industries, Japan), and ethanol (EtOH, JIS Special Grade, Wako Pure Chemical Industries, Japan). The water used in this study was ultrapure water (Direct-Q 3 UV, Millipore, USA), which had a specific resistivity of 18.2 MΩ cm.

### Preparation of OSA Modified Rice Starch and Determination of the Degree of Modification

Rice starch was isolated in a semi-technical scale. Briefly, 8 kg of rice were steeped in 16 kg of a 0.4% NaOH-solution for 16 h at 4°C, in order to soften the endosperm and to enhance protein solubilization. The supernatant was then separated, 30 kg of fresh water added and the rice wet milled with a colloid-mill (150 μm). Afterwards, the protein and the fiber were separated from the starch by repeated centrifugation (decanter) and wet-sieving (vibration sieve) steps. Finally, the starch suspension was neutralized and spray dried using a spray dryer (type minor production, Niro A/S, Kopenhagen, Denmark) (Marefati et al., 2017). Next, 50.0 g of the starch was suspended in 200.0 g of distilled water. The pH-value was adjusted to 8.2–8.4 and maintained constant during the reaction by addition of a 0.5 N NaOH solution. A solution of OSA in acetone (100 mg OSA/mL solution) was added at 32°C with intensive stirring for 5–40 min. The mixture was still stirred until the reaction had finished (90–120 min). The pH did not decrease further with time after the reaction had finished. The amount of OSA in relation to starch dry matter (44.7 g) was 0.6, 1.2, 1.8, 2.4, and 3.0% by mass (Marefati et al., 2017). The modified starch was isolated by centrifugation (7 min, 3,350–5,580 × g), washed with 350 mL of distilled water (5 min suspension followed by centrifugation) and finally with 300 mL of acetone. The third sediment was first dried at room temperature overnight and then in a convection dryer at 30°C for 4 h. Finally, the products were conditioned to their equilibrium moisture content for 2 days at room temperature. All yields varied between 50.1 and 51.1 g (Marefati et al., 2017). The degree of substitution (DS) of these starches was determined by hydrolysis of 2 g of the modified starch with 60 mL of distilled water and 20.00 ± 0.03 mL of a 0.1 N NaOH at 35°C for 24 h in a closed Erlenmeyer flask and by back titration of the excess sodium hydroxide with 0.1 N $H_2SO_4$ to pH = 7.0 ± 0.1. The starch/water-suspension was adjusted to pH = 7.0 ± 0.1 before the addition of the sodium hydroxide solution (Marefati et al., 2017).

The native rice starch particles (NRS) and rice starch particles modified by OSA to different degrees were used in this study. The rice starch particles were modified with OSA to give surface hydrophobized starches with a modification level of 0.46 ± 0.01, 0.97 ± 0.03, 1.40 ± 0.05, 1.90 ± 0.05, 2.36 ± 0.02% OSA by mass in dry matter of the sample. These values correspond to degrees of substitution (DS) of 0.0036, 0.0077, 0.0108, 0.0149, and 0.0186, respectively (Marefati et al., 2017). In this study, we refer to these particles as 0.6RS, 1.2RS, 1.8RS, 2.4RS, 3.0RS, respectively. The diameter of the native rice particles was determined in earlier studies to be 6.92 ± 0.17 μm (Marefati et al., 2017). Scanning Electron Micorspy images from that studied also showed that the NRS and 3.0RS particles had comparable sizes and shapes (Marefati et al., 2017). As the same batch of rice particles used in this present study was the same as that used in these previous studies, the size of the rice particles was treated as 6.92 ± 0.17 μm.

## Preparation of the NRS and RS Starch Particle Spreading Solutions

The starch particles were firstly dispersed in ethanol to give a concentration of $7.97 \times 10^4 \pm 0.24 \times 10^4$ starch particles per μL of ethanol by adding ∼0.05 g of the dry particles to 2.5 mL of the ethanol. This solution was then sonicated for 10 min, so as to disperse the particles in the ethanol. Ethanol acted as the solvent to spread the particles at the air/aqueous interface. Organic solvents, such as chloroform, which are commonly used to spread and prepare insoluble Langmuir films at air/aqueous interfaces could not be used in this study, because the starch particles were seen to aggregate in chloroform. Ethanol, however, allowed the starch particles to be well-dispersed. Ethanol also has a positive spreading coefficient (Barnes and Gentle, 2005), which enabled it to spread at an air/water interface and form the films of the starch particles.

## Methods

### Langmuir Trough

A Langmuir Trough (Large microscopy Langmuir trough, Nima Technology Ltd, Coventry, UK) was used to prepare the films of starch particles at the air/aqueous interface. The surface pressure was measured using a Wilhelmy plate of wet filter paper (Barnes and Gentle, 2005) (No.2 240 mm, Toyo, Japan) that was attached to a strain gauge (Nima PS4 surface pressure sensor, Nima Technology Ltd, Coventry, UK).

The Langmuir trough was cleaned with chloroform and then with ethanol, before the surface pressure-area isotherms were measured. Water was next added to the trough and then removed, in order to remove any solvent remaining in the trough. The solution that was to be used as the subphase was subsequently added to the trough and the barriers compressed to maximum. The liquid surface was then cleaned by suctioning the water surface between the two barriers, after which the barriers were fully expanded. The temperature of the subphase was maintained at 20°C by controlling the temperature of the experimental room. Next, 2,000–2,250 μL of the starch particles in ethanol solution was spread drop-wise onto the water surface by using a 1,000 μL syringe (Hamilton, Switzerland). A time of 10 min was allowed for the ethanol to evaporate. The particle films were then compressed with a speed of 80 $cm^2$ $min^{-1}$. The surface pressure-area isotherms were recorded during this time.

Each isotherm was measured a minimum of three times, in order to ensure the reproducibility of the results.

The surface pressure ($\prod$)-area isotherms were converted to $\prod$-area per starch particle ($A_{starch}$) isotherms so as to enable the isotherms of the different starch particle types to be directly compared. This was necessary, as different volumes of spreading solutions needed to be spread to the air/aqueous interfaces for the different particle types, so as to measure both the loose packing and tight packing regions in each film. The area values were converted to area per starch particle ($A_{starch}$) values by calculating the number of starch particles spread at the air/aqueous interface ($N_{starch}$). This was achieved by using

$$N_{starch} = \frac{\rho_{starch}\ V\ \rho_{EtOH}}{W_{starch}} \quad (1)$$

The parameters $\rho_{starch}$, V, and $\rho_{EtOH}$ are the weight fraction of the starch particles in the ethanol spreading solution, the volume spread at the air/water interface and the density of ethanol (0.789 g/mL), respectively. $W_{starch}$ is the mass of one particle and was calculated using

$$W_{starch} = \frac{\rho_{starch} 4\pi R^3}{3} \quad (2)$$

Here, $\rho_{starch}$ is the density of starch, approximated by the standard value of 1.5 g/cm$^3$ (Odeku and Itiola, 2007), and R is the radius of one particle.

The maximum volume fraction of close-packed spheres is reported to be 0.74 (Israelachvili, 2011). Thus, the area expected for a hexagonal packed layer of particles ($A_{hex}$) with mean starch size was calculated using

$$A_{hex} = \frac{\pi R^2}{0.74} \quad (3)$$

## Optical Imaging of Films of Starch Particles at Air/Aqueous Interfaces

The combined optical microscope-Langmuir trough set-up used in this study has been described elsewhere (Ngyugen and McNamee, 2014). The Langmuir films were prepared in the same way described to measure the surface pressure-area isotherms. Briefly, the starch particles in ethanol spreading solutions were applied to the air/aqueous interface by using a 1,000 μL syringe (Hamilton, Switzerland), and 10 min was allowed for the solvent to evaporate. The films were then compressed to the desired surface pressure. The surface pressure was maintained at the desired value by using the surface pressure control option on the Langmuir trough, during which time the images of the air/aqueous interface were taken. The images were taken in the order of low to high surface pressures.

## Monolayer Interaction Particle Apparatus (MPIA)

The colloid probes to be used in the MPIA measurements were prepared by using a light microscope (BX51, Olympus) and a micro-manipulator (Model MMO-202D, Narishige) to attach a rice starch particle (native or OSA modified) to a gold-plated $Si_3N_4$ cantilever (V-shaped, nominal spring constant $k = 0.15$ N/m, OTR8-PS-W, Olympus) with an epoxy resin (Araldite Rapid).

The MPIA was used to measure the forces between a film of starch particles at an air/aqueous interface and the colloid probe in the water. The MPIA is comprised of a force measurement unit that is attached to a Langmuir trough (Riegler & Kirstein GmbH, Potsdam, Germany). Detailed information about the MPIA can be found elsewhere (Gillies et al., 2005; McNamee et al., 2011).

The MPIA was used in the following way. First, the Langmuir trough was cleaned using chloroform and ethanol. Any remaining solvent was eliminated from the trough by adding water to the trough and then by removing it. The colloid probe was next inserted into the MPIA cantilever holder and the cantilever holder attached to the MPIA. Water was then added to the trough and its surface suctioned cleaned. The temperature of the subphase was maintained at 20.0 ± 0.1°C by running thermostated water through the base of the trough by using a circulation system (C25P, ThermoHaake, Karlsruhe, Germany). A calibration factor ($CF_{mica}$) was required to convert the raw force curves (force [V] vs. piezo position [nm] curves) to the calibrated force curves (force [nN] vs. piezo position [nm] curves). This was achieved by measuring the force curves between the probe and a clean mica substrate that was placed across the edges of the Langmuir trough filled with water. $CF_{mica}$ was obtained from the constant compliance region (the region where the probe was in contact with the mica substrate) of these force curves. The water in the trough was removed after the calibration. The solution to be used as the subphase was then added to the trough, and that surface cleaned. The particle in ethanol spreading solution was next spread at the air/aqueous interface, after which 10 min was allowed for the ethanol to evaporate. The films were then compressed to a certain surface pressure, and the forces measured between that film and the same probe that was used to measure $CF_{mica}$. A minimum of 50 force curves was recorded at each surface pressure. $CF_{mica}$ was used to convert the raw force curves (force [V] vs. piezo position [nm] curves) measured between the film of starch particles at the air/aqueous interface and the probe in the aqueous phase to the calibrated force curves (force [nN] vs. piezo position [nm] curves). Zero force was defined at large probe-film separations, where no surface forces acted on the cantilever. Zero distance was defined at the onset of the linear contact region in the force curves; the contact region was defined as the area where the probe was in contact with the particle film at the air/aqueous interface.

The magnitude of the adhesive force between the probe and the film of starch particles at the air/aqueous interface was obtained from the force curve minimum that was measured in the retraction force curves. The average adhesion force ($F_{ad}$) was calculated by fitting a Gaussian curve to a histogram of the adhesive forces that were calculated from the measured force curves taken at the same conditions (same surface pressure, same particle type, and same subphase solution conditions). The effective stiffness ($S_N$) (McNamee et al., 2010) of the film of starch particles at the air/aqueous interface was calculated by dividing the slope of the linear contact region of the force curves measured between the probe and film of starch particles at the air/aqueous interface ($S_1$) by the slope of the linear contact region of the force

curves measured between the same probe and the mica substrate in water ($S_2$).

### Zeta Potential Measurements

The Zeta potential (ζ) values of the starch particles were measured with a Zetasizer (Zetasizer Nano ZS, Malvern Instruments Ltd, Wostershire, UK) by preparing a 1,000 ppm concentration of native or modified starches dispersed in water or aqueous solutions containing NaCl. Briefly, the electrophoretic mobility was measured for each sample five times. These values were then converted into zeta potential values by using the Helmholtz-Smoluchowski approximation, assuming that the particles were spherical and large compared to the Debye length of the system. The zeta potential values of each sample type were then averaged.

## RESULTS AND DISCUSSION

### Effect of the Degree of Modification of the Rice Starch Particle on the Physical Properties of a Film of the Rice Particles at an Air/Water Interface

The effect of modifying the structure of rice starch on its ability to form films of starch particles at air/water interfaces was firstly investigated by spreading native rice starch particles (NRS) and OSA modified rice starch particles at air/water interfaces and then by measuring their surface pressure-area per rice starch particles ($A_{starch}$) isotherms, see **Figure 2**. The rice starch particles that were modified with an OSA modification percentage of 0.46 ± 0.01, 0.97 ± 0.03, 1.40 ± 0.05, 1.90 ± 0.05, 2.36 ± 0.02 are referred to as 0.6RS, 1.2RS, 1.8RS, 2.4RS, 3.0RS, respectively. The NRS particles gave positive surface pressure values for the $A_{starch}$ values $< \sim 120\ \mu m^2$. The surface pressure increased gradually with an $A_{starch}$ decrease, suggesting a loose particle packing in the film of the NRS particles at the air/water interface. OSA modification of the rice particles caused the isotherms to shift to lower $A_{starch}$ values than those measured with the NRS particles, when the same surface pressure values were compared. The isotherms also showed a change in slope from a flatter to a steeper isotherm as the particles were compressed. These two slope regions are thought to indicate films of loose packing and tight packing, respectively. The $A_{starch}$ values where the phase transition from loose to tight packing films occurred moved to higher values as the degree of modification of the rice particles increased. A change in the inter-particle interactions and therefore the particle packing at the air/water interface may explain this shift in the critical $A_{starch}$ values and this change in the particle packing ability.

The area expected for a hexagonal packed layer of particles with a mean starch size ($A_{hex}$) was calculated using equation 4 and is shown in **Figure 2** by the dashed line. If the area where the tight packing region commenced in the surface pressure-$A_{starch}$ isotherms of the native rice starch and the OSA modified rice particles are to the left of this line, then some of the particles may have been lost from the air/water interface to the subphase. The $A_{starch}$ corresponding to the commencement of the tight packing region for the films of NRS, 0.6RS and 1.2RS particles were less than the $A_{hex}$ value. The 1.8RS, 2.4RS, and 3.0RS particles gave films, where the $A_{starch}$ corresponding to the commencement of the tight packing region was larger than $A_{hex}$. Thus, the NRS, 0.6RS and 1.2RS particles are thought to have been less stable at the air/water interface than the 1.8RS, 2.4RS, and 3.0RS particles.

The effect of the structural modification of the starch particles on the packing of the starch particle at the air/water interface can be determined by using an optical microscope to image the starch particles in the Langmuir films at the air/water interface. **Figures 3–5** show the images of the Langmuir films of the native starch particles (NRS), and the OSA modified starch particles (0.6RS, 1.2RS, 1.8RS, 2.4RS, and 3.0RS) at air/water interfaces, when the films were compressed to surface pressure values of 5, 15, and 25 mN/m, respectively. These values were chosen as the surface pressure-$A_{starch}$ isotherms indicated that these three values should allow the different packing densities to be studied. The NRS particles can be seen to aggregate to give large, 3-dimensional types of aggregates at the air/water interface, regardless of the surface pressure (see the white boxes in **Figures 3–5**). These aggregates were compressed as the film was compressed, resulting in a surface pressure increase with an $A_{starch}$ decrease. A closely packed film of particles without holes could therefore not be formed at the air/water interface with the NRS particles due to this aggregation. This inability to form a closely packed film of particles may also be related to a loss of material to the subphase, due to the hydrophilicity of the native starch particles. In the case of the modified starch particles, films with holes were seen at $\Pi = 5$ mN/m. An increase in the degree of modification of the starch particles improved the packing of the particles in the film and consequently decreased the size of these holes seen in the film. The dark colored patches (see white circle in **Figure 3F**) in the film of 3.0RS particles showed that the 3.0RS particles could closely pack in the film or that multilayer aggregates were being formed in the film. The area occupied by these closely packed particles was much smaller than the ones seen in film of NRS particles. Thus, the mechanism causing these particles to closely pack or aggregate is thought to be different than that which caused the NRS particles to form the large aggregates in the interfacial film. Increasing the surface pressure to 15 mN/m reduced the size of the holes in the films of OSA modified starch particles (**Figure 4**). This result was explained by the fact that the air/water interfacial area available for the starch particles decreased as the surface pressure increased. This would cause the starch particles to pack closer together and to therefore reduce the area of bare air/water interfacial area. The number and size of the holes in the films decreased as the degree of modification was increased. The 1.2RS, 1.8RS, 2.4RS, and 3.0RS particles formed films without detectable holes. Areas of closely packed particles or aggregates were also observed at the air/water interface, see the dark patches of closely packed particles highlighted by the circles in the images in **Figure 4**. An increase in the surface pressure to 25 mN/m resulted in the 0.6RS, 1.2RS, 18RS, 2.4RS, and 3.0RS particles forming films of particles without detectable holes (**Figure 5**) and with dark patches of closely packed particles (see the white circles in **Figure 5**). The number of these dark patches appeared to increase with the

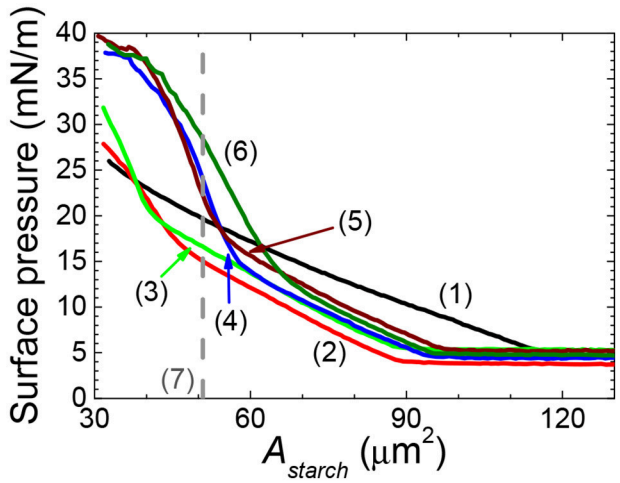


**FIGURE 2 |** Surface pressure-area per rice starch particle ($A_{starch}$) isotherm of films of native and OSA modified rice starch particles spread at an air/water interface. NRS: black solid line (1); 0.6RS: red solid line (2); 1.2RS: green solid line (3); 1.8RS: blue solid line (4); 2.4RS: wine color solid line (5); 3.0RS: olive color solid line (6). Area expected for a hexagonal packed layer of particles with mean starch size is shown by the dashed line (7).

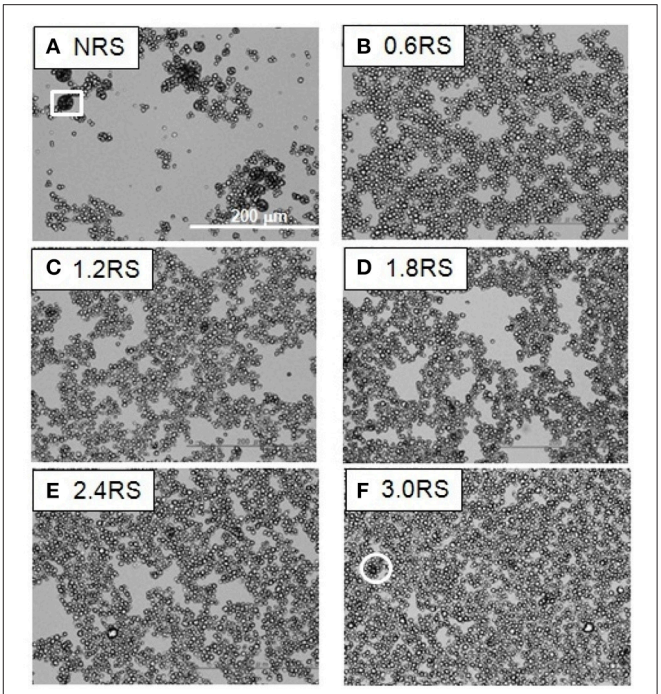


**FIGURE 3 |** Optical microscope images of films of native and OSA modified starch particles compressed to $\prod = 5$ mN/m at air/water interfaces. The white square shows an example of the large aggregates formed by the NRS particles. The white circles show examples of dark patches of closely packed OSA modified particles or aggregates in the films.

degree of modification of the rice starch particles. Comparison of the number of the dark patches in the films of 3.0RS particles measured at different surface pressures showed that a surface pressure increase caused the number of these patches to increase.

The packing type assigned to each film of particles at the air/water interface by analyzing the surface pressure-$A_{starch}$ isotherms was the same as those obtained by interpreting the optical images. This result indicates the reliability of the interpretation of the isotherms.

Information about the stability of the films of rice starch particles at the air/water interface and the interactions between the particles in the films can be obtained by measuring the compression-expansion cycle surface pressure-$A_{starch}$ isotherms of the films. **Figure 6** shows two cycle compression-expansion surface pressure-$A_{starch}$ isotherms for the native and OSA modified rice starch particles. In the first cycle of all of the isotherms, the expansion isotherms shifted to lower surface areas of the compression isotherms, when the $A_{starch}$ values measured at the same surface pressure were compared. This result indicates that the particles remained adhered to each other to some degree and did not immediately re-disperse at the air/water interface after compression, and/or that some of the starch particles were lost from the air/water interface to the subphase. Comparison of the isotherms measured in the first cycle with those measured in the second cycle also allows information about the strength of the adhesive force between the starch particles within the film and the stability of the particles at the interface to be obtained. If the isotherms move to lower surface areas, then the particles remained adhered to each other after the first compression, due to inter-particle attractions. Alternatively, some of the particles may have detached from the air/water interface into the water subphase. The compression-expansion isotherms shifted less to the left as the degree of modification of the rice starch particles was increased. Thus, the inter-particle attractions are thought to decrease with an increase in the degree of modification of the rice starch particles. An increase in the OSA modification is also thought to improve the stability of the particles at the air/water interface.

Increasing the degree of OSA modification of the rice starch particles increases the number of octenyl succcinate derivatives per glucose unit on the starch particle (Sweedman et al., 2013). The OSA modification is also reported to increase the hydrophobicity of the starch while also rendering the starch anionic (Nilsson and Bergenståhl, 2007a). This is because the octenyl succcinate substituent is hydrophobic and contains a carboxylic acid, which can also be negatively charged (Nilsson and Bergenståhl, 2007a), see **Figure 1B**.

In order to determine if the charge of the starch particles increased with an increase in the degree of the OSA modification, the zeta potential values of dispersions of native starch particles and dispersions of OSA modified starch particles in water were measured. These values are shown in **Table 1**. The zeta potential values increased from −19.8 mV for the NRS particles to −36.2 and −35.1 mV for the 2.4RS and the 3.0RS particles, respectively. In general, the zeta potential values became larger as the degree of the OSA modification was increased. The particles therefore tend to become more negatively charged

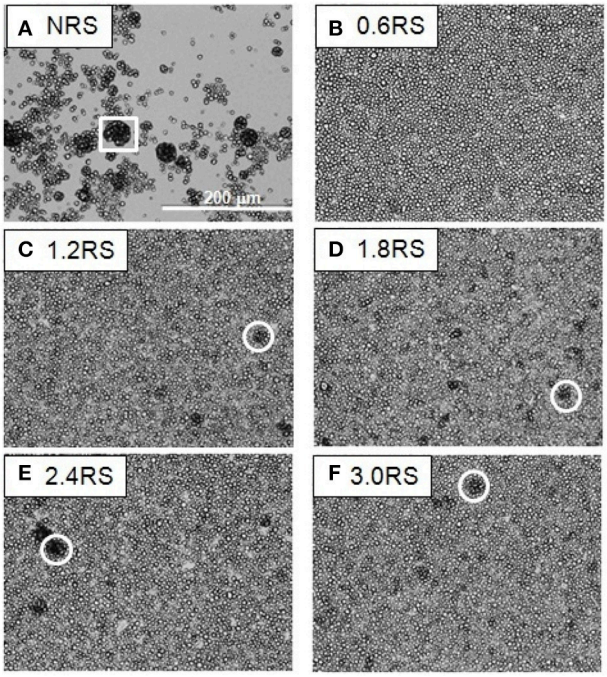


**FIGURE 4 |** Optical microscope images of films of native and OSA modified starch particles compressed to $\prod = 15$ mN/m at air/water interfaces. The white square shows an example of the large aggregates formed by the NRS particles. The white circles show examples of dark patches of closely packed OSA modified particles or aggregates in the films.

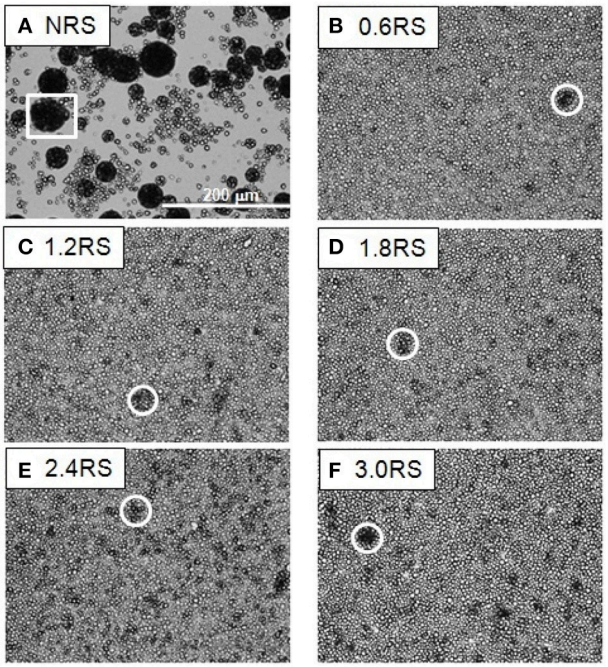


**FIGURE 5 |** Optical microscope images of films of native and OSA modified starch particles compressed to $\prod = 25$ mN/m at air/water interfaces. The white square shows an example of the large aggregates formed by the NRS particles. The white circles show examples of dark patches of closely packed OSA modified particles or aggregates in the films.

as the degree of OSA modification increases. This increase is explained by the increase in the number of octenyl succcinate derivatives per glucose unit on the starch particles as the degree of the OSA modification is increased, where the negative charge is resulting from by the carboxylic acid substituent. The zeta potential of O/W emulsions stabilized by starch has also been reported to become more negative as the degree of OSA substitution is increased (Miao et al., 2014). The presence of the charge on the starch particle from the OSA modification would increase the inter-particle electrostatic repulsions in the film, causing the aggregation of the starch particles at the air/water interface to be reduced. The hydrophobicity of the OSA substituent gives the starch particle a degree of hydrophobicity, resulting in the starch particle showing surface active properties. It may also increase the inter-particle hydrophobic attractions within the film of particles at the air/water interface.

Attractive hydrophobic interactions can result between surfaces containing hydrophobic groups, such as long-chain alkanes, when they come in close proximity in aqueous systems. The strength of this hydrophobic interaction is thought to increase with the hydrophobicity of the surface. Increasing the degree of OSA modification of the starch particle would increase the number of the octenyl succcinate derivatives on the starch, which should cause the hydrophobicity of the starch particles to increase. Thus, the inter-particle hydrophobic attractions between the starch particles at the air/water interface were expected to increase with the degree of OSA modification. This therefore should have increased the aggregation of particles in the film at the air/water interface. A very strong attraction between the particles is expected to lead to a fractal type of aggregation (Joanicot et al., 1990; Mastushita et al., 1997), which therefore would increase the number of holes seen in the particle film at the air/water interface. Decreasing the surface area by closing the barriers causes the packing density of the particles in the film to increase. Thus, we would expect an increased attraction between the particles and aggregation with an increased compression of the film, due to capillary forces. The capillary forces would cause particles to aggregate more as the particles become more hydrophobic. The particles were therefore expected to aggregate more with an increased OSA modification. This was, however, not observed. The isotherms and optical images of the films of rice starch particles at the air/water interface shown in **Figures 1–5** indicated that the packing of the particles in the film improved with the degree of modification of the rice starch particles and the surface pressure of the film. These results suggest that the presence of charged groups from the octenyl succcinate derivatives modulates the inter-particle hydrophobic interactions between the octenyl succcinate derivatives on the starch particles. This effect caused us not to observe this fractal type of aggregation.

The difference in the physical properties of the films of the native and modified starch particles at the air/water interface

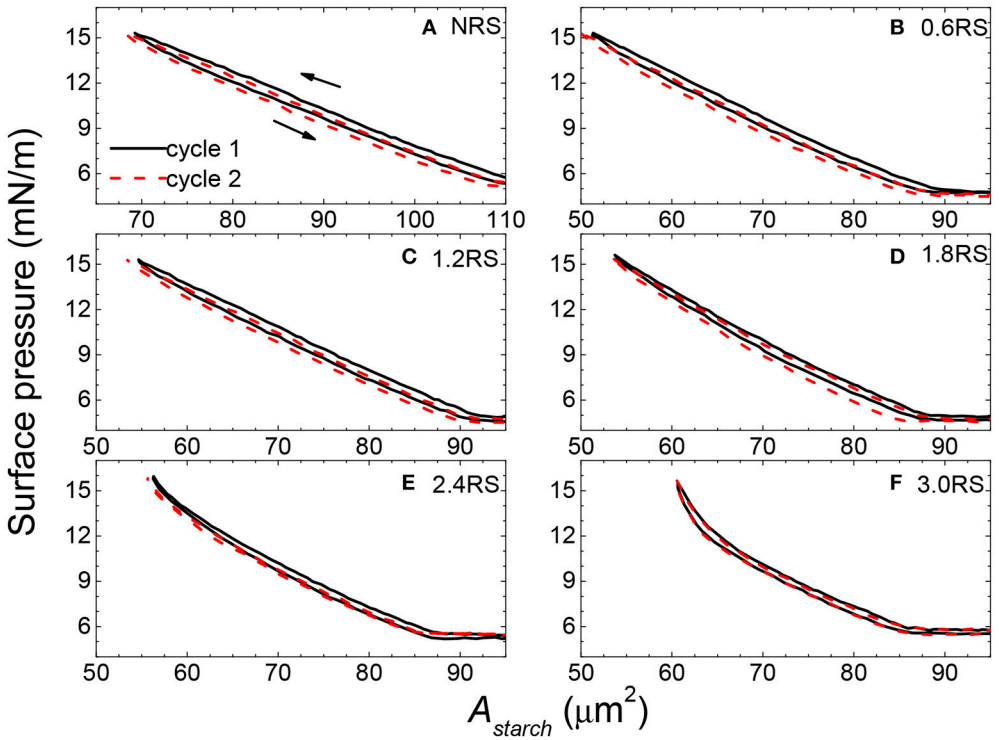


**FIGURE 6 |** Two compression-expansion cycle surface pressure-area per rice starch particle ($A_{starch}$) isotherm of films of native and OSA modified rice starch particles spread at an air/water interface. The black solid line and the red dashed line show the first and second cycle compression-expansion isotherms, respectively.

**TABLE 1 |** Zeta potential (ζ) values measured of 100 ppm concentration of native or modified starches dispersed in water or aqueous solutions containing NaCl, where the concentration of NaCl is given by [NaCl].

| Sample | [NaCl] (mM) | ζ (mV) |
|---|---|---|
| NRS | 0 | −19.8 ± 1.2 |
| 0.6RS | 0 | −27.8 ± 1.0 |
| 1.2RS | 0 | −34.1 ± 0.7 |
| 1.8RS | 0 | −32.5 ± 2.5 |
| 2.4RS | 0 | −36.2 ± 1.1 |
| 3.0RS | 0 | −35.1 ± 1.8 |
| 3.0RS | 1 | −29.7 ± 0.7 |
| 3.0RS | 10 | −24.9 ± 1.1 |
| 3.0RS | 100 | −8.4 ± 0.7 |

was further investigated by measuring the force-distance curves between a starch particle attached to an AFM cantilever (probe) in the water phase and a film of starch particles at the air/water interface. The same starch particle type that was used to form the film of particles was used as the probe. Forces were measured for the NRS, 0.6RS, and 3.0RS systems, in order to determine the effect of modifying the rice starch structure and the degree of modification. **Figures 7A–C** show example approach force curves for the NRS starch particles, the 0.6RS starch particles, and the 3.0RS starch particles, respectively, when the films were compressed to $\prod$=5, 10, and 15 mN/m. The zero of the separation distance in the approach force curves was set as the distance where the linear contact region commenced, i.e., the distance where the probe started to be in contact with the particle films at the air/water interface. An attraction was observed in the approach force curves for the NRS particles for all the surface pressures, while the approach force curves for 0.6RS and 3.0RS gave a repulsion. The insets in **Figure 7** show the force vs. separation distance curves on a magnified scale, showing the shift from the attraction to repulsion more clearly. The strength of this repulsion increased with the degree of modification of the rice starch particle. Increasing the degree of modification of the rice starch particles increases the number of octenyl succcinate derivatives per glucose unit on the starch particle. The increase in repulsion with the degree of modification of the rice starch particles can therefore be explained by this increase in number of octenyl succcinate derivatives, which are charged. The slope of the approach force in the linear contact region in the approach force curves changed with the degree of modification and surface pressure. The stiffness ($S_N$) of the film of particles at the air/water interface was calculated from the slope of this region. An increase in the slope of this region indicates an increase in the interface stiffness. The retract force curves (not shown) showed an adhesion, the strength of this adhesion was calculated to give the adhesive force ($F_{ad}$).

**Figure 8A** shows the effect of the degree of modification of the rice starch particles and the surface pressure of the film of particles at the air/water interface on the adhesive force

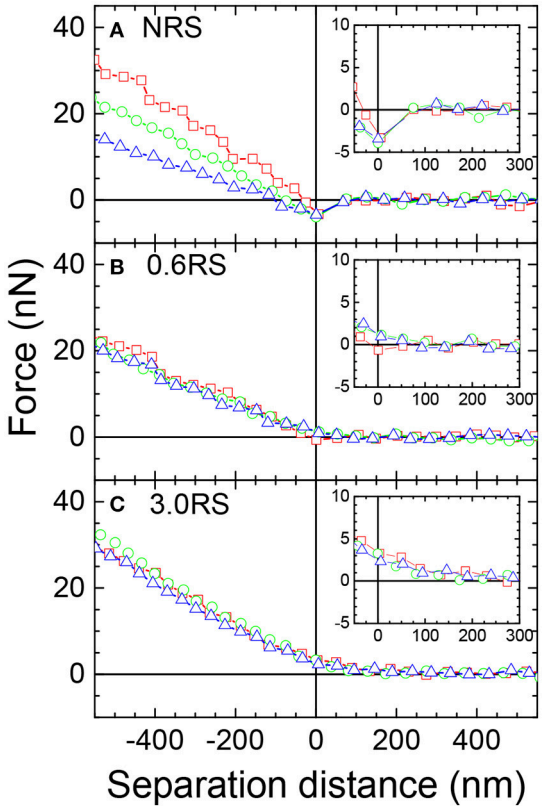


**FIGURE 7 |** Example approach force curves between a starch particle (probe) in the water phase and a bare air/water interface or a starch film at an air/water interface, where the same particle type used to prepare the films was used as the probe. Red open squares: starch particle film compressed to $\Pi = 5$ mN/m; green open circles: starch particle film compressed to $\Pi = 10$ mN/m; blue open triangles: starch particle film compressed to $\Pi = 15$ mN/m. The insets show the force vs. separation distance curves on a magnified scale, showing the shift from the attraction to repulsion more clearly.

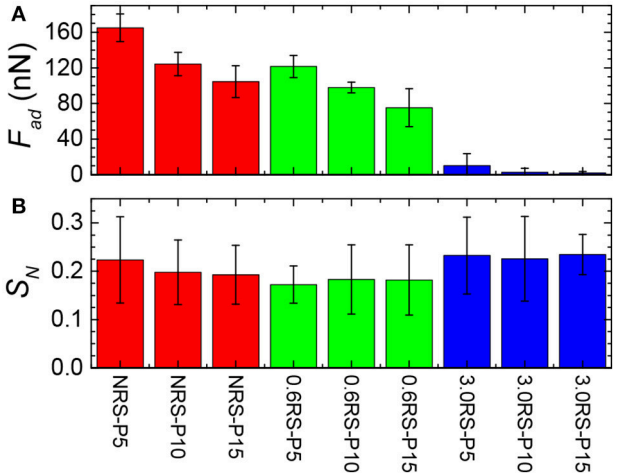


**FIGURE 8 |** Effect of degree of modification of starch particle on the adhesion ($F_{ad}$) of the starch particle to the film composed of the same starch particles at an air/water interface and the stiffness of the film ($S_N$). **(A)** Adhesive force; **(B)** stiffness of the films at the air/water interface. NRS-P5: Film of NRS particles compressed to $\Pi = 5$ mN/m; NRS-P10: Film of NRS particles compressed to $\Pi = 10$ mN/m; NRS-P15: Film of NRS particles compressed to $\Pi = 15$ mN/m; 0.6RS-P10: Film of 0.6RS particles compressed to $\Pi = 5$ mN/m; 0.6RS-P10: Film of 0.6RS particles compressed to $\Pi = 10$ mN/m; 0.6RS-P15: Film of 0.6RS particles compressed to $\Pi = 15$ mN/m; 3.0RS-P10: Film of 3.0RS particles compressed to $\Pi = 5$ mN/m; 3.0RS-P10: Film of 3.0RS particles compressed to $\Pi = 10$ mN/m; 3.0RS-P15: Film of 3.0RS particles compressed to $\Pi = 15$ mN/m.

($F_{ad}$) measured between a rice starch particle in the water phase and the film of particles at the air/water interface. The adhesive force tended to decrease with an increase in the degree of modification of the rice starch particles and with an increase in the surface pressure of the film of particles at the air/water interface. A decrease in the adhesive force indicates that the attractive forces between two starch particles separated by water have decreased. The introduction of an inter-particle electrostatic repulsion could explain this decrease in the adhesive force. The increase in number of charged octenyl succcinate derivatives on the rice starch particles with an increased degree of modification of the rice starch particles could cause this increase in the electrostatic repulsion between two rice starch particles. Additionally, compressing the film, i.e., decreasing the separation distance between the particles in the film, would increase the charge density of the film, causing the magnitude of the electrostatic repulsion to increase. The surface pressure was observed to increase with the film compression. Thus, the adhesive force may also have decreased with a surface pressure increase, due to this increased electrostatic repulsion.

**Figure 8B** shows the effect of the degree of modification of the rice starch particles and the surface pressure of the film of particles at the air/water interface on the stiffness ($S_N$) of the film of particles at the air/water interface. There was only a small change in the measured surface stiffness between systems formed using the NRS, 0.6RS, and 3.0RS particles, when the same surface pressure values were compared. The stiffness of the films of 0.6RS particles was seen to be a little less than that of the film formed by the NRS particles. The stiffness of the film of 3.0RS particles was, however, a little greater than that of the films of NRS or 0.6RS particles. The lack of change in the stiffness for the particle types is thought to be related to the surface pressures used in the MPIA experiments. If the interface was held at a high enough surface pressure, then there would have been little flexibility in the interface. The forces measured would then have been dominated by the probe particle and the immediate particle in the interface that it contacts. This would have caused the influence of the surrounding network to be reduced.

**Figure 8B** also showed that the stiffness of the films of particles tended to decrease with a surface pressure increase for the NRS particles. The stiffness, however, either increased with the surface pressure or was independent of the surface pressure for the 0.6 RS and 3.0 RS particles. This change in the stiffness with surface pressure tendency indicates that the mechanism controlling the stiffness of the air/water interface in the presence of a film

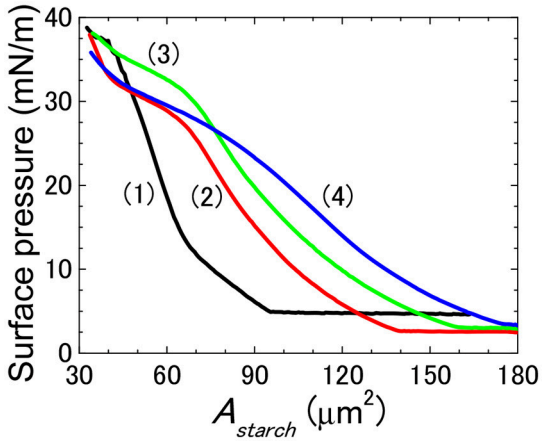


**FIGURE 9 |** Effect of adding NaCl to the water to the surface pressure-$A_{starch}$ isotherms of films of 3.0RS starch particles at air/aqueous interface. Water subphase: black solid line (1); 1 mM NaCl subphase: red solid line (2); 10 mM NaCl subphase: green solid line (3), and 100 mM NaCl subphase: blue solid line (4).

of particles were different for the native and modified starch particles.

The stiffness of a film of particles at the air/water interface is controlled by the surface tension of the interface, the stiffness of the particles, and continuity or integrity of the film. The stiffness of an interface decreases with the surface tension (or increased surface pressure) of the film. A film of loosely packed particles would contain areas of air/water interface that are bare and areas that are covered by particles. The size of the area of the air/water interface that is bare and therefore not covered by particles decreases with an increase in the particle packing density. As the surface tension of a bare air/water interface is higher than the surface tension of an air/water interface with adsorbed matter, the surface tension of a film of particles at the air/water interface would decrease with a surface pressure increase. This would cause the stiffness of the air/water interface with the particles to decrease with a surface pressure increase. The stiffness of an interface would also increase with an increased stiffness or hardness of the material adsorbed at the air/water interface. A change in the stiffness of the particles with the modification of the starch particles would therefore also affect the stiffness of the film of particles at the air/water interface. Starch gels made from OSA starch are reported to be softer than starch gels made from native starch (Ovando-Martinez et al., 2017). Thus, the stiffness of the starch particles is expected to decrease with an increase in the degree of OSA modification. The stiffness of the interface is also affected by the discontinuity of a film of particles at an air/water interface. The particles in a film of particles without holes would be capable of being moved more by a particle colliding with it from the bulk water than a film of particles without holes, causing its stiffness to be less than a film without holes (Azakami et al., 2017).

The decrease in the stiffness of the film of NRS particles at an air/water interface with a surface pressure increase shows that the surface tension effect affected the stiffness of that film. This result is also supported by that fact that the optical images of the films of NRS particles at air/water interfaces showed areas of bare water surface and areas covered by large aggregates of particles. A film of closely packed particles was not formed by the NRS particles, indicating that the film also contained a large degree of discontinuity, which would also tend to decrease the stiffness of the film.

The stiffness of the films of 0.6RS and 3.0RS particles did not decrease with the surface pressure. This result indicates that the surface tension effect was not the determining factor controlling the film stiffness for these particle types. The 3.0RS film was also seen to give a stiffer film than the 0.6RS film. As the stiffness of the starch particles are expected to decrease with an increase in the degree of OSA modification, this increase cannot be explained by the change in the stiffness of the actual starch particle resulting from a change in the degree of OSA modification.

An increase the surface pressure of a film of OSA modified rice starch particles at the air/water interface caused the particles to pack closer in the film and the number of holes in the film to decrease. An increase in the degree of OSA modification also decreased the number of holes in the film and allowed the particles to pack closer in the film. The increase in the stiffness of the film with the degree of OSA modification and surface pressure increase is therefore explained by the decrease in the number of holes in the film of particles at the air/water interface, due to an improved ability of the particles to pack in the film. This improved packing is explained by the increase in the inter-particle electrostatic repulsions resulting from the OSA modification. The particles in a film of loosely packed particles would be moved by the starch particle probe in the bulk water that is brought in contact with the film of starch particles. This lateral movement of particles within the film would cause the film to be disturbed and partially broken. The particles in a film that is made up of closely packed particles would be less capable of moving laterally at the air/water interface, due to a lack of free area and the presence of the inter-particle electrostatic repulsions acting within the film. Thus, the film would be less perturbed by the starch particle probe in the bulk water, causing this film to be stronger than the film with aggregating particles and holes. Thus, the stiffness increase with a surface pressure increase or an increase in the degree of OSA modification is explained by a decrease in the discontinuity in the film of particles at the air/water interface, i.e., a decrease in the number of holes in the film of particles. The increased surface pressure caused the particles to be pushed together, resulting in a more homogenous film without holes.

## Effect of the Addition of Salt to the Physical Properties of Films of 3.0RS Particles at an Air/Aqueous Interfaces

The results of the above section suggested that the well-dispersed and tight packing film of 3.0RS particles was obtained due to the presence of charged groups on the starch particle, which were introduced due to the OSA modification of the starch particles. If the starch particles are forming the tight packing film without

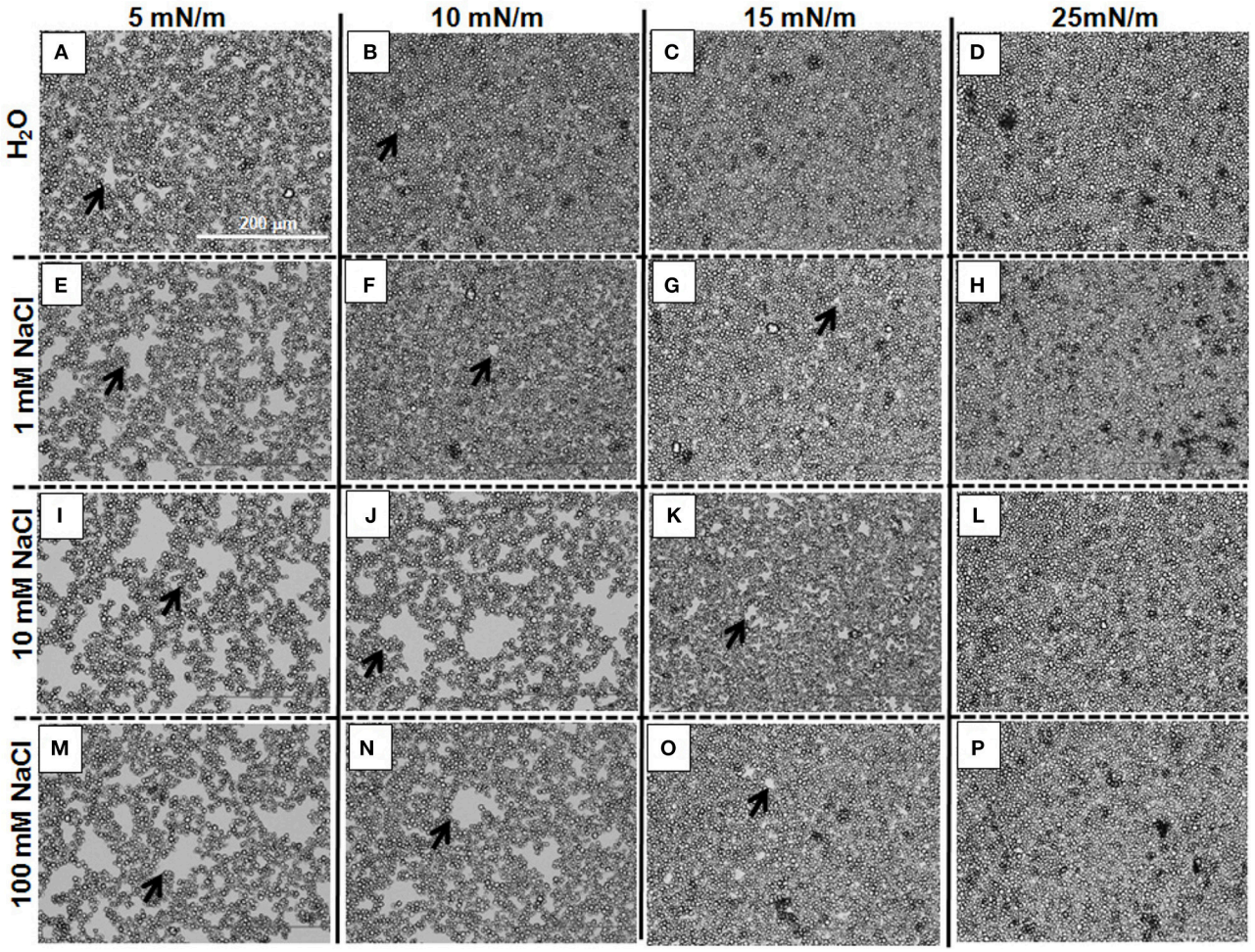


**FIGURE 10 |** Optical microscope images showing the effect of adding NaCl to the water of films of 3RS particles at air/aqueous interfaces compressed to 5, 10, 15, and 25 mN/m. Water subphase: **(A–D)**; 1 mM NaCl subphase: (**E–H)**; 10 mM NaCl subphase: **(I–L)**; 100 mM NaCl subphase: **(M–P)**. $\Pi = 5$ mN/m: **(A,E,I,M)**; $\Pi = 10$ mN/m: **(B,F,J,N)**; $\Pi = 15$ mN/m: **(C,G,K,O)**; $\Pi = 25$ mN/m: **(D,H,L,P)**. The black arrows show examples of holes in the films of particles at the air/aqueous interfaces.

holes due to the inter-particle electrostatic repulsions resulting from these charged groups, then the introduction of salt into the water subphase should change these inter-particle interactions.

The effect of adding salt to water on which the particles formed the films was firstly investigated by measuring the surface pressure-$A_{starch}$ isotherms for the films of 3.0RS particles spread on water, and on aqueous solutions containing 1, 10, and 100 mM NaCl (**Figure 9**). The isotherms are seen to shift to larger $A_{starch}$ values for surface pressures $< \sim$25 mN/m, as the concentration of salt in the water increased. The isotherms converged to the same area per 3.0RS particle value for high surface pressure values (>35 mN/m), i.e., highly compressed films.

The surface tension of air/aqueous solutions containing NaCl can be calculated to increase by 0.28% when the concentration of NaCl was increased from 0.1 to 100 mM, if the values of the apparent relative surface tensions of air/NaCl aqueous solutions are compared (Jones and Ray, 1941). As the surface tension change accompanying an NaCl concentration increase is small, the shift in the isotherms due to the NaCl concentration increase is thought to be due to another reason.

Information as to why the isotherms shift to larger $A_{starch}$ values with a salt concentration increase was obtained by using an optical microscope to observe the films of 3.0RS particles at the different subphases. **Figure 10** shows the images obtained for the films of 3.0RS particles on subphases of water, 1, 10, and 100 mM NaCl, when the films were compressed to 5, 10, 15, and 25 mN/m. The size and number of the holes in the films (examples shown by the black arrows in **Figure 10**) tended to increase with the concentration of salt in the water subphase. The size and number of these holes also decreased with a surface pressure increase. Few holes were visible at the high surface pressure value of 25 mN/m. These holes are thought to be formed due to the aggregation of particles within the films at the air/aqueous interface. An increase in the number and size of holes can be explained by an increase in the particle aggregation. The holes were no longer visible when the films were highly compressed, i.e., at high surface pressures.

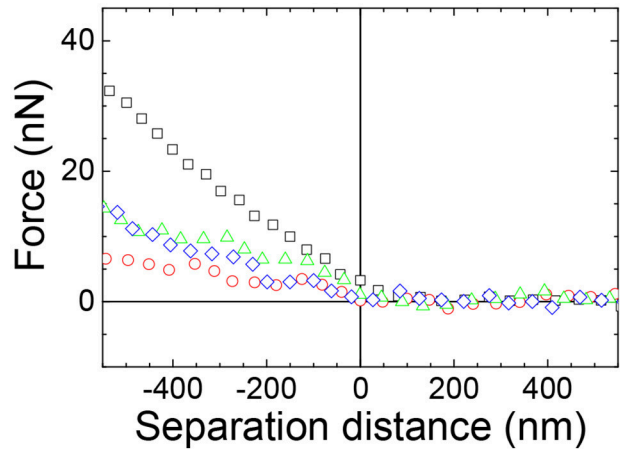


**FIGURE 11 |** Example approach force curves between a 3.0RS starch particle (probe) in the aqueous phase and a 3.0RS starch film at an air/aqueous interface compressed to 10 mN/m showing the effect of adding NaCl to the water. Water subphase: black squares; 1 mM NaCl subphase: red circles; 10 mM NaCl subphase: green triangles; 100 mM NaCl subphase: blue diamonds.

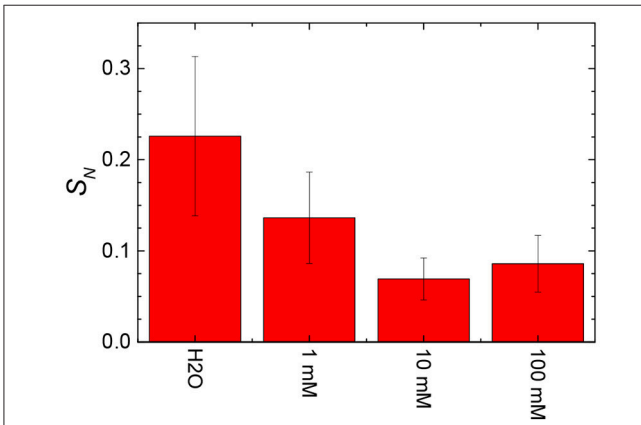


**FIGURE 12 |** Effect of the addition of salt to the water on the stiffness of films ($S_N$) of 3.0RS particles compressed to $\Pi = 10$ mN/m at air/aqueous interfaces.

The shift in the isotherms to higher $A_{starch}$ values with a salt concentration increase can be explained by the presence of these holes.

The effect of the presence of the holes formed at higher ionic strength of the aqueous subphase on the stiffness of the films of particles was next investigated. The force curves between a 3.0RS particle in the subphase and films of 3.0RS particle compressed to 10 mN/m at air/aqueous interfaces were recorded with 0, 1, 10, and 100 mM NaCl in the subphase (**Figure 11**). The surface pressure of 10 mN/m was chosen, as this surface pressure best showed the influence of the salt presence. A repulsive force was observed, regardless of the concentration of NaCl in the subphase. The slope of the approach force in the linear contact region in the approach force curves changed with the concentration of NaCl added to the water. The retract force curves (not shown) showed a repulsion, causing the strength of the adhesion to be very small or negligible.

The stiffness values obtained from the slope of the linear contact area of the approach force curves were calculated and are shown in **Figure 12** as a function of the concentration of NaCl in the subphase. The stiffness values tended to decrease with an increase in the NaCl concentration from 0 to 10 mM. An increase in the concentration from 10 to 100 mM NaCl appeared to slightly increase the stiffness of the film of particles at the air/aqueous interface.

In general, the stiffness of the film of particles tended to decrease with an increase in the number and size of holes in the film of particles. The decreased stiffness can be explained by an increased discontinuity in the particle film, due to the presence of the holes.

Previous studies investigating the physical properties of a monolayer of charged surfactants at air/aqueous interfaces showed that the addition of salt to the water subphase changed the packing of the monolayer and caused the stiffness of the interface to increase with high NaCl concentrations (McNamee et al., 2012). This increase was explained by either the increased stiffness of the air/aqueous interface itself for highly concentrated salt solutions and/or an increased dehydration of the monolayer. Thus, the slight increase in the stiffness of the film of particles at the air/100 mM NaCl interface that was seen in this present study is thought to be related to the dehydration of the interface by the high salt concentration. Here we also note, though, that the starch particles themselves are expected to be hydrated.

The formation of holes due to the increased aggregation of particles within the films at the air/aqueous interface with a salt concentration increase can be explained by a decrease in the magnitude of the inter-particle electrostatic repulsions. The electrostatic repulsion between two charged surfaces separated by an aqueous solution decreases with an ionic strength increase due to an increase in the screening of the charged surfaces (Israelachvili, 2011). This decrease in the electrostatic repulsion can also be understood by the decrease in the Debye length (Israelachvili, 2011) of a charged surface in aqueous solutions containing NaCl, when the NaCl concentration was increased from 1 to 100 mM. The Debye length for an aqueous solution containing 1, 10, and 100 mM NaCl can be calculated to be 9.62, 3.04, and 0.96 nm, respectively. The effect of adding NaCl to the water on the charge of the 3.0RS particles was also determined by measuring the zeta potentials of the 3.0RS particles dispersed in water and in aqueous solutions containing NaCl. **Table 1** shows that the zeta potential of the 3.0RS particles decreased from −35.1 to −8.4 mV, as the concentration of NaCl was increased from 0 to 100 mM. Thus, NaCl was concluded to screen the charges on the 3.0RS particles.

The force acting between two particles is the resultant of the attractive and repulsive forces. The effect of the inter-particle attractive forces would therefore be more prevalent in the total forces acting between the two particles in the presence of salt. Other studies have also shown that the addition of salt to starch granule stabilized emulsions for starch modified with OSA to 4.66% increased the size of the droplet, which was explained by an

increased droplet aggregation (Rayner et al., 2012a). These results also therefore indicate that the addition of salt can increase the attractions in the system. Screening of the charge on the particles by an increased NaCl concentration would cause the rice particle to appear more hydrophobic. The lateral capillary force would cause particles to aggregate more as the particles become more hydrophobic.

Modification of the rice starch particles caused octenyl succcinate derivatives to be introduced on the starch particle, which contained both charge and hydrophobicity. In the absence of salt in the water subphase, the presence of the charge reduced the aggregation of the particles at the air/aqueous interface. This was explained by the inhibition of the inter-particle hydrophobic attractions resulting from the charge of the octenyl succcinate derivatives. The addition of salt to the water subphase caused these charges to be screened. As a result, the hydrophobic octenyl succcinate derivatives could have come into contact closer, causing the strength of the inter-particle hydrophobic attractions to increase. These attractions would have caused the particles to aggregate and form islands at the air/aqueous interface. Holes would be present in the film of particles, when the particles are not compressed enough to remove the spaces between the islands. The stiffness of the film of particles with holes is lower than one without holes. It would therefore be necessary to compress the films to higher amounts in order to achieve a dense packing density, if a stiff and strong film of particles is required with OSA modified starch particles used at air/aqueous interfaces containing salts.

## CONCLUSIONS

Native rice starch particles formed large aggregates at air/water interfaces. A two-dimensional film of particles could not be formed with these particles at an air/water interface. The modification of the rice starches particles decreased the aggregation of the starch particles, due to the introduction of a charged group on the starch particle. Increasing the degree of modification improved the particle packing within the film of particles at the air/water interface, due to the increase in the magnitude of the inter-particle electrostatic interactions arising from the greater number of charged groups on the particles. The stiffness of the film also increased with the degree of modification, due to this improved particle packing. Introduction of salt to the water phase caused the particles to aggregate and form holes within the film, due to screening of the charged groups on the starch particles. The presence of these holes decreased the stiffness of the films.

The packing and stiffness of films of starch particles formed at hydrophobic/hydrophilic interfaces in the absence of salt can be improved by increasing the degree of modification of the starch particles. In the presence of salt, the films of particles must be compressed to give a high packing density, in order to remove holes in the films of the particles. Such holes would decrease the stiffness of the films.

## AUTHOR CONTRIBUTIONS

CM: Designed the study, performed the research, wrote the manuscript; YS and IF: Performed the research; MK: Provided new methods; BW: Prepared the starch particles; TN, MR, and AM: Designed the study and wrote the manuscript; and all authors approved the revisions.

## ACKNOWLEDGMENTS

The authors would like to thank Prof. Hans-Jürgen Butt (Max Planck Institute for Polymer Research, Germany) for support and discussions concerning this study.

## REFERENCES

Aussillous, P., and Quéré, D. (2001). Liquid marbles. *Nature* 411, 924–927. doi: 10.1038/35082026

Aveyard, R., Clint, J. H., Nees, D., and Paunov, V. N. (2000). Compression and structure of monolayers of charged latex particles at air/water and octanve/water interfaces. *Langmuir* 15, 1969–1979. doi: 10.1021/la990887g

Azakami, Y., Kappl, M., Fujii, S., Yusa, S., and McNamee, C. E. (2017). Effect of the addition of a cross-linker and the water pH on the physical properties of pH-responsive polymer particles at air/water interfaces. *ACS Omega* 2, 7837–7848. doi: 10.1021/acsomega.7b01241

Barnes, G. T., and Gentle, I. R. (2005). *Interfacial Science an Introduction*. Oxford: Oxford University Press.

Bleibel, J., Domínguez, A., and Oettel, M. (2013). Colloidal particles at fluid interfaces: effective interactions, dynamics and a gravitation-like instability. *Eur. Phys. J. Spec. Top*. 222, 3071–3087. doi: 10.1140/epjst/e2013-02076-9

Bormashenko, E. (2011). Liquid marbles: properties and applications. *Curr. Opin. Colloid Interface Sci.* 16, 266–271. doi: 10.1016/j.cocis.2010.12.002

Chevalier, Y., and Bolzinger, M. (2013). Emulsions stabilized with solid nanoparticles: pickering emulsions. *Colloid Surf. A Physicochem. Eng. Asp*. 439, 23–34. doi: 10.1016/j.colsurfa.2013.02.054

Dinsmore, A. D., Hsu, M. F., Nikolaides, M. G., Marquez, M., Bausch, A. R., and Weitz, D. A. (2002). Colloidosomes: selectively permeable capsules composed of colloidal particles. *Science* 298, 1006–1009. doi: 10.1126/science.1074868

Gillies, G., Büscher, K., Preuss, M., Kappl, M., Butt, H.-J., and Graf, K. (2005). Contact angles and wetting behaviour of single micron-sized particles. *J. Phys. Condens. Matter*. 17, S445–S464. doi: 10.1088/0953-8984/17/9/011

Hui, R., Qi-he, C., Ming-liang, F., and Guo-qing, H. (2009). Preparation and properties of octenyl anhydride modified potato starch. *Food Chem*. 114, 81–86. doi: 10.1016/j.foodchem.2008.09.019

Israelachvili, J. N. (2011). *Intermolecular and Surface Forces*. Amsterdam: Academic Press.

Jane, J.-L., Kasemsuwan, T., Leas, S., Zobel, H., and Robyt, J. F. (1994). Anthology of starch granule morphology by scanning electron microscopy Starch. *Starch* 46, 121–129. doi: 10.1002/star.19940460402

Joanicot, M., Wong, K., Maquet, J., Chevalier, Y., Pichot, C., Graillat, C., et al. (1990). Ordering of latex particles during film formation. *Progr. Colloid Polym. Sci*. 81, 175–183. doi: 10.1007/BFb0115548

Jones, G., and Ray, W. A. (1941). The surface tension of solutions of electrolytes as a function of the concentration. III. Sodium Chloride. *J. Am. Chem. Soc*. 63, 3262–3263. doi: 10.1021/ja01857a007

Kralchevsky, P. A., and Nagayama, K. (2000). Capillary interactions between particles bound to interfaces, liquid films and biomembranes. *Adv. Colloid Interface Sci*. 85, 145–192. doi: 10.1016/S0001-8686(99)00016-0

Li, C., Li, Y., Sun, P., and Yang, C. (2013). Pickering emulsions stabilized by native starch granules. *Colloid Surf. A Physicochem. Eng. Asp*. 431, 142–149. doi: 10.1016/j.colsurfa.2013.04.025

Marefati, A., Wiege, B., Haase, N. U., Matos, M., and Rayner, M. (2017). Pickering emulsifiers based on hydrophobically modified small granular starches – Part I: manufacturing and physico-chemical characterization. *Carbohydr. Polym*. 175, 473–483. doi: 10.1016/j.carbpol.2017.07.044

Mastushita, S., Miwa, T., and Fujishima, A. (1997). Distribution of components in composite two-dimensional arrays of latex particles and evaluation in terms of the fractal dimension. *Langmuir* 13, 2582–2584. doi: 10.1021/la960710b

McNamee, C. E., Fujii, S., Yusa, S., Azakami, Y., Butt, H.-J., and Kappl, M. (2015). The forces and physical properties of polymer particulate monolayers at air/aqueous interfaces. *Colloid Surf. A Physicochem. Eng. Asp*. 470, 322–332. doi: 10.1016/j.colsurfa.2014.12.035

McNamee, C. E., Graf, K., Butt, H.-J., Higashitani, K., and Kappl, M. (2011). Interaction between a silica particle and the underside of a polymer monolayer at the air/water interface in the presence of an anionic surfactant. *Colloid Surf. A Physicochem. Eng. Asp*. 383, 32–40. doi: 10.1016/j.colsurfa.2010.11.030

McNamee, C. E., and Kappl, M. (2016). Forces and physical properties of Langmuir monolayers of TiO2 particles at air/water interfaces after collisions by a particle in the water. *RSC Adv*. 6, 54440–54448. doi: 10.1039/C6RA09499F

McNamee, C. E., Kappl, M., Butt, H.-J., Higashitani, K., and Graf, K. (2010). Interfacial forces between a Silica particle and phosphatidylcholine monolayers at the air-water interface. *Langmuir* 26, 4574–14581. doi: 10.1021/la1019839

McNamee, C. E., Kappl, M., Butt, H.-J., Nguyen, H., Sato, S., Graf, K., et al. (2012). Effect of the degree of dissociation of molecules in a monolayer at an air/water interface on the force between the monolayer and a like-charged particle in the subphase. *J. Phys. Chem. B*. 116, 274–281. doi: 10.1021/jp307343a

Miao, M., Li, R., Cui, S. W., Zhang, T., and Jin, Z. (2014). Structure and physicochemical properties of octenyl succinic esters of sugary mainz soluble starch and waxy maize starch. *Food Chem*. 151, 154–160. doi: 10.1016/j.foodchem.2013.11.043

Min, Y., Akbulut, M., Kristiansen, K., Golan, Y., and Israelachvili, J. (2008). The role of interparticle and external forces in nanoparticle assembly. *Nat. Mater*. 7, 527–538. doi: 10.1038/nmat2206

Ngyugen, H., and McNamee, C. E. (2014). Determination and comparison of how the chain number and chain length of a lipid affects its interactions with a phospolipid at an air/water interface. *J. Phys. Chem. B*. 118, 5901–5912. doi: 10.1021/jp500840a

Nilsson, L., and Bergenståhl, B. (2007a). Adsorption of hydrophobically modified anionic starch at oppositely charged oil/water interfaces. *J. Colloid Interface Sci*. 308, 508–513. doi: 10.1016/j.jcis.2007.01.024

Nilsson, L., and Bergenståhl, B. (2007b). Emulsification and adsorption properties of hydrophobically modified potato and barley starch. *J. Agric. Food Chem*. 55, 1469–1474. doi: 10.1021/jf062087z

Odeku, O. A., and Itiola, O. A. (2007). Compaction properties of three types of starch. *Iran. J. Pharm. Res.* 6, 17–23.

Ovando-Martinez, M., Whitney, K., Ozsisli, B., and Simsek, S. (2017). Physicochemical properties of octenyl succinic esters of cereal, tuber and root starches. *J. Food Process Preserv*. 41, 1745–4549. doi: 10.1111/jfpp.12872

Pickering, S. U. (1907). Emulsions. *J. Chem. Soc*. 91, 2001–2021. doi: 10.1039/CT9079102001

Rayner, M., Sjöö, M., Timgren, A., and Dejmek, P. (2012a). Quinoa starch granules as stabilizing particles for production of Pickering emulsions. *Faraday Discuss*. 158, 139–155. doi: 10.1039/c2fd20038d

Rayner, M., Timgren, A., Sjöö, M., Dejmek, P., and Walgren, M. (2012b). Quinoa starch granules: a candidate for stabilizing food-grade Pickering emulsions. *J. Sci. Food Agric*. 92, 1841–1847. doi: 10.1002/jsfa.5610

Saari, H., Heravifar, K., Rayner, M., Wahlgren, M., and Sjöö, M. (2016). Preparation and characterization of starch particles for use in pickering emulsions. *Cereal Chem*. 93, 116–124. doi: 10.1094/CCHEM-05-15-0107-R

Schultz, D. G., Lin, X.-M., Li, D., Gebhardt, J., Meron, M., Viccaro, P. J., et al. (2006). Structure, wrinkling, and reversibility of langmuir monolayers of gold nanoparticles. *J. Phys. Chem. B*. 110, 24522–24529. doi: 10.1021/jp063820s

Shogren, L., Viswanathan, A., and Felker, F., Gross, R. A. (2000). Distribution of octenyl succinate groups in octenyl succinic anhydride modified waxy maize starch. *Starch Starke* 52, 196–204. doi: 10.1002/1521-379X(200007)52:6/7<196::AID-STAR196>3.0.CO;2-4

Song, X., Pei, Y., Zhu, W., Fu, D., and Ren, H. (2014). Particle-stabilizers modified from indica rice starches differing in amylose content. *Food Chem*. 153, 74–80. doi: 10.1016/j.foodchem.2013.12.046

Sweedman, M. C., Tizzotti, M. J., Schäfer, C., and Gilbert, R. G. (2013). Structure and physicochemical properties of octenyl succinic anhydride modified starches: a review. *Carbohydr. Polym.* 92, 905–920. doi: 10.1016/j.carbpol.2012.09.040

Tesch, S., Gerhards, C. H., and Schubert, H. (2002). Stabilization of emulsions by OSA starches. *J. Food Eng*. 54, 167–174. doi: 10.1016/S0260-8774(01)00206-0

Thompson, K. L., Williams, M., and Armes, S. P. (2015). Colloidosomes: synthesis, properties and applications. *J. Colloid Interface Sci.* 447, 217–228. doi: 10.1016/j.jcis.2014.11.058

Trubiano, P. C. (1986). "Succinate and substituted succinate derivations of starch," in *Modified Starches: Properties and Uses*, ed O. B. Wurzburg (Roca Raton, FL: CRC Press), 131–148.

Whitney, K., Reuhs, B. L., Martinez, M. O., and Simsek, S. (2016). Analysis of ocetenylsuccinate rice and tapioca starches: distribution of octenylsuccinic anhydride groups in starch granules. *Food Chem*. 211, 608–615. doi: 10.1016/j.foodchem.2016.05.096

Yusoff, A., and Murray, B. S. (2011). Modified starch granules as particle-stabilizers of oil-in-water emulsions. *Food Hydrocoll*. 25, 42–55. doi: 10.1016/j.foodhyd.2010.05.004

**Conflict of Interest Statement:** The authors declare that the research was conducted in the absence of any commercial or financial relationships that could be construed as a potential conflict of interest.

frontiers in Chemistry

ORIGINAL RESEARCH
published: 02 July 2018
doi: 10.3389/fchem.2018.00259

# Dynamic Surface Wetting and Heat Transfer in a Droplet-Particle System of Less Than Unity Size Ratio

*Subhasish Mitra* and Geoffrey Evans*

*Discipline of Chemical Engineering, School of Engineering, Faculty of Engineering and Built Environment, University of Newcastle, Callaghan, NSW, Australia*

Dynamic surface wetting of particles in contact with droplet is a complex phenomenon ubiquitously encountered in many multiphase systems of industrial importance. In this study, we address this aspect by investigating impact behavior of a water droplet (diameter = 2.9 ± 0.1 mm) in the Weber number (*We*) range from ~4 to 104 on a stationary spherical brass particle (diameter = 10 mm) with and without heat transfer using a combination of high speed imaging and computational fluid dynamics (CFD) modeling approach. In cold state interactions (20°C), droplet exhibited oscillatory interfacial motion comprising periodic spreading and recoiling motion. Interactions involving heat transfer were studied in film boiling regime (350°C) and two outcomes were noted—droplet rebound and disintegration. A coupled Level Set and Volume of Fluid (VOF) approach based multiphase CFD model was utilized to predict the dynamic spread ratio and transient evolution of droplet shape during the interaction. To capture the complex contact line motion realistically, a continuous time varying profile of experimentally measured dynamic contact angles was used as a wall boundary condition for the cold interactions which provided good agreement with experimentally measured droplet spread ratio. In film boiling regime, droplet spread ratio was correlated to impact Weber number and a power law trend was obtained. Rebound and disintegration outcomes were characterized by the droplet-particle contact time. For simulating interactions in film boiling regime, a constant contact angle in the limit of super-hydrophobic surface was implemented in the CFD model to account for the apparent non-wetting effect due to vapor film formation at the contact area. A sensitivity analysis was performed involving three different contact angle boundary conditions ($\theta_S$ = 150, 160, and 170°) to represent the surface hydrophobicity. CFD model predicted interaction outcomes and droplet spread ratios were in reasonable agreement with the experiment at different impact Weber numbers. Increase in spherical surface heat flux and corresponding rise in droplet temperature at different impact Weber numbers were also quantified which showed an increasing trend up to a critical Weber number for droplet disintegration.

**Keywords: droplet-particle interaction, surface wetting, spreading, recoiling, dynamic contact angle, film-boiling, droplet evaporation, VOF-CFD**

OPEN ACCESS

***Edited by:***
*Syuji Fujii,*
*Osaka Institute of Technology, Japan*

***Reviewed by:***
*Sujata Tarafdar,*
*Jadavpur University, India*
*Petra Foerst,*
*Technische Universität München, Germany*

****Correspondence:***
*Subhasish Mitra*
*subhasish.mitra@newcastle.edu.au*

***Specialty section:***
*This article was submitted to Chemical Engineering, a section of the journal Frontiers in Chemistry*

***Received:*** *04 April 2018*
***Accepted:*** *08 June 2018*
***Published:*** *02 July 2018*

***Citation:***
*Mitra S and Evans G (2018) Dynamic Surface Wetting and Heat Transfer in a Droplet-Particle System of Less Than Unity Size Ratio. Front. Chem. 6:259. doi: 10.3389/fchem.2018.00259*

## INTRODUCTION

Dynamic wetting of particle surface is an important research aspect in the area of multiphase flows. Ample process applications such as spray coating of tablets in pharmaceutical applications (Hardalupas et al., 1999), vaporization of vacuum gas oil feed droplets in contact with catalyst particles in fluid catalytic cracking unit (Ge and Fan, 2007; Mitra et al., 2013, 2015, 2016, 2017; Nguyen et al., 2015; Banitabaei and Amirfazli, 2017), spray drying (Charalampous and Hardalupas, 2017), thermal cracking of bitumen feed in fluid coking unit, scrubbing of particulate matters from off-gas stream (Mitra et al., 2013, 2015, 2016, 2017) require adequate surface wetting of particles. Dynamic wetting of particle surface resulting from such interactions contribute significantly to the liquid distribution on particle surface, associated heat-mass transport processes, and chemical reactions each of which governs the process performance. Admittedly, a complete theoretical description of the droplet collision process with particles is a difficult problem due to the complex interplay among various hydrodynamic and thermodynamic factors such as deformable interface, three phase contact line motion, heat transfer at solid-liquid interface and evaporation at gas-liquid interface which occurs at different length and time scales.

Central to the surface wetting behavior is the three-phase contact line motion which changes drastically as a consequence of the several outcomes that are possible based on interacting droplet-particle size ratio ($\Delta$) such as deposition, rebound, disintegration ($\Delta < 1$) (Ge and Fan, 2007; Mitra et al., 2013, 2016); capture, penetration, disintegration ($\Delta > 1$) (Mitra et al., 2015), deposition, film formation and disintegration ($\Delta \sim 1$) (Bakshi et al., 2007; Gac and Gradon, 2014; Banitabaei and Amirfazli, 2017; Mitra et al., 2017). For $\Delta < 1$ scenario, upon impact on the solid surface, droplet spreads into a liquid lamella wherein the impact kinetic energy is transformed into the surface energy and the spreading process continues until the kinetic energy is completely dissipated and a maximum spreading state is reached. Following this, the spread-out lamella is retracted by the restoring surface tension force to minimize the surface area and initiates the recoiling phase.

The contact line motion in both spreading and recoiling phase is primarily governed by the competition between the inertia, capillary, viscous, and gravity force. Relative dominance of these forces are often expressed in terms of relevant dimensionless numbers i.e., Reynolds number $\left(Re = \frac{d_d v_d \rho_d}{\mu_d}\right)$ as ratio of inertia to viscous force; Weber number $\left(We = \frac{\rho_d v_d^2 d_d}{\gamma_{lg}}\right)$ as ratio of inertia to surface tension force; Capillary number $\left(Ca = \frac{\mu_d v_d}{\gamma_{lg}}\right)$ as ratio of viscous force to surface tension force and Froude number $\left(Fr = \frac{v_d}{\sqrt{g d_d}}\right)$ as ratio of inertia to gravity force. From the fundamental research aspect, motion of this three-phase contact line is significant as it governs the contact angle condition on solid surface and directly affects the evolution of interface and wetted contact area. The apparent unsteady contact angle differs significantly from the equilibrium static contact angle or Young's contact angle value and exhibits a hysteresis involving a maximum (dynamic advancing) and minimum (dynamic receding) value.

Previous studies investigated different aspects of this short duration (order of few milliseconds) droplet-particle interaction phenomena utilizing high speed visualization technique. These aspects included droplet deposition behavior on particle surface involving spreading and recoiling phase (Mitra et al., 2013; Malgarinos et al., 2016); rebound behavior in film boiling regime (Ge and Fan, 2007; Mitra et al., 2013, 2016); liquid film coating on particle surface and temporal variation in film thickness (Bakshi et al., 2007; Banitabaei and Amirfazli, 2017; Mitra et al., 2017); and disintegration behavior (Hardalupas et al., 1999; Mitra et al., 2013, 2016, 2017; Charalampous and Hardalupas, 2017).

Alongside experimental studies, numerical modeling involving complete solution of viscous form of the Navier-Stokes equation with moving gas-liquid interface incorporating surface tension force is considered to be a useful tool to gain insights into the complex interaction mechanisms and quantify the wetting behavior and associated heat transfer where applicable. Although significant effort could be noted in the numerical modeling aspect on droplet impact behavior on a flat surface due to its application in spray cooling, fewer studies are indeed available on the droplet impact behavior on particle surface. Of few reported studies, mainly three numerical approaches could be noted—a combined level-set and immersed boundary method (Ge and Fan, 2007), VOF (Mitra et al., 2013, 2015; Malgarinos et al., 2016, 2017a,b); and Lattice Boltzmann Method (Gac and Gradon, 2014).

Ge and Fan (2007) simulated surface wetting behavior of an acetone droplet on a brass particle ($\Delta < 1$) in film boiling regime (200–300°C) in low Weber number range ($We = 3$–$20$). A thin intervening vapor layer was assumed to exist at the liquid-solid interfacial area which was accounted by a 2D vapor flow model without requiring a contact angle boundary condition. Mitra et al. (2013) utilized an experimentally measured dynamic contact angle profile set over discrete time interval into their CFD model to simulate spreading ratio and droplet shape evolution in cold state interactions ($We = 8$) and a constant contact angle of 180° for film boiling simulations ($We = 8$ and 84, $T_p = 250$°C). Malgarinos et al. (2016) used a constant static contact angle boundary condition ($\theta_s = 90°$) in their CFD model with adaptive mesh refining and showed reasonable agreement with the time varying spread ratio for a low Weber number case ($We = 8$) reported in Mitra et al. (2013).

Noting relatively limited effort in quantifying the surface wetting dynamics in a droplet-particle system specifically when heat transfer is involved, objective of the present study was to examine the particle surface wetting behavior at low droplet impact Weber number range using high speed visualization and CFD modeling both in absence and presence of heat transfer. More specifically, aims were to quantify;

1. Role of contact angle boundary condition on the surface wetting dynamics in low Weber number impact regime in absence of any heat transfer and

2. Sensitivity of varying contact angle boundary condition in film boiling regime and effect of impact Weber number on maximum spreading ratio, and heat transfer involving change in droplet temperature and heat flux during impact.

## EXPERIMENTAL

A schematic of the experimental setup is presented in **Figure 1**. Experiments were performed using RO filtered water droplets of diameter ∼2.9 ± 0.1 mm at both cold state ambient condition (20°C) and film boiling regime (350°C) at different Weber numbers on a 10 mm solid brass sphere. Before each droplet deposition, the sphere surface was carefully cleaned with acetone and allowed for sufficient time to dry. Surface temperature was controlled by a PID controller connected with an embedded T-type thermocouple and a cartridge heater placed in a well-insulated billet. A droplet delivery system with adjustable height (∼10–150 mm from the apex point of the sphere) was utilized using a 21G hypodermic nozzle and a precision syringe pump. A single droplet was generated at the nozzle tip at ∼2.4 ml/h flow rate by adjusting the pump stroke length which was found to be suitable for deposition purpose. Droplet-sphere interactions were captured using a Phantom v311 high speed camera at 2000 frames per second in shadowgraphy mode using backlighting and a diffuser screen.

An in-house developed MATLAB image processing script was utilized to extract useful data from the captured images. Droplet boundary was marked to separate it from the background and area equivalent diameter was determined. Centroid of the marked droplet was tracked prior to impact to estimate the impingement velocity. Contact angles were determined on both left and right side of the marked interface by computing the inside angle between the two tangents—one drawn to the interface and the other on the spherical surface both passing through the three-phase contact line intersection points (**Figure 3**). Details of the image processing algorithm can be found in Mitra et al. (2016).

## COMPUTATIONAL MODEL

### Geometry and Mesh

The computational domain (12 mm × 12 mm × 9 mm) for 3D simulations is presented in **Figure 2**. Hexahedral meshing tool Ansys ICEM was used to generate the mesh comprising ∼0.32 million hexahedral cells. Size of cells were kept lower in the vicinity of spherical surface for better resolution of the three-phase contact line and gradually coarser away from the solid surface. Total 10,592 cells were patched to resolve the droplet. In the present work, total cell number was decided based on a trade-off between a reasonable agreement with the experimental data and computational time which took on average ∼2–4 days per case to simulate ∼10–20 ms of physical time on a 32 processors workstation.

### Governing Equations

A 3D CFD model in Cartesian coordinate system based on the interface capturing coupled level-set and VOF (CLSVOF) (Ansys Fluent theory guide, 2013) approach was implemented in the finite volume method based commercial solver ANSYS Fluent (version: 17). The continuity equation for the liquid phase

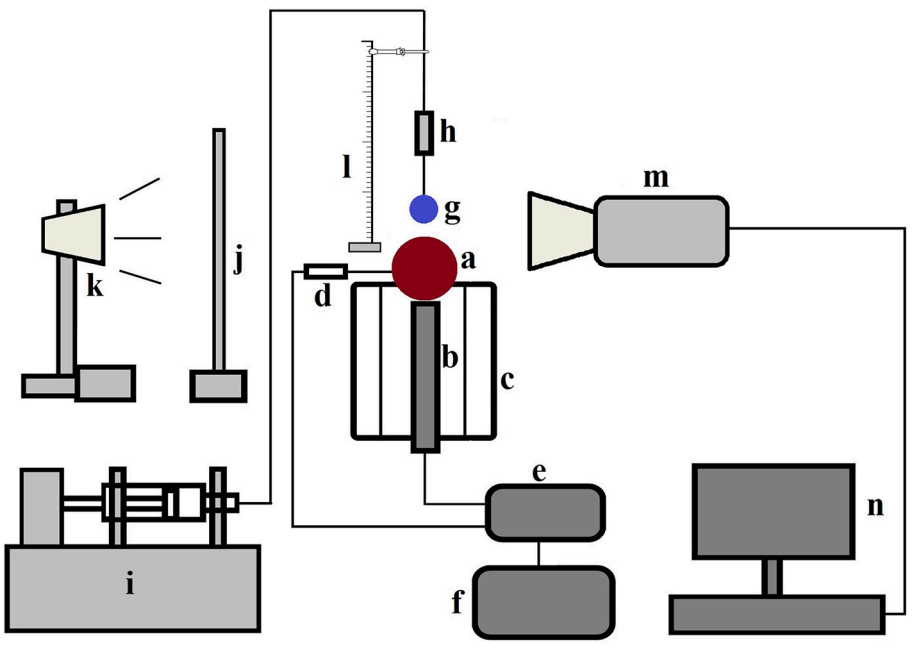


**FIGURE 1 |** Schematic diagram of the experimental set up—(a) brass particle (b) cartridge heater placed inside the grooved heating billet (c) heating billet with insulation (d) T type thermocouple (e) temperature controller (f) variac with transformer (g) droplet (h) nozzle assembly containing hypodermic needle (i) syringe pump (j) diffuser screen (k) light source (l) height adjustment facility with scale (m) camera (n) computer (Mitra et al., 2016) (With permission from Elsevier).

accounting for the evaporation loss at droplet interface was written as,

$$\frac{\partial\left(\rho_{mix}\alpha_l\right)}{\partial t}+\vec{v}.\nabla\left(\rho_{mix}\alpha_l\right)=-\dot{m}_{evap} \quad (1)$$

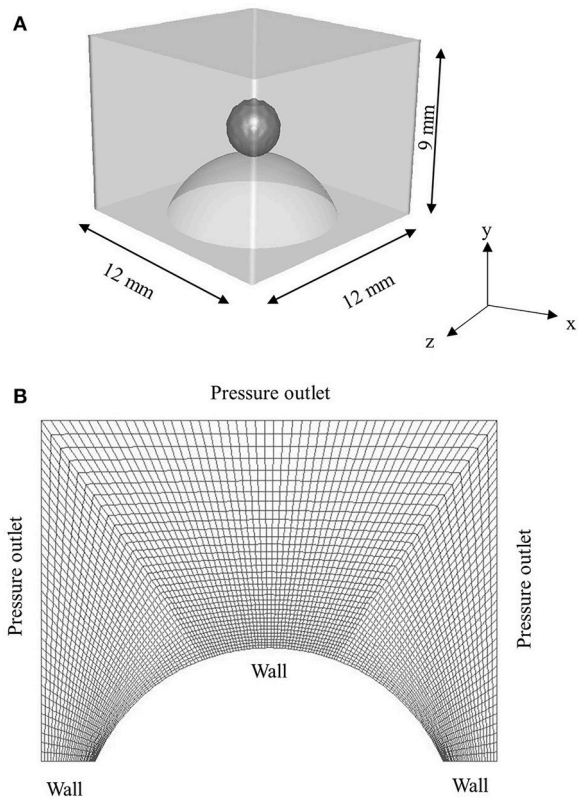


**FIGURE 2 | (A)** 3D Computational domain used for simulation **(B)** sectional view of the hexahedral mesh with boundary conditions.

where $\alpha_l$ is the liquid phase volume fraction, $\rho_{mix}$ = mixture phase density, $v$ is velocity, and $\dot{m}_{evap}$ is the volumetric evaporation rate.

The volume fraction of the continuous phase can be calculated from mass conservation following $\alpha_g+\alpha_l=1$. The evaporative source term at interface $\dot{m}_{evap}$in Equation (1) was derived as follows:

$$\dot{m}_{evap}=6\alpha_l\left(1-\alpha_l\right)\left|\nabla\alpha\right|\left(\frac{dm_d}{dt}\right) \quad (2)$$

where $|\nabla\alpha|$ is interfacial area per unit volume and $dm_d/dt$ is the evaporative mass flux obtained from Hertz-Knudsen-Schrage kinetic evaporation model as follows (Barrett and Clement, 1992):

$$\frac{dm_d}{dt}=\left(\frac{M_v}{2\pi R}\right)^{0.5}\left(\frac{2\chi_e}{2-\chi_e}\frac{P_{sat}}{T_l^{0.5}}-\frac{2\chi_c}{2-\chi_c}\frac{P_v}{T_v^{0.5}}\right) \quad (3)$$

where $M_v$ is the vapor molecular weight, $R$ is universal gas constant, $\chi_e$ and $\chi_c$ are the evaporation and condensation coefficient, respectively, $P_{sat}$ is liquid phase saturation vapor pressure corresponding to liquid temperature $T_l$ computed from the Antoine equation and $P_v$ is pressure at vapor side corresponding to temperature $T_v$.

Equation (3) assumes that both incoming (absorption/condensation) and outgoing (reflection/evaporation) molecular fluxes at droplet interface exhibit Maxwellian distribution behavior which is characterized by the temperature and pressure in the liquid phase near the interface alone. Further assumptions include that molecular transport mechanism depends only on the state variables (pressure and temperature) of the liquid and vapor phase and is independent of the net transfer of mass, momentum, and energy. To depict the probabilistic behavior of molecular interactions with the interface, evaporation coefficient ($\chi_e$) is defined as the ratio of number of molecules transferred to the vapor phase to

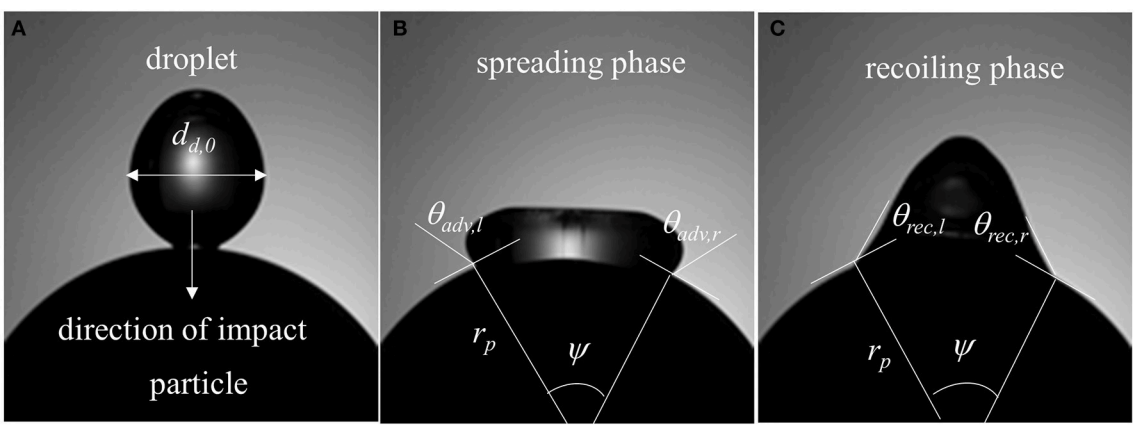


**FIGURE 3 |** Surface wetting behavior (Case-1, *We = 4*) and relevant parameters **(A)** droplet at the instant of impact in the direction of gravity **(B)** spreading phase ($\psi$ = central angle, $r_p$ = particle radius, $\theta_{adv,l}$ = dynamic advancing contact angle at left, $\theta_{adv,r}$ = dynamic advancing contact angle at right) and **(C)** recoiling phase ($\theta_{rec,l}$ = dynamic receding contact angle at left, $\theta_{adv,r}$ = dynamic receding contact angle at right).

number of total molecules escaped from the interface. Similarly, condensation coefficient ($\chi_c$) is defined as the ratio of number of the molecules absorbed by the liquid phase to the total number of vapor molecules impinging at the interface. Considering a specific scenario wherein all vapor molecules have the same probability for condensation and both specular (energy of molecules remains conserved) and diffuse reflection (energy of molecules is not conserved) at the interface are possible, under equilibrium assumption, both evaporation and condensation coefficients can be replaced with a single thermal accommodation coefficient for the purpose of simplicity. Nonetheless in real cases, specifically for interface with high curvature, departure from equilibrium state is quite possible which would eventually lead to a lower evaporation rate compared to Equation (3). Accommodation coefficient parameter is strictly determined from experiment and known to have large uncertainty even for a simple molecule like water which varies in the range ∼0.01–1.0 (Marek and Straub, 2001). For simulation purpose in the present study, a median value of 0.5 was considered which has been reported in a number of related studies previously (Nikolopoulos et al., 2007; Malgarinos et al., 2017a,b).

A species transport equation was separately solved to account for generation of the vapor phase during evaporation as

$$(1-\alpha_l)\,\rho_g\frac{\partial y_{vap}}{\partial t}+\nabla.[\vec{v}\,(1-\alpha_l)\,\rho_g y_{vap}]= \nabla.[\rho_g\,(1-\alpha_l)\,D_{vap}\nabla y_{vap}]+\dot{m}_{vap} \quad (4)$$

where $\rho_g$ is gas phase density and $y_{vap}$ is vapor mass fraction.

The momentum equation in addition to pressure, gravity and viscous stress, included a surface tension force $\vec{F}_s$ to model the interfacial deformation as follows:

$$\frac{\partial(\rho_{mix}\vec{v})}{\partial t}+\nabla.(\rho_{mix}\vec{v}\vec{v}) = -\nabla P+\left[\nabla.\mu_{mix}(\nabla\vec{v}+\nabla\vec{v})^T\right]+ \rho_{mix}\vec{g}+\vec{F}_s \quad (5)$$

where the mixture density and viscosity were calculated based on the volume fraction of each phase as shown below,

$$\rho_{mix}=\alpha_l\rho_l+(1-\alpha_l)\,\rho_g \quad (6)$$

$$\mu_{mix}=\alpha_l\mu_l+(1-\alpha_l)\,\mu_g \quad (7)$$

Any additional momentum source term due to evaporation was however not considered in the present modeling framework.

In Equation (5), $\vec{F}_s$ was modeled according to the continuum surface force model (Brackbill et al., 1992),

$$\vec{F}_s=\sigma_{\lg}\kappa\delta\,(\varphi_{LS})\,\vec{n} \quad (8)$$

where $\sigma_{lg}$ is surface tension parameter, $\kappa$ is interface curvature, $\delta$ is dirac-delta function and $\vec{n}$ is a unit normal at the interface.

To capture the interface efficiently, a level-set function was used in addition to the phase volume fraction parameter based interface tracking capability of the VOF approach. As the level-set function is smooth and continuous as opposed to the VOF function (discontinuous across the interface), its spatial gradients are computed more accurately. Consequently, accurate estimates of interface curvature and associated surface tension force are obtained. The surface normal at interface was defined as gradient of a level set function $\phi_{LS}$, and corresponding unit normal was expressed as $\vec{n}=\frac{\nabla\varphi_{LS}}{|\nabla\varphi_{LS}|}$. Curvature at interface was then written as divergence of the unit normal as $\kappa=\nabla.\left(\frac{\nabla\varphi_{LS}}{|\nabla\varphi_{LS}|}\right)$.

In Equation (8) and definition of unit normal and interface curvature, $\phi_{LS}$ is a signed function which takes positive value $(+\varepsilon)$ in the gas phase, negative value $(-\varepsilon)$ in liquid phase, and zero value at the interface and can be written as:

$$\varphi_{LS}(x,y,z,t)=\begin{cases}+\varepsilon, if\ x,y,z\in\alpha_g\\ 0\quad at\ \text{interface}\\ -\varepsilon, if\ x,y,z\in\alpha_l\end{cases}. \quad (9)$$

The $\delta$ function in Equation (8) ensures that surface tension force in Equation (5) is only computed at the interface and takes zero value elsewhere which was given as

$$\delta(\varphi_{LS})=\begin{cases}\dfrac{1+\cos\left(\frac{\pi\varphi_{LS}}{a_l}\right)}{2a_l}, for\ |\varphi_{LS}|<a_l\ where\ a_l=1.5h_{gs}\\ 0\qquad\qquad for\ |\varphi_{LS}|>a_l\end{cases} \quad (10)$$

where $a$ is interface thickness and $h_{gs}$ is grid spacing.

Transient evolution of both the volume fraction parameter $\alpha_l$and level set parameter $\varphi_{LS}$ were solved as per the general advection equation $\left(scalar\ \varsigma=\alpha_l,\varphi_{LS}\right)$ given below:

$$\frac{\partial\varsigma}{\partial t}+\vec{v}.\nabla\varsigma=0 \quad (11)$$

It is important to mention that level set function is not mass conserving due to deformation of interface and it needs to be reinitialised at every time step using geometrical interface-front construction method. In this method, both VOF and the LS function values are utilized to reconstruct the interface-front wherein VOF model provides the size of the cut in the cell based on the probable interface location while the direction of the interface is determined by the gradient of the LS function.

Wall adhesion is significant for partial wetting fluids with non-zero contact angle on solid surface. This effect was incorporated in the CFD model expressing unit normal at the wall ($\hat{n}_w$) boundary in terms of unit vectors for fluid and for wall ($\hat{t}_w$) and the contact angle $\theta$ as follows,

$$\hat{n}=\hat{n}_w\cos(\theta_w)+\hat{t}_w\sin(\theta_w) \quad (12)$$

Finally, a single energy balance equation was solved for the mixture phase considering that both primary (gas) and secondary phase (liquid) share the same temperature. Additionally, accounting for the phase change source term due to latent heat vaporization, this equation was written as,

$$\frac{\partial}{\partial t}(\rho_{mix}C_{p,mix}T_{mix})+\nabla.(\vec{v}(\rho_{mix}C_pT_{mix}+P_{mix}))= \nabla.\left(k_{mix}\nabla T\right)-\dot{m}_{evap}\lambda \quad (13)$$

where $C_{p,mix}$ and $k_{mix}$ are mass averaged heat capacity and thermal conductivity of the mixture respectively, and $P_{mix}$ and $T_{mix}$ are mixture pressure and temperature and λ is latent heat of vaporization.

The source terms due to phase change in Equations (1), (4), and (13) were implemented through a UDF (user defined function) based on the source term expression given in Equation (2).

## Model Parameters and Solution Procedure

All the thermo-physical properties (density, viscosity, surface tension, heat capacity, and thermal conductivity) of the gas and liquid phase used in the simulations were set as temperature dependent polynomials. No slip boundary condition was applied at the sphere wall in the cold simulation cases. Both static contact angle ($\theta_s = 75 \pm 3^{\circ}$) and an experimentally measured time dependent continuous dynamic contact angle profile (through user defined function) were used to depict adhesion behavior at solid surface. Pressure outlet boundary condition with zero gauge pressure was applied on all the surrounding faces. For simulating film boiling regime cases, it was assumed that intense vaporization at the solid-liquid interface forms an intervening thin vapor film which renders the surface to be non-wetting and contributes to significant reduction in friction. Without explicitly modeling this vapor layer, a free slip boundary condition (zero shear stress) was rather applied at the solid surface to represent this physical condition (Karl et al., 1996; Mitra et al., 2013; Gumulya et al., 2015). In conjunction with this slip condition, a range of static contact angle boundary condition in the limit of super-hydrophobic surface condition was utilized (see section Dynamic Surface Wetting in Presence of Heat Transfer).

The computational domain was first initialized with zero velocity, pressure, liquid volume fraction, vapor mass fraction and temperature of 293 K. A droplet of diameter 2.9 mm was then patched in the computational domain setting liquid volume fraction equal to 1.0, level-set parameter close to zero and initial velocity equal to the impingement velocity as obtained from the experimental measurement for a particular *We* number case. Governing equations were then solved sequentially in a spatial iteration loop within an outer time loop starting with momentum (Equation 5), mass continuity (Equation 1) with mass loss source term due to evaporation (Equation 2), and correction of velocity and pressure field using a pressure velocity coupling scheme. Energy (Equation 13) was solved next with the energy source term to determine the mixture temperature. Vapor concentration equation (Equation 4) was solved then with the mass source term. Displacement of droplet interface was next obtained by solving the advection equation for phase volume fraction and level set parameter (Equation 11). All user-defined temperature dependent physical properties were updated at the end of the sequence.

For discretization of the momentum and energy equation, a second order upwind scheme was used. Volume fraction parameter and level set parameter were discretised using the Geo-Reconstruct and second order upwind scheme, respectively. PRESTO scheme was used for pressure variable and pressure-velocity coupling required for incompressible flow field was obtained by the SIMPLE algorithm. A residual of $10^{-4}$ was set for convergence of continuity, momentum, species, volume fraction, and level-set equations while a residual of $10^{-6}$ was

**TABLE 1 |** Operating conditions used in the cold state interactions.

| Case | $d_{d,0}$ (mm) | $v_0$ (m.s$^{-1}$) | *Re* | *We* | *Ca* |
|---|---|---|---|---|---|
| 1 | 2.9 ± 0.1 | 0.32 | 932 | 4 | 0.004 |
| 2 | 2.9 ± 0.1 | 0.54 | 1,594 | 12 | 0.007 |
| 3 | 2.9 ± 0.1 | 0.70 | 2,039 | 19 | 0.009 |

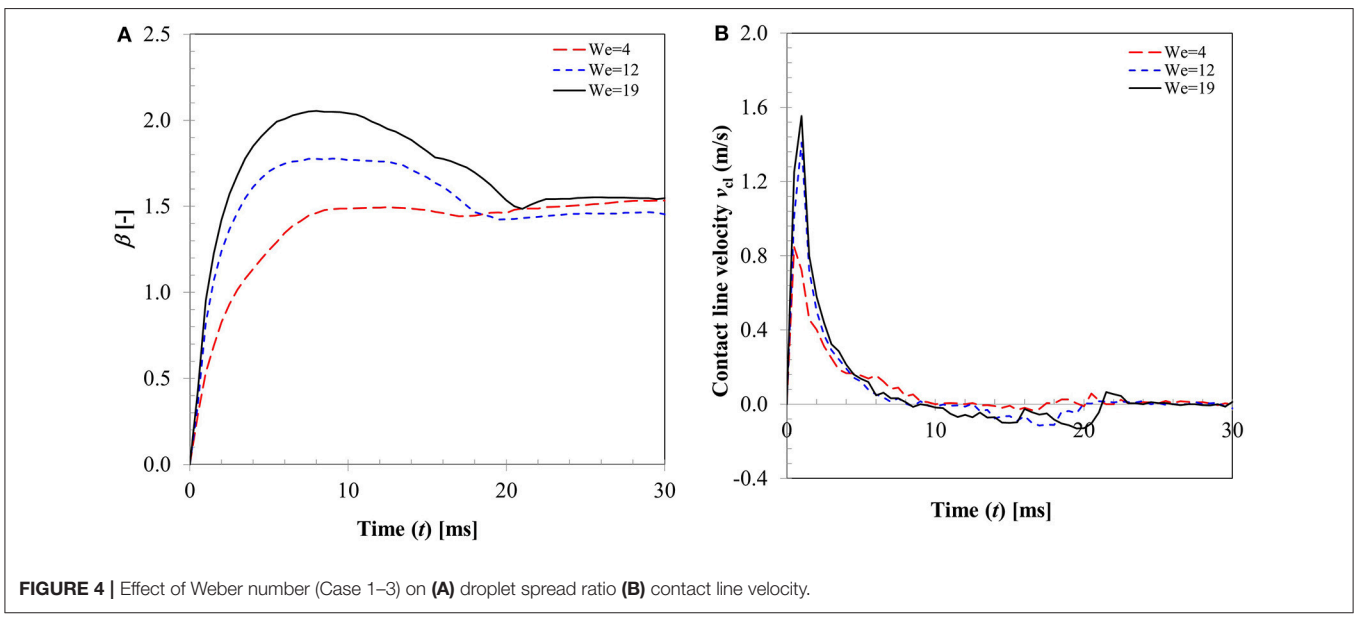


**FIGURE 4 |** Effect of Weber number (Case 1–3) on **(A)** droplet spread ratio **(B)** contact line velocity.

used for the energy equation. All simulations were performed for a duration of 10–20 ms depending on impact Weber number using a time step of $10^{-6}$ s with 50 iterations per time step. A first order implicit time stepping method was used in all the simulations ensuring global Courant number ∼0.1 throughout the simulation.

# RESULTS AND DISCUSSION

## Dynamic Surface Wetting at Cold State

In the absence of heat transfer, ($T_p$ = 20°C), solid sphere (henceforth referred to as particle) surface wetting behavior was studied at three different water droplet impact velocities. Physical properties of droplet used to report the dimensionless numbers are $\rho_l$ = 998.2 kg. m$^{-3}$; $\mu$ = 0.001 kg.m$^{-1}$.s$^{-1}$, $\sigma_{lg}$ = 0.073 N.m$^{-1}$. Details of the operating conditions are given in **Table 1**.

In a typical low Weber number impact case (case 1–3) below the breakup (disintegration) limit, surface tension and viscous force resist impact inertia which results in deposition outcome (**Figure 3**). Surface wetting behavior here comprises two distinct phases—spreading and recoiling. An important parameter of interest is the extent of surface wetting which was defined as the spread ratio $\beta$ (arc length between the two three-phase intersection points) normalized with initial droplet diameter, $d_{d,0}$. The wetted perimeter was determined from images by measuring the central angle $\psi$ subtended at the sphere center and sphere radius to give $d_d = \psi r_p$. Effect of Weber numbers on the temporal variations of this non-dimensional wetting parameter is shown in **Figure 4A** for three different Weber number cases (case: 1–3) in the increasing order. Following impact, due to dominating inertia, in all three cases, droplet quickly reaches the maximum spreading state which is identified by the distinct peaks. The magnitude of the wetting parameter peaks could be noted increasing (∼1.5–2.0) with corresponding Weber numbers. Time required to reach the maximum spreading state shows slight left shift in all the three cases which occurs in the time range $t$ ∼8–10 ms with decreasing order of Weber number. After reaching the maximum spreading state, all three cases exhibit recoiling phase indicated by a sharp decline in the spread ratio parameter which is more prominent in the higher Weber number cases ($We$ ∼ 12 and 19). This could be explained by the greater rate of conversion of surface energy into kinetic energy in the recoiling phase due to more interfacial area produced at higher Weber number. After the first cycle of spreading and recoiling, few such cycles follow but with much weaker magnitudes due to the dampening effect from competing surface tension and viscous force.

**Figure 4B** illustrates the temporal variation in contact line velocity obtained in the three representative Weber number cases. Magnitudes of the contact line velocity, as can be noticed, increases with impact Weber number with a slight right shift. The contact line velocity ratios were in the range from ∼0.9 to 1.55 which provide an estimation of the maximum possible spreading velocity just after impact. All three velocity profiles pass through a zero cross-over point at $t$ ∼8–10 ms which denotes the maximum spreading state where momentarily contact line velocity becomes zero (zero kinetic energy). Past this point, contact line velocity profiles exhibit reversal of sign indicating commencement of the recoiling state. The velocity magnitude in the recoiling phase can be noted to be much smaller (−0.1 to −0.15 m/s) compared to spreading phase which indicates weak influence of inertia in the recoiling phase wherein dynamics are primarily controlled by the surface tension, viscosity and gravity force.

A key parameter in interpreting the surface wetting behavior is the variation in contact angles as the three phase contact line advances or recedes which has been an area of active research for

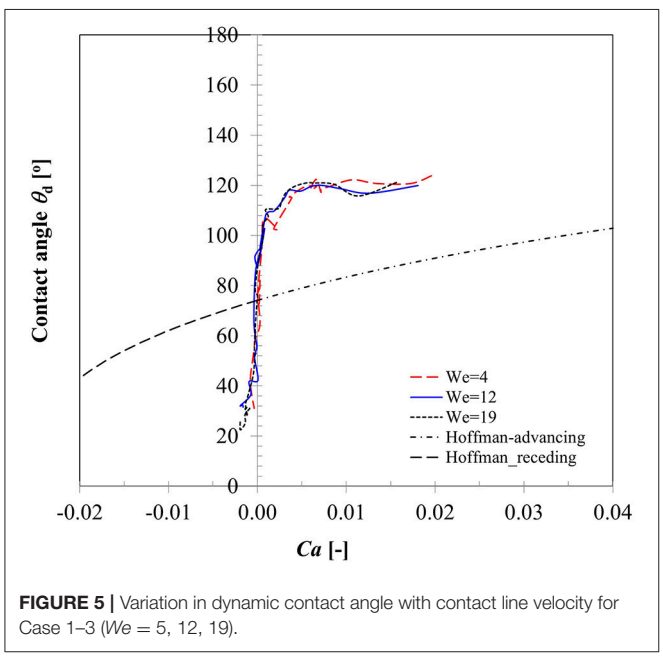


**FIGURE 5 |** Variation in dynamic contact angle with contact line velocity for Case 1–3 ($We$ = 5, 12, 19).

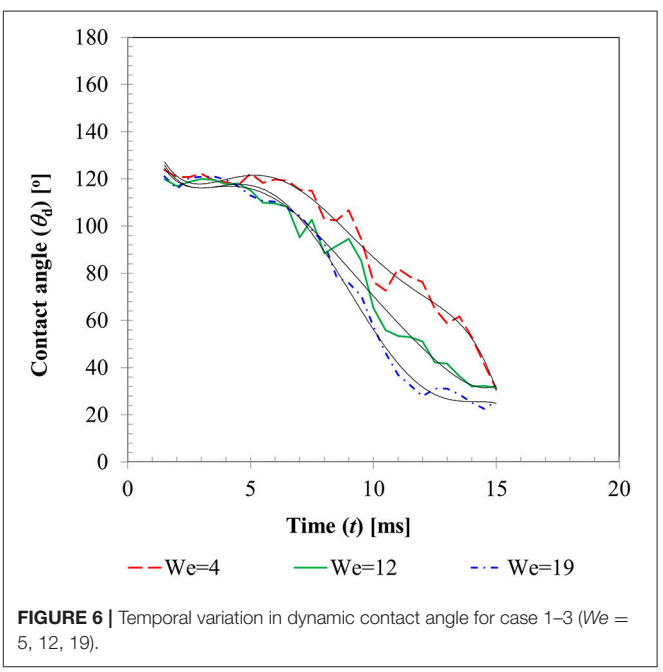


**FIGURE 6 |** Temporal variation in dynamic contact angle for case 1–3 ($We$ = 5, 12, 19).

decades (Hoffman, 1975; Dussan, 1979; Kistler, 1993; Hocking, 1995; Ganesan, 2013). Dependency of dynamic contact angles on Capillary number (contact line velocity) for case 1–3 is presented in **Figure 5**. It could be noted that in the spreading phase due to inertia dominated behavior of contact line motion, contact angle remains almost constant ($\theta_{d,adv} \sim 120^{\circ}$) in all the three Weber number cases. In an earlier CFD modeling study on droplet impact on flat surface, Sikalo et al. (2005) also noted that spreading state is essentially inertia dominated which is indicated by high *Ca* number at the contact line region. Apparent increase in contact angle from the static value at this stage was reasoned to occur due to viscous stress initiating the rolling motion at the advancing gas-liquid interface. A drastic change in the contact angle value is evident near the transition region from spreading to recoiling phase where the contact line velocity passes through a zero cross-over point signifying the maximum spreading state. All contact line dynamics related to droplet impact is located in this transition zone wherein the dynamic contact angle value changes from the advancing to receding mode. Due to weaker velocity magnitude as shown in **Figure 4B**, dynamic contact angle values were much smaller in the recoiling phase ($\theta_{d,rec} \sim 30^{\circ}$) compared to spreading phase. All the three contact line motion profiles could be seen passing through the zero cross-over point which on the vertical axis reads $\sim 90^{\circ}$ and should in principle produce the equilibrium static contact angle. The measured average static contact angle value ($\theta_s = 75 \pm 3^{\circ}$) however was lower than this value for the same droplet size on brass sphere surface which could be attributed to presence of some hysteresis due to contact line motion.

To compare the prediction capability of an available dynamic contact angle model with these measured values, also plotted here is the well-known Hoffman's (1975) model originally developed for advancing contact angles of a gas-liquid meniscus rising in glass capillary tube for a wide range of Capillary numbers ($4 \times 10^{-5} \leq Ca \leq 36$). The data was later fitted in Kistler (1993) to produce a useful form widely known as Kistler's law which is given as follows:

$$\theta_{dyn} = f_{Hoff}\left(Ca + f_{Hoff}^{-1}(\theta_s)\right) \tag{14}$$

where $f_{Hoff}$ and $f_{Hoff}^{-1}$ are the Hoffman and inverse Hoffman function, respectively and written for any independent variable $x$ as,

$$f_{Hoff}(x) = \cos^{-1}\left(1 - 2\tanh\left[5.16\left(\frac{x}{1 + 1.31x^{0.99}}\right)^{0.706}\right]\right). \tag{15}$$

Equation 14 represents a nearly *sigmoidal* (*s* shape curve) indicating dynamic contact angle reaches 180° at very large Capillary number. In Equation (14), using directional sign of contact line velocity (positive and negative) in the definition of capillary number (*Ca*), corresponding dynamic advancing contact angles ($\theta_{dyn,adv}$), and receding contact angles ($\theta_{dyn,rec}$) were computed and plotted in **Figure 5**. Apparently, Equation (14) indicates significant deviations both in the spreading and recoiling phase from the measured values. Sikalo et al. (2005) showed that the existing empirical models for the dynamic contact angles, such as Hoffman's model only provide satisfactory agreement with the experimental data at low capillary numbers ($Ca < 0.1$) and produce significant deviations especially at high capillary numbers. We however note that Hoffman's model significantly under-predicts contact angles even at low Capillary numbers (maximum $Ca \sim 0.04$ in case 1–3) in depicting the three-phase contact line behavior. Similar deviations in the predicted dynamic contact angle values were also noted in the Bracke et al.'s (1989) model (not shown).

**Figure 6** presents the temporal variations of contact angles (dynamic advancing and receding) obtained for the three different Weber number cases. From the instant of impact ($t = 0$) when droplet and particle are almost at point contact with each other, to $t \sim 1.0$–$1.5$ ms, contact angles could not be determined due to insufficient resolution of the interface curvature at the liquid-solid contact area. Afterwards, up to $t \sim 4$–$5$ ms, still in the spreading phase, all the contact angle profiles exhibit a relatively flat regime which can be explained by the relative dominance of inertia over the surface tension force. A steep decline in the contact angle value in the transition zone from advancing to receding phase could be observed in all the three cases with decreasing slopes at higher Weber numbers. This is explained by the larger duration of spreading and recoiling phase observed in higher Weber number cases. Having shown that available empirical models such as Equation (14) do not capture the temporal variations in contact angles well, these experimentally measured contact angle profiles were utilized as wall boundary condition in the CFD model. A sixth order polynomial was fitted to each of these contact angle profiles for interpolating temporal variation in contact angle value in the corresponding time range. Coefficients of these polynomials are provided in **Table 2**.

A comparison of time varying behavior of droplet shape evolution predicted by the CFD model using dynamic contact angle boundary condition and the experimental visualization for $We = 4$ case is presented in **Figure 7**. A very reasonable agreement was obtained in the predicted dynamics which shows the gradual sinking behavior of the lamella tip into a toroidal shape ring as the droplet spreads and eventually reaches a maximum spreading state ($t = 8$ ms) followed by a gradual increase in the lamella height in the recoiling phase due to retracting action of surface tension force. A definite improvement was achieved using the contact angle profile as a continuous function of time compared to the earlier predicted droplet shape variation presented in Mitra et al. (2013) wherein a discrete time sequence implementation of contact angle boundary condition rendered a relatively coarse interface structure for a similar low Weber number deposition case ($We = 8$).

**Figure 8** presents a comparison of the CFD model predicted wetting parameter using both static and dynamic contact angle boundary conditions with the experimental measurement for $We = 4$ case. Also presented here are the effects of the two extremities of slip conditions at particle surface (no-slip and full slip) and interface treatment approach based on VOF and CLSVOF methodology. In CFD computation, wetted surface area hence droplet spread was obtained by integrating the volume fraction

**TABLE 2 |** Polynomial coefficients of time varying contact angle profiles.

| Case | *We* | $a_0$ | $a_1$ | $a_2$ | $a_3$ | $a_4$ | $a_5$ | $a_6$ |
|---|---|---|---|---|---|---|---|---|
| 1 | 4 | 180 | −59.428 | 20.181 | −2.923 | 0.176 | −0.003 | $-4 \times 10^{-5}$ |
| 2 | 12 | 180 | −67.116 | 26.504 | −4.923 | 0.453 | −0.021 | $4 \times 10^{-4}$ |
| 3 | 19 | 180 | −61.5 | 21.206 | −3.129 | 0.187 | −0.003 | $-3 \times 10^{-5}$ |

*Subscript of the coefficients denotes the corresponding exponent of time variable.*

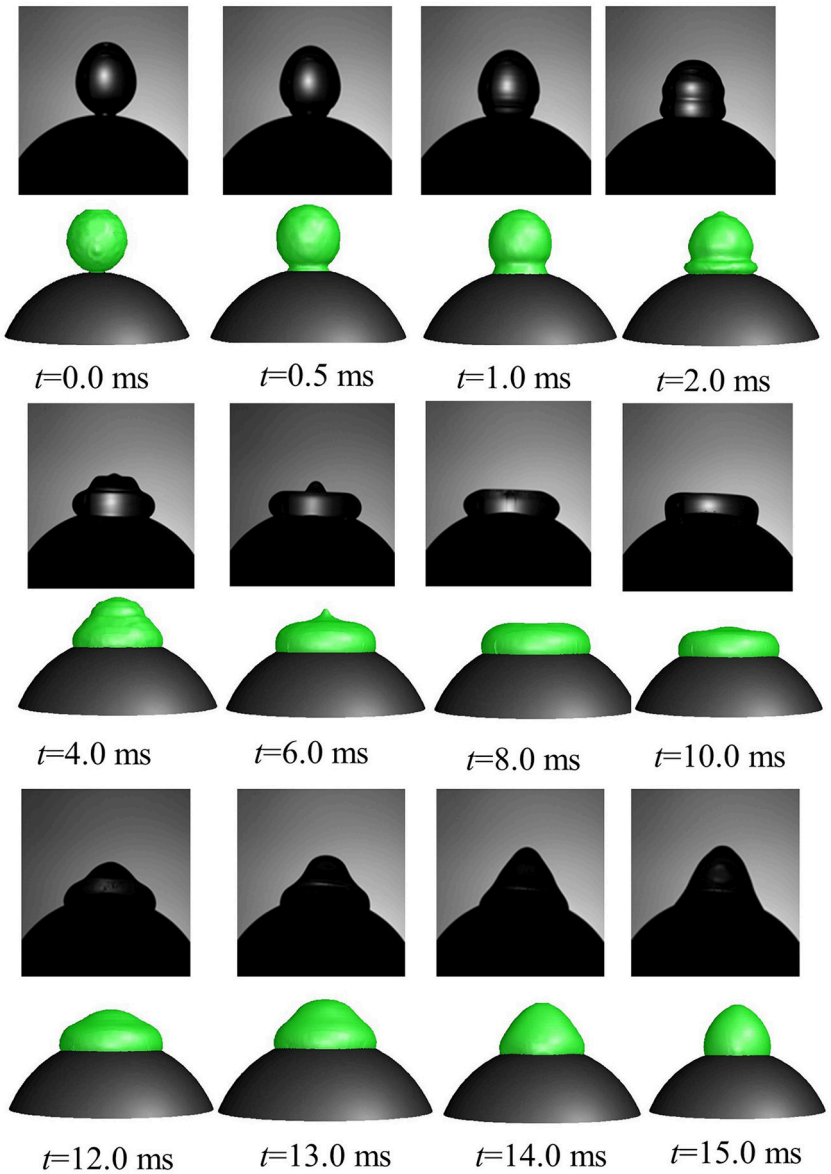


**FIGURE 7 |** Comparison of CFD model predicted temporal evolution of droplet shape (row 2, 4, 6 in color) with high speed visualizations (row 1, 3, 5 in black and white) (Case 1, $We = 4$).

of liquid phase in the cells adjacent to particle surface. Clearly, with static contact angle boundary condition, there was almost no difference in the spreading ratio up to $t \sim 8$ ms which covers the spreading phase for all these different combinations. It is quite apparent that even the slip or no-slip boundary conditions do not affect the droplet spreading behavior much where inertia prevails. Past $t \sim 8$ ms, in the recoiling regime, some deviations are apparent in the spread ratio profile which results from different

boundary conditions. Between VOF and CLSVOF methodology for interface treatment, deviations in the simulated spread ratio are almost negligible for the no-slip boundary condition however the slip BC condition predicts relatively higher spread ratio as would be expected intuitively due to zero viscous dissipation at the contact line. It was previously noted in Sikalo et al. (2005) that most of the available CFD codes predict droplet shape evolution reasonably well in the spreading phase when droplet motion is primarily controlled by inertia, however they are often not successful in predicting the receding phase which is controlled by the surface tension and surface hydrophobicity.

It is a well-known fact that imposing a no-slip boundary condition on solid surface creates a non-integrable shear stress singularity at the contact line (Huh and Scriven, 1971; Dussan, 1979). To overcome, this issue, often a slip condition (Navier slip condition) is used to capture all the relevant flow and geometry details near the contact line. However, for this purpose, mesh size requires to be of the order of the slip length which is much less than the physical dimension of the droplet but comparable with the intermolecular distance. Any mesh size larger than this slip length leads to mesh size dependent results. Nonetheless using such small slip length entails direct numerical simulation requiring enormous computational resources. In the present study, a VOF based approach was used which utilizes cell face normal velocity in the computation meaning that an implicit slip condition proportional to mesh spacing exists at the no-slip boundary condition near wall (Afkhami et al., 2009). To keep the simulation time reasonable, mesh size near the contact line was kept ∼40 μm. Apparently, with this implicit slip condition and the experimentally measured dynamic contact angle profile, a better agreement with the experimentally measured spreading ratio was obtained compared to static contact angle condition without requiring a local mesh adaptation for finer resolution.

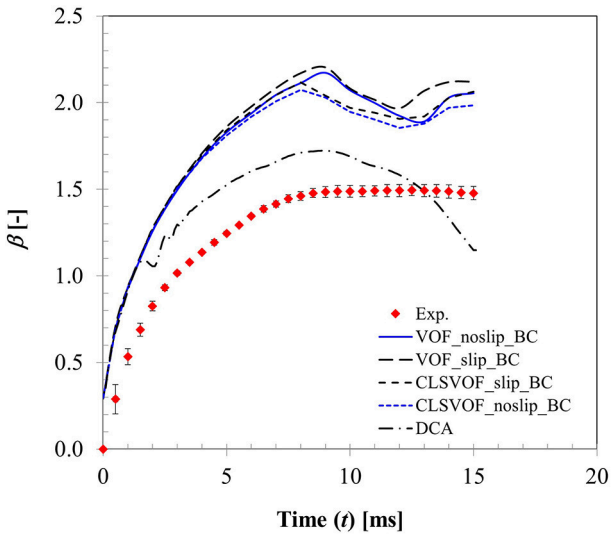


**FIGURE 8 |** Comparison of CFD model predicted surface wetting behavior based on both static and dynamic contact angle boundary condition (Case 1, *We* = 4).

A similar observation on the advantage of dynamic contact angle was also noted in Pasandideh-Fard et al. (2001) on their CFD simulation of droplet impact on a flat surface. It was reported that use of dynamic contact angle condition produces more accurate predictions during the spreading and at equilibrium. However, when the contact angle was assumed to be equal to the measured equilibrium value (static contact angle), model predictions were less accurate which over-predicted droplet diameter during recoil. This behavior was also noted in the present study. It is however possible to predict reasonable droplet shape evolution and associated spread ratio with static contact boundary condition alone by local mesh refinement which has been recently demonstrated in Malgarinos et al. (2016).

In previous studies, use of different mesh resolutions has been reported to simulate droplet impact behavior on a solid surface. For example, Nikolopoulos et al. (2007) used ∼0.5 million cells (with local mesh refinement) for a geometry size of 15 mm × 15 mm × 10 mm; Malgarinos et al. (2016) used 1.55–2.45 million cells (with 5 levels of local mesh refinement) for a physical geometry size of 60 mm × 30 mm × 30 mm and Gumulya et al. (2015) utilized a 15 mm × 10.85 mm cylindrical boundary involving 1.85 million cells. It is known that interface resolving VOF method bears the computation intensive DNS (direct numerical simulation) characteristic and obtaining truly mesh independent solution is difficult which has dependency on the size of flow structures of interest that need to be resolved. On that note, selection of mesh size in such scenarios is governed by a trade-off between the reasonable model predictions and associated computational cost.

## Dynamic Surface Wetting in Presence of Heat Transfer

Droplet-particle interactions involving heat transfer was studied in film boiling regime ($T_p$ = 350°C) at ten different droplet impact velocity (see operating conditions in **Table 3**).

### Surface Wetting Parameter

**Figure 9** presents variation in maximum spread diameter ratio with increasing droplet impact Weber number (5–104) obtained for case 4–13. Due to increase in impact kinetic energy, spread

**TABLE 3 |** Operating conditions used in the hot state interactions.

| Case | $d_{d,0}$ (mm) | $v_0$ (m.s$^{-1}$) | *Re* | *We* | *Ca* |
|---|---|---|---|---|---|
| 4 | 2.9 ± 0.1 | 0.35 | 1,008 | 5 | 0.005 |
| 5 | 2.9 ± 0.1 | 0.56 | 1,601 | 12 | 0.008 |
| 6 | 2.9 ± 0.1 | 0.71 | 2,039 | 20 | 0.01 |
| 7 | 2.9 ± 0.1 | 0.84 | 2,414 | 28 | 0.011 |
| 8 | 2.9 ± 0.1 | 0.94 | 2,690 | 34 | 0.013 |
| 9 | 2.9 ± 0.1 | 1.11 | 3,177 | 48 | 0.015 |
| 10 | 2.9 ± 0.1 | 1.27 | 3,644 | 63 | 0.017 |
| 11 | 2.9 ± 0.1 | 1.41 | 4,041 | 78 | 0.019 |
| 12 | 2.9 ± 0.1 | 1.52 | 4,356 | 90 | 0.021 |
| 13 | 2.9 ± 0.1 | 1.63 | 4,672 | 104 | 0.022 |

diameter ratio increases leading to increased wetted contact area. A power law trend is quite evident here indicating Weber number dependency of ∼0.39. The obtained correlation is very close to Akao et al.'s (1980) correlation $\beta_{\max} = 0.61We^{0.39}$(deviation<15%) obtained from droplet impingement on flat hot metal surface at 400 to 800°C. The empirical Weber number exponent is consistent with the theoretical limit of 0.25 and 0.5 obtained based on a scaling analysis suggested in Clanet et al. (2004) equating kinetic energy to surface energy and disregarding any viscous dissipation on a super-hydrophobic surface.

**Figure 10** shows droplet-particle contact time variation for the same range of impact Weber numbers. Droplet-particle interactions are known to exhibit two outcomes—rebound (droplet bounce off the particle surface) and disintegration (droplet breaks up to produce multiple secondary droplets) in the film boiling regime. These two regimes can be distinctly identified in **Figure 10** demarcated by a critical threshold at $We \sim 50$. In rebound regime, droplet exhibits both spreading and recoiling phase however at the end of recoiling phase droplet loses contact with the particle due to intense vapor force at the contact area. Contact times are in the range of ∼18–19 ms which are higher compared with the first order droplet vibration time $\tau = \pi\sqrt{\frac{\rho_l d_d^3}{16\sigma_{lg}}}$ suggested in Wachters and Westerling (1966) which estimates this contact time ∼14 ms.

When Weber number is increased past a critical threshold, droplet upon impact continues spreading and liquid mass accumulates in the outer rim. On a non-wetting surface, the larger contact angle creates a greater interface curvature at the periphery of the drop which increases the surface tension force and decreases inertia effect and consequently leads to more mass accumulation at the periphery. Following mass conservation, the connecting lamella on the particle apex decreases in thickness. Eventually due to conduction heat transfer, vapor bubbles are generated within this lamella which erupt and destabilizes the expanding film leading to disintegration outcome (Nikolopoulos et al., 2007; Mitra et al., 2017). Surface tension force then retracts the residual lamella to minimize surface area which leads to ejection of multiple secondary droplets from the rim leading to disintegration. Contact time in the regime drastically reduces due to absence of the recoiling phase. Noticeably, with increasing Weber number, over all contact time decreases however in both regimes separately, contact time remains somewhat independent of the impact Weber number. It was noted that identifying maximum spreading state for a disintegration event at higher impact Weber number had some uncertainties due to side view imaging and a state just before the ejection of secondary droplets from the rim was considered as the maximum spreading state.

The apparent non-wetting behavior in droplet-particle interactions in film boiling regime is attributed to the presence of a thin vapor layer at liquid-solid interface (Harvie and Fletcher, 2001; Ge and Fan, 2007; Mitra et al., 2013, 2016) which renders the surface to appear super-hydrophobic. To investigate effect of this non-wetting behavior on the flow dynamics, a sensitivity study was carried out using different contact angle boundary conditions ($\theta_s = 150, 160, 170°$) in the limit of super-hydrophobicity.

In **Figure 11**, CFD model predicted spread diameter ratio for different contact angle boundary conditions is compared with the experimental measurement for $We = 5$ case. All the contact angle boundary conditions provide reasonable agreement with experimental measurement producing average deviations in the predicted maximum spread ratio as ∼9, 13, and 17% for $\theta_s = 150, 160, 170°$, respectively. Contact times obtained with these boundary conditions are ∼18, 16.5, and 15 ms for the three contact angle cases which are also in good agreement with experimental value ∼18.3 ms. Clearly, $\theta_s = 150°$ boundary

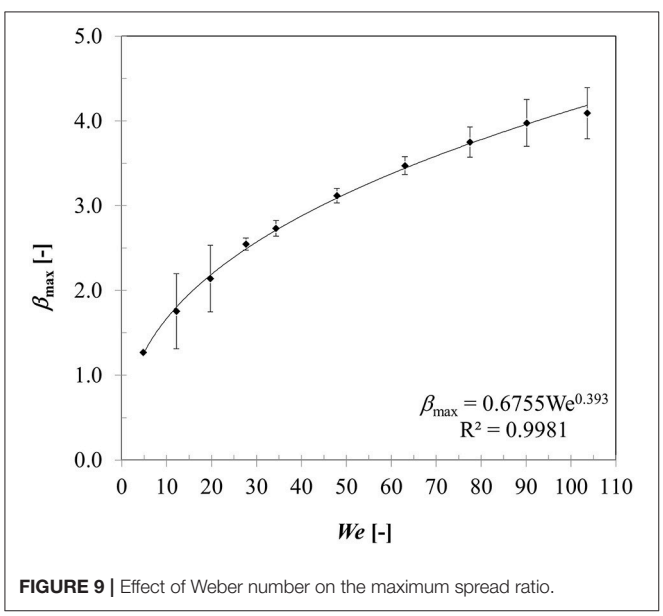


**FIGURE 9 |** Effect of Weber number on the maximum spread ratio.

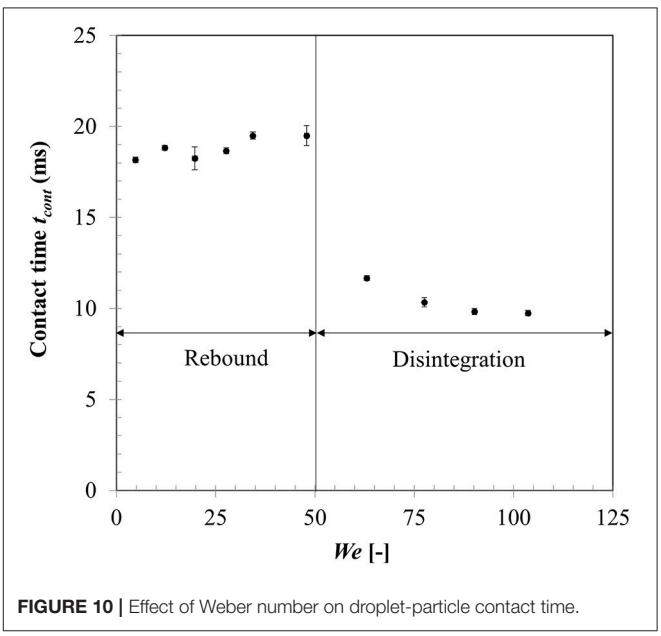


**FIGURE 10 |** Effect of Weber number on droplet-particle contact time.

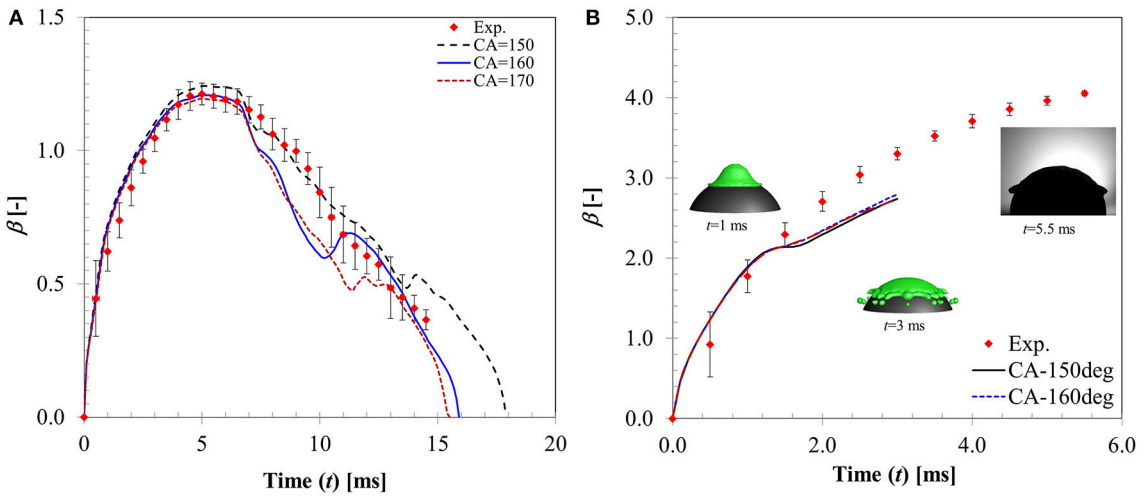


**FIGURE 11 |** Influence of contact angle boundary condition on the temporal flow dynamics for **(A)** $We = 5$ **(B)** $We = 104$.

condition provides a better match. Increasing contact angle has an effect on shortening of contact time due to increased surface tension force which is evident from the decreasing contact time trend obtained with increasing contact angle values. This observation is consistent with a contact time value reported in Gumulya et al. (2015) for similar operating conditions ($T_p$ = 250°C, $We = 24.8$) which was 11.5 ms for $\theta_s = 180°$.

An intermediate Weber number case ($We$ = 20, case 6) was also simulated (not shown). Although the model predicted rebound behavior was similar to experiment, deviations in the CFD model prediction were higher (∼21% for $\theta_s = 150°$ and ∼23% for $\theta_s = 170°$) specifically toward the maximum spreading and recoiling stage. Both contact angle boundary conditions produce less maximum spread diameter (∼1.84 for $\theta_s = 150°$, ∼1.7 for $\theta_s = 170°$ compared with 2.12 in experiment) but the predicted contact times ∼22 and 19 ms for $\theta_s = 150°$ and $\theta_s = 170°$, respectively, were comparable with experiment (∼18.3 ms). It is clear from the model predictions that increasing contact angle decreases the maximum spreading ratio but at the same improve contact time prediction due to higher recoiling action.

**Figure 11B** shows a higher Weber number case ($We$ = 104) where disintegration outcome was observed. CFD model also predicts the same outcome however droplet disintegration was predicted earlier. Apparently, all contact angle boundary conditions predict almost identical spread ratio within the time sequence presented with deviations ∼15–16% in all cases. CFD simulations indicate that contact angle boundary condition has no observable influence on the flow dynamics in the inertia dominated regime past the critical Weber number for droplet disintegration.

Insignificant effect of contact angle boundary condition on the droplet flow dynamics in non-wetting regime has been identified in few recent studies. Ganesan (2013) compared the effect of four different contact angle boundary conditions—static/equilibrium contact angle, Hocking's model (Hocking, 1995), Jiang et al. (1979), and Bracke et al. (1989) using a finite element based CFD model to simulate droplet impact process. This study demonstrated that contact angle boundary condition does not affect the flow dynamics of droplets on non-wetting surface however for wetting and partially wetting surface, different contact angle models induce different flow dynamics, especially during the recoiling phase. Recently, Banitabaei and Amirfazli (2017) investigated droplet-particle interaction in a $\Delta \sim 1$ system over a range of Weber number (∼0.1–1,146) and noted that increasing the contact angle has a considerable effect on geometry of the liquid film and lamella formation, however, increasing the contact angle on a hydrophobic surface beyond a threshold value of 110° did not produce significant effect on the observed lamella geometry.

From the energy balance perspective, droplet dynamics is primarily governed by the competition between the kinetic energy ($E_{kin} = \frac{1}{2} m_d v_{d,0}^2$) and surface energy ($E_{surf} = \sigma_{lg} A_{int}$) considering the fact that energy loss due to viscous dissipation can be ignored on a non-wetting surface. **Figure 12** presents the temporal variations of these two energy components for three different Weber number cases (case 4, 6, 13) with respect to a reference line where the surface to kinetic energy ratio is unity. For case 4 ($We$ = 5), SE/KE ratio shows rapid increase as the droplet spreads over the particle surface and the ratio reaches a maximum (SE/KE ∼14) at $t$ ∼7 ms which corresponds to the maximum spreading state. This is clearly an unstable state from the energy minimization point of view as surface energy is maximum due to excessive deformation of the interface. Due to this instability, droplet interface is retracted by the surface tension force to minimize the interfacial area and consequently kinetic energy commences to increase from a minimum in the recoiling phase eventually resulting in rebound. It could be noted that throughout the entire dynamics, surface energy always dominates the kinetic energy. For case 5 ($We$ = 20), initial kinetic energy of the droplet was higher than its surface energy (SE/KE<1 at $t$ = 0)),

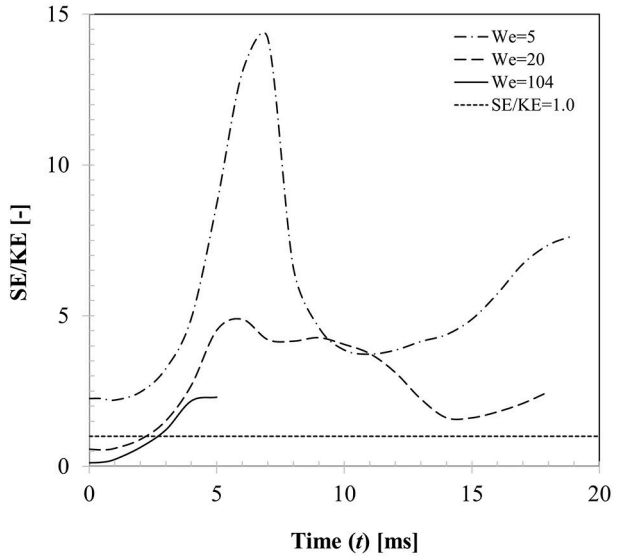


**FIGURE 12 |** Temporal variation in kinetic and surface energy during interaction at different impact Weber numbers (Case 4, 6, 13, $We = 5$, 20, 104, $\theta_S = 150°$).

however this case also showed rebound outcome indicating maximum spreading ratio at $t \sim 6$ ms where SE/KE ratio was much lower (∼4.9) compared to case 4. For case 13 ($We = 104$), again initial kinetic energy of the droplet was higher than its surface energy, however during spreading phase itself, although surface energy increased, due to dominant inertia and vaporization of connecting lamella, droplet exhibited disintegration outcome.

## Heat Transfer Between Droplet and Particle

A time sequence of droplet shape evolutions for $We = 5$ and corresponding CFD simulations with propagation of vapor field (colored by vapor mass fraction) is presented in **Figure 13**. Upon impact, droplet spreads in radial direction wherein impact kinetic energy is converted into surface energy and reaches the maximum spreading state at $t = 5$ ms. During the spreading phase, heat is transferred from the solid to the liquid phase. This energy transfer to the droplet increases its mean temperature while liquid vaporizes at the solid-liquid interface due to elevated temperature gradient between droplet and the particle. If the heat transfer rate is large enough during impact, a thin vapor film forms at the solid-liquid interface. The theoretically minimum temperature required for this vapor film to exist (Leidenfrost or minimum film boiling temperature) can be estimated as $T_{Leid} = \frac{27}{32} T_c$ (Chandra and Avedisian, 1991) where $T_c$ is the critical temperature. For water $T_c = 647$ K which estimates the theoretical temperature to be ∼545 K (273°C). In the experiment, solid surface temperature was kept 350°C which was well above the minimum film boiling temperature and ensured that film boiling scenario actually occurred.

At the maximum spreading stage, vapor production rate is highest due to formation of maximum wetted contact area. Droplet in this state rests on a thin vapor film (<< droplet radius or wetted contact area) and the produced vapor escapes sideways through this narrow film (order of few microns). In the limit of very low Reynolds number ($Re$ <1), flow and pressure drop can be related using the lubrication theory which equates only the pressure gradient term to the viscous diffusion term in the Navier-Stokes equation (Equation 5) while discarding the effect of other terms. Below the disintegration limit, after the maximum spreading state (wetted area) is reached, vapor force due to pressure drop at the liquid-solid interface becomes maximum which causes the spread-out lamella to retract. Eventually, when the upward acting vapor force due to flow pressure drop in the film is able to overcome the downward acting gravity force on droplet, rebound occurs ($t = 17.5$ ms).

Stability of the vapor layer at the wetted contact area has significant impact on the observed interaction outcome. Burton et al. (2012) showed that smaller diameter Leidenfrost drops having wetted contact area length scale much smaller than the capillary length scale $l_{cap} = \sqrt{\frac{\sigma_{lg}}{\rho_l g}}$ (∼2.73 mm for water), have a more stable vapor layer compared to larger size drops where pressure drop in the vapor layer cannot balance the gravity force. In the present study, average droplet diameter was ∼2.9 mm and considering the $\beta$ ratio from the various cases (**Figure 9**), it could be realized that for wetted contact area length scale ($\beta d_{d,0}$) fluctuates around the capillary length. Due to associated inertia, contact line motion is dynamic which overcomes the droplet gravity in the initial stages of spreading. It could be expected that a uniform vapor layer possibly is never established under the operating conditions used in the present study and fluctuations in the vapor layer thickness are indeed inevitable.

An estimate of this thin film thickness can be obtained from the expression for Leidenfrost drop as $e_{film} = \left(\frac{d_{d,0}}{2}\right)^{4/3} \left[\frac{g \mu_{vap} k_{vap} \rho_l (T_p - T_b)}{\sigma_{lg}^2 \lambda \rho_{vap}}\right]^{1/3}$ suggested in Biance et al. (2003) which gives ∼8 μm using water physical properties for liquid and gas phase at ambient condition (20°C) and saturation condition (100°C), respectively. Clearly, resolving such small thickness in the CFD framework leads to a computationally prohibitive multiscale problem. In the earlier work of Harvie and Fletcher (2001) on droplet impact on a heated flat surface, the vapor film was modeled separately based on lubrication approximation as a one-dimensional sub-model outside their 2D CFD code. Later Ge and Fan (2007) extended the approach into two dimensions into their 3D CFD model. The present CFD model includes an evaporation model (Equation 2) which directly accounts for this vapor field however due to limitation in cell resolution at the contact area, the vapor layer contribution could not be directly substantiated.

Also shown here is the evolution of vapor field around the droplet interface on a cross sectional plane colored by the vapor mass fraction which shows a distribution of vapor phase with maximum vapor fraction at the interface and zero (initial vapor fraction in the CFD model was taken as zero) further away from the interface. All heat transfer takes place during the brief period (contact time ∼18 ms in rebound regime and ∼9 ms in disintegration regime) when the droplet makes a

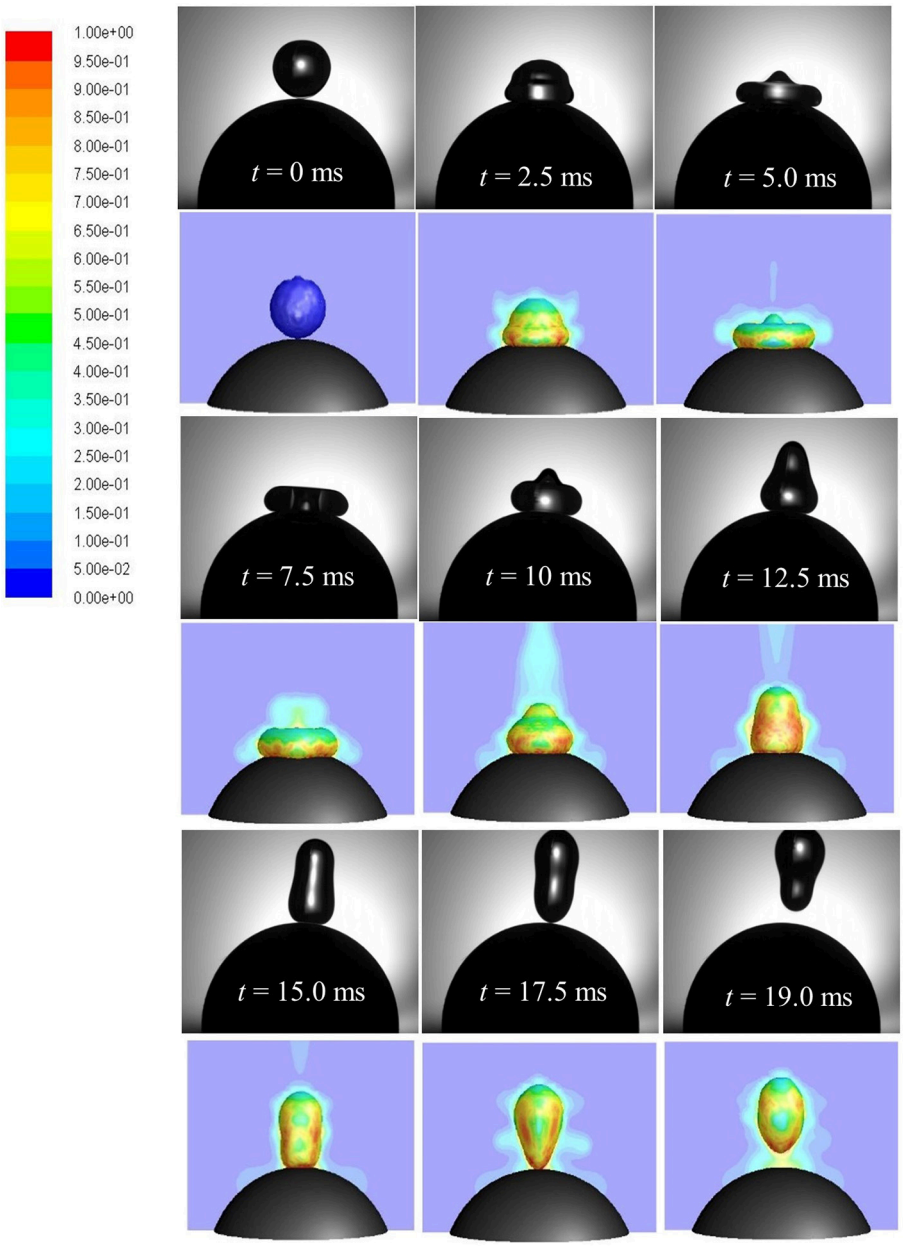


**FIGURE 13 |** Comparison of CFD model predicted (row 2, 4, 6) droplet rebound behavior with high speed imaging (row 1, 3, 5). Vapor profile around the droplet interface is colored by vapor mass fraction (Case 4, $We = 5$).

physical contact with the hot particle surface. In absence of any external convection, dominant heat transfer mechanism here is the conduction at solid-liquid interface and internal convection within the droplet. Due to smaller contact duration, droplet temperature increase was small and consequently computed vaporized droplet mass was found to be insignificant ($<<1\%$ in all cases). This is consistent with the earlier results on droplet vaporization under similar operating conditions ($\sim$0.16% in Nikolopoulos et al., 2007; <0.6% in Ge and Fan, 2007; and <0.1% in Gumulya et al., 2015).

Change in droplet temperature during impact was computed based on volume averaging as follows $T_{d,avg} = \frac{\int_V \alpha_d T_{mix} dV}{\int_V \alpha_d dV}$ where $\alpha_d$ = droplet volume fraction, $T_{mix}$ = mixture temperature and $V$ = domain volume. **Figure 14A** presents a comparison of the estimated droplet temperature for the three contact angle boundary conditions $\theta_s$ = 150, 160, and 170° for case 4 ($We = 5$). All boundary conditions predict similar temperature rise ($\sim$4–5°C) during the spreading phase ($t$ $\sim$7–10 ms) and temperature trends almost collapse on each other. In the

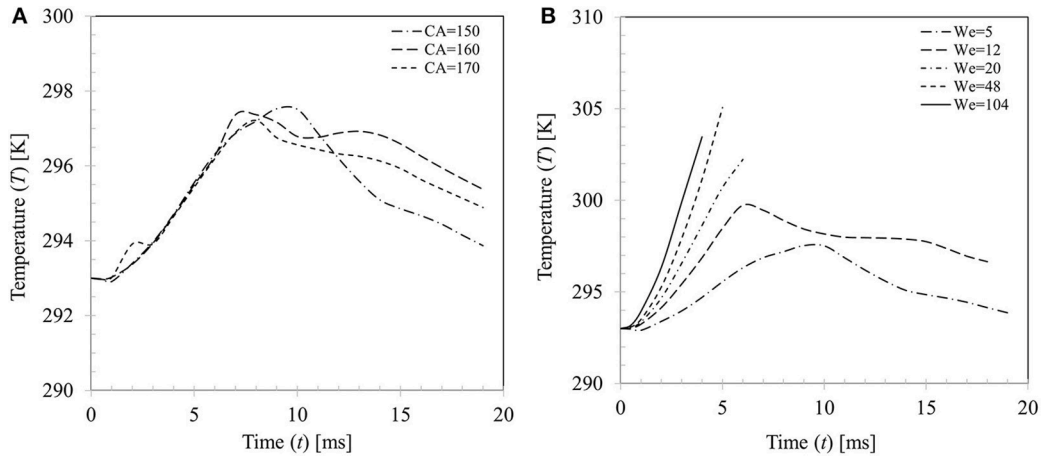


**FIGURE 14 | (A)** Effect of contact angle boundary condition on droplet temperature ($We = 5$). **(B)** Variation in droplet temperature for different impact Weber number cases ($We = 5$, 20, 34, 48, and 104 for $\theta_S = 150°$).

recoiling phase, due to retraction of droplet hence reduction in wetted contact area, heat input to droplet decreases and at the same time due to evaporative cooling effect, droplet temperature decreases. There are some apparent discrepancies in the predicted droplet temperature in the recoiling phase for different contact angle boundary conditions which vary within ±2°C.

**Figure 14B** shows variations in the average droplet temperature at different impact Weber numbers. Generally, droplet temperature increases with increase in Weber number up to $We = 48$. This can be explained by the increasing maximum spread ratio hence the wetted contact area for heat transfer at higher Weber number. The discernible peaks in temperature profiles (∼298–305 K) indicate the maximum spreading state where wetted area for heat transfer is maximum. A left shift in the observed peaks is apparent at the corresponding Weber numbers which indicates early occurring of the maximum spreading phase. It could however be noted that at the highest Weber number case ($We = 104$), peak temperature $T_d \sim 303.5$ K is somewhat lower than the $We = 48$ case ($T_d \sim 305$ K) This could be explained by the fact that even if a larger wetted area is created at higher Weber number, further heat transfer hence increase in temperature is limited by the disintegration process past a critical threshold ($We \sim 50$) which restricts contact time for conduction heat transfer of the droplet on particle surface.

**Figure 15A** presents the effect of contact angle boundary conditions on the computed transient heat flux profile at particle surface for case 4 ($We = 5$). Peak heat flux is slightly higher ($5.22 \times 10^5$ W.m$^{-2}$) for $\theta_s = 150°$ compared with other two contact angle conditions ($4.93 \times 10^5$ W.m$^{-2}$ for $\theta_s = 160°$ and $4.84 \times 10^5$ W.m$^{-2}$ for $\theta_s = 170°$) due to decrease in the contact time at higher contact angle boundary condition. **Figure 15B** shows effect of increasing Weber number on the heat flux profile for $\theta_s = 150°$. It can be seen that increasing Weber number ($We = 5$–104) leads to increasing heat flux at particle surface which increases by almost an order of magnitude ($\sim 5.22 \times 10^5 - 3.23 \times 10^6$ W/m$^2$). It could however be noted that after a critical threshold for Weber number is reached ($We \sim 50$), further increase in Weber number, even by doubling it, increase in heat flux is only marginal (∼7%). This trend could be explained by the limitation in droplet-particle contact time responsible for the conduction heat transfer duration as explained in **Figure 14B**. Two more heat flux profiles from the earlier work of Ge and Fan (2007) under similar operating conditions (acetone droplet on brass particle, $d_{d,0} = 1.8$ mm, $d_p = 3.2$ mm, $T_p = 300$°C, $We = 8$ and 18) are presented in **Figure 15B** for a comparison. In these two cases, droplet exhibits rebound outcome and heat flux profiles follow the same trend as obtained in the present study, however peak heat flux in these two cases are comparatively higher for the similar Weber number cases ($We = 5$ and 20) investigated in the present study. This phenomenon could be attributed to the relatively larger droplet-particle size ratio ($\Delta = 0.56$) used in Ge and Fan's (2007) work compared to present study ($\Delta = 0.29$) which led to larger spread ratio hence wetted contact for heat transfer.

A similar observation on the heat flux behavior in the temperature range from $T_{surf} = 50$ to 120°C was also noted in Pasandideh-Fard et al. (2001) for droplet impact on a flat heated stainless-steel surface. Increasing impact velocity of droplet was found to marginally increase heat flux from the substrate and the only apparent effect was increase in the wetted contact area over which heat transfer takes place. In another study, using a VOF based CFD model, Nikolopoulos et al. (2007) quantified heat flux for water droplets impinging onto a stainless-steel surface ($T_{surf} = 180$°C) which was ∼3 $\times 10^7$ W/m$^2$. The reported heat flux value in their work was higher by an order of magnitude compared with the present study. The discrepancy could be attributed to the lower surface temperature used in their work, $T_{surf} = 180$°C which defines a nucleate to film boiling transition regime. In this regime,

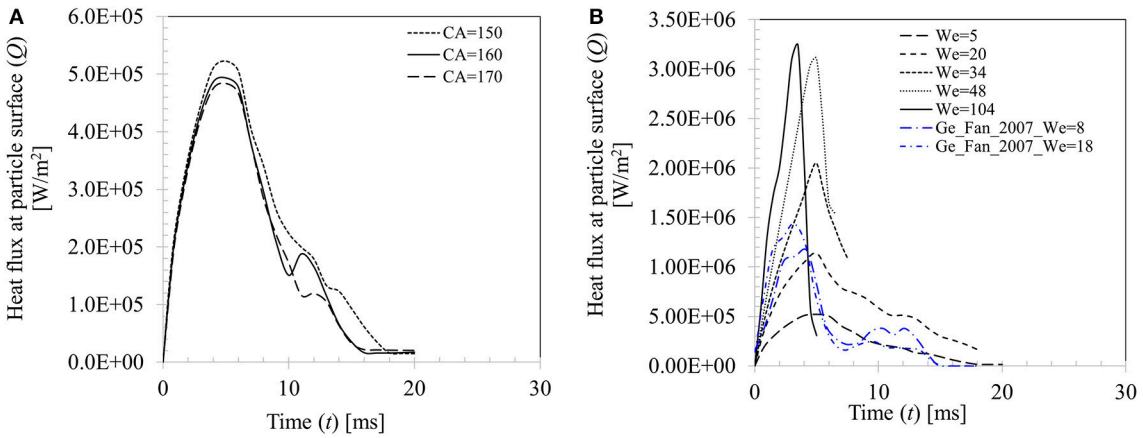


**FIGURE 15 | (A)** Effect of contact angle boundary condition on heat flux for Case 4, $We = 5$. **(B)** Effect of Weber number on heat flux at particle surface ($We = 5$, 20, 34, 48, and 104 for $\theta_S = 150°$).

surface was moderately hydrophobic which was characterized by a contact angle value of 100°. In absence of an insulating vapor film at the contact area, direct droplet-surface contact was inevitable which resulted in comparatively higher heat flux.

## CONCLUSION

In the present study, surface wetting behavior of a spherical particle with and without heat transfer was reported at different droplet impact Weber numbers in the range from 4 to 104. In absence of heat transfer, it was shown that implementation of a continuous time varying measured dynamic contact angle boundary condition provides better agreement to spread ratio. It also produces better interface shape evolution behavior specifically in the recoiling phase when compared with the discrete time implementation of contact angle boundary condition earlier reported in Mitra et al. (2013).

Effect of heat transfer on the droplet-particle interaction was studied in the film boiling regime. Maximum droplet spread ratio was correlated to Weber number which exhibited a power law trend. Two distinct outcomes were observed—rebound and disintegration based on droplet-particle contact time and were clearly demarcated by a critical Weber number ∼50. Droplet-particle contact time in the rebound regime decreased almost by half in the disintegration regime due to absence of the recoiling phase. Flow dynamics in the film boiling regime was studied for different surface hydrophobicity using three contact angle boundary conditions in the limit of super-hydrophobicity ($\theta_s = 150, 160, 170°$) to account for an intervening vapor film at the liquid-solid interface. In general, contact angle boundary condition appears to have less influence on the flow dynamics specifically in the spreading phase, which was confirmed by the relative invariance of maximum spread ratio, droplet temperature and heat flux parameter for all three contact angle conditions. Heat flux and droplet temperature increased with increasing Weber number due to creation of larger spread ratio (wetted contact). Droplet temperature rise was predicted to be in the range from ∼4 to 12°C while heat flux increased by almost an order of magnitude. Although increasing droplet impact velocity (Weber number) augments heat transfer on particle surface, maximum possible heat flux was shown to be largely limited by the contact time which cannot be increased by increasing impact velocity beyond the critical Weber number threshold for droplet disintegration.

Summarizing, this study aimed to analyse the particle surface wetting phenomenon based on its impact dynamics which is critical for a number of multiphase applications of industrial importance. The interface resolved computational model coupling hydrodynamics with the physics of surface tension, contact angle and heat and mass transfer process provides advanced level of details such as wetted contact area, maximum possible heat transfer, evaporation rate and corresponding variation in droplet temperature. The model is also capable of predicting uneven temperature distribution within the particle body (although not shown) as a result of localized transient surface wetting. All this information is essential to gain insight into the complex phase interactions closely associated with process applications such as spray coating, spray drying, fluid coking, and fluid catalytic cracking and cannot be solely obtained from experiment. Further studies in this area will focus on the collision induced chemical reactions that occur during transient heat transfer at particle surface and has relevance specifically to the fluid catalytic cracking process.

## ETHICS STATEMENT

This manuscript has not been previously published or is not currently under consideration for publication elsewhere, either in whole or in part.

## AUTHOR CONTRIBUTIONS

SM conducted the experiment, performed CFD modeling, analyzed data and drafted the manuscript. GE provided valuable inputs to the work through insightful discussions and revised the manuscript.

## FUNDING

The authors would like to gratefully acknowledge the financial support (LP110100717) received from Australian Research Council (ARC) and British Petroleum (BP), Kwinana, Western Australia for this work.

## ACKNOWLEDGMENTS

The authors would like to thank Dr. Mayur Sathe (Institute of Chemical Technology, India), Prof. J. B. Joshi (Homi Bhabha National Institute, India), Prof. Vishnu Pareek (Curtin University of Technology, Western Australia) for engaging discussion and inputs to the work. Authors would also like to thank doctoral student Ms. Thi Bang Tuyen Nguyen (University of Newcastle) for her participation in the experimental part of this work.

## REFERENCES

Afkhami, S., Zaleski, S., and Bussmann, M. (2009). A mesh-dependent model for applying dynamic contact angles to VOF simulations. *J. Comput. Phys.* 228, 5370–5389. doi: 10.1016/j.jcp.2009.04.027

Akao, F., Araki, K., Mori, S., and Moriyama, A. (1980). Deformation behaviours of a liquid droplet impinging onto hot metal surface. *Trans. Iron Steel Inst.* 20, 737–743.

Ansys Fluent theory guide (2013). *Release 15.* Canonsburg, PA: Ansys Inc.

Bakshi, S., Roisman, I. V., and Tropea, C. (2007). Investigations on the impact of a drop onto a spherical target. *Phys. Fluids* 19, 1–12. doi: 10.1063/1.2716065

Banitabaei, S. A., and Amirfazli, A. (2017). Droplet impact onto a solid sphere: effect of wettability and impact velocity. *Phys. Fluids* 29, 1–14. doi: 10.1063/1.4990088

Barrett, J., and Clement, C. (1992). Kinetic evaporation and condensation rates and their coefficients. *J. Colloid Interface Sci.* 150, 352–364. doi: 10.1016/0021-9797(92)90205-Z

Biance, A.-L., Clanet, C., and Quere, D. (2003). Leidenfrost drops. *Phys. Fluids* 15, 1632–1637. doi: 10.1063/1.1572161

Brackbill, J. U., Kothe, D. B., and Zemach, C. (1992). A continuum method for modelling surface tension. *J. Comput. Phys.* 100, 335–354. doi: 10.1016/0021-9991(92)90240-Y

Bracke, M., Voeght, F. D., and Joos, P. (1989). The kinetics of wetting: the dynamic contact angle. *Prog. Colloid Polym Sci.* 79, 142–149. doi: 10.1007/BFb0116200

Burton, J. C., Sharpe, A. L., van der Veen, R. C. A., Franco, A., and Nagel, S. R. (2012). Geometry of the vapor layer under a Leidenfrost drop. *Phys. Rev. Lett.* 109:074301. doi: 10.1103/PhysRevLett.109.074301

Chandra, S., and Avedisian, C. T. (1991). On the collision of a droplet on a solid surface. *Proc. R. Soc. Lond. A* 432, 13–41. doi: 10.1098/rspa.1991.0002

Charalampous, G., and Hardalupas, Y. (2017). Collisions of droplets on spherical particles. *Phys. Fluids* 29, 1–15. doi: 10.1063/1.5005124

Clanet, C., Beguin, C., Richard, D., and Quere, D. (2004). Maximal deformation of an impacting drop. *J. Fluid Mech.* 517, 199–208. doi: 10.1017/S0022112004000904

Dussan, E. B. (1979). On the spreading of liquids on solid surfaces: static and dynamic contact lines. *Ann. Rev. Fluid Mech.* 11, 371–400. doi: 10.1146/annurev.fl.11.010179.002103

Gac, J. M., and Gradon, L. (2014). Lattice-Boltzmann modelling of collisions between droplets and particles. *Colloid Surfaces A Physicochem. Engin. Aspects* 441, 831–836. doi: 10.1016/j.colsurfa.2012.11.078

Ganesan, S. (2013). On the dynamic contact angle in simulation of impinging droplets with sharp interface methods. *Microfluid Nanofluid* 14, 615–625. doi: 10.1007/s10404-012-1080-x

Ge, Y., and Fan, L.-S. (2007). Droplet-particle collision dynamics with film boiling evaporation. *J. Fluid Mech.* 573, 311–337. doi: 10.1017/S0022112006003922

Gumulya, M., Utikar, R. P., Pareek, V., Mead-Hunter, R., Mitra, S., and Evans, G. M. (2015). Evaporation of droplet on a heated spherical particle. *Chem. Eng. J.* 278, 309–319. doi: 10.1016/j.cej.2014.11.024

Hardalupas, Y., Taylor, A. M. K. P., and Wilkins, J. H. (1999). Cooling effectiveness of a water drop impinging on a hot surface. *Int. J. Heat Fluid Flow* 20, 477–485. doi: 10.1016/S0142-727X(99)00045-4

Harvie, D. J. E., and Fletcher, D. F. (2001). A hydrodynamic and thermodynamic simulation of droplet impacts on hot surfaces, part-I: theoretical model. *Int. J. Heat Mass Transf.* 44, 2633–2642. doi: 10.1016/S0017-9310(00)00303-3

Hocking, L. (1995). On the contact angels in evaporating liquids. *Phys. Fluids* 7, 2950–2955. doi: 10.1063/1.868672

Hoffman, R. L. (1975). A study of the advancing interface. I. Interface shape in liquid–gas systems. *J. Colloid Interface Sci.* 50, 228–241. doi: 10.1016/0021-9797(75)90225-8

Huh, C., and Scriven, L. E. (1971). Hydrodynamic model of steady movement of a solid/liquid/fluid contact line. *J. Colloid Interface Sci.* 35, 85–101. doi: 10.1016/0021-9797(71)90188-3

Jiang, T. -S., Soo-Gun, O. H., and Slattery, J. C. (1979). Correlation for dynamic contact angle. *J. Colloid Interface Sci.* 69, 74–77. doi: 10.1016/0021-9797(79)90081-X

Karl, A., Anders, K., Rieber, M., and Frohn, A. (1996). Deformation of liquid droplets during collisions with hot walls: experimental and numerical results. *Part.Part.Syst.Char.* 13, 186–191. doi: 10.1002/ppsc.19960130304

Kistler, S. F. (1993). "Hydrodynamics of wetting," in *Wettability,* ed J. Berg (New York, NY: Marcel Dekker), 311–429.

Malgarinos, I., Nikolopoulos, N., and Gavaises, M. (2016). A numerical study on droplet-particle collision dynamics. *Int. J. Heat Fluid Flow* 61, 499–509. doi: 10.1016/j.ijheatfluidflow.2016.06.010

Malgarinos, I., Nikolopoulos, N., and Gavaises, M. (2017a). Numerical investigation of a heavy fuel droplet-particle collisions in the injection zone of Fluid Catalytic Cracking reactor, Part I: numerical model and 2D simulations. *Fuel Process. Technol.* 156, 317–330. doi: 10.1016/j.fuproc.2016.09.014

Malgarinos, I., Nikolopoulos, N., and Gavaises, M. (2017b). Numerical investigation of heavy fuel droplet-particle collisions in the injection zone of Fluid Catalytic Cracking reactor, Part II: 3D simulations. *Fuel Process. Technol.* 156, 43–53. doi: 10.1016/j.fuproc.2016.09.012

Marek, R., and Straub, J. (2001). Analysis of the evaporation coefficient and the condensation coefficient of water. *Int. J. Heat Mass Trans.* 44, 39–53. doi: 10.1016/S0017-9310(00)00086-7

Mitra, S., Doroodchi, E., Pareek, V., Joshi, J. B., and Evans, G. M. (2015). Collision behaviour of a smaller particle into a larger stationary droplet. *Adv. Powder Tech.* 26, 280–295. doi: 10.1016/j.apt.2014.10.008

Mitra, S., Doroodchi, E., Pareek, V., Joshi, J. B., and Evans, G. M. (2016). On wetting characteristics of droplet on a spherical particle in film boiling regime. *Chem. Eng. Sci.* 149, 181–203. doi: 10.1016/j.ces.2016.04.003

Mitra, S., Doroodchi, E., Pareek, V., Joshi, J. B., and Evans, G. M. (2017). Interactions in droplet-particle system of near unity size ratio. *Chem. Eng. Sci.* 170, 154–175. doi: 10.1016/j.ces.2017.03.059

Mitra, S., Sathe, M. J., Doroodchi, E., Utikar, R., Shah, M., Pareek, V., et al. (2013). Droplet impact dynamics on a spherical particle. *Chem. Eng. Sci.* 100, 105–119. doi: 10.1016/j.ces.2013.01.037

Nguyen, T. B., Mitra, S., Pareek, V., Joshi, J. B., and Evans, G. M. (2015). Comparison of vaporization models for feed droplet in fluid catalytic cracking risers. *Chem. Eng. Res. Des.* 101, 82–97. doi: 10.1016/j.cherd.2015.03.020

Nikolopoulos, N., Theodorakakos, A., and Bergeles, G. (2007). A numerical investigation of the evaporation process of a liquid droplet impinging onto a hot substrate. *Int. J. Heat Mass Transf.* 50, 303–319. doi: 10.1016/j.ijheatmasstransfer.2006.06.012

Pasandideh-Fard, M., Aziz, S. D., Chandra, S., and Mostaghimi, J. (2001). Cooling effectiveness of a water drop impinging on a hot surface. *Int. J. Heat Fluid Flow* 22, 201–210. doi: 10.1016/S0142-727X(00)00086-2

Sikalo, S., Wilhelm, H.-D., Roisman, I. V., Jakirli, S., and Tropea, C. (2005). Dynamic contact angle of spreading droplets: experiments and simulations. *Phys. Fluids* 17:062103. doi: 10.1063/1.1928828

Wachters, L. H. J., and Westerling, N. A. J. (1966). The heat transfer from a hot wall to impinging water drops in the spheroidal state. *Chem. Eng. Sci.* 21, 1047–1056. doi: 10.1016/0009-2509(66)85100-X

**Conflict of Interest Statement:** The authors declare that the research was conducted in the absence of any commercial or financial relationships that could be construed as a potential conflict of interest.

## NOMENCLATURE

$A$ area ($m^2$)
$a$ interfacial thickness (m)
$C_p$ heat capacity ($J.kg^{-1}.K^{-1}$)
$d$ diameter (m)
$F_s$ surface tension force ($N/m^3$)
$g$ gravitational constant ($m.s^{-2}$)
$h_{GS}$ grid spacing (m)
$k$ thermal conductivity ($W.m^{-1}.K^{-1}$)
$l$ length scale (m)
M molecular weight ($kg.kmol^{-1}$)
$m$ mass kg
$\dot{m}$ volumetric evaporation rate ($kg.m^{-3}.s^{-1}$)
$n$ unit normal (-)
$P$ pressure (Pa)
Q heat flux ($W/m^2$)
$r$ radius (m)
$R$ universal gas constant ($J.\ kmol^{-1}.K^{-1}$)
$T$ temperature (K)
$t$ time (s)
$t^*$ non-dimensional time (-)
$V$ volume ($m^3$)
$v$ velocity ($m.s^{-1}$)
$y$ species mass fraction (-)

**Dimensionless numbers**

*Ca* Capillary number
*Fr* Froude number
*Re* Reynolds number
*We* Weber number

**Greek letters**

$\alpha$ dispersed phase volume fraction (-)
$\beta$ droplet spread ratio (-)
$\delta$ Dirac delta function (-)
$\Delta$ droplet particle size ratio (-)
$\varepsilon$ level set function value (-)
$\zeta$ scaler variable (-)
$\theta$ contact angle ($^\circ$)
$\kappa$ interface curvature ($m^{-1}$)
$\lambda$ latent heat of vaporization ($J.kg^{-1}$)
$\mu$ viscosity ($Kg.m^{-1}.s^{-1}$)
$\rho$ density ($kg.m^{-3}$)
$\sigma$ surface tension ($N.m^{-1}$)
$\tau$ characteristic time scale (s)
$\phi$ level set function (-)
$\chi$ accommodation coefficient (-)
$\psi$ central angle ($^\circ$)

**Super/Subscript**

*adv* advancing
*avg* average
*c* condensation
*cap* capillary
*cl* contact line
*d* droplet
*e* evaporation
*g* gas
*hoff* Hoffman function
0 initial state
*int* interface
*kin* kinetic
*l* liquid
*LS* level-set
max maximum
*mix* mixture
*p* particle
*rec* receding
*s* static
*sat* saturation
*surf* surface
*vap* vapor
*w* wall

frontiers in Chemistry

ORIGINAL RESEARCH
published: 24 September 2018
doi: 10.3389/fchem.2018.00435

# Effects of Contact Angle and Flocculation of Particles of Oligomer of Tetrafluoroethylene on Oil Foaming

*Ryo Murakami*[1]*, *Syuji Kobayashi*[1], *Manami Okazaki*[1], *Alexander Bismarck*[2,3] and *Masahiro Yamamoto*[1]

[1] Department of Chemistry, Konan University, Kobe, Japan, [2] Polymer and Composite Engineering (PaCE) Group, Department of Material Chemistry, University of Vienna, Vienna, Austria, [3] Polymer and Composite Engineering (PaCE) Group, Department of Chemical Engineering, Imperial College London, London, United Kingdom

Oil foams have been stabilized by using particles of oligomer of tetrafluoroethylene (OTFE). OTFE particles were dispersed in oil mixtures prior to aeration, to exclude the oil-repellency nature of the particles due to the formation of the metastable Cassie-Baxter state and properly evaluate the effects of contact angle on the foaming behavior. The particle contact angle ($\theta^{Y}$) against air/oil surfaces were controlled by changing a composition of two oils with different surface tension (*n*-heptane and methyl salicylate). The $\theta^{Y}$ value increases with increasing a mole fraction of methyl salicylate, from 42° (for pure *n*-heptane) to 89° (for pure methyl salicylate). The air volume incorporated in the oils after aerating OTFE dispersions in the oil mixtures shows a maximum when $\theta^{Y}$ = 55°. The flocculation of OTFE particles in bulk oils is responsible for the unexpected behavior of foaming observed when $\theta^{Y}$ is relatively high. The increase in the degree of the flocculation reduces the effective concentration of OTFE particles in bulk oil, leading to the inefficient bubble stabilization. These findings suggest the efficient oil foaming using particles as a stabilizer is achieved by optimizing both the particle contact angle and the degree of flocculation in oils.

**Keywords: oil foams, Pickering-Ramsden foams, contact angle, adsorption, flocculation**

OPEN ACCESS

***Edited by:***
*Grant Bruce Webber, University of Newcastle, Australia*

***Reviewed by:***
*Hongbo Zeng, University of Alberta, Canada*
*Seher Ata, University of New South Wales, Australia*

***Correspondence:**
*Ryo Murakami*
*murakami@konan-u.ac.jp*

***Specialty section:***
*This article was submitted to Chemical Engineering, a section of the journal Frontiers in Chemistry*

***Received:*** *11 April 2018*
***Accepted:*** *03 September 2018*
***Published:*** *24 September 2018*

***Citation:***
*Murakami R, Kobayashi S, Okazaki M, Bismarck A and Yamamoto M (2018) Effects of Contact Angle and Flocculation of Particles of Oligomer of Tetrafluoroethylene on Oil Foaming. Front. Chem. 6:435. doi: 10.3389/fchem.2018.00435*

## INTRODUCTION

Liquid foams are utilized in industries such as foods and cosmetics but also in the chemical processes such as froth flotation and foam fractionation. Molecular and polymeric surfactants have been frequently used to stabilize liquid foams. Particulate materials (colloidal particles) are also adsorbed at air/liquid surfaces, usually forming adsorbed films of densely packed particles, which prevents coalescence and disproportionation, as has been reported for particle-stabilized emulsions (Pickering-Ramsden emulsions) (Binks and Horozov, 2006). Water is the most frequently used liquid for foaming with particulate materials, there are a large of number studies on particle-stabilized aqueous foams (Alargova et al., 2004; Binks and Horozov, 2005; Binks and Murakami, 2006; Gonzenbach et al., 2006; Kostakis et al., 2006; Binks et al., 2007; Horozov, 2008; Wege et al., 2008; Stocco et al., 2011). Non-aqueous liquids that are practically not miscible with water and show a relatively low surface tension, that is, oils can be also aerated in the presence of particles (Friberg, 2010; Fameau, 2017). One of the important factors for stabilizing foams and emulsions with particles is the particle wettability against air/liquid surfaces, quantified by a contact angle

($\theta$). For dispersed systems consisting of air and liquids, if a particle is relatively liquid-philic, air-in-liquid systems (liquid foams) are stabilized, while relatively liquid-phobic particles stabilize liquid-in-air systems, such as liquid marbles and dry liquids. The phase inversion between the two systems has been achieved by controlling the particle wettability (Binks and Murakami, 2006; Binks et al., 2007; Murakami and Bismarck, 2010).

The driving force of adsorption of a particle to an air/liquid surface is the free energy gain ($\Delta G$) by losing an area of the surface and crucially dependent on $\theta$ (Binks and Horozov, 2006). If a particle is spherical and the line tension effect is neglected, $\Delta G$ can be calculated as an energy to remove the particle already adsorbed at a liquid surface into bulk;

$$\Delta G = \pi r^2 \gamma_{\mathrm{al}} (1 - |\cos\theta|)^2 . \quad (1)$$

Here $r$ is a particle radius, $\gamma_{\mathrm{al}}$ is a surface tension between air and liquid. For dispersed systems of air and liquids $\theta$ is measured through the liquid phase. At fixed surface tension and particle size, $\Delta G$ shows a maximum at 90° and sharply decreases with $\theta$ either decreasing to 0° or increasing to 180°. The $\Delta G$ for the particles with moderate wettability is typically higher than hundreds of $kT$, implying such particles are irreversibly adsorbed at fluid interfaces. This irreversible adsorption has been thought to be the origin of the stability of particle-stabilized dispersed systems. Aqueous foams stabilized solely by nano-sized silica particles with different hydrophobicity have been prepared (Binks and Horozov, 2005; Binks and Murakami, 2006; Binks et al., 2007). When the hydrophobicity is intermediate, stable aqueous foams are formed and the foaming efficiency increases with increasing the hydrophobicity. If the particles are very hydrophilic, that is, $\theta$ is relatively close to 0°, the particles are easily desorbed from an air/water surface and prefer remaining in a water phase, leading to the formation of particle dispersions.

Compared to particle-stabilized aqueous foams, particle-stabilized oil foams have been sparsely studied (Friberg, 2010; Fameau, 2017). The stabilization of oil foams have been reported using particles with low surface energy (particles with fluorinated surfaces and fluoro-particles such as PTFE) and various kinds of pure oils (Thareja et al., 2008; Binks et al., 2011, 2015; Binks and Tyowua, 2013). The types of materials formed by mixing air, the oils and the particles have been considered in terms of air-oil surface tension, particle surface energy and mixing methods. However, the mechanisms regarding oil foam stabilization, for example, the dependence of foam volume on the contact angle, has not been studied. In our previous study, we have prepared oil foams using oligomer of tetrafluoroethylene (OTFE) particle (Murakami and Bismarck, 2010). The particle contact angle was controlled by mixing two oils with different surface tension. The foam volume shows a maximum when the particle intrinsic (Young's) contact angle ($\theta^{\mathrm{Y}}$), which is the contact angle determined by the particle surface chemistry, is around 46°. When the contact angle is relatively high, say, between 50 and 80°, oil foams are barely formed, instead, agglomerated particles containing small amount of trapped air bubbles are obtained. From the viewpoint of $\Delta G$, the foaming efficiency is expected to increase with increasing $\theta^{\mathrm{Y}}$ when $\theta^{\mathrm{Y}} < 90°$, as is found for particle-stabilized aqueous foams (Binks and Horozov, 2005; Binks and Murakami, 2006). The reason of the poor oil foaming at a relatively high $\theta^{\mathrm{Y}}$ is that OTFE particles are oil-repellent due to the metastable Cassie-Baxter state. The particles are highly agglomerated in air due to the surface force between the particles and air/oil surfaces can be suspended between the primary particles in the agglomerates, leading to the formation of the metastable Cassie-Baxter state, when $\theta^{\mathrm{Y}}$ is higher than a critical angle (46°). Bubbles formed during aeration are barely adsorbed by OTFE particles, as they are not readily wetted by oils when $\theta^{\mathrm{Y}}$ is higher than 46°. Such oil-repellent agglomerated particles preferably stabilize oil marbles and dry oils, instead of oil foams.

We have hypothesized that if OTFE particles are properly dispersed in oil *prior to aeration*, oil foam volume would increase with increasing $\theta^{\mathrm{Y}}$ and hence with increasing $\Delta G$. In this study, we prepare dispersions of OTFE particles in two oils with a low surface tension oil (*n*-heptane) and a high surface tension one (methyl salicylate). To eliminate the effects of the metastable Cassie-Baxter state on oil foaming behavior, a dispersion of OTFE particles in methyl salicylate is prepared by using the solvent replacement method; initially the particles are dispersed in an oil with a low surface tension (hence low $\theta^{\mathrm{Y}}$) and the oil is gradually replaced with an oil with a high surface tension (hence high $\theta^{\mathrm{Y}}$). The two dispersions of OTFE particles are mixed at a fixed content of OTFE particles and $\theta^{\mathrm{Y}}$ is increased with increasing a mole fraction of methyl salicylate in the oil mixture. By aerating the dispersions of OTFE particles with showing different $\theta^{\mathrm{Y}}$, we investigate the dependence of oil foaming on the contact angle and discuss the oil foaming mechanism. The aim of this study is to find out important factors to control properties of oil foams stabilized by particulate materials.

# EXPERIMENTAL

## Materials

OTFE particles (surface area = 2.17–3.26 $m^2\ g^{-1}$, supplier information) were supplied by Central Glass Co. Ltd., Japan. The particle density is 2.3 g $cm^{-3}$, but the bulk density is 0.30 g $cm^{-3}$, indicating that the powder contains about 90 vol.% air. The degree of polymerization is 5 to 145, corresponding to the molecular weight of 700 to 4,000. Scanning electron microscope images of OTFE particles without any conductive coating are shown in **Figure 1**. The primary particles are nearly spherical with diameters of 0.3 to 1.4 μm (**Figure 1B**). Each primary particle is strongly agglomerated in air due to surface forces. The size of the particle agglomerates is tens to hundreds of micrometers (**Figure 1A**).

Two oils were used. The one is an oil with a low surface tension, *n*-heptane [$\gamma$ = 19.66 mN $m^{-1}$ at 25°C (Lide, 2006)], and the other is an oil with a high surface tension [39.2 mN $m^{-1}$ at 25°C (Lide, 2006)], methyl salicylate. Methyl salicylate, *n*-heptane (SAJ special grade, ≥ 99.0%, Sigma-Aldrich Japan) were passed through alumina columns twice prior to use.

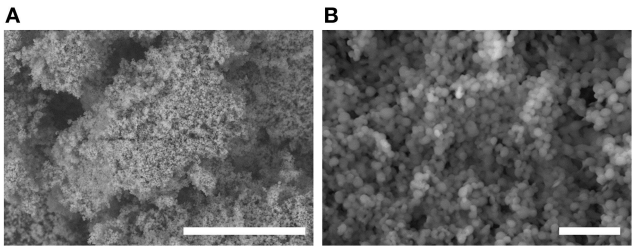


**FIGURE 1 |** Variable pressure-SEM images of OTFE particles taken at **(A)** lower and **(B)** higher magnification. Scale bar = 50 μm for **(A)** and = 5 μm for **(B)**.

## Contact Angle Measurement

To estimate a contact angle of OTFE particles against air/oil surfaces ($\theta^Y$), compressed tablets of OTFE particles were prepared by pressing 0.21 g of the particles in evacuable pellet dies (diameter 13 mm, Specac) at 81.2 MPa for 30 min. Contact angle measurements were conducted using a LSE-B100 (NiCK Corp., Japan) at room temperature (22 ± 2°C). About 10 μL of mixtures of the two oils was placed on the tablet and then advancing contact angles were measured. The error of the measurement is typically < 2°. The compressed tablets are reasonably smooth, judging the difference between advancing and receding contact angles, i.e. the contact angle hysteresis of oils on the tablets is smaller than 3°.

## Preparation of Particle Dispersions in Oil Mixtures and Non-aqueous Foams

Two dispersions of OTFE particles in different oils were prepared. The dispersion of OTFE particles in *n*-heptane was prepared simply by contacting OTFE particles with the oil, as the particles were spontaneously wetted by the oil. The dispersion of OTFE particles in methyl salicylate was prepared by the following several steps (solvent replacement method). Firstly, an amount of OTFE dispersion in *n*-heptane was centrifuged. Secondly, the supernatant brought about by the centrifugation was removed and pure methyl salicylate was added on top of the sedimented OTFE particles. OTFE particles were then re-dispersed by sonication and sedimented again by centrifugation. By repeating these re-dispersion and sedimentation several times, *n*-heptane was practically completely removed and an OTFE dispersion in methyl salicylate was obtained; the final *n*-heptane concentration in OTFE dispersion in methyl salicylate was < 0.01 wt%.

By mixing the OTFE dispersions in *n*-heptane and methyl salicylate, we have prepared OTFE dispersions with desired mole fractions of methyl salicylate ($x_{MS}$) and particle concentrations (1.0, 2.0 and 3.0 vol.% relative to the total volume). The liquid volume was fixed at 5.0 mL. Aeration of OTFE dispersions in glass vials with a volumetric capacity of about 20 mL was carried out by shaking the dispersions by hand at 4 Hz for 15 s, at room temperature (22 ± 2°C).

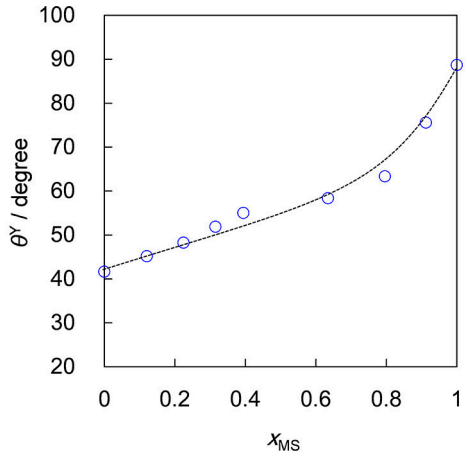


**FIGURE 2 |** Contact angle of OTFE particles against air/oil surface ($\theta^Y$) as a function of mole fraction of methyl salicylate ($x_{MS}$).

## Characterization

The air volume incorporated in oil mixtures was measured manually at a certain time. The error for the volume measurement is typically ± 0.1 mL. Photographs of samples were taken with a CX2 digital camera (Ricoh). Optical micrographs of samples placed on a glass slide with a depression were taken with an Olympus BX51 transmission/reflection microscope fitted with a CMOS camera (Moticam 2000, Shimazu). SEM observation without prior conductive coating was conducted using a Hitachi S-3400N Variable Pressure SEM at an accelerating voltage of 15 kV and at 60-80 Pa with an environmental secondary electron detector.

# RESULTS AND DISCUSSION

## Contact Angle

It is challenging to measure the contact angle of a small particle adsorbed at a liquid surface (Binks et al., 2011). Instead we have measured contact angles of oil drops on tablets of OTFE particles prepared by compression molding, which could mimic the particle surface (Murakami and Bismarck, 2010). The $\theta^Y$ value measured through an oil phase monotonically increases from 42° (for pure *n*-heptane) to 89° (for pure methyl salicylate) with increasing $x_{MS}$, as shown in **Figure 2**. The $\theta^Y$ value for pure *n*-heptane (42°) is lower than the critical contact angle for the formation of the metastable Cassie-Baxter transition (46°). In fact, a dispersion of OTFE particles in *n*-heptane was obtained by simply placing the particles on the top of the surface of the oil. On the other hand, OTFE particles repels the oil mixture when $x_{MS} > 0.22$ ($\theta^Y > 48°$) due to the formation of the metastable Cassie-Baxter state (Murakami and Bismarck, 2010). To properly disperse OTFE particles and study the effect of the contact angle on the foaming behavior in the whole range of $x_{MS}$, the solvent replacement method was used.

## Oil Foaming Behavior

To remove the oil-repellent character and evaluate effects of contact angle on oil foaming, we have dispersed OTFE into oils by the solvent replacement. The upper part of **Figure 3** shows a digital photographs of vials containing 3.0 vol.% dispersions of OTFE particles in oil mixtures at different $x_{MS}$ (and $\theta^Y$) before aeration. All the OTFE dispersions with different $x_{MS}$ ($\theta^Y$) show the same total volume, showing OTFE particles are completely wetted by the oil mixtures and they are properly dispersed in the oils. The particles sediment on the bottom of the glass vials, as the particle density is much higher than the oil one. It should be noted that the apparent volume of the sedimented particles increases with increasing $\theta^Y$, when $\theta^Y \geqq 55°$, while the volume is identical when $42° \leqq \theta^Y \leqq 55°$. This increase is due to the flocculation of the particles and the relationship between the flocculation and oil foaming behavior is discussed later.

OTFE dispersions at different $x_{MS}$ ($\theta^Y$) and particle concentrations were vigorously shaken by a hand. An example of OTFE dispersions after aeration (3.0 vol.%) is shown in **Figure 3**, lower part. For pure *n*-heptane ($x_{MS} = 0$, $\theta^Y = 42°$), the volume of the dispersion is unchanged from the original one upon aeration, implying no stable bubbles (hence foam) was formed. The case for pure methyl salicylate ($x_{MS} = 1.0$, $\theta^Y = 89°$) also shows no practical change of the volume, but a white layer has appeared, which could be highly flocculated particles containing a relatively small number of air bubbles, as shown in **Figure 5D**. The flocculated particles with the air bubbles creams up due to a decrease in the apparent particle density, leading to the formation of the white layer. When the oil mixtures were used ($0.12 \leqq x_{MS} \leqq 0.91$, $45° \leqq \theta^Y \leqq 76°$), the dispersions show not only the formation of white layers but also an increase in the total volume, indicating air is incorporated into the samples as bubbles; oil foams are formed. It is found that the extent of volume increase is quite dependent on $x_{MS}$ (and $\theta^Y$).

The air volume incorporated into the dispersions with different OTFE concentrations after aeration are dependent on both $\theta^Y$ and OTFE concentration, as shown in **Figure 4**. The total volume after aeration has unchanged with time, while a clear subphase appeared with time when $\theta^Y \geq 45°$, indicating creaming of bubbles. It should be stressed that the incorporated air volume has unchanged with time for all the $\theta^Y$ and the particle concentration for at least 3 months, suggesting the particle-stabilized bubbles and foams are stable against coalescence and disproportionation. On the dependence of the incorporated air volume on $\theta^Y$ (**Figure 4A**), there is a maximum of the incorporated air volume at $\theta^Y = 55°$, irrespective of OTFE concentration; oil foams are efficiently formed when the contact angle is intermediate. For particle-stabilized foams prepared using water and ethanol mixture, there is also a maximum in foam height when the contact angle is between 75 and 85° (Sun and Gao, 2002). The existence of the maximum at the intermediate contact angle is not explained in terms of $\Delta G$ which increases with $\theta^Y$ approaching to 90° and is contradict with the behavior observed for the particle-stabilized aqueous foams (Binks and Horozov, 2005; Binks and Murakami, 2006; Binks et al., 2007). We discuss this unexpected oil foaming behavior later.

**Figure 4B** shows that the incorporated air volume monotonically increases with increasing OTFE concentration at a fixed $\theta^Y$. Binks and Tyiwua observed an increase in

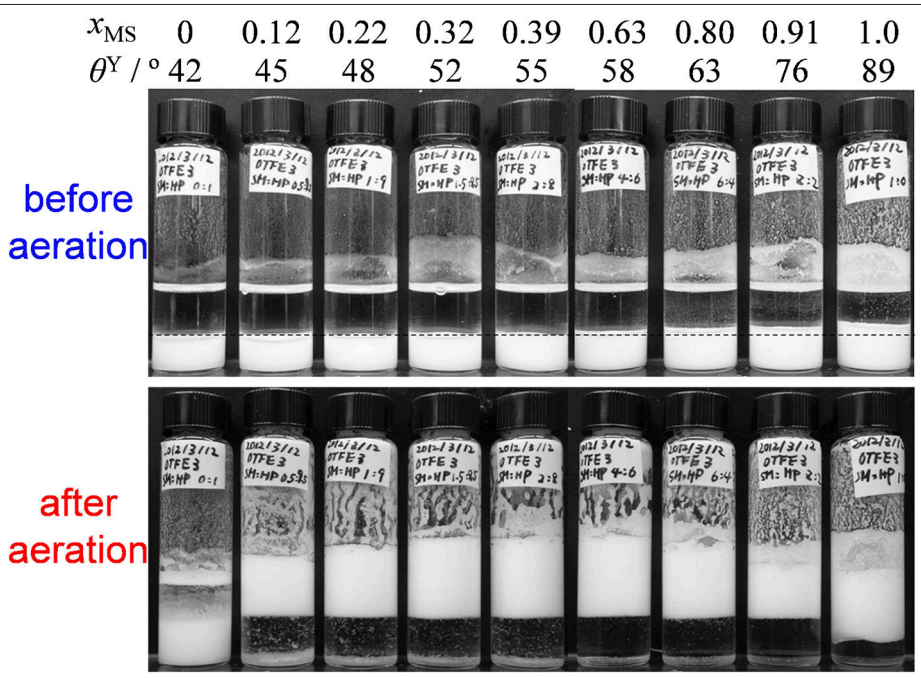


**FIGURE 3 |** Digital photographs of vials containing 3.0 vol.% dispersions of OTFE particles in oil mixtures at different $x_{MS}$ (and $\theta^Y$) before and after aeration. Dotted line is guide for apparent volume of sedimented OTFE particles.

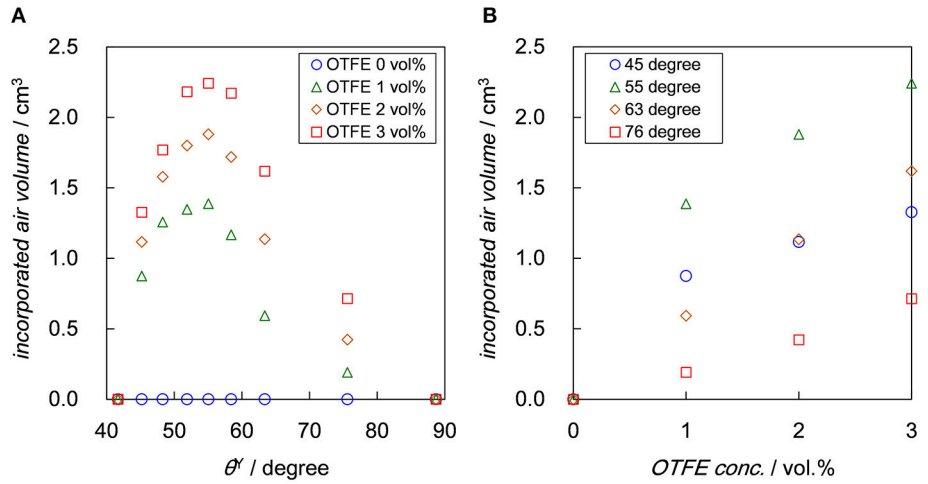


**FIGURE 4 |** Air volume incorporated into the dispersion with different OTFE concentration after aeration plotted as a function of: **(A)** $\theta^{Y}$ and **(B)** OTFE concentration. Air volume measured after 1 month is plotted.

volume of particle-stabilized oil foams with increasing a particle concentration and pointed out the resemblance to surfactant foaming agents below the critical micelle concentration (Binks and Tyowua, 2013). It is assumed that during aeration bare bubbles are initially formed and if the bubbles are adsorbed by enough amount of particles during aeration, they remain as particle-stabilized bubbles after the cease of aeration. The size of bubbles stabilized by particles might be larger than the original bare bubble due to the limited coalescence (Arditty et al., 2003; Tcholakova et al., 2008). The increase in the particle concentration facilitate the bubble stabilization, which is driven by an increase in the potential total area to be covered by particles, leading to an increase in the incorporated air volume. However the drawback of the increase in the particle concentration is a decrease in the rate of energy dissipation, which is consumed by the formation bubble surfaces and the agitation of the total mass (Tsabet and Fradette, 2015). The air volume incorporated in oils is determined by a balance between these two factors; the air volume could initially increase and practically reach a plateau with increasing the particle concentration.

**Figure 5** shows optical micrographs of aerated OTFE dispersions with 3.0 vol.% of particle concentration. When $\theta^{Y} =$ 48 and 55°, a large amount of air bubbles are seen (**Figures 5A,B**). The typical bubble size ranges from tens micrometer to hundreds micrometer and the average size appears to be not dependent on $\theta^{Y}$. Most of the bubbles are deformed from a sphere, suggesting OTFE particles are jammed at the bubble surfaces (Subramaniam et al., 2005, 2006). When $\theta^{Y} = 63°$ (**Figure 5C**), less amount of bubbles are observed and some bubbles appear to be covered by the flocculated particles. There are only a few bubbles and a large amount of highly flocculated particles at a relatively high $\theta^{Y}$ ($\theta^{Y} = 76°$, **Figure 5D**). The bubbles appear to be entrapped by the network of the flocculated particles. The extent of the deformation appears to become more severe with increasing $\theta^{Y}$; the particle networking might also retard the shape relaxation of the bubbles due to the air/oil surface tension.

## Oil Foaming Mechanism

To investigate the reasons why the foaming efficiency decreases when $\theta^{Y} > 55°$. We have observed OTFE dispersions before aeration by an optical microscopy. When the contact angle is relatively low (for the case of pure *n*-heptane, $\theta^{Y} =$ 42°, **Figure 6A**), the particles appear reasonably dispersed. With increasing $\theta^{Y}$ (a mole fraction of methyl salicylate), however, OTFE particles are progressively flocculated in the oils **Figures 6B–D**). These findings are consistent with an increase in the apparent volume of the sedimented particles increasing $\theta^{Y}$ when $\theta^{Y} > 55°$, as shown in **Figure 3**. It is thought that the particle packing in the sedimented layer progressively becomes loose with increasing the degree of the flocculation.

The flocculation is induced by either an increase in attractive interactions or a decrease in repulsive interactions. There would be no effective repulsive interactions between OTFE particles in oils, while it is reasonably assumed that the van der Waals interaction between OTFE particle surfaces is the origin of the attractive interaction. We have estimated the non-retarded Hamaker constant *A* for two OTFE particle surfaces interacting across an oil according to the Lifshitz theory (Israelachvili, 2011):

$$A = \frac{3}{4}kT\left(\frac{\varepsilon_p - \varepsilon_o}{\varepsilon_p + \varepsilon_o}\right)^2 + \frac{3h\nu_e}{16\sqrt{2}}\frac{\left(n_p^2 - n_o^2\right)^2}{\left(n_p^2 + n_o^2\right)^{3/2}}, \quad (2)$$

where $\varepsilon_p$ and $\varepsilon_o$ are the dielectric constant of OTFE particle and oil and $n_p$ and $n_o$ are the refractive index of OTFE particle and oil. *k*, *T*, *h*, and $\nu_e$ are the Boltzmann constant, the absolute temperature, the Plank constant and the main electronic absorption frequency in the UV, respectively. The Hamaker constants estimated for two OTFE particles in either *n*-heptane or methyl salicylate are shown in **Table 1**. The $\varepsilon_p$

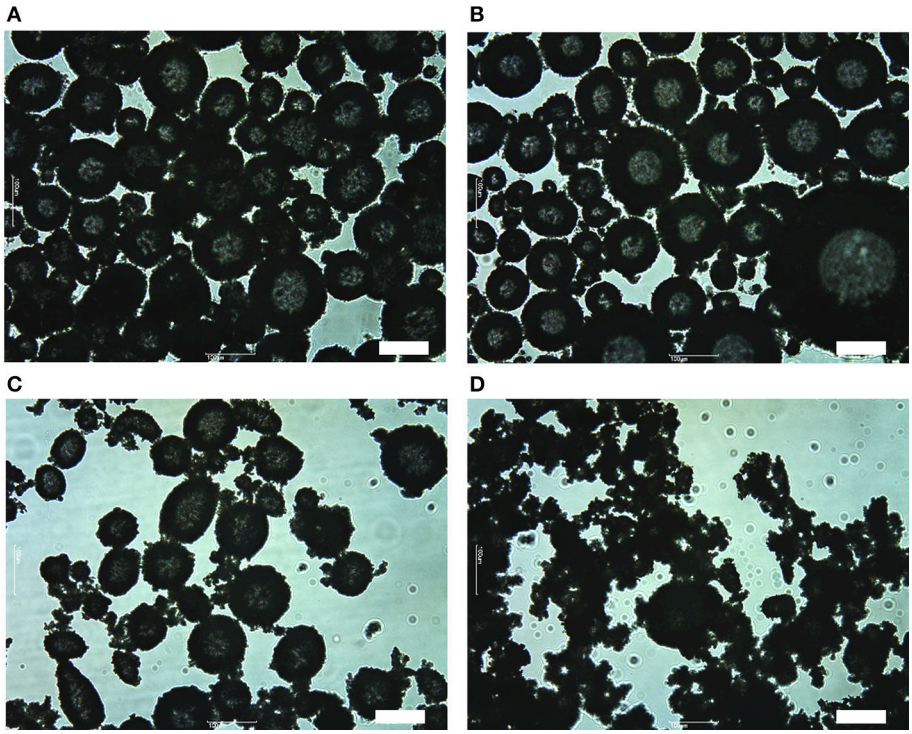


**FIGURE 5 |** Optical micrographs of aerated OTFE dispersions with 3.0 vol.% of particle concentration at different $\theta^Y : \theta^Y =$ **(A)** 48°, **(B)** 55°, **(C)** 63°, and **(D)** 76°. Scale bar = 100 μm.

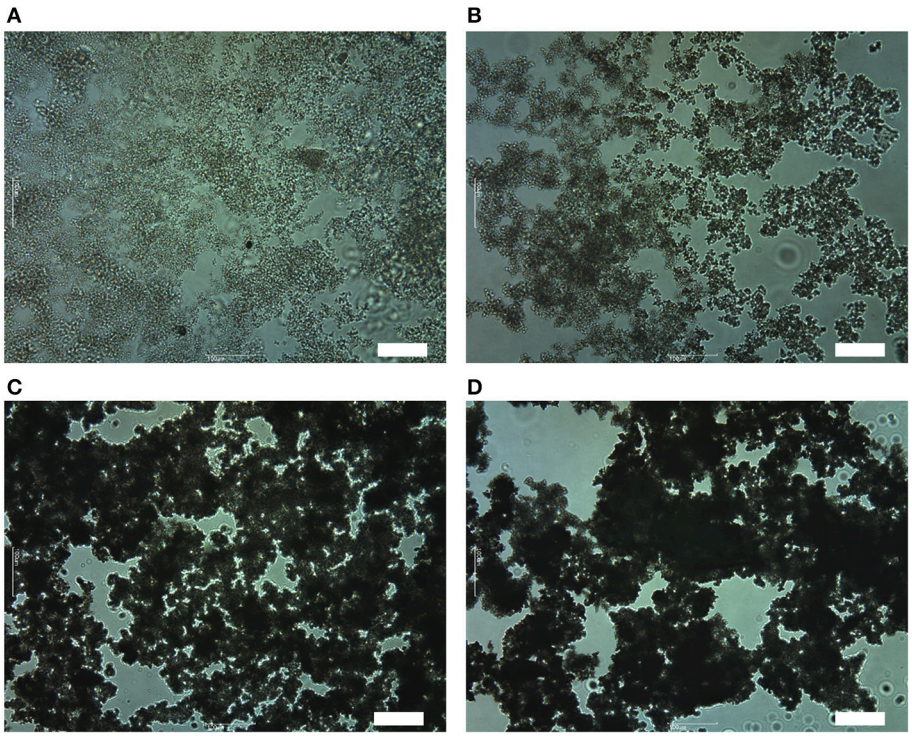


**FIGURE 6 |** Optical micrographs of 1.0 vol.% dispersions of OTFE particles in oil mixtures at different $\theta^Y : \theta^Y =$ **(A)** 42°, **(B)** 55°, **(C)** 63°, and **(D)** 76°. Scale bar = 100 μm.

**TABLE 1 |** Dielectric constant, refractive index and Hamaker constants for two OTFE particles in oils at 293.15 K.

| Oil | $\varepsilon_o$ | $n_o$ | A / $10^{-21}$ J | $\gamma_{al}$ / mN m$^{-1}$ (298.15 K) | $\theta^Y$/° |
|---|---|---|---|---|---|
| *n*-heptane | 1.92 | 1.38776[a] | 0.23 | 19.66 | 42 |
| Methyl salicylate | 9.64 | 1.535 | 8.9 | 39.2 | 89 |
| Cyclohexanone | 16.1 | 1.507 | 7.3 | 34.57 | – |
| Methyl benzoate | 6.642[b] | 1.5164 | 7.0 | 37.17 | – |
| Benzaldehyde | 17.85 | 1.5463 | 10.5 | 38.00 | – |

*Referenced from Lide (2006), except*
[a] *(Rodriguez et al., 1999).*
[b] *Value at 302.7 K.*

and $n_p$ values were assumed to be same as those for PTFE ($\varepsilon_p = 2.1$ and $n_p = 1.359$) and the $\nu_e$ value was set to be $2.9 \times 10^{-15}$ s$^{-1}$, which is a typical value for aliphatic hydrocarbons and PTFE (Israelachvili, 2011). The Hamaker constant for methyl salicylate is about 40 times higher than that for *n*-heptane. It is expected that the Hamaker constant for mixtures of *n*-heptane and methyl salicylate increases with increasing $x_{MS}$ (and $\theta^Y$). The increase in the Hamaker constant could be the reason for the increase in the degree of the flocculation.

The Hamaker constants were estimated for other three oils (cyclohexanone, methyl benzoate and benzaldehyde), whose surface tension is close to that for methyl salicylate and hence would show a relatively high contact angle. The Hamaker constants for the three oils are again much higher than that for *n*-heptane. By mixing an oil with a low surface tension and a high surface tension, the contact angle can be precisely controlled as shown the above, but the flocculation of OTFE particles is inevitable and the efficient oil foaming is not expected when a composition of an oil with a high surface tension in the oil mixture is relatively high.

Here we propose that the flocculation of the particles is closely related to the foaming behavior. One of the possible reasons for less foaming with highly flocculated particles could be a decrease in the effective particle concentration with increasing the degree of flocculation. In the field of mineral flotation, it is well-known that the rate of flotation is a first order to a bulk particle concentration;

$$\frac{dN}{dt} = -kN, \tag{3}$$

where $N$ is the number of floatable particles and $k$ is the rate constant (Mao and Yoon, 1997; Arai et al., 2009). Upon aeration, as stated in the previous section (the dependence of OTFE concentration on the incorporated air volume), bare bubbles could be initially formed and the bubbles become stable against coalescence if the bubbles are enoughly covered by the particles during aeration. The finding that the incorporated air volume increases with increasing the bulk OTFE concentration has suggested that the efficiency of the coverage could increase with increasing the particle concentration around bubbles. Not well-covered bubbles could be formed at a low effective particle concentration for flocculated particles and they are prone to coalesce during aeration, eventually less amount of foam is produced compared to the more dispersed particles. On one hand, the low degree of flocculation might be advantageous to the formation of oil foams. The degree of the flocculation could monotonically increase with increasing the contact angle in this study (see **Figure 6**). The maximum foaming at the intermediate contact angle (55°) might be associated with the particle adsorption energy but also the moderately flocculated particles that can retard drainage and improve the stability of oil foams. Another reason might be that flocculated particles are so large that they are more slowly transferred to an air/oil surface than the deflocculated ones.

## CONCLUSION

Foaming of oils using a particulate material (particles of oligomer of tetrafluoroethylene) was carried out by controlling the particle contact angle against air/oil surfaces and the particle concentration. OTFE particles were properly dispersed in the oils to eliminate the oil-repellency character due to the metastable Cassie-Baxter state. The particle contact angle was controlled by changing a composition of mixtures of two oils with different surface tensions. Oil foaming efficiency shows a maximum at an intermediate contact angle (55°), which is contradict to the findings for particle-stabilized aqueous foams. The reason for the poor oil foaming when the contact angle is relatively high could be a decrease in the effective particle concentration with increasing the degree of flocculation. Less covered bubbles are formed for the flocculated particles and they could be less stable against coalescence. If particles are well dispersed even at a high contact angle, the efficient formation of particle-stabilized oil foams is expected. It is worth using sterically stabilized particles, such as particles with a hairy polymer layer solvated with oil, to test this idea.

## AUTHOR CONTRIBUTIONS

RM designed the study, and wrote the initial draft of the manuscript. MY and AB contributed to analysis and interpretation of data, and assisted in the preparation of the manuscript. SK and MO have contributed to data collection and interpretation.

## FUNDING

We thank Foundation, Oil & Fat Industry Kaikan (Japan), CREST, Japan Science and Technology Agency (Grant No.: JPMJCR12C1) and the Challenging Engineering programme of the UK Engineering and Physical Sciences Research Council (EPSRC, Grant no.: EP/E007538/1) for funding.

## ACKNOWLEDGMENTS

We thank Central Glass Co., Ltd. (Japan), for kindly supplying OTFE particles.

## REFERENCES


Alargova, R. G., Warhadpande, D. S., Paunov, V. N., and Velev, O. D. (2004). Foam superstabilization by polymer microrods. *Langmuir* 20, 10371–10374. doi: 10.1021/la048647a

Arai, H., Matsumoto, K., Shimasaki, S., and Taniguchi, S. (2009). Model experiment on inclusion removal by bubble flotation accompanied by particle coagulation in turbulent flow. *Isij Int.* 49, 965–974. doi: 10.2355/isijinternational.49.965

Arditty, S., Whitby, C. P., Binks, B. P., Schmitt, V., and Leal-Calderon, F. (2003). Some general features of limited coalescence in solid-stabilized emulsions. *Eur. Phys. J. E* 11, 273–281. doi: 10.1140/epje/i2003-10018-6

Binks, B. P., Duncumb, B., and Murakami, R. (2007). Effect of pH and salt concentration on the phase inversion of particle-stabilized foams. *Langmuir* 23, 9143–9146. doi: 10.1021/la701393w

Binks, B. P., and Horozov, T. S. (2005). Aqueous foams stabilized solely by silica nanoparticles. *Angew. Chem. Int. Ed.* 44, 3722–3725. doi: 10.1002/anie.200462470

Binks, B. P., and Horozov, T. S. (2006). "Ch. 1. colloidal particles at liquid interfaces: an introduction" in *Colloidal Particles at Liquid Interfaces*, eds B. P. Binks, and T. S. Horozov (Cambridge: Cambridge University Press), 1–74.

Binks, B. P., Johnston, S. K., Sekine, T., and Tyowua, A. T. (2015). Particles at oil-air surfaces: powdered oil, liquid oil marbles, and oil Foam. *ACS Appl. Mater. Interfaces* 7, 14328–14337. doi: 10.1021/acsami.5b02890

Binks, B. P., and Murakami, R. (2006). Phase inversion of particle-stabilized materials from foams to dry water. *Nat. Mater.* 5, 865–869. doi: 10.1038/nmat1757

Binks, B. P., Rocher, A., and Kirkland, M. (2011). Oil foams stabilised solely by particles. *Soft Matter* 7, 1800–1808. doi: 10.1039/C0SM01129K

Binks, B. P., and Tyowua, A. T. (2013). Influence of the degree of fluorination on the behaviour of silica particles at air-oil surfaces. *Soft Matter* 9, 834–845. doi: 10.1039/C2SM27395K

Fameau, A.-L. (2017). "Ch13. non-aqueous foams based on edible oils" in *Edible Oil Structuring: Concepts, Methods and Applications,* eds. A. R. Patel (London: The Royal Society of Chemistry), 275–307.

Friberg, S. E. (2010). Foams from non-aqueous systems. *Curr. Opin. Colloid Interface Sci.* 15, 359–364. doi: 10.1016/j.cocis.2010.05.011

Gonzenbach, U. T., Studart, A. R., Tervoort, E., and Gauckler, L. J. (2006). Ultrastable particle-stabilized foams. *Angew. Chem. Int. Ed.* 45, 3526–3530. doi: 10.1002/anie.200503676

Horozov, T. S. (2008). Foams and foam films stabilised by solid particles. *Curr. Opin. Colloid Interface Sci.* 13, 134–140. doi: 10.1016/j.cocis.2007.11.009

Israelachvili, J. N. (2011). *Intermolecular and Surface Forces, 3rd Edn.* Oxford: Academic Press.

Kostakis, T., Ettelaie, R., and Murray, B. S. (2006). Effect of high salt concentrations on the stabilization of bubbles by silica particles. *Langmuir* 22, 1273–1280. doi: 10.1021/la052193f

Lide, D. R ed. (2006). *CRC Handbook of Chemistry and Physics, 87th Edn.* Boca Raton, FL: Taylor and Francis.

Mao, L. Q., and Yoon, R. H. (1997). Predicting flotation rates using a rate equation derived from first principles. *Int. J. Min. Proces.* 51, 171–181. doi: 10.1016/S0301-7516(97)00025-2

Murakami, R., and Bismarck, A. (2010). Particle-stabilized materials: dry oils and (polymerized) non-aqueous foams. *Adv. Funct. Mater.* 20, 732–737. doi: 10.1002/adfm.200902007

Rodriguez, A., Canosa, J., and Tojo, J. (1999). Binary mixture properties of methyl tert-butyl ether with hexane or heptane or octane or nonane from 288.15 K to 298.15 K. *J. Chem. Eng. Data* 44, 666–671. doi: 10.1021/je990009k

Stocco, A., Rio, E., Binks, B. P., and Langevin, D. (2011). Aqueous foams stabilized solely by particles. *Soft Matter* 7, 1260–1267. doi: 10.1039/c0sm01290d

Subramaniam, A. B., Abkarian, M., Mahadevan, L., and Stone, H. A. (2005). Non-spherical bubbles. *Nature* 438, 930–930. doi: 10.1038/438930a

Subramaniam, A. B., Abkarian, M., Mahadevan, L., and Stone, H. A. (2006). Mechanics of interfacial composite materials. *Langmuir* 22, 10204–10208. doi: 10.1021/la061475s

Sun, Y. Q., and Gao, T. (2002). The optimum wetting angle for the stabilization of liquid-metal foams by ceramic particles: experimental simulations. *Metal. Mat. Trans. Phys. Metal. Mat. Sci.* 33, 3285–3292. doi: 10.1007/s11661-002-0315-y

Tcholakova, S., Denkov, N. D., and Lips, A. (2008). Comparison of solid particles, globular proteins and surfactants as emulsifiers. *Phys. Chem. Chem. Phys.* 28, 1608–1627. doi: 10.1039/b715933c

Thareja, P., Ising, B. P., Kingston, S. J., and Velankar, S. S. (2008). Polymer foams stabilized by particles adsorbed at the air/polymer interface. *Macromol. Rapid Commun.* 29, 1329–1334. doi: 10.1002/marc.200800262

Tsabet, E., and Fradette, L. (2015). Effect of processing parameters on the production of Pickering emulsions. *Ind. Eng. Chem. Res.* 54, 2227–2236. doi: 10.1021/ie504338d

Wege, H. A., Kim, S., Paunov, V. N., Zhong, Q. X., and Velev, O. D. (2008). Long-term stabilization of foams and emulsions with *in-situ* formed microparticles from hydrophobic cellulose. *Langmuir* 24, 9245–9253. doi: 10.1021/la801634j


**Conflict of Interest Statement:** The authors declare that the research was conducted in the absence of any commercial or financial relationships that could be construed as a potential conflict of interest.

frontiers in Chemistry

ORIGINAL RESEARCH
published: 17 July 2018
doi: 10.3389/fchem.2018.00269

# pH-Responsive Aqueous Bubbles Stabilized With Polymer Particles Carrying Poly(4-vinylpyridine) Colloidal Stabilizer

*Masaya Ito*[1], *Koki Takano*[2], *Haruka Hanochi*[1], *Yuta Asaumi*[1], *Shin-ichi Yusa*[3], *Yoshinobu Nakamura*[2,4] *and Syuji Fujii*[2,4]*

[1] Graduate Course in Applied Chemistry, Environmental and Biomedical Engineering, Graduate School of Engineering, Osaka Institute of Technology, Osaka, Japan, [2] Department of Applied Chemistry, Faculty of Engineering, Osaka Institute of Technology, Osaka, Japan, [3] Department of Applied Chemistry, Graduate School of Engineering, University of Hyogo, Hyogo, Japan, [4] Nanomaterials Microdevices Research Center, Osaka Institute of Technology, Osaka, Japan

Free radical dispersion polymerization was conducted to synthesize near-monodispersed, micrometer-sized polystyrene (PS) particles carrying pH-responsive poly(4-vinylpyridine) (P4VP) colloidal stabilizer (P4VP-PS particles). The P4VP-PS particles were extensively characterized in terms of morphology, size, size distribution, chemical composition, surface chemistry, and pH-response using optical and scanning electron microscopies, elemental microanalysis, X-ray photoelectron spectroscopy, laser diffraction particle size analysis, and zeta potential measurement. The P4VP-PS particles can work as a pH-responsive stabilizer of aqueous bubbles by adsorption at the air-water interface. At and above pH 4.0, where the particles have partially protonated/non-protonated P4VP stabilizer with relatively hydrophobic character, particle-stabilized bubbles were formed. Optical and scanning electron microscopy studies confirmed that the P4VP-PS particles were adsorbed at the air-water interface of the bubbles in aqueous media. At and below pH 3.0, where the particles have cationic P4VP stabilizer with water-soluble character, no bubble was formed. Rapid disruption of the bubbles can be induced by decreasing the pH; the addition of acid caused the *in situ* protonation of pyridine groups in P4VP, which impart water-soluble character to the P4VP stabilizer, and the P4VP-PS particles were desorbed from the air-water interface. The bubble stabilization/destabilization cycles could be repeated at least five times.

**Keywords: bubbles, stimulus-responsive, polymer, particles, interface, adsorption**

OPEN ACCESS

***Edited by:***
*Heqing Jiang,*
*Qingdao Institute of Bioenergy and Bioprocess Technology (CAS), China*

***Reviewed by:***
*Yuchao Wang,*
*Qingdao Institute of Bioenergy and Bioprocess Technology (CAS), China*
*Clemens Kilian Weiss,*
*Fachhochschule Bingen, Germany*

***Correspondence:**
*Syuji Fujii*
*syuji.fujii@oit.ac.jp*

***Specialty section:***
*This article was submitted to Chemical Engineering, a section of the journal Frontiers in Chemistry*

***Received:*** *10 February 2018*
***Accepted:*** *14 June 2018*
***Published:*** *17 July 2018*

***Citation:***
*Ito M, Takano K, Hanochi H, Asaumi Y, Yusa S, Nakamura Y and Fujii S (2018) pH-Responsive Aqueous Bubbles Stabilized With Polymer Particles Carrying Poly(4-vinylpyridine) Colloidal Stabilizer. Front. Chem. 6:269. doi: 10.3389/fchem.2018.00269*

## INTRODUCTION

For a long time, it has been known that gas bubbles can be stabilized solely by solid colloidal particles in aqueous media (Ramsden, 1903; Binks and Horozov, 2006; Studart et al., 2006; Fujii and Murakami, 2008; Hunter et al., 2008; Kruglyakov et al., 2011; Stevenson, 2012; Pugh, 2016; Fujii and Nakamura, 2017). The hydrophilicity-hydrophobicity balance of the particle surfaces determines the adsorption behavior of such particles at the air-water interface, and the bubbles stabilized by solid particles of the suitable hydrophilicity-hydrophobicity balance show excellent long-term stability. Disruption of bubbles is also often required in practical applications. It has

been shown that the stability of bubbles stabilized with stimulus-responsive solid particles can be controlled *in situ* by application of external stimulus such as pH, temperature, light and magnetic fields, as reviewed recently (Fujii and Nakamura, 2017). In such cases, disruption of bubbles can be realized by decreasing the adsorption energy of the solid particles at the interface or by application of external energy exceeding the adsorption energy.

Recently, we synthesized polystyrene (PS) particles carrying poly[2-(diethylamino)ethyl methacrylate] (PDEA) colloidal stabilizer (PDEA-PS particles), and evaluated their ability as a pH-responsive particulate bubble stabilizer (Fujii et al., 2011; Nakayama et al., 2015b, 2016). Using this system, bubbles stabilized under basic conditions (>pH 7) can be destabilized by the addition of an acidic solution. This addition leads to protonation of the PDEA on the PS particle surfaces, which makes the PDEA hydrophilic, and afterward the PDEA-PS particles are desorbed from the air-water interface, leading to disruption of the bubbles. The critical maximum pH required for destabilization of the bubbles correlates closely with the p$K_a$ value of 7.6 for PDEA chains. These results indicated that the threshold pH value which determines bubble stability depends on the pH-responsive nature (p$K_a$ value) of the colloidal stabilizer on the particle surfaces. We also demonstrated that PS particles carrying poly[2-(dimethylamino)ethyl methacrylate] (PDMA) colloidal stabilizer can work as the pH-responsive particulate bubble stabilizer. The p$K_a$ value of PDMA is 7.0 and the threshold pH value determining the bubble stability was near pH 7 (Fujii et al., 2015). In order to widen application ranges of the stimulus-responsive particle-stabilized bubbles, it is crucial to control the threshold pH value which determines their stability.

In the present study, there are two objectives: (i) synthesis and characterization of near-monodispersed, micrometer-sized PS particles carrying poly(4-vinylpyridine) (P4VP) colloidal stabilizer on their surfaces (P4VP-PS particles) by free radical dispersion polymerization, and (ii) investigation of their ability as a pH-responsive particulate bubble stabilizer (**Figure 1**). P4VP shows a p$K_a$ value of ∼4.5 (Wang et al., 2017), which is lower than those of PDEA and PDMA, and it is expected that stability of aqueous bubbles stabilized with the P4VP-PS particles should be changed at around pH 4.5. The P4VP-PS particles were characterized in terms of morphology, size, size distribution, chemical composition, surface chemistry, and pH-response. The particle-stabilized bubbles were characterized in detail with respect to their stability, microstructure and pH response.

# EXPERIMENTAL

## Materials

Styrene, $\alpha$,$\alpha'$-azobisisobutyronitrile (AIBN), isopropanol (IPA, 99%), hydrochloric acid (HCl, 0.5 M aqueous solution), sodium hydroxide (NaOH, ≥ 98%), 4-vinylpyridine (4VP, 95%), PS homopolymer (M.W. 45,000), and aluminum oxide (activated, basic, Brockmann 1, standard grade) were purchased from Sigma-Aldrich. Ethyl 2-cyanoacrylate (Aron Alpha Extra Sokkotayoto) was purchased from Toagosei Co. The inhibitors in styrene and 4VP monomers were removed by treatment with the basic alumina. Water was first ion exchanged and then distilled (Advantec MFS RFD240NA: GA25A-0715).

## Preparation of P4VP Homopolymer by Solution Polymerization

Solution of IPA (100 mL) and the free radical initiator AIBN (0.1 g, 0.61 mmol) was prepared in a 250 mL flask and gas phase was replaced with nitrogen gas to purge oxygen at room temperature. Then, the monomer 4VP (10.0 g, 95 mmol) was introduced to the flask in order to start the free radical solution polymerization using a temperature-controlled magnetic stirrer with constant stirring at 250 rpm at 70°C. The resulting solution was cooled to room temperature after the polymerization for 24 h.

## Preparation of P4VP-Stabilized PS (P4VP-PS) Particles by Dispersion Polymerization

The IPA solution of P4VP homopolymer prepared by the free radical solution polymerization (4.55 g, 10.24 wt%), the initiator AIBN (50 mg, 0.30 mmol) and ethanol (44.5 mL) were mixed in a 250 mL flask equipped with a magnetic stirrer bar, and gas phase was replaced with nitrogen gas. The polymerization was started by injection of styrene (5.0 g, 48.0 mmol) to the flask at 70°C with constant stirring at 250 rpm. After 24 h, P4VP-PS latex was cooled down to 25°C to stop the polymerization. Purification of the latex was conducted by centrifugation/redispersion cycles with ethanol (3 cycles) and then deionized water (5 cycles) using a centrifuge.

## Characterization of P4VP-PS Particles and Bubbles

### Optical Microscopy (OM)

A drop of an aqueous dispersion of the P4VP-PS particles or aqueous bubbles was placed on a microscope slide glass and observed using an OM (Shimadzu Motic BA200; Shimadzu Corp., Kyoto, Japan) fitted with an objective lens and a digital system (Shimadzu Moticam, 2000). For observation of the P4VP-PS particles, a cover glass was placed on the sample.

### Scanning Electron Microscopy (SEM)

The purified latex droplets dried on an aluminum stub were sputter-coated with thin layer of Au using an Au coater. SEM studies were conducted using a Keyence VE-8800 SEM operated at 5 kV. Number-average diameter of the P4VP-PS particles was evaluated from the SEM images. Dried bubbles were also observed using SEM.

### Particle Size Analysis

A laser diffraction particle size analyzer (Malvern Mastersizer, 2000), which is equipped with a small volume sample dispersion unit, a solid-state blue laser (466 nm) and a HeNe laser (633 nm), was utilized to determine volume equivalent sphere mean diameter ($D_v$). The resulting data are presented as mean diameter ± standard deviation.

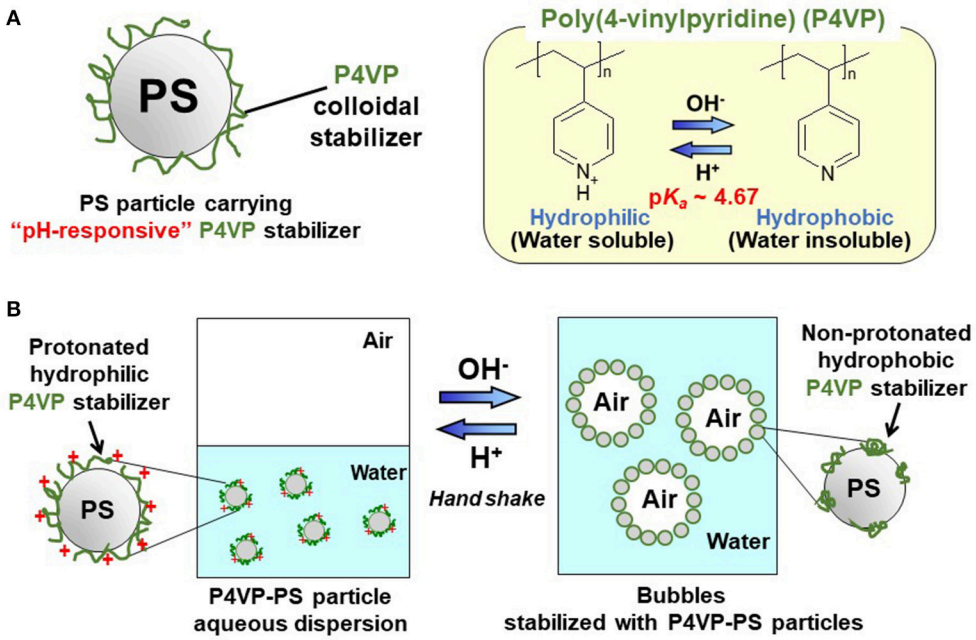


**FIGURE 1 | (A)** Diagram of polystyrene particle carrying pH-responsive poly(4-vinylpyridine) colloidal stabilizer (P4VP-PS particle) and **(B)** schematic diagram illustrating pH-responsive bubbles stabilized with the P4VP-PS particles.

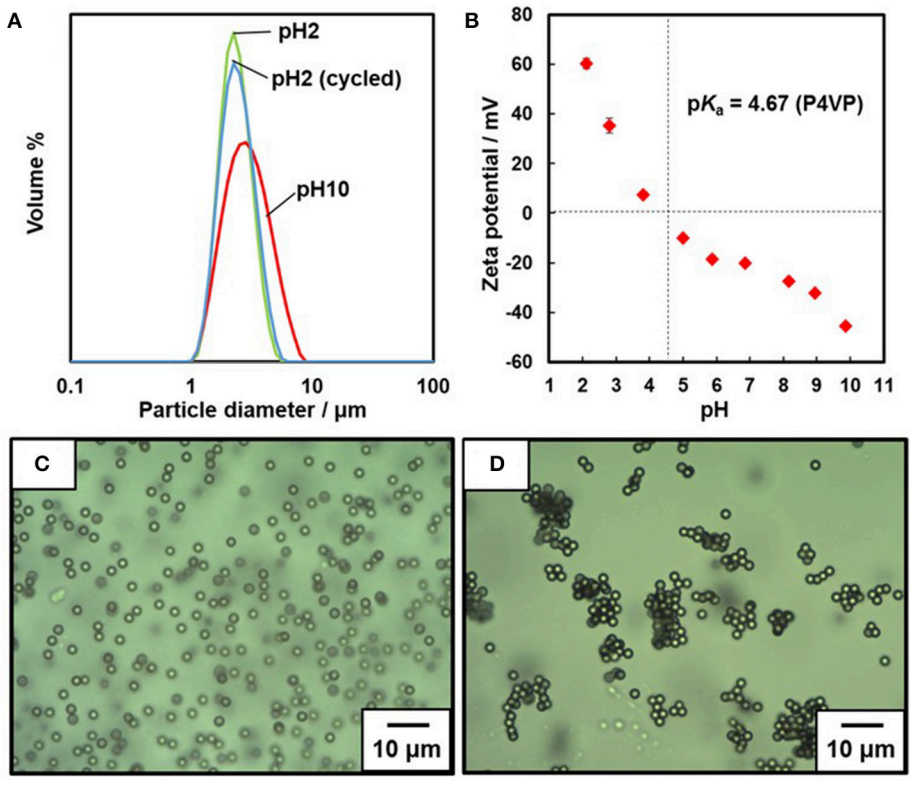


**FIGURE 2 | (A)** Particle size distribution curves measured by laser diffraction method. **(B)** Relationship between pH and zeta potential measured for the P4VP-PS particles. Optical micrographs of aqueous dispersions of P4VP-PS particles observed at **(C)** pH 2.2 and **(D)** pH 10.4.

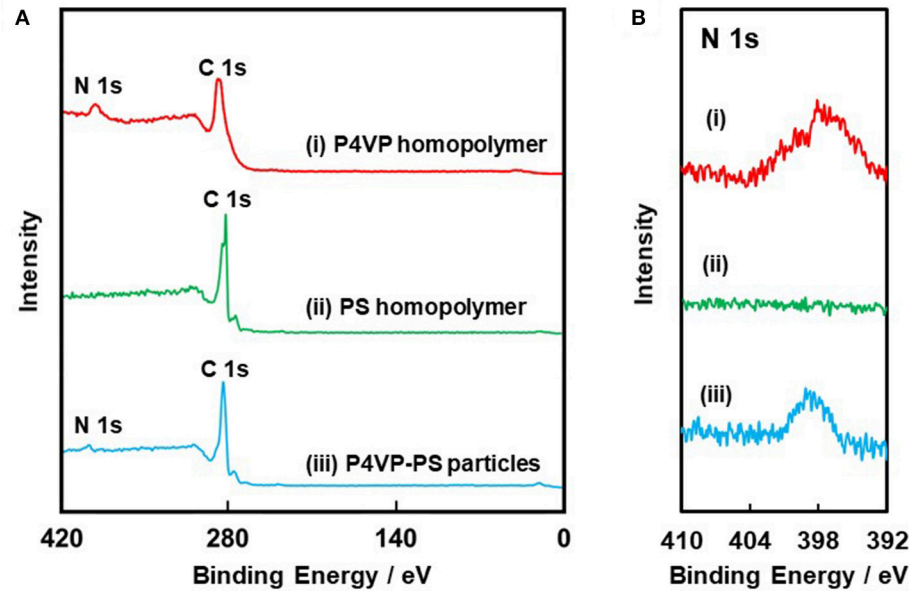


**FIGURE 3 | (A)** XPS survey spectra obtained for (i) P4VP homopolymer, (ii) PS homopolymer, and (iii) P4VP-PS particles. **(B)** Core-level N 1s spectra.

### Chemical Composition

The P4VP loading of the P4VP-PS particles after washing was determined by comparing the nitrogen contents evaluated by elemental microanalysis (Yanaco CHN-Corder MT-5) with that of the P4VP homopolymer.

### X-Ray Photoelectron Spectroscopy (XPS)

The XPS measurements were obtained on the samples mounted onto sample stubs using conductive tape using an XPS spectrometer (Axis Ultra) with a monochromated Al $K_\alpha$ X-ray gun.

### Zeta Potential

The electrophoretic mobilities were measured to determine zeta potentials using a Malvern Zetasizer Nano ZS. Measurements were carried out as a function of pH with diluted latex by a gradual addition of HCl or NaOH starting from an initial pH of 6.9.

## Interfacial Particle Trapping Method

Particle trapping at air-water interface was carried out following the method reported in 2014. (Vogel et al., 2014). Aqueous dispersion of P4VP-PS particles (pH 10.0 adjusted using NaOH aqueous solution) placed in a petri dish was magnetically stirred at 450 rpm for 10 min. The ethyl 2-cyanoacrylate monomer (0.7 g) is placed in the other petri dish on a hotplate (50°C). Both petri dishes were placed in a closed glass container for 15 min. The monomer can evaporate and polymerize at the air–water interface. The anionic polymerization of cyanoacrylate occurs by contact with water surface, resulting in generation of the polycyanoacrylate film at the air-water interface. The P4VP-PS particles were trapped at the air-water interface in their equilibrium position.

## Bubble Preparation

The pH of the original dispersion after centrifugal washing was 6.9; the pH was controlled by the addition of concentrated aqueous solutions of either NaOH or HCl. The aqueous latex (2.0 mL, solid content, 5.0 wt%) prepared in a glass vessel (4 mL) with a screw cap was hand shaken for 30 s (70 cycles; amplitude of a swing, 30 cm). The same experiments were also conducted using 5.0 mL aqueous latex in a glass vessel (13.5 mL). Prepared bubbles were stored at 25°C and their heights were measured using a ruler. (The bubble height was determined to be 0 mm, if the planar air-aqueous latex interface could be observed).

# RESULTS AND DISCUSSION

P4VP is a pH-responsive polybase with a p$K_a$ value of ∼4.5 (Wang et al., 2017), which is lower than those of PDEA and PDMA. Relationship between degree of protonation of the pyridine group ($\alpha$) and pH can be expressed using Equation (1)

$$\alpha = 1/(1 + 10^{\mathrm{pH}-\mathrm{p}Ka}) \quad (1)$$

where $K_a$ is proton dissociation constant of the pyridine group. P4VP is soluble in aqueous media below pH at around 3 because of protonation of its pyridine groups (>96%). At pH around 5 or above, P4VP has either very low or zero charge density, which results in precipitation. P4VP-based polymers have been used for syntheses of polymeric micelles (Koh et al., 2007), microgels (Ma and Fukutomi, 1991; Kim and Vincent, 2005), nanocomposite particles (Fujii et al., 2005, 2006a), surface-modifier for immobilization of nanoparticles (Malynych et al., 2002) and polymer brushes (Wang et al., 2017). Here, P4VP

homopolymer was used as a colloidal stabilizer to synthesize PS latex particles.

The number-average molecular weight ($M_n$) and molecular weight distribution ($M_w/M_n$) values of the P4VP stabilizer were determined to be 13,200 g/mol and 1.5 by gel-permeation chromatography (GPC). Free radical dispersion polymerization of styrene was carried out using the P4VP colloidal stabilizer, which led to colloidally stable milky dispersion of P4VP-PS particles. SEM studies clarified that the P4VP-PS particles were nearly monodisperse and had a number-average diameter ($D_n$) of 2.44 ± 0.13 μm (Supplementary Figure 1). Elemental microanalysis indicates a P4VP loading% of 1.05 wt%: we compared the nitrogen content of the P4VP-PS particles ($N = 0.12\%$) to that of the P4VP homopolymer ($N = 11.41\%$). After replacing the dispersing media from ethanol to distilled water (∼pH 6.3), particle size distributions were obtained by the laser diffraction method for dilute dispersion at acidic and basic pHs (**Figure 2A**). The volume average diameter $D_v$ was 2.58 ± 0.76 μm at pH 2.1 with a narrow particle size distribution, which indicated that the P4VP-PS particles were well dispersed. The P4VP-PS particles were flocculated at pH 10.4, reflected in an increase in the apparent particle diameter and diameter distribution ($D_v$, 3.29 ± 1.39 μm). These laser diffraction results agree with observations made by OM (**Figures 2C,D**): colloidally stable particles at pH 2.2 were detected, whereas a few micrometer to a few tens micrometer-sized flocs were observed at pH 10.4. Adjustment of the solution pH from 10.4 back to 2.3 led to redispersion of the P4VP-PS particles: the $D_v$ was 2.65 ± 0.85 μm, which is almost the same as that obtained originally at pH 2.1 (**Figure 2A**). This flocculation/redispersion cycle is reversible at least five times. $D_v$ determined by the laser diffraction method at pH 10.4 was smaller than $D_n$ estimated for aqueous dispersion by using OM at pH 10.4. This difference could be caused by breakage of flocs under shear stress during the laser diffraction particle size measurements. (Note that no shear stress was applied during OM observation).

XPS survey spectra and nitrogen core-line spectra obtained for the P4VP-PS particles, the P4VP homopolymer, and PS homopolymer are shown in **Figure 3**. For both the P4VP-PS particles and the P4VP homopolymer, carbon and nitrogen were detected. On the other hand, nitrogen was not detected, while carbon was observed, for the PS homopolymer. Considering that the XPS can investigate surface chemical compositions with typically ∼10 nm, these results verify that the particles are covered by P4VP. Furthermore, a surface coverage by P4VP was determined to be ∼27% by comparing the intensity of the N1s signal observed for the P4VP-PS particles to that of the P4VP homopolymer (**Table 1**). From these XPS and the above-mentioned elemental microanalyses results, it can be confirmed that the P4VP is mainly located at the surface of the PS particles, rather than buried within the PS particles: If the P4VP (1.05 wt% loading on the P4VP-PS particles) existed within the PS particles, nitrogen could not be detected in the XPS spectrum. It is also expected that P4VP exists on the particle surface in aqueous media, because hydrophilicity of the P4VP is higher than that of the PS; Solubility parameters are calculated to be 20.05 $(MPa)^{1/2}$ and 23.31 $(MPa)^{1/2}$ for PS and P4VP (Fedors, 1974). P4VP is expected to be adsorbed to PS particle surface physically in loop-train-tail manner. There is a possibility that the P4VP is chemically grafted *via* chain transfer reaction followed by formation of P4VP-*g*-PS during free radical dispersion polymerization of styrene. The P4VP strongly adsorbed to the PS particles, because the P4VP-PS particles can be dispersed in acidic medium even after five times pH cycles between 2 and 10. Diameter of gyration of the P4VP stabilizer chain was calculated to be 2.5 nm, which was less than the square root of the occupied molecular area (7.45 $nm^2$) determined under assumption that the P4VP exists only on the surface of PS particles.

**TABLE 1 |** Quantitative surface composition of PS homopolymer, P4VP homopolymer, and P4VP-PS particles determined by XPS.

| | Atom. % | | Surface coverage % | |
|---|---|---|---|---|
| | C content/% | N content/% | P4VP/% | PS/% |
| PS homopolymer | 100 | 0.0 | — | 100 |
| P4VP homopolymer | 85.6 | 14.4 | 100 | — |
| P4VP-PS particles | 95.3 | 4.7 | 32.5 | 67.5 |

The relationship between zeta potential of the P4VP-PS particles and pH is shown in **Figure 2B**. At and below approximately pH 4, the zeta potentials are positive and have values up to ∼+60 mV. The particle surface is positively charged because of protonation of the pyridine groups of the P4VP stabilizer. The zeta potential values were negative at and above ∼pH 5 (near the $pK_a$ value of P4VP), which is due to deprotonation of the P4VP stabilizer. The non-charged neutral P4VP stabilizer collapsed onto the PS surfaces due to dehydration and the electrophoretic mobility of the particles was determined by the hydroxide anion adsorption amount on the particle surfaces (Beattie and Djordjev, 2004; Roger and Cabane, 2012). The same phenomenon has been observed for PS particles carrying PDEA colloidal stabilizer (Fujii et al., 2009; Sekido et al., 2017a). The aqueous electrophoresis studies confirmed that surface charge density on the P4VP-PS particle surfaces can be controlled by pH. (Note that it is not possible to determine real surface charge density, because the zeta potential is an electric potential in the interfacial double layer at the location of the slipping plane). This zeta potential result also indicated that surface hydrophilicity-hydrophobicity balance depends on pH.

Bubble stability depends on the hydrophilicity-hydrophobicity balance of the particle surfaces, in other words, the wettability of the particles at the air-water interface (Ramsden, 1903; Binks and Horozov, 2006; Studart et al., 2006; Fujii and Murakami, 2008; Hunter et al., 2008; Kruglyakov et al., 2011; Stevenson, 2012; Pugh, 2016; Fujii and Nakamura, 2017); therefore, the behavior of bubbles stabilized with these P4VP-PS particles is expected to change at pH values close to the $pK_a$ of the P4VP stabilizer in a significant manner. To evaluate bubble forming ability and bubble stability, the bubble formation was estimated after shaking aqueous dispersions of the P4VP-PS aqueous latex particles (5.0 wt%) at different pHs. It appears that reasonably stable bubbles, which were stable for at least 4 days, were formed under conditions where the P4VP colloidal

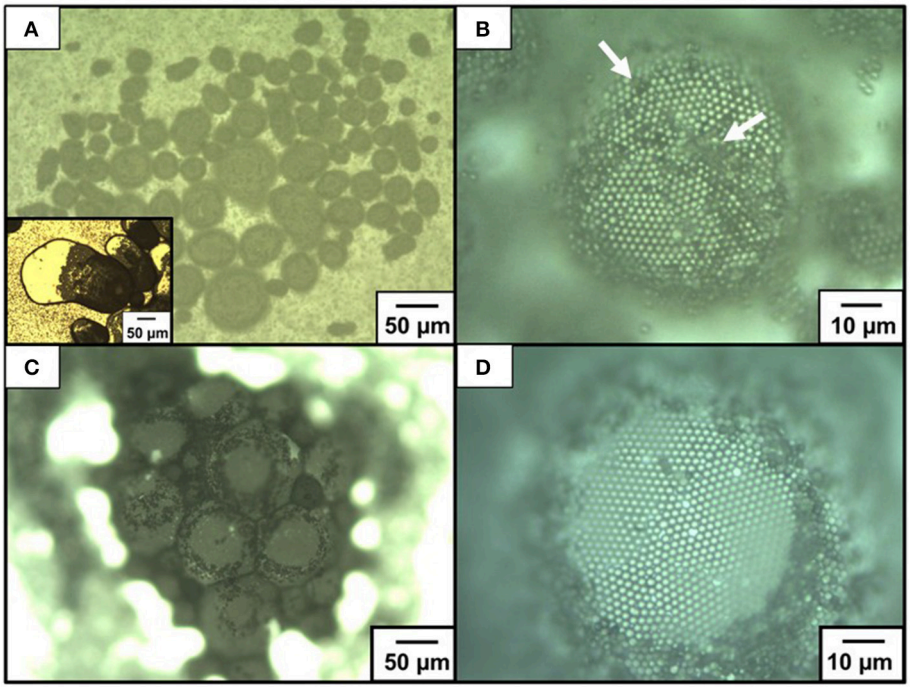


**FIGURE 4 |** Optical micrographs of bubbles stabilized with P4VP-PS particles at pH 10.4: **(A,B)** before and **(C,D)** after drying. **(B,D)** are magnified images of **(A,C)**, respectively. White arrows indicate flocs of the P4VP-PS particles on bubble surface. An inset of **(A)** shows the bubbles after application of pressure between glass substrates.

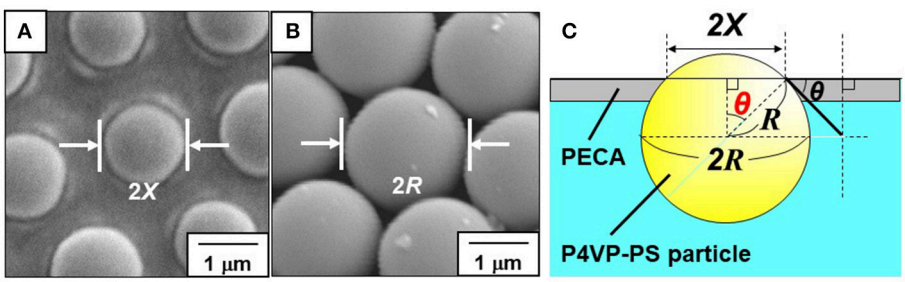


**FIGURE 5 | (A,B)** SEM images of P4VP-PS particles trapped with PECA films recorded from the **(A)** air-exposed and **(B)** water-exposed sides of the films. **(C)** Determination of the contact angle (through water) of the P4VP-PS particle at the air–water interface using SEM images.

stabilizer shows hydrophobic nature and the particles are weakly flocculated in bulk (pH $\geq$ 4.0). In these cases, the bubbles floated up to planar air-water interface of the aqueous dispersion due to buoyancy. On the other hand, no bubble could be prepared at low pH (e.g., 2.0, 3.0), where the particles have cationic and water soluble P4VP colloidal stabilizer.

OM and SEM studies were conducted to investigate the microstructures of the particle-stabilized bubbles (**Figures 4–6**). An OM study of an aqueous dispersion of the P4VP-PS particles at pH 2.2 after hand shaking, where ∼100% of the P4VP colloidal stabilizer is protonated, confirms that the particles do not stabilize the bubbles and are dispersed in the aqueous medium rather than adsorbed at air-water interface. At and above pH 4.0, where less than 76% of the pyridine unit of P4VP colloidal stabilizer is protonated (calculated using Equation 1) and the particles are weakly flocculated in the aqueous media, near spherical and non-spherical, polydisperse bubbles (size range from ∼10 μm to ∼1 mm) with the P4VP-PS particles adsorbed at the bubble surfaces were observed in the continuous aqueous media (**Figure 4A**, Supplementary Figures 2, 3). The non-spherical bubbles could be formed by elongation during the hand shaking due to uneven shearing, followed by covering with the P4VP-PS particles before relaxing back to a spherical shape. These non-spherical bubbles might also be formed due to the coalescence of multiple particle-coated bubbles. The bubbles could not become spherical owing to the solid-like properties conferred to the interface by the presence of the P4VP-PS particles (*i.e.*, the particles were irreversibly adsorbed

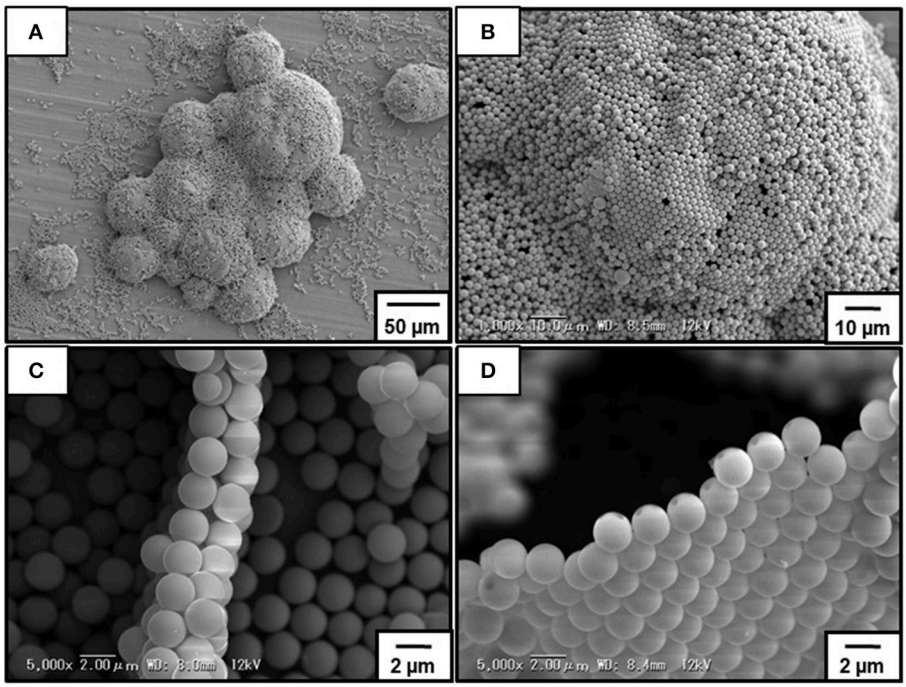


**FIGURE 6 |** SEM images of dried bubbles stabilized with P4VP-PS particles prepared at pH10.4. **(B)** is a magnified image of **(A)**. **(C,D)** are cross-section SEM images of the bubbles after deliberate rupture using a scalpel.

at the air-water interface). Similarly, non-spherical bubbles (Subramaniam et al., 2005; Fujii et al., 2018) and oil droplets (Kim et al., 2008; Fujii et al., 2013), which are stabilized with solid particles, have been observed in aqueous media in other studies. Highly magnified OM images of the bubble surface indicated the formation of hexagonal-close-packed arrays of the particles with some flocs on them (**Figure 4B**) (white arrows indicate the flocs). These particle arrays at air-water interface have been observed in previous studies (Fujii et al., 2006b,c, 2012; Dupin et al., 2008; Nakayama et al., 2015a; Fukuoka et al., 2016; Sekido et al., 2017a,b). It is worth noting that the bubbles were not fully covered with flocculated P4VP-PS particles. There is a possibility that only the P4VP-PS particles adsorbed at air-water interface could remain on the bubble surfaces and flocculated particles detached from the floating bubble surfaces and precipitated in continuous aqueous media. After manual application of light pressure to aqueous gas bubbles placed between a glass slide and a cover glass, the air escaped from the P4VP-PS particle-stabilized bubbles, which indicated encapsulation of air bubble (**Figure 4A** inset). Magnified image of the crushed bubble indicates that single P4VP-PS particle monolayers were formed at air-water interface to stabilize the bubbles (Supplementary Figure 4). Contact angle $\theta$ of the P4VP-PS particles at the air-water interface was evaluated by the interfacial particle trapping method and neglecting gravity (Vogel et al., 2014). The P4VP-PS particles adsorbed at air-water interface was exposed to ethyl 2-cyanoacrylate vapor. Contact of ethyl 2-cyanoacrylate monomer with the interface induced anionic polymerization to form poly(ethyl 2-cyanoacrylate) (PECA) films, which trapped the P4VP-PS particles at the air-water interface. In the SEM images, a spherical cap of each particle was observed on the air phase-exposed side of the film and the spherical particles was observed on the water-exposed side for the film prepared at pH 10.0 (**Figures 5A,B**). The contact angle $\theta$ of the P4VP-PS particles was determined to be 43°, which accorded well with that measured for poly(*N*-vinylpyrolidone)-stabilized PS particle (Fujii et al., 2012), using the diameter of spherical cap of PS particles and the diameter of original P4VP-PS particles (**Figure 5C**). The adsorption energy of the P4VP-PS particle adsorbed at an air-water interface from the liquid phase ($\Delta G$) can be calculated to be $4.1 \times 10^6$ $k_B T$ with the contact angle using Equation (2) (Levine et al., 1989):

$$\Delta G = -\gamma_{aw} \pi a^2 (1 - \cos\theta)^2 \quad (2)$$

where $k_B$ is the Boltzmann constant and $T$ is temperature, $\gamma_{aw}$ is the surface tension of water, $a$ is the particle radius, and $\theta$ is the contact angle measured through the aqueous phase.

After evaporation of the continuous water phase from the aqueous bubbles prepared at pH 10.4 overnight at ambient temperature, solid bubbles with three-dimensional structures were obtained (**Figure 4C**). A little coalescence was observed and the bubble size increased during/after drying, which was confirmed by OM studies. After the water evaporation, near-spherical bubble shapes observed when dispersed in water medium were significantly deformed. Due to capillary forces

working among the particle-stabilized bubbles during drying, the bubbles were forced to deviate from their near-spherical shape. Because of the deformability of the P4VP-PS particle layer formed at bubble surface, the bubble deformation could not be avoided during/after drying. It is worth noting that the particle arrays remained even after drying (**Figure 4D**).

**Figure 6** shows SEM images obtained for dried bubbles prepared at pH 10.4. Even under high vaccuum condition, the bubbles kept their three-dimensional structure (**Figure 6A**). Observation of the top surface of the dried bubbles indicated the presence of the P4VP-PS particles, which were near close-packed (**Figure 6B**). The internal particle microstructure was examined after deliberate rupture of the bubbles using a scalpel. Well-defined particle bilayers were observed in most cases (**Figure 6C**), which strongly indicates that most bubbles were stabilized by P4VP-PS particle monolayers. During water drainage from the drying foams, these monolayers should be forced together to form bilayers. Similar results were reported previously (Fujii et al., 2006b,c; Dupin et al., 2008; Nakayama et al., 2015a; Fukuoka et al., 2016). In some cases, monolayers and multilayers (mainly triple layers) were observed. The monolayers should be due to the top surface of dried bubbles that contacted with bulk air phase in direct manner and was not overlapped with other bubbles (**Figure 6D**). The multilayers should be formed due to flocs on the bubble surfaces and/or excess free particles trapped between two bubble surfaces.

Finally, the possibility of inducing destabilization of the particle-stabilized bubbles by subsequent pH control was investigated. The bubbles formed at pH 9.9 and allowed to stand for 10 min after preparation were rapidly (< 1 min) destabilized (coalesced) by decreasing the pH of the aqueous phase to pH 2.2, followed by vigorous hand shaking at 25°C. This should be due to *in situ* protonation of the P4VP colloidal stabilizer on the P4VP-PS particles, which rendered the particle surface highly hydrophilic. Therefore, the P4VP-PS particles are detached from the air-water interface and are not adsorbed at the interface anymore, which leads to disruption of the bubbles. The bubbles could be reformed after pH adjustment back to pH 10 followed by hand shaking. This stabilization/destabilization cycle is readily reversible at least five times (**Figure 7**).

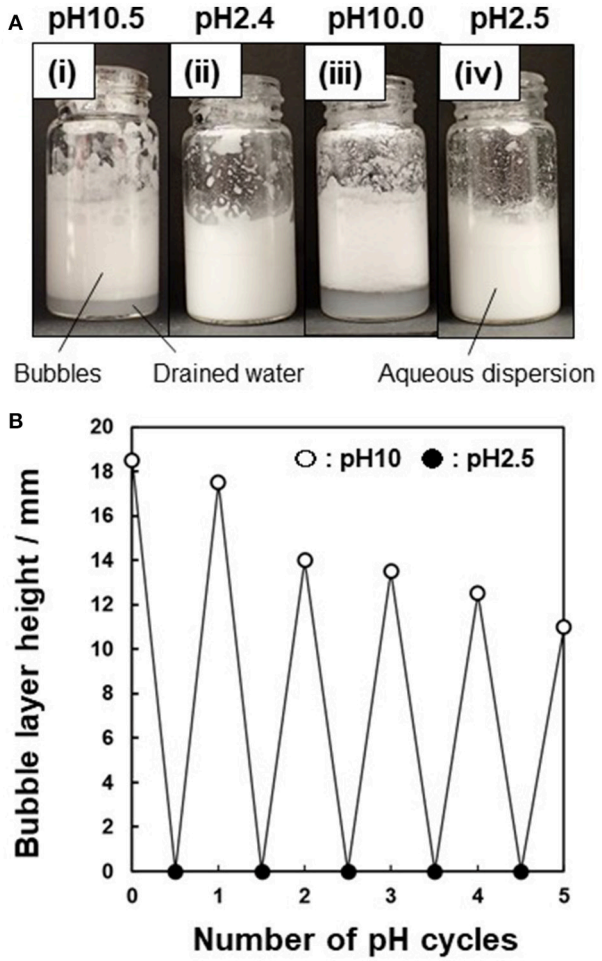


**FIGURE 7 | (A)** Photographs illustrating pH-responsive behavior of bubbles prepared using P4VP-PS particles (5.0 wt %): (i) at pH 10.5 after 10 min, (ii) pH adjustment from pH 10.5 to pH 2.4 after 10 min, (iii) pH adjustment from pH 2.4 to pH 10.0 after 10 min, and (iv) pH adjustment from pH 2.4 to pH 10.0 to pH 2.5 after 10 min. **(B)** Height of the bubbles layer vs. the number of pH cycles.

## CONCLUSION

In summary, near-monodispersed, micrometer-sized PS particles carrying P4VP colloidal stabilizer on their surfaces were successfully synthesized by free radical dispersion polymerization. The particle were characterized in terms of the morphology, size, size distribution, chemical composition, surface chemistry, and pH-response. The ability of the P4VP-PS particles was evaluated as a pH-dependent and pH-responsive particulate bubble stabilizer. Aqueous bubbles can be stabilized with the P4VP-PS particles at and above pH 4.0, where the particles have relatively hydrophobic surfaces. On the other hand, no bubble was stabilized at and below pH 3.0, where the particles are positively charged and colloidally stable. Destabilization of the bubbles prepared at pH ∼10 could be induced by subsequent pH adjustment to ≤3.0, and the stabilization/destabilization cycles were reversible. Recently, it has been confirmed that there are lots of similarities among particle-stabilized bubbles, emulsions and liquid marbles/dry liquids (Fujii et al., 2016). The principles demonstrated in this study should also be applicable to predict the stabilities and microstructures of these particle-stabilized soft dispersed systems. The encapsulation of air bubbles in liquid phase using solid particles with stimuli-responsive character should be useful in food manufacturing, personal care products and cosmetic formulations.

## AUTHOR CONTRIBUTIONS

MI, KT, HH, YA, and SY carried out the experiments with respect to synthesis and characterization of the P4VP-PS particles and bubble formation and characterization experiments.

SF organized the project and wrote the manuscript. All authors discussed the results and edited the manuscript. YA conducted additional experiments (XPS studies and contact angle measurement of the P4VP-PS particle at air-water interface) and discussed the results.

## FUNDING

This work was supported by Grant-in-Aid for Scientific Research (B) (JSPS KAKENHI Grant Number JP16H04207) and Scientific Research on Innovative Areas Engineering Neo-Biomimetics (No. 4402) (JSPS KAKENHI Grant Numbers JP15H01602 and JP25120511), New Polymeric Materials Based on Element-Blocks (No.2401) (JSPS KAKENHI Grant Numbers JP15H00767 and JP25102542), Molecular Soft Interface Science (No. 2005) (JSPS KAKENHI Grant Numbers 23106720), and Electrostatic Formation of Liquid Marbles (Australian Research Council Discovery Project, DP170100578).

## ACKNOWLEDGMENTS

We thank Mr. Hisato Kawashima for XPS measurements.

## SUPPLEMENTARY MATERIAL

The Supplementary Material for this article can be found online at: https://www.frontiersin.org/articles/10.3389/fchem.2018.00269/full#supplementary-material

## REFERENCES

Beattie, J. K., and Djordjev, A. M. (2004). The pristine oil/water interface: surfactant-free hydroxide-charged emulsions. *Angew. Chem. Int. Ed.* 43, 3568–3571. doi: 10.1002/anie.200453916

Binks, B. P., and Horozov, T. S. (ed.) (2006). *Colloidal Particles at Liquid Interfaces*. Cambridge: Cambridge University Press.

Dupin, D., Howse, J. R., Armes, S. P., and Randall, D. P. (2008). Preparation of stable foams using sterically stabilized pH-responsive latexes synthesized by emulsion polymerization. *J. Mater. Chem.* 18, 545–552. doi: 10.1039/B714261G

Fedors, R. F. (1974). A method for estimating both the solubility parameters and molar volumes of liquids. *Polym. Eng. Sci.* 14, 147–154. doi: 10.1002/pen.760140211

Fujii, S., Akiyama, K., Nakayama, S., Hamasaki, S., Yusa, S., and Nakamura, Y. (2015). pH- and temperature-responsive aqueous foams stabilized by hairy latex particles. *Soft Matter* 11, 572–579. doi: 10.1039/C4SM02236J

Fujii, S., Armes, S. P., Binks, B. P., and Murakami, R. (2006a). Stimulus-responsive particulate emulsifiers based on lightly cross-linked poly(4-vinylpyridine)-silica nanocomposite microgels. *Langmuir* 22, 6818–6825. doi: 10.1021/la060349l

Fujii, S., Iddon, P. D., Ryan, A. J., and Armes, S. P. (2006b). Aqueous particulate foams stabilized solely with polymer latex particles. *Langmuir* 22, 7512–7520. doi: 10.1021/la060812u

Fujii, S., Kakigi, S., Suzaki, M., Yusa, S., Muraoka, M., and Nakamura, Y. (2009). Synthesis of stimuli-responsive macroazoinitiators and their use as an inistab toward hairy polymer latex particles. *J. Polym. Sci. Part A. Polym. Chem.* 47, 3431–3443. doi: 10.1002/pola.23424

Fujii, S., Kappl, M., Butt, H.-J., Sugimoto, T., and Nakamura, Y. (2012). Soft Janus colloidal crystal film. *Angew. Chem. Int. Ed.* 51, 9809–9813. doi: 10.1002/anie.201204358

Fujii, S., Mochizuki, M., Aono, K., Hamasaki, S., Murakami, R., and Nakamura, Y. (2011). pH-responsive aqueous foams stabilized by hairy latex particles. *Langmuir* 27, 12902–12909. doi: 10.1021/la203062b

Fujii, S., and Murakami, R. (2008). Smart particles as foam and liquid marble stabilizers. *KONA Powder Part. J.* 26, 153–166. doi: 10.14356/kona.2008014

Fujii, S., and Nakamura, Y. (2017). Stimuli-responsive bubbles and foams stabilized with solid particles. *Langmuir* 33, 7365–7379. doi: 10.1021/acs.langmuir.7b01024

Fujii, S., Read, E. S., Armes, S. P., and Binks, B. P. (2005). Stimulus-responsive emulsifiers based on nanocomposite microgel particles. *Adv. Mater. Weinheim.* 17, 1014–1018. doi: 10.1002/adma.200401641

Fujii, S., Ryan, A. J., and Armes, S. P. (2006c). Long-range structural order, moiré patterns, and iridescence in latex-stabilized foams. *J. Am. Chem. Soc.* 128, 7882–7886. doi: 10.1021/ja060640n

Fujii, S., Yokoyama, Y., Miyanari, Y., Shiono, T., Ito, M., Yusa, S., et al. (2013). Micrometer-sized gold-silica Janus particles as particulate emulsifiers. *Langmuir* 29, 5457–5465. doi: 10.1021/la400697a

Fujii, S., Yokoyama, Y., Nakayama, S., Ito, M., Yusa, S., and Nakamura, Y. (2018). Gas bubbles stabilized by Janus particles with varying hydrophilic–hydrophobic surface characteristics. *Langmuir* 34, 933–942. doi: 10.1021/acs.langmuir.7b02670

Fujii, S., Yusa, S., and Nakamura, Y. (2016). Stimuli-responsive liquid marbles: controlling structure, shape, stability, and motion. *Adv. Funct. Mater.* 26, 7206–7223. doi: 10.1002/adfm.201603223

Fukuoka, K., Tomikawa, A., Nakamura, Y., and Fujii, S. (2016). Aqueous foams stabilized with several tens of micrometer-sized polymer particles: effects of surface hydrophilic–hydrophobic balance on foamability and foam stability. *Chem. Lett.* 45, 667–669. doi: 10.1246/cl.160182

Hunter, T. N., Pugh, R. J., Franks, G. V., and Jameson, G. J. (2008). The role of particles in stabilising foams and emulsions. *Adv. Colloid Interface Sci.* 137, 57–81. doi: 10.1016/j.cis.2007.07.007

Kim, J.-W., Lee, D., Shum, H. C., and Weitz, D. A. (2008). Colloid surfactants for emulsion stabilization. *Adv. Mater. Weinheim* 20, 3239–3243. doi: 10.1002/adma.200800484

Kim, K. S., and Vincent, B. (2005). pH and temperature-sensitive behaviors of poly(4-vinyl pyridine-*co*-*N* isopropyl acrylamide) microgels. *Polym. J.* 37, 565–570. doi: 10.1295/polymj.37.565

Koh, H. D., Kang, N. G., and Lee, J. S. (2007). Fabrication of an open Au/nanoporous film by water-in-oil emulsion-induced block copolymer micelles. *Langmuir* 23, 12817–12820. doi: 10.1021/la702891q

Kruglyakov, P. M., Elaneva, S. I., and Vilkova, N. G. (2011). About mechanism of foam stabilization by solid particles. *Adv. Colloid Interface Sci.* 165, 108–116. doi: 10.1016/j.cis.2011.02.003

Levine, S., Bowen, B., and Partridge, S. J. (1989). Stabilization of emulsions by fine particles I. Partitioning of particles between continuous phase and oil/water interface. *Colloids Surf.* 38, 325–343. doi: 10.1016/0166-6622(89)80271-9

Ma, G. H., and Fukutomi, T. (1991). Studies on the preparation and characterization of poly(4-vinylpyridine) microgel. I. Preparation with polymer emulsifier. *J. Appl. Polym. Sci.* 43, 1451–1457. doi: 10.1002/app.1991.070430806

Malynych, S., Luzinov, I., and Chumanov, G. (2002). Poly(vinyl pyridine) as a universal surface modifier for immobilization of nanoparticles. *J. Phys. Chem. B.* 106, 1280–1285. doi: 10.1021/jp013236d

Nakayama, S., Fukuhara, K., Nakamura, Y., and Fujii, S. (2015a). Hollow microspheres fabricated from aqueous bubbles stabilized with latex particles. *Chem. Lett.* 44, 773–775. doi: 10.1246/cl.150161

Nakayama, S., Hamasaki, S., Ueno, S., Mochizuki, M., Yusa, S., Nakamura, Y., et al. (2016). Foams stabilized with solid particles carrying stimuli-responsive polymer hairs. *Soft Matter* 12, 4794–4804. doi: 10.1039/C6SM00425C

Nakayama, S., Yusa, S., Nakamura, Y., and Fujii, S. (2015b). Aqueous foams stabilized by temperature-sensitive hairy polymer particles. *Soft Matter* 11, 9099–9106. doi: 10.1039/C5SM02187A

Pugh, R. J. (2016). *Bubble and Foam Chemistry*. Cambridge: Cambridge University Press.

Ramsden, W. (1903). Separation of solids in the surface-layers of solutions and 'suspensions' (Observations on surface-membranes, bubbles, emulsions, and mechanical coagulation). – Preliminary account. *Proc. R. Soc. Lond.* 72, 156–164. doi: 10.1098/rspl.1903.0034

Roger, K., and Cabane, B. (2012). Why are hydrophobic/water interfaces negatively charged? *Angew. Chem. Int. Ed.* 51, 5625–5628. doi: 10.1002/anie.201108228

Sekido, T., Kappl, M., Butt, H.-J., Yusa, S., Nakamura, Y., and Fujii, S. (2017a). Effects of pH on structure and mechanical properties of dried pH-responsive latex particles. *Soft Matter* 13, 7562–7570. doi: 10.1039/C7SM01625E

Sekido, T., Wooh, S., Fuchs, R., Kappl, M., Nakamura, Y., Butt, H.-J., et al. (2017b). Controlling the structure of supraballs by pH-responsive particle assembly *Langmuir* 33, 1995–2002. doi: 10.1021/acs.langmuir.6b04648

Stevenson, P. (ed.) (2012). *Foam Engineering: Fundamentals and Applications*. Chichester: Wiley.

Studart, A. R., Gonzenbach, U. T., Tervoort, E., and Gauckler, L. J. (2006). Processing routes to macroporous ceramics: a review. *J. Am. Ceram. Soc.* 89, 1771–1789. doi: 10.1111/j.1551-2916.2006.01044.x

Subramaniam, A. B., Abkarian, M., Mahadevan, L., and Stone, H. A. (2005). Colloid science: non-spherical bubbles. *Nature* 438:930. doi: 10.1038/438930a

Vogel, N., Ally, J., Bley, K., Kappl, M., Landfester, K., and Weiss, C. K. (2014). Direct visualization of the interfacial position of colloidal particles and their assemblies. *Nanoscale* 6, 6879–6885. doi: 10.1039/C4NR00401A

Wang, M., Yan, F., Zhao, L., Zhang, Y., and Sorci, M. (2017). Preparation and characterization of a pH-responsive membrane carrier for meso-tetraphenylsulfonato porphyrin. *RSC Adv.* 7, 1687–1696. doi: 10.1039/C6RA26414J

**Conflict of Interest Statement:** The authors declare that the research was conducted in the absence of any commercial or financial relationships that could be construed as a potential conflict of interest.

The reviewer, YW, and handling Editor declared their shared affiliation.

frontiers in Chemistry

ORIGINAL RESEARCH
published: 05 June 2018
doi: 10.3389/fchem.2018.00201

# Influence of Shell Thickness on the Colloidal Stability of Magnetic Core-Shell Particle Suspensions

*Frances Neville*[1] *and Roberto Moreno-Atanasio*[2]*

[1] School of Environmental and Life Sciences, University of Newcastle, Callaghan, NSW, Australia, [2] School of Engineering, University of Newcastle, Callaghan, NSW, Australia

We present a Discrete Element study of the behavior of magnetic core-shell particles in which the properties of the core and the shell are explicitly defined. Particle cores were considered to be made of pure iron and thus possessed ferromagnetic properties, while particle shells were considered to be made of silica. Core sizes ranged between 0.5 and 4.0 μm with the actual particle size of the core-shell particles in the range between 0.6 and 21 μm. The magnetic cores were considered to have a magnetization of one tenth of the saturation magnetization of iron. This study aimed to understand how the thickness of the shell hinders the formation of particle chains. Chain formation was studied with different shell thicknesses and particle sizes in the presence and absence of an electrical double layer force in order to investigate the effect of surface charge density on the magnetic core-shell particle interactions. For core sizes of 0.5 and 4.0 μm the relative shell thicknesses needed to hinder the aggregation process were approximately 0.4 and 0.6 respectively, indicating that larger core sizes are detrimental to be used in applications in which no flocculation is needed. In addition, the presence of an electrical double layer, for values of surface charge density of less than 20 mC/m$^2$, could stop the contact between particles without hindering their vertical alignment. Only when the shell thickness was considerably larger, was the electrical double layer able to contribute to the full disruption of the magnetic flocculation process.

**Keywords: Discrete Element Method, computer simulations, core-shell particles, magnetic chains, electrical double layer**

OPEN ACCESS

***Edited by:***
*Syuji Fujii,*
*Osaka Institute of Technology, Japan*

***Reviewed by:***
*Timothy Nie Hunter,*
*University of Leeds, United Kingdom*
*Victor Sans Sangorrin,*
*University of Nottingham,*
*United Kingdom*

***Correspondence:**
*Roberto Moreno-Atanasio*
*roberto.moreno-atanasio@newcastle.edu.au*

***Specialty section:***
*This article was submitted to Chemical Engineering, a section of the journal Frontiers in Chemistry*

***Received:*** *02 March 2018*
***Accepted:*** *15 May 2018*
***Published:*** *05 June 2018*

***Citation:***
*Neville F and Moreno-Atanasio R (2018) Influence of Shell Thickness on the Colloidal Stability of Magnetic Core-Shell Particle Suspensions. Front. Chem. 6:201. doi: 10.3389/fchem.2018.00201*

## INTRODUCTION

Core-shell particles are particles whose cores are made of different component materials to those of the shell surrounding them (Cao et al., 2009; Mora-Huertas et al., 2010). In general, there is an inorganic or organic particle core which is surrounded by a layer or multilayer of a different inorganic or organic material. These core-shell particles have the advantage of possessing properties of both the core and its surrounding shell. This not only gives benefits in terms of improving the stability and surface chemistry of the core particle but also gives unique physical and chemical properties that are impossible to have if only one type of material is used (Caruso et al., 1999; Cao et al., 2009).

The structure of core-shell particles may be comprised of the core being a particle and the shell consisting of a different solid material. However, the shell could also be a soft layer of attached molecules, such as functional polymers which can be used to tune the specific surface interactions

of the particles (Vakurov et al., 2009; Mora-Huertas et al., 2010; Yuan et al., 2010; Amelia et al., 2011; Arsianti et al., 2011). Core-shell particles are fabricated via a range of methods including dispersion polymerization, self-assembly techniques (Cao et al., 2009) and microfluidic jet-spray drying (Amelia et al., 2012). The properties of the hybrid multifunctional particles formed can be controlled by altering the composition, dimension and structure of the cores and the shells.

Core-shell particles possess a high level of complexity in terms of structure and behavior under external forces including mechanical interaction with other particles (Centi and Perathoner, 2011; Sacanna and Pine, 2011; Strydom et al., 2014). It is quite common that either the core or the shell are made of a magnetic material (Zeng et al., 2004a,b) and these suspensions are known as magnetic or magnetorheological fluids (Bossis et al., 2011). Nevertheless, a larger degree of sophistication has been achieved by creating magnetic patches (Sacanna et al., 2012) or controlling shell thickness (Strydom et al., 2014).

Traditionally, magnetorheological fluids are suspensions of micron sized or smaller, magnetizable particles in a liquid (Vekas et al., 2000; Tao, 2001; Lopez-Lopez et al., 2005; Patel and Chudasama, 2009; Bossis et al., 2011; de Vicente et al., 2011). A special case of these magnetic fluids are ferrofluids in which the particles are ferromagnetic materials at the nanoscale (Rosensweig, 1985, 2011; Popplewell et al., 1995; Odenbach, 2009). These fluids are of interest to researchers and engineers due to their unique properties, since under an applied magnetic field their viscosity and other physical properties can be altered by orders of magnitude, depending on the intensity of the field (Bossis et al., 2011; de Vicente et al., 2011). At a more fundamental level, one of the main areas of research on magnetorheological fluids is the formation of self-organized structures, whether experimentally or using computer simulations, under the influence of an external magnetic field (Wang et al., 2002; Li et al., 2005; Han et al., 2010; Lim and Feng, 2012; Ku et al., 2015; Lagger et al., 2015a,b). Different interactions may lead to the formation of several types of structures, including linear chains, which align parallel to the external magnetic field (Parker et al., 1982; Perez-Castillo et al., 2000; Vekas et al., 2000; Martinez-Pedrero et al., 2007a; Mousavi et al., 2015). However, in applications such as drug delivery when either functionalized magnetic or core-shell particles are introduced into the blood system, the formation of magnetic chains is highly undesirable (Freund and Shapiro, 2012).

Computer simulations and theoretical studies have mainly focused on understanding particle aggregation (Hovorka et al., 2005; Zubarev et al., 2010) and rheological behavior (Chirikov et al., 2010; Kang et al., 2012; Segovia-Gutierrez et al., 2013) in constant or oscillating magnetic fields (Li et al., 2012). The trajectory of magnetic particles in a magnetic gradient (Li et al., 2007; van Netten et al., 2013), the influence of particle density on separation efficiency (Murariu et al., 2005) and simply the demonstration of the separation concept using model systems (Moeser et al., 2004; Nakai et al., 2011) has also been studied.

Simulation of core-shell particles has been performed by using molecular dynamics (MD) to study the actual properties of the particles but not their bulk behavior in suspension (Dalgic, 2016; Wang and Shin, 2017). It is only in recent years that a technique such as Discrete Element Method (DEM) has been applied to colloidal suspensions (Li et al., 2003; Moreno-Atanasio et al., 2009; MacPherson et al., 2012) and core-shell particles (Moreno-Atanasio et al., 2009; Weber et al., 2017). The main difference between DEM and MD is that the latter focuses on the analysis of molecules (Mijajlovic and Biggs, 2007) and the former, DEM, on the behavior of single particles (mesoscopic) whose material properties have been defined. DEM is easily coupled with Brownian dynamics to simulate the hydrodynamic interactions based on the Langevin equation (Li et al., 2003; Moreno-Atanasio et al., 2009). The main advantage of DEM is that the treatment of the bulk material (such as a particle suspension) is mesoscopic and the dimensions of the simulated systems are more realistic than in molecular dynamics. In addition, DEM simulations usually employ the material properties of the whole particle to analyze the contact between structures and the interaction which is provided by an external shell or coating as determined by atomic force microscopy (AFM) or by atomistic or molecular simulations (Patrick et al., 2003; Bose et al., 2005).

Despite the wide use of DEM in studying colloidal systems, the literature on using DEM to study magnetic colloidal systems is still incipient. Golovnia et al. (2014) studied the alignment of the magnetic particles with the external field. However, other published DEM studies considered the particles to be aligned along the external magnetic field. Zhenghua et al. (2010) investigated particle motion in a fluidization assisted by a magnetic gradient and they observed the fluidization at high values of external magnetic strength. Similar observations were reported by Wang et al. (2013). Lindner et al. (2013) combined DEM with FEM to determine the external magnetic field and the fluid flow around cylindrical wires. Other DEM studies focused on predicting the magnetic particle behavior during compression, shearing and breakage of magnetic chains were published by Kargulewicz et al. (2012); Lagger et al. (2015a,b); Soda et al. (2015). Ke et al. (2017) coupled DEM with Lattice Boltzmann Method and Immersed Boundary Method to simulate the settling of two individual magnetic particles. In addition, Son (2018) studied the hindered settling of magnetic particles coated with a surfactant layer, thus increasing the effective hydrodynamic radius of the particles. Despite the abovemetioned studies, the actual bulk behavior of magnetic core-shell colloidal particles has never been studied by considering the shell explicitly.

This paper presents the first DEM study of the behavior of magnetic core-shell particles where the shell and core components were independently considered in the simulations rather than just averaging the core and shell of the core-shell particles. In this study the particle shells were simulated as silica. Ferromagnetic cores of different sizes (0.5, 1.0, 2.0, and 4.0 $\mu$m) were simulated with a large overall particle size range of core-shell particles (0.6–21 $\mu$m) in order to vary the thickness of the shell layer and study its effect on chain formation. In addition, core-shell particles were simulated with different shell thicknesses and particle sizes in the presence and absence of an electrical double layer force in order to investigate the effect of surface charge density on the magnetic core-shell particle interactions.

# METHODOLOGY: DEM COMPUTER SIMULATION OPTIMIZATION OF COATED IRON PARTICLES

## Theory

Discrete Element Method (DEM) is a computational technique in which particles are assigned individual physical and mechanical properties. Although initially developed for the study of rock mechanics (Cundall and Strack, 1979) this technique has also been used to investigate the behavior of colloidal suspensions, especially in flocculation (Zhu and Yu, 2006; An et al., 2008) and in other colloidal systems (Moreno-Atanasio et al., 2009; Fang et al., 2012).

DEM uses Newton's second law to simulate particle motion. The equation of motion is integrated numerically using an explicit finite difference method, such as the Euler method (Cundall and Strack, 1979), to determine the accelerations, velocities and positions of the particles at any time. More detail on the DEM working procedure can be found elsewhere (MacPherson et al., 2012). The forces acting on the particles can be decomposed into several components: elastic contact, magnetic, electric double layer, Brownian and drag. Therefore, the general equation of motion can be written as:

$$m\frac{d^2\vec{x}}{dt^2} = \overrightarrow{F}_{cont} + \overrightarrow{F}_{mag} + \overrightarrow{F}_{edl} + \overrightarrow{F}_{brw} + \overrightarrow{F}_{drag} \quad (1)$$

where $m$ is the mass of the particle, $\vec{x}$is the vector position of the particle, $t$ the time, $\vec{F}$the force and the subscripts *cont*, *mag*, edl, *brw* and *drag* refer to contact, magnetic, electric double layer, Brownian and drag forces respectively.

The elastic force experienced by two contacting particles is given by Hertz's law:

$$\vec{F}_{cont,n} = \frac{4}{3}E^* R^{*1/2}\,\delta_n^{3/2} \quad (2)$$

where $\delta_n$ is the normal contact deformation, $R^*$ is the reduced particle radius ($1/R^* = 1/R_1 + 1/R_2$), and E* the reduced elastic modulus ($1/E^* = (1-\upsilon_1^2)/E_1 + (1-\upsilon_2^2)/E_2$), of two contacting particles, respectively, as given by their individual radii, $R_i$, Poisson's ratio, $\upsilon_i$ and elastic moduli, $E$.

The fluid in these simulations was assumed to be stationary. The Stokes' drag force for a stationary fluid used in the simulations is given by:

$$\vec{F}_{drag} = 6\pi\nu R\left(\frac{d\vec{r}}{dt}\right) \quad (3)$$

where $\nu$ is the fluid viscosity.

Brownian forces describe the random motion of particles in a fluid. The direction is randomly determined and the magnitude of the force follows a Gaussian, or normal distribution, with variance ($< \Delta F_B^2 >$), for a given direction (x, y, or z) in the form (MacPherson et al., 2012):

$$< \Delta F_B^2 > = \frac{12K_B T\pi R\nu}{\Delta t} \quad (4)$$

Where $k_B$ is the Boltzmann constant, $T$ the absolute temperature and $\Delta t$ the time step.

The electrical double layer force ($F_{edl}$) was incorporated into the simulations by using the Debye-Huckel approximation for constant surface charge density in the form (Warren, 2000; Li et al., 2010; Szilagyi et al., 2014):

$$\vec{F}_{EDL} = \frac{q_i q_j}{4\pi\varepsilon_0\varepsilon_r r^3} exp^{-(r-(a+b))\kappa}\frac{1+r\kappa}{(1+a\kappa)(1+b\kappa)}\vec{r} \quad (5)$$

Where $\kappa^{-1}$ is the Debye length, $a$ and $b$ are the particle radii of particles $i$ and $j$ respectively, $d$ is the particle center to particle center distance, $r$ is the distance between charges, $\varepsilon_0$ is the permittivity of free space, $\varepsilon_R$ is the relative dielectric constant and $q_i$and $q_j$are the total surface charge for particles $i$ and $j$ respectively.

The magnetic force between two particles ($i$ and $j$) was calculated as a function of the initial magnetic susceptibility ($\chi$) of iron whose value is equal to 150. The expression used for the force between two magnetic dipoles ($F_m$) was (Rosensweig, 1985; Patel and Chudasama, 2009; Lim and Feng, 2012; Ku et al., 2016):

$$\vec{F}_m = \frac{3\mu_0}{4\pi r^5}\left[(\vec{m}_i\vec{r})\vec{m}_j + (\vec{m}_j\vec{r})\vec{m}_i + (\vec{m}_i\vec{m}_j)\vec{r} - \frac{5(\vec{m}_i\vec{r})(\vec{m}_j\vec{r})}{r^2}\vec{r}\right] \quad (6)$$

where $\vec{m}_i$ and $\vec{m}_j$ are the magnetic dipolar moment of the particles $i$ and $j$ and $\vec{r}_{ij}$ is the vector that joins the center of particle $i$ with the center of particle of $j$.

## Simulation Details

A summary of the particle properties used in the simulations is given in **Table 1**. Particles were randomly positioned within a cubic space whose dimensions were varied in order to keep the volume fraction constant at the value of 0.0039, which is close to published experimental and simulation work (Ezzaier et al., 2017; Hyde et al., 2017). No overlap between the particles was allowed in the initial configuration and no initial velocity was given to the particles. Therefore, particle motion was a direct consequence of the magnetic, van der Waals forces and Brownian forces.

The cores and shells were simulated as made of pure iron and silica respectively (Neville and Moreno-Atanasio, 2012; Hyde et al., 2017). The magnetization of the particles was set at $1/10^{th}$ of the saturation magnetization value of iron 0.228 T/$\mu_0$ (Reitz et al., 2008; Kargulewicz et al., 2012).

**TABLE 1** | Particle physical properties and fluid properties.

| Property | Value |
|---|---|
| Core density (kg/m$^3$) | 7,860 |
| Shell density (kg/m$^3$) | 2,200 |
| Elastic modulus–shell (GPa) | 70 |
| Magnetization (A/m) | $1.8 \times 10^5$ |
| Volume fraction (v/v) | 0.004 |
| Water viscosity (Pa s) | 0.001 |

### Absence of Electrical Double Layer Forces

The first study was conducted in the absence of an electrical double layer force with the objective of understanding the influence of the magnetic force on particle aggregation. In addition, these cases can be considered as the limiting case of a situation with an electrical double layer force but high ionic strength and therefore would constitute a special case of our second study which was carried out in the presence of an electrical double layer interaction.

Particle sizes ranged between 0.5 and 21 μm while the core diameters considered were 0.5, 1.0, 2.0, and 4 μm (**Table 2**). **Table 2** also shows the relative shell thickness, RST, which is defined as:

$$RST = \frac{d_p - d_c}{d_p} \tag{7}$$

where $d_p$ and $d_c$ are the particle and core diameters. Eq. (7) can also be interpreted as a function of the particle and core radii, $r_p$ and $r_c$, as:

$$RST = \frac{r_p - r_c}{r_p} \tag{8}$$

It is important to note that the difference between particle radius and core radius, $r_p$–$r_c$, is the actual thickness of the shell. Both, Equations (7, 8) can take values between 0 and 1 which correspond to the cases of a particle with no shell and a particle in which there is no magnetic core, respectively.

Each simulation was labeled in terms of particle and core sizes and thus, the two first numbers represent the particle size in units of 100 nm and the two numbers following the letter C represent the core size, also in units of 100 nm. For example, case 06-C05 has a central core of 500 nm diameter ("C05"), with a 50 nm shell layer, giving an overall particle diameter of 600 nm ("06"). Therefore, the relative shell thickness, RST, would be according to Equations (7) or (8), 1/6 or 0.17.

### In the Presence of EDL Forces

The first part of the analysis of the influence of the electrical double layer was carried out by varying the surface charge density. Surface charge densities in the range of 0.1 to 20 $mC/m^2$ were assigned to the particles while the Debye length was kept constant at 3 nm (equivalent to a 10 mM monovalent salt solution). These surface charge densities correspond to surface potentials of 0.42–84 mV. In the case of unmodified silica, these values would be negative (Hyde et al., 2015). However, if the silica formed contained a basic polymer, the surface potentials would be positive, but of the same magnitude (Neville et al., 2013; Hyde et al., 2015). Therefore, the sign of the surface charge is irrelevant in this study as all the particles were considered to have the same sign of the surface potential and therefore, they will always experience repulsion due to the electrical double layer.

In order to elucidate if either the absolute or relative shell thickness are the most important parameters controlling aggregation, our study in the presence of electrical double layer considered the cases of a shell thickness of 50 nm with core sizes of 0.5 and 4 μm in diameter (cases 06-C05 and 41-C40), respectively. In order to compare the effect of relative shell thickness, RST, two cases with relative shell thickness equal to 0.17 and 0.64 for two different core diameters 0.5 and 4 μm were investigated. Here, the four cases were 06-C05 (RST = 0.17), 48-C40 (RST = 0.17), 15-C05 (RST = 0.64) and 120-C40 (RST = 0.64). Here the coordination number (number of neighbors per particle), singlet ratio (single particles/total particles) and largest fragment ratio (chain) (particles in largest fragment/total particles) were analyzed. After this, the minimum interparticle distance between particles that showed no contacts was analyzed. In addition, the minimum surface charge density for the particles to not be in contact was studied in order to obtain the relationship between this value and the ratio of the core to total particle diameter.

**TABLE 2 |** Properties of the different core-shell particles studied at the limit of the range for each core diameter.

| Simulation label | Particle diameter, $d_p$, (μm) | Core diameter, $d_c$ (μm) | Relative shell thickness | Concentration (g/l) |
|---|---|---|---|---|
| 05-C05 | 0.50 | 0.50 | 0.00 | 29.9 |
| 20-C05 | 2.00 | 0.50 | 0.75 | 8.60 |
| 10-C10 | 1.00 | 1.00 | 0.00 | 29.9 |
| 40-C10 | 4.00 | 1.00 | 0.75 | 8.60 |
| 20-C20 | 2.00 | 2.00 | 0.00 | 29.9 |
| 120-C20 | 12.0 | 2.00 | 0.83 | 8.40 |
| 40-C40 | 4.00 | 4.00 | 0.00 | 29.9 |
| 210-C40 | 15.0 | 4.00 | 0.81 | 8.50 |

## RESULTS AND DISCUSSION

The focus of this paper was to investigate the influence of the shell thickness of magnetic core-silica shell particles on their colloidal stability, for different values of surface charge density. The properties of the cores and the shells were explicitly considered rather than the use of an overall average of the particle. Four different core sizes were simulated with a large overall particle size range (**Table 2**).

### Magnetic Aggregation in the Absence of Electrical Double Layer (High Ionic Strength)

All the simulations conducted here used the properties given in **Tables 1**, **2**. **Figure 1** shows the visualization of the system for the cases in which the relative shell thickness (RST) were 0.0 (top), and 0.70 and 0.73 (left and right, bottom respectively).

The simulations in **Figure 1** clearly demonstrate that the presence of a shell (**Figure 1**, bottom) can disrupt the chain formation process that can be seen when the particles had no shell (**Figure 1**, top). In fact, although some chains were formed in the presence of a thick shell, their linearity as well as their length seem to be greatly affected. Furthermore, in the absence of a shell, the chains seem to transverse the system from top to bottom as typically encountered in magnetic fluids studies (Popplewell and Rosensweig, 1996; Chin et al., 2000). However, the case 40-C40 shows a smaller number of chains which seem

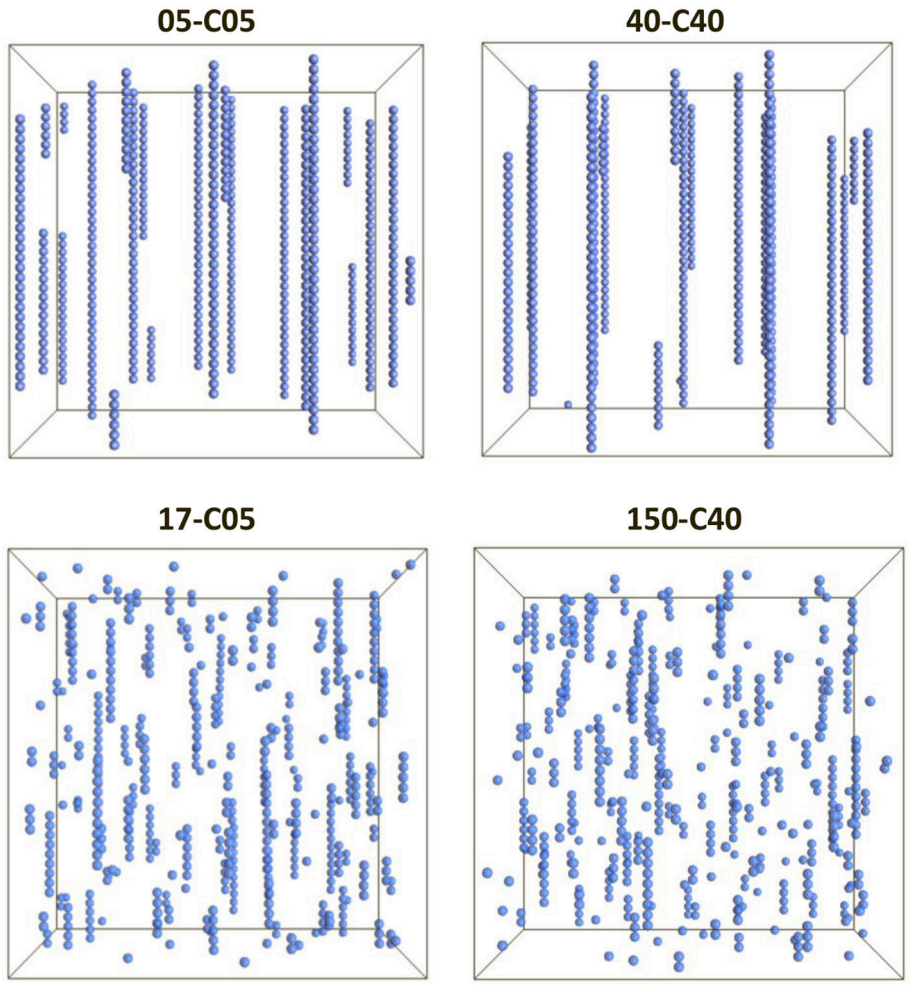


**FIGURE 1 |** Visualization of 4 cases corresponding to two different core sizes (0.5 and 4.0 μm, left and right respectively) and situations in which no shell was present, and thus RST = 0 (top) or a thick shell was present (RST = 0.70, bottom left and RST = 0.73, bottom right). The images have been scaled for easier viewing. However, the dimensions of the system were different to keep a constant volume fraction of 0.0039.

to be longer than in the 05-C05 case, corroborating that larger magnetic particles aggregate more easily. However, a microscopic analysis is necessary in order to understand the influence of the presence of a shell and the differences between the different cases.

The data in **Figure 2** show the singlet ratio (number of particles without contacts divided by the total number of particles) against the relative shell thickness for different core sizes. The general trend for all core diameters is that the ratio of the singlets increases with the increase in relative shell thickness. In addition, the actual size of the core has a strong influence on the behavior of the system as a magnetic core of 4.0 μm would need a shell thickness of around 6.0 μm to start to hinder aggregation as reflected by the increase in singlet ratio, while for the smallest core (0.5 μm) the required shell thickness is 0.46 μm.

A clearer picture is provided in **Figure 3** where the coordination number as a function of the relative shell thickness is presented. Coordination number is defined as twice the number of contacts divided by the number of particles. The reason for the factor of two is that a contact is shared by two particles. It can be seen that a coordination number of around 2 was observed for low values of relative shell thickness, indicating that each particle has two contacts. This is indicative of the formation of linear chains due to the magnetic force and this coordination number is clearly much smaller than in self-assembly cases due van der Waals force (MacPherson et al., 2012). It can also be observed that the coordination number decreased with the increase in relative shell thickness, suggesting the occurrence of disruption of the chain formation process. Finally, the increase in the actual value of the size of the core is associated to an increase in the coordination number and thus, this observation confirms that the larger the size of the core, the largest the relative shell thickness needed to disrupt the magnetic aggregation.

In order, to fully understand the degree of aggregation, we have plotted the largest fragment ratio (number of particles contained in the largest fragment divided by the number of

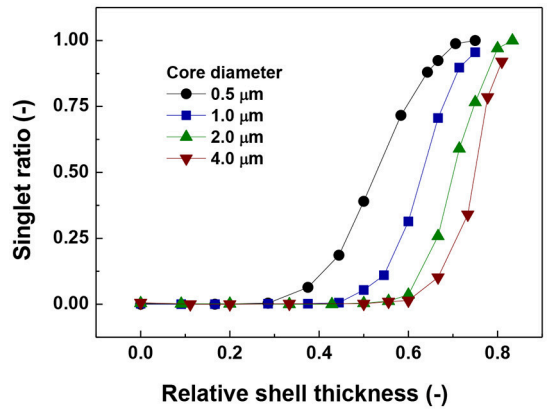


**FIGURE 2 |** Ratio of number of singlets to the total number of particles vs. relative shell thickness.

particles in the system) a function of the relative shell thickness in **Figure 4**. As can be seen in **Figure 4**, there is a decrease in the size of the largest fragment with increasing relative shell thickness (RST). All the curves trend to around 0.08 for the smallest values of RST. This value of the largest fragment ratio although seemingly small, corresponds to an actual length of 40 particles which can be easily demonstrated to coincide with the length of the working space, L /$d_p$ is

$$\frac{L}{d_p} = \left(\frac{\pi N}{6\phi}\right)^{1/3} \tag{9}$$

where N is the number of particles in the system and $\varphi$ is solid volume fraction (**Table 1**). As the number of particles in the system as well as the packing were fixed for all the simulations at 500 and 0.0039, L/$d_p$ is equal to 40.6 particles.

The value of 0.08 starts to decrease approximately at the same relative shell thickness value at which the coordination number started to decrease (**Figure 2**) and the number of singlets started to increase (**Figure 1**). The coincidence of these points suggests a predominant behavior of single particle addition rather than cluster-cluster aggregation.

Another important aspect is the fluctuation that appears in the curves of the largest fragment (**Figure 4**) in comparison to the singlets and coordination number plots (**Figures 2**, **3**). This is more likely to be due to a statistical process in which the random nature of the Brownian forces produces aggregates of slightly different sizes. This result is consistent with the trend of coordination number and number of singlets suggesting that there is a maximum value of shell thickness below which the presence of the shell does not have an important influence on the behavior of the system. Nevertheless, it is important to note that this maximum value increases with increasing core size.

## In the Presence of an Electrical Double Layer Contribution

After the initial study where no electrical double layer contribution was included, chain formation in the presence of an electrical double layer force was investigated in order to determine the surface charge density required to act on the shell layer for particle contacts not to occur in chains. The effect of the electrical double layer on particles with different shell thicknesses was also studied to determine magnetic core-shell particle interaction behavior.

**Figures 5–7** show the singlet ratio, coordination number and largest fragment ratio as a function of the surface charge density for the five different cases considered in the simulations. For the smallest core (0.5 μm) there is a drastic difference between both plotted cases correlating well with the strong difference in shell thicknesses that are 50 nm and 500 nm. For the smallest particles (06-C05) a surface charge density of about 10 mC/$m^2$ was required to start to observe the hindering of the magnetic aggregation. In contrast, for the largest shell thickness (15-C05) the magnetic core was unable to produce aggregation. This result is consistent with **Figure 6** where we observed that the coordination number of the system is close to 2 for the former case and close to zero for the latter.

For the cases in which a 4.0 μm core size was simulated, the differences were not as abrupt as for the case of 0.5 μm core diameter. **Figure 5** shows that the singlet ratio was close to zero or in the case of the largest relative shell thickness (0.67, case 120-C40) only about 20% of particles had no contacts, indicating that significant aggregation occurred. This is further corroborated by **Figures 6**, **7** as the coordination number and largest size ratio were close to 1.3 and 0.03, respectively, for the case 120-C40. Given that a relative shell thickness for the core of 0.5 μm was enough to completely hinder aggregation, we can conclude as the size of the core increases, even with the combined effect of the electric double layer repulsion and the thickness of the shell the possibility of stopping magnetic aggregation reduces considerably. This is a consequence of the magnetic force being proportional to the volume of the core (Equation 6) while the electrical double layer and the Brownian forces are proportional to the surface of the particles (Equation 4) and the square root the particle size (Equation 5), respectively.

By comparing the cases with a shell thickness of 50 nm (06-C05 and 41-C40), the presence of an electrical double layer was not sufficient to stop the aggregation process despite the magnetization was only 1/10th of the saturation magnetization of iron. The exception was observed for the smallest core and surface charge densities of 10 mC/$m^2$ (42 mV). Therefore, within the range of particle size analyzed here the presence of a charged shell unless, further functionalized, has no role in the colloidal stability of the system.

**Figure 8** shows the minimum interparticle distance between particles for the cases plotted in **Figures 5–7** that show no contacts for any value of surface charge density. These cases are 06-C05 at 15 mC/$m^2$, 15-C05 at 3 mC/$m^2$, and 120-C40 at 5 mC/$m^2$. The values were obtained by averaging the minimum surface distance taken from the simulations between 0.2 and 1.0 s at 0.0001 s intervals. **Figure 8** shows that the minimum surface distance increases "linearly" with surface charge density on the linear-log scale presented. This result is consistent with the experimental data of Chin et al. (2000) which observed that as zeta potential increased, the distance between particle increased

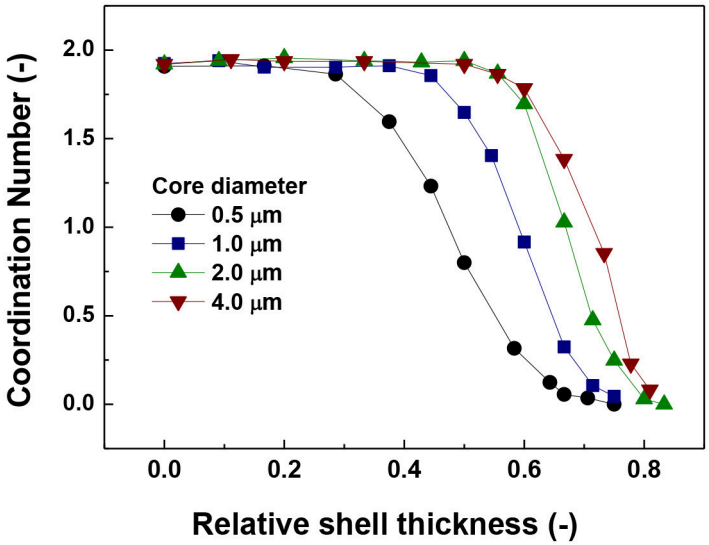


**FIGURE 3 |** Coordination number vs. relative shell thickness.

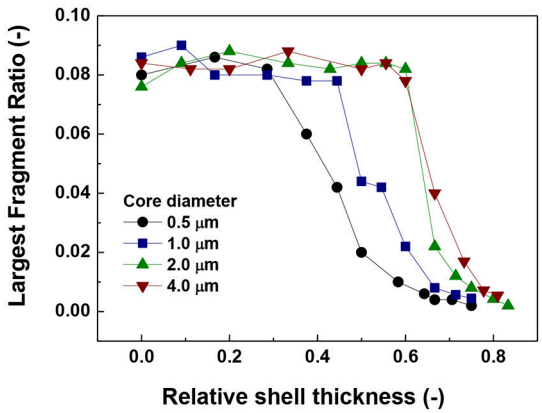


**FIGURE 4 |** Largest fragment ratio vs. relative shell thickness.

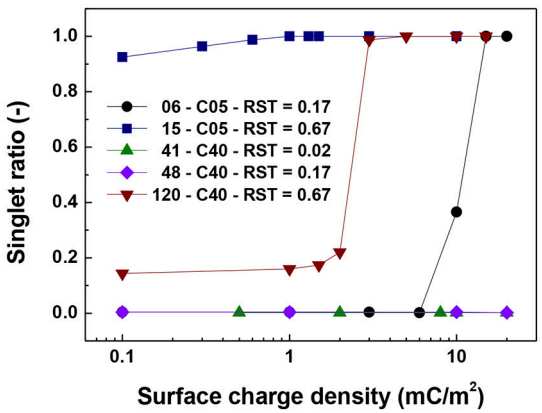


**FIGURE 5 |** Singlet ratio vs. surface charge density. The figure presents the comparison for cases of shell thickness equal to 50 nm (06-C05 and 41-C40) and two values of relative shell thickness of 0.17 (06-C05, 48-C40) and 0.67 (15-C05 and 120-C40).

with a natural logarithmic-shaped trend. They reasoned that this was because as the surface charge density increases the electrostatic repulsion increases and so the separation distance is larger (Chin et al., 2000). It is important to note that this minimum separation distance is orders of magnitude smaller than the particle diameter.

Most of the work published in the literature has focused on the aggregation of nanoparticles for which Brownian forces are mainly dominant. Chin et al. (2000) studied the superparamagnetic chain formation and breakage for particles of 0.89 μm diameter dispersed at different pH values and ionic strengths. Their suspension concentration was very dilute with $2.4 \times 10^8$ particles/mL, which corresponds to a volume fraction of $8.9 \times 10^{-5}$ (around 50 times smaller than ours). They first created the magnetic chains using magnetic field induction values in the range 0.5–0.8 T and once the chains were formed, the magnetic field induction was reduced to 0.0004 T. The latter value yields a magnetisation of 31.8 A/m and a magnetic moment for their particles of $1.17 \times 10^{-17}$ Am$^2$, which is significantly smaller than ours ($9.5 \times 10^{-14}$ Am$^2$ and $1.2 \times 10^{-14}$ Am$^2$ for the 1 and 0.5 μm particles respectively). However, despite their much lower magnetization they still found formation of linear chains that were stable and did not break. Therefore, the chain formation and stability for the core-particles of 0.5 and 1.0 μm is consistent with the results of Chin et al. (2000).

Chin et al. (2000) studied the position of a secondary minimum for a range of magnetic field induction values and ionic strengths. They reported the position of the secondary minimum

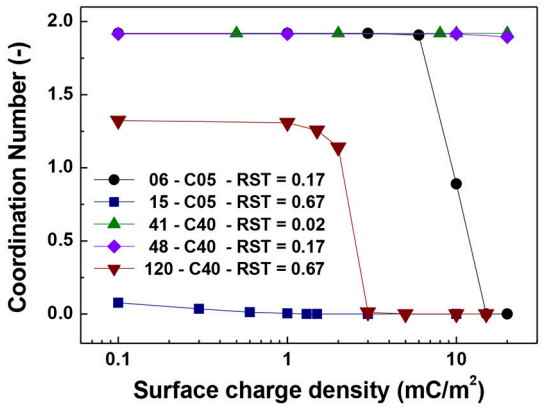


**FIGURE 6 |** Coordination number vs. surface charge density. The figure presents the comparison for cases of shell thickness equal to 50 nm (06-C05 and 41-C40) and two values of relative shell thickness of 0.17 (06-C05, 48-C40) and 0.67 (15-C05 and 120-C40).

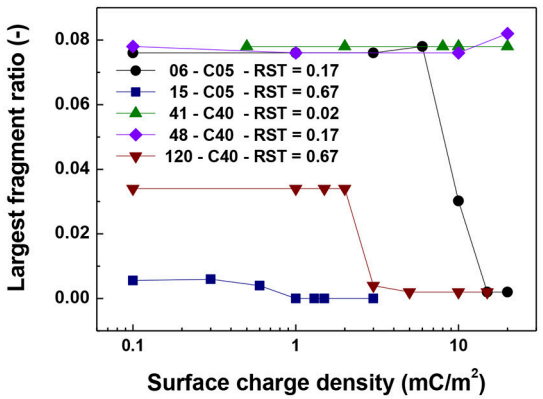


**FIGURE 7 |** Largest fragment ratio vs. surface charge density. The figure presents the comparison for cases of shell thickness equal to 50 nm (06-C05 and 41-C40) and two values of relative shell thickness of 0.17 (06-C05, 48-C40) and 0.67 (15-C05 and 120-C40).

to be at 18 nm (surface to surface distance) for an ionic strength of 10 mM and 66 mV surface potential. This result (Chin et al., 2000) seems to be weakly independent of particle size as the value was very similar when either a 0.89 or 4 μm diameter particle was used. With this data the equivalent surface charge density calculated using

$$\sigma = \frac{\psi \varepsilon_r \varepsilon_0 (1 + \kappa R)}{R} \tag{10}$$

is 15 mC/m$^2$. Using their values of magnetic field induction of 0.05 T and magnetic susceptibility of 0.1, an equivalent magnetic moment of $1.47 \times 10^{-15}$ Am$^2$ is obtained.

Since the particles of Chin et al. (2000) are superparamagnetic composites of polystyrene and magnetic and our particles may be thought of as composite core-shell particles of silica and ferromagnetic iron, of similar but not identical sizes, a direct comparison is not straightforward. Nevertheless, according to **Figure 8** for the same value of the electrical double layer, a separation distance 4–15 nm was obtained for the 0.5 μm core particles (with 0.6 and 1.5 μm total diameters), which is comparable to the value of Chin et al. (2000).

A visualization of the 06-C05 and 120-C40 cases at 15 and 5 mC/m$^2$ is provided in **Figure 9**. The differences in **Figure 9** are remarkable as despite the fact that no contacts were detected in either case, there are still clearly visible linear particle chains, more so in the 06-C05 case than in the 120-C40. As shown in **Figure 8** the minimum interparticle distance was much smaller than the particle size therefore, deceptively, the particles seem to be in contact in **Figure 9** although this is not the case. More importantly, the level of disruption is much larger in the case of 120-C40, arguably due to the combined effect of shell thickness and electrical double layer. This is consistent with the results of **Figures 2–4** where a RST of 0.67 started to affect chain formation in the absence of an electrical double layer. In contrast, an RST of 0.17 for a 0.5 μm core (06-C05 case), is too small to affect the aggregation process as this phenomenon would have required a

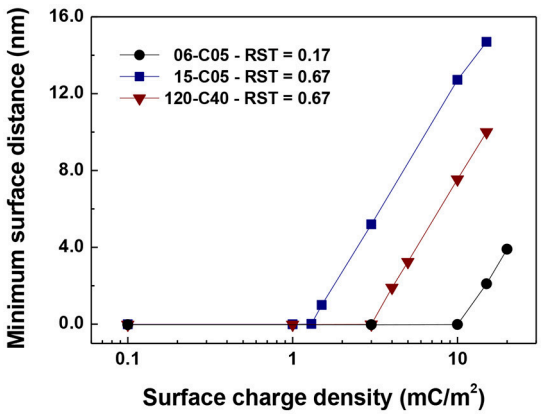


**FIGURE 8 |** Minimum interparticle distance between particles for the cases plotted in **Figures 5–7** that show no contacts (15-C05 and 120-C40 and 06-C05).

RST of 0.35–0.40 (**Figures 2–4**) to start to observe the effects of its shell thickness in the case of 06-C05 (RST = 0.17). Therefore, chains seem to be forming without the particles being in physical contact in the 06-C05 cases as a consequence of the combination of magnetic and electrical double layer interactions having a primary (Gao et al., 2017) or a secondary minimum (Chin et al., 2000) outside the particle.

## CONCLUSIONS

Computer simulations based on the Discrete Element Method have been carried out to study the influence of shell thickness of magnetic core-silica shell particles. The investigation was carried assuming an arbitrary value of magnetization of the cores equivalent to one 10th of the saturation magnetization of iron ($0.228/\mu_0$).

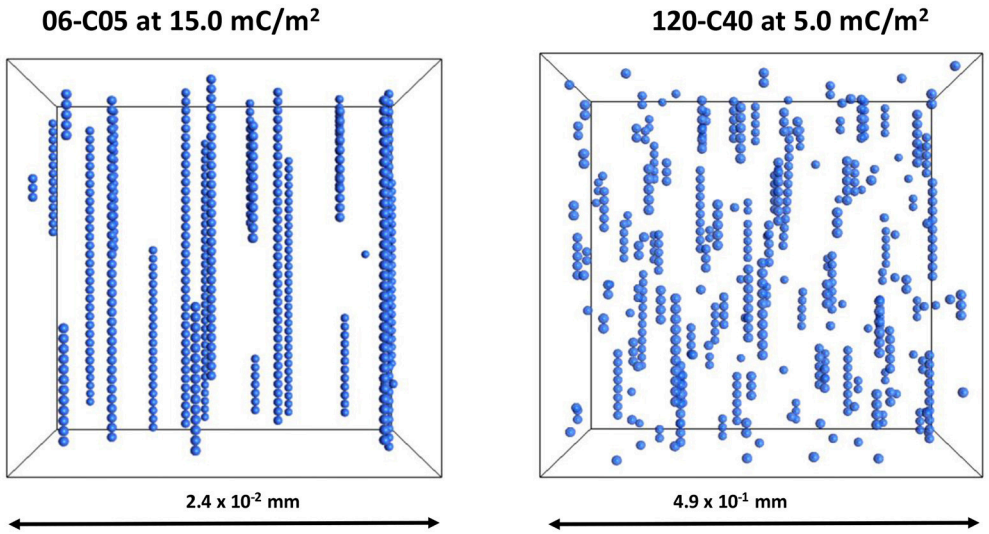


**FIGURE 9 |** Visualization of the cases 06-C05 and 120-C40 at 15 and 5 mC/m$^2$. These cases have relative shell thickness of 0.17 and 0.67. The images have been scaled for easier viewing. However, the dimensions of the system were different to keep a constant volume fraction of 0.0039.

The results have shown that the presence of a shell could contribute to the disruption of chain formation due to magnetic dipole-dipole interactions even in the absence of an electrical double layer. In addition, the increase in the size of the magnetic core produced an increase in the relative shell thickness needed to affect magnetic aggregation. This was attributed to the dependency on particle volume of the magnetic moments of the cores in comparison to the square root dependency of the Brownian forces and the physical presence of the shell whose influence could be considered to be linear with particle size.

The presence of an electrical double layer repulsion for particles of 0.5 μm core with a shell thickness of 50 nm was not sufficient to hinder the aggregation process until a surface charge density above 10 mC/m$^2$ was achieved. In fact, although particles were shown not be in contact, it was possible to still observe the formation of linear chains with the particles probably positioned at a primary minimum located outside the particles. Nevertheless, the fact that particles were not in contact and thus fluid was present between the particles, suggests that a shear flow could easily disrupt the chain process and these particles could be useful in micro or nanofluidic devices. In contrast, when the shell thickness was sufficiently large to start to produce the disruption of the formation of linear chains, the electrical double layer repulsion could produce a total disruption of the magnetic aggregation.

This study suggests that it is necessary to tune the thickness of magnetic core-silica shell particles able to hinder the aggregation process in the absence of other steric repulsions (Almusallam and Sholl, 2007), as the electrical double layer was only effective when large shell thicknesses were considered (Martinez-Pedrero et al., 2007a,b; Baldasarre et al., 2015). Future work will include the incorporation of further parameters such as van der Waals force and the redefinition of contacts and singlets to include particles that are aligned in a chain formation, but not in physical contact.

## AUTHOR CONTRIBUTIONS

RM-A designed the computer code, ran simulations, and carried out a large amount of the analysis. FN also ran simulations using the code written by RM-A and obtained the additional results. RM-A and FN drafted the work. FN concentrated on the introduction and method sections and RMA on the results and discussion. RM-A and FN both corrected the full paper several times through.

## ACKNOWLEDGMENTS

This work was partially funded by a small project grant from the Priority Research Centre for Advanced Particle Processing and Transport, The University of Newcastle.

## REFERENCES

Almusallam, A. S., and Sholl, D. S. (2007). Brownian dynamics simulations of copolymer-stabilized nanoparticles in the presence of an oil–water interface. *J. Colloid Interf. Sci*, 313, 345–352. doi: 10.1016/j.jcis.2007.04.017

Amelia, R., Wu, W. D., Cashion, J., Bao, P., Zheng, R., Chen, X. D., et al. (2011). Microfluidic spray drying as a versatile assembly route of functional particles. *Chem. Eng. Sci*. 66, 5531–5540. doi: 10.1016/j.ces.2011.07.059

Amelia, R., Xu, W. D., Chen, Z. D., and Selomulya, C. (2012). Assembly of magnetic microcomposites from low pH precursors using a novel micro-fluidic-jet-spray-dryer. *Chem. Eng. Res. Des.* 90, 150–157. doi: 10.1016/j.cherd.2011.06.014

An, X. Z., Yang, R. Y., Zou, R. P., and Yu, A. B. (2008). Effect of vibration condition and inter-particle frictions on the packing of uniform spheres. *Powder Technol.* 188, 102–109 doi: 10.1016/j.powtec.2008.04.001

Arsianti, M., Lim, M., Lou, S. N., Goon, I. Y., Marquis, C. P., and Amal, R. (2011). Bi-functional gold-coated magnetite composites

with improved biocompatibility. *J. Colloid Interf. Sci.* 354, 536–545. doi: 10.1016/j.jcis.2010.10.061

Baldasarre, F., Cacciola, M., and Ciccarella, G. J. (2015). A predictive model of iron oxide nanoparticles flocculation tuning Z-potential in aqueous environment for biological application. *Nanopart. Res.* 17:377. doi: 10.1007/s11051-015-3163-6

Bose, K., Moreno, R., Antony, S. J., Ding, Y., Biggs, S. R., Ghadiri, M., et al. (2005). "Effect of Contact Stiffness on the fluidization behaviour of cohesive powders," in *Powder & Grains,* eds R. García-Rojo, H. J. Herrmann, S. McNamara (London: CRC Press), 555–558.

Bossis, G., Iskakova, I., Kostenko, V. and Zubarev, A. (2011). Statistical mechanics and its applications. *Physica A* 390, 2655–2663. doi: 10.1016/j.physa.2011.02.044

Cao, S., Chen, J., and Hu, J. (2009). The fabrication and progress of core-shell composite materials Aust. *J. Chem*. 62, 1561–1576. doi: 10.1071/CH08420

Caruso, F., Susha, A. S., Giersig, M., and Möhwald, H. (1999). Magnetic core–shell particles: preparation of magnetite multilayers on polymer latex microspheres. *Adv. Mater*, 11, 950–953. doi: 10.1002/(SICI)1521-4095(199908)11:11<950::AIDADMA950>3.0.CO;2-T

Centi, G., and Perathoner, S. (2011). Creating and mastering nano-objects to design advanced catalytic materials. *Coordin. Chem. Rev*., 255, 1480–1498. doi: 10.1016/j.ccr.2011.01.021

Chin, C. J., Yiacoumi, S., Tsouris, C., Relle, S., and Grant, S. B. (2000). Secondary-minimum aggregation of superparamagnetic colloidal particles. *Langmuir* 16, 3641–3650. doi: 10.1021/la991201n

Chirikov, D. N., Fedotov, S. P., Iskakova, L. Y., and Zubarev, A. Y. (2010). Viscoelastic properties of ferrofluids. *Physic. Rev. E* 82:51405. doi: 10.1103/PhysRevE.82.051405

Cundall, P. A., and Strack, O. D. L. (1979). A discrete numerical model for granular assemblies. *Geotechnique* 29, 47–65. doi: 10.1680/geot.1979.29.1.47

Dalgic, S. S. (2016). Size dependent properties of hollow gold nanoparticles: a theoretical investigation. *Acta Phys. Polon. A* 129, 531–534. doi: 10.12693/APhysPolA.129.531

de Vicente, J., Klingerberg, D. J., and Hidalgo-Alvarez, R. (2011). Magnetorheological fluids: a review. *Soft Matter* 7, 3701–3710. doi: 10.1039/c0sm01221a

Ezzaier, H., Alves Marins, J., Razvin, I., Abba, M., Ben Haj Amara, A., Zubarev, A., et al. (2017). Two-stage kinetics of field-induced aggregation of medium-sized magnetic nanoparticles. *J. Chem. Phys*. 146:114902 doi: 10.1063/1.4977993

Fang, H., Tade, M. O., and Li, Q. (2012). A numerical study on the role of geometry confinement and fluid flow in colloidal self-assembly. *Powder Technol*. 214, 283–291. doi: 10.1016/j.powtec.2011.08.023

Freund, J. B., and Shapiro, B. (2012). Transport of particles by magnetic forces and cellular blood flow in a model microvessel. *Phys. Fluids* 24:051904. doi: 10.1063/1.4718752

Gao, Y., Evans, G. M., Wanless, E. J., and Moreno-Atanasio, R. (2017). DEM modelling of particle-bubble capture through extended DLVO theory. *Colloids Surf. A Physicochem. Eng. Aspects* 529, 876–885. doi: 10.1016/j.colsurfa.2017.06.082

Golovnia, O. A., Popov, A. G., Sobolev, A. N., and Hadjipanayis, G. C. (2014). Alignment of magnetic uniaxial particles in a magnetic field: simulation. *J. Magn. Magn. Mater*. 365, 64–69. doi: 10.1016/j.jmmm.2014.04.037

Han, K., Feng, Y. T., Owen. (2010) Three-dimensional modelling and simulation of magnetorheological fluids. *Int. J. Numer. Meth. Eng.* 84, 1273–1302. doi: 10.1002/nme.2940

Hovorka, O., Dan, Y. N., and Friedman, G. (2005). Self-consistent model of field gradient driven particle aggregation in magnetic fluids. *J. Appl. Phys*. 97:10Q306. doi: 10.1063/1.1860811

Hyde, E. D. E. R., Moreno-Atanasio, R., and Neville, F. (2017). Fabrication of magnetic core PEI-silica shell particles. *Mater. Res. Bull*. 96, 222–232. doi: 10.1016/j.materresbull.2017.02.045

Hyde, E. D., Moreno-Atanasio, R., Millner, P. A., and Neville, F. (2015). Surface charge control through the reversible adsorption of a biomimetic polymer on silica particles. *J. Phys. Chem. B* 119, 1726–1735 doi: 10.1021/jp5100439

Kang, T. G., Julsen, M. A., and den Toonder, M. J. (2012). Dynamics of magnetic chains in a shear flow under the influence of a uniform magnetic field. *Phys. Fluids* 24:42001. doi: 10.1063/1.4704822

Kargulewicz, M., Iordanoff, I., Marrero, V., and Tichy, J. (2012). Modeling of magnetorheological fluids by the discrete element method. *J. Tribol.* 134:31706. doi: 10.1115/1.4006021

Ke, C.-H., Shu, S., Zhang, H., and Yuan, H.-Z. (2017). LBM-IBM-DEM modelling of magnetic particles in a flui. *Powder Technol*. 314, 264–280. doi: 10.1016/j.powtec.2016.08.008

Ku, J. G., Liu, X. Y., Chen, H. H., Deng, R. D., and Yan, Q. X. (2016). Interaction between two magnetic dipoles in a uniform magnetic field. *AIP Adv*. 6:25004 doi: 10.1063/1.4941750

Ku, J., Chen, H., He, K., and Yan, Q. (2015). Simulation and observation of magnetic mineral particles aggregating into chains in a uniform magnetic field. *Min. Eng.* 79, 10–16. doi: 10.1016/j.mineng.2015.05.002

Lagger, H. G., Bierwisch, C., Korvink, J. G., and Moseler, M. (2015a). Discrete element study of viscous flow in magnetorheological fluids. *Rheol. Acta* 53, 417–443 doi: 10.1007/s00397-014-0768-0

Lagger, H. G., Breinlinger, T., Korvink, J. G., Moseler, M., Di Renzo, A., Di Maio, F., et al. (2015b). Influence of hydrodynamic drag model on shear stress in the simulation of magnetorheological fluids. *J. Non Newtonian Fluid Mech.* 218:16026 doi: 10.1016/j.jnnfm.2015.01.010

Li, D., Lam, C. N., and Biswal, S. L. (2010). Measuring short-range repulsive forces by imaging directed magnetic-particle assembly title. *Soft Matter* 6, 239–242 doi: 10.1039/B917675F

Li, H., Peng, X., and Chen, W. (2005). Simulation of the chain-formation process in magnetic fields. *J. Intell. Mater. Syst. Struct*. 16, 653–658. doi: 10.1177/1045389X05052598

Li, J., Yu, W., Chen, C., and Wei, W. (2003). Modeling nanosized colloidal particle interactions with Brownian dynamics using discrete element method. 2003 Nanotechnology Conference and Trade Show. *Nanotech* 2, 566–569.

Li, X. L., Yao, K. L., Liu, H. R., and Liu, Z. L. (2007). The investigation of capture behaviors of different shape magnetic sources in the high-gradient magnetic field. *J. Magn. Magn. Mater*. 311, 481–488. doi: 10.1016/j.jmmm.2006.07.040

Li, Y. H., Chen, C. Y., Sheu, S. T., and Pai, J. M. (2012). Dynamics of a microchain of superparamagnetic beads in an oscillating field. *Microfluid Nanofluid* 13, 579–588. doi: 10.1007/s10404-012-0974-y

Lim, E. W., and Feng, R. (2012). Agglomeration of magnetic nanoparticles. *J. Chem. Phys*. 136:124109. doi: 10.1063/1.3697865

Lindner, J., Menzel, K., and Nirschl, H. (2013). Simulation of magnetic suspensions for HGMS using CFD, FEM and DEM modelling. *Comp. Chem. Eng.* 54, 111–121. doi: 10.1016/j.compchemeng.2013.03.012

Lopez-Lopez, M. T., de Vicente, J., Bossis, G., and González-Caballero, F. (2005). Preparation of stable magnetorheological fluids based on extremely bimodal iron–magnetite suspensions. *J. Mat Res*. 20, 874–881 doi: 10.1557/JMR.2005.0108

MacPherson, S. A., Webber, G. B., and Moreno-Atanasio, R. (2012). Aggregation of nanoparticles in high ionic strength suspensions: effect of Hamaker constant and particle concentration. *Adv. Powder Technol*. 23, 478–484 doi: 10.1016/j.apt.2012.04.008

Martínez-Pedrero, F., Tirado-Miranda, M., Schmitt, A., and Callejas-Fernández, J. (2007a). Formation of magnetic filaments: a kinetic study. *Phys Rev. E* 76:11405. doi: 10.1103/PhysRevE.76.011405

Martinez-Pedrero, F., Tirado-Miranda, M., Schmitt, A., Vereda, F., and Callejas-Fernandez, J. (2007b). Structure and stability of aggregates formed by electrical double-layered magnetic particles. *Colloids Surf. A Physicochem. Eng. Aspects* 306, 158–165. doi: 10.1016/j.colsurfa.2007.03.029

Mijajlovic, M., and Biggs, M. J. (2007). Study of conformational switching in polyalanine at solid surfaces using molecular simulation. *J. Phys. Chem. C*. 111, 15839–15847. doi: 10.1021/jp074378w

Moeser, G. D., Roach, K. A., Green, W. H., and Hatton, T. A. (2004). High-gradient magnetic separation of coated magnetic nanoparticles. *AIChE J.* 50, 2835–2848. doi: 10.1002/aic.10270

Mora-Huertas, C. E., Fessi, H., and Elaissari, A. (2010). Polymer-based nanocapsules for drug delivery. *Int. J. Pharm*. 385, 113–142. doi: 10.1016/j.ijpharm.2009.10.018

Moreno-Atanasio, R., Antony, S. J., and Williams, R. A. (2009). 'Influence of interparticle interactions on the kinetics of self-assembly and mechanical strength of nanoparticulate aggregates. *Particuology* 7, 106–113 doi: 10.1016/j.partic.2009.01.008

Mousavi, N. S.., Khapli, S. D., and Kumar, S. (2015). Direct observations of field-induced assemblies in magnetite ferrofluids. *J. Appl. Phys.* 117:103907 doi: 10.1063/1.4914484

Murariu, V., Svoboda, J., and Sergeant, P. (2005). The modelling of the separation process in a ferrohydrostatic separator. *Miner. Eng.* 18, 449–457. doi: 10.1016/j.mineng.2004.06.015

Nakai, Y., Senkawa, K., Mishima, F., Akiyama, Y., and Nishijima, S. (2011). Study on interparticle interaction for dry HGMS system using pneumatic conveyance. *Phys. C.* 471:15331537. doi: 10.1016/j.physc.2011.05.232

Neville, F., and Moreno-Atanasio, R. (2012). "Magnetic interactions of core-shell composite particles: a combined experimental and simulation approach," in *Chemeca 2012: Quality of Life through Chemical Engineering (Proceedings)* (Wellington).

Neville, F., Murphy, T., and Wanless, E. (2013). The formation of polyethyleneimine-trimethoxymethylsilane organic-inorganic hybrid particles. *Colloid. Surf. A Physicochem. Eng. Aspects* 431, 42–50. doi: 10.1016/j.colsurfa.2013.04.022

Odenbach, S. (2009). *Colloidal Magnetic Fluids: Basics, Development and Applications of Ferrofluids*. Berlin: Springer.

Parker, M. R., van Leef, R. P. A. R., Myron, H. W., and Wyder, P. (1982). Particle aggregation in colloids in high magnetic fields. *J. Magm. Mag. Mat*. 27, 250–256. doi: 10.1016/0304-8853(82)90085-3

Patel, R., and Chudasama, B. (2009). Hydrodynamics of chains in ferrofluid-based magnetorheological fluids under rotating magnetic field. *Phys. Rev. E*. 80:12401. doi: 10.1103/PhysRevE.80.012401

Patrick, D. L., Flanagan, J. F., Kohl, P., and Lyden-Bell, R. M. (2003). Atomistic molecular dynamics simulations of chemical force microscopy. *J. Am. Chem. Soc*. 125, 6762–6773. doi: 10.1021/ja0345367

Perez-Castillo, I., Perez-Madrid, A., and Tubi, J. M. (2000). Chaining in magnetic colloids in the presence of flow. *J. Chem. Phys.* 113, 6443–6448. doi: 10.1063/1.1308541

Popplewell, J., and Rosensweig, R. E. (1996). Magnetorheological fluid composites. *J. Phys. D Appl. Phys.* 29, 2297–2303. doi: 10.1088/0022-3727/29/9/011

Popplewell, J., Rosensweig, R. E., and Siller, J. K. (1995). Magnetorheology of ferrofluid composites. *J. Magm. Mag. Mat*. 149, 53–56. doi: 10.1016/0304-8853(95)00336-3

Reitz, J. R., Milford, F. J., and Christy, R. W. (2008). *Foundations of Electromagnetic Theory, 4th Edn*. Boston: Addison-Wesley.

Rosensweig, R. E. (1985). Ferrohydrodynamics. Cambridge: Cambridge University Press.

Rosensweig, R. E. (2011). Towards ferrofluids with enhanced magnetization. *J. Mag. Mag. Mater*. 323, 1191–1197. doi: 10.1016/j.jmmm.2010.11.004

Sacanna, S., and Pine, D. J. (2011). Shape-anisotropic colloids: building blocks for complex assemblies. *Curr. Op. Coll. Interf. Sci*. 16, 96–105. doi: 10.1016/j.cocis.2011.01.003

Sacanna, S., Rossi, L., and Pine, D. J. (2012). Magnetic click colloidal assembly. *J. Am. Chem. Soc*. 134, 6112–6115. doi: 10.1021/ja301344n

Segovia-Gutierrez, J. P., de Vicent, J., Hidalgo-Alvarez, R., and Puertas, A. M. (2013). Brownian dynamics simulations in magnetorheology and comparison with experiments. *Soft Matt.* 9, 6970–6977. doi: 10.1039/c3sm00137g

Soda, R., Takagi, K., and Ozaki, K. (2015). Extended particle-based simulation for magnetic-aligned compaction of hard magnetic particles. *J. Magn. Magn. Mater*. 396, 128–134. doi: 10.1016/j.jmmm.2015.08.018

Son, K. J. (2018). A discrete element model for the influence of surfactants on sedimentation characteristics of magnetorheological fluids. *Korea Aus. Rheol. J*. 30, 29–29 doi: 10.1007/s13367-018-0004-z

Strydom, S., Otto, D. P., Stieger, N., Aucamp, M. E., Liebenberg, W., and de Villiers, M. M. (2014). Self-assembled macromolecular nanocoatings to stabilize and control drug release from nanoparticles. *Powder Technol*. 256, 470–476. doi: 10.1016/j.powtec.2014.01.088

Szilagyi, I., Trefalt, G., Tiraferri, A., Maroni, P., and Borkovec, M. (2014). Polyelectrolyte adsorption, interparticle forces, and colloidal aggregation. *Soft Matter* 10, 2469–2502. doi: 10.1039/c3sm52132j

Tao, R. (2001). Super-strong magnetorheological fluids. *J. Phys. Cond. Matter* 13, R979–R999. doi: 10.1088/0953-8984/13/50/202

Vakurov, A., Pchelintsev, N. A., Forde, J., Ó'Fágáin, C., Gibson, T., and Millner, P. (2009). The preparation of size-controlled functionalized polymeric nanoparticles in micelles. *Nanotechology* 20:295605. doi: 10.1088/0957-4484/20/29/295605

van Netten, K., Zhou, J., Galvin, K. P., and Moreno-Atanasio, R. (2013). 'Influence of magnetic and hydrodynamic forces on chain-aggregation and motion of magnetisable particles and composites. *Chem. Eng. Sci*. 93, 229–237. doi: 10.1016/j.ces.2013.01.028

Vékás, L., Rasa, M., and Bica, D. (2000). Physical Properties of Magnetic Fluids and Nanoparticles from Magnetic and Magneto-rheological measurements. *J. Colloid Interface Sci*. 231, 247–254. doi: 10.1006/jcis.2000.7123

Wang, J., and Shin, S. (2017). Room temperature nanojoining of Cu-Ag core-shell nanoparticles and nanowires. *J. Nanopart. Res.* 19:53. doi: 10.1007/s11051-017-3761-6

Wang, S., Sun, Z., Li, X., Gao, J., Lan, X., and Dong, Q. (2013). Simulation of flow behavior of particles in liquid–solid fluidized bed with uniform magnetic field. *Powder Technol*. 237, 314–325. doi: 10.1016/j.powtec.2012.12.013

Wang, Z., Holm, C., and Müller, H. W. (2002). Molecular dynamics study on the equilibrium magnetization properties and structure of ferrofluids. *Phys. Rev. E.* 66:21405. doi: 10.1103/PhysRevE.66.021405

Warren, P. B. (2000). A theory of void formation in charge-stabilized colloidal suspensions at low ionic strength. *J. Chem. Phys*. 112, 4683–4698 doi: 10.1063/1.481024

Weber, M., Spettl, A., Dosta, M., Heinrich, S., and Schmidt, V. (2017). Simulation-based investigation of core-shell agglomerates: influence of spatial heterogeneity in particle sizes on breakage characteristics. *Comput. Mater. Sci*. 137, 100–106. doi: 10.1016/j.commatsci.2017.05.014

Yuan, Q., Cayre, O. J., Fujii, S., Armes, S. P., Williams, R. A., and Biggs, S. (2010). Responsive core–shell latex particles as colloidosome microcapsule membranes. *Langmuir* 26, 18408–18414. doi: 10.1021/la1033564

Zeng, H., Li, J., Wang, Z. L., Liu, J. P., and Sun, S. (2004a). Bimagnetic Core/Shell FePt/Fe3O4 Nanoparticles. *Nano Lett.* 4, 187–190. doi: 10.1021/nl035004r

Zeng, H., Sun, S., Li, J., Wand, Z. L., and Liu, J. P. (2004b). Tailoring magnetic properties of core/shell nanoparticles. *Appl. Phys. Lett*. 85, 792–794. doi: 10.1063/1.1776632

Zhenghua, H., Xiang, L., Huilin, L., Guodong, L., Yurong, H., Shuai, W., et al. (2010). Numerical simulation of particle motion in a gradient magnetically assisted fluidized bed. *Powder Technol.* 203, 555–564. doi: 10.1016/j.powtec.2010.06.022

Zhu, H. P., and Yu, A. B. (2006). A theoretical analysis of the force models in discrete element method. *Powder Technol.* 161, 122–129. doi: 10.1016/j.powtec.2005.09.006

Zubarev, A. Y., Iskakova, L. Y., and Kostenko, V. O. (2010). Kinetics of growth of chain aggregates in magnetic suspensions. *Colloid J.* 72, 799–805. doi: 10.1134/S1061933X10060104

**Conflict of Interest Statement:** The authors declare that the research was conducted in the absence of any commercial or financial relationships that could be construed as a potential conflict of interest.

frontiers in Chemistry

REVIEW
published: 19 June 2018
doi: 10.3389/fchem.2018.00225

# Tailoring the Wettability of Colloidal Particles for Pickering Emulsions via Surface Modification and Roughness

*Meina Xiao, Anli Xu, Tongtong Zhang and Liangzhi Hong**

*Department of Polymer Materials Science and Engineering, South China University of Technology, Guangzhou, China*

Pickering emulsions are water or oil droplets that are stabilized by colloidal particles and have been intensely studied since the late 90s. The surfactant-free nature of these emulsions has little adverse effects such as irritancy and contamination of environment and typically exhibit enhanced stability compared to surfactant-stabilized emulsions. Therefore, they offer promising applications in cosmetics, food science, controlled release, and the manufacturing of microcapsules and porous materials. The wettability of the colloidal particles is the main parameter determining the formation and stability of Pickering emulsions. Tailoring the wettability by surface chemistry or surface roughness offers considerable scope for the design of a variety of hybrid nanoparticles that may serve as novel efficient Pickering emulsion stabilizers. In this review, we will discuss the recent advances in the development of surface modification of nanoparticles.

**Keywords: Pickering emulsions, wettability alteration, interfaces, surface modification, surface roughness**

OPEN ACCESS

***Edited by:***
*Grant Bruce Webber,*
*University of Newcastle, Australia*

***Reviewed by:***
*Sonia Iurian,*
*Iuliu Haţieganu University of Medicine and Pharmacy, Romania*
*Catherine Whitby,*
*Massey University, New Zealand*

****Correspondence:***
*Liangzhi Hong*
*mslzhong@scut.edu.cn*

***Specialty section:***
*This article was submitted to Chemical Engineering, a section of the journal Frontiers in Chemistry*

***Received:*** *05 January 2018*
***Accepted:*** *30 May 2018*
***Published:*** *19 June 2018*

***Citation:***
*Xiao M, Xu A, Zhang T and Hong L (2018) Tailoring the Wettability of Colloidal Particles for Pickering Emulsions via Surface Modification and Roughness. Front. Chem. 6:225. doi: 10.3389/fchem.2018.00225*

## INTRODUCTION

Emulsions stabilized by solid particles, so-called Pickering emulsions, offer promising applications in cosmetics, food science, controlled release, and the manufacturing of microcapsules and porous materials (Aveyard et al., 2003; Dickinson, 2010; Rayner et al., 2014; Silverstein, 2014; Marquis et al., 2016; Marto et al., 2016; Wu and Ma, 2016). The surfactant-free nature of Pickering emulsions has seldom adverse effects such as irritancy and contamination of environment and typically exhibit enhanced stability compared to surfactant-stabilized emulsions. Generally, a wide range of colloidal particles including polystyrene latexes, inorganic particles, microgels, organic pigment particles, and gelatin particles have been demonstrated to be effective Pickering emulsion stabilizers (Ashby and Binks, 2000; Binks and Lumsdon, 2001; Binks and Whitby, 2004; Li and Ngai, 2013; Binks and Olusanya, 2017; Tan et al., 2017).

The stability of Pickering emulsion is influenced by many factors, including particle size, shape and concentration, as well as surface wettability. Most research has concluded that the main parameter controlling the particle interfacial behaviors and the emulsion stability is the wettability of particles, which can be measured by the three phases contact angle at the oil-particle-water interface. The particles have to be partially wettable by both water and oil phases. If the particle is too hydrophilic, it will prefer to stay in aqueous phase rather than go to the interface. If the particle is too hydrophobic, it will prefer to stay in the oil phase. The energy required to remove a particle from an oil/water interface is given by the following equation:

$$\Delta E = \pi r^2 \gamma_{O/W} (1 - |\cos\theta_w|)^2 \quad (1)$$

where $r$ is the radius of particles, $\gamma_{o/w}$ is the oil/water interfacial tension and $\theta_w$ is the three phase contact angle (Binks, 2002). For microparticles with intermediate contact angles, the detach energy is much greater than the thermal energy and the absorption of particles at the oil/water interface is irreversible. Empirically, the emulsion type is correlated to which phase the particle prefer to disperse. Preferentially water-wetted particles favor to stabilize oil-in-water (O/W) emulsions, and preferentially oil-wetted particles favor to stabilize water-in-oil (W/O) emulsions.

In this review, we highlight recent advances in tuning the wettability of colloidal particles for Pickering emulsions and related applications, especially focus on switchable Pickering emulsions, environmentally-responsive properties, and the effect of surface roughness. There have been several reviews published devoted to Pickering emulsions (Tang et al., 2015; Wang and Wang, 2016). Wang and coworkers provide a review of controllable Pickering emulsions by adjusting amphiphilicity of soft particles, rigid particles and Janus particles (Wang and Wang, 2016). Tang and coworkers provide a comprehensive review of stimuli-responsive Pickering emulsions (Tang et al., 2015). However, our goal in this short review is to provide detail discussion of surface modification methods of tuning the particle wettability by either surface chemistry or surface topology. In addition to tune the wettability by surface chemistry with small molecules or polymers, surface topology such as surface roughness also contributes to the wettability of particles. The typical functionalization methods of particles is summarized in **Table 1** with short comments.

## TAILORING THE WETTABILITY BY SURFACE CHEMISTRY

Particle surface chemistry regulates particle retention, wettability alteration, ability to stabilize emulsions and foams. There are two main approaches developed for adjusting the surface chemistry for controllable wettability of particles: physical adsorption and chemical anchoring of small molecules or polymers.

### Surface Modification by Physical Adsorption

Surface modification by physiosorbed small molecules has attracted significant interest due to its simple preparation and efficacy. The pristine nanoparticles are typically too hydrophilic to form stable emulsion. The adsorption of surface inactive small molecules can efficiently enhance the hydrophobicity of nanoparticles, so that the modified particles preferentially stay at the oil/water interfaces and correspondingly bring out stable emulsion. Frith and coworkers explored the trivalent $La^{3+}$ cations to tune the hydrophilicity of negatively charged silica nanoparticles (Frith et al., 2008). The adsorption of $La^{3+}$ onto the silica particles reduce their effective charge and synergistically promote to form stable O/W Pickering emulsions. Also, Hasse and coworkers revealed that the adsorption of 8-hydroquinoline (8-HQ) onto the surface of hydrophilic silica particles rendering them hydrophobicity and therefore more interfacially active, as shown in **Figure 1** (Haase et al., 2010). O/W Pickering emulsions with dispersed diethyl phthalate droplets containing 8-HQ stabilized by 20 nm Ludox TMA silica nanoparticles were stable in a narrow pH range from 4.4 to 5.5 (Haase et al., 2010). Above pH 5.5, only small fractions of 8-HQ was protonated and dissolved in aqueous phase. Because of this, insufficient adsorption of protonated 8-HQ onto silica particles leads to unstable emulsions. In contrast, excess adsorption of protonated 8-HQ below pH 4.4 forms bilayer structure on silica particles, which also causes emulsion destabilization. Binks and coworkers demonstrated that the inherently hydrophilic particles can be hydrophobilized *in situ* by the adsorption of dissolved oil molecules (dialkyl adipate) in the aqueous phase and enable them to stabilize O/W emulsions (Binks and Yin, 2016). This kind of surface modification method is mainly dependent on the solubility of dialkyl adipate in water, which can be systematically adjusted by altering the chain length of alkyl group. Based on adsorption of palmitic acid (PA) onto silica nanoparticles, Santini and coworkers pointed out that emulsions stability is associated with the hydrophobicity of nanoparticles-surfactant complexes, in which the surfactant concentration and the volume ratio between the dispersed liquids are extremely important. The most stable emulsions can be produced only when surfactant molecules form single layers at the particle surface (Santini et al., 2014). By optimizing the parameters, submicrometer-sized Pickering emulsions were produced with silica nanoparticles and adsorbed oleic acid for a wide range of oils (Sadeghpour et al., 2013). Similar results have also been reported for the surface modification of other inorganic nanoparticles such as Laponite, layered double hydroxide (LDH), aluminum oxide and clay through electrostatic attraction or hydrogen bonding interaction (Li et al., 2012, 2013; Reger et al., 2012; Sturzenegger et al., 2012).

Besides interfacially inactive small molecules, the adsorption of surfactants onto colloidal particles can also synergistically enhance the formation of Pickering emulsions. Yuan and coworkers proposed two distinct co-stabilization mechanisms that arise from interactions between the nanoparticles and surfactant molecules (Yuan and Williams, 2016). Generally, significant interaction generate faster wetting process for nanoparticles at the oil/water interface and yields enhanced stabilization. On the contrary, competitive adsorption of nanoparticles and surfactant molecules occurs to stabilize the droplets when significant interaction is not existed. The adsorption/desorption equilibrium between surfactant molecules regulates the droplet stability. Cui and coworkers demonstrated that the *in situ* surface modification of pristine $CaCO_3$ nanoparticles by the adsorption of a series of sodium carboxylates could stabilize Pickering emulsions (Cui et al., 2012). The negatively charged headgroups of sodium carboxylates can absorb onto the positively charged $CaCO_3$ nanoparticles and form a monolayer, resulting in enhanced hydrophobicity of the particle surface. When the particle surface is modified to a particular hydrophobicity, emulsion type inversed from O/W(1) to W/O as shown in **Figure 2**. As for sodium dodecanoate, a second phase inversion from W/O to O/W(2) emulsions occurred at high amphiphile concentration. This phase inversion was attributed to the bilayer or hemimicelle formation of sodium

**TABLE 1 |** Typical fabrication methods of tuning wettability of particles for Pickering emulsions.

| Method | Modifiers | Particles | Emulsion types and characteristics | References |
|---|---|---|---|---|
| Physical adsorption | 8-hydroxyquinoline | Silica | O/W; stable emulsions in a narrow pH range from 4.4 to 5.5 | Haase et al., 2010 |
| | Dialkyl adipate | Silica and Zirconia | O/W; the formation of Hydrogen bonds between oils and particle surfaces renders partially hydrophobicity | Binks and Yin, 2016 |
| | Palmitic acid | Silica | W/O; simplicity, formation of nanoparticle-PA complexes at oil/water interfaces | Santini et al., 2014 |
| | Oleic acid | Silica | O/W; long-term stability, biocompatible materials | Sadeghpour et al., 2013 |
| | Surfactants and polymers | Clay | O/W; emulsions have either viscous or gel-like properties | Reger et al., 2012 |
| | Octyl gallate | Aluminum oxide | W/O, *in situ* hydrophobization | Sturzenegger et al., 2012 |
| | Methyl orange | Layered double hydroxide | O/W, enhanced emulsion stability, *in situ* confocal fluorescence microscopic images at interface | Li et al., 2013 |
| | Fatty Acids | $CaCO_3$ | O/W or W/O, switchable Pickering emulsions depending on the absorbed amount of amphiphile | Cui et al., 2012 |
| | CTAB and SDS | Silica | O/W; switchable Pickering emulsions with the sequential addition of oppositely charged surfactants | Zhu et al., 2015 |
| | Cationic surfactants | Silica | O/W, W/O; double phase inversion achieved with two-tails cationic surfactants | Cui et al., 2010 |
| | *N′*-dodecyl-*N,N*-dimethylacetamidine | Silica | O/W; switchable Pickering emulsion triggered by $CO_2$ responsive surfactant | Jiang et al., 2013 |
| | PDMAEMA-*b*-PMMA | PS latex nanoparticle | O/W, W/O; switchable Pickering emulsion triggered by temperature responsive PDMA blocks | Binks et al., 2005 |
| | PEI | Silica | O/W, W/O, W/O/W; the emulsion type can be easily tuned by the adsorbed amount of PEI | Williams et al., 2014a,b |
| | PLLA | HAp | O/W, biocompatible microspheres, *in situ* modification at interfaces | Fujii et al., 2009 |
| | PS | HAp | O/W, *in situ* modification at interfaces | Okada et al., 2012 |
| | Amine end-capped PDMS | Carboxylated PS nanoparticles | O/W; *in situ* modification at interfaces, interfacial jamming | Cui et al., 2013 |
| | Amine end-cappd PS | Cellulose nanocrystal | W/O; *in situ* modification at interfaces, liquid tubule | Liu et al., 2017 |
| | PDMS | Carboxylated PS nanoparticles | O/W/O, W/O, bicontinuous jammed emulsions | Huang et al., 2017 |
| Chemical anchoring | Silane coupling agents | $Fe_3O_4$ nanoparticles | O/W; stable magnetic Pickering emulsions | Zhou et al., 2012 |
| | Carboxyl containing spiropyran | UCNP@$SiO_2$ | W/O, O/W; switchable Pickering emulsions triggered by NIR/visible light, interfacial catalysis | Chen et al., 2014 |
| | organosilanes | Silica | O/W; switchable Pickering emulsions triggered by pH | Yang et al., 2013 |
| | PNIPAM | Cellulose nanocrystals | O/W; thermoresponsiveness of Pickering emulsions | Zoppe et al., 2012 |
| | PMETAC | Silica | O/W; ion-specific responsive Pickering emulsions | Tan et al., 2011 |
| | *N,N*-dimethylacetamidine | Silica | O/W, W/O; switchable Pickering emulsions triggered by $CO_2$ | Liang et al., 2014 |
| | thiol-terminated PEG chains and short alkane-thiol molecules | Gold | O/W; emulsions with enhanced stability stabilized by gold particles with both hydrophilic and hydrophobic chains | Larson-Smith and Pozzo, 2012 |
| | hydrophilic & hydrophobic organosilanes | Silica | O/W; particles modified by both hydrophilic and hydrophobic groups generate emulsions with highest stability | Björkegren et al., 2017 |
| | Sulfonated PS | Silica | Double emulsions; interfacial catalysis for biphasic reactions | Shi et al., 2015 |
| | PS-*b*-P2VP-*b*-PEO | Silica | O/W, W/O; switchable Pickering emulsions triggered by pH | Motornov et al., 2007 |
| | $\mu$-PEG-*b*-PS-*b*-PIPSMA | Silica | O/W, W/O, O/W/O; tuning the wettability of the modified nanoparticles by solvent environment and host-guest complexation, initial location effect and one-step fabrication of multiple emulsions | Liu et al., 2016 |

*(Continued)*

**TABLE 1** | Continued

| Method | Modifiers | Particles | Emulsion types and characteristics | References |
|---|---|---|---|---|
| Roughness | Eudragit S100 nanoparticles | Amine modified silica particles | O/W; surface roughness benefits emulsions stability in Wenzel regime and destabilize emulsion in Cassie-Baxter regime | San-Miguel and Behrens, 2012 |
| | Negatively charged silica nanoparticles | Positively charged silica microparticles | O/W, W/O; initial location effect | Zanini et al., 2017 |

*CTAB, cetyltrimethylammonium bromide; SDS: sodium dodecyl sulfate; PDMAEMA-b-PMMA: poly(2-(dimethylamino)ethyl methacrylate)-b-poly(methyl methacrylate); PEI, poly(ethylene imine); PLLA, poly(L-lactic acid); Hap, hydroxyapatite; PS, polystyrene; PDMS, polydimethylsiloxane; PMETAC, poly((2-(methacryloyloxy)ethyl)- trimethylammonium chloride); Poly(N-isopropylacrylamide): PNIPAM; PS-b-P2VP-b-PEO: polystyrene-b-poly(2-vinylpyridine)-b-poly(ethylene oxide); μ-PEG-b-PS-b-PIPSMA: μ-poly(ethylene glycol)-b-polystyrene-b-poly[(3-triisopropyloxysilyl)propyl methacrylate] miktoarm star terpolymers; Eudragit S100 nanoparticles: poly(methacrylic acid-co-methyl methacrylate) nanoparticles, 50 nm.*

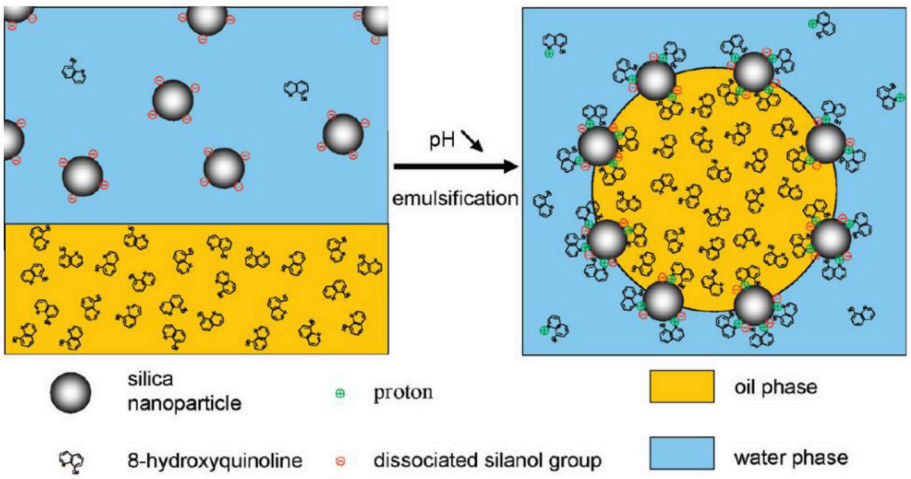


**FIGURE 1 |** Schematic representation of pH-sensitive Pickering emulsion stabilized by silica nanoparticles and hydrophobizing agent 8-hydroxyquinoline (8-HQ) (Haase et al., 2010). Reprinted with permission from Haase et al. (2010). Copyright 2010 American Chemical Society.

dodecanoate at high concentration, which endowed the particle surface hydrophilicity again and induced desorption of the particles from the interface. Consequently, the emulsion droplets were stabilized solely by the surfactants (Cui et al., 2012).

The switchable Pickering emulsions were reported with negatively charged silica nanoparticles and the consequent addition of cationic and anionic surfactants (Zhu et al., 2015). The *in situ* hydrophobization of silica nanoparticles with cetyltrimethylammonium bromide (CTAB) enable them to stabilize stable O/W emulsions. The destabilization of emulsions can be triggered by adding an equimolar amount of sodium dodecyl sulfate (SDS) because of the stronger electrostatic interaction between cationic and anionic surfactants. The same authors further investigated the effect of the architecture of the ionic surfactants on the *in situ* hydrophobization of the oppositely charged particles (Cui et al., 2010). They found that using single-chain trimethylammonium bromide surfactants or a double-head gemini cationic surfactant, only O/W emulsions can be prepared. In contrast, using didodecyldimethylammonium bromide with double alkyl tail-group, the hydrophobicity of silica particles is sufficient to stabilize W/O emulsions, and phase inversion from O/W to W/O occurred. Jiang and coworkers have also prepared a switchable Pickering emulsion by using a combination of silica nanoparticles and a trace amount of switchable surfactant *N*'-dodecyl-*N*,*N*-dimethylacetamidine (Jiang et al., 2013). Upon the addition of $CO_2$, the neutral amidine group converts to cationic amidinium group, which adsorbed onto the silica particles and then stable *n*-octane-in-water emulsion were prepared with the *in situ* formed nanoparticle surfactant. Demulsification of the as-prepared Pickering emulsion could be achieved by bubbling $N_2$.

Compared to small molecules, anchoring polymer chains onto particles by physical adsorption or chemical bonding makes the particles extremely efficient Pickering emulsion stabilizers (Binks et al., 2005; Saleh et al., 2005a; Saigal et al., 2010; Isa et al., 2011). Generally, pristine particles do not reduce the interfacial tension, whereas grafted polymer chains reduce the interfacial tension by penetrating the oil/water interface and (Saigal et al., 2010). Furthermore, the desorption of a particle grafted with polymer corresponds to the simultaneous detachment of many polymer chains from oil/water interfaces. For this kind of emulsifiers, the solubility of the grafted polymer chains in oil and water may significantly influence the emulsion characteristics.

Lucio and coworkers have demonstrated that surface modification with nitro catechol-endcapped polyethylene glycol

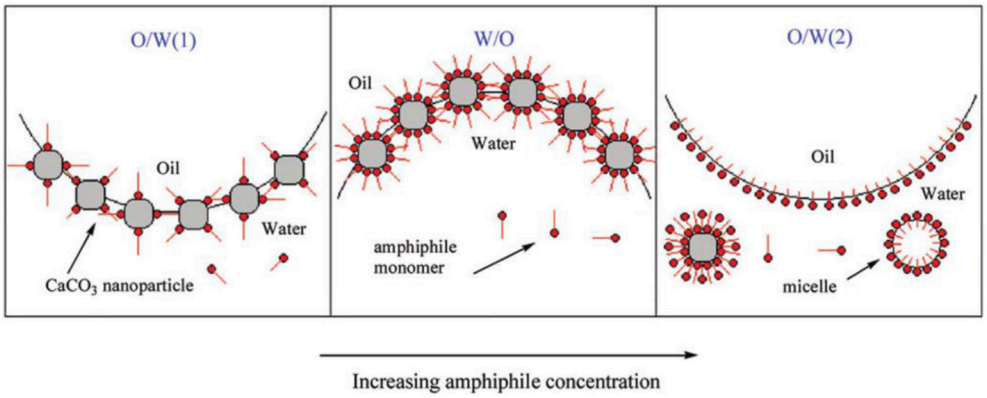


**FIGURE 2 |** Schematic representation of phase inversion induced by the adsorption of sodium carboxylates onto $CaCO_3$ nanoparticles (Cui et al., 2012). Reprinted with permission from Cui et al. (2012). Copyright 2012 American Chemical Society.

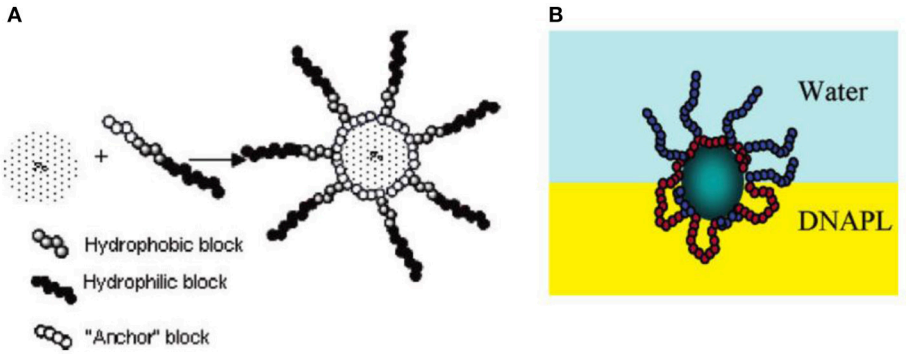


**FIGURE 3 |** Schematics representation of triblock copolymer-modified iron nanoparticles **(A)** and proposed chain rearrangement at oil/water interface **(B)**, the oil phase is toxic non-aqueous phase liquids (NAPL) (Saleh et al., 2005a). Reprinted with permission from Saleh et al. (2005a). Copyright 2005 American Chemical Society.

(PEG) endows $Fe_3O_4$ nanoparticles with superior stability. They showed that the thermodynamics adsorption of the functionalized particles at water/n-decane interface is dominated by the solubility of PEG in each phase (Isa et al., 2011). Binks and coworkers have employed poly(2-(dimethylamino)ethyl methacrylate-*b*-poly(methyl methacrylate) (PDMAEMA-*b*-PMMA) stabilized polystyrene latex nanoparticles to prepare thermos-responsive Pickering emulsions (Binks et al., 2005). Hydrophobic PMMA block acts as the anchoring block and hydrophilic PDMAEMA acts as steric stabilizer. The wettability of the particles can be tailored by temperature because of thermos-responsive properties of PDMAEMA block, which resulted in the phase inversion from O/W below the lower critical solution temperature (LCST) and to W/O above the LCST. Saleh and coworkers have reported that physisorbed layers of amphiphilic poly(methacrylic acid)-*b*-poly(methyl methacrylate)-*b*-poly(styrene- sulfonate) (PMAA-*b*-PMMA-*b*-PSS) triblock copolymers can improve the stability of $Fe^0/Fe_3O_4$ nanoparticles in water and render them amphiphilicity at the oil/water interfaces via chain rearrangement, as shown in **Figure 3** (Saleh et al., 2005a). The adsorption of copolymer-modified iron nanoparticles at oil/water interfaces and the formation of O/W Pickering emulsions have potential application in the remediation of chlorinated organic-contaminated groundwater.

It has been demonstrated that poly(ethylene imine) (PEI) can be physisorbed onto fumed silica particles to tune their surface wettability (Williams et al., 2014a,b). The wettability of such hybrid PEI/silica particles can be easily tailored by changing the PEI/silica weight ratio (Williams et al., 2014a). Systematic variation of the PEI/silica weight ratio induces the phase inversion from O/W to W/O emulsions. Stable water-in-oil-in-water (W/O/W) multiple emulsions can be prepared with the combination of two kind of PEI/silica hybrid particles with mass ratios of 0.075 and 0.50 at pH 10, respectively. Therefore, the hydrophilic hybrid particles with mass ratio of 0.075 stabilized the O/W interface and the hydrophobic hybrid particles with mass ratio of 0.50 stabilized the W/O interface. The authors further demonstrated the wettability of PEI/silica hybrid particles could be tailored by *in situ* Schiff base chemistry between primary or secondary amine groups of PEI and long chain aldehyde (1-undecanal) in oil phase, as shown in **Figure 4**

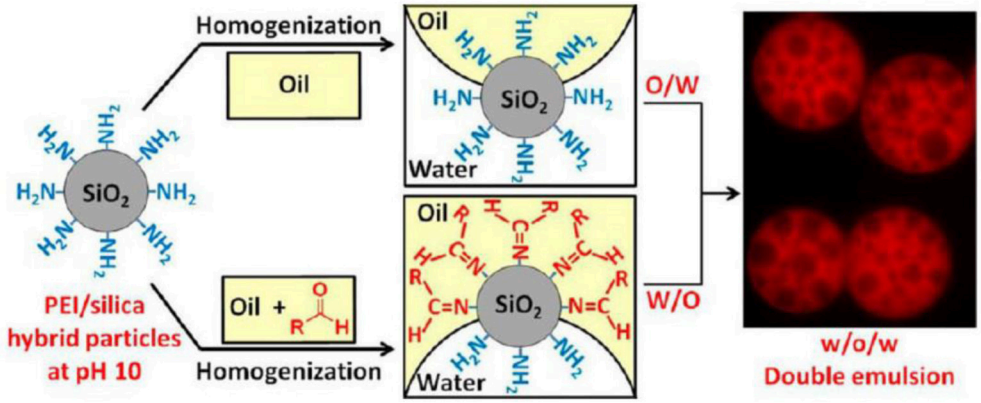


**FIGURE 4 |** Schematic illustration of the preparation of W/O/W multiple emulsions using hybrid PEI/silica particles with adjustable wettability via Schiff base chemistry (Williams et al., 2014b). Reprinted with permission Williams et al. (2014b). Copyright 2014 American Chemical Society.

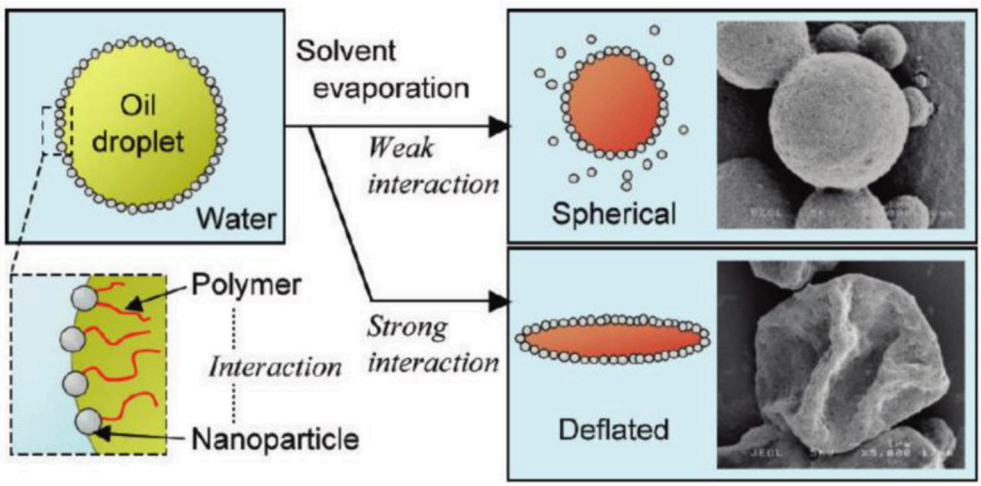


**FIGURE 5 |** Schematic representation of O/W emulsion stabilized by the combination of hydroxyapatite (HAp) particles in aqueous solution and polystyrene containing end groups in oil phase; and the effect of interaction between HAp particles and polymer on the morphology of microparticles after evaporation of oil phase (Okada et al., 2012). Reprinted with permission from Okada et al. (2012). Copyright 2012 American Chemical Society.

(Williams et al., 2014b). This interfacial reaction increases the hydrophobicity of PEI/silica hybrid particles. In accordance to the surface wettability of hybrid particles, various type of Pickering emulsions can be obtained including O/W, W/O, and W/O/W emulsions.

Fujii and coworkers found that hydroxyapatite (HAp) stabilized O/W emulsions were prepared only for the oils containing ester group such as methyl myristate (Fujii et al., 2007). They further demonstrated that dichloromethane-in-water emulsions could be stabilized by HAp particles when poly(L-lactic acid) (PLLA) was dissolved in oil phase (Fujii et al., 2009). Instead of the interactions between HAp and ester groups of polymer chain at the interface, Okada and coworkers prepared O/W Pickering emulsions stabilized by the combination of HAp particles and polystyrene containing end groups in oil phase (Okada et al., 2012). The driving force for the formation of the stable O/W emulsions is the interaction between HAp particles and carboxyl group of polystyrene at oil/water interfaces. After evaporation of dichloromethane for the emulsions, HAp particles coated microspheres were fabricated as shown in **Figure 5** (Okada et al., 2012). When weak interactions are involved, HAp particles may desorb from the interface during the evaporation of dichloromethane and shrinkage of the interface. However, strong interactions between HAp particles and polymer in oil phase prevent desorption of HAp particles from the interface, resulting in deflated microspheres.

Cui and coworkers detailly investigated the interfacial jamming of nanoparticles at the oil/water interfaces with the aid of end-functionalized polymer chains in oil phase (Cui et al., 2013). Aqueous dispersion of 15 nm carboxylated polystyrene (PS-COOH) nanoparticles was dispersed in silicone oil containing amine end-capped polydimethylsiloxane. The

water droplets were stabilized by the nanoparticle surfactants formed *in situ* at the interface via the carboxylate-amine interactions. It is worth noting that neither PS-COOH particles nor functionalized polydimethylsiloxane (PDMS) alone is interfacially active to arrest the coalescence of water droplets. Under the external electric field, the water droplets could deform from spherical to ellipsoidal shapes. Consequently, more nanoparticles surfactants were formed at the interface because of the increase of the oil/water interface from the deformation. More interestingly, the water droplets maintained the deformed shape stabilizing by the interfacially jammed nanoparticle surfactants after the removal of the electric field. Based on the same principle, Liu and coworkers described the interfacial activity of nanoparticle surfactants formed at the toluene/water interface with rod-like cellulose nanocrystal (CNC) dispersed in water and amine end-capped polystyrene in toluene (Liu et al., 2017). Under the optimized experimental conditions, the formation of CNC-surfactants at the interface can arrest the Rayleigh instability and generate aqueous tubules in toluene.

Previously, bicontinuous jammed emulsions (bijels) were mainly produced through spinodal decomposition process and the formed two continuous, interconnected domains were stabilized by particles with equal affinity with the two liquids (Stratford et al., 2005; Herzig et al., 2007). Recently, Huang and coworkers fabricated bijels with sub-micrometer domains using nanoparticle surfactants (Huang et al., 2017). It was found the combination of 15 nm PS-COOH particles with low molecular weight PDMS (1,000 g/mol) tends to produce either oil-in-water-in-oil (O/W/O) multiple emulsions or W/O emulsions, the combination of PS-COOH particles with high molecular weight PDMS tends to produce W/O emulsions. By contrast, bijels were produced by the combination of PS-COOH particles with a mixture of low and high molecular weight PDMS.

In addition to the electrostatic interaction, supramolecular complexation between particles and modifiers has also been employed in assembling supramolecular colloidosomes at the oil/water interface (Mathapa and Paunov, 2013; Stephenson et al., 2014). Mathapa and coworkers have reported that O/W Pickering emulsion can be stabilized by the *in situ* formed inclusion complex of cyclodextrin (CD) and tetradecane. Similarly, W/O emulsions can be formed when highly viscous silicone oil was used as continuous phase (Mathapa and Paunov, 2013). Stephenson and coworkers have explored the cucurbi[8]uril (CB[8]) host-guest system to interfacially crosslink methyl viologen-functionalized polystyrene nanoparticles by naphthol-functionalized polyacrylamide as shown in **Figure 6** (Stephenson et al., 2014). Triggered release of cargoes from the supramolecular colloidosomes has been demonstrated by disassembly of the supramolecular complex with the addition of competitive guest such as 1-adamanthlamine (ADA) for CB[8] under mild condition.

Besides, temperature induced phase separation was applied to tune the wettability of hybrid particles of polymer@silica (Fuchs and Avnir, 2013). Under thermal treatment, most of the entrapped hydrophobic polymers emerge at particles surface and endow the hybrid particles with amphiphilic properties for stabilizing W/O or O/W emulsions (Fuchs and Avnir, 2013). Zhou and coworkers designed a thermally switched release system consisted of aqueous colloidosomes stabilized by $\beta$-cyclodextrin ($\beta$-CD) nanoparticles (Zhou et al., 2013). Pluronic L31, the poly(ethylene oxide)-*b*-poly(propylene oxide)-*b*-poly(ethylene oxide) (PEO-*b*-PPO-*b*-PEO) triblock copolymer, was dissolved in the inner aqueous phase with 6.0 wt%. The release of active materials was triggered by the temperature change. Under ambient temperature (21°C), the interstitial pores were blocked by the adsorption of PEO-*b*-PPO-*b*-PEO triblock copolymers and then inhibited the release of active materials from inner to outer aqueous phase. By contrast, at 37°C, PEO-*b*-PPO-*b*-PEO triblock copolymers self-assembled into micelles and the pores were opened by the desorption of the triblock copolymers.

## Surface Modification by Chemical Anchoring

It was demonstrated that silane coupling agents-modified $Fe_3O_4$ nanoparticles can stabilize emulsions with both non-polar oil (dodecane) and polar oil (butyl butyrate) (Zhou et al., 2012). The hydrophobicity of $Fe_3O_4$ nanoparticles increased with the modification by either fatty acids or silane coupling agents with different chain lengths. However, fatty acids-coated $Fe_3O_4$ nanoparticles can only stabilize emulsions containing non-polar oil and are incapable to stabilize emulsions composed of butyl butyrate. Thermal gravimetric analysis indicates that the adsorbed amount of carboxylic acid via physical adsorption is less than silane coupling agents via chemical anchoring (Zhou et al., 2012).

A novel NIR/visible light controlled Pickering emulsion stabilized by photochromic spiropyran conjugated upconversion nanophosphors (UCNPs) was developed and applied for biocatalytic applications as shown in **Figure 7** (Chen et al., 2014). Under NIR excitation, the UCNPs emit UV light and induce the formation of hydrophilic open-ring form of spiropyran. This isomerization process can be reversed by exposure to visible light. Light-triggered emulsion inversion was attributed to the surface switchable of UCNPs. Based on this intelligent Pickering emulsion, catalytic performance was enhanced, and substrate inhibition effect was relieved (Chen et al., 2014).

Yang and coworkers fabricated pH-responsive and interfacially active modified silica particles with a mixture of hydrophobic $(CH_3O)_3Si(CH_2)_7CH_3$ and hydrophilic, pH sensitive $(CH_3O)_3SiCH_2CH_2CH_2(NHCH_2CH_2)_2NH_2$ organosilanes by covalent linkage via sol-gel chemistry (Yang et al., 2013). After loading catalysts, the functionalized silica particle-stabilized emulsions show higher catalysis efficiency than its analogous biphasic systems. More interestingly, the separation and recycling of sub-micrometer solid catalyst can be achieved by changing the pH value based on pH-triggered emulsion phase inversion (Yang et al., 2013).

Tilton and coworkers investigated the Pickering emulsions stabilized by thermally responsive polymer grafted silica nanoparticles (Saigal et al., 2010). Poly(2-(dimethylamino)ethyl

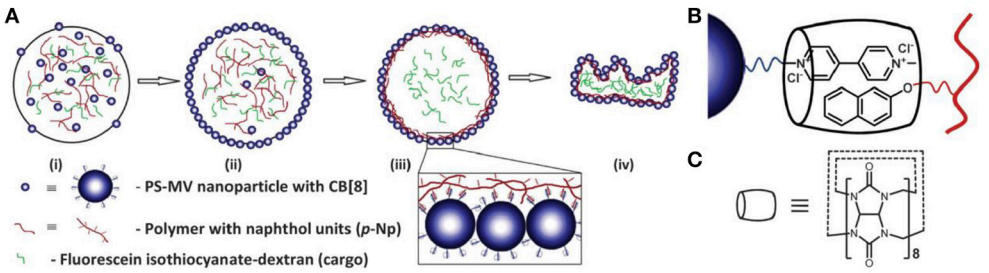


**FIGURE 6 |** Schematic representation of supramolecular colloidosomes through the interfacially host-guest crosslinking between cucurbi[8]uril (CB[8]), methyl viologen-functionalized polystyrene nanoparticles and naphthol-functionalized polyacrylamide (Stephenson et al., 2014). **(A)** Schematic of colloidosome formation. **(B)** Schematic of the ternary supramolecular complex formed between PS-MV, p-Np and CB[8]. **(C)** The molecular structure of CB[8]. Reprinted with permission from Stephenson et al. (2014). Copyright 2014 The Royal Society of Chemistry.

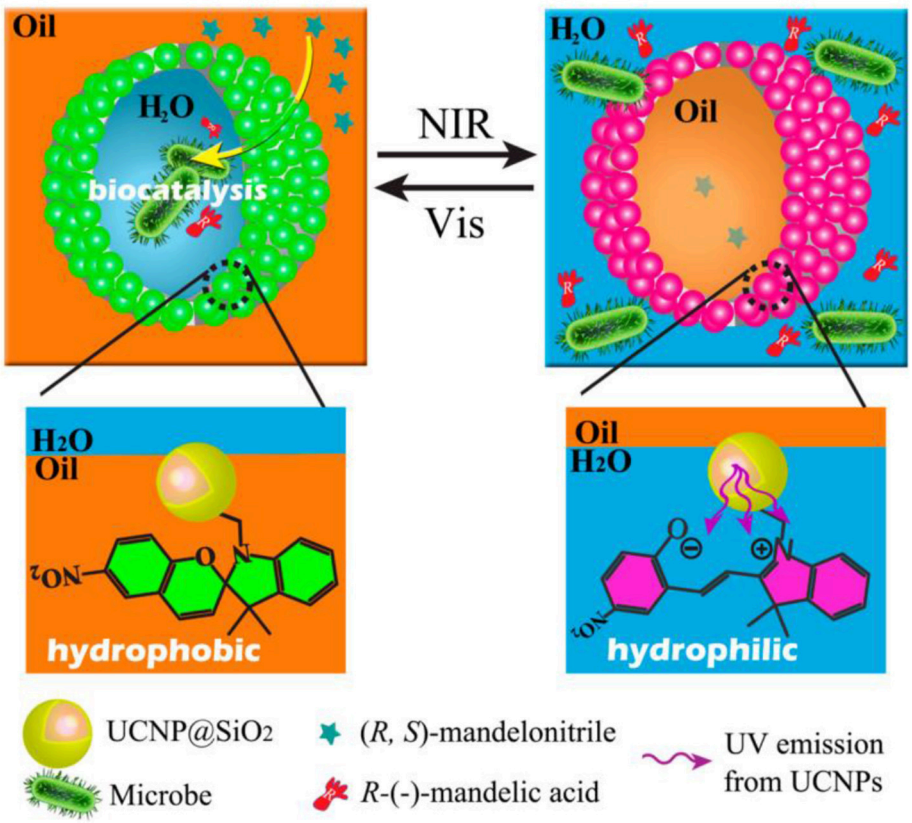


**FIGURE 7 |** Schematic representation of NIR/visible light controlled Pickering emulsions for biphasec enantioselective biocatalysis (Chen et al., 2014). Reprinted with permission from Chen et al. (2014). Copyright 2014 American Chemical Society.

methacrylate) (PDMAEMA) chains displaying pH- and thermo-responsive behaviors, were grafted from 20 nm silica particles with controlled chain length and grafting density by atom-transfer radical polymerization (ATRP). These functionalized silica particles can be used to form highly stable O/W emulsions at extremely low concentrations. Emulsions prepared according to this method were thermos-responsive, and rapidly demulsified upon increasing the temperature above the critical flocculation temperature (CFT) of the $SiO_2$-PDMAEMA particles. The lowest grafting density particles were observed to be more efficient and robust emulsifiers than high grafting density particles, which stemmed from the chain configurational freedom of the grafted polymer chain as shown in **Figure 8** (Saigal et al., 2010). For the lowest grafting density particles, these particles can emulsify both the xylene (a good solvent for PDMAEMA) and cyclohexane (a poor solvent for PDMAEMA) below and

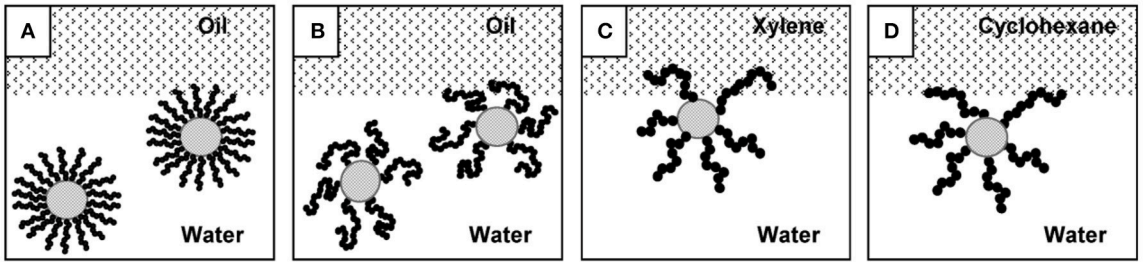


**FIGURE 8 |** Effect of grafting density and the solubility of the grafted polymer chain in oil and water phases on the location of the hybrid silica nanoparticles (Saigal et al., 2010). Particles with high grafting density **(A)** are restricted in their ability to reorganize and penetrate the interface compared to particles with a low grafting density **(B)**. Proposed configurations of a $SiO_2$-PDMAEMA particle at an oil/water interface, with chains able to penetrate xylene **(C)**, but not cyclohexane **(D)**. Reprinted with permission from Saigal et al. (2010). Copyright 2010 American Chemical Society.

above the CFT. However, for high grafting density particles, although the solvent quality of oil phase had no influence below CFT, it was an important factor above CFT. At 70°C, emulsions were formed with cyclohexane but not with xylene. Thermo-responsive Pickering emulsions were also prepared with cellulose nanocrystals (CNCs) grafted with poly(*N*-isopropylacrylamide) (PNIPAM) brushes (Zoppe et al., 2012). The emulsions were observed to be stable at a temperature below the LCST of PNIPAM. It was proposed that the partial collapse of PNIPAM brushes above LCST rendered the nanoparticle surfaces less hydrophilic and produced less stable emulsion.

Saigal and coworkers investigated the interactions between poly(2-(dimethylamino)ethyl methacrylate) (PDMAEMA)-grafted silica nanoparticles and three kinds of molecular surfactants, the anionic surfactant SDS, the non-ionic water-soluble surfactant Triton X-100 and the non-ionic oil-soluble surfactant Span 85, respectively (Saigal et al., 2015). Emulsification efficacy was improved with SDS at low concentrations range, where particle absorption is enhanced due to the complexation between PDMAEMA and SDS. At high SDS concentration, the SDS at interface repel the $SiO_2$-PDMAEMA-SDS complexes due to charge reversal. Synergism was also observed for Triton-100, while Span 85 had no observable effect on the emulsification efficacy.

Stable O/W emulsions can also be stabilized by silica nanoparticles grafted with highly charged polyelectrolyte (Saleh et al., 2005b). Fully sulfonated poly(styrenesulfonate) (PSS) were grafted from silica by ATRP. The emulsifying effectiveness of such modified particles was ascribed to the hydrophobic vinylic polymer backbone, which rendered this highly charged polyelectrolyte surface interfacially active. Similarly, cationic poly (2-(methacryloyloxy)ethyltrimethyl-ammonium chloride) (PMETAC) brushes were grafted from 320 nm silica nanoparticles by ATRP, which can be used to produce stable O/W Pickering emulsions (Tan et al., 2011). PMETAC brushes show ion-specific collapse behavior, which induce the switching of surface hydrophilicity. The resulting colloidal dispersion was responsive to perchlorate ions ($ClO^{4-}$), which triggered particle aggregation and then enabled the formation of emulsions. The formation of stable emulsions was not simply due to brush collapse but also due to shielding of electrostatic repulsion.

When two kinds of agents were grafted onto particle surface, the wettability can be easily controlled by the balance between hydrophilic and hydrophobic components on the surface. Liang and coworkers showed that silica particles with only $CO_2$-responsive groups are capable of stabilizing O/W emulsions, while particles grafted with both $CO_2$-responsive and hydrophobic chemical functional groups are capable of stabilizing W/O emulsions (Liang et al., 2014). Larson-Smith and coworkers modified gold nanoparticles with thiol-terminated polyethylene glycol (PEG) and alkane-thiol molecules (Larson-Smith and Pozzo, 2012). The resulting nanoparticles showed effective stabilization for emulsions because of strong adsorption at oil/water interfaces. Similarly, Sanna Björkegren has prepared colloidal silica particles modified with hydrophilic PEG silane and hydrophobic organosilanes containing propyl and methyl groups for Pickering emulsions (Björkegren et al., 2017). It was determined that particles containing hydrophobic groups produced emulsions with smaller droplets and higher stability. The emulsification performance was further improved by amphiphilic groups.

Besides balance between two kinds components, the wettability of colloidal particles can also be adjusted by functionalization of the grafted surface modifiers (Shi et al., 2015). Shi and coworkers have prepared amphiphilic nanoparticles with tunable properties by sulfonation of polystyrene-grafted silica nanoparticles. The sulfonic acid centers were designed to catalyze the biphasic etherification reaction of glycerol with dodecanol at the interfaces (Shi et al., 2015). By optimizing the wettability of the particles, multiple Pickering emulsions could be produced with enhanced diffusion of glycerol and dodecanol to the acid centers.

Recently, remarkable advances have been made in fabricating functionalized particles grafted with environmentally responsive polymer for Pickering emulsions (Zhao and Zhu, 2009). Those functionalized particles can form stable dispersion in both oil and aqueous phase with the reorganization of polymer chains based on surrounding solvent condition. Zhao and coworkers first reported the switching behavior

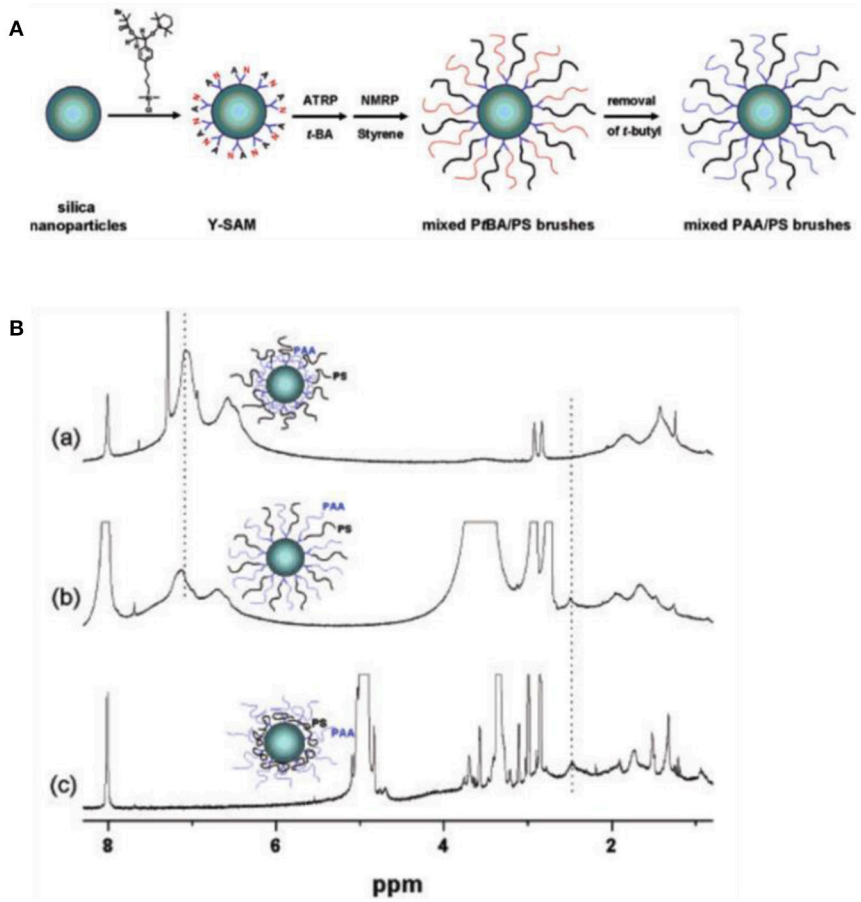


**FIGURE 9 |** Schematic illustration of mixed polymer brushes on silica nanoparticles **(A)** and environmentally responsive properties of hairy particles in different deuterated solvent demonstrated by $^{1}$H NMR (Li et al., 2005). **(B)** $^{1}$H NMR spectra of PAA/PA particles dispersed in (a) CDCl3, (b) DMF-d7, and (c) CD3OD. Reprinted with permission from Li et al. (2005). Copyright 2005 American Chemical Society.

of silica nanoparticles coated by mixed polymer brushes (Li et al., 2005). As shown in **Figure 9**, poly(*tert*-butyl acrylate) (P*t*BA) and polystyrene (PS) brushes were grafted from silica nanoparticles by ATRP and nitroxide-mediated radical polymerization (NMP), respectively. Subsequent hydrolysis of P*t*BA produced silica nanoparticles coated with amphiphilic poly(acrylic acid) (PAA) and PS mixed brushes. Environmentally responsive properties of the as-prepared hairy particles were demonstrated by $^{1}$H NMR in different deuterated solvent (Li et al., 2005). Later on, Minko and coworkers reported the application of mixed polymer brushes to tune the wettability of nanoparticles for Pickering emulsions (Motornov et al., 2007). Particles grafted with amphiphilic mixed polymer brush were prepared by quaternization reaction between bromo groups on the surface of silica particles and pyridine groups in the middle block of polystyrene-*b*-poly(2-vinylpyridine)-*b*-poly(ethylene oxide) (PS-*b*-P2VP-*b*-PEO). The wettability of functionalized particles can be precisely tuned by solvent and pH. The emulsion type is closely related to the balance between hydrophobic PS and hydrophilic P2VP and PEO in the particle surface. At pH <4, the fraction of hydrophilic components is fairly high and O/W emulsions were formed. While at pH >4, the deprotonated P2VP collapsed and contributed to the hydrophobic behavior, consequently W/O emulsions were formed. Following this central linking approach, nanoparticles grafted with poly(methyl methacrylate)-*b*-poly(glycidyl methacrylate)-*b*-polystyrene or poly(methyl methacrylate)-*b*-poly(glycidyl methacrylate)-*b*-poly(*tert*-butyl methacrylate) showed similar swithcing properties for Pickering emulsions (Cheng et al., 2008; Wang et al., 2011). The emulsion types can be tuned between O/W and W/O by altering the relative chain length of hydrophobic and hydrophilic blocks (Wang et al., 2011).

It has been reported that amphiphilic poly(ethylene glycol)-*b*-polystyrene (PEG-*b*-PS) block copolymer can stabilize multiple emulsions via one-step phase inversion process (Hong et al., 2012). The multiple emulsions stabilized by block copolymer are highly stable and impart the ability to encapsulate both polar and non-polar cargos. The ratio of the block length, namely asymmetric ratio, greatly affects the catastrophic phase

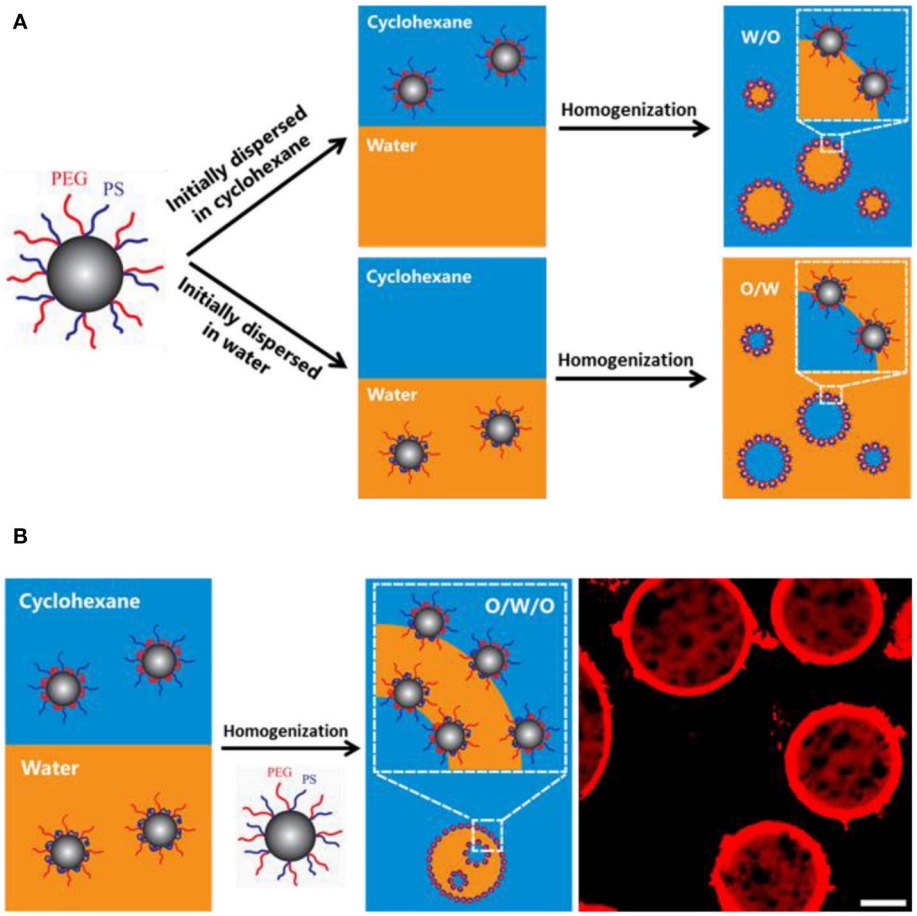


**FIGURE 10 |** Schematic representation of the initial location of silica nanoparticles on the emulsion type **(A)** and emulsification of multiple emulsions **(B)** (Liu et al., 2016). Reprinted with permission from Liu et al. (2016). Copyright 2016 American Chemical Society.

inversion as well as the emulsion type and stability (Sun et al., 2014). Recently, PEG and PS blocks have been alternately grafted onto silica nanoparticles via the sol-gel reaction between silane coupling groups of ABC miktoarm star terpolymers consisting of PEG, PS and poly[(3-triisopropyloxysilyl)propyl methacrylate] ($\mu$-PEG-*b*-PS-*b*-PIPSMA) and silanol groups on silica surface (Liu et al., 2016). It was found that the wettability of the resulting nanoparticles can be finely tuned by the solvent environment and host-guest chemistry. The $^1$H NMR results confirmed that the wettability change is attributed to the reorganization polymer chains in different deuterated solvents. The initial location effect was shown in **Figure 10**. When the functionalized particles were first dispersed in oil, W/O emulsion was prepared. Also O/W emulsion was prepared when the functionalized particles were first dispersed in water. These results imply the initial location of the particles is the determining factor for the emulsion type. Inspired by the effect of initial location, multiple emulsions were fabricated with one half of the hairy particles in water, another half in oil. The hairy particle's wettability can also be tuned by supramolecular chemistry. The hydroxyl group of $\alpha$-CD will increase the hydrophilicity of the hairy particle.

## TAILORING THE WETTABILITY BY SURFACE ROUGHNESS

In addition to the surface chemistry, the surface topology such as roughness can also affect the wetting behavior of colloidal particles and consequently affect the adsorption of particles at oil/water interfaces (San-Miguel and Behrens, 2012; Zanini et al., 2017). The roughness of surface enlarges the surface area of the colloidal particles and consequently increases the adsorption energy of particles at oil/water interface, which is shown as follows:

$$\Delta F = -\pi r^2 \gamma_{O/W}(1 - \alpha|cos\theta|)^2 \quad (2)$$

where $\alpha$ is the surface area magnification factor, $\theta$ is the contact angle for the smooth particles with the same surface chemistry (Nonomura et al., 2006).

San-Miguel and coworkers first reported the connection between particle roughness and the stability of related Pickering emulsions (San-Miguel and Behrens, 2012). Rough particles were fabricated by electrostatically adsorbing of negatively charged 50 nm poly(methacrylic acid-*co*-methyl methacrylate)

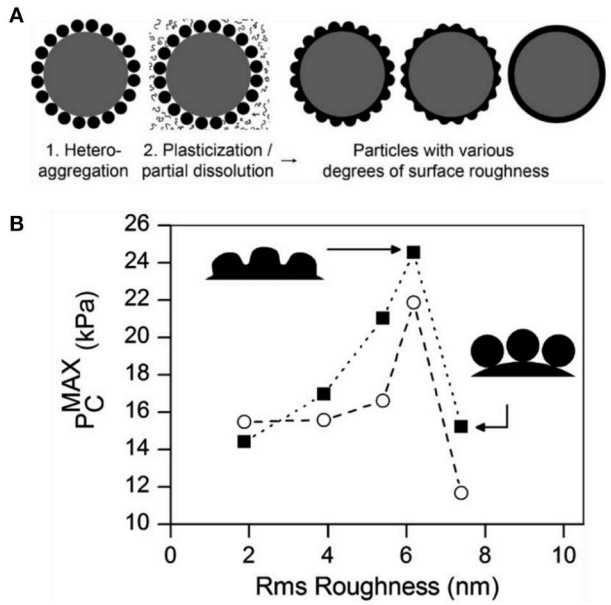


**FIGURE 11 |** Schematic illustration of fabrication of particles with different surface roughness **(A)** and maximum capillary pressure for decane-in-water emulsions stabilized by particles with different surface roughness **(B)** (San-Miguel and Behrens, 2012). Reprinted with permission from San-Miguel and Behrens (2012). Copyright 2012 American Chemical Society.

nanoparticles onto amine modified silica particles as shown in **Figure 11**. The surface roughness was finely tuned by fusing the polymer nanoparticles through exposure to aqueous solutions of acetone or ethanol with different concentrations. The emulsion stability stabilized by the as-prepared rough particles was quantitatively measured by maximum capillary pressure ($P_C^{MAX}$), which was determined by centrifugation. It was found that the emulsion stability was greatly increased with the surface roughness in the Wenzel regime (with roughness below 6 nm). As the roughness increased further, the wetting regime of particles inverted to Cassie-Baxter wetting and consequently the benefit of surface roughness for emulsion stability was lost.

Zanini and coworkers employed the similar protocol to fabricate rough particles through electrostatic-driven absorption of negatively charged silica nanoparticles onto positively charged silica microparticles (Zanini et al., 2017). By contrast, the surface roughness was tuned by growing silica layer on the surface of raspberry-like particles using a modified Stöber process. It was found that surface roughness provides plenty of pinning points for the three-phase contact line and the pinning induces contact angle hysteresis. Consequently, the inversion of particle wettability happens for sufficient roughness. In other words, the particles with specific roughness can stabilize both W/O and O/W emulsions and the emulsion type only depend on the initial location of the particles.

## CONCLUSIONS AND PROSPECT

The review describes the up-to-date examples of tailoring wettability of particulate emulsifiers for Pickering emulsions. There are many reports tuning the wettability by changing the surface chemistry with small molecules or polymers via either physical adsorption or chemical anchoring. The *in situ* modification with amphiphiles render particles tunable wettability depending on the interaction between particles and amphiphiles. Especially, there has been an increasing interest in switchable Pickering emulsions, which are triggered by wettability change depending on environmental stimuli. Recently, the surface roughness was found to be another main factor affecting the wettability of particles. In addition to tune the surface chemistry, precisely control of the surface roughness also adjust the wetting behavior of particles at oil/water interface and consequently affect emulsion characteristics of the resultant Pickering emulsions. We foresee that complexed Pickering emulsions including multiple emulsions, water-in-water (W/W) emulsions, and oil-in-oil (O/O) emulsions can be produced with finely tailoring both the surface chemistry and surface roughness. With the incorporation of functional and responsive building blocks to particulate emulsifiers, the as-prepared Pickering emulsions may find emerging applications in biphasic catalysis, oil recovery and biomedical applications (Pera-Titus et al., 2015; Tang et al., 2015; Wu and Ma, 2016; Binks, 2017).

## AUTHOR CONTRIBUTIONS

LH and MX searched the literatures for the article and produced the first draft. All the authors discussed the content and contributed to review and edit the manuscript.

## ACKNOWLEDGMENTS

We gratefully acknowledge financial support from the National Natural Science Foundation of China (21374031, 21774035).

## REFERENCES

Ashby, N. P., and Binks, B. P. (2000). Pickering emulsions stabilised by Laponite clay particles. *Phys. Chem. Chem. Phys.* 2, 5640–5646. doi: 10.1039/b007098j

Aveyard, R., Binks, B. P., and Clint, J. H. (2003). Emulsions stabilised solely by colloidal particles. *Adv. Colloid Interface Sci.* 100, 503–546. doi: 10.1016/S0001-8686(02)00069-6

Binks, B. P. (2002). Particles as surfactants - similarities and differences. *Curr. Opin. Colloid Interface Sci.* 7, 21–41. doi: 10.1016/S1359-0294(02)00008-0

Binks, B. P. (2017). Colloidal particles at a range of fluid–fluid interfaces. *Langmuir* 33, 6947–6963. doi: 10.1021/acs.langmuir.7b00860

Binks, B. P., and Lumsdon, S. O. (2001). Pickering emulsions stabilized by monodisperse latex particles: effects of particle size. *Langmuir* 17, 4540–4547. doi: 10.1021/la0103822

Binks, B. P., Murakami, R., Armes, S. P., and Fujii, S. (2005). Temperature-induced inversion of nanoparticle-stabilized emulsions. *Angew. Chem. Int. Ed.* 44, 4795–4798. doi: 10.1002/anie.200501073

Binks, B. P., and Olusanya, S. O. (2017). Pickering emulsions stabilized by coloured organic pigment particles. *Chem. Sci.* 8, 708–723. doi: 10.1039/C6SC03085H

Binks, B. P., and Whitby, C. P. (2004). Silica particle-stabilized emulsions of silicone oil and water: aspects of emulsification. *Langmuir* 20, 1130–1137. doi: 10.1021/la0303557

Binks, B. P., and Yin, D. (2016). Pickering emulsions stabilized by hydrophilic nanoparticles: in situ surface modification by oil. *Soft Matter* 12, 6858–6867. doi: 10.1039/C6SM01214K

Björkegren, S., Nordstierna, L., Törncrona, A., and Palmqvist, A. (2017). Hydrophilic and hydrophobic modifications of colloidal silica particles for Pickering emulsions. *J. Colloid Interface Sci.* 487, 250–257. doi: 10.1016/j.jcis.2016.10.031

Chen, Z., Zhou, L., Bing, W., Zhang, Z., Li, Z., Ren, J., et al. (2014). Light controlled reversible inversion of nanophosphor-stabilized pickering emulsions for biphasic enantioselective biocatalysis. *J. Am. Chem. Soc.* 136, 7498–7504. doi: 10.1021/ja503123m

Cheng, J., He, J., Li, C., and Yang, Y. (2008). Facile approach to functionalize nanodiamond particles with V-shaped polymer brushes. *Chem. Mater.* 20, 4224–4230. doi: 10.1021/cm800357g

Cui, M., Emrick, T., and Russell, T. P. (2013). Stabilizing liquid drops in nonequilibrium shapes by the interfacial jamming of nanoparticles. *Science* 342, 460–463. doi: 10.1126/science.1242852

Cui, Z. G., Cui, C. F., Zhu, Y., and Binks, B. P. (2012). Multiple phase inversion of emulsions stabilized by *in situ* surface activation of $CaCO_3$ nanoparticles via adsorption of fatty acids. *Langmuir* 28, 314–320. doi: 10.1021/la204021v

Cui, Z. G., Yang, L. L., Cui, Y. Z., and Binks, B. P. (2010). Effects of surfactant structure on the phase inversion of emulsions stabilized by mixtures of silica nanoparticles and cationic surfactant. *Langmuir* 26, 4717–4724. doi: 10.1021/la903589e

Dickinson, E. (2010). Food emulsions and foams: stabilization by particles. *Curr. Opin. Colloid Interface Sci.* 15, 40–49. doi: 10.1016/j.cocis.2009.11.001

Frith, W. J., Pichot, R., Kirkland, M., and Wolf, B. (2008). Formation, stability, and rheology of particle stabilized emulsions: influence of multivalent cations. *Ind. Eng. Chem. Res.* 47, 6434–6444. doi: 10.1021/ie071629e

Fuchs, I., and Avnir, D. (2013). Induction of amphiphilicity in polymer@silica particles: ceramic surfactants. *Langmuir* 29, 2835–2842. doi: 10.1021/la3048246

Fujii, S., Okada, M., and Furuzono, T. (2007). Hydroxyapatite nanoparticles as stimulus-responsive particulate emulsifiers and building block for porous materials. *J. Colloid Interface Sci.* 315, 287–296. doi: 10.1016/j.jcis.2007.06.071

Fujii, S., Okada, M., Sawa, H., Furuzono, T., and Nakamura, Y. (2009). Hydroxyapatite nanoparticles as particulate emulsifier: fabrication of hydroxyapatite-coated biodegradable microspheres. *Langmuir* 25, 9759–9766. doi: 10.1021/la901100z

Haase, M. F., Grigoriev, D., Moehwald, H., Tiersch, B., and Shchukin, D. G. (2010). Encapsulation of amphoteric substances in a pH-sensitive Pickering emulsion. *J. Phys. Chem. C* 114, 17304–17310. doi: 10.1021/jp104052s

Herzig, E. M., White, K. A., Schofield, A. B., Poon, W. C. K., and Clegg, P. S. (2007). Bicontinuous emulsions stabilized solely by colloidal particles. *Nat. Mater.* 6, 966–971. doi: 10.1038/nmat2055

Hong, L., Sun, G., Cai, J., and Ngai, T. (2012). One-step formation of W/O/W multiple emulsions stabilized by single amphiphilic block copolymers. *Langmuir* 28, 2332–2336. doi: 10.1021/la205108w

Huang, C., Forth, J., Wang, W., Hong, K., Smith, G. S., Helms, B. A., et al. (2017). Bicontinuous structured liquids with sub-micrometre domains using nanoparticle surfactants. *Nat. Nanotechnol.* 12, 1060–1064. doi: 10.1038/nnano.2017.182

Isa, L., Amstad, E., Schwenke, K., Del Dado, E., IIg, P., Kroger, M., et al. (2011). Adsorption of core-shell nanoparticles at liquid-liquid interfaces. *Soft Matter* 7, 7663–7675. doi: 10.1039/c1sm05407d

Jiang, J., Zhu, Y., Cui, Z., and Binks, B. P. (2013). Switchable Pickering emulsions stabilized by silica nanoparticles hydrophobized *in situ* with a switchable surfactant. *Angew. Chem. Int. Ed.* 52, 12373–12376. doi: 10.1002/anie.201305947

Larson-Smith, K., and Pozzo, D. C. (2012). Pickering emulsions stabilized by nanoparticle surfactants. *Langmuir* 28, 11734–11741. doi: 10.1021/la301896c

Li, D. J., Sheng, X., and Zhao, B. (2005). Environmentally responsive "Hairy" nanoparticles: mixed homopolymer brushes on silica nanoparticles synthesized by living radical polymerization techniques. *J. Am. Chem. Soc.* 127, 6248–6256. doi: 10.1021/ja0422561

Li, W., Yu, L., Liu, G., Tan, J., Liu, S., and Sun, D. (2012). Oil-in-water emulsions stabilized by Laponite particles modified with short-chain aliphatic amines. *Colloids Surf. A* 400, 44–51. doi: 10.1016/j.colsurfa.2012.02.044

Li, W., Zhao, C., Tan, J., Jiang, J., Xu, J., and Sun, D. (2013). Roles of methyl orange in preparation of emulsions stabilized by layered double hydroxide particles. *Colloids Surf. A* 421, 173–180. doi: 10.1016/j.colsurfa.2012.12.058

Li, Z., and Ngai, T. (2013). Microgel particles at the fluid-fluid interfaces. *Nanoscale* 5, 1399–1410. doi: 10.1039/c2nr33503d

Liang, C., Liu, Q., and Xu, Z. (2014). Surfactant-free switchable emulsions using $CO_2$-responsive particles. *ACS Appl. Mater. Interfaces* 6, 6898–6904. doi: 10.1021/am5007113

Liu, M., Chen, X., Yang, Z., Xu, Z., Hong, L., and Ngai, T. (2016). Tunable Pickering emulsions with environmentally responsive hairy silica nanoparticles. *ACS Appl. Mater. Interfaces* 8, 32250–32258. doi: 10.1021/acsami.6b11931

Liu, X., Shi, S., Li, Y., Forth, J., Wang, D., and Russell, T. P. (2017). Liquid tubule formation and stabilization using cellulose nanocrystal surfactants. *Angew. Chem. Int. Ed.* 59, 12594–12598. doi: 10.1002/anie.201706839

Marquis, M., Alix, V., Capron, I., Cuenot, S., and Zykwinska, A. (2016). Microfluidic encapsulation of Pickering oil microdroplets into alginate microgels for lipophilic compound delivery. *ACS Biomater. Sci. Eng.* 2, 535–543. doi: 10.1021/acsbiomaterials.5b00522

Marto, J., Ascenso, A., Simoes, S., Almeida, A. J., and Ribeiro, H. M. (2016). Pickering emulsions: challenges and opportunities in topical delivery. *Expert Opin. Drug Del.* 13, 1093–1107. doi: 10.1080/17425247.2016.1182489

Mathapa, B. G., and Paunov, V. N. (2013). Cyclodextrin stabilised emulsions and cyclodextrinosomes. *Phys. Chem. Chem. Phys.* 15, 17903–17914. doi: 10.1039/c3cp52116h

Motornov, M., Sheparovych, R., Lupitskyy, R., MacWilliams, E., Hoy, O., Luzinov, I., et al. (2007). Stimuli-responsive colloidal systems from mixed brush-coated nanoparticles. *Adv. Funct. Mater.* 17, 2307–2314. doi: 10.1002/adfm.200600934

Nonomura, Y., Komura, S., and Tsujii, K. (2006). Adsorption of microstructured particles at liquid-liquid interfaces. *J. Phys. Chem. B* 110, 13124–13129. doi: 10.1021/jp0617017

Okada, M., Maeda, H., Fujii, S., Nakamura, Y., and Furuzono, T. (2012). Formation of pickering emulsions stabilized via interaction between nanoparticles dispersed in aqueous phase and polymer end groups dissolved in oil phase. *Langmuir* 28, 9405–9412. doi: 10.1021/la3015964

Pera-Titus, M., Leclercq, L., Clacens, J.-M., De Campo, F., and Nardello-Rataj, V. (2015). Pickering interfacial catalysis for biphasic systems: from emulsion design to green reactions. *Angew. Chem. Int. Ed.* 54, 2006–2021. doi: 10.1002/anie.201402069

Rayner, M., Marku, D., Eriksson, M., Sjoo, M., Dejmek, P., and Wahlgren, M. (2014). Biomass-based particles for the formulation of Pickering type emulsions in food and topical applications. *Colloids Surf. A* 458, 48–62. doi: 10.1016/j.colsurfa.2014.03.053

Reger, M., Sekine, T., and Hoffmann, H. (2012). Pickering emulsions stabilized by amphiphile covered clays. *Colloids Surf. A* 413, 25–32. doi: 10.1016/j.colsurfa.2011.12.005

Sadeghpour, A., Pirolt, F., and Glatter, O. (2013). Submicrometer-sized Pickering emulsions stabilized by silica nanoparticles with adsorbed oleic acid. *Langmuir* 29:6004. doi: 10.1021/la4008685

Saigal, T., Dong, H. C., Matyjaszewski, K., and Tilton, R. D. (2010). Pickering emulsions stabilized by nanoparticles with thermally responsive grafted polymer brushes. *Langmuir* 26, 15200–15209. doi: 10.1021/la1027898

Saigal, T., Xu, J., Matyjaszewski, K., and Tilton, R. D. (2015). Emulsification synergism in mixtures of polyelectrolyte brush-grafted nanoparticles and surfactants. *J. Colloid Interface Sci.* 449, 152–159. doi: 10.1016/j.jcis.2014.12.047

Saleh, N., Phenrat, T., Sirk, K., Dufour, B., Ok, J., Sarbu, T., et al. (2005a). Adsorbed triblock copolymers deliver reactive iron nanoparticles to the oil/water interface. *Nano Lett.* 5, 2489–2494. doi: 10.1021/nl0518268

Saleh, N., Sarbu, T., Sirk, K., Lowry, G. V., Matyjaszewski, K., and Tilton, R. D. (2005b). Oil-in-water emulsions stabilized by highly charged polyelectrolyte-grafted silica nanoparticles. *Langmuir* 21, 9873–9878. doi: 10.1021/la050654r

San-Miguel, A., and Behrens, S. H. (2012). Influence of nanoscale particle roughness on the stability of Pickering emulsions. *Langmuir* 28, 12038–12043. doi: 10.1021/la302224v

Santini, E., Guzmán, E., Ferrari, M., and Liggieri, L. (2014). Emulsions stabilized by the interaction of silica nanoparticles and palmitic acid at the water–hexane interface. *Colloids Surf. A* 460, 333–341. doi: 10.1016/j.colsurfa.2014.02.054

Shi, H., Fan, Z., Ponsinet, V., Sellier, R., Liu, H., Pera-Titus, M., et al. (2015). Glycerol/dodecanol double pickering emulsions stabilized by polystyrene-grafted silica nanoparticles for interfacial catalysis. *ChemCatChem* 7, 3189–3189. doi: 10.1002/cctc.201501070

Silverstein, M. S. (2014). PolyHIPEs: recent advances in emulsion-templated porous polymers. *Prog. Polym. Sci.* 39, 199–234. doi: 10.1016/j.progpolymsci.2013.07.003

Stephenson, G., Parker, R. M., Lan, Y., Yu, Z., Scherman, O. A., and Abell, C. (2014). Supramolecular colloidosomes: fabrication, characterisation and triggered release of cargo. *Chem. Commun.* 50, 7048–7051. doi: 10.1039/C4CC01479K

Stratford, K., Adhikari, R., Pagonabarraga, I., Desplat, J. C., and Cates, M. E. (2005). Colloidal jamming at interfaces: a route to fluid-bicontinuous gels. *Science* 309, 2198–2201. doi: 10.1126/science.1116589

Sturzenegger, P. N., Gonzenbach, U. T., Koltzenburg, S., and Gauckler, L. J. (2012). Controlling the formation of particle-stabilized water-in-oil emulsions. *Soft Matter* 8, 7471–7479. doi: 10.1039/c2sm25176k

Sun, G., Liu, M., Zhou, X., Hong, L., and Ngai, T. (2014). Influence of asymmetric ratio of amphiphilic diblock copolymers on one-step formation and stability of multiple emulsions. *Colloids Surf. A* 454, 16–22. doi: 10.1016/j.colsurfa.2014.04.015

Tan, H., Zhao, L. F., Tian, S. S., Wen, H., Gou, X. J., and Ngai, T. (2017). Gelatin particle-stabilized high-internal phase emulsions for use in oral delivery systems: protection effect and *in vitro* digestion study. *J. Agric. Food Chem.* 65, 900–907. doi: 10.1021/acs.jafc.6b04705

Tan, K. Y., Gautrot, J. E., and Huck, W. T. S. (2011). Formation of Pickering emulsions using ion-specific responsive colloids. *Langmuir* 27, 1251–1259. doi: 10.1021/la102904r

Tang, J. T., Quinlan, P. J., and Tam, K. C. (2015). Stimuli-responsive Pickering emulsions: recent advances and potential applications. *Soft Matter* 11, 3512–3529. doi: 10.1039/C5SM00247H

Wang, Y., Fan, D., He, J., and Yang, Y. (2011). Silica nanoparticle covered with mixed polymer brushes as Janus particles at water/oil interface. *Colloid Polym. Sci.* 289, 1885–1894. doi: 10.1007/s00396-011-2506-9

Wang, Z., and Wang, Y. (2016). Tuning amphiphilicity of particles for controllable Pickering emulsion. *Materials* 9:903. doi: 10.3390/ma9110903

Williams, M., Armes, S. P., Verstraete, P., and Smets, J. (2014a). Double emulsions and colloidosomes-in-colloidosomes using silica-based pickering emulsifiers. *Langmuir* 30, 2703–2711. doi: 10.1021/la500219m

Williams, M., Warren, N. J., Fielding, L. A., Armes, S. P., Verstraete, P., and Smets, J. (2014b). Preparation of double emulsions using hybrid polymer/silica particles: new pickering emulsifiers with adjustable surface wettability. *ACS Appl. Mater. Interfaces* 6, 20919–20927. doi: 10.1021/am505581r

Wu, J., and Ma, G. H. (2016). Recent studies of Pickering emulsions: particles make the difference. *Small* 12, 4633–4648. doi: 10.1002/smll.201600877

Yang, H., Zhou, T., and Zhang, W. (2013). A strategy for separating and recycling solid catalysts based on the pH-triggered pickering-emulsion inversion. *Angew. Chem. Int. Ed.* 125, 7603–7607. doi: 10.1002/ange.201300534

Yuan, Q., and Williams, R. A. (2016). CO-stabilisation mechanisms of nanoparticles and surfactants in Pickering Emulsions produced by membrane emulsification. *J. Membr. Sci.* 497, 221–228. doi: 10.1016/j.memsci.2015.09.028

Zanini, M., Marschelke, C., Anachkov, S. E., Marini, E., Synytska, A., and Isa, L. (2017). Universal emulsion stabilization from the arrested adsorption of rough particles at liquid-liquid interfaces. *Nat. Commun.* 8:15701. doi: 10.1038/ncomms15701

Zhao, B., and Zhu, L. (2009). Mixed polymer brush-grafted particles: a new class of environmentally responsive nanostructured materials. *Macromolecules* 42, 9369–9383. doi: 10.1021/ma902042x

Zhou, J., Wang, L., Qiao, X., Binks, B. P., and Sun, K. (2012). Pickering emulsions stabilized by surface-modified $Fe_3O_4$ nanoparticles. *J. Colloid Interface Sci.* 367, 213–224. doi: 10.1016/j.jcis.2011.11.001

Zhou, S. B., Fan, J., Datta, S. S., Guo, M., Guo, X., and Weitz, D. A. (2013). Thermally switched release from nanoparticle colloidosomes. *Adv. Funct. Mater.* 23, 5925–5929. doi: 10.1002/adfm.201301030

Zhu, Y., Jiang, J., Liu, K., Cui, Z., and Binks, B. P. (2015). Switchable Pickering emulsions stabilized by silica nanoparticles hydrophobized *in situ* with a conventional cationic surfactant. *Langmuir* 31, 3301–3307. doi: 10.1021/acs.langmuir.5b00295

Zoppe, J. O., Venditti, R. A., and Rojas, O. J. (2012). Pickering emulsions stabilized by cellulose nanocrystals grafted with thermo-responsive polymer brushes. *J. Colloid Interface Sci.* 369, 202–209. doi: 10.1016/j.jcis.2011.12.011

**Conflict of Interest Statement:** The authors declare that the research was conducted in the absence of any commercial or financial relationships that could be construed as a potential conflict of interest.

frontiers in Chemistry

ORIGINAL RESEARCH
published: 19 September 2018
doi: 10.3389/fchem.2018.00409

# Pickering Emulsions Electrostatically Stabilized by Cellulose Nanocrystals

*Swambabu Varanasi[1,2], Leeav Henzel[1], Llyza Mendoza[1], Ragesh Prathapan[3], Warren Batchelor[1], Rico Tabor[3] and Gil Garnier[1]**

[1] Department of Chemical Engineering, Bioresource Processing Research Institute of Australia, Monash University, Clayton, VIC, Australia, [2] Department of Chemical Engineering, Indian Institute of Petroleum and Energy, Visakhapatnam, India, [3] School of Chemistry, Monash University, Melbourne, VIC, Australia

Cellulose Nanocrystals (CNC) are explored to stabilize oil/water emulsions for their ability to adsorb at the oil/water interface. In this work, the role of electrostatic forces in the CNC ability to stabilize oil/water emulsions is explored using canola oil/water and hexadecane/water as model systems. Canola oil/water and Hexadecane/ water (20/80, v/v) emulsions were stabilized with the addition of CNCs using ultrasonication. Emulsion droplet sizes range from 1 to 4 μm as measured by optical microscopy. It is found that CNC can stabilize oil/water emulsions regardless of their charge density. However, reducing the surface charge density, by adding salts and varying pH, can reduce the amount of CNC's required to form a stable emulsion. Just by adding 3 mM $Na^{+}$ or 1 mM or less $Ca^{+2}$ to a CNC suspension, the amount of CNC reduced by 30% to stabilized 2 mL of Canola oil. On the other hand, adding salt increases the emulsion volume. The addition of 100 mM $Na^{+}$ or the reduction of pH below 2 leads to the aggregation of CNC; emulsions formed under these conditions showed gel-like behavior. This work shows the potential of nanocellulose crystal in stabilizing food and industrial emulsions. This is of interest for applications where biodegradability, biocompatibility, and food grade requirements are needed.

**Keywords: cellulose nanocrystals (CNC), Pickering emulsions, oil in water, gels, electrostatic stabilization**

OPEN ACCESS

***Edited by:***
*Erica Wanless, University of Newcastle, Australia*

***Reviewed by:***
*Catherine Whitby, Massey University, New Zealand*
*Patrick Spicer, University of New South Wales, Australia*

***Correspondence:**
*Gil Garnier*
*gil.garnier@monash.edu*

***Specialty section:***
*This article was submitted to Chemical Engineering, a section of the journal Frontiers in Chemistry*

***Received:*** *15 May 2018*
***Accepted:*** *20 August 2018*
***Published:*** *19 September 2018*

***Citation:***
*Varanasi S, Henzel L, Mendoza L, Prathapan R, Batchelor W, Tabor R and Garnier G (2018) Pickering Emulsions Electrostatically Stabilized by Cellulose Nanocrystals. Front. Chem. 6:409. doi: 10.3389/fchem.2018.00409*

## INTRODUCTION

Cellulose is the most abundant natural polymer. It consists of anhydroglucose units linearly linked through β-1,4-glycosidic bonds. Cellulose nanocrystals (CNC) and cellulose nanofibers (CNF) are two types of exciting green nanomaterials prepared from cellulosic sources (Safari et al., 2014). Nanocellulose has recently been investigated for a multitude of applications because of their renewable nature and unique properties such as wettability, large surface area, high aspect ratio, biocompatibility, being optically transparent, and amphiphilic nature, their strength and ease of chemical modification (Hosseinidoust et al., 2015; Trache et al., 2017). CNC particles are processed from native cellulose sources by controlled acid hydrolysis (Moon et al., 2011). Sulfuric acid hydrolysis dissolves the amorphous fraction, releasing the cellulose nanocrystals (CNC) with sulfate ester groups surface, resulting in electrostatically stabilized aqueous suspensions of CNC (Dong and Gray, 1997). In a dilute aqueous system, CNC particles are well dispersed and orient randomly due to electrostatic repulsion among negatively charged sulfate ester groups (Dong and Gray, 1997). The surface charge of CNC is primarily controlled by the hydrolysis conditions. Higher acid concentration, reaction time and temperature produces CNC of higher surface charge as promoted

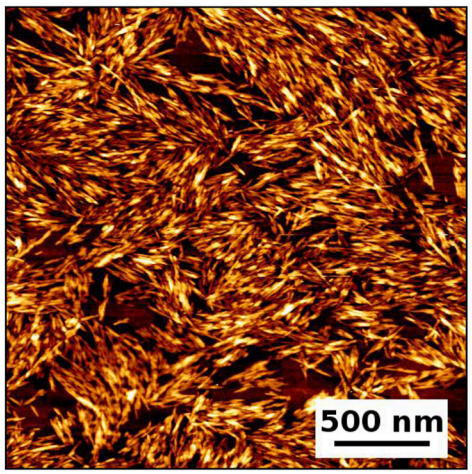


**FIGURE 1 |** AFM Image of CNC deposited on a glass surface and dried.

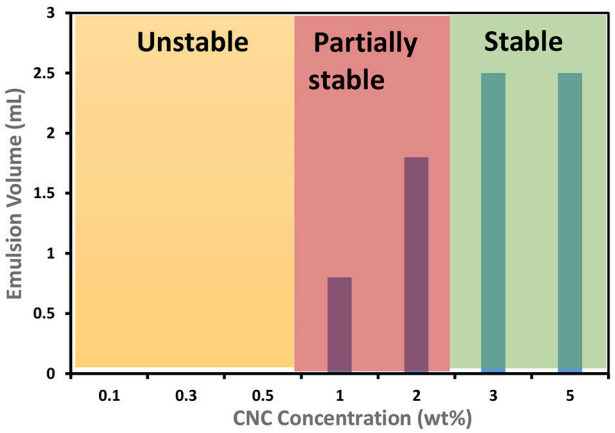


**FIGURE 2 |** Effect of CNC concentration on stability of emulsions prepared with canola oil and hexadecane (oil to water ratio is 2:8 mL) at room temperature, pH = 7.

by sulphuric acid diffusion into fibers (Nishio et al., 2016). Zeta-potential of CNC produced by sulphuric acid hydrolysis varies from −20 to −80 mV. In contrast, if hydrochloric acid is used to produce CNC, the resulting CNC has almost no charge (Nishio et al., 2016).

Many types of nano or microscale particles are used to stabilize the oil/water interface of emulsions, commonly known as Pickering emulsions (Wu and Ma, 2016). Pickering emulsions possess many unique features over classical surfactant stabilized emulsions, such as low toxicity and superior stability (Yang et al., 2017). Particle size, shape, wettability, surface properties, and particle concentration all influence the stability and drop size of emulsions (Wu and Ma, 2016). A key factor to form Pickering emulsions is wettability, which can be indicated by the contact angle at the interface. Binks et al. reported that particles of very low hydrophilicity or very high hydrophobicity are not suitable to form stable emulsions (Binks and Lumsdon, 2000). Particles having an intermediate contact angle (close to 90°) can easily accumulate at the oil/water interface and form stable emulsions (Binks and Lumsdon, 2000). The optimum contact angle to prepare stable oil/water emulsion is around 70° and water/oil emulsion is 110° (Kaptay, 2006). Particles having smaller size will have faster adsorption kinetics and more efficient packing at the oil/water interface than bigger particles (Wu and Ma, 2016). Particle size should be at least one order of magnitude smaller than droplet size to prepare stable emulsion (Wang, 2013). Cylindrical or elliptical shaped particles showed superior stability than spherical shape particles since cylindrical particles pack like network structure and also their ability to shape capillary force between absorbed particles at the interface is superior (Dugyala et al., 2013; Wang, 2013). In order to keep large surface area particles stable in suspension, there must be a steric hindrance or electrostatic repulsion between the particles. However, this force between particles acts as an activation barrier for particle adsorption. At present, there is very little information in the literature to describe the governing laws between surface charge and particle adsorption of CNC (Wu and Ma, 2016).

In this study, CNCs were investigated to prepare very strong and stable Pickering emulsions because of their high aspect ratio. Cellulose Nanofibers (CNF) are also being used in Pickering emulsions (Kalashnikova et al., 2011; Capron and Cathala, 2013; Carrillo et al., 2015; Wang et al., 2016; Capron et al., 2017). Although both CNCs and CNFs are not surface active, they position efficiently at the oil/water or water/oil interface because of their amphiphilic nature (Capron et al., 2017). A presence of hydrophobic edge plane is attributed to its amphiphilic nature. Kalashnikova et al. first reported preparing Pickering emulsions with bacterial CNC (Kalashnikova et al., 2011). Later they described that when sulphated cotton cellulose nanocrystals (CNC) were used, no emulsion was observed (Kalashnikova et al., 2012). To prepare Pickering emulsions with sulphated CNC, the surface charge density has to be modulated to 0.033 e/nm$^2$ or lower. The charge density of CNC can be modulated by treating sulphated CNC with mild HCl or adding salts. However, thermodynamically amphiphilic particles can form stable emulsions regardless of their charge density. Many reports concluded that the surface charge of CNCs and CNFs play a key role in the stability of emulsions (Marinova et al., 1996; Kalashnikova et al., 2011, 2012; Fujisawa et al., 2017; Miao et al., 2017). However, there is no systematic study on the role of electrostatics in CNC based emulsions.

CNCs are also being used for preparing high internal phase emulsions (HIPE) (Marinova et al., 1996; Fujisawa et al., 2017; Miao et al., 2017). Capron and Cathala reported a two-step procedure to prepare HIPEs with CNCs (Fujisawa et al., 2017). First, a low internal phase emulsion having 10% oil content was prepared using an ultrasonicator. In the second step, extra oil was added into the already formed emulsion, followed by shearing with a double cylinder-type homogenizer. The resulting final emulsions had a gel-like appearance. Miao et al. also reported another type of two-step procedure to prepare HIPEs with CNC (Marinova et al., 1996). In their study, homogenization at low shear (approximately 2,000 rpm for 1 min) was followed by high shear (10,000 rpm for 1 min). However, the viscoelastic properties of these gel-like emulsions were not reported.

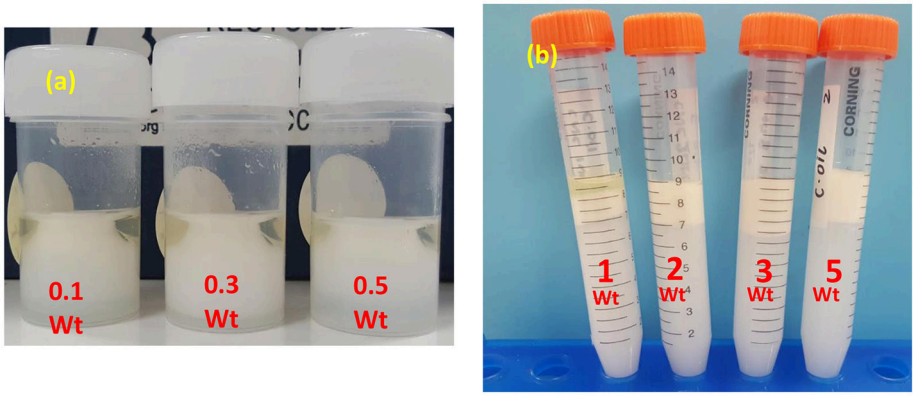


**FIGURE 3 |** Photographs of CNC stabilized C. Oil/water emulsion after centrifugation. **(a)** Low CNC concentrations and **(b)** high CNC concentrations.

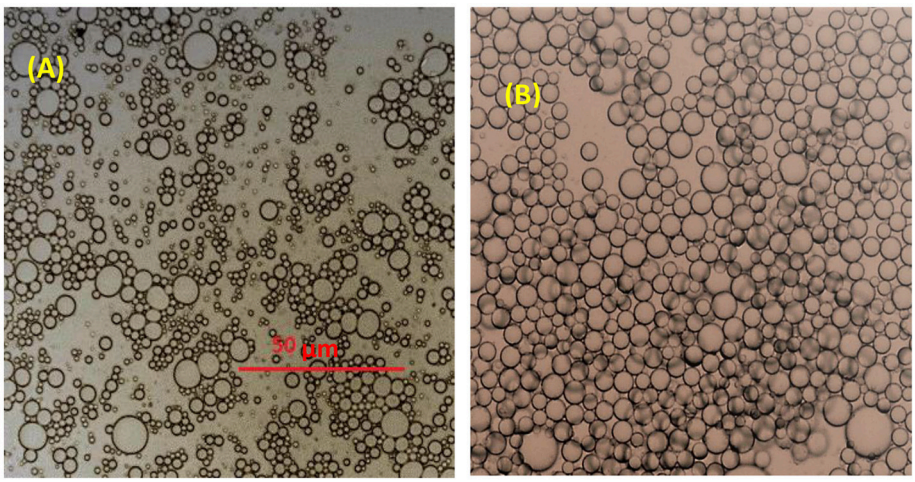


**FIGURE 4 |** Microscopic image of emulsions stabilized with 3 wt% CNC **(A)** C. Oil/water **(B)** hexadecane/water emulsions.

This study aims at exploring whether stable emulsions can be prepared from CNCs having surface charge density higher than 0.033 e/nm$^2$ and if modulating their charge density, by adding salts and varying pH, can reduce the amount of CNC's required to form a stable emulsion. This paper investigates the role played by electrostatic forces in CNC based emulsions and whether these are completely charge driven systems. This study also describes a method to prepare CNC based on emulsified gels on a single shearing method.

## EXPERIMENTAL SECTION

### Materials

Cellulose nanocrystals (CNC, 12.6 wt %) were purchased from the University of Maine Process Development Center as a dispersion in water (sulfur content of 1–2%), with an average width of 8 nm and length 138 nm. Canola oil was purchased from the local supermarket. Hexadecane, Sodium Chloride (NaCl) and Calcium Chloride ($CaCl_2$) were purchased from Sigma Aldrich, Australia. Oils were used as supplied- without further purification.

### Methods

1. **Emulsion preparation:** All the emulsions were prepared using an oil/water ratio of 20/80 (v/v). Typically, 2 mL of canola oil was added to 8 mL of the CNC aqueous suspension in a 50 mL vial and was sonicated with a titanium probe (Sonics Vibracell High Intensity Ultrasonic Processor, VCX 500–VCX 750) immersed in the solution under the following conditions: 3 s on and 3 s off for an interval of 3 min, with 44 Watts power input. The sonicated emulsions were then poured into 15 mL centrifuge tubes (without any separation) and centrifuged at 4,000G for 10 min to estimate the stability of CNC-palm oil emulsion. Cream volume after centrifugation is noted as emulsion volume.
2. **Conductometric Titration:** Conductometric titration was performed to determine the surface charge density as reported in Kalashnikova et. al. (Kalashnikova et al., 2012). In brief, a

total of 50 mL of a CNC suspension at 1 g/L in water was titrated with freshly prepared 2 mM NaOH with a TIM900 titration manager and a CDM230 conductimeter equipped with a CDC749 titration cell (Kalashnikova et al., 2012; Zhong et al., 2012). CNC samples showed low conductance values because of their small amounts of charge so HCl and NaCl were added prior to titration.

3. **Z-potential measurement:** The electrophoretic mobility of aliquots of aqueous CNC suspensions at 0.1 g/L was measured in triplicate with a NanoBrook Omni (Brookhaven's Instruments).
4. The optical micrographs of the prepared emulsions on transparent glass slides were taken using a microscope (Nikon upright motorized microscope Eclipse Ni-E) immediately after each preparation. Drop sizes and distribution were measured using ImageJ software.
5. **Rheology:** All rheological testing of the gel like emulsions were performed with an Anton Paar MCR302 rheometer. A cone (0.997°) and plate (49.975 mm) geometry were selected. Testing was done at ambient temperature (25°C). To ensure stable temperature during the testing, a solvent trap was used. Viscosity was measured at shear rate ranging from 0.5 to 100 $s^{-1}$. Oscillatory strain sweep was performed from 0.01 to 100% at a constant 1 Hz frequency. Frequency sweep was measured from 0.1 to 100 rad/s and at 0.1% strain. All measurements were in triplicates.
6. **Atomic Force Microscopy imaging:** Atomic force microscopy (AFM, JPK Nanowizard 3) was used in alternating contact, AC mode to obtain images of CNC morphology and particle size. CNC suspension drop was casted and air died on glass slide.

## RESULTS

An AFM image of the CNC studied is shown in **Figure 1**. Cellulose nanocrystals (CNC) having an average diameter 8 nm, a length 138 nm, a surface charge density of 0.11 e/$nm^2$ and a zeta potential of −70 mV were used to prepare a series of canola oil (C. Oil)/water and hexadecane/water emulsions. The CNC rods exhibit a strongly negatively charged surface because of the presence of hydroxyl and sulfate groups. CNC concentration was varied to study this effect on the stability of oil/water emulsions prepared with two types of oils. Results are shown in **Figure 2**. Hexadecane behaves similarly to C. Oil. CNCs could not stabilize the emulsions at concentrations ranging from 0.1 to 0.5 wt%. This supports the work of Kalashnikova et.al also reporting that CNC could not stabilize hexadecane/water emulsion at a concentration of 0.1 wt% (Kalashnikova et al., 2012). Interestingly, CNC stabilizes emulsions at a concentration higher than 1 wt% CNC for both types of oils, even though the CNC surface charge density is higher than 0.033 e/$nm^2$. Canola oil/water and hexadecane/water samples were centrifuged at 4,000G for 10 min to test their stability.

**Figure 3** shows the appearance of C. Oil/water emulsions after centrifugation in vials and centrifuge tubes. Emulsions were prepared with CNC concentration ranging from 0.1 to 0.5 wt% **(Figure 3a)** and from 1 to 5 wt% **(Figure 3b).** The oil and aqueous layers separated clearly. At CNC concentrations of 1 and 2 wt%, a stable emulsion is formed between the oil and the aqueous layers where the emulsion volume is lower than the initial oil volume. In

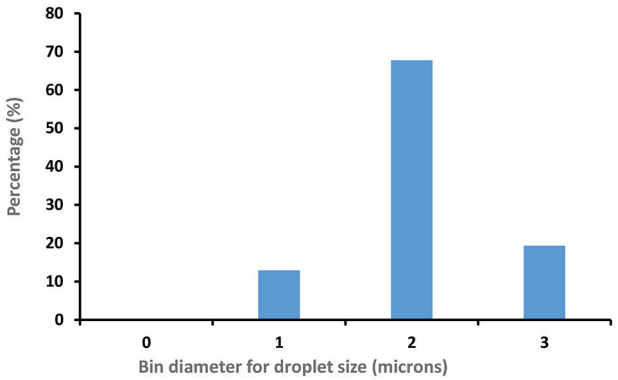


**FIGURE 5 |** CNC (3 wt %) stabilized Hexadecane/water Emulsion droplet size distribution (100 droplets measured).

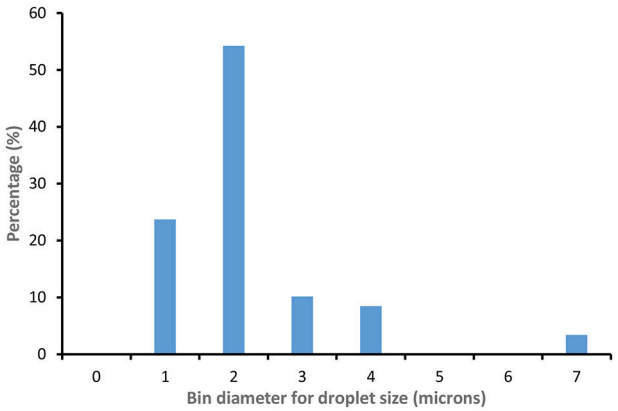


**FIGURE 6 |** CNC (3 wt %) stabilized C. Oil/water Emulsion droplet size distrubution (100 droplets measured).

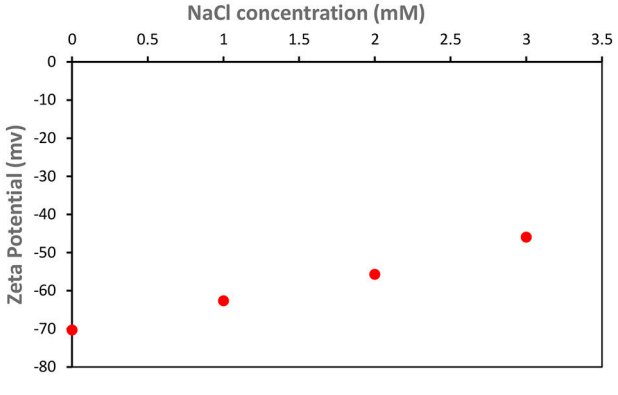


**FIGURE 7 |** Effect of NaCl addition on the zeta potential of CNC Suspension at pH = 7 and room temperature.

contrast, at CNC concentrations of 3 and 5 wt%, stable emulsions and aqueous layers were observed, with the emulsion volume higher than the initial oil volume. Completely stable emulsions are formed at 3 wt% CNC and higher concentrations.

**Figure 4** displays optical microscopy images of CNC stabilized C. Oil and hexadecane in water emulsions. Droplets of hexadecane/water emulsion are uniformly dispersed, with an average diameter of 2.5 μm (std. dev−0.3 μm) microns **(Figure 5)**. However, C. Oil/water emulsions with an average diameter of 2.7 μm and a high standard deviation of 1.2 μm **(Figure 6)** are more polydispersed and have random aggregates.

## Effect of Salts on Emulsions Stability

Salt greatly affects the stability of C. Oil/water emulsions. Salts are well known for screening the electrostatic repulsion on CNC surfaces (Kalashnikova et al., 2012). The zeta potential of CNC decreased linearly from (–)70 mV to (–)50 mV with the addition of 0 to 3 mM NaCl **(Figure 7)**. The limiting conditions of CNC based Pickering emulsions in the presence of NaCl were studied **(Figure 8)**. Experiments were initially conducted with the addition of 100 Mm NaCl solution to varying CNC concentrations ranging from 3 to 0.1 wt%. After identifying that 0.1 wt% CNC can stabilize C. Oil/water emulsions with 100 mM NaCl, the NaCl concentration was varied, keeping the CNC concentration constant at 0.1 wt%. It was found that CNC could stabilize C. Oil/water emulsions at 0.1 wt% concentration with as little as 3 mM NaCl concentration. Emulsion volume remained constant for NaCl concentration ranging from 3 to 20 mM. As the NaCl concentration increased from 20 to 50 mM, the emulsion volume increased by 15%. At 1 wt% CNC concentration, the emulsion volume is 2.5 mL which is 3 times higher than in absence of salt. Interestingly, the emulsion volume at 3 wt% CNC and 100 mM NaCl concentration correspond to the total volume of the aqueous suspension and oil used. Even with the centrifuge tube placed upside down, the emulsion after stability test did not flow, forming a gel-like network **(Figure 9)**. Rheological properties of this gel are discussed in the last part of the discussion section.

Similarly, the effect of $CaCl_2$ addition on the stability of C. Oil/water emulsion was tested **(Figure 10)**. It was found that CNC could stabilize C. Oil/water emulsions at 0.1 wt% concentration with $CaCl_2$ concentration as low as 1 mM or even lower.

## Effect of pH on C. Oil/Water EMULSIONS Stability

Varying pH from 7 to 3 had no effect on the stability of C. Oil/water emulsions **(Table 1)**. 0.1 wt% CNC could not form stable C. Oil/water emulsions for pH ranging between 7 and 3. In contrast, at pH 2 or below, 0.1 wt% CNC formed stable emulsions. On the other hand, 3 wt% CNC could form stable C. Oil/water emulsion at pH 7 or below. At pH below 2, the emulsion volume represented the combined volume of the aqueous suspension and oil used. The emulsion prepared with 3 wt% CNC at pH 3.9 flowed when the centrifuge tube was turned upside down; the emulsion formed with 3 wt% CNC at pH 1 did not. At lower pH, the emulsion formed a gel network **(Figure 11)**.

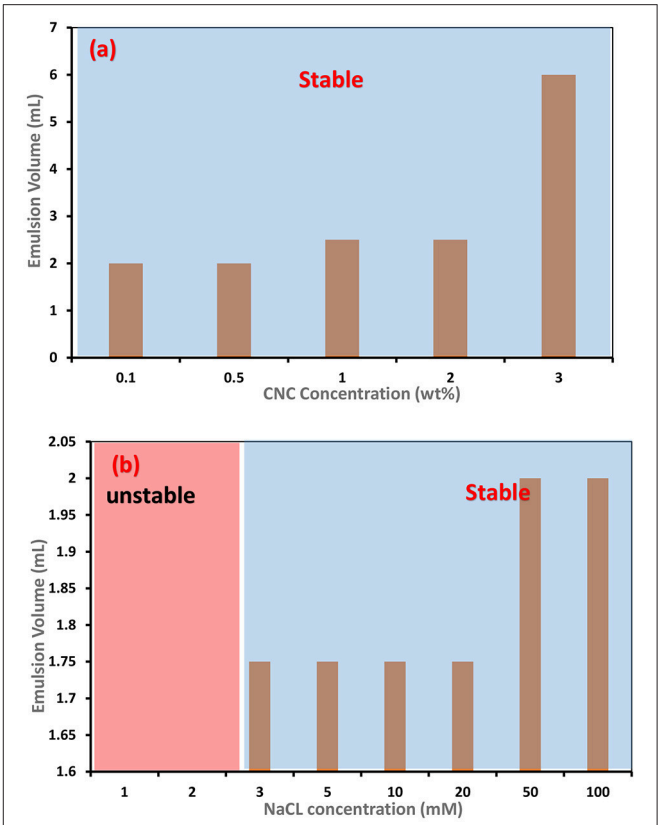


**FIGURE 8 |** Effect of NaCl addition on the stability of C. Oil/Water emulsions– **(a)** CNC concentration varied keeping NaCl concentration constant at 100 mM **(b)** NaCl concentration varied keeping CNC concentration constant at 0.1 wt.

The rheological properties of the C. Oil in water gel are shown in **Figures 12**, **13**. Gel-like emulsions are subjected to strain **(Figure 12)** and frequency **(Figure 13)** sweeps. In a strain sweep, the range of viscoelastic behavior can be quantified for gels. The elastic modulus G' describes the solid-like behavior of gel whereas the loss or viscous modulus G" defines the liquid-like behavior of the material.

# DISCUSSION

Particle concentration is an important factor in the formation of particle stabilized emulsions, commonly known as Pickering emulsions. It has a remarkable influence on the emulsion stability. Stable Pickering emulsion formation is a two-step process. Firstly, particles migrate from the aqueous dispersion onto the oil–water interface. Then, particles adsorb at the oil/water interface replacing and decreasing the oil-water contact area. The adsorbed particles act as emulsifiers, by lowering the interfacial free energy primarily by reducing the interfacial area between the two phases and makes the system stable (Wang, 2013).

The amphiphilic nature of negatively charged CNC's is the driving force for their migration from solution toward the

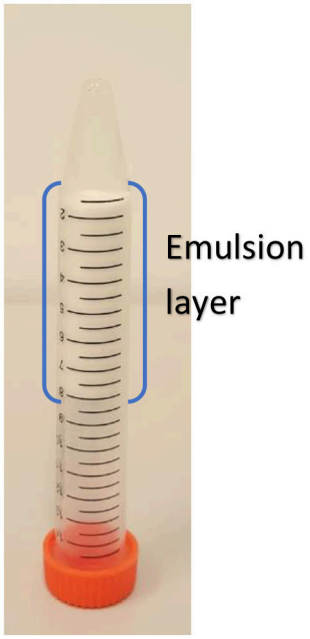


**FIGURE 9 |** Photograph of C. Oil/water emulsion with 3 wt% CNC and 100 mM NaCl after centrifugation.

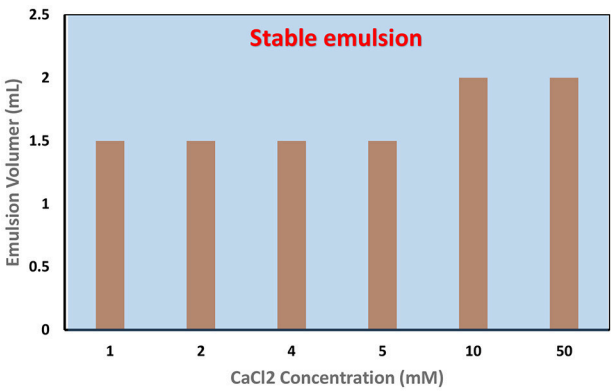


**FIGURE 10 |** Effect of $CaCl_2$ addition on the stability of CNC (0.1 wt%) stabilized C.Oil/Water emulsions.

oil/water interface during emulsification. However, significant electrostatic repulsion occurs when a negatively charged CNC (because of sulfate ester groups on the surface) approaches the oil-water interface that is also negatively charged due to the preferential adsorption of hydroxide ions (Capron and Cathala, 2013). Such repulsion can create an energy barrier preventing particle adsorption to the interface, and hinder the formation of emulsions (Danov et al., 2005; Golemanov et al., 2006). Hence, stable emulsions could not form at low concentrations of CNCs ranging from 0.1 to 0.5 wt% (**Figures 2**, **3**).

At higher concentrations, starting from 1 wt%, CNC tend to aggregate in aqueous solution (Xu et al., 2017) because of chemical interaction (for example hydrogen bond) and

**TABLE 1 |** Effect of pH on the stability of C. Oil/water emulsions.

| CNC concentration (wt%) | pH | Emulsion condition | Emulsion Volume (mL) |
|---|---|---|---|
| 0.1 | 7 | No Emulsion | 0 |
| | 6 | No Emulsion | 0 |
| | 5 | No Emulsion | 0 |
| | 4 | No Emulsion | 0 |
| | 2 | Stable | 2 |
| | 1.1 | Stable | 2 |
| 3 | 3.9 | Stable | 2 |
| 3 | 1.1 | Stable | 9 |

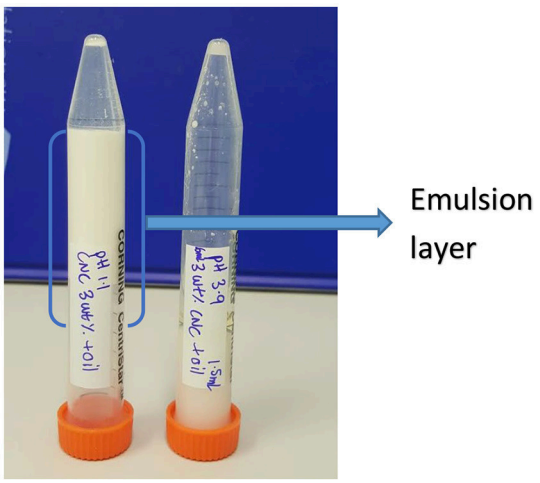


**FIGURE 11 |** Photograph of C. Oil/water emulsion with 3 wt% CNC and pH 1.1 and 3.9.

strong affinity toward material containing hydroxyl groups (hydrogen bonding between CNC and water molecules) (Li et al., 2015). CNC aggregates have higher adsorption energy (force of attraction) that dominates the repulsion force between CNCs and oil/water interface (Paunov et al., 2002). Adsorbed CNC aggregates minimize the interfacial free energy primarily by reducing the interfacial area between the oil/water interfaces. Hence, CNC's can stabilize the emulsions at higher concentrations than 1 wt%.

## Effect of Salts Addition on Emulsion Stability

The amount of CNC required to stabilize the emulsion reduced greatly with the addition of either NaCl or $CaCl_2$. **Figure 7** shows that the zeta potential of CNC suspension reduced gradually with increasing NaCl concentration. Zhong et al. (2012) and Prathapan et al. (2016) reported similar observations. This is because of the electrostatic screening effect from the cation counter ion $Na^+$ and the Debye-Huckel screening strength augments upon increasing salt concentration; therefore, the Debye length decreases. For example, the Debye length and ionic strength of NaCl at

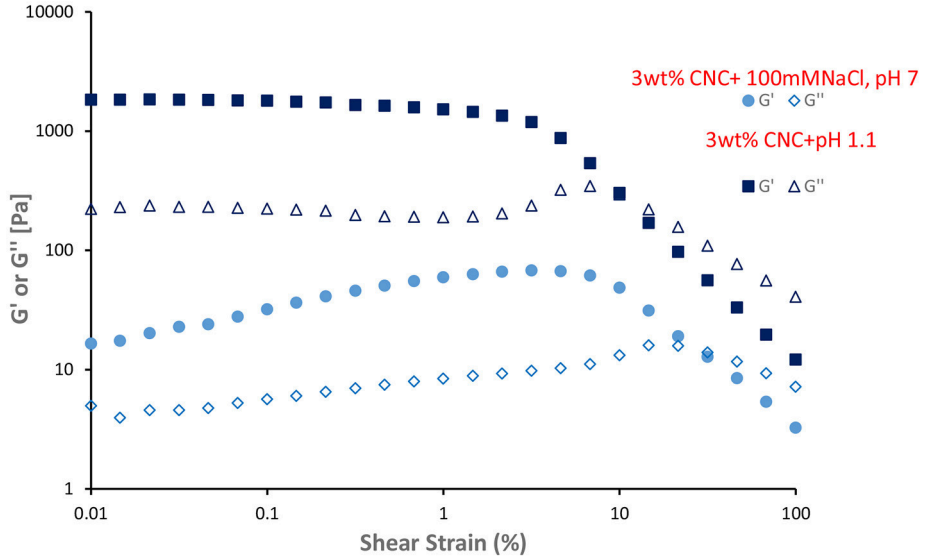


**FIGURE 12 |** Dynamic strain sweep of gel like emulsions (3 wt% CNC and 100 mM NaCl, 3 wt% CNC and pH 1.1) at 25° C and frequency of 1 Hz. Filled symbol indicate elastic moduli (G') and unfilled symbol indicate loss moduli (G").

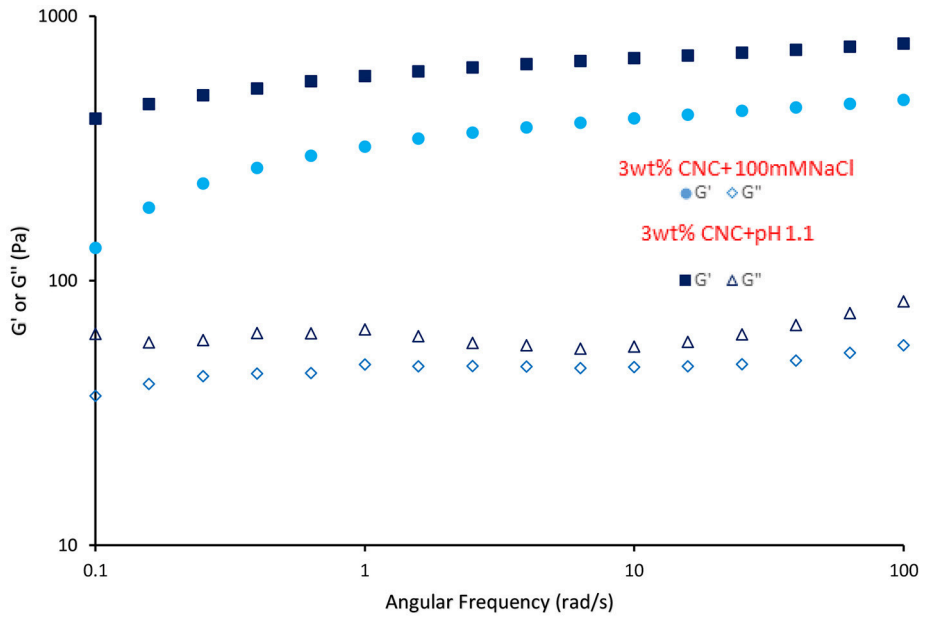


**FIGURE 13 |** Dynamic frequency sweep of gel like CNC emulsion (3 wt% CNC and 100 mM NaCl, 3 wt% CNC and pH 1.1) at 25° C and 0.1% strain. Filled symbol indicate elastic moduli (G') and unfilled symbol indicate loss moduli (G").

1 mM concentration are 9.6 nm and 1 mol/$m^3$, respectively; at 3 mM concentration, these are 5.54 nm and 3 mol/$m^3$. Prathapan et al. (2016) further reported that $Ca^{2+}$ ions screen stronger than $Na^{+}$ ions. Hence, there was a greater reduction in CNC zeta potential with the addition of $Ca^{2+}$ ions. The Debye length of $CaCl_2$ at 1 mM concentration is 4.52 nm, which is lower than that of NaCl at 3 mM concentration (5.54 nm).

Double layer principles imply that the adsorption of ions and ion pairs to the CNC surface shield the surface charge of CNC and reduces the electrostatic repulsion, which facilitates the CNC to migrate and adsorb onto the oil/water interface in the presence of Na+ and Ca2+ ions, even at 0.1 wt% CNC concentration. Hence, a stable C. Oil/water emulsion could form at 0.1 wt% CNC in the presence of Na+ and Ca2+ ions. The amount of CNC required to stabilize 2 mL of C. Oil is 30 times less in the presence

of salts. Interestingly, to stabilize C. Oil/water emulsion with a 0.1 wt% CNC suspension, <1 mM $CaCl_2$ addition to the CNC suspension is required, which is 3 times lower than for NaCl. This directly corroborates the Debye length of $CaCl_2$ and NaCl. These results indicate that stabilization of oil/water emulsion with CNC is governed by the surface charge in the presence of electrolytes.

Zhong et al. reported that a 0.15 wt% CNC suspension is clear and transparent, indicating a stable suspension because of charge repulsion among CNC's (Zhong et al., 2012). When ionic strength increased to 50 mM $Na^+$, CNC particles tend to aggregate to a size of 980 nm, which is 10 times higher than their initial size. This is because of van der Waals forces dominating the electrostatic repulsion. Xu et al. reported that CNC tends to aggregate even in the absence of electrolytes at concentrations higher than 1 wt% (Xu et al., 2017). When the suspension concentration is higher than 3 wt%, aggregation of CNC became denser through long-range electrostatic interactions (Xu et al., 2017). When 100 mM NaCl is added to a 3 wt% CNC suspension, CNC aggregates grew in size and connected into a percolating network. Macroscopically, gel-like behavior is observed. Peddireddy et al. also reported similar observations with CNC concentrations higher than 12 g/L and 70 mM NaCl (Peddireddy et al., 2016). Emulsions prepared with a 3 wt% CNC suspension and ionic strength of 100 mM $Na^+$ behave like gels. The emulsion volume is 9 mL, corresponding to the total volume of oil and aqueous suspension.

## Effect of pH on Emulsion Stability

Prathapan et al. (2016) and Zhong et al. (2012) reported that when the pH is varied from 11 to 2, the change in CNC suspension zeta potential is very low. This is because pH did not significantly alter the disassociation state of the sulfate ester groups present on the CNC surface since the $pK_a$ of covalently bound sulfate ester group ($pK_a = 1.9$) is very low. However, for pH below 2, a considerable reduction in zeta potential–i.e., net charge on CNC surface, and agglomeration of CNC results because of the protonation of the sulfonic acids starting to occur. Again, reduction in the net charge of CNC at pH below 2 helps their migration and adsorption at the oil/water interface to form stable emulsions with 0.1 wt% CNC. When emulsions are prepared with 3 wt% CNC at pH 1.1, aggregates of CNC grew in size and connect into a percolating network gel.

Emulsions prepared with 3 wt% CNC, 100 mM NaCl, and pH 1.1 show gel behavior. Viscoelastic properties of these gels were presented in **Figures 12**, **13**. G' and G" of gel-like emulsions obtained at pH 1.1 are higher than those with 100 mM NaCl. At low shear stresses, both gel emulsions possess a linear viscoelastic region (LVR) wherein the elastic modulus G' and viscous modulus G" are independent of shear stress. Within this region, G' is dominant over G", indicating that the material is acting as a solid; elastic behavior dominates over viscous comportment. At a critical shear stress, the gel yields as shown by the decrease in G', and then reaches a "cross-over point" where G" becomes dominant and the gel begins to flow. Past this critical stress, the viscous regime dominates (G" > G') indicating that the network structure has yielded and begins to behave as a non-Newtonian shear thinning fluid. **Figure 13** gives the frequency sweep i.e., the time-dependent behavior of the gel emulsion. For both gel emulsions, the G' and G" values are non-intersecting with G' increasing gradually with angular frequency. This slight increase in moduli shows these gels to be weakly cross-linked (Mendoza et al., 2018).

# CONCLUSION

Cellulose nanocrystals (CNC) can form stable oil/water emulsions regardless of their charge density. This contradicts the limiting condition of charge density below 0.033 e/nm$^2$ reported in the literature for the formation of stable emulsions with CNC. However, higher charge density CNC requires higher amounts of CNC and higher concentrations. At high CNC concentrations, the adsorption forces of CNC aggregates dominate the electrostatic repulsion between CNC and the oil/water interface. As the charge density reduces through the addition of salts, lower concentrations of CNC are required because of the salt induced reduction in electrostatic repulsion. The amount of CNC required to stabilize 2 mL of oil is 30 times less in the presence of salts. The ratio of minimum ionic strength required to prepare a stable emulsion with $CaCl_2$ and NaCl directly corroborates with the Debye length ratio of $CaCl_2$ and NaCl. This indicates that stabilization of oil/water emulsion with CNC is governed by surface charge in the presence of electrolytes. Emulsions prepared with 3 wt% CNC suspensions have an ionic strength of 100 mM $Na^+$ and behaved like a gel. Varying pH from 7 to 3 had no effect on the stability of emulsions. However, the emulsion prepared with 3 wt% CNC and at pH below 2 behaved like a gel. These gels are weakly cross-linked. Cellulose nanocrystal offers a new way to stabilize oil in water by forming Pickering emulsions. The systems are completely biodegradable and biocompatible and can form robust gels or not, opening new innovation avenues in food and biomedical applications.

# AUTHOR CONTRIBUTIONS

SV, WB, and GG prepared manuscript. SV, LH, and LM performed experiments. RP and RT performed AFM measurements.

# ACKNOWLEDGMENTS

Financial support was from Australian Research Council, Australian Paper, Carter Holt Harvey, Circa, Norske Skog and Visy through the Industry Transformation Research Hub grant IH130100016. Thanks to Monash Centre for Electron Microscopy for training and facilities, Dr. C. Henderson for assisting with an optical microscope and Dr. V. Raghuwanshi for discussion and manuscript preparation.

## REFERENCES


Binks, B. P., and Lumsdon, S. O. (2000). Influence of particle wettability on the type and stability of surfactant-free emulsions. *Langmuir* 16, 8622–8631. doi: 10.1021/la000189s

Capron, I., and Cathala, B. (2013). Surfactant-free high internal phase emulsions stabilized by cellulose nanocrystals. *Biomacromolecules* 14, 291–296. doi: 10.1021/bm301871k

Capron, I., Rojas, O. J., and Bordes, R. (2017). Behavior of nanocelluloses at interfaces. *Curr. Opin. Colloid Interf. Sci.* 29(Suppl. C), 83–95.doi: 10.1016/j.cocis.2017.04.001

Carrillo, C. A., Nypelö, T. E., and Rojas, O. J. (2015). Cellulose nanofibrils for one-step stabilization of multiple emulsions (W/O/W) based on soybean oil. *J. Colloid Interf. Sci.* 445(Suppl. C), 166–173. doi: 10.1016/j.jcis.2014.12.028

Danov, K. D., Kralchevsky, P. A., Naydenov, B. N., and Brenn, G. (2005). Interactions between particles with an undulated contact line at a fluid interface: Capillary multipoles of arbitrary order. *J. Colloid Interf. Sci.* 287, 121–134. doi: 10.1016/j.jcis.2005.01.079

Dong, X. M., and Gray, D. G. (1997). Effect of counterions on ordered phase formation in suspensions of charged rodlike cellulose crystallites. *Langmuir* 13, 2404–2409. doi: 10.1021/la960724h

Dugyala, V. R., Daware, S. V., and Basavaraj, M. G. (2013). Shape anisotropic colloids: synthesis, packing behavior, evaporation driven assembly, and their application in emulsion stabilization. *Soft Matter* 9, 6711–6725. doi: 10.1039/c3sm50404b

Fujisawa, S., Togawa, E., and Kuroda, K. (2017). Nanocellulose-stabilized pickering emulsions and their applications. *Sci. Technol. Adv. Mater.* 18, 959–971. doi: 10.1080/14686996.2017.1401423

Golemanov, K., Tcholakova, S., Kralchevsky, P. A., Ananthapadmanabhan, K. P., and Lips, A. (2006). Latex-particle-stabilized emulsions of anti-bancroft type. *Langmuir* 22, 4968–4977. doi: 10.1021/la0603875

Hosseinidoust, Z., Alam, M. N., Sim, G., Tufenkji, N., and van de Ven, T. G. (2015). Cellulose nanocrystals with tunable surface charge for nanomedicine. *Nanoscale* 7, 16647–16657. doi: 10.1039/C5NR02506K

Kalashnikova, I., Bizot, H., Cathala, B., and Capron, I. (2011). New pickering emulsions stabilized by bacterial cellulose nanocrystals. *Langmuir* 27, 7471–7479. doi: 10.1021/la200971f

Kalashnikova, I., Bizot, H., Cathala, B., and Capron, I. (2012). Modulation of cellulose nanocrystals amphiphilic properties to stabilize oil/water interface. *Biomacromolecules* 13, 267–275. doi: 10.1021/bm201599j

Kaptay, G. (2006). On the equation of the maximum capillary pressure induced by solid particles to stabilize emulsions and foams and on the emulsion stability diagrams. *Colloids Surf. A* 282–283(Suppl. C), 387–401.doi: 10.1016/j.colsurfa.2005.12.021

Li, M. C., Wu, Q., Song, K., Lee, S., Qing, Y., and Wu, Y. (2015). Cellulose nanoparticles: structure–morphology–rheology relationships. *ACS Sustain. Chem. Eng.* 3, 821–832. doi: 10.1021/acssuschemeng.5b00144

Marinova, K. G., Alargova, R. G., Denkov, N. D., Velev, O. D., Petsev, D. N., Ivanov, I. B., et al. (1996). Charging of oil–water interfaces due to spontaneous adsorption of hydroxyl ions. *Langmuir* 12, 2045–2051. doi: 10.1021/la950928i

Mendoza, L., Batchelor, W., Tabor, R. F., and Garnier, G. (2018). Gelation mechanism of cellulose nanofibre gels: A colloids and interfacial perspective. *J. Coll. Interface Sci.* 509(Suppl. C), 39–46. doi: 10.1016/j.jcis.2017.08.101

Miao, C., Tayebi, M., and Hamad, W. Y. (2017). Investigation of the formation mechanisms in high internal phase Pickering emulsions stabilized by cellulose nanocrystals. *Philos. Trans. R. Soc. A* 376:20170039. doi: 10.1098/rsta.2017.0039

Moon, R. J., Martini, A., Nairn, J., Simonsen, J., Youngblood, J., (2011). Cellulose nanomaterials review: structure, properties and nanocomposites. *Chem. Soc. Rev.* 40, 3941–3994. doi: 10.1039/c0cs00108b

Nishio, Y., Sato, J., and Sugimura, K. (2016). "Liquid crystals of cellulosics: fascinating ordered structures for the design of functional material systems," in *Cellulose Chemistry and Properties: Fibers, Nanocelluloses and Advanced Materials*, ed O. J. Rojas (Cham: Springer International Publishing), 241–286.

Paunov, V. N., Binks, B. P., and Ashby, N. P. (2002). Adsorption of charged colloid particles to charged liquid surfaces. *Langmuir* 18, 6946–6955. doi: 10.1021/la0203584

Peddireddy, K. R., Capron, I., Nicolai, T., and Benyahia, L. (2016). Gelation kinetics and network structure of cellulose nanocrystals in aqueous solution. *Biomacromolecules* 17, 3298–3304. doi: 10.1021/acs.biomac.6b01061

Prathapan, R., Thapaa, R., Garnierb, G., and Tabora, R. F. (2016). Modulating the zeta potential of cellulose nanocrystals using salts and surfactants. *Coll. Surf. A Physicochem. Eng. Aspec.*509(Suppl. C), 11–18. doi: 10.1016/j.colsurfa.2016.08.075

Safari, S., Sheikhi, A., and van de Ven, T. G. (2014). Electroacoustic characterization of conventional and electrosterically stabilized nanocrystalline celluloses. *J. Colloid Interface Sci.* 432(Suppl. C), 151–157. doi: 10.1016/j.jcis.2014.06.061

Trache, D., Hussin, M. H., Haafiz, M. K. M., and Thakur, V. K. (2017). Recent progress in cellulose nanocrystals: sources and production. *Nanoscale* 9, 1763–1786. doi: 10.1039/C6NR09494E

Wang, H. (2013). *Understanding of Charge Effects in Pickering Emulsions and Design of Double Pickering Emulsion Templated Composite Microcapsules*. Chemical and Biomolecular Engineering. Georgia Instituite of Technology.

Wang, W., Du, G., Li, C., Zhang, H., Long, Y., and Ni, Y. (2016). Preparation of cellulose nanocrystals from asparagus (Asparagus officinalis L.) and their applications to palm oil/water Pickering emulsion. *Carbohydrate Polymers* 151(Suppl. C), 1–8. doi: 10.1016/j.carbpol.2016.05.052

Wu, J., and Ma, G.-H. (2016). Recent studies of pickering emulsions: particles make the difference. *Small* 12, 4633–4648. doi: 10.1002/smll.201600877

Xu, H. N., Tang, Y. Y., and Ouyang, X. K. (2017). Shear-induced breakup of cellulose nanocrystal aggregates. *Langmuir* 33, 235–242. doi: 10.1021/acs.langmuir.6b03807

Yang, Y., Fang, Z., Chen, X., Zhang, W., Xie, Y., Chen, Y., et al., (2017). An overview of pickering emulsions: solid-particle materials, classification, morphology, and applications. *Front. Pharmacol.* 8:287. doi: 10.3389/fphar.2017.00287

Zhong, L., Fu, S., Peng, X., Zhan, H., and Sun, R. (2012). Colloidal stability of negatively charged cellulose nanocrystalline in aqueous systems. *Carbohydrate Polymers* 90, 644–649. doi: 10.1016/j.carbpol.2012.05.091


**Conflict of Interest Statement:** The authors declare that the research was conducted in the absence of any commercial or financial relationships that could be construed as a potential conflict of interest.

frontiers in Chemistry

ORIGINAL RESEARCH
published: 20 July 2018
doi: 10.3389/fchem.2018.00301

# Influence of pH-Responsive Monomer Content on the Behavior of Di-Block Copolymers in Solution and as Stabilizers of Pickering Latex Particle Emulsifiers

*Mohamed S. Manga*[1]*, *Olivier J. Cayre*[1], *Simon Biggs*[1,2] and *Timothy N. Hunter*[1]

[1] Faculty of Engineering, School of Chemical and Process Engineering, University of Leeds, Leeds, United Kingdom, [2] The University of Western Australia, Perth, WA, Australia

In this study, diblock copolymers poly(methyl methacrylate)—block—poly (2-dimethylaminoethyl methacrylate) (pMMA-b-pDMAEMA) are investigated for the steric stabilization of latex particles and the subsequent use of these latex particles as Pickering emulsifiers. Solution properties of the diblock copolymers highlight that the pDMAEMA block length influences the critical micelle concentration (CMC) and micelle hydrodynamic diameter in response to changes in pH and the p$K_a$. The block length can also be used as a way to control the particle size of sterically stabilized polystyrene latex particles prepared via emulsion polymerization. The suspension properties of these latex particles are also presented. Emulsion studies using these latex particles as emulsifiers show that both continuous phase pH and electrolyte concentration affect emulsion stability to coalescence. At high pH, stable emulsions are formed due to the affinity of the particles to the interface. At low pH, protonation of the amine groups reduces the affinity and thus droplet coalescence is observed. Increasing the electrolyte concentration improves emulsion stability, but causes an increase in droplet size due to adsorption of flocculated/aggregated particles. Finally, it is shown that these latex particles can be used in conjunction with membrane emulsification techniques to produce emulsions with low polydispersity.

**Keywords: pH-responsive polymer, pDMAEMA, core-shell particles, Pickering emulsions, membrane emulsification**

OPEN ACCESS

***Edited by:***
*Syuji Fujii,*
*Osaka Institute of Technology, Japan*

***Reviewed by:***
*To Ngai,*
*The Chinese University of Hong Kong, Hong Kong*
*Yanqing Tian,*
*Southern University of Science and Technology, China*

***Correspondence:**
*Mohamed S. Manga*
*m.s.manga@leeds.ac.uk*

***Specialty section:***
*This article was submitted to Chemical Engineering, a section of the journal Frontiers in Chemistry*

***Received:*** *28 March 2018*
***Accepted:*** *29 June 2018*
***Published:*** *20 July 2018*

***Citation:***
*Manga MS, Cayre OJ, Biggs S and Hunter TN (2018) Influence of pH-Responsive Monomer Content on the Behavior of Di-Block Copolymers in Solution and as Stabilizers of Pickering Latex Particle Emulsifiers. Front. Chem. 6:301. doi: 10.3389/fchem.2018.00301*

## INTRODUCTION

The preparation and stabilization of emulsions and foams using colloidal particles (commonly referred to as Pickering systems) has been well documented for over a century (Ramsden, 1903; Pickering, 1907; Binks and Horozov, 2006; Hunter et al., 2008; Dickinson, 2010; Lam et al., 2014; Binks, 2017). For interfacial stabilization to occur, these Pickering stabilizers self-assemble at the fluid-fluid interface and remain irreversibly adsorbed once attached, preventing coalescence (Finkle et al., 1923; Binks and Horozov, 2006). In addition, their size and wettability (defined by their contact angle) play an important role in dictating the amount of energy that is required to detach them from the interface (Binks, 2002; Binks and Horozov, 2006).

The majority of research into Pickering systems has been conducted with inorganic particles such as silica, owing to their well-defined shape, availability of different sizes and ability to chemically tune the surface properties (Binks and Lumsdon, 1999; Binks and Horozov, 2005). The use of organic particles (e.g., polymer latex) as stabilizers has also received significant attention (Velev et al., 1996; Velev and Nagayama, 1997; Dinsmore et al., 2002), and as a consequence of developments in polymer chemistry, this has further expanded to include stimuli-responsive latex systems (Tang et al., 2015; Fujii and Nakamura, 2017). A key driver for this development, is the ability to form new "smart" materials with these responsive particles such as microcapsules (Biggs et al., 2008; San Miguel et al., 2010; Thompson et al., 2010, 2015; Cayre et al., 2012).

While there are numerous examples of Pickering emulsions produced using stimuli-responsive latex emulsifiers in the literature with various stimuli, the focus on this present study is on pH-responsive systems. Tu and co-workers developed pH-responsive Janus polymeric particles based on polystyrene and polyacrylic acid (Tu and Lee, 2014). They report that the particles can change shape based on changes in suspension pH due to the protonation/deprotonation of the acrylic acid. When used as emulsifiers, it was demonstrated that these particles were able to induce phase inversion of the emulsions when the continuous phase pH was switched. The authors stated that this occurred due to protonation of the acrylic acid at low pH (lowering charge) increasing wettability with oil phase to form a w/o emulsion, whilst deprotonation occurred at high pH (increasing charge) leading to o/w emulsions. Microgel latex particles have been successfully utilized by numerous groups with the most extensively studied being poly(N-isopropylacrylamide) based microgels (Li and Ngai, 2011; Liu et al., 2012; Richtering, 2012). Other similar systems that have been studied are poly(4-vinylpyridine)/silica (P4VP/$SiO_2$) (Fujii et al., 2005, 2006), and 2-vinylpyridine (2VP) (Dupin et al., 2007), where emulsion stability is based on the continuous phase pH used in relation to the p$K_a$ of the polymer. For example in the case of P4VP/$SiO_2$, lowering the pH below the p$K_a$ caused the particles to protonate and desorb from the interface leading to emulsion instability. A similar mechanism exists with cross-linked poly(tert-butylamino)ethyl methacrylate (pTBAEMA) latex emulsifiers (Morse et al., 2012).

Alternatively, poly(methyl methacrylate)—block—poly(2-dimethylaminoethyl methacrylate) (pMMA-b-pDMAEMA) has previously been used as a pH-responsive steric stabilizer for the synthesis of polymer latex particles by Armes et al. and the current authors (Amalvy et al., 2003, 2004; Read et al., 2004; Reis et al., 2010; Cayre et al., 2012). The pDMAEMA block is pH-responsive exhibiting a p$K_a$ of 7–7.5 (Baines et al., 1996), which influences its behavior in solution and when used as a steric stabilizer. As a result, these latex particles have been used as emulsifiers to produce pH-responsive emulsions (Amalvy et al., 2003; Cayre et al., 2012), i.e., a similar mechanism to that of P4VP and pTBAEMA described above.

To date, there are very few studies that have investigated the influence of polymer chain length on the adsorption behavior of sterically stabilized particles at fluid-fluid interfaces. Reed et al. (2012) observed the influence of latex particles sterically stabilized with different chain lengths of a non-ionic macromonomer, pGMA (glycerol monomethacrylate) on particle wettability at fluid-fluid interfaces. Here, the interfacial contact angle was measured using a gel trapping technique (GTT) and a film caliper method (FCM). The equilibrium interfacial particle contact angle was found to be insensitive to pGMA chain length, because the high grafting densities achieved during particle synthesis meant that the polymer brushes were compact, forming a dense surface layer. The dense layer limited the access of the non-polar solvent to the particle surface and hence changes in the interfacial contact angle was found to be limited. Alternatively, Saigal et al. (2010), investigated inorganic silica particles stabilized with a pDMAEMA homopolymer as a thermo-responsive Pickering emulsifier. At high pH values, pDMAEMA has a low critical solubility temperature above which particle dispersions begin to flocculate. It was found that the pDMAEMA content at similar grafting densities did not affect emulsion stability regardless of the oil-type or emulsification temperature used at a continuous phase pH of 7–9.

It is evident that while the role of responsive polymer chain length may be critical to defining latex particle behavior and overall Pickering emulsion stability, grafted chain interactions are complex and difficult to predict from the free polymer behavior. To further understand these links, we present a comprehensive study that tracks the effect of a pH-responsive block on polymer solution behavior to bulk resulting effects on latex particles as stabilizers and finally to their performance as Pickering emulsifiers. While previous studies have investigated the use of well-defined steric stabilizers to exert control over the synthesis of sterically-stabilized latexes and covalently cross-linkable colloidosomes (Thompson and Armes, 2010; Thompson et al., 2017), the chain length of the steric stabilizer used was fixed. Here, four pMMA-b-pDMAEMA di-block copolymers with different DMAEMA block lengths (where the MMA block length was fixed at ∼14–16 units and the DMAEMA content was varied from ∼60 to 95 mol%) were investigated in terms of their free polymer behavior and the dispersion stability of synthesized core-shell latex particles. The ability of particles to stabilize emulsions and undergo rapid phase separation and release from pH changes are also characterized. Finally, these sterically stabilized latex particles are used to produce size-controlled low polydispersity droplets using membrane emulsification, for continuous scalable manufacture.

# MATERIALS AND METHODOLOGY

## Materials

The chemicals used in this study are listed with details of purity and suppliers. Methyl methacrylate (MMA, purity ≥99%, Sigma Aldrich) and dimethylaminoethyl methacrylate (DMAEMA, ≥98%, Sigma Aldrich) monomers were purified by distillation prior to use. Cyanopropyl dithiobenzoate (CPDB) was synthesized and purified according to the protocol described elsewhere (Moad et al., 2000) and is used as a Reversible addition–fragmentation chain transfer (RAFT) agent. Azoisobutylnitrile (AIBN, >98%, Fluka) was purified by recrystallization from hot methanol prior to use. All other

chemicals listed as follows were used as received: toluene (>99%, Fisher Scientific), dichloromethane (>99%, Acros Organics), hexane (>97%, Sigma), styrene (>99%, Sigma-Aldrich), ammonium persulfate (APS, >98%, Sigma-Aldrich).

## Synthesis of the Responsive Copolymer

The pMMA-b-pDMAEMA di-block copolymer used in this study was prepared, purified and characterized according to the protocol described by Cayre et al. (2012) (where $DMAEMA_{245}$ was used). For this study, the MMA block length was fixed (14–16 units) and the DMAEMA length was altered to 20, 54, 108, and 245 units (equating to a DMAEMA content of ∼60–95 mol% of the total polymer molecular weight) to compare their properties in solution, as a steric stabilizer and finally as an emulsifier. A summary of the four copolymers and their molecular weights used in this study are presented in **Table 1**.

## Characterization of Solution Properties of the Di-Block Copolymer

### Dynamic Light Scattering (DLS)

Measurements were made at 25°C using a Brookhaven BI-200SM instrument equipped with a 633 nm Helium-Neon (He-Ne) laser. To estimate the critical micelle concentration (CMC) of the di-block copolymers, changes in the hydrodynamic diameter were measured in polymer solutions prepared at different concentrations. Typically, a stock polymer solution was prepared at pH 4 at a concentration of 1,000 ppm. This was diluted with Milli-Q water also at pH 4, to obtain different polymer solution concentrations varying from 50 to 1,000 ppm (in this case there is no further dilution). The angle studied for the light scattering measurements was 90°. All copolymer solutions analyzed by DLS were passed through a syringe-mounted 0.2 μm filter.

### Potentiometric Titrations

All aqueous solutions were prepared by molecularly dissolving the copolymer in dilute $HNO_3$ (pH 2; Milli-Q grade water), with constant background electrolyte of 0.01 M $KNO_3$. Potentiometric titrations were performed by titrating 1,000 ppm copolymer solutions with 0.01M KOH from pH 2 to 11 (Figure S1 in Supplementary Information). Probe calibration was carried out using pH 4, 7, and 10 buffers.

## Synthesis and Characterization of the Responsive Latex Particles

### Synthesis Protocol

The responsive polystyrene latex particles were prepared via emulsion polymerization at different reaction temperatures, based on the method described in previous work (Cayre et al., 2012). Typically, the diblock copolymer stabilizer (0.5 g) was added to Milli-Q water (45 ml) (adjusted to pH 3–4 using $HNO_3$) in a three necked 100 mL round bottom flask fitted with a reflux condenser and a magnetic stirrer. This mixture was stirred at room temperature to allow the stabilizer to dissolve, before placing the flask in an oil bath and heating it to a working temperature of 70°C. The reaction was purged with nitrogen and an aqueous solution of ammonium persulfate initiator (0.05 g) (1.0 wt% based on styrene) was added to the vessel. The styrene (5 ml) was then added and the polymerization was allowed to proceed for approximately 24 h. Serum replacement was used to remove excess stabilizer, trace monomer and initiator, and was performed by using dialysis tubing (Fisher, $M_w$ = 12–14 kDa) over a time period of 1 week.

### Dynamic Light Scattering (DLS) and Zeta (ζ)-Potential

Measurements were performed using the Zetasizer Nano ZS (Malvern, U.K.) equipped with a helium-neon laser with a wavelength of 633 nm. DLS was used to measure the changes in hydrodynamic diameter of sterically-stabilized latex particles as a function of pH, electrolyte concentration and temperature. The angle studied for the light scattering measurements was 173°. The influence of pH and electrolyte concentration on the zeta potential was also measured. The solution pH was adjusted by adding either $HNO_3$ or KOH.

### $^1$H NMR Spectroscopy

The grafting density of the stabilizing diblock copolymer on the particles was determined through NMR studies of particles dissolved in deuterated chloroform. The intensity signals from the polystyrene and stabilizer were analyzed via integration of the relevant proton signals (Amalvy et al., 2004). It was assumed that the stabilizer was uniquely located on the surface of the particles. The grafting density, Γ, was calculated by comparing the stabilizer content (which takes into account the integration peaks) with the available particle surface area (based on intensity-averaged particle diameter using DLS).

## Preparation of Batch Emulsions via Homogenization

For the bulk emulsions study, an IKA T25 Ultra-Turrax homogenizer operating at 15,000 rpm for 2 min was used. The aqueous phase was prepared at a 2 wt% latex dispersion into Milli-Q water (5 ml) and was adjusted using $HNO_3$ or KOH to obtain the desired solution pH. Prior to emulsification, the latex dispersion was sonicated for 20 min before the emulsification experiments were carried out. An equal volume of n-hexadecane was added and the two phases were homogenized. The final

**TABLE 1 |** Summary of the copolymer block length, molecular weight, and polydispersity of the four pMMA-b-pDMAEMA copolymers used in this study.

| Stabilizer | Copolymer block length | Average molecular weight, $M_n$ (g mol$^{-1}$) | DMAEMA mol % | Polydispersity (PDI) |
|---|---|---|---|---|
| $DMAEMA_{20}$ | $pMMA_{14}$-b-$pDMAEMA_{20}$ | 4,770 | 58 | 1.1 |
| $DMAEMA_{54}$ | $pMMA_{14}$-b-$pDMAEMA_{54}$ | 10,110 | 79 | 1.2 |
| $DMAEMA_{108}$ | $pMMA_{14}$-b-$pDMAEMA_{108}$ | 18,600 | 88 | 1.2 |
| $DMAEMA_{245}$ | $pMMA_{16}$-b-$pDMAEMA_{245}$ | 40,340 | 94 | 1.1 |

emulsions were then placed in a water bath at 25°C for 24 h to assess their stability, and were characterized using laser diffraction and by monitoring the movement of the oil-emulsion and emulsion-water phases.

## Preparation of Emulsions Using Rotational Membrane Emulsification

Membrane emulsification studies were conducted using a stainless steel membrane mounted on an overhead stirrer motor (IKA, Eurostar digital agitator) that was carefully positioned in a stationary cylindrical container. The steel membrane had an array of 108 square pores with a pore size of 80 μm × 80 μm used in a previous study with silica nanoparticles (Manga et al., 2012). The membrane rotational speed was kept constant in a given experiment; rotational speeds were systematically varied here from 500 to 1,500 rpm. The oil injection rate was controlled using a syringe pump (Razel A99FMZ, Fisher Scientific, UK) with a wide range of pumping rates from $0.075 \times 10^{-6}$ to $75 \times 10^{-6}$ $m^3\ h^{-1}$ (corresponding to oil flow rates of $10^{-3}$ to 1 ml $min^{-1}$) and a total oil volume of 5 mL was injected for each experiment. The continuous phase used in each experiment was 25 mL with particle concentrations of 2 and 4 wt%. The optimal pH and electrolyte concentration to prepare emulsions were based on the findings from the bulk emulsion studies prepared using the homogenizer. Prior to emulsification, the latex dispersion was sonicated for 20 min before the emulsification experiments were carried out.

These emulsions were characterized to obtain the number average droplet diameter measured from optical microscopy images. To minimize distortion of the droplets during analysis pipettes with a wide opening were used and were imaged without glass cover slides. Optical microscopy was used here, as some of the droplets produced were too large for size measurement using standard laser diffraction techniques (e.g., Malvern Mastersizer). The average diameter and standard deviation of the emulsions was determined by manually measuring several hundred droplets.

# RESULTS AND DISCUSSION

## Solution Properties of the Copolymer

The di-block copolymers used are comprised of a hydrophobic block (MMA) and a hydrophilic block (DMAEMA). The latter allows for the resulting polymer to be readily soluble in weakly acidic aqueous environments (pH ≈ 4) due to the homopolymer exhibiting a p$K_a$ value between 7 and 7.5 (Baines et al., 1996). Indeed, the DMAEMA block contains a tertiary amine group that protonates as the pH decreases below the polymer p$K_a$, thus dictating the block solubility in water as a function of pH. Similar block copolymers have been reported to form micelle structures in solvents, which are selective for one of the blocks (Tuzar and Kratochvíl, 1976; Price, 1982; Munk et al., 1992). The study and characterization of such micellar structures is important when considering their role in the synthesis of latex particles via emulsion polymerization (Lovell and El-Aasser, 1997).

DLS measurements were performed to measure the changes in hydrodynamic diameter as a function of polymer concentration and DMAEMA block length, prepared at pH = 4 (below the pKa of the DMAEMA block, resulting in a protonated and thus water-soluble polymer) in the presence of 0.01 M $KNO_3$ electrolyte. The resulting changes, for all four DMAEMA block lengths synthesized are shown in **Figure 1**.

Although information regarding the individual size of the micelle core and corona cannot be gathered using DLS (Brookhaven), the measured hydrodynamic diameter gives indication of the overall size of the copolymer aggregates in solution. The data in **Figure 1** show that at low polymer concentrations (below 400–500 ppm) the copolymer exists as unimers, which results in smaller hydrodynamic diameters being measured. When the polymer concentrations reach a critical concentration and above, these individual chains self-assemble into micellar structures consisting of a hydrophobic core (MMA block) and a hydrophilic corona (DMAEMA block). The variation associated with the values presented in **Figure 1** are large, but they do seem to suggest that as the DMAEMA block length increases, the overall micellar aggregate diameter at pH 4 (at the cmc value) appears to decrease. This apparent decrease in hydrodynamic size matches similar observations reported by Xiao et al. (2012) where the change can be described by the packing parameter theory (Eastoe, 2005). As the DMAEMA block length increases, it leads to a hydrophilic head group occupying a larger volume, driving a higher degree of curvature for the assemblies with a corresponding smaller aggregate size.

The transition from unimers to equilibrium micellar aggregates occurs at different values as the DMAEMA content changes. An increase in the block length leads to an overall decrease in the CMC (in accordance with the standard definition, and known as CMC). This relationship is due to the fact that as the DMAEMA block length increases, the overall volume occupied by the headgroup also increases leading to greater separation distances between neighboring hydrophobic chains within the core (reduced density of unimer chains participating in the micelle structure). Therefore the energy transition point (where micelles represent the lower energy state to minimize solvophobic interactions) is reached at lower concentrations (Karayianni and Pispas, 2016). The cmc values reported here using dynamic light scattering are of the same order that were reported by Baines et al. (1996), i.e., 0.5 g/L using surface tension measurements, where the diblock copolymer studied was comprised of ∼80 mol% DMAEMA (similar to $DMAEMA_{54}$ in our case).

The changes in hydrodynamic diameter of the micellar aggregates (at 1,000 ppm i.e., above cmc at pH 4) as a function of solution pH was also measured to study the effect of DMAEMA block protonation/deprotonation (**Figure 2A**). The hydrodynamic diameter of the micellar aggregates increases as a function of increasing solution pH, which can be explained by examining the data from the pH titration of the polymer (**Figure 2B**). At low pH values (pH 4 and below) the amine groups are fully protonated leading to high surface charge densities. This protonation increases the electrostatic repulsive forces exhibited between neighboring chains and as a result the chain packing density will reduce to accommodate for the larger volume occupied by the hydrophilic block, leading to an

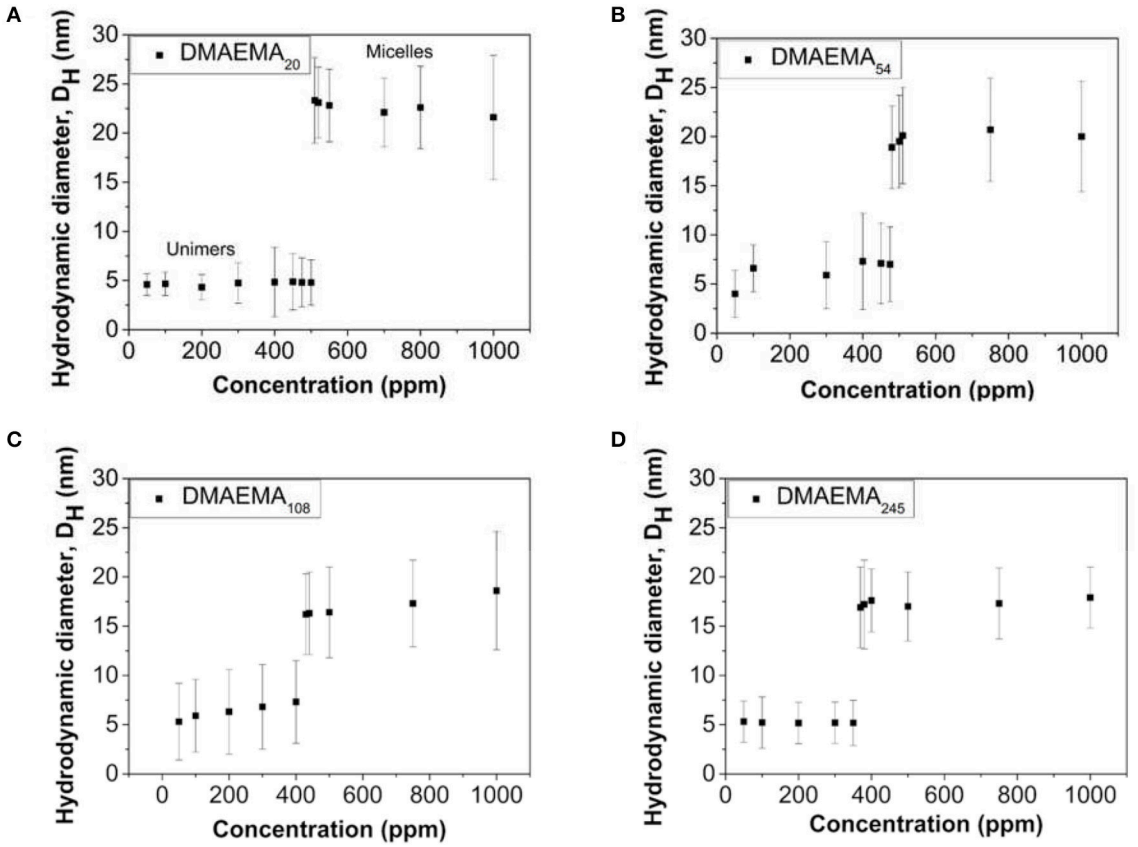


**FIGURE 1 |** Variation in the diblock copolymer (or the formed micellar aggregates) hydrodynamic diameter as a function of polymer concentration for four different DMAEMA block lengths; **(A)** 20, **(B)** 54, **(C)** 108, and **(D)** 245. The polymer solutions are prepared at pH 4 in the presence of 0.01 M $KNO_3$ ($T = 25°C$).

evolution of the self-assembled objects toward smaller aggregates containing fewer polymer chains. As the pH is increased, the DMAEMA block becomes increasingly deprotonated (majority of the polymer dissociation occurs over a narrow pH range), resulting in weaker electrostatic repulsive forces, which allows for more efficient packing of the polymer chains leading to micellar growth (Wesley et al., 2005). These trends are confirmed by similar observations found by Xiao et al. (2012). The degree of protonation data confirms that the DMAEMA block is weakly basic with a p$K_a$ value of around 7–7.5 (Amalvy et al., 2004), which slightly decreases with increasing pDMAEMA block length matching similar observations made in previous work (Van De Wetering et al., 1998). Similarly, increasing the DMAEMA monomer content at low pH values leads to the formation of seemingly smaller micellar aggregates, likely containing fewer polymer chains, due to the stronger repulsive forces resulting from the higher concentration of charges in the micelle coronas.

## Synthesis of Sterically Stabilized Latex Particles

### Effect of DMAEMA Block Length

Emulsion polymerization of styrene in the presence of the di-block copolymers was performed to investigate the influence of the DMAEMA block length stabilizer on the size of the resulting latex particles and their bulk properties. To determine the effect on particle size only, measurements using DLS and Scanning Electron Microscopy were performed at pH 8. At this pH, it was assumed that the polymer would retract back onto the surface of the latex particles, but not lead to flocculation and therefore, allow comparisons of the particle core size using both techniques. Size measurements of the latex particles are presented in **Table 2**, scanning electron micrographs are presented in Supplementary Information (Figures S2.1, S2.2) where all particles synthesized were spherical in shape.

The polymerization in the presence of the smallest diblock, i.e., $DMAEMA_{20}$ (LP-$DMAEMA_{20}$) led to an uncontrolled process that resulted in the formation of particles with high polydispersity on numerous occasions and was therefore not further evaluated as part of this study. This issue was not observed with the other three di-block copolymers. The data in **Table 2** illustrates that the latex particle diameter generally increases as the pDMAEMA block length increases. For the polymerization reaction, the mass of polymeric stabilizers was fixed at 0.5 g which was well above the polymer CMC values (>10,000 ppm) outlined in **Figure 1**. However, it is worth noting that fixing the mass of polymer corresponded to a decrease in the molar concentration of the polymer in solution (i.e., number of polymer chains) with

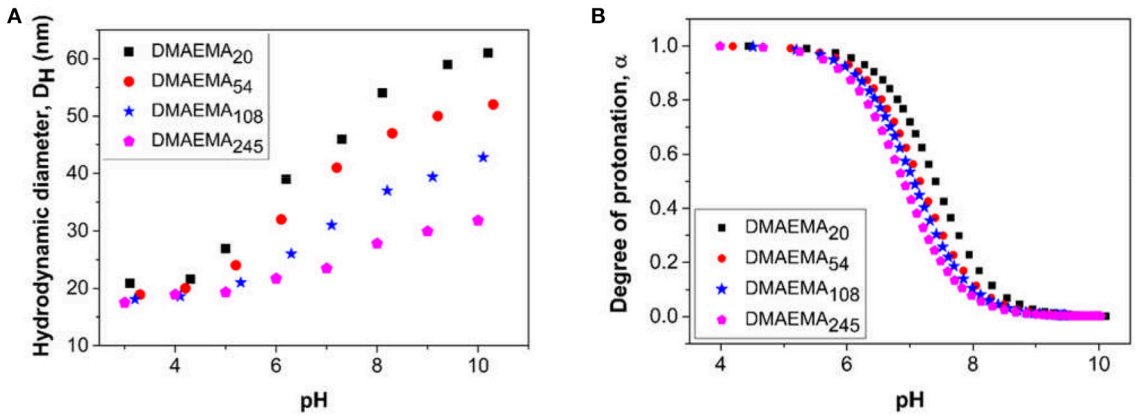


**FIGURE 2 |** Changes in **(A)** hydrodynamic diameter and **(B)** degree of polymer protonation as a function of solution pH for the four diblock copolymers prepared at a concentration of 1,000 ppm (above the CMC). The polymer solutions are prepared in the presence of 0.01 M $KNO_3$, ($T = 25°C$). The $pK_a$ of the copolymers obtained are; $DMAEMA_{20} = 7.41$, $DMAEMA_{54} = 7.16$, $DMAEMA_{108} = 7.08$, and $DMAEMA_{245} = 6.92$.

**TABLE 2 |** Influence of DMAEMA block length on latex particle diameters synthesized with the various diblock copolymers used as stabilizers in the emulsion polymerization process.

| Sample | Number of DMAEMA units in the block copolymer. | DLS latex particle hydrodynamic diameter (nm) (polydispersity) | SEM latex particle (dry) diameter (nm) (polydispersity) |
|---|---|---|---|
| LP-$DMAEMA_{20}$ | 20 | – | – |
| LP-$DMAEMA_{54}$ | 54 | 57 (0.06) | 53 (0.06) |
| LP-$DMAEMA_{108}$ | 108 | 68 (0.08) | 64 (0.09) |
| LP-$DMAEMA_{245}$ | 245 | 87 (0.05) | 84 (0.07) |

*Mass of polymer stabilizers and reaction temperatures (70°C) were kept constant.*

increasing DMAEMA content (by virtue of increasing molecular weight) which is summarized in Table S3 in the Supplementary Information. It was assumed the molar reduction may play a role in the reaction initiation process, as well as clearly particle growth and stability. Indeed, it is evident that the increase in latex particle size may be caused by the reduction in stabilizer units for the larger DMAEMA block copolymers, as the lower total number of chains would therefore not be able to stabilize the same total particle surface area as the smaller units.

### Polymer Grafting Density

The grafting density of the polymer chains onto the latex particle provides important information about how the polymer stabilizer molecular weight may influence the properties of the resulting core-shell latex particles. To measure the polymer chain grafting density on the surface of the particles, $^1$H NMR spectroscopy experiments were performed after dissolution of the latex particles in $CDCl_3$. The block copolymer grafting densities of all successful latex particles samples are presented in **Table 3**.

The data in **Table 3** show that the number of polymer chains occupied per unit surface area of the particle decreases with increasing DMAEMA block length. As discussed, because the mass of the stabilizer used in the polymerization process was fixed, increasing the DMAEMA meant that there are fewer chains in solution to begin with (due to higher polymer molecular weight) and a resultant formation of larger particles. Additionally, the fact that the grafting density also reduced, is also indicative of the greater steric repulsions of the larger DMAEMA head groups.

The grafting densities obtained by $^1$H NMR can be compared with theoretical values that one would expect (summarized in Table S3 in the Supplementary Information) assuming that (i) all the styrene monomer is converted into polystyrene particles, (ii) using mean particle size to calculate total particle surface area based on SEM measurements and (iii) all the polymer chains are located on the particle surface. These theoretical grafting densities also decrease with increasing DMAEMA content using particle sizes (based on mean diameters via SEM) obtained during polymerization. The theoretical grafting density values are around 20–30% higher than those calculated using $^1$H NMR, as in reality the polymerization conversion is less than 100%. The reduced number of polymer chains and grating density in turn affects the number of amine groups available per particle, which ultimately dictates the behavior of the particles in suspension and as emulsifiers in response to environmental pH and electrolyte conditions.

## Influence of pH and Electrolyte Concentration on the Latex Particle Suspension Properties

The effect of pH and electrolyte concentration on the properties of the particle dispersions was investigated by measuring changes to the hydrodynamic diameter and electrophoretic mobility, for the successful particle synthesis samples (LP-$DMAEMA_{54}$ to LP-$DMAEMA_{245}$) and are presented in **Figure 3**. The behavior of the samples in suspension is

**TABLE 3 |** Number of polymer chains and amine groups per particle derived from $^1$H NMR experiments carried out in $CDCl_3$ after dissolution of the synthesized particles.

| Sample code | Molecular Weight | Adsorbed amount, Γ (mg.m$^{-2}$) | Chains/nm$^2$ | Chains per particle | Amine groups per particle |
|---|---|---|---|---|---|
| LP-DMAEMA$_{54}$ | 10,110 | 0.23 | 0.018 | 53 | 2,862 |
| LP-DMAEMA$_{108}$ | 18,600 | 0.24 | 0.0072 | 42 | 4,536 |
| LP-DMAEMA$_{245}$ | 40,340 | 0.3 | 0.0045 | 29 | 7,105 |

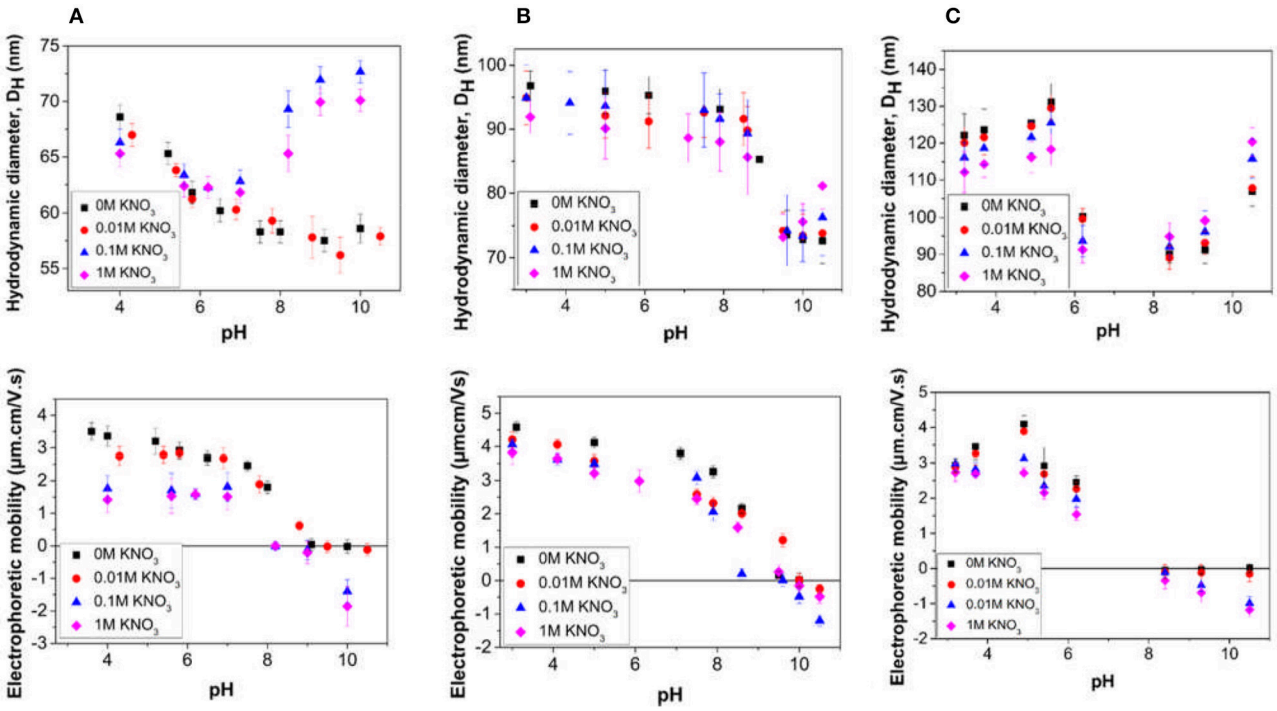


**FIGURE 3 |** Influence of pH and electrolyte concentration on the properties of particle dispersions obtained from emulsion polymerizations conducted in the presence of the different diblock copolymers **(A)** LP-DMAEMA$_{54}$, **(B)** LP-DMAEMA$_{108}$ and **(C)** LP-DMAEMA$_{245}$. Electrolyte concentrations used for the measurements were (■) 0 M (i.e., no added) $KNO_3$, (●) 0.01 M $KNO_3$, (▲) 0.11 M $KNO_3$, and (♦) 1 M $KNO_3$.

observed to be significantly dependent on the stabilizer chain length.

For sample LP-DMAEMA$_{54}$ (**Figure 3A**), as the pH is decreased from around pH 8 to pH 4, there is a clear increase in the electrophoretic mobility toward a plateau value, as a result of the protonation of the amine groups on the DMAEMA. This behavior is consistent with the pure polymer protonation (**Figure 2**).The charging also results in an observed slight increase in the measured particle diameter, assumed to be due to extension of the grafted and charged polymer stabilizer chains. It is interesting that for this sample, at very low pH values, the mobility is relatively constant, whereas the diameter seems to further increase as the pH reduces. Although the number of polymer chains present per surface area is highest for this system (**Table 3**) the number of amine groups present per particle is the lowest of the three samples. Steric hindrance from the relatively high grafting density may influence the hydrodynamic response of the polymer at these low pH conditions and further work is needed to fully understand this behavior.

Increasing the pH of the LP-DMAEMA$_{54}$ particle dispersions above 8 results in an increase to the measured particle size (especially at higher salt levels) whilst the measured mobility remains close to zero. At high pH, the polymer on the particle surface is deprotonated and as a result it is no longer soluble in the bulk, therefore collapsing onto the particle surface. The measured increase in the hydrodynamic diameter is most likely caused by the formation of particle aggregates driven by inter-segmental attraction between the uncharged DMAEMA chains on the surface of approaching particles. Such changes will be further driven through salt coagulation.

For the latex particles sterically stabilized by LP-DMAEMA$_{245}$ (**Figure 3C**) there is a contrast in the particle hydrodynamic diameter changes below the polymer p$K_a$, where the measured size reaches a maximum value at pH 5 before decreasing with lower solution pH. A potential reason for this behavior is that while the number of polymer chains per particle is lower than LP-DMAEMA$_{54}$, the larger chain length occupies a larger volume per particle surface area, and overall, there are many more

charge groups per particle (**Table 3**). These differences make it more susceptible to changes in pH and electrolyte conditions. Therefore, as the pH is decreased, it is more likely that there is a salting effect from the high electrolyte levels at low pH, which reduces the electrostatic repulsion between the chains and hence a reduction in overall size is observed. The effect of electrolyte is more evident for LP-DMAEMA$_{245}$ at low pH, with measured diameters being lower for high salt conditions (attributed to greater salting-out effect). At high pH, there is also evident aggregation of the dispersions from destabilization of the particles as a result of the collapsed chains.

Aggregation of the particles appears to be less pronounced for the LP-DMAEMA$_{108}$ sample (**Figure 3B**), which does not appear to be related to the amine moiety density (that varies with increasing block length). Instead, it is thought that this is a direct consequence of the surface charge distribution on the three different samples. Indeed, the electrophoretic measurements carried out for the LP-DMAEMA$_{108}$ sample show clearly a shift to higher pHs for the point of zero charge of the particles. This is likely due to differences of initiator species incorporation on the particle surfaces between the different latex samples, as these species carry a negative charge, which can compensate for some of the positive charges resulting from the polymer. Nevertheless, the observed difference in the point of zero charge is likely to be responsible for the lack of aggregation of the LP-DMAEMA$_{108}$ sample at the high pH values tested in this study, although it is expected that aggregation for this sample is likely to occur at slightly higher pHs.

## Influence of DMAEMA Block Length on Pickering Emulsion Stability

The three latex samples were investigated to determine their performance as Pickering stabilizers. Since the base particle size and the pMMA block lengths are similar, the influence of DMAEMA content on emulsion stability across the pH range can be assessed. Emulsions created at varying solution pH values with no added background electrolyte to the continuous phase are illustrated in **Figure 4**. The emulsions were left to stand at 25°C for 24 h prior to characterization.

The digital micrographs and droplet size data show varying degrees of emulsion stability as a function of solution pH. When examining emulsions created with LP-DMAEMA$_{54}$, a highly stable emulsion with a mean droplet size of 25 μm is produced at pH 9.6, as the pDMAEMA chains become deprotonated at this pH and therefore collapse back on the surface of the particle (increasing the hydrophobic character of the particles) and thus improving particle wettability at the o/w interface. Increasing the pH to 10.9 leads to droplet coalescence (large polydisperse droplets) and macroscopic phase separation occurs. It is assumed this instability is due to adsorption of latex aggregates, driven by intersegmental attraction of the deprotonated pDMAEMA chains (as observed from increased dispersion size data in **Figure 3**) producing larger droplets that are destabilized. When the pH is decreased below 9.6 (pH 7.9–3), emulsions with macroscopic phase separation are observed. This change is due to the pDMAEMA chains becoming protonated, i.e., more cationic with increased solubility in the water phase, thus reducing their affinity for the interface. The observed behavior is in agreement with studies on similar responsive emulsion stabilizers reported previously (Amalvy et al., 2003, 2004).

When sample LP-DMAEMA$_{245}$ is used as an emulsifier, the trend in emulsion stability/instability differs somewhat (as evidenced by differences in deprotonation pH from latex size and mobility in **Figure 3**). Although the same trend is found at pH 9.5 and above, decreasing the pH results in a wider band of pH for stable emulsions down to pH 6.6. Such changes may

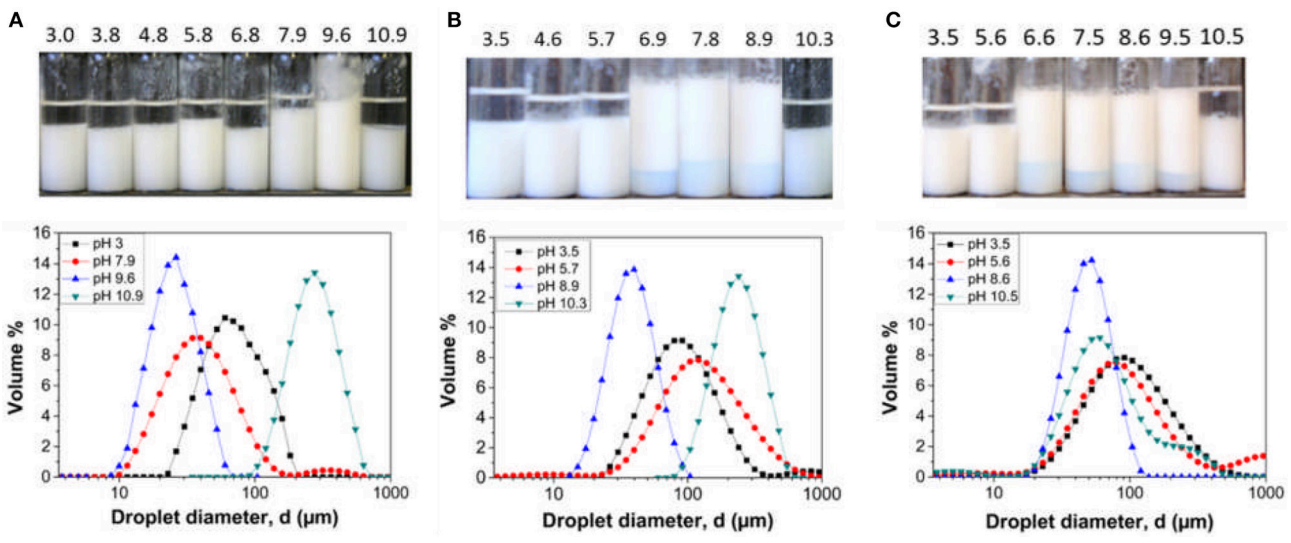


**FIGURE 4 |** Hexadecane in water emulsions stabilized by **(A)** LP-DMAEMA$_{54}$, **(B)** LP-DMAEMA$_{108}$ and **(C)** LP-DMAEMA$_{245}$ as a function of pH. Digital micrographs of the emulsions 24 h after production (top) and the droplet diameter distribution based on volume % (bottom). No background electrolyte was added to the continuous phase and measurements were performed a 25°C.

be explained by considering how the polymer chains behave as free polymers in solution vs. grafted onto a particle surface. In solution, the amine groups are highly susceptible to pH changes, and therefore the pH range for protonation is markedly narrow (as shown in **Figure 2**). When the same chains are grafted onto a particle surface, their response to environmental pH may be modified in magnitude or range. For larger chemically grafted polyelectrolytes, parts of the chain that are closer to the particle surface may remain unchanged, due to local screening effects leading to a distribution of charges along the polymer chain. Furthermore, at pH 9.5 where the polymer is deprotonated (i.e., in a collapsed state on the particle surface), decreasing the pH should begin to increase the degree of polymer protonation (based on the free polymer data presented in **Figure 2**). In reality, the protonation is most likely to be slower on a surface than when the polymer is dissolved in the bulk due to steric hindrance between the collapsed polymer chains. Lastly, the strength of the particle adsorption at the interface will be dictated by the polymer charge and its corresponding influence on the overall contact angle. Decreasing the pH below 6.6, the polymer degree of protonation increases and will drive a much larger affinity for the bulk for the particles, resulting in decreased particle adsorption energies and thus a more likely emulsion droplet coalescence with eventually macroscopic phase separation occurring.

The trend in emulsion stability when using LP-DMAEMA$_{108}$ exhibits similar characteristics to LP-DMAEMA$_{54}$ at low pH values and LP-DMAEMA$_{245}$ around the polymer p$K_a$ and above. The grafting density of LP-DMAEMA$_{108}$ is similar to that of LP-DMAEMA$_{54}$, but because of the larger polymer block length, the number of amine groups per particle is higher and thus their adsorption behavior as a function of pH lies in between that observed with LP-DMAEMA$_{54}$ and LP-DMAEMA$_{245}$.

The effect of adding background electrolyte on emulsion stability across the pH range was also examined. Digital micrographs and droplet size data of the emulsions created with 0.01 M $KNO_3$ is presented in **Figure 5**.

The addition of background electrolyte to emulsions created with LP-DMAEMA$_{54}$ shows an improvement in emulsion stability (volume of coalesced oil noticeably decreased) especially at the lower pH values. By adding electrolyte, screening of the protonated amine groups results in the polymer becoming less soluble in the continuous phase and it adopts a less extended configuration, enhancing the interfacial wettability of the latex particles. Additionally, low levels of background electrolyte (below levels causing bulk coagulation) may promote stronger interfacial films, with greater interfacial elasticity (Yu et al., 2017). This trend is confirmed by a shift in the droplet size data toward smaller sizes when compared to emulsion droplets created in the absence of background electrolyte. With LP-DMAEMA$_{245}$, the effect of adding background electrolyte leads to improvements in emulsion stability at the extreme pH values examined. However, phase separation still occurs at pH 4.9 and 5.7, as the combination of adding background electrolyte and the electrolyte formed due to pH alteration (to reach these moderately acidic pH's) appears to not sufficiently screen the polymer charges in this case (as the number of charge groups is larger).

It is noted that, importantly, the emulsion droplet sizes (in the most stable pH region) are larger for the LP-DMAEMA$_{245}$ samples than the particles with smaller charged block length. This difference is likely partially due to the particles being larger (as it is well known that smaller nanoparticles attain higher packing efficiencies and thus are better Pickering emulsifiers (Hunter et al., 2008). Differences may also be due to changes in particle wettability as the polymer length is altered, although, a previous study by Reed et al. (2012) on similar latex systems found that

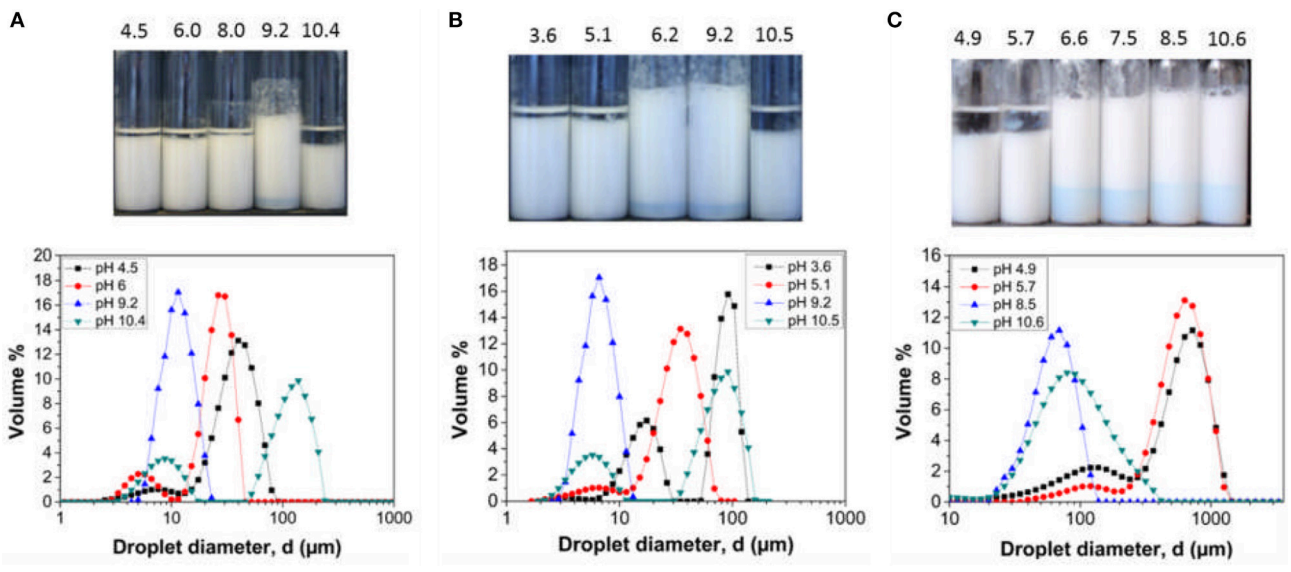


**FIGURE 5 |** Digital images (top) and droplet size data (bottom) for hexadecane in water emulsions stabilized by **(A)** LP-DMAEMA$_{54}$, and **(B)** LP-DMAEMA$_{108}$, and **(C)** LP-DMAEMA$_{245}$ as a function of pH in the presence of 0.01 M $KNO_3$. Measurements were performed at 25°C.

the particle contact angle at the interface was insensitive to the polymer chain length ($PGMA_n$), as the polymer grafting density was high (larger than unity for all $PGMA_n$–PS latexes studied). The grafting densities we obtain however are significantly lower, and as a result, the chain length may induce larger changes in particle wettability.

Despite the larger minimum droplet sizes, emulsions produced from LP-$DMAEMA_{245}$ were considered more "responsive" than the other particles, as droplet sizes at lower pHs increased much more markedly (with mean sizes in the order of 1,000 μm). As a key potential application of such responsive Pickering systems would be the retention and release of oil-phase actives with a pH trigger, it was clear the LP-$DMAEMA_{245}$ samples provided a better response envelope overall.

It is additionally noted, that increasing the concentration of the background electrolyte further resulted in larger emulsion droplets across the pH range investigated, although no macroscopic phase separation was observed (Figures S4.1, S4.2).

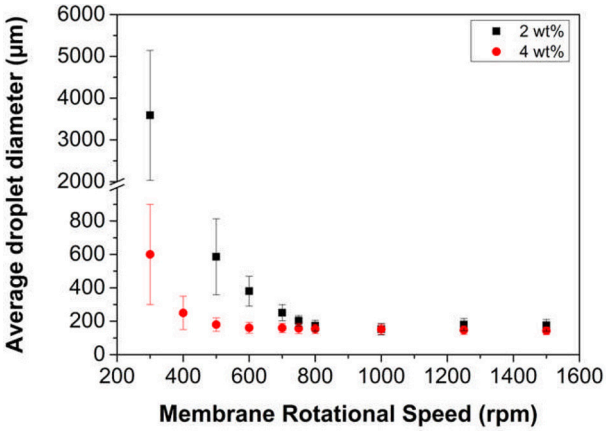


**FIGURE 6 |** Variation in mean droplet size of hexadecane in water emulsions as a function of membrane rotation speed at 2 and 4 wt% particle loading of LP-$DMAEMA_{245}$. The continuous phase contained an electrolyte concentration of 0.01 M $KNO_3$ at pH 9. The oil injection rate was fixed at 0.01 mL $min^{-1}$.

## Improving Droplet Size Control via Membrane Emulsification Techniques

Membrane emulsification is a technique to produce controlled droplets by expressing the dispersed phase through a porous membrane (with well-defined pores) in a drop by drop manner into a continuous phase containing the emulsifier. Droplet detachment occurs, due to shear forces acting on the membrane surface created by either a crossflow of the continuous phase over the membrane surface (Schröder et al., 1998; Williams et al., 1998; Bux et al., 2016), rotation/vibration of the membrane (Vladisavljević and Williams, 2006; Manga et al., 2012), or by mechanical stirring (Dragosavac et al., 2008; Thompson et al., 2011; Manga and York, 2017).

In this study, rotational membrane emulsification (RME) is used to explore the potential of using the sterically stabilized particles to produce controlled emulsions. The RME is a sensible rig to conduct such studies, as it allows for small scale experiments to be performed easily without the need for substantial quantities of the latex emulsifier. Based on the bulk emulsion studies, it was decided to perform the experiments at a solution pH of 9 and at a background electrolyte of 0.01 M $KNO_3$ to ensure successful particle adsorption and stable emulsions (see **Figure 5**).

The residence time of the droplet at the membrane surface prior to detachment plays an important role in controlling the droplet size and size distribution of the emulsion (Manga et al., 2012). The residence time is controlled by the shear rate imparted at the membrane surface and in the case of RME this is done by the rotation of the membrane within the continuous phase. The influence of this rotation speed on droplet size and size distribution data when using LP-$DMAEMA_{245}$ latex particles is presented in **Figure 6**. The oil injection rate was fixed at 0.01 mL $min^{-1}$, which was selected based on the optimized conditions found previously when studying with 800 nm silica colloids (Manga et al., 2012).

In the case where a 2 wt% concentration of the latex emulsifier is used, large polydisperse droplets form at the lowest membrane rotation speed (i.e., 300 rpm). During the emulsification process at this speed, it is difficult to determine if these large droplets are a result of coalescence occurring in the bulk due to the opacity of the latex dispersion. The solution conditions as well as fast diffusion times of the particles from the bulk to the interface (due to their hydrodynamic diameter) should result in a stable emulsion with small diameters. However, the shear rate at the membrane surface is low and thus the droplets either (a) grow to a large size before detaching or (b) merge together from adjacent pores. As the speed is increased, both the droplet size and size distribution decreases with an apparent minimum occurring around 1,000 rpm. The increase in shear rate and fast particle adsorption times allow for such controlled droplets to be produced. It should be noted that there is very little difference in the droplet size for samples created between 800 and 1,500 rpm, representing the minimum size distributions possible from the membrane pore size.

Increasing the particle emulsifier concentration to 4 wt%, effectively increases the collision frequency between the particles and the interface from the greater particle loading, and resulted in improvements to both size and size distribution at the lower rotation speeds (300–600 rpm). This difference is driven by two significant factors. It is known that the grafted pDMAEMA is surface active, and will reduce the interfacial tension to equilibrium values much faster at higher particle loading (Manga et al., 2016) (higher collision rate with the interface). Additionally, the greater particle number will increase the total surface area that is able to be stabilized for a given particle loading, which together with surface tension reduction leads to the production of smaller droplets evident at the lower rotation speeds. However, at greater speeds, the size is similar for both particle concentrations, as the droplet breakup tends toward a minimum size value for a given oil flow rate, regardless of shear

rate (over a certain threshold) dependent on the membrane pore size. This behavior is analogous to surfactant systems that have been studied (Vladisavljević and Williams, 2006) and matches a similar trend that was observed when 800 nm silica colloids were used (Manga et al., 2012). However, improvements in size and polydispersity are more pronounced with the latex particles, due to the influence of faster adsorption kinetics (from the smaller particle size) and surface active nature of the particles (Manga et al., 2016).

The oil injection rate through the porous membrane governs the rate at which new interfacial area is created, and therefore plays a critical role in controlling the droplet size and size distribution obtained. Additionally, from a production scale-up perspective, it is imperative to understand what are the maximum stable emulsion production rates possible for a given membrane size. Changes in mean droplet size with oil injection rate are presented in **Figure 7**, with a fixed membrane rotation speed of 1,000 rpm, again at two particle loadings.

At the fastest injection rate studied (1 mL $min^{-1}$), emulsions with large polydisperse droplets are produced when using a latex concentration of 2 wt%. Increasing the concentration to 4 wt% dramatically causes a reduction in both the observed mean droplet diameter and associated size distribution. This reduction highlights the importance of adsorption kinetics, as by increasing the particle concentration the particle collision rate with the newly forming interface also increases. Decreasing the oil injection rate reduces the droplet sizes further to ~150 μm at 0.01 mL $min^{-1}$. Since the shear force acting at the membrane surface is fixed, growth and detachment of the droplets from the membrane pore will occur at a fixed timescale. Therefore, size invariance at low injection rates, will most likely be due to high particle effective collision frequency and reduction of the interfacial tension, as the interface production rates are reduced below a certain critical threshold to produce stable droplets.

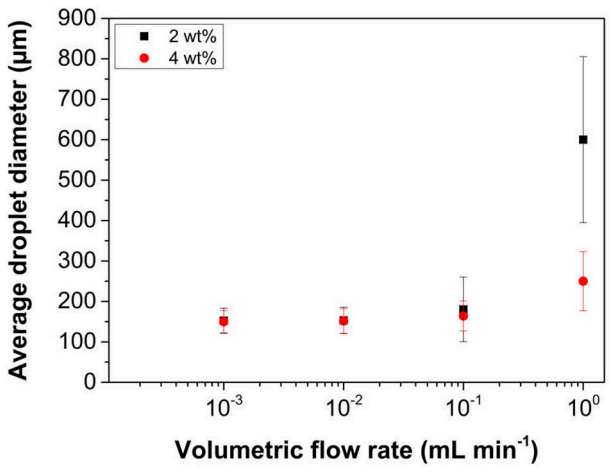


**FIGURE 7 |** Variation in mean droplet size of hexadecane in water emulsions as a function of oil injection rate at 2 and 4 wt% particle loading of LP-$DMAEMA_{245}$. The continuous phase contained an electrolyte concentration of 0.01 M $KNO_3$ at pH 9. The membrane rotation speed was fixed at 1,000 rpm.

These data illustrate that the sterically stabilized latex particles can act as very efficient emulsifiers when using membrane emulsification technologies, provided the emulsification parameters have been fully optimized. With this single membrane device, for a production rate of 1 mL $min^{-1}$ (where droplet coefficient of variation is 30% at a particle loading of 4 wt%) a 100 mL of emulsion (with a volume fraction of 20%) can be produced in 20 min. In comparison, microfluidic devices such as T-junctions are able to generate highly monodisperse droplets (size variation as low as 3%) however the flow rate of the disperse flow rate is very low, typically 0.01–10 mL $h^{-1}$ (Basile and Charcosset, 2015). Taking the fastest rate, the example emulsion mentioned above would take almost 120 min to produce. The productivity can be increased by parallelization of the fluidic channels, however issues arise with regards to pressure drops, channel blockages and controlling the flow rates of individual streams in long channel networks. This is less of an issue in membrane emulsification, so by increasing the active membrane surface area or by parallelization, the overall throughput can be further increased.

## CONCLUSIONS

This study has demonstrated that DMAEMA monomer content plays a critical role in the synthesis of latex particles sterically stabilized by pMMA-b-pDMAEMA diblock copolymers, and their resulting performance as pH responsive Pickering emulsifiers. Increasing the pDMAEMA block length alters the solution behavior of these polymers, leading to a reduction in the CMC, which is an important parameter in latex synthesis via emulsion polymerization, as well as their hydrodynamic diameters and p$K_a$. During synthesis of the latex emulsifiers, increasing the DMAEMA content of the steric stabilizer leads to formation of larger particles, due to the influence of monomer content on micelle numbers when a fixed polymer concentration by weight is used.

When used as emulsifiers, pH-responsive emulsions are obtained, which were typically stable above the polymer p$K_a$, where macroscopic phase separation occurred below it, caused by the reduction in contact angle from particle charging. Destabilization was also evident at very high pH, and was assumed to be driven by particle aggregation in the bulk. The transition between emulsion stability and instability in the presence of very low electrolyte concentrations was dictated by the DMAEMA monomer content and its grafting density onto the latex emulsifiers. Overall, the largest block length stabilizer, resulted in the most pH responsive emulsions. Finally, it was shown that emulsions with well controlled sizes can be produced using a RME, providing the emulsification parameters are well optimized. In particular, the importance of the interplay between particle concentration vs. shear rate and rate of interfacial area production is presented.

## AUTHOR CONTRIBUTIONS

MM was primarily responsible for the collection of all data reported here and its initial analysis as well as aspects of the

experimental design. MM was also the primary author of the article and was responsible for various drafts and final approval. OC, SB, and TH contributed to the analysis and interpretation of the data along with critical revisions to the draft manuscript. OC, SB, and TH also gave approval to the final version of the paper.

## FUNDING

This work was supported by the EPSRC (grant number EP/G501521/1) and case support from Procter & Gamble.

## ACKNOWLEDGMENTS

The authors thank Dr. G. Bacquey, Dr. M. Manguian, and Dr. N. Chagneux for their help with the synthesis and characterization of the pH-responsive polymer used in this study. Dr. A. Richez is thanked for his help in characterizing the grafting density of the particles.

## SUPPLEMENTARY MATERIAL

The Supplementary Material for this article can be found online at: https://www.frontiersin.org/articles/10.3389/fchem.2018.00301/full#supplementary-material

## REFERENCES

Amalvy, J., Armes, S., Binks, B., Rodrigues, J., and Unali, G. (2003). Use of sterically-stabilised polystyrene latex particles as a pH-responsive particulate emulsifier to prepare surfactant-free oil-in-water emulsions. *Chem. Commun.* 1826–1827. doi: 10.1039/b304967a

Amalvy, J. I., Unali, G. F., Li, Y., Granger-Bevan, S., Armes, S. P., Binks, B. P., et al. (2004). Synthesis of sterically stabilized polystyrene latex particles using cationic block copolymers and macromonomers and their application as stimulus-responsive particulate emulsifiers for oil-in-water emulsions. *Langmuir* 20, 4345–4354. doi: 10.1021/la035921c

Baines, F. L., Billingham, N. C., and Armes, S. P. (1996). Synthesis and solution properties of water-soluble hydrophilic–hydrophobic block copolymers. *Macromolecules* 29, 3416–3420. doi: 10.1021/ma951699+

Basile, A., and Charcosset, C. (2015). *Integrated Membrane Systems and Processes*. Chichester, UK: John Wiley & Sons.

Biggs, S., Williams, R., Cayre, O., and Yuan, Q. (2008). *Microcapsules and Methods*. US20110008427A1.

Binks, B. P. (2002). Particles as surfactants - similarities and differences. *Curr. Opin. Colloid Interface Sci.* 7, 21–41. doi: 10.1016/S1359-0294(02)00008-0

Binks, B. P. (2017). Colloidal particles at a range of fluid–fluid interfaces. *Langmuir* 33, 6947–6963. doi: 10.1021/acs.langmuir.7b00860

Binks, B. P., and Horozov, T. S. (2005). Aqueous foams stabilized solely by silica nanoparticles. *Angew. Chem. Int. Ed.* 44, 3722–3725. doi: 10.1002/anie.200462470

Binks, B. P., and Horozov, T. S. (2006). *Colloidal Particles at Liquid Interfaces*. Cambridge, UK: Cambridge University Press. doi: 10.1017/CBO9780511536670

Binks, B. P., and Lumsdon, S. O. (1999). Stability of oil-in-water emulsions stabilised by silica particles. *Phys. Chem. Chem. Phys.* 1, 3007–3016. doi: 10.1039/a902209k

Bux, J., Manga, M. S., Hunter, T. N., and Biggs, S. (2016). Manufacture of poly(methyl methacrylate) microspheres using membrane emulsification. *Philos. Trans. Royal Soc. A.* 374:20150134. doi: 10.1098/rsta.2015.0134

Cayre, O. J., Hitchcock, J., Manga, M. S., Fincham, S., Simoes, A., Williams, R. A., et al. (2012). pH-responsive colloidosomes and their use for controlling release. *Soft Matter* 8, 4717–4724. doi: 10.1039/c2sm00002d

Dickinson, E. (2010). Food emulsions and foams: stabilization by particles. *Curr. Opin. Colloid Interface Sci.* 15, 40–49. doi: 10.1016/j.cocis.2009.11.001

Dinsmore, A. D., Hsu, M. F., Nikolaides, M. G., Marquez, M., Bausch, A. R., and Weitz, D. A. (2002). Colloidosomes: selectively permeable capsules composed of colloidal particles. *Science* 298, 1006–1009. doi: 10.1126/science.1074868

Dragosavac, M. M., Sovilj, M. N., Kosvintsev, S. R., Holdich, R. G., and Vladisavljević, G. T. (2008). Controlled production of oil-in-water emulsions containing unrefined pumpkin seed oil using stirred cell membrane emulsification. *J. Membr. Sci.* 322, 178–188. doi: 10.1016/j.memsci.2008.05.026

Dupin, D., Armes, S. P., Connan, C., Reeve, P., and Baxter, S. M. (2007). How does the nature of the steric stabilizer affect the Pickering emulsifier performance of lightly cross-linked, acid-swellable poly(2-vinylpyridine) latexes? *Langmuir* 23, 6903–6910. doi: 10.1021/la063170j

Eastoe, J. (2005). *Surfactant Chemistry*. Wuhan: Wuhan University Press.

Finkle, P., Draper, H. D., and Hildebrand, J. H. (1923). The theory of emulsification 1. *JACS* 45, 2780–2788. doi: 10.1021/ja01665a002

Fujii, S., Armes, S. P., Binks, B. P., and Murakami, R. (2006). Stimulus-responsive particulate emulsifiers based on lightly cross-linked poly(4-vinylpyridine)–silica nanocomposite microgels. *Langmuir* 22, 6818–6825. doi: 10.1021/la060349l

Fujii, S., and Nakamura, Y. (2017). Stimuli-responsive bubbles and foams stabilized with solid particles. *Langmuir* 33, 7365–7379. doi: 10.1021/acs.langmuir.7b01024

Fujii, S., Read, E. S., Binks, B. P., and Armes, S. P. (2005). Stimulus-responsive emulsifiers based on nanocomposite microgel particles. *Adv. Mater.* 17, 1014–1018. doi: 10.1002/adma.200401641

Hunter, T. N., Pugh, R. J., Franks, G. V., and Jameson, G. J. (2008). The role of particles in stabilising foams and emulsions. *Adv. Colloid Interface Sci.* 137, 57–81. doi: 10.1016/j.cis.2007.07.007

Karayianni, M., and Pispas, S. (2016). "Self-assembly of amphiphilic block copolymers in selective solvents," in *Fluorescence Studies of Polymer Containing Systems*, ed. K. Procházka (Gewerbestrasse: Springer), 27–63. doi: 10.1007/978-3-319-26788-3_2

Lam, S., Velikov, K. P., and Velev, O. D. (2014). Pickering stabilization of foams and emulsions with particles of biological origin. *Curr. Opin. Colloid Interface Sci.* 19, 490–500. doi: 10.1016/j.cocis.2014.07.003

Li, Z., and Ngai, T. (2011). Stimuli-responsive gel emulsions stabilized by microgel particles. *Colloid. Polym. Sci.* 289, 489–496. doi: 10.1007/s00396-010-2362-z

Liu, T., Seiffert, S., Thiele, J., Abate, A. R., Weitz, D. A., and Richtering, W. (2012). Non-coalescence of oppositely charged droplets in pH-sensitive emulsions. *Proc. Natl. Acad. Sci. U.S.A.* 109, 384–389. doi: 10.1073/pnas.1019196109

Lovell, P. A., and El-Aasser, M. S. (1997). *Emulsion Polymerization and Emulsion Polymers*. Chichester, UK: Wiley.

Manga, M. S., Cayre, O. J., Williams, R. A., Biggs, S., and York, D. W. (2012). Production of solid-stabilised emulsions through rotational membrane emulsification: influence of particle adsorption kinetics. *Soft Matter* 8, 1532–1538. doi: 10.1039/C1SM06547E

Manga, M. S., Hunter, T. N., Cayre, O. J., York, D. W., Reichert, M. D., Anna, S. L., et al. (2016). Measurements of submicron particle adsorption and particle film elasticity at oil–water interfaces. *Langmuir* 32, 4125–4133. doi: 10.1021/acs.langmuir.5b04586

Manga, M. S., and York, D. W. (2017). Production of concentrated Pickering emulsions with narrow size distributions using stirred cell membrane emulsification. *Langmuir* 33, 9050–9056. doi: 10.1021/acs.langmuir.7b01812

Moad, G., Chiefari, J., Chong, Y. K., Krstina, J., Mayadunne, R. T. A., Postma, A., et al. (2000). Living free radical polymerization with reversible addition – fragmentation chain transfer (the life of RAFT). *Polym. Int.* 49, 993–1001. doi: 10.1002/1097-0126(200009)49:9<993::AID-PI506>3.0.CO;2-6

Morse, A. J., Dupin, D., Thompson, K. L., Armes, S. P., Ouzineb, K., Mills, P., et al. (2012). Novel Pickering emulsifiers based on pH-responsive poly(tert-butylaminoethyl methacrylate) latexes. *Langmuir* 28, 11733–11744. doi: 10.1021/la301936k

Munk, P., Ramireddy, C., Tian, M., Webber, S. E., Procházka, K., and Tuzar, Z. (1992). Block copolymer micelles in aqueous media. *Makromol. Chem. Macromol. Symp.* 58, 195–199. doi: 10.1002/masy.19920580115

Pickering, S. U. (1907). CXCVI.-emulsions. *J. Chem. Soc.* 91, 2001–2021. doi: 10.1039/CT9079102001

Price, C. (1982). "Colloidal properties of block copolymers," in *Developments in Block Copolymers-1*, ed I. Goodman (London: Applied Science Publishers), 39–80.

Ramsden, W. (1903). Separation of solids in the surface-layers of solutions and 'suspensions' (observations on surface-membranes, bubbles, emulsions, and mechanical coagulation).—Preliminary account. *Proc. Royal Soc. Lond.* 72, 156–164.

Read, E., Fujii, S., Amalvy, J., Randall, D., and Armes, S. (2004). Effect of varying the oil phase on the behavior of pH-responsive latex-based emulsifiers: demulsification versus transitional phase inversion. *Langmuir* 20, 7422–7429. doi: 10.1021/la049431b

Reed, K. M., Borovicka, J., Horozov, T. S., Paunov, V. N., Thompson, K. L., Walsh, A., et al. (2012). Adsorption of sterically stabilized latex particles at liquid surfaces: effects of steric stabilizer surface coverage, particle Size, and chain length on particle wettability. *Langmuir* 28, 7291–7298. doi: 10.1021/la300735u

Reis, B. M., Armes, S. P., Fujii, S., and Biggs, S. (2010). Characterisation of the dispersion stability of a stimulus responsive core–shell colloidal latex. *Colloids Surf. A* 353, 210–215. doi: 10.1016/j.colsurfa.2009.11.015

Richtering, W. (2012). Responsive emulsions stabilized by stimuli-sensitive microgels: emulsions with special non-Pickering properties. *Langmuir* 28, 17218–17229. doi: 10.1021/la302331s

Saigal, T., Dong, H., Matyjaszewski, K., and Tilton, R. D. (2010). Pickering emulsions stabilized by nanoparticles with thermally responsive grafted polymer brushes. *Langmuir* 26, 15200–15209. doi: 10.1021/la1027898

San Miguel, A., Scrimgeour, J., Curtis, J. E., and Behrens, S. H. (2010). Smart colloidosomes with a dissolution trigger. *Soft Matter* 6, 3163–3166. doi: 10.1039/c002930k

Schröder, V., Behrend, O., and Schubert, H. (1998). Effect of dynamic interfacial tension on the emulsification process using microporous, ceramic membranes. *J. Colloid Interface Sci.* 202, 334–340. doi: 10.1006/jcis.1998.5429

Tang, J., Quinlan, P. J., and Tam, K. C. (2015). Stimuli-responsive Pickering emulsions: recent advances and potential applications. *Soft Matter* 11, 3512–3529. doi: 10.1039/C5SM00247H

Thompson, K., Armes, S., and York, D. (2011). Preparation of pickering emulsions and colloidosomes with relatively narrow size distributions by stirred cell membrane emulsification. *Langmuir* 27, 2357–2363. doi: 10.1021/la104970w

Thompson, K. L., and Armes, S. P. (2010). From well-defined macromonomers to sterically-stabilised latexes to covalently cross-linkable colloidosomes: exerting control over multiple length scales. *Chem. Commun.* 46, 5274–5276. doi: 10.1039/c0cc01362e

Thompson, K. L., Armes, S. P., Howse, J. R., Ebbens, S., Ahmad, I., Zaidi, J. H., et al. (2010). Covalently cross-linked colloidosomes. *Macromolecules* 43, 10466–10474. doi: 10.1021/ma102499k

Thompson, K. L., Cinotti, N., Jones, E. R., Mable, C. J., Fowler, P. W., and Armes, S. P. (2017). Bespoke diblock copolymer nanoparticles enable the production of relatively stable oil-in-water Pickering nanoemulsions. *Langmuir* 33, 12616–12623. doi: 10.1021/acs.langmuir.7b02267

Thompson, K. L., Williams, M., and Armes, S. P. (2015). Colloidosomes: synthesis, properties and applications. *J. Colloid Interface Sci.* 447, 217–228. doi: 10.1016/j.jcis.2014.11.058

Tu, F., and Lee, D. (2014). Shape-changing and amphiphilicity-reversing Janus particles with pH-responsive surfactant properties. *JACS* 136, 9999–10006. doi: 10.1021/ja503189r

Tuzar, Z., and Kratochvíl, P. (1976). Block and graft copolymer micelles in solution. *Adv. Colloid Interface Sci.* 6, 201–232. doi: 10.1016/0001-8686(76)80009-7

Van De Wetering, P., Zuidam, N. J., Van Steenbergen, M. J., Van Der Houwen, O. A. G. J., Underberg, W. J. M., and Hennink, W.E. (1998). A mechanistic study of the hydrolytic stability of poly(2-(dimethylamino)ethyl methacrylate). *Macromolecules* 31, 8063–8068. doi: 10.1021/ma980689g

Velev, O., Furusawa, K., and Nagayama, K. (1996). Assembly of latex particles by using emulsion droplets as templates. 1. Microstructured hollow spheres. *Langmuir* 12, 2374-2384. doi: 10.1021/la9506786

Velev, O., and Nagayama, K. (1997). Assembly of latex particles by using emulsion droplets. 3. Reverse (water in oil) system. *Langmuir* 13, 1856–1859. doi: 10.1021/la960652u

Vladisavljević, G. T., and Williams, R. A. (2006). Manufacture of large uniform droplets using rotating membrane emulsification. *J. Colloid Interface Sci.* 299, 396–402. doi: 10.1016/j.jcis.2006.01.061

Wesley, R. D., Dreiss, C. A., Cosgrove, T., Armes, S. P., Thompson, L., Baines, F. L., et al. (2005). Structure of a hydrophilic–hydrophobic block copolymer and its interactions with salt and an anionic surfactant. *Langmuir* 21, 4856–4861. doi: 10.1021/la046830y

Williams, R., Peng, S., Wheeler, D., Morley, N., Taylor, D., Whalley, M., et al. (1998). Controlled production of emulsions using a crossflow membrane: part II: industrial scale manufacture. *Chem. Eng. Res. Des.* 76, 902–910. doi: 10.1205/026387698525702

Xiao, G., Hu, Z., Zeng, G., Wang, Y., Huang, Y., Hong, X., et al. (2012). Effect of hydrophilic chain length on the aqueous solution behavior of block amphiphilic copolymers PMMA-b-PDMAEMA. *J. Appl. Polym. Sci.* 124, 202–208. doi: 10.1002/app.33734

Yu, K., Zhang, H., Hodges, C., Biggs, S., Xu, Z., Cayre, O. J., et al. (2017). Foaming behavior of polymer-coated colloids: the need for thick liquid films. *Langmuir* 33, 6528–6539. doi: 10.1021/acs.langmuir.7b00723

**Conflict of Interest Statement:** The authors declare that the research was conducted in the absence of any commercial or financial relationships that could be construed as a potential conflict of interest.

frontiers in Chemistry

ORIGINAL RESEARCH
published: 01 May 2018
doi: 10.3389/fchem.2018.00148

# Comparing the Relative Interfacial Affinity of Soft Colloids With Different Crosslinking Densities in Pickering Emulsions

*Man-hin Kwok*[1] *and To Ngai*[1,2]*

[1] Department of Chemistry, The Chinese University of Hong Kong, Shatin, Hong Kong, [2] Shenzhen Municipal Key Laboratory of Chemical Synthesis of Medicinal Organic Molecules, Shenzhen Research Institute, The Chinese University of Hong Kong, Shenzhen, China

Pickering emulsions prepared by various kinds of soft colloids such as the poly(*N*-isopropylacrylamide) (PNIPAM)-based microgels, have been studied for decades in order to fabricate stimuli-responsive emulsions. It has been generally viewed that the interfacial properties of the microgel monolayers and the emulsion stability are dominated by the softness or deformability of the microgel particles. However, there is still no convenient way to characterize the adsorption/desorption energy of the microgels at the interface although this is an essential topic for microgel-stabilized emulsions. This paper presents a novel method for directly comparing the relative interfacial affinity of microgel particles with comparable size but different crosslinking densities, therefore, different softness at the oil/water interface. Typical micron-sized PNIPAM-based microgels were synthesized and used in this study. With advanced fluorescent labeling techniques, we are capable of distinguishing different kinds of microgels in a Pickering emulsion. During vigorous agitation, particles with higher adsorption energy are more likely to be found at the oil/water interface instead of the loosely adsorbed counterparts. By counting the ratio of interfacial area occupied by two microgels, the interfacial affinity of them can be compared. It is found that interfacial affinity of microgels is not only dependent on the softness but also strongly correlated with the core-shell morphology of the microgels, especially the outmost collapsed polymer layer at the interface. This result is consistent with the interfacial morphology model proposed by other researchers. The understanding of the stabilization of such Pickering emulsions can help us to design and develop responsive Pickering emulsions with better controlled stability.

**Keywords: Pickering emulsions, microgels, PNIPAM, soft colloids, microgel-stabilized emulsions**

OPEN ACCESS

***Edited by:***
*Erica Wanless,*
*University of Newcastle, Australia*

***Reviewed by:***
*Ryo Murakami,*
*Konan University, Japan*
*Alexander Francis Routh,*
*University of Cambridge,*
*United Kingdom*

***Correspondence:**
*To Ngai*
*tongai@cuhk.edu.hk*

***Specialty section:***
*This article was submitted to Chemical Engineering, a section of the journal Frontiers in Chemistry*

***Received:*** *14 February 2018*
***Accepted:*** *16 April 2018*
***Published:*** *01 May 2018*

***Citation:***
*Kwok M and Ngai T (2018) Comparing the Relative Interfacial Affinity of Soft Colloids With Different Crosslinking Densities in Pickering Emulsions. Front. Chem. 6:148. doi: 10.3389/fchem.2018.00148*

## INTRODUCTION

Pickering emulsion was first described by Ramsden (1904) and S. U. Pickering more than 100 years ago (Pickering, 1907). Submicron or micron-sized solid particles like surfactants or amphiphilic polymers, can adsorb at oil-water interfaces, and provided long-term kinetic stability. Such particle-stabilized emulsions are now commonly called Pickering (or Pickering–Ramsden) emulsions. These stabilizing particles are wetted by both phases in the system and they are interfacially active.

Unlike the conventional small molecule surfactants, the particle stabilizers are usually considered to be irreversibly adsorbed to the interface and cannot be removed by thermal energy (Schmitt and Ravaine, 2013).

Since the early 1900's studies on solid particles at interfaces, the issue of correlating the properties of individual particles at the interface with emulsion stability has remained largely unexplored until the last couple of decades. Nevertheless, with the advancement in preparation of various kinds of colloidal particles, the topic has attracted so much more attention in physical science research (Binks, 1998; Chen et al., 2007; Li and Stover, 2008; Liu et al., 2008; Tsuji and Kawaguchi, 2008; Richtering, 2012; Destribats et al., 2014; Style et al., 2015). Pickering emulsions retain the basic properties of classical emulsions stabilized by surfactants or proteins so that they can be substituted for classical emulsions in most industrial and technological applications. Moreover, Pickering emulsions offer several remarkable advantages over conventional surfactant-stabilized emulsions, such as high resistance to coalescence and reduced foaming (by hydrophobic particles) (Aveyard et al., 1994). The "surfactant-free" character makes them more attractive in personal care and pharmaceutical applications where surfactants often cause adverse effects such as irritancy and even cell damage (Tang et al., 2015). Therefore, they have received intense attention in the past decade.

Besides hard spherical particles, Pickering emulsions stabilized by soft polymeric particles have also been developed (Ngai et al., 2005, 2006). Particles made of soft matter are able to significantly change their properties when they are triggered by external stimulations, such as temperature (Pelton and Chibante, 1986) pH (Hoare and Pelton, 2004, 2008; Khan, 2007) ionic strength (Saunders and Vincent, 1999) or even magnetic field (Khan, 2008). Therefore, the use of soft particles in stabilizing Pickering emulsions allows a convenient way to prepare responsive emulsions, which are also known as "smart emulsions." The responsiveness of the soft particles can be transferred to the corresponding Pickering emulsions. The development of such responsive emulsions leads to even more potential applications, for example, biocatalysis (Wiese et al., 2013), oil transportation (Li and Stover, 2008), oil refinery (Brugger et al., 2008), and drug delivery (Frelichowska et al., 2009; Zhang et al., 2010; Chevalier and Bolzinger, 2013).

Whilst soft particles have been demonstrated as being interesting stabilizers for Pickering emulsions, the mechanism and detail of the stabilization given by these soft particles are still not fully understood. In the past few years, many reports studied Pickering emulsions stabilized by soft particles, especially poly(*N*-isopropylacrylamide) (PNIPAM)-based microgel particles (Brugger et al., 2010; Geisel et al., 2012, 2014a,b; Destribats et al., 2013, 2014; Monteillet et al., 2014; Pinaud et al., 2014). The softness or the deformability of microgels has been emphasized to play an important role in the stabilization of emulsions. For example, Destribats et al. (2011) obtained the images of PNIPAM-based microgel particles at the oil/water interface using cryo-scanning electron microscopy (cyro-SEM) techniques. Based on their SEM images, they concluded that microgel particles are often deformed and stretched at the interface. They described the conformation as "fried egg-like structure" and suggested that the deformability of the microgel particles was important in stabilizing the corresponding Pickering emulsions. It is reasonable to attribute the high stability of the emulsion to the deformability of the stabilizers because the flattening of microgel particles would increase the coverage of each particle and form a better and elastic protecting layer.

However, in our recent study, we observed individual, micron-sized microgel particle at the oil/water interface under confocal laser scanning microscopy (CLSM) (Kwok and Ngai, 2016). It was found that the deformation of the overall shape of micron-sized microgel is not significant. Compared with cryo-SEM, CLSM does not offer images with very high resolution but the images can be taken in aqueous solution, the native state instead of high vacuum, dried state of soft particles. Therefore, CLSM is likely a better choice for characterizing these water swollen gel particles. We argued that larger microgel only significantly deform at extremely swollen condition, which refers to the pH-responsive swelling. For PNIPAM microgel without pH-responsiveness, the corresponding deformation might not be significant as shown in cryo-SEM of the sub-micron-sized microgels.

Besides our CLSM images, Geisel et al. obtained images of microgel-stabilized Pickering emulsions in aqueous state using novel transmission X-ray microscopy (Geisel et al., 2014a). In their images, the main body of the particles do not show any significant flattening or deformation. Nevertheless, deformation near the interface is found. Recently, Style et al. took cryo-SEM images of a fractured water-decane interface populated by PNIPAM microgel particles with good resolution (Style et al., 2015). In this peculiar side-view as shown in **Figure 1**, soft microgel particles show asymmetric conformations across the interface, with two different sizes and shapes of the particle portions exposed to the two fluids. However, it can be clearly found that the main part of the microgel particle is not significantly deformed. It seems that the oil/water interface in between the particles is covered by a layer of the collapsed polymer which is connected into networks. Their results are consistent with our previous confocal results and the measurement of the elastic modulus of PNIPAM-based microgel particles from other AFM based studies (Hashmi and Dufresne, 2009; Burmistrova et al., 2011; Kwok and Ngai, 2016). Moreover, Zielinska et al. have recently used neutron reflectivity to study the PNIPAM-based nanogels at the water/air interface (Zielinska et al., 2016). They found that the nanogels at the interface have a collapsed polymer layer in contact with air. This collapsed polymer layer has a low water content which is similar to that for a collapsed microgel at temperatures above the volume transition temperature (VTP). However, it is still an open question how the morphology of the microgels and this outermost collapsed polymer layer influence the adsorption/desorption energy of individual microgel particles at the interface which is not easy to be measured. In order to connect interfacial properties between soft particles and emulsion stability, in this study, we have developed a novel method to compare the relative interfacial affinity or surface activity of the microgels with different

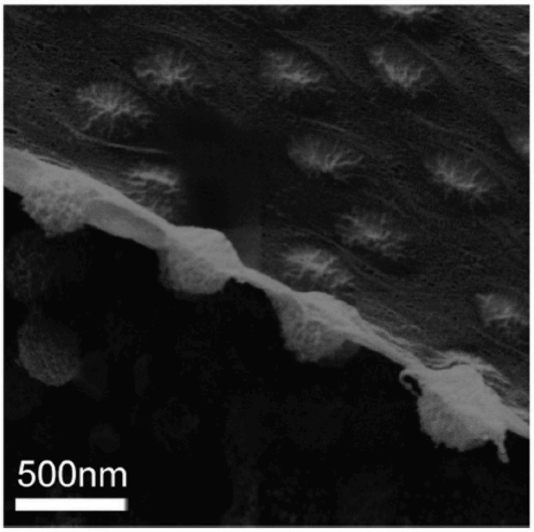


**FIGURE 1 |** Cryo-SEM image of a fracture water-decane interface populated by PNIPAM microgel particles (Style et al., 2015). Reproduced with permission of The Royal Society of Chemistry.

softness. PNIPAM-based microgels with different crosslinking densities were firstly synthesized and mixed together to stabilize emulsions. By using excess microgel particles, the number of microgels at the oil/water interface was no longer limited by the total number of particles. Instead, the number of a specific microgel sample populated at the interface depended on its affinity to the interface, which directly reflected its desorption energy. With optimized labeling techniques, microgels with different softness within the same emulsion sample can be distinguished clearly. Combining with the deformation model suggested by other literatures, which also matches our previous CLSM images, the stabilization of soft microgels with different softness and morphology on resulting Pickering emulsion can be explained. By keeping the sizes of our microgel samples the same, we found that the interfacial affinities of the microgel stabilizers are not only dependent on the crosslink density but also strongly correlated with the outermost collapsed polymer layer of the microgel in controlling the emulsion stability. The results presented in this paper bring new insights for controlling the stability of Pickering emulsions, particularly using soft colloids as stabilizers.

# MATERIALS AND METHODS

## Materials

*N*-isopropylacrylamide (NIPAM, Fluka) was recrystallized using a 1:1 toluene/n-hexane mixture twice. *N*, *N*′-Methylenebisacrylamide (MBA, Fluka) was recrystallized using methanol. Potassium persulfate (KPS, Merck), decane (Sigma Aldrich), methacryloxyethyl thiocarbonyl rhodamine B (RB, Polysciences), and fluorescein sodium salt (FSS, Sigma Aldrich) were used as received. Milli-Q deionized water was used in all the experiments.

## Preparation of PNIPAM Microgels

The procedures to prepare micrometer-sized microgel particles with tailored structure and different cross-linker contents have been documented in our previous publication (Kwok et al., 2013). We briefly describe different types of microgels prepared for this work as below.

### PNIPAM Microgels of Diameter Around 1.4 μm With 10 mg MBA Cross-Linker

First, 1.0 g of NIPAM, 1 mg of RB, and 0.01 g of MBA were dissolved in 90 ml deionized water and filtered to remove any solid impurities. The solution was then transferred to a 250 ml round-bottomed flask. The solution was purged with nitrogen gas and the solution was stirred in a 43°C water bath for 1 h so that the dissolved oxygen was removed. Then, 0.09 g KPS was dissolved in around 3 ml deionized water and added to the reaction vessel with a syringe for initiation of the polymerization. Once the solution started to turn opalescent, which typically happened within 4–6 min, the temperature was immediately ramped to 60°C with a constant ramp rate of 2°C/min. Finally, the reaction mixture was stirred for 3 h at 60°C. This sample was labeled as L10 (meaning large size of microgel with 10 mg of MBA). Three more microgels with diameters also around 1.4 μm were synthesized with similar procedures but without the RB fluorescent labeling. Their specific conditions and sample names were shown in **Table 1**. L50A was prepared by the same procedures as L50, except that after the temperature reached to 60°C for 30 min, an extra 10 mg of MBA was added to the reaction mixture. The addition of MBA at the late stage is for cross-linking the dangling chains on the periphery of the microgel particles.

### PNIPAM Microgels of Diameter Around 900 nm With 30 mg MBA Cross-Linker

Similar to the procedures of synthesizing L30, the monomer solution was prepared, but with a volume of 60 ml and 1 mg of RB dissolved in the solution. After 0.05 g of KPS was added to the reaction vessel at 55°C, the temperature was immediately ramped to 70°C in half an hour. Finally, the reaction mixture was stirred for 3 h at 70°C. This sample was called M30.

All of the synthesized microgels were purified by centrifugation in order to remove any unreacted monomers, oligomer chains and the unreacted initiator. The microgels were

**TABLE 1 |** The experimental conditions for synthesizing L10, L30, L50, L80 PNIPAM micogel particles.

| Sample name | MBA content | Reaction temperature | Volume of solution |
|---|---|---|---|
| L10 | 10 mg | 43°C | 90 |
| L30 | 30 mg | 43°C | 110 |
| L50 | 50 mg | 42°C | 120 |
| L50A | 50 ± 10 mg | 42°C | 120 |
| L80 | 80 mg | 40°C | 140 |

*Underline values indicates "50 + 10 mg" –50 mg of MBA was used initially and 10 mg of MBA was added in the middle of the reaction.*

purified at a constant maximum centrifugal force of 28,000 g for 1 h. After that, the supernatant was removed and the microgels were dispersed again in deionized water (or microgel solution for concentrating the sample) by stirring overnight. The purification cycle was repeated four times for each of the samples.

## Physical Measurements

### Laser Diffraction Measurement

Deionized water was used to fill up the sample chamber of the Coulter LS230 laser diffraction size analyser. Background measurements and detector alignment were done by the provided software. Then 1% wt/wt microgel samples were added to the analyzer and the measurements of the particle sizes were performed.

### Concentration Determination

The mass of a clean glass vial was recorded accurately by an analytical balance. After that, about 0.5 mL of the purified microgel sample was transferred to the glass vial, and the total mass of it was measured carefully. Then the glass vial was put in an oven at 150°C to evaporate the water. After the vial was cooled to room temperature, the total mass of the residue and the vial was measured again. Finally, the concentration of the microgel was calculated as a weight percentage.

### Pickering Emulsion Stability Measurement

0.7 mL of decane was added to 0.7 mL of 1.0% wt/wt microgel solution. Then, the emulsion was prepared by an Ultra Turrax T25 homogenizer (with 10 mm head) operating at 9,500 rpm. After that, the emulsion was placed in a centrifuge for 30 min. The centrifugal force was set at 1,000 g. The centrifugation was repeated until the oil released did not change anymore. Finally, a photo of the emulsion after centrifugation was taken to measure the oil released.

### Relative Interfacial Affinity of Different Microgels

Fifty microliters of decane was added to 1 mL of the 1% wt/wt mixed microgel solution 0. 30 μL of 0.3 mg/mL FSS solution, and 10 μL of 0.075 M sulfuric acid were also added. Then, the emulsion was prepared by the homogenizer operating at 9,500 rpm for 2 min. CLSM images of the emulsion were taken with a Nikon Eclipse Ti inverted microscope (Nikon). The wavelength of the excitation laser for FSS and RB were 488 nm and 543 nm respectively. A 60× (NA = 1.49) oil immersion objective was used. Images were taken from many different portions of the emulsion.

# RESULTS AND DISCUSSION

## Microgel Preparations and Characterizations

To synthesize the required microgel particles, surfactant free emulsion polymerization (SFEP), which is also known as precipitation polymerization, was applied. **Figure 2** shows schematics of the syntheses. It is found that among numerous synthetic parameters, cross-linker content, nucleation temperature and the total monomer concentration are the key parameters for controlling the particle size. All of the syntheses in this work were based on batch synthesis. The monomers were all added to the reaction mixtures, except for sample L50A. It is worth noting that many reports have indicated that batch polymerization at high temperature can result in a poorly controlled microgel network structure since the cross-linker MBA monomer was commonly incorporated into the microgels faster than the NIPAM monomer. This suggests that the microgel particles prepared in this study would have a core-shell morphology with a highly cross-linked core surrounded a shell of dangling polymer chains. We used only one such kind of particle morphology because the Pickering emulsions stabilized by microgel particles are complicated. Therefore, the comparison of emulsion stabilities was limited to only one variable, the total cross-linker content or softness of the microgels.

For the syntheses of micron-sized microgels with different cross-linking densities (samples named as L10, L30, L50, L80, L50A), temperature-programmed emulsion polymerization was applied. Large PNIPAM particles can be prepared at lower temperature, which is typically around 45°C. However, the yield of the reaction is relatively low and a lot of oligomeric chains, not involved in particle growth, will be formed. Therefore, applying a temperature ramp right after the nucleation state can produce stable micron-sized microgel dispersions with reasonable yield. High cross-linking density on the other hand prevents the microgel from dissolving in water at low temperature. Therefore, it was important to note that the temperature of each synthesis was slightly different. In order to prepare microgels with different cross-linker contents and similar diameter, L10 was prepared at a slightly higher temperature so that the size of it could be reduced and L80 was prepared at a slightly lower temperature. The volume of reaction mixtures was different so that aggregation in the syntheses could be minimized.

We used a laser diffraction particle size analyser and dynamic light scattering (DLS) to characterize the diameters of the synthesized PNIPAM microgels. **Figure 3** shows the laser diffraction measurements of the microgels. The size distributions of large microgels were very similar, with means around 1.4 μm. In **Table 2**, the size measurements of all five microgels were summarized. We calculated the thermal responsive swelling ratios (Q) by dividing the diameters measured by DLS $D_h$ at 25°C with $D_h$ at 40°C. This swelling ratio was affected by the softness of the particles. The swelling ratio increased as the softness of the particle increased. From the diameter swelling ratios shown in **Table 2**, it was found that the difference in diameter swelling ratios between L10 and L80 were consistent with the corresponding cross-linker content.

## Determining the Stability of the Pickering Emulsions Stabilized by Microgels Using Centrifugation

For measuring the stability of the microgel stabilized emulsion, centrifugation was applied as it is a widely utilized method to quantitatively measure emulsion stability. The advantage of this method relies in the fact that it is direct and easy to perform. The method determines the maximum pressure which can be

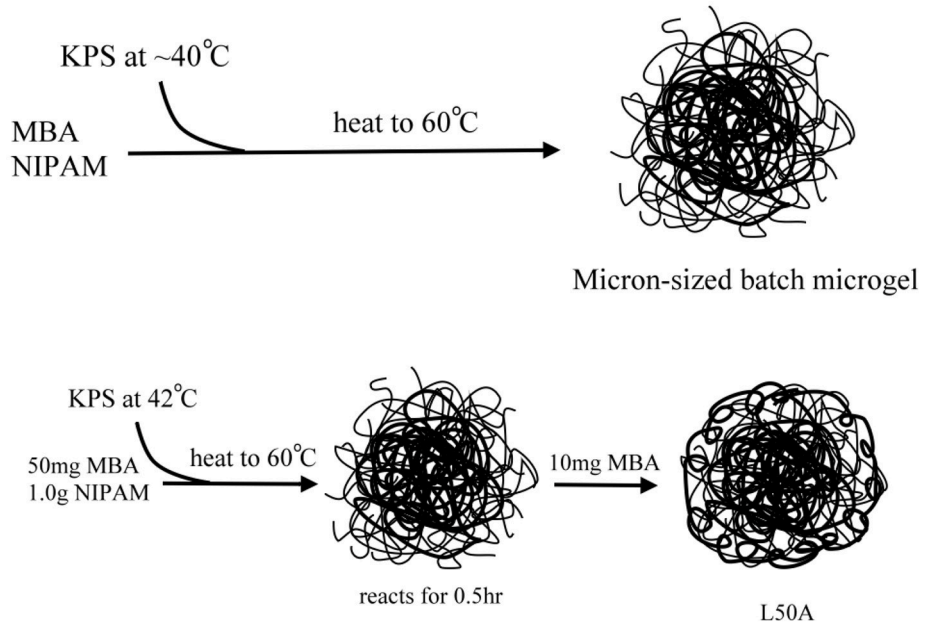


**FIGURE 2 |** Schematic illustration of the preparation of the micron-sized PNIPAM-based microgel samples.

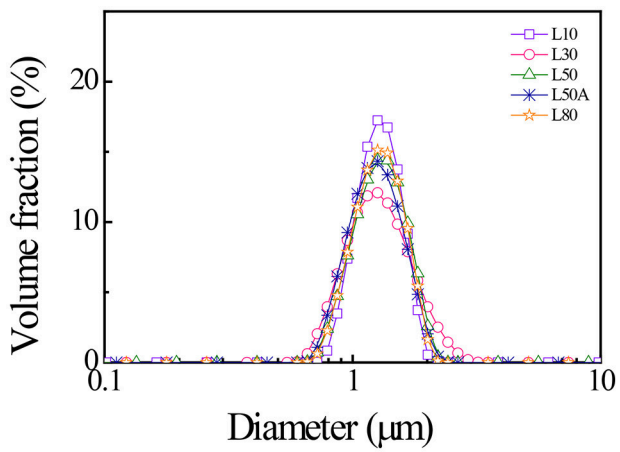


**FIGURE 3 |** Laser diffraction results of the synthesized micron-sized PNIPAM with different cross-linker contents measured at 25°C.

withstood by the water thin film between oil droplets before coalescence occurs. This pressure is called the maximum osmotic pressure $P_{osm}$. Campbell et al. have suggested that this maximum osmotic pressure is a complete analogy with the maximum capillary pressure (Tcholakova et al., 2002). Therefore, emulsions with a higher $P_{osm}$, are able to resist coalescence for a longer period of time, the emulsions are thus more stable. To calculate this $P_{osm}$ from the centrifugation data, the following equation was used:

$$P_{osm} = \Delta\rho \, g_{max}(H_{oil} - H_r) \quad (1)$$

**TABLE 2 |** The $D_h$, $D_{LD}$ and the corresponding VPT diameter swelling ratios (Q) of the PNIPAM microgels.

| Sample | $D_h$ (nm) at 25°C | $D_{LD}$ (nm) at 25°C | $D_h$ (nm) at 40°C | Q |
|---|---|---|---|---|
| M30 | 960 ± 110 | 940 ± 270 | 408 ± 60 | 2.3 |
| L10 | 1400 ± 240 | 1360 ± 260 | 470 ± 46 | 3.0 |
| L30 | 1450 ± 240 | 1390 ± 420 | 518 ± 80 | 2.8 |
| L50 | 1400 ± 260 | 1380 ± 320 | 518 ± 86 | 2.7 |
| L50A | 1350 ± 210 | 1330 ± 310 | 504 ± 79 | 2.7 |
| L80 | 1370 ± 220 | 1360 ± 300 | 522 ± 101 | 2.6 |

In this equation, $g_{max}$ is the maximum centrifugal acceleration; $\Delta\rho$ is the density difference between the oil and water; $H_r$ is the height of the oil released by the centrifugation process, and $H_{oil}$ is the height of the oil when there is total phase separation.

**Figure 4** shows the emulsion stability measurements of the large microgel stabilized emulsions after centrifugation at 1,000 g. Although the energy of the particle desorption is usually a few orders larger than the centrifugal potential energy, it was essential to further confirm that the centrifugal force was not large enough to actively remove microgel particles from the oil-water interface. Therefore, the centrifugation was repeated and it was found that the amount of oil released was unchanged after a few centrifugations.

In **Figure 4**, it can be seen that the stability of the emulsion decreased as the MBA content increased for the microgel stabilized emulsion samples. Note that sample L50A was an exception. By comparing the maximum osmotic pressures of emulsions were stabilized by L50 and L80 with L50A, we found

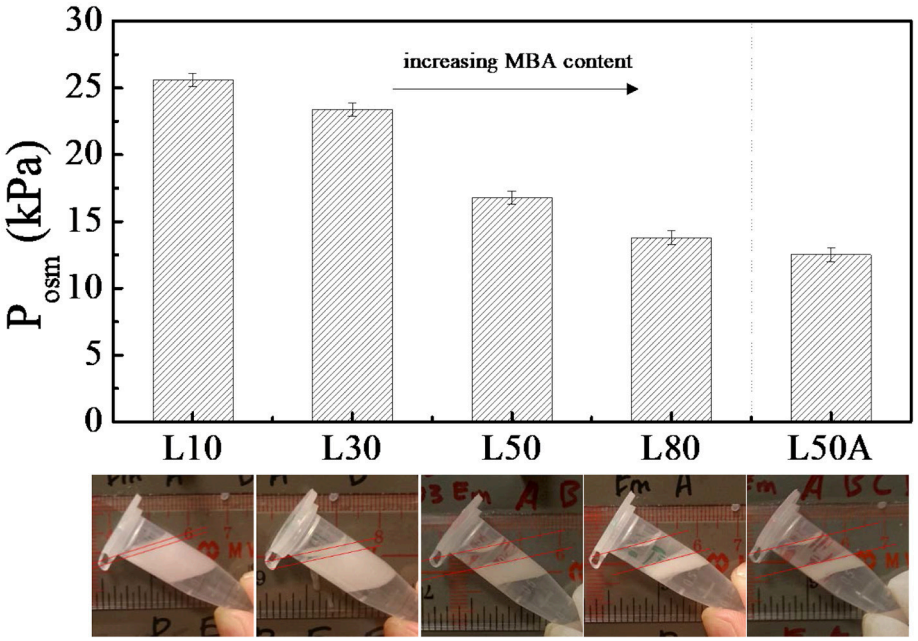


**FIGURE 4 |** The maximum osmotic pressure ($P_{osm}$) of emulsions stabilized by large microgels with different cross-linker contents. The centrifugation was done at 1,000 g (g is gravitational acceleration). The images below the bars are the corresponding photos of the emulsion samples after centrifugation.

that L50A stabilized emulsions were the least stable. However, L50 and L50A just differed by the surface property and L80 possessed even more MBA content that L50A. We will discuss more about this stability difference in the next section.

## Comparison of Surface Affinity Between Microgels With Different Size

It is often suggested that Pickering emulsion stability is strongly related to the interfacial energy of the particles because they reduce the area of the interface between the two immiscible liquid. Also, the energy is usually a few orders of magnitude larger than thermal energy, which leads to an ultra-strong anchoring of particles at the interface. The energy required when a single rigid spherical particle was desorbed from the interface is given by:

$$\Delta E = \gamma \pi r^2 (1 - |cos\theta|)^2 \text{ (ChevalierandBolzinger, 2013)} \quad (2)$$

where $r$ is the radius of the particle, $\gamma$ is the surface tension and $\theta$ is the contact angle of the particle. This desorption energy is affected by many factors, such as size, contact angle, roughness, etc. If the particles are adsorbed to the interface with higher energy, they form a particle shell around the emulsion droplet with higher strength and the shell is capable of stabilizing the emulsion better. Therefore, the desorption energy is one of the crucial factors in Pickering emulsion stability and this energy can be compared by the surface affinity of the particle. The contact angle of microgel at the oil-water interface was around 40°, which was estimated by the effective contact angle of Richtering's work (Geisel et al., 2012). Therefore, the desorption energy of our larger microgels is around $1.9 \times 10^6$ $k_BT$.

CLSM is a chosen for this study because the sample preparation is much easier and there is almost no disturbance to the emulsion sample. Also, the emulsion can be visualized in solution instead of vacuum as commonly viewed by electron microscopy. To compare the relative surface affinity of different microgel particles, we mixed two microgel samples, which were labeled differently, and prepared the emulsion with the homogenizer after adding oil. CLSM images were taken and the number of each particle type at the oil-water interface counted. We call this number ratio $\phi$. As the diameters of the particles were well-characterized, the relative surface coverage, which is defined to be our relative interfacial affinity $\Phi$ can be easily calculated. The method is based on the equilibrium established by the two kinds of microgel and the energy input by the homogenizer. With rigorous agitation, individual microgel particles in the bulk solution are capable of displacing another particle which has been adsorbed at the interface. The probability of this process is depended on their relative desorption energy. A particle with lower desorption energy is less likely to displace a particle with higher desorption energy and vice versa. Therefore, higher interfacial affinity indicated higher desorption energy of the particles.

We synthesized microgel M30, which has diameter of around 900 nm and polymerizable red fluorescent dye, RB, was also added in the synthesis. The reason that we used sample M30 instead of L10 in the demonstration was because RB could be much better incorporated into the microgel at high temperature synthesis so that the image quality was better. In **Figure 5**, we can clearly see that M30 and L30 showed different colors under

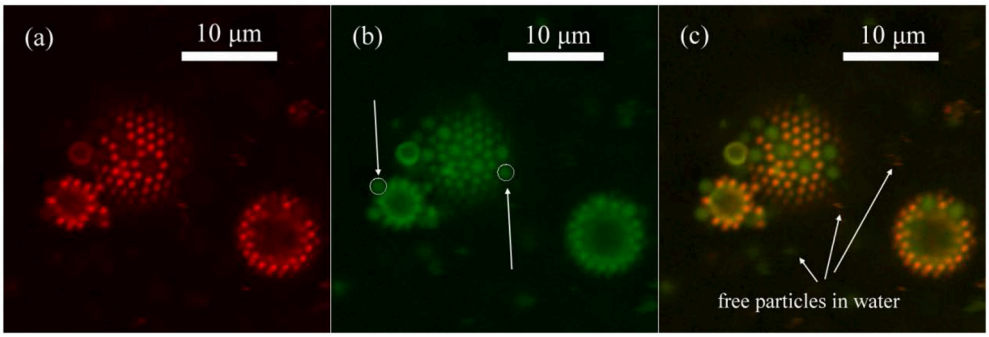


**FIGURE 5 |** CLSM image of emulsion prepared by M30 and L30 microgels in 1:1 weight concentration ratio in bulk **(a)** Red channel of Rhodamine B fluorescence, which was only given by M30 microgels. **(b)** Green channel of fluorescein fluorescence, which was given by M30 and also L30 microgels. **(c)** Combined image of both channels. Free M30 and L30 microgel particles presented in water, indicating that microgel particles were in excess in the system.

CLSM. M30 is orange and L30 is mostly green. In the synthesis of M30, RB was added so that the red fluorescent dye was covalently bonded onto the M30 microgel. Next, both of the microgels were labeled by diffusing fluorescein (from fluorescein sodium salt). The adsorption of fluorescein to the microgel was based on the H-bond interaction. (Kwok et al., 2013) Therefore, the two microgels were clearly distinguishable at the oil-water interface. The initial bulk ratio (weight concentration) between M30 and L30 was 1:1. To obtain a statistically valid result, over 4,000 particles were counted from different portions of the emulsion.

.

In addition, for the smaller emulsion droplet in **Figure 5b**, the CLSM image was taken near half of the height of the droplet. On the other hand, the CLSM image of the middle sized droplet in **Figure 5b** was taken near the bottom of the droplet. A white circle of the same size was put onto one L30 particle on each droplet. Obviously, the two L30 particles were identical in either shape or size under CLSM. Therefore, we also could confirm that the main body of the particles were not deformed significantly.

In **Figure 5c**, we can see that there were free M30 and L30 microgel particles, which were not adsorbed at the interface, in the bulk solution. This is because only a very small amount of oil was used to prepare the emulsion. Both M30 and L30 were in excess while the emulsion was prepared under the vigorous stirring of the homogenizer. In order to further confirm that the current CLSM image results were representing the equilibrium distribution between M30 and L30 on the interface, we prepared the emulsion in four different ways. The initial bulk ratio between M30 and L30 was changed to 2:1 and 1:2, respectively. Also, the emulsion was first prepared by M30 (or L30), then L30 (or M30) was added and the homogenizing process repeated. **Table 3** summarizes all five results and the results of (A), (B), (D), and (E) were statistically the same. Result (D) and (E) showed that under homogenization, particle desorption and displacement was allowed. Both M30 and L30 microgel particles were capable of displacing each other from the oil-water interface. Therefore, these particle counting results were not kinetically controlled by the initial adsorption. From result (A) and (B) shown in **Table 3**, it was confirmed that both M30 and L30 microgels were in excess at an initial ratio of 1:1 and 2:1. It was because the excess particles in the solution did not affect the equilibrium of the adsorption of different particles at the interface. However, from result (C) in **Table 3**, it was believed that at a M30 to L30 ratio of 1:2, M30 microgel was limited in the system, so that the excess interface was covered by L30 instead. Hence, result (C) in **Table 3** was smaller than results (A) and (B).

We determined the equilibrium number ratio $\phi$ of M30 to L30 on the oil-water interface to be 5.62 at 9,500 rpm

**TABLE 3 |** Particle counting results of M30 and L30 at the interface.

| Image no. | 1 | 2 | 3 | Total |
|---|---|---|---|---|
| **(A) M30 TO L30 WT. CONC. RATIO = 1:1 (# RATIO = 3.4: 1), EMULSION PREPARED BY ONE STEP** | | | | |
| No. of M30 | 701 | 3,776 | 1,863 | 6,340 |
| No. of L30 | 127 | 672 | 329 | 1,128 |
| M30: L30 at interface | 5.52 | 5.62 | 5.66 | 5.62 ± 0.05 |
| **(B) M30 TO L30 Wt. CONC. RATIO = 2:1 (# Ratio = 6.8:1), EMULSION PREPARED BY ONE STEP** | | | | |
| No. of M30 | 1,633 | 1,702 | 1,380 | 4,715 |
| No. of L30 | 290 | 302 | 249 | 841 |
| M30: L30 at interface | 5.63 | 5.64 | 5.54 | 5.61 ± 0.05 |
| **(C) M30 TO L30 WT. CONC. RATIO = 1:2 (# RATIO = 1.7: 1), EMULSION PREPARED BY ONE STEP** | | | | |
| No. of M30 | 625 | 1,459 | 1,179 | 3,263 |
| No. of L30 | 215 | 513 | 421 | 1149 |
| M30: L30 at interface | 2.90 | 2.84 | 2.80 | 2.84 ± 0.05 |
| **(D) M30 TO L30 WT. CONC. RATIO = 1:1 (# RATIO = 3.4: 1), EMULSION PREPARED BY M30 FIRST** | | | | |
| No. of M30 | 1,912 | 1,759 | 1,089 | 4,760 |
| No. of L30 | 351 | 305 | 196 | 852 |
| M30: L30 at interface | 5.45 | 5.77 | 5.56 | 5.59 ± 0.17 |
| **(E) M30 TO L30 WT. CONC. RATIO = 1:1 (# RATIO = 3.4: 1), EMULSION PREPARED BY L30 FIRST** | | | | |
| No. of M30 | 1,066 | 1,455 | 2,415 | 4,936 |
| No. of L30 | 191 | 261 | 431 | 883 |
| M30: L30 at interface | 5.58 | 5.57 | 5.60 | 5.59 ± 0.02 |

*The overall ratio is the average of $\varphi$ and its weighted standard deviation. The initial bulk # ratio was also calculated based on the assumption that M30 and L30 have the same density.*

stirring, from result (A) in **Table 3**. However, it was important to note that small and large particles occupied different areas at the interface. Therefore, to compare their desorption energy obviating the size effect in equation (2), equilibrium interfacial coverage ratio $\Phi$ was calculated. This ratio $\Phi$ indicated the ratio of interfacial area covered by the two microgels when the exchanging particles established equilibrium with the energy input by the stirring. From the CLSM image in **Figure 5**, the areas occupied by each M30 particle and L30 particle on the interface were determined to be 0.72 and 1.65 $\mu m^2$, respectively. Therefore, $\Phi$ of M30 to L30 was determined to be 2.44, larger than 1. That meant for a given oil-water interface with a certain area, the adsorption of small microgel particles was more energetically favorable than the adsorption of the large microgel particles. Unfortunately, we could not quantify the difference of their desorption energy. It was because we could not quantify the energy which was given by the homogenizer. Nevertheless, this method provided an effective way to qualitatively compare the relative desorption energy of particles per unit area.

## Comparison of Interfacial Affinity Between Microgels With Different Cross-Linker Contents

Similar to the previous comparison of surface affinity between microgels with different sizes, microgels with different cross-linker contents were mixed together and emulsions were prepared by the homogenizer. As we had five micron-sized microgel samples, the interfacial affinity of L10 was compared with L30, L50, L80, and L50A. Although the laser diffraction measurements of these samples were not exactly the same, their diameters in the CLSM images in **Figure 6** were similar. Different types of the particles could mix with each other and achieve hexagonal packing on the interface. **Table 4** summarizes the particle counting results. As each of these particles occupied almost the same area, we could compare their interfacial affinity simply having the number ratio equaled to the coverage ratio (i.e., $\varphi = \Phi$).

According to the results in **Table 4**, when the cross-linker content of the microgel increased from 30 mg (L30) to 80 mg

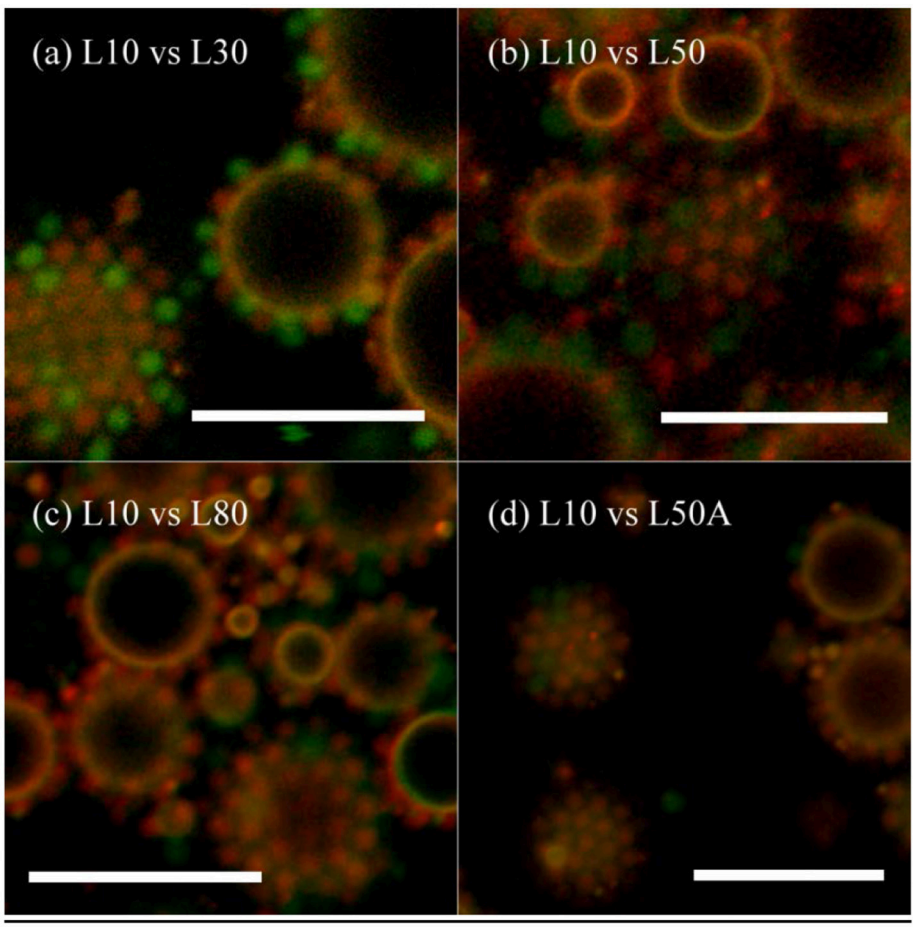


**FIGURE 6 |** CLSM image of emulsion prepared by L10 and other micron-sized microgels in 1:1 wt. conc. ratio. **(a)** L10 + L30, **(b)** L10 + L50, **(c)** L10 + L80, and **(d)** L10 + L50A. Red Rhodamine B fluorescence was only given by L10. Green fluorescein fluorescence was given both of the particles. The scale bars are all 10 μm.

**TABLE 4 |** Particle counting results of large microgels at the interface.

| **(A) L10 MIXED WITH L30** | | | | | | | | | |
|---|---|---|---|---|---|---|---|---|---|
| **Image no.** | **1** | **2** | **3** | **4** | **5** | **6** | **7** | **8** | **Total** |
| No. of L10 | 120 | 151 | 192 | 275 | 181 | 130 | 130 | 462 | 1,641 |
| No. of L30 | 59 | 76 | 97 | 163 | 92 | 64 | 58 | 243 | 852 |
| L10: L30 at interface | 2.03 | 1.99 | 1.98 | 1.69 | 1.97 | 2.03 | 2.24 | 1.90 | 1.93 ± 0.15 |
| **(B) L10 MIXED WITH L50** | | | | | | | | | |
| **Image no.** | **1** | **2** | **3** | **4** | **5** | **6** | **7** | **Total** | |
| No. of L10 | 318 | 345 | 434 | 243 | 245 | 342 | 295 | 2,222 | |
| No. of L50 | 118 | 131 | 158 | 92 | 102 | 126 | 112 | 839 | |
| L10: L50 at interface | 2.69 | 2.63 | 2.75 | 2.64 | 2.40 | 2.71 | 2.63 | 2.65 ± 0.11 | |
| **(C) L10 MIXED WITH L80** | | | | | | | | | |
| **Image no.** | **1** | **2** | **3** | **4** | **Total** | | | | |
| No. of L10 | 708 | 897 | 837 | 846 | 3,288 | | | | |
| No. of L80 | 190 | 248 | 244 | 240 | 922 | | | | |
| L10: L80 at interface | 3.73 | 3.62 | 3.43 | 3.53 | 3.57 ± 0.12 | | | | |
| **(D) L10 MIXED WITH L50A** | | | | | | | | | |
| **Image no.** | **1** | **2** | **3** | **4** | **Total** | | | | |
| No. of L10 | 855 | 747 | 745 | 723 | 3,070 | | | | |
| No. of L50A | 232 | 193 | 204 | 198 | 827 | | | | |
| L10: L50A at interface | 3.69 | 3.87 | 3.65 | 3.65 | 3.71 ± 0.10 | | | | |

*The overall ratio is the weighted average of $\Phi$ and its weighted standard deviation.*

(L80), their interfacial affinity relative to microgel with 10 mg cross-linker (L10) decreased. More importantly, when we looked at the interfacial affinity of L50A relative to L10, it was smaller than that of L50 and L80. The calculated relative interfacial affinity is shown in **Figure 7**. The relative interfacial affinity is defined to be the reciprocal of the coverage ratio $\Phi$. Note that the relative interfacial affinity of L10 was by definition set to be 1.

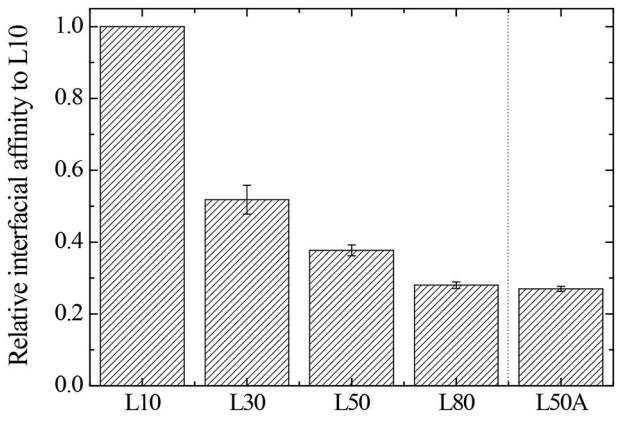


**FIGURE 7 |** The relative interfacial affinity of micron-sized microgels compared to L10.

## Stability of Microgel Stabilized Pickering Emulsions: Effect of Cross-Linker Content

Here, we focus the discussion on the effect of cross-linker content. The stabilities of the emulsions showed the same dependence on cross-linker content of microgel (L10, L30, L50 and L80). The stability of the resulting emulsion decreased as the cross-linking content of the stabilizing microgel increases. The main body of our micron-sized microgel particles (cross-linker content between 1.0 and 7.4% wt/wt) were not significantly deforming at the interface. Therefore, we apply the conformation proposed by Geisel et al. in our discussion and focus at the periphery, the collapsed polymer layer at the interface (Geisel et al., 2012). **Figure 8** shows a schematic illustration of the proposed conformation of microgel particle and the outermost collapsed polymer layer at the interface.

As mentioned above, in microgel batch synthesis, the cross-linker MBA was more reactive than the NIPAM monomer. As a result, the cross-linking density of the inner part of the microgel is higher. Also, the cross-linking density decreases gradually to the periphery of the particle. Here, we suggest that microgels with less cross-linker content also have a more deformable periphery. Therefore, they deformed more at the oil/water interface. Then, each of them was capable of covering and replacing more area at the interface. These outermost collapsed polymer chains on one hand act as anchors and help the particle attachment to the interface. On the other hand, because of low water content and the strong inter—and interapolymer interaction, the collapsed polymer layers at the interface also have a higher elastic modulus compared to the swollen microgels. As a resulting, the desorption energy of these particles, which has softer outer collapsed polymer layer, is higher.

In the previous section, the relative interfacial affinity was compared to the desorption energy of each of our microgel samples. Therefore, the desorption energy decreased from L10 to L80 gradually. It is consistent with our hypothesis and the stability measurement.

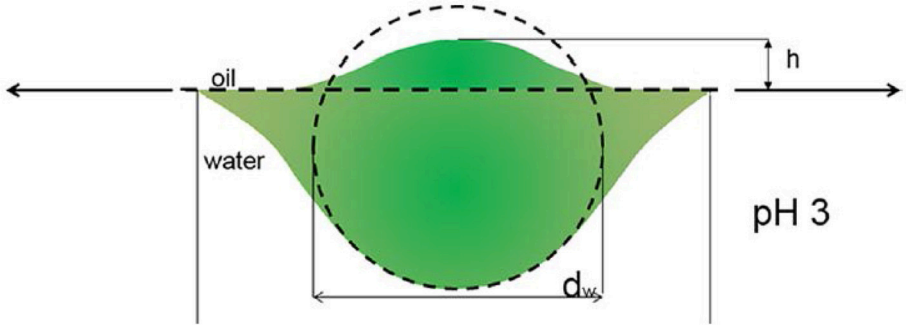


**FIGURE 8 |** The conformation of microgel particle at oil/water interface proposed by Geisel et al. (2012) Reprinted with permission from. Copyright (2012) American Chemical Society.

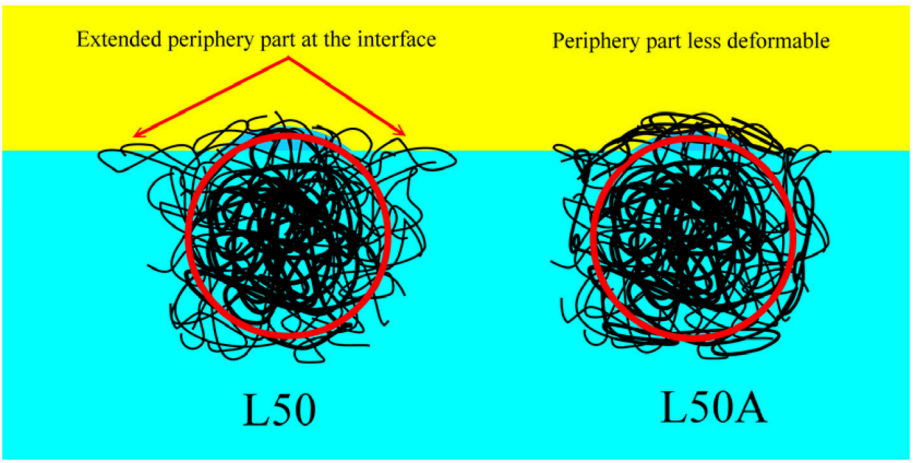


**FIGURE 9 |** The schematic illustrations of microgel L50 and L50A at oil/water interface. The red circles indicate the part which was labeled effectively by fluorescent dye. The soft periphery part and the main body of the microgel were not drawn in scale.

However, in order to verify this hypothesis, we prepared L50A. As mentioned above, the extra 10 mg of cross-linker MBA was not involved in the particle growth at such low monomer concentrations. Therefore, it changed the microgel particle surface property by cross-linking some of the surface dangling chains. It decreased the deformability of the particle surface and outer portion collapsed polymer layer. It is very important to note that the overall deformability indicated by the thermo-responsive swelling ratios of L50 and L50A were very similar as they were synthesized by the same procedures. From the relative interfacial affinity results, the 10 mg of extra cross-linker significantly reduced the interfacial affinity of the L50A microgel. It is important to point out that the overall cross-linker content of L80 was 33% higher than that of L50A. These interfacial affinity results are also consistent with the stability measurements of the emulsions. In **Figure 9**, the schematic illustrations of microgel L50 and L50A at oil/water interface are shown. We show that if the outermost collapsed polymer layer portion of the particle was cross-linked, the desorption energy is lower compared to its counterpart, verifying our hypothesis.

## CONCLUSIONS

We have demonstrated a new approach for comparing the relative interfacial affinity of soft colloids at the oil/water interface. Microgel samples demonstrated the good confocal image quality. By changing the preparation procedures and the amount of the microgels, it has been confirmed that the final ratio of interfacial particles is not kinetically controlled by the initial adsorption. Once the amount of oil is limited, the ratio is not affected by the amount of particles. Therefore, the interfacial coverage ratio of different microgels derived by this number ratio is capable of representing the relative affinity of the particles. The method was applied to study the effects of cross-linker content and surface deformability on the corresponding microgel-stabilized Pickering emulsions. It was found that microgels with less cross-linker content have higher interfacial affinity and better emulsion stability. Furthermore, the effect is more pronounced for the outermost collapsed polymer layer of the microgel. This result is consistent with the interfacial morphology proposed by other researches and

provides direct connection between the deformability and the corresponding Pickering emulsion stability. The improvement in understanding the mechanism of soft colloids stabilized Pickering emulsions will be beneficial for further development of responsive Pickering emulsions with well-controlled stability and performance.

## AUTHOR CONTRIBUTIONS

TN: conceived and managed the research. MK: performed the soft colloids synthesis, emulsion fabrication, and characterizations. TN and MK: reviewed the results and provided the technical guidelines. TN and MK: wrote and drafted the article. TN and MK: reviewed and approved the article.

## ACKNOWLEDGMENTS

The financial support of this work by the Hong Kong Special Administration Region (HKSAR) General Research Fund (CUHK14306617, 2130535), the National Natural Science Foundation of China (21574110), and the Direct Grant for Research (3132681, 3132682, and 4053109) of the Chinese University of Hong Kong is gratefully acknowledged.

## REFERENCES

Aveyard, R., Binks, B., Fjetcher, P., and Rutherford, C. (1994). Contact angles in relation to the effects of solids on film and foam stability. *J. Disp. Sci. Tech.* 15, 251–271. doi: 10.1080/01932699408943557

Binks, B. P. (1998). "Emulsions—Recent advances in understanding," in *Modern Aspects of Emulsion Science* (Royal Society of Chemistry), 1–55.

Brugger, B., Rosen, B. A., and Richtering, W. (2008). Microgels as stimuli-responsive stabilizers for emulsions. *Langmuir* 24, 12202–12208. doi: 10.1021/la8015854

Brugger, B., Vermant, J., and Richtering, W. (2010). Interfacial layers of stimuli-responsive poly-(N-isopropylacrylamide-co-methacrylicacid)(PNIPAM-co-MAA) microgels characterized by interfacial rheology and compression isotherms. *Phys. Chem. Chem. Phys.* 12, 14573–14578. doi: 10.1039/c0cp01022g

Burmistrova, A., Richter, M., Uzum, C., and Klitzing, R. V. (2011). Effect of cross-linker density of P (NIPAM-co-AAc) microgels at solid surfaces on the swelling/shrinking behaviour and the Young's modulus. *Colloid Polym. Sci.* 289, 613–624. doi: 10.1007/s00396-011-2383-2

Chen, T., Colver, P. J., and Bon, S. A. (2007). Organic–inorganic hybrid hollow spheres prepared from $TiO_2$-stabilized pickering emulsion polymerization. *Adv. Mater.* 19, 2286–2289. doi: 10.1002/adma.200602447

Chevalier, Y., and Bolzinger, M.-A. (2013). Emulsions stabilized with solid nanoparticles: Pickering emulsions. *Colloids Surf. A* 439, 23–34. doi: 10.1016/j.colsurfa.2013.02.054

Destribats, M., Eyharts, M., Lapeyre, V., Sellier, E., Varga, I., Ravaine, V., et al. (2014). Impact of pNIPAM microgel size on its ability to stabilize Pickering emulsions. *Langmuir* 30, 1768–1777. doi: 10.1021/la4044396

Destribats, M., Lapeyre, V., Wolfs, M., Sellier, E., Leal-Calderon, F., Ravaine, V., et al. (2011). Soft microgels as Pickering emulsion stabilisers: role of particle deformability. *Soft Matter* 7, 7689–7698. doi: 10.1039/c1sm05240c

Destribats, M., Wolfs, M., Pinaud, F., Lapeyre, V., Sellier, E., Schmitt, V., et al. (2013). Pickering emulsions stabilized by soft microgels: influence of the emulsification process on particle interfacial organization and emulsion properties. *Langmuir* 29, 12367–12374. doi: 10.1021/la402921b

Frelichowska, J., Bolzinger, M. A., Pelletier, J., Valour, J. P., and Chevalier, Y. (2009). Topical delivery of lipophilic drugs from o/w Pickering emulsions. *Int. J. Pharm.* 371, 56–63. doi: 10.1016/j.ijpharm.2008.12.017

Geisel, K., Henzler, K., Guttmann, P., and Richtering, W. (2014a). New insight into microgel-stabilized emulsions using transmission X-ray microscopy: nonuniform deformation and arrangement of microgels at liquid interfaces. *Langmuir* 31, 83–89. doi: 10.1021/la503959n

Geisel, K., Isa, L., and Richtering, W. (2012). Unraveling the 3D localization and deformation of responsive microgels at oil/water interfaces: a step forward in understanding soft emulsion stabilizers. *Langmuir* 28, 15770–15776. doi: 10.1021/la302974j

Geisel, K., Richtering, W., and Isa, L. (2014b). Highly ordered 2D microgel arrays: compression versus self-assembly. *Soft Matter* 10, 7968–7976. doi: 10.1039/C4SM01166J

Hashmi, S. M., and Dufresne, E. R. (2009). Mechanical properties of individual microgel particles through the deswelling transition. *Soft Matter* 5, 3682–3688. doi: 10.1039/b906051k

Hoare, T., and Pelton, R. (2004). Highly pH and temperature responsive microgels functionalized with vinylacetic acid. *Macromolecules* 37, 2544–2550. doi: 10.1021/ma035658m

Hoare, T., and Pelton, R. (2008). Characterizing charge and crosslinker distributions in polyelectrolyte microgels. *Curr. Opin. Colloid Interface Sci.* 13, 413–428. doi: 10.1016/j.cocis.2008.03.004

Khan, A. (2007). Preparation and characterization of N-isopropylacrylamide/acrylic acid copolymer core–shell microgel particles. *J. Colloid Interface Sci.* 313, 697–704. doi: 10.1016/j.jcis.2007.05.027

Khan, A. (2008). Preparation and characterization of magnetic nanoparticles embedded in microgels. *Mater. Lett.* 62, 898–902. doi: 10.1016/j.matlet.2007.07.011

Kwok, M. H., Li, Z., and Ngai, T. (2013). Controlling the synthesis and characterization of micrometer-sized PNIPAM microgels with tailored morphologies. *Langmuir* 29, 9581–9591. doi: 10.1021/la402062t

Kwok, M. H., and Ngai, T. (2016). A confocal microscopy study of micron-sized poly (N-isopropylacrylamide) microgel particles at the oil–water interface and anisotopic flattening of highly swollen microgel. *J. Colloid Interface Sci.* 461, 409–418. doi: 10.1016/j.jcis.2015.09.049

Li, J., and Stöver, H. D. (2008). Doubly pH-responsive pickering emulsion. *Langmuir* 24, 13237–13240. doi: 10.1021/la802619m

Liu, B., Wei, W., Qu, X., and Yang, Z. (2008). Janus colloids formed by biphasic grafting at a Pickering emulsion interface. *Angew. Chem.* 120, 4037–4039. doi: 10.1002/ange.200705103

Monteillet, H., Workamp, M., Appel, J., Kleijn, J. M., Leermakers, F. A., and Sprakel, J. (2014). Ultrastrong anchoring yet barrier-free adsorption of composite microgels at liquid interfaces. *Adv. Mater. Interfaces* 1:1300121. doi: 10.1002/admi.201300121

Ngai, T., Auweter, H., and Behrens, S. H. (2006). Environmental responsiveness of microgel particles and particle-stabilized emulsions. *Macromolecules* 39, 8171–8177. doi: 10.1021/ma061366k

Ngai, T., Behrens, S. H., and Auweter, H. (2005). Novel emulsions stabilized by pH and temperature sensitive microgels. *Chem. Commun.* 331–333. doi: 10.1039/b412330a

Pelton, R., and Chibante, P. (1986). Preparation of aqueous latices with N-isopropylacrylamide. *Colloids Surf.* 20, 247–256. doi: 10.1016/0166-6622(86)80274-8

Pickering, S. U. (1907). Cxcvi.—emulsions. *J. Chem. Soc. Trans.* 91, 2001–2021. doi: 10.1039/CT9079102001

Pinaud, F., Geisel, K., Massé, P., Catargi, B., Isa, L., Richtering, W., et al. (2014). Adsorption of microgels at an oil–water interface: correlation between packing and 2D elasticity. *Soft Matter* 10, 6963–6974. doi: 10.1039/C4SM00562G

Ramsden, W. (1904). Separation of solids in the surface-layers of solutions and 'suspensions'(observations on surface-membranes, bubbles, emulsions, and mechanical coagulation).—Preliminary account. *Proc. R. Soc. Lond.* 72, 156–164. doi: 10.1098/rspl.1903.0034

Richtering, W. (2012). Responsive emulsions stabilized by stimuli-sensitive microgels: emulsions with special non-Pickering properties. *Langmuir* 28, 17218–17229. doi: 10.1021/la302331s

Saunders, B. R., and Vincent, B. (1999). Microgel particles as model colloids: theory, properties and applications. *Adv. Colloid Int. Sci.* 80, 1–25. doi: 10.1016/S0001-8686(98)00071-2

Schmitt, V., and Ravaine, V. (2013). Surface compaction versus stretching in Pickering emulsions stabilised by microgels. *Curr. Opin. Colloid Int. Sci.* 18, 532–541. doi: 10.1016/j.cocis.2013.11.004

Style, R. W., Isa, L., and Dufresne, E. R. (2015). Adsorption of soft particles at fluid interfaces. *Soft Matter* 11, 7412–7419. doi: 10.1039/C5SM01743B

Tang, J., Quinlan, P. J., and Tam, K. C. (2015). Stimuli-responsive Pickering emulsions: recent advances and potential applications. *Soft Matter* 11, 3512–3529. doi: 10.1039/C5SM00247H

Tcholakova, S., Denkov, N. D., Ivanov, I. B., and Campbell, B. (2002). Coalescence in β-lactoglobulin-stabilized emulsions: effects of protein adsorption and drop size. *Langmuir* 18, 8960–8971. doi: 10.1021/la0258188

Tsuji, S., and Kawaguchi, H. (2008). Thermosensitive Pickering emulsion stabilized by poly (N-isopropylacrylamide)-carrying particles. *Langmuir* 24, 3300–3305. doi: 10.1021/la701780g

Wiese, S., Spiess, A. C., and Richtering, W. (2013). Microgel-Stabilized Smart Emulsions for Biocatalysis. *Angew. Chem.* 125, 604–607. doi: 10.1002/ange.201206931

Zhang, K., Wu, W., Guo, K., Chen, J., and Zhang, P. (2010). Synthesis of temperature-responsive poly (N-isopropyl acrylamide)/poly (methyl methacrylate)/silica hybrid capsules from inverse pickering emulsion polymerization and their application in controlled drug release. *Langmuir* 26, 7971–7980. doi: 10.1021/la904841m

Zielinska, K., Sun, H., Campbell, R. A., Zarbakhsh, A., and Resmini, M. (2016). Smart nanogels at the air/water interface: structural studies by neutron reflectivity. *Nanoscale* 8, 4951–4960. doi: 10.1039/C5NR07538F

**Conflict of Interest Statement:** The authors declare that the research was conducted in the absence of any commercial or financial relationships that could be construed as a potential conflict of interest.

frontiers in Chemistry

ORIGINAL RESEARCH
published: 04 May 2018
doi: 10.3389/fchem.2018.00132

# Mixing Time, Inversion and Multiple Emulsion Formation in a Limonene and Water Pickering Emulsion

*Laura Sawiak*[1], *Katherine Bailes*[2], *David Harbottle*[2] *and Paul S. Clegg*[1]*

[1] School of Physics and Astronomy, University of Edinburgh, Edinburgh, United Kingdom, [2] School of Chemical and Process Engineering, University of Leeds, Leeds, United Kingdom

It has previously been demonstrated that particle-stabilized emulsions comprised of limonene, water and fumed silica particles exhibit complex emulsification behavior as a function of composition and the duration of the emulsification step. Most notably the system can invert from being oil-continuous to being water-continuous under prolonged mixing. Here we investigate this phenomenon experimentally for the regime where water is the majority liquid. We prepare samples using a range of different emulsification times and we examine the final properties in bulk and via confocal microscopy. We use the images to quantitatively track the sizes of droplets and clusters of particles. We find that a dense emulsion of water droplets forms initially which is transformed, in time, into a water-in-oil-in-water multiple emulsion with concomitant changes in droplet and cluster sizes. In parallel we carry out rheological studies of water-in-limonene emulsions using different concentrations of fumed silica particles. We unite our observations to propose a mechanism for inversion based on the changes in flow properties and the availability of particles during emulsification.

**Keywords: droplet, interface, emulsification, colloid, cluster**

OPEN ACCESS

***Edited by:***
*Erica Wanless,*
*University of Newcastle, Australia*

***Reviewed by:***
*To Ngai,*
*The Chinese University of Hong Kong, China*
*Cathy Elizabeth McNamee,*
*Shinshu University, Japan*

***Correspondence:**
*Paul S. Clegg*
*paul.clegg@ed.ac.uk*

***Specialty section:***
*This article was submitted to Chemical Engineering, a section of the journal Frontiers in Chemistry*

***Received:*** *16 February 2018*
***Accepted:*** *09 April 2018*
***Published:*** *04 May 2018*

***Citation:***
*Sawiak L, Bailes K, Harbottle D and Clegg PS (2018) Mixing Time, Inversion and Multiple Emulsion Formation in a Limonene and Water Pickering Emulsion. Front. Chem. 6:132. doi: 10.3389/fchem.2018.00132*

## INTRODUCTION

That emulsions can turn "inside out" with prolonged mixing is a phenomenon which has been exploited in butter making for millennia. In the butter churn the fat droplets from cream become the continuous medium (Rønholt et al., 2013). The process is quite complex, involving very many components some of which are lost to the buttermilk. The same phenomenon has been noted much more recently, under high shear, for particle-stabilized emulsions. These emulsions are simpler: they incorporate only three components, most commonly none of them is close to its solidification temperature. In spite of its simplicity this type of inversion process is not yet fully understood. Without this understanding predictive control of emulsification using particles is not possible.

Particle-stabilized emulsions (also called Pickering emulsions) have droplet interfaces stabilized by colloidal particles rather than molecular surfactants (Binks and Horozov, 2006; Ngai and Bon, 2015). Preparing a stable Pickering emulsion involves optimizing the particle wettability, the liquid and particle concentrations, the order of ingredient addition, the liquid flow properties and the mixing protocol. At different points within this highly multi-dimensional phase space a whole slew of different types of emulsions can be fabricated (Vignati et al., 2003; Destribats et al., 2012; Clegg et al., 2016; Domenech and Velankar, 2017) and, by varying one or more of the control variables, transitions between emulsion types are observed (Binks et al., 2010; French et al., 2016).

The simplest Pickering emulsions are made up of dispersed droplets covered by a more-or-less complete layer of particles. Droplet coalescence is prevented by the mechanical barrier provided by the particles. Early on in Pickering emulsion research it was observed that inversions between water-in-oil and oil-in-water Pickering emulsions could be achieved by either changing the wettability of the particles (transitional inversion) or, in some cases, by changing the proportion of the two liquid phases (catastrophic inversion) (Whitby and Wanless, 2016). Subsequently, the number of inversion routes discovered has multiplied.

Crucial aspects of Pickering emulsion inversion behavior were revealed in a study of perfume oils emulsified using fumed silica particles (Binks et al., 2010). This research built on the existing understanding of transitional and catastrophic inversion; in particular, the authors were aware that dispersing the particles in one solvent would bias the system to form an emulsion with that solvent as the continuous phase. In order to minimize this effect, they sprinkled the particles between the two phases prior to emulsification. Alongside confirming transitional and catastrophic emulsion behavior for industrially relevant oils, this study also highlighted the fact that some of these Pickering emulsions could be induced to invert by either increasing the concentration of particles or by increasing the emulsification time. It was suggested that the clusters of particles typical of a high particle concentration/short mixing time sample were more hydrophobic than the well-dispersed particles seen at lower concentrations/longer mixing times. This effect was presented in most detail for a system of water, limonene and fumed silica particles in which the liquid volumes were equal. For example, in one study water droplets in oil form at short times, these grow in size and become oil-in-water-in-oil droplets before finally undergoing an inversion to oil-droplets in water after several minutes of high shear. Below we study related behavior in a somewhat different composition range where we have the added benefit that we are able to observe the size of silica clusters and the details of the droplet size distribution.

Choosing the appropriate combination of mixing time, shear rate and particle concentration is also an important part of designing a stable emulsion in the limit of very high concentrations of droplets. Such systems are called high internal phase emulsions (HIPEs); in Zang and Clegg (2013) the dense emulsions were made up of water droplets stabilized by fumed silica particles. This system can be destabilized into an oil-in-water Pickering emulsion by using too few particles, shearing too fast or for too long. Using confocal microscopy and analysis of the bulk emulsion composition it was possible to show that, in the formation of a HIPE, both droplet size and excess water decrease with time. Provided that the particle concentration is sufficiently high, water droplets are gradually packed into the oil continuous phase even though it is already well populated. It was tentatively suggested that this occurs if the oil phase is sufficiently viscous. Hence oil droplet formation occurs at low particle concentration, after long mixing times or at high shear rates because, under these conditions, the viscosity of the oil phase has markedly decreased.

Close to the point at which an emulsion undergoes inversion it is quite common to observe the formation of a multiple emulsion, i.e., droplets of one liquid phase inside droplets of another. The region of the multi-dimensional parameter space where this occurs is of fundamental interest because it represents the point at which the opposite mean curvatures of the same interfaces are captured in the same sample. It is also of interest for applications because it holds the promise of a simple route to preparing these relatively complex samples. For example, a water-in-oil-in-water emulsion can be used to reduce the fat content of foods or to address a variety of encapsulation challenges. The absence of a simple mixing protocol for preparing multiple emulsions with long-term stability is currently a barrier to their exploitation (Clegg et al., 2016). Very recently a generic pathway for the creation of oil-in-water-in-oil multiple emulsions has been proposed based on phase inversion (Kim et al., 2018). Here we consider one scenario for the production of water-continuous multiple emulsions.

Below we present experimental results on the emulsification of combinations of water, limonene and fumed silica particles. We target the behavior when the aqueous phase is in the majority ($\varphi_w = 0.8$). Qualitatively, we show using bulk observations combined with fluorescence confocal microscopy that a dense emulsion of water droplets rapidly forms which undergoes an inversion after tens of minutes of high shear. The inverted emulsion is a water-in-limonene-in-water multiple emulsion. Quantitatively, we use image analysis to show the complex evolution of the water-droplet size and the size distribution of particle clusters as inversion is approached. We find that the droplets bifurcate into a dense population of small droplets and a small number of very large water droplets which go on to become the continuous phase after inversion. We separately study the flow properties of dense populations of small droplets to support our proposed explanation of the inversion process.

# MATERIALS AND METHODS

## Materials

The fumed silica, type H3O, is partially hydrophobic and was a gift from Wacker, the manufacturing company. Fumed silica is formed of primary particles 30 nm in diameter which aggregate irreversibly into group sizes of 100–1,000 nm. These often cluster further to give final sizes in the micron range. The oil, limonene (R-+, 97%, Sigma-Aldrich), was filtered with activated alumina three times to remove polar impurities. Water was distilled and then passed through a Milli-Q machine giving an initial resistivity of 18 MΩ cm.

## Preparation of Emulsions for Phase Inversion Studies

The powdered particle method from Binks et al. (2010) was used to minimize the extent to which the system is biased to being either oil or water-continuous. The densest phase, water, was put in the vial first. Then a known amount of silica was sprinkled on top before limonene was finally added.

Emulsions had a water volume fraction of 80%, and a silica weight fraction of 0.5%. Nile red was added to the water phase before it was measured out. The concentration of dye in the water was 2.1 μM. A Polytron PT 3100 rotor stator with a 12 mm head was used at 10,300 rpm to emulsify each sample for varying lengths of time. Emulsification durations of 1, 5, 10, 15, 20, and 25 min were used for a series of separate samples.

Preparation of water-in-oil emulsions for rheology studies: To make water-in-oil (w/o) emulsions, which are free of particle clusters and have no tendency to undergo inversion, a dispersion of silica in limonene was first prepared. A known amount of fumed silica was added to a given volume of limonene with dispersion being performed via three cycles of first 2 min. vortex mixing and second ultra-sonication using a probe (VCX 500, Sonics and Materials Inc., Newtown USA) for 2 min. at 20% maximum amplitude. The 25 mL emulsions were made up with a water volume fraction of 0.7. The silica weight fractions were 0.11, 0.19, 0.27, 0.35, 0.44, and 0.52% w/w respectively. A Silverson L5M-A mixer was used to homogenize each sample for 10 min at 10,000 rpm.

## Rheology Experiments

A rheology study was carried out using a TA Instruments DHR-2 rheometer using a Couette geometry. Here, the bob length = 42 mm, bob diameter = 28 mm, cup diameter = 30.4 mm. The freshly loaded sample was allowed to rest for 120 s. This was followed by a frequency sweep for which the stress was 1.0 Pa and the angular frequency varied from 0.3 to 100 rad/s. For each step, there were 5 conditioning cycles, and 5 acquisition cycles. This was followed by an upsweep in shear stress from 0.9 to 200 Pa in order to measure a flow curve with an equilibration time of 5 s, and an acquisition time of 20 s.

## Optical Microscopy

To characterize w/o emulsions, an optical microscope was used with a ×20 objective, Olympus BX51 with a GXCAM HiChrome-MET (GT Vision) camera system. A curved spatula was used to scoop some emulsion onto a cover slip for observation. Droplet sizing was done using Matlab. More than 100 droplets from each sample were measured by diameter.

## Confocal Fluorescence Microscopy

A Zeiss Observer.Z1 inverted microscope in conjunction with a Zeiss LSM 700 scanning system was used to visualize emulsions following various emulsification times. For confocal microscopy studies, the limonene was dyed with Nile Red (2.1 μM, Technical Grade, Sigma-Aldrich). Deployment of two channels allowed separate visualization of dyed oil, and silica in the presence of dyed oil. The first channel was for fluorescence from molecules excited using a laser with wavelength 488 nm and second channel for 555 nm. A short pass filter at 555 nm and a dichroic mirror was used to separate the light for these two channels. A spatula was used to scoop some of each emulsion onto a cover slip for examination. For phase inverted samples, a pipette was used instead.

# RESULTS AND DISCUSSION

## Macroscale

**Figure 1** shows six separate emulsions prepared by high-shear mixing for different periods of time. These vials all contain water, limonene and silica particles with water and silica fractions 80 vol% and 0.5 wt% respectively. Each vial was emulsified for a different period of time indicated by the numbers in each frame. After 1 min of high shear mixing the sample is fully emulsified and appears white and gel-like. As will be confirmed using fluorescence confocal microscopy below, the sample is full of water droplets indicating that it is a particle-stabilized high internal phase emulsion (HIPE). Once the samples had begun to gel it was necessary to move the vial around to give a stirring effect in addition to the localized high shear.

The images of the vials at 15 and 20 min evidence the presence of excess water at the base of the vials. Hence, it is likely that inversion has begun to occur in some parts of the sample. Subsequently, the emulsion begins to yield more substantially and flows fast, before jammed droplets intermittently stop the flow. After a number of flow-stops, the emulsion flows easily throughout the sample. The result can be seen at 25 min of emulsification: the emulsion can now cream. The water is now the continuous phase and the emulsion is no longer a HIPE. The final small vial shows emulsion scraped off the rotor stator. This part of the emulsion had not inverted, and so still exhibits a yield stress.

## Microscale

**Figure 2** shows typical fluorescence confocal micrographs, each corresponding to a particular mixing time, shown top left of each panel. Water (black), Nile Red dyed limonene (pale gray) and the silica (white) are all clearly visible via the merging of separate channels. These micrographs demonstrate that both the size and shape of droplets and clusters of particles change with emulsification time. In the panel at 1 min many non-spherical droplets can be seen reflecting both the dense packing of the droplets and the likely role of coalescence. Smaller droplets are also visible. By 5 min there is less difference in size between small and large droplets in general while the larger ones are more regular in shape than before. At 10 min the emulsion looks less uniform: there are some small droplets, some large droplets with a couple of droplets apparently bigger than at the 5 min point. At 15 min, the difference between big and small droplets continues to grow with the big droplets being few in number. In the 20 min panel only a few large droplets can be seen, the rest are small. Recalling **Figure 1**, at this point water has been expelled from the emulsion which presumably is the natural limit of large water droplets. At 25 min, the phase inversion is captured. No large droplets can be seen anymore, but the continuous phase can clearly be identified as water. Many multiple emulsion droplets can be seen as indicated by the white arrow in the final panel. The

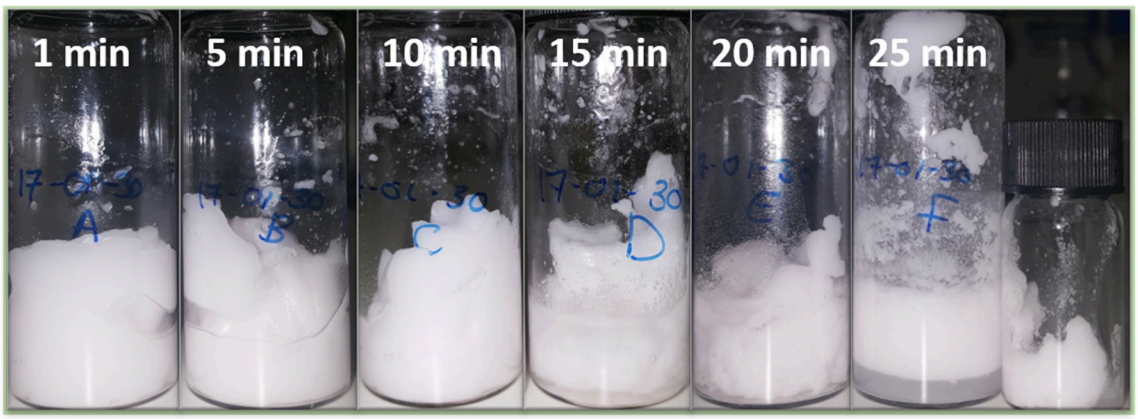


**FIGURE 1 |** Six different emulsion samples created by high shear mixing for different periods of time. The samples are 80 vol.% water and the oil is limonene. Initially a dense emulsion of water droplets is formed stabilized by fumed silica particles. After 15 min a continuous phase of water is beginning to become visible at the base of the sample. The final smaller vial contains dense gelled droplets recovered from the rotor stator head after 25 min.

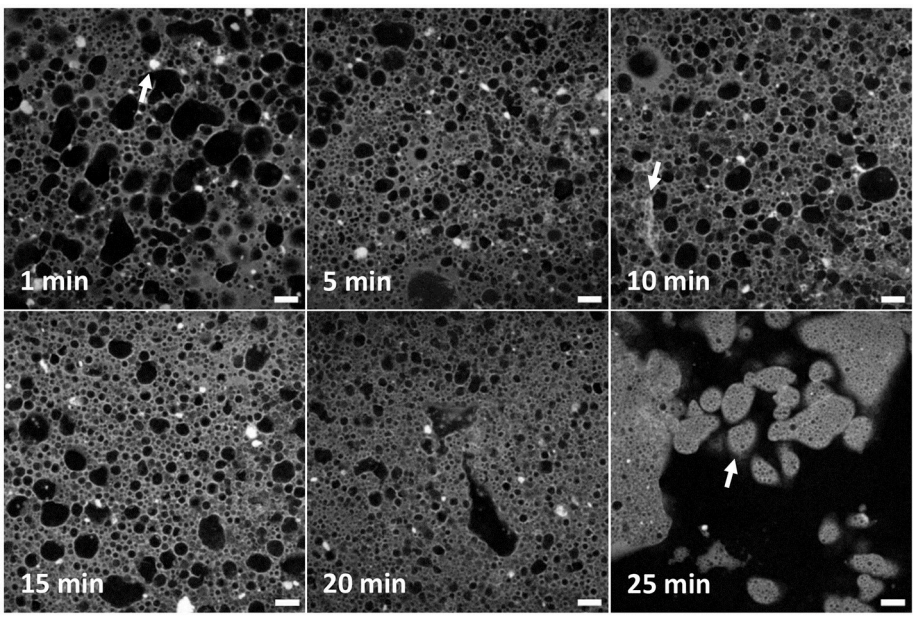


**FIGURE 2 |** A series of confocal micrographs taken using a ×10 objective lens of different emulsion samples prepared by high-shear mixing for different periods of time. All scale bars are 100 μm. The darker phase is water and the lighter phase is limonene dyed with Nile Red. Clusters of poorly dispersed fumed silica are evident as solid bright regions. An example is given by an arrow in the first panel. The changes to the droplet and cluster size distribution are analyzed and discussed in the text. The second arrow shows an elongated structure of silica. The arrow in the final panel points to multiple emulsion droplets of water-in-oil-in-water.

inner water droplets are very small, and uniform over large areas.

In addition to droplets, many clusters of silica can be seen (**Figure 2**, 1 min panel, as indicated by a white arrow). These have been speculated about previously (Binks et al., 2010) as outlined in the Introduction but are imaged here for the first time. The prevalence of these clusters reflects the manner in which the samples were created, i.e., pre-dispersal of particles was avoided. In the confocal micrographs the clusters are very bright and have a low aspect ratio. They appear both in the bulk oil phase and stuck to the interface of droplets. At 5 min, clusters appear smaller on average. This trend continues throughout the time sequence until only a handful of clusters can be seen in the final image. In the 10 min panel, near the bottom left corner an elongated structure can be seen as indicated by an arrow. Its brightness indicates that it is a structure of silica. It is less bright than other silica features and has a different shape to those before. It seems likely that these occur as a side-product of the other processes which lead to emulsion inversion. This will be discussed in more detail later.

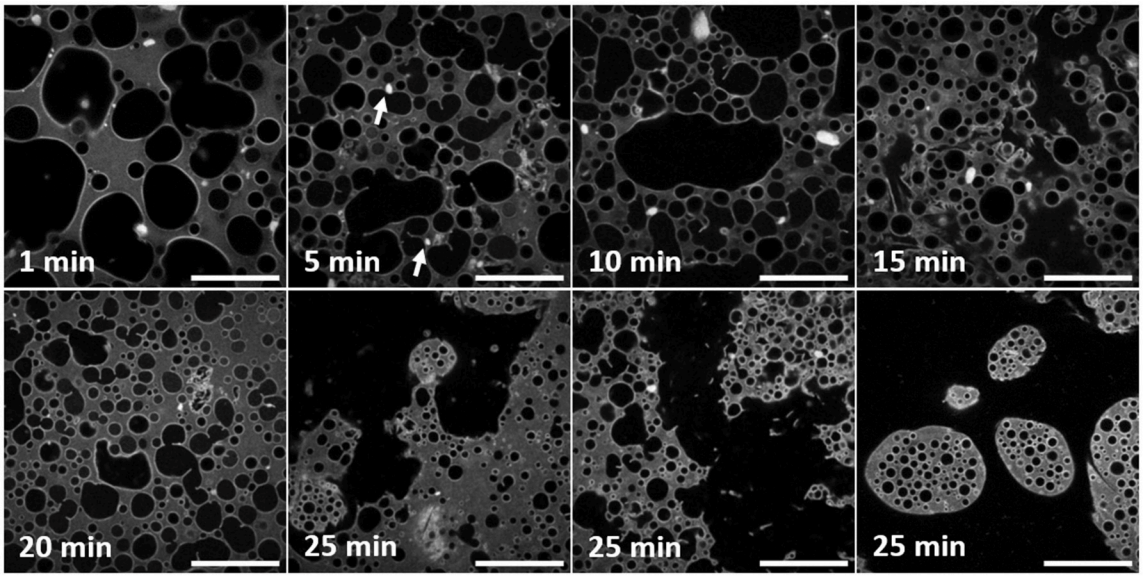


**FIGURE 3 |** A series of confocal micrographs taken using a ×40 objective lens of different emulsion samples prepared by high-shear mixing for different periods of time. All scale bars are 100 μm. The darker phase is water and the lighter phase is limonene dyed with Nile Red. Both particles on droplet interfaces and clusters of particles are visible at this magnification. The changes to the droplet and cluster size distribution are analyzed and discussed in the text. The white arrows in the second panel point out examples of clusters of particles stuck to interfaces of droplets.

**Figure 3** (objective ×40) reveals more details of the water droplets and particle clusters but over a smaller area, compared to **Figure 2**, which will be important for the quantitative analysis that follows. For the first 20 min these images confirm the droplet development described in relation to **Figure 2**. The three confocal micrographs corresponding to 25 min of high-shear mixing, **Figure 3**, demonstrate how heterogeneous the sample has become. The large and very irregular water spaces dominate the images. Within the water, there is floating debris. This is presumed to stem from the emulsification smashing up jammed regions of droplets. This section of water can be considered continuous. Pinch off events, where an interface bulges out in a spherical shape, before the neck of the bulge thins and breaks forming a new droplet are also suggested by these images. In the final 25 min confocal micrograph, multiple emulsion droplets can be seen. There are no large emulsion droplets. Phase inversion has occurred. The inner droplets are small and have a narrow size distribution.

Observing all of the particle clusters in **Figure 3**, the same trend as in **Figure 2** can be seen. The higher resolution of these images highlights features invisible at lower magnification. Here, fewer bright regions of silica can be spotted and the density of particles on the droplet interfaces is reflected in brighter patches. At 5 min clusters are visible on the right-hand side of the image and stuck to droplets of varying size. Two examples are highlighted by white arrows. In the 15 min panel, brighter, straighter segments of silica can be seen. They appear near the boundary of large, irregularly shaped droplets. At 25 min, the edge of the multiple emulsion droplet visible at the top of the image has a textured interface.

**Figure 4** illustrates quantitative segmentation of the micrographs. On the left-hand side the originals are shown, after a Gaussian filter has been used to reduce random noise. At this point a threshold was selected by hand in order to separate the maximum number of droplets. Even with an optimum threshold, some droplets appear stuck together. A morphological opening was used to remove spurious bridges with a disk as the structuring element. The results can be seen in the right-hand side of this figure where the segmentation is overlaid in color. Red signifies droplets with a radius larger than 20 μm, while blue shows smaller droplets. Green indicates particle clusters. Throughout, objects touching the image border of the high resolution images were not included in the analysis. A similar procedure was used to segment the particle clusters which appear bright white in the micrographs.

**Figure 5** shows that normalization of cluster sizes matters. Normalization was carried out separately by volume or by number. Number averaging is an unweighted calculation of the mean. To find the volume-averaged diameter of a particle, d, the sum of $d^4$ divided by the sum of $d^3$ must be calculated. This method of averaging is weighted by the volume each particle takes up, rather than just the number of particles as in the case of a number-average. This graph presents the average cluster size segmented for all micrographs taken from emulsions emulsified for specific times. The cluster radius depends on whether the sizes were normalized by volume (red) or by number (blue). Both trends show that the cluster size at 25 min is less than that initially, but they take different routes. The blue curve shows the clusters gradually getting smaller with time, whereas the red curve shows cluster growth before they are finally broken down.

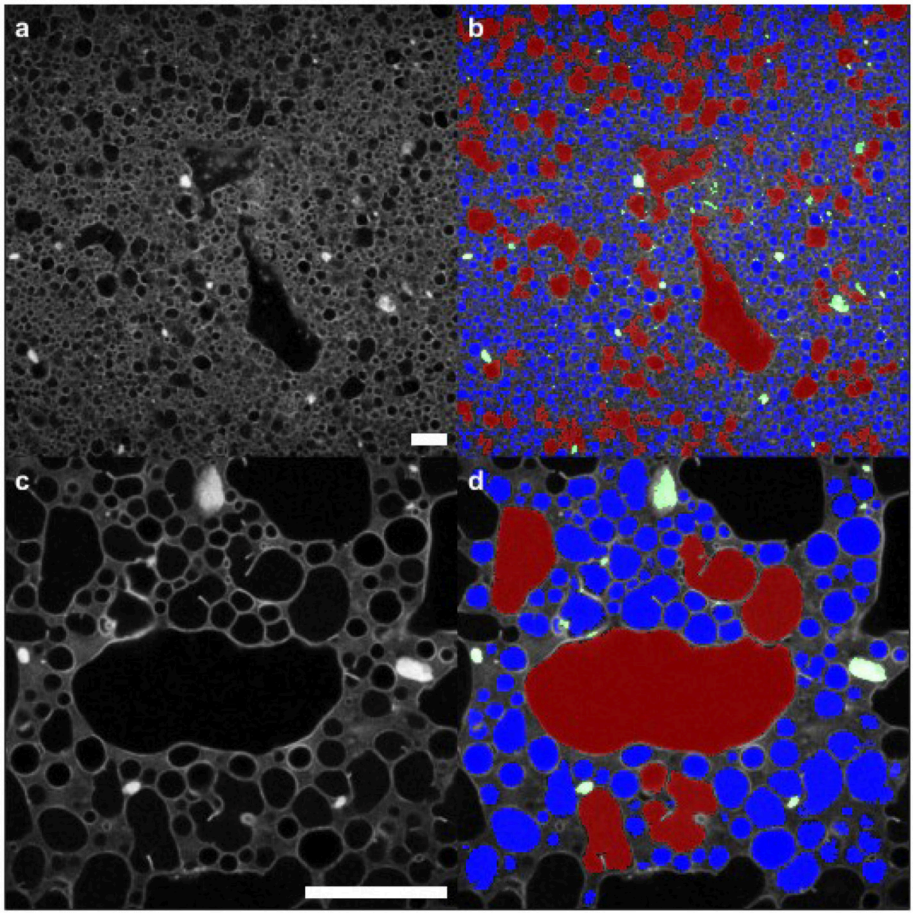


**FIGURE 4 |** Segmentation of droplets and clusters of particles from the confocal image data. **(a,b)** images using ×10 objective (**c,d**) images using ×40 objective. Red signifies droplets larger than 20 μm in their largest dimension; blue indicates the smaller droplets. The segmentation procedure is described in the text; a selection of the resulting parameters are presented in subsequent images. Scale bars in **(a,c)** are 100 μm.

The reason for this is as follows: at all times there are a number of small clusters, bringing the average down. At 10–20 min a very small number of very large objects can be seen. These sometimes occur at the edge of a jagged boundary between oil and water, and sometimes are elongated and rounded. They look like the remnants of a large droplet folded over many times. These cluster sizes were segmented from low magnification data. The larger area of view allows better statistics. Error bars are the standard error. The conclusion that clusters generally break up with time is broadly in agreement with (Binks et al., 2010) although the behavior for our compositions is markedly more complex.

**Figure 6** shows quantitative changes in droplet sizes with emulsification time. The droplet sizes are normalized by volume, and the droplet radius is given. Since there were two data sets with different magnification, the large and small droplets come from the images with the most suitable magnification. The threshold between small (blue) and large (red) droplets is taken as a radius of 20 μm. The two sets of droplets follow different trends. The small droplets begin small, and get smaller and more numerous. Large droplets initially get broken up too. Around 15 min they stop shrinking and instead begin to grow. This is curious and unexpected and is discussed further below.

## Rheology

Several rheology studies have already explored the flow properties of Pickering emulsions fabricated from a range of ingredients (Arditty et al., 2005; Binks et al., 2005; Wolf et al., 2007; Frith et al., 2008; Braisch et al., 2009; Hermes and Clegg, 2013; Katepalli et al., 2017). Early studies focused on systems which had a yield stress at relatively low volume fractions due to the influence of strong attractive interactions between droplets. Unlike with many surfactant-stabilized emulsions, a shear thickening signature was observed at high volume fraction (Wolf et al., 2007). More recently, rheology was combined with imaging for attractive and repulsive Pickering droplets (Hermes and Clegg, 2013) while the flow properties of droplets stabilized by fumed silica have now been explored in some detail (Katepalli et al., 2017) at least in the presence of salt.

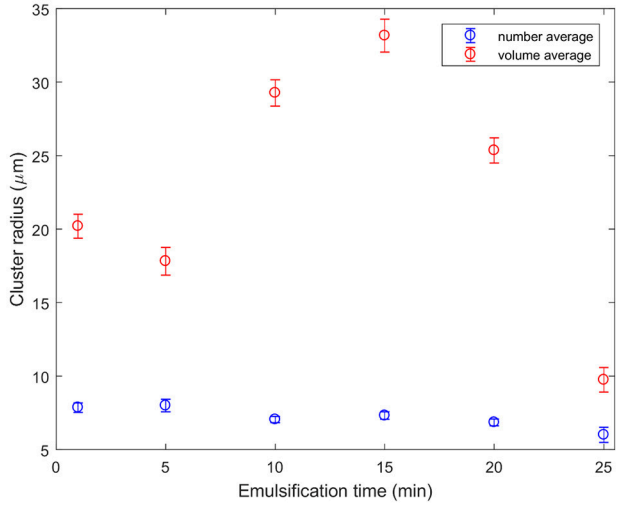


**FIGURE 5 |** Particle cluster sizes segmented from the ×10 objective confocal micrographs as a function of emulsification time. The number average indicates that typical clusters are getting slightly smaller as they are sheared for longer. By contrast, a few very large clusters which appear to be created as large droplets fold over on themselves dominate the volume averages at intermediate emulsification times.

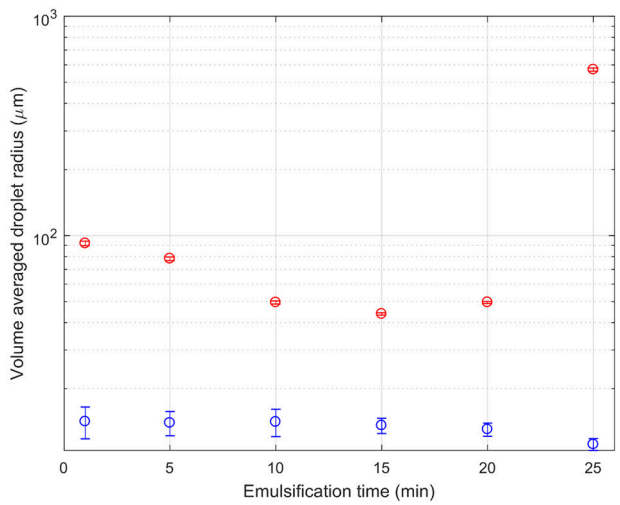


**FIGURE 6 |** A composite graph of the droplet size as a function of emulsification time. The red symbols indicate the volume average of the size of droplets which are above 20 μm in size as determined from the ×10 confocal micrographs. The blue symbols indicate the volume average of the size of droplets which are below 20 μm in size as determined from the ×40 confocal micrographs.

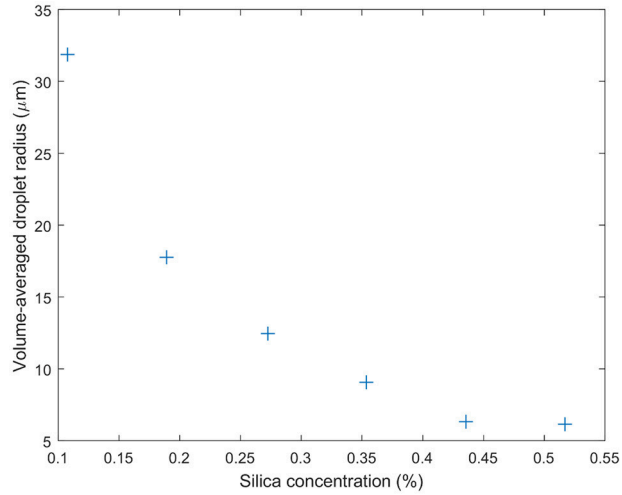


**FIGURE 7 |** Droplet sizes determined using bright-field microscopy for the emulsions designed for rheology studies. The volume average of the water droplet radius is found to steadily decrease with the concentration of silica particles. The particles were pre-dispersed in the limonene oil phase which occupied 30 vol.% of the sample.

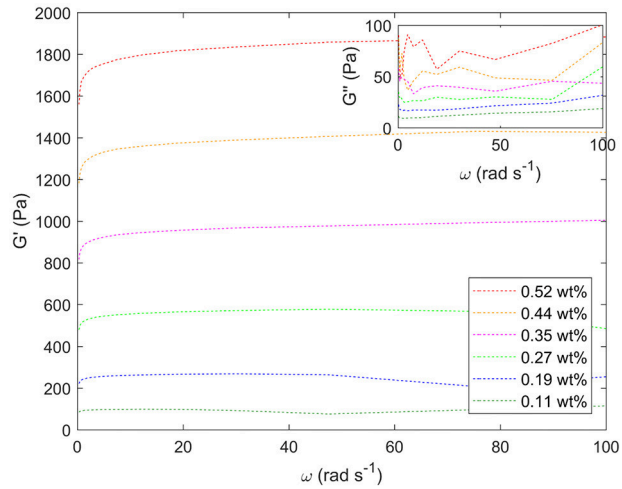


**FIGURE 8 |** Storage moduli (G') for a series of different water-in-limonene Pickering emulsion samples determined for a frequency (ω) sweep at a strain of 0.6 carried out using a Couette geometry. Inset: the corresponding loss moduli (G"). The storage moduli increase systematically with increasing particle concentration / decreasing droplet size. Weight percentages of silica are given in the legend.

The emulsions prepared for the rheology experiments here needed to be stable with respect to shear. Additionally we wanted to avoid large silica clusters to allow us to study the effect of droplet size alone on the flow of an emulsion (see Methods). Silica was dispersed in limonene with its concentration controlling the droplet size. This stock solution was then diluted in order to make a 70% oil fraction emulsion. **Figure 7** illustrates the range of droplet sizes achieved by this route, ranging from around 6–31 μm.

**Figure 8** shows the response to oscillating shear of a range of emulsions with varying droplet size. In the main graph, the effect of changing droplet size on the storage modulus, G', can be seen for angular velocities between 0 and 100 rad $s^{-1}$. Decreasing the droplet size systematically increases the storage modulus. For example, at intermediate angular frequencies the storage modulus increases from ∼100 to 1,800 Pa as the droplet size

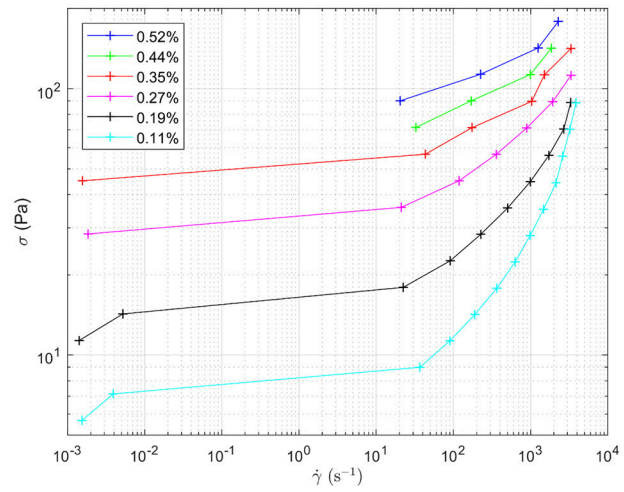


**FIGURE 9 |** Flow curves for the different water-in-limonene Pickering emulsion samples. The shape of the curve is indicative of the samples having a yield stress which is overcome at higher shear rates. Shear stress ($\sigma$) is plotted against shear rate ($\dot{\gamma}$).The legend details the concentration of silica within each emulsion, which controls the size distribution of the droplets making up each emulsion respectively.

decreases, **Figure 7**. The smaller the droplet radius, the more elastic the droplets are. This makes it more difficult for the system to flow. The corresponding loss moduli can be seen inset. The absolute values of the loss moduli are small compared to the storage moduli. With the same range of emulsions, the loss modulus increase is just under an order of magnitude. **Figure 9** shows flow curves (the change in shear rate with varying shear stress) for the range of different emulsions with differing droplet sizes. Larger droplets show lower yield stresses. At higher shear rates, the larger droplets have a stronger dependence between the stress and the shear rate in comparison to the more gentle slopes for the smaller droplets. This relationship has been seen before for surfactant-stabilized emulsions (Pal, 1996, 1998).

## Role of Emulsification Time

Considering together the flow properties (**Figures 8**, **9**) and the evolution of the droplet size (**Figure 6**), some light is shed upon the underlying mechanism of phase inversion for our composition range. At short times, droplets of all sizes are being broken up as the macroscopic domains and rough emulsion droplets become the droplet size distribution observed in our images. Curiously, at around 15 min of emulsification the larger droplets stop shrinking while the small droplets are becoming less flowable. Indeed the regions of dense droplets in the sample are likely to have a significant yield stress. The break-up and deformation of the larger droplets is the easiest way for the system to flow, however, break-up into smaller droplets appears not to be happening with any permanence. Instead we see these large droplets growing and becoming increasingly folded and deformed. The folding is evident in the growth of new, less bright, silica clusters leading to the apparent increased cluster size in the volume averaged curve in **Figure 5**. Ultimately, the large population of droplets appear to develop progressively into the continuous phase of a multiple emulsion.

We suggest that the large population of water droplets develops a separate mode of behavior due to exhaustion of the supply of particles. It appears that most particles are: either bound up on the interfaces of a robust population of small droplets or formed into new particle clusters when large droplets are distorted and fold. At the same time, the dense population of small droplets and everything bound around them does not easily flow. By contrast the large droplets can be broken up and deformed easily. Following break up they also rapidly coalesce, giving rise to the many examples of arrested coalescence which are evident in **Figures 2**, **3**. (It is possible that in some cases the droplets form particle bridges, in place of coalescence, although this is difficult to diagnose for the particle sizes we are using here).

This process of multiple emulsion formation is quite different from that observed by Binks and coworkers (Binks et al., 2010). Those authors worked with a range of particle surface chemistries but their studies included a focus on the water/limonene system we have used here. They show that, for an equal volume of water and limonene, the system forms an oil-continuous emulsion at short times but that the water droplets become larger, on average, as mixing continues. They suggest that the sharp increase in droplet size is due to the inclusion of oil droplets within the water droplets, i.e., the opposite type of multiple emulsion to that which we observe. Finally, these large multiple emulsion droplets invert to give a water-continuous simple emulsion.

It is also important to consider whether the behavior we observe could be due to a change in wettability of particle clusters with mixing time. Binks suggested that the changes in emulsion state with increasing duration of high-shear mixing could be due to the improved dispersal of particle clusters (Binks et al., 2010). We have demonstrated here that these clusters exist and that they are broken down during mixing to some extent. While we cannot rule out that two populations of particles exist or that some clusters include a trapped solvent (Clegg et al., 2016) it is far from obvious that the interfaces of the small and large droplets are in anyway different. There is no immediate suggestion that there are two classes of interface leading to a variation in the sign of the mean curvature of the interfaces.

# CONCLUSIONS

Using bulk observations, confocal microscopy and rheology we have explored the behavior of Pickering emulsions comprised of water, limonene and fumed silica as a function of mixing time. From a very early stage the samples are completely comprised of water droplets. With continuing mixing time, particle clusters break up and the droplet sizes decrease. As the water droplets break up a subset of large droplets is left behind and some of these even grow. Most of the sample is a dense rigid population of small water droplets and we separately find that such emulsions become increasingly gel-like as the droplet size decreases. By contrast, the remaining larger droplets are floppy and unstable.

During the continuing mixing, the large droplets are never permanently broken down to the typical small droplet size. We argue that this is because the supply of accessible particles has been exhausted. Instead large floppy water droplets with low Laplace pressures are folded over on themselves and become crumpled leading to some new (but less dense) particle clusters being formed. Eventually the large water droplets coalesce to form a continuous phase around limonene droplets which contain a dense population of small water droplets.

## AUTHOR CONTRIBUTIONS

Mixing time and confocal microscopy studies were carried out by LS under the guidance of PC. Rheology studies were carried out by LS and KB under the guidance of DH. The manuscript was drafted by PC with contributions from all of the other authors.

## FUNDING

LS gratefully acknowledges a studentship from the Soft Matter and Functional Interfaces EPSRC Centre for Doctoral Training.

## ACKNOWLEDGMENTS

We thank N. Koumakis for his assistance with quantitative image processing.

## REFERENCES

Arditty, S., Schmitt, V., Lequeux, F., and Leal-Calderon, F. (2005). Interfacial properties in solid-stabilized emulsions. *Europhys. J. B.* 44, 381–393. doi: 10.1140/epjb/e2005-00137-0

Binks, B. P., Clint, J. H., and Whitby, C. P. (2005). Rheological behavior of water-in-oil emulsions stabilized by hydrophobic bentonite particles. *Langmuir* 21:5307. doi: 10.1021/la050255w

Binks, B. P., and Horozov, T. S. (2006). *Colloidal Particles at Liquid Interfaces.* Cambridge: CUP.

Binks, B. P., Fletcher, P. D., Holt, B. L., Beaussoubre, P., and Wong, K. (2010). Phase inversion of particle-stabilised perfume oil-water emulsions: experiment and theory. *Phys. Chem. Chem. Phys.* 12, 11954–11966. doi: 10.1039/c0cp00558d

Braisch, B., Kohler, K., Schuchmann, H., and Wolf, B. (2009). Preparation and flow behaviour of oil-in-water emulsions stabilized by hydrophilic silica particles. *Chem. Eng. Technol.* 32, 1107–1112. doi: 10.1002/ceat.200900064

Clegg, P. S., Tavacoli, J. W., and Wilde, P. J. (2016). One-step production of multiple emulsions: microfluidic, polymer-stabilized and particle-stabilized approaches. *Soft Matter* 12:998. doi: 10.1039/C5SM01663K

Destribats, M., Lapeyre, V., Sellier, E., Leal-Calderon, F., Ravaine, V., and Schmitt, V. (2012). Origin and control of adhesion between emulsion drops stabilized by thermally sensitive soft colloidal particles. *Langmuir* 28:3744. doi: 10.1021/la2043763

Domenech, T., and Velankar, S. S. (2017). Microstructure, phase inversion and yielding in immiscible polymer blends with selectively wetting silica particles. *J. Rheol.* 2:363. doi: 10.1122/1.4975931

French, D. J., Brown, A. T., Schofield, A. B., Fowler, J., Taylor, P., and Clegg, P. S. (2016). The secret life of Pickering emulsions: particle exchange revealed using two colours of particle. *Sci. Rep.* 6:31401. doi: 10.1038/srep31401

Frith, W. J., Pichot, R., Kirkland, M., and Wolf, B. (2008). Formation, stability, and rheology of particle stabilized emulsions: influence of multivalent cations. *Indus. Eng. Chem. Res.* 47:6434. doi: 10.1021/ie071629e

Hermes, M., and Clegg, P. S. (2013). Yielding and flow of concentrated Pickering emulsions. *Soft Matter* 9:7568. doi: 10.1039/c3sm50889g

Katepalli, H., John, V. T., Tripathi, A., and Bose, A. (2017). Microstructure and rheology of particle stabilized emulsions: effects of particle shape and inter-particle interactions. *J. Coll. Interf. Sci.* 485:11. doi: 10.1016/j.jcis.2016.09.015

Kim, S., Kim, K., and Choi, S. Q. (2018). Controllable one-step double emulsion formation. *Soft Matter* 14, 1094–1099. doi: 10.1039/C7SM02134H

Ngai, T., and Bon, S. A. F. (2015). *Particle-Stabilized Emulsions and Colloids.* Cambridge: RSC.

Pal, R. (1996). Effect of droplet size on the rheology of emulsions. *AIChE J.* 42, 3181–3190. doi: 10.1002/aic.690421119

Pal, R. (1998). Scaling of viscoelastic properties of emulsions. *Chem. Eng. J.* 70, 173–178. doi: 10.1016/S0923-0467(98)00082-7

Rønholt, S., Mortensen, K., and Knudsen, J. C. (2013). The effective factors on the structure of butter. *Compr. Rev. Food Sci. Food Safety.* 12, 468–482. doi: 10.1111/1541-4337.12022

Vignati, E., Piazza, R., and Lockhart, T. P. (2003). Pickering emulsions: interfacial tension, colloidal layer morphology, and trapped-particle motion. *Langmuir* 19:6650. doi: 10.1021/la034264l

Whitby, C. P., and Wanless, E. J. (2016). Controlling pickering emulsion destabilisation: a route to fabricating new materials by phase inversion. *Materials* 9:626. doi: 10.3390/ma9080626

Wolf, B., Lam, S., Kirkland, M., and Frith, W. J. (2007). Shear thickening of an emulsion stabilized with hydrophilic silica. *J. Rheol.* 51:465. doi: 10.1122/1.2714642

Zang, D., and Clegg, P. S. (2013). Relationship between high internal-phase Pickering emulsions and catastrophic inversion. *Soft Matter* 9:7042 doi: 10.1039/c3sm00133d

**Conflict of Interest Statement:** The authors declare that the research was conducted in the absence of any commercial or financial relationships that could be construed as a potential conflict of interest.

frontiers in Chemistry

MINI REVIEW
published: 30 August 2018
doi: 10.3389/fchem.2018.00383

# Particle-Stabilized Fluid-Fluid Interfaces: The Impact of Core Composition on Interfacial Structure

*Alison Tasker*[1,2]*, *Frank Sainsbury*[1] *and Simon Puttick*[1,2]

[1] *Australian Institute for Bioengineering and Nanotechnology, University of Queensland, Brisbane, QLD, Australia,*
[2] *Commonwealth Scientific and Industrial Research Organisation, Probing Biosystems Future Science Platform, Brisbane, QLD, Australia*

The encapsulation of small molecule drugs in nanomaterials has become an increasingly popular approach to the delivery of therapeutics. The use of emulsions as templates for the synthesis of drug impregnated nanomaterials is an exciting area of research, and a great deal of progress has been made in understanding the interfacial chemistry that is critical to controlling the physicochemical properties of both the encapsulated material and the templated material. For example, control of the interfacial tension between an oil and aqueous phase is a fundamental concern when designing drug delivery vehicles that are stabilized by particulate surfactants at the fluid interface. Particles in general are capable of self-assembly at a fluid interface, with a preference for one or the other of the phases, and much work has focussed on modification of the particle properties to optimize formation and stability of the emulsion. An issue arises however when a model, single oil system is translated into more complex, real-world scenarios, which are often multi-component, with the incorporation of charged active ingredients and other excipients. The result is potentially a huge change in the properties of the dispersed phase which can lead to a failure in the capability of particles to continue to stabilize the interface. In this mini-review, we will focus on two encapsulation strategies based on the selective deposition of particles or proteins on a fluid-fluid interface: virus-like particles and polymer microcapsules formed from particle-stabilized emulsion templates. The similarity between these colloidal systems lies in the fact that particulate entities are used to stabilize fluid cores. We will focus on those studies that have described the effect of subtle changes in core composition on the self-assembly of particles at the fluid-fluid interface and how this influences the resulting capsule structure.

**Keywords: VLPs, pickering emulsions, polymer microcapsules, interfacial chemistry, drug delivery**

OPEN ACCESS

***Edited by:***
*Syuji Fujii,*
*Osaka Institute of Technology, Japan*

***Reviewed by:***
*Javier Ereña,*
*University of the Basque Country (UPV/EHU), Spain*
*Ryo Murakami,*
*Konan University, Japan*

***Correspondence:**
*Alison Tasker*
*a.tasker@uq.edu.au*

***Specialty section:***
*This article was submitted to Chemical Engineering, a section of the journal Frontiers in Chemistry*

***Received:*** *29 March 2018*
***Accepted:*** *09 August 2018*
***Published:*** *30 August 2018*

***Citation:***
*Tasker A, Sainsbury F and Puttick S (2018) Particle-Stabilized Fluid-Fluid Interfaces: The Impact of Core Composition on Interfacial Structure. Front. Chem. 6:383. doi: 10.3389/fchem.2018.00383*

## INTRODUCTION

Encapsulation in nanomaterials is a powerful approach to the delivery of active components that require protection from harsh external environments. Encapsulation strategies range from mimicking natural delivery vehicles using virus coat protein self-assembly, through to the stabilization of hydrophobic cores by inorganic nanoparticles or polymeric surfactants to form microcapsules. In the case of delivery vehicles based on a capsule structure, significant effort is directed to optimizing the interface used to template the capsule material, be it polymeric or

protein in nature. Based on observations in our laboratory and others (Manuela et al., 2017), the physicochemical properties of the active component itself can have a profound effect on the stability of this interface and this has prompted us to review existing literature in this area.

Whilst it is well-known that the contact angle is a key parameter for stabilization of emulsions using particles (Binks et al., 2007), the literature surrounding the effect of core composition on the organization of stabilizers at the interface is scarce. Thus, in this mini-review, we aim to capture emerging knowledge around the impact of core compositions on interfacial architectures and particle morphology. As compositions are developed with increasing complexity, for example by drug loading, there is an increasing need for fundamental understanding on the assembly of nanoscale to microscale capsules. We aim to bring together information of core effects intended to highlight the importance of consideration of the core properties in particle-stabilized fluid-fluid systems. Herein we consider the selective deposition of both proteins and particles on a fluid-fluid interface: virus-like particles and particle-stabilized emulsion templates. In virus-derived particles, the influence of the core on particle structure can often be mapped to specific changes in the interactions between coat protein subunits. However, for polymer microcapsules, how the changing interactions between the core and particles at the interface affects interfacial organization is somewhat less clear. Here we will focus on capsule-like structures and not solid microparticles where the active ingredient is absorbed into a solid matrix, or covalently bonded to a micro/nanostructure or protein, and the interested reader is instead directed to several recent reviews in these areas (Duncan, 2011; Kopecek, 2013; Chudasama et al., 2016; Han et al., 2016; Ramazani et al., 2016).

## VIRUSES AND VIRUS-LIKE PARTICLES

Nature's prototypical delivery vehicles, viruses, are assembled from particulate protein subunits around a nucleic acid or nucleoprotein core. The structural fidelity of capsid subunits enables the rational genetic or chemical modification of solvent-exposed amino acid side chains, which has led to their application in biomedical nanotechnology (Wen and Steinmetz, 2016). The packaging density of viral genomes is such that it is considered to be in a liquid crystalline state (Speir and Johnson, 2012) and the net charge of the interior face of capsid protein subunits is commonly highly positive, imparting a strong preference to assemble around this polyanionic fluid-like core. This feature of capsid subunits has been used to drive the encapsidation of cargo proteins (Glasgow et al., 2012; Brasch et al., 2017) into particles that may be subsequently surface-modified for cellular uptake (Ashley et al., 2011). As spherical virus capsids can undergo elastic deformation (Marchetti et al., 2016), it is perhaps not surprising that there is some plasticity in the interfacial arrangement of coat protein subunits around various core compositions. For example, the packaging of DNA-tagged enzymes into Cowpea chlorotic mottle virus (CCMV) capsids results in a radial swelling that changes the way capsid subunits interact with each other at the interface, although the particle remains stable (Brasch et al., 2017).

While capsid morphologies are constrained by a limited range of subunit interactions, these interactions can be altered by the encapsidated cargo. For example, Hu et al. demonstrated that the capsid subunits of CCMV assembled around an anionic polymer, poly(styrene-sulfonate) can be forced into assemblies of 120 or 180 subunits depending on the molecular weight of the polymer (Hu et al., 2008). Capsids of the related Brome mosaic virus (BMV) assembled around different segments of the BMV genome, while all the same size and composed of 180 capsid subunits, display different physical properties that impact the rate of interfacial disassembly and cargo release (Vaughan et al., 2014). In these examples, regular subunit lattices are maintained by the conformational switching of capsid protein subunits that allows them to occupy non-equivalent positions on the native icosahedron. Conversely, CCMV subunits deposited on poly(dimethylsiloxane) cores, stabilized by anionic sodium dodecyl sulfate to impart negative charge, forces the subunits into larger and non-icosahedral particles as well as multi-shell structures (Chang et al., 2008). Areas of local subunit organization reminiscent of the native capsid were observed, however, the presence of "scars" indicated core induced disorder at a smaller scale than the subunit (**Figure 1A**).

The classically pleomorphic members of the Polyomaviridae have been subject to numerous studies on the impact of core composition on capsid geometry. For example, varying the ratio of linear DNA to capsid subunit of SV40 can be used to control size, shape, and stability of virus-like particles (Mukherjee et al., 2010). unrivaled flexibility in the lateral interactions between polyomavirus capsid subunits allows them to assemble on cores considerably larger or smaller than the native 50 nm capsid, while maintaining a regular subunit lattice, for example polystyrene beads of 100 and 200 nm (**Figure 1B**; (Kawano et al., 2015)), or the much smaller 8, 20, and 27 nm citrate-coated oleate-iron nanoparticles (Enomoto et al., 2013).

Whole virus capsids have also been used to stabilize fluid-fluid interfaces. Their amenability to genetic or chemical modification makes them particularly attractive for the formation of hierarchically ordered structures based on Pickering emulsions. In an early example, Russell et al. showed that chemically labeled Cowpea mosaic virus (CPMV) particles assembled as a monolayer at the interface of perfluorodecalin emulsions (**Figure 1C**; (Russell et al., 2005)). Chemical crosslinking of unmodified particles, or biochemically linking biotinylated particles with streptavidin, resulted in non-equilibrium stability of the capsules and the dual fluorescence-biotin labeling demonstrated the excellent potential for further functionalization. Turnip yellow mosaic virus (TYMV) was similarly used to stabilize a perfluorodecalin emulsion with fluorescent functionalization of the TYMV particles (Kaur et al., 2009). Kaur et al. report that among six different core compositions stable emulsions could only be formed with perfluorodecalin, highlighting the importance of particle-core compatibility in the formation of such capsules (Kaur et al., 2009). Furthermore, this study showed that under the dynamic conditions of emulsification the monolayer of particles is

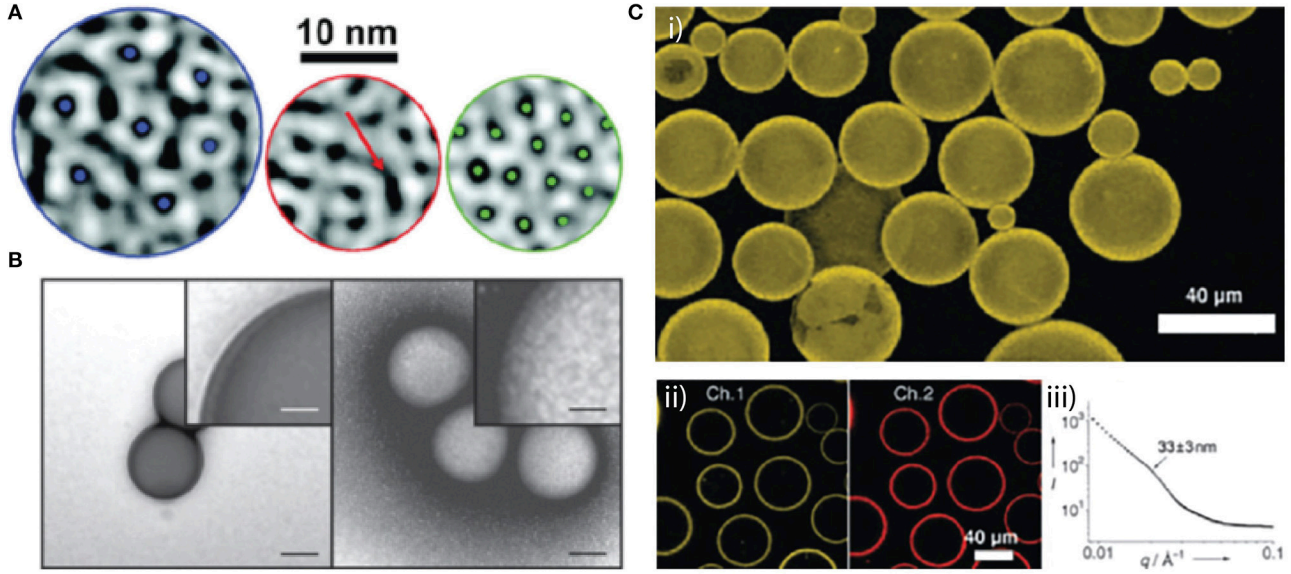


**FIGURE 1 |** Examples of virus interfacial arrangements around various core compositions. **(A)** Local CCMV protein structures observed on the surfaces of nanodroplets have different degrees of order and disorder. **(A)** Left: six-fold-coordinated capsomers (blue dots at center) represent a high degree of order seen mostly on smaller droplets. Middle: an example of a trough-like scar that consists of an elongated dark region (red arrow) surrounded by a protruding white region. Right: hexagonal web structure, typically seen on larger droplets, consisting of dark spots (green dots) surrounded by an interconnected white network of protein protruding from the interface. Reprinted with permission from Chang et al. (2008). **(B)** Polystyrene beads incubated with (right) or without (left) SV40 VP1 pentamers. The samples were visualized by TEM with negative staining. Scale bar = 100 and 25 nm (insets). Reprinted with permission from Kawano et al. (2015). **(C)** (i) A 3D reconstruction of a confocal fluorescence microscope image of perfluorodecalin droplets coated with CPMV/biotin after being cross-linked with avidin for 3 h at 48°C. (ii) A two-channel confocal fluorescence microscope image of particle assemblies after cross-linking with fluorescently tagged streptavidin: Channel 1 shows the CPMV/biotin fluorescence and channel 2 shows the ATTO-655-streptavidin fluorescence. (iii) SAXS data of the cross-linked CPMV/biotin shell around the perfluodecalin droplets. Reprinted with permission from Russell et al. (2005).

disorganized, despite the ability of the icosahedral virus capsid to form ordered hexagonal arrays. While both CPMV and TYMV are spherical viruses with icosahedral symmetry, Tobacco mosaic virus (TMV) is helical with a rod-shaped morphology. In a further example, He et al. showed that the anisotropic morphology of TMV could be exploited to generate dramatically different interfacial organization of the particle. At low particle concentrations rod-shaped particles were oriented parallel to the interface of a perfluorodecalin core, however, at high concentrations segregation at the interface forced the rods to orient perpendicular to the interface, overcoming inter-particle electrostatic repulsion (He et al., 2009).

## POLYMER MICROCAPSULES TEMPLATED ON A PARTICLE-STABILIZED FLUID-FLUID INTERFACE

The use of a fluid-fluid interface as a template for the synthesis of polymer microcapsules encapsulating an active component is an exciting area and a great deal of progress has been made in understanding the interfacial chemistry that is critical to controlling the physicochemical properties of both the encapsulated material and the templated material. Control of the interfacial tension between the three phases in an emulsion system (core, aqueous, and stabilizer) is a fundamental concern when designing a template emulsion and one approach is to use solid nanoparticles as the stabilizer to form a Pickering emulsion. Particles in general are capable of self-assembly at a fluid interface, for example in an oil-water (o/w) emulsion, with a preference for one or the other of the phases and much work has focussed on tailoring the surface chemistry of the particle to control properties such as surface activity and to optimize emulsion properties such as stability and cargo release (Aveyard et al., 2003; Amalvy et al., 2004; Read et al., 2004; Ngai et al., 2006; Tasker et al., 2018). An issue arises however when a model, single oil system is translated into more complex, real-world scenarios, which are often multi-component, with the incorporation of charged active ingredients and other excipients. This potentially alters the properties of the dispersed phase leading to changes in the particle contact angle, which may result in a reduced capacity of particles to stabilize the interface.

For example, graphene oxide (GO) sheets have been successfully used to stabilize emulsions with either a water-oil-water (w/o/w) or oil-water (o/w) morphology, depending on the oil used as the dispersed phase, via a Pickering emulsion formation (Ali et al., 2017). The authors found that for both toluene and olive oil dispersed phases, when the GO concentration was increased, the formed droplets became smaller, suggesting that GO was acting as a limiting interfacial stabilizer. Toluene emulsions required more energy than the olive oil emulsions due to the higher interfacial

tension of toluene/water compared to olive oil/water. They also discovered that when olive oil was used as the dispersed phase, multiple emulsions were formed spontaneously, a phenomenon which was not observed with toluene as the dispersed phase (**Figure 2A**). They suggest that this unusual multiple emulsion formation is due to the more complex mixture of components in the olive oil. Free fatty acids present in the oil contributed to the stability of the internalized water droplets in the w/o/w emulsions that were formed. Furthermore, with toluene, droplet size increased with pH while droplet stability decreased, resulting in mostly coalescence at pH 11, however when olive oil was used, the opposite was seen to be the case—droplets became smaller and more stable with an increase in pH. A minor component of olive oil, oleic acid, is deprotonated at pH 11 to form sodium oleate which is an effective emulsifier and acts to stabilize the emulsions at higher pH. This work highlights the potential for minor components of the core material to play a critical role in the formation and stability of the final emulsion.

Work conducted by Tasker et al. also indicates that the relationship between the interfacial tensions of the three phases involved in polymer microcapsule synthesis, namely the oil, polymer, and aqueous phase, are crucial in determining the final microcapsule morphology as they determine the wettability of the core oil by the polymer in the aqueous phase (Tasker et al., 2016). Although a surfactant is not considered a particle in the traditional sense, this work demonstrates how changing interfacial properties resulting from substitution of the core phase can impact the formation of an emulsion-based polymer microcapsule template. In their study the authors used poly(methyl methacrylate) as the shell-forming polymer using the solvent evaporation method of microcapsule formation with a range of oils and aqueous phases to understand the importance of the correct interfacial behavior. The authors found that when cetyltrimethylammonium bromide was used as the stabilizer and hexadecane was used as the oil phase, acorn morphology microcapsules were formed, whereas when hexadecane was substituted for toluene, cyclamen aldehyde, dihydromyrcenol, or hexyl salicylate, core-shell microcapsules were produced (**Figure 2B**). This is likely an effect of the hydrophobicity of the oils chosen, as the partition coefficient of hexadecane is much higher than that of the other oils tested. The work demonstrated that interfacial tension and contact angle measurements can help predict whether a given oil-polymer surfactant combination chosen to create a polymer microcapsule will result in desired morphologies. Polarity of the oil phase is a further physicochemical property that has been considered in depth when considering the formation of Pickering emulsions. The polarity of the oil phase can determine what type of emulsion is formed, if any, which again highlights the importance of considering interfacial tension and contact angle measurements in the design of any complex emulsion situation (Binks and Clint, 2002; Read et al., 2004).

The effect of core composition on emulsion stability is also evident when using complex cores with melting points near room temperature. Veverka et al. (2018) made oil-in-gel emulsions using β-glucan as the aqueous phase with a range of natural oils. They found that using conjugated linoleic acid (CLA) as the oil phase in a 1:1 molar ratio with the aqueous phase, using no additional stabilizer, yielded an emulsion which was fully phase separated within 48 h. In comparison, when using cocoa butter as the oil phase, again in a 1:1 ratio, a stable emulsion (up to 12 months) was produced. The authors state that this stability is due to the nature of the cocoa butter, as it contained crystalline particles of saturated fatty acids, as demonstrated by cryo-SEM, and saturated fatty acids are known to behave as solids at the oil-gel interface (Macierzanka et al., 2009; Frasch-Melnik et al., 2010; Ghosh and Rousseau, 2011). This work demonstrates how the core composition is an important parameter to consider when forming an emulsion, as in this case, the presence of particles within the oil actually allowed the unintentional formation of a Pickering emulsion. It is worth noting that when β-glucan particles were added to the gel phase, CLA emulsions were stabilized however no differences in oil droplet properties were observed.

The chain length of core oils can also affect microcapsule morphologies. For example, Wagdare et al. investigated how the use of different oils as the core of Eudragit microcapsules impacted the morphology of the capsule shell (Wagdare et al., 2011). The authors used long chain triglycerides, such as olive oil, coconut oil, and vegetable oil, and the medium chain triglyceride Miglyol, in addition to jojoba oil which is a mixture of monoesters. They found that for the long chain triglycerides, a single core-shell morphology was obtained, but when the medium chain triglyceride was used, multi-compartment core-shell morphologies were obtained. They explain the differences in behavior between the long- and medium-chain triglyceride core oils to be due to their compatibility with the shell material. As the solvent diffuses out of the formed droplets, the concentrations of both the polymer and the oil in the droplet increase. There comes a point at which the polymer is no longer soluble in the remaining solvent and so precipitation/gelation occurs. If the oil has already phase separated before the polymer solidifies, the oil can diffuse through the polymer matrix to form a large droplet in the middle of the capsule. However, if the oil does not phase separate before precipitation/gelation of the polymer, small pockets of oil will become trapped throughout the polymer matrix, resulting in the observed multi-component capsules. Higher molecular weight molecules are less soluble in general than their smaller counterparts and so phase separation will occur at an earlier stage in the capsule formation which explains the difference in morphologies seen for capsules formed using the different oils in this study.

In other cases it has been found that the ratio of components that make up a microcapsule core can also affect the resulting capsule morphology. Wang et al. prepared microcapsules using particle-stabilized emulsion polymerization for applications such as the selective adsorption of bisphenol A (BPA), an endocrine-disrupting chemical found in a wide range of food and drink products (Wang et al., 2018). They first formed an o/w Pickering emulsion, stabilized with silica nanoparticles, with a complex core containing the monomer, 4-vinylpyridine; crosslinker, divinylbenzene; initiator, azobisisobutyronitrile (AIBN); solvent, hexadecane, and the template molecule, BPA. They found that the resulting morphology of the formed polymer capsules could

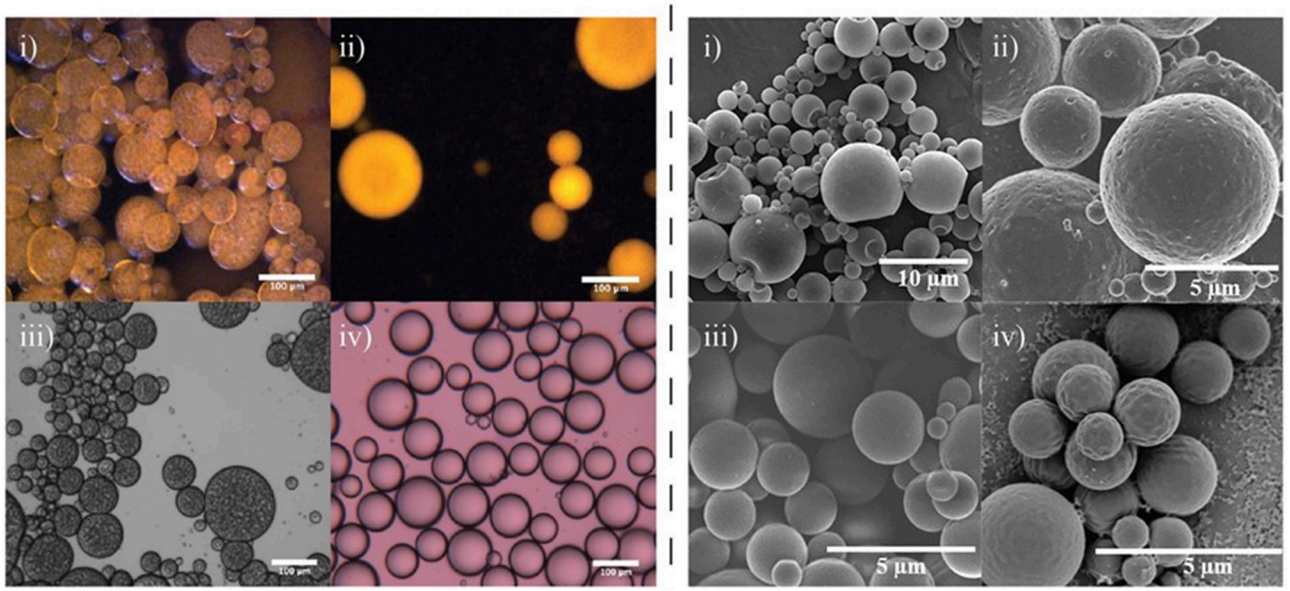


**FIGURE 2 |** Examples of how core composition can affect the structure of fluid-fluid interfaces and resultant templated microcapsules. **(A)** Fluorescence and transmission optical micrographs showing multiple emulsion formation for olive oil and single emulsion formation for toluene with aqueous GO solutions; (i) fluorescence image of an olive oil emulsion, (ii) fluorescence image of a toluene emulsion, (iii) optical microscopy image of an olive oil emulsion, (iv) optical microscopy image of a toluene emulsion. All samples were prepared with 1 mg/mL GO at pH 1. Reprinted with permission from Ali et al. (2017). **(B)** The changing morphology of poly(methyl methacrylate) microcapsules when the core composition is modified between (i) Hexadecane, (ii) hexyl salicylate, (iii) cyclamen aldehyde, and (iv) toluene. Reprinted with permission from Tasker et al. (2016).

be controlled by adjusting the composition of the oil phase, resulting in either a single void inside the polymer shell, or a multi-component core. Firstly, they note that in the absence of BPA, a single void structure is formed, and this is attributed to the presence of hexadecane, which acts as a non-solvent for the formed polymer, driving it to the oil-water interface where it forms a shell. However, when BPA is added to the oil phase, the internal structure of the capsule changes to what appears to be a series of sub capsules within the external shell. They found that by increasing the BPA concentration in the oil phase, the number of internal cores increases but the cores also decrease in size and, as expected, the shell thickness of the whole capsule decreases as less polymer migrates to the interface. BPA will dissolve in the oil phase if it contains hexadecane at <50% volume fraction, however, as polymerization occurs the volume fraction of hexadecane increases and so the BPA precipitates, creating nucleation sites for the internal sphere growth. In contrast, when the authors reduced the initial volume fraction of hexadecane to just 30%, no significant differences were observed between the capsules formed with and without BPA. This article demonstrates the importance of considering the effect that changing the composition of a complex cargo could have on the morphology of microcapsules. In other works which exemplify this, Liu et al. found that when forming polymer microcapsules from a Pickering emulsion template, the ratio between block lengths of a block copolymer within the oil core affected the distribution of hydroxyapatite particles at the oil-water interface, which in turn affected the surface morphology of the resulting microparticles (Liu et al., 2011). The microparticles are formed as the solvent evaporates from the core, resulting in shrinkage of the emulsion droplets, and polymer precipitation. When changing the block lengths of poly(L-lactide-co-ε-caprolactone) P(LA/CL) from 50:50 to 75:25, the interaction between the particles and the polymer becomes weaker due to the reduced carboxyl groups per unit mass, resulting in easier detachment of the particles as shrinkage occurs, and leading to a smoother surface as compared to the crinkled surface of the P(LA/CL) 50:50 microparticles. Similarly, Hitchcock et al. found that adsorption of platinum nanoparticles to a polymer-water interface was affected by the oil core contained within the polymer microcapsule (Tasker et al., 2017; Hitchcock et al., 2018). They found that by replacing toluene with hexyl salicylate in the microcapsule core, the nanoparticles adsorbed to the polymer microcapsules in an aggregated, fractal pattern on the polymer surface, with the equivalent of up to eight monolayers forming on one surface as opposed to the dense monolayer coverage observed on the toluene core microcapsules.

## CONCLUSION

The increasing use of particle-stabilized fluid-fluid interfaces to template the formation of micro/nanostructured capsules that encapsulate an active component has ultimately led to increasing complexity of the components that make up the template

emulsion. This is particularly relevant in the field of drug delivery where the drive to incorporate higher concentrations of drug increases the influence of the physicochemical properties of the drug on the emulsion core. The formation and resulting structure of nature's highly defined self-assembling nanocapsules, viruses, is highly sensitive to the composition of the core template and serves as a guiding example to other microcapsule fields. Indeed, computational simulation of assembly has shown that the strength of the interactions between viral subunits and the core, relative to inter-subunit interactions, is a governing principle on assembly around cores that do not match the preferred empty particle geometry (Elrad and Hagan, 2008). Our review of recent literature suggests that minor changes in core composition, particularly toward more complex systems, can play a critical role in the stability of many fluid-fluid interfaces, by altering the interfacial properties of the system, ultimately impacting the final structure of templated capsules. We believe that continued efforts to understand the fundamental forces that drive the stability of fluid-fluid interfaces in complex mixtures will ultimately underpin further advancement in the field.

## AUTHOR CONTRIBUTIONS

AT and FS jointly led the initial literature search and drafting. All authors contributed equally to the final writing of the manuscript.

## ACKNOWLEDGMENTS

AT and SP gratefully acknowledge funding from the CSIRO Probing Biosystems Future Science Platform and the Australian Institute for Bioengineering and Nanotechnology.

## REFERENCES

Ali, M., McCoy, T. M., McKinnon, I. R., Majumder, M., and Tabor, R. F. (2017). Synthesis and characterization of graphene oxide–polystyrene composite capsules with aqueous cargo via a water–oil–water multiple emulsion templating route. *ACS Appl. Mater. Interfaces* 9, 18187–18198. doi: 10.1021/acsami.7b02576

Amalvy, J. I., Unali, G. F., Li, Y., Granger-Bevan, S., Armes, S. P., Binks, B. P., et al. (2004). Synthesis of sterically stabilized polystyrene latex particles using cationic block copolymers and macromonomers and their application as stimulus-responsive particulate emulsifiers for oil-in-water emulsions. *Langmuir* 20, 4345–4354. doi: 10.1021/la035921c

Ashley, C. E., Carnes, E. C., Phillips, G. K., Durfee, P. N., Buley, M. D., Lino, C. A., et al. (2011). Cell- specific delivery of diverse cargos by bacteriophage MS2 virus-like particles. *ACS Nano* 5, 5729–5745. doi: 10.1021/nn201397z

Aveyard, R., Binks, B. P., and Clint, J. H. (2003). Emulsions stabilised solely by colloidal particles. *Adv. Colloid Interfaces Sci.* 100–102, 503–546. doi: 10.1016/S0001-8686(02)00069-6

Binks, B. P., and Clint, J. H. (2002). Solid wettability from surface energy components: relevance to pickering emulsions. *Langmuir* 18, 1270–1273. doi: 10.1021/la011420k

Binks, B. P., Dyab, A. K. F., and Fletcher, P. D. I. (2007). Contact angles in relation to emulsions stabilised solely by silica nanoparticles including systems containing room temperature ionic liquids. *Phys. Chem. Chem. Phys.* 9, 6391–6397. doi: 10.1039/b711174f

Brasch, M., Putri, R. M., De Ruiter, M. V., Luque, D., Koay, M. S., Caston, J. R., et al. (2017). Assembling enzymatic cascade pathways inside virus-based nanocages using dual-tasking nucleic acid tags. *J. Am. Chem. Soc.* 139, 1512–1519. doi: 10.1021/jacs.6b10948

Chang, C. B., Knobler, C. M., Gelbart, W. M., and Mason, T. G. (2008). Curvature dependence of viral protein structures on encapsidated nanoemulsion droplets. *ACS Nano* 2, 281–286. doi: 10.1021/nn700385z

Chudasama, V., Maruani, A., and Caddick, S. (2016). Recent advances in the construction of antibody-drug conjugates. *Nat. Chem.* 8, 113–118. doi: 10.1038/nchem.2415

Duncan, R. (2011). Polymer therapeutics as nanomedicines: new perspectives. *Curr. Opin. Biotechnol.* 22, 492–501. doi: 10.1016/j.copbio.2011.05.507

Elrad, O. M., and Hagan, M. F. (2008). Mechanisms of size control and polymorphism in viral capsid assembly. *Nano Lett.* 8, 3850–3857. doi: 10.1021/nl802269a

Enomoto, T., Kawano, M., Fukuda, H., Sawada, W., Inoue, T., Haw, K. C., et al. (2013). Viral protein-coating of magnetic nanoparticles using simian virus 40 VP1. *J. Biotechnol.* 167, 8–15. doi: 10.1016/j.jbiotec.2013.06.005

Frasch-Melnik, S., Norton, I. T., and Spyropoulos, F. (2010). Fat-crystal stabilised w/o emulsions for controlled salt release. *J. Food Eng.* 98, 437–442. doi: 10.1016/j.jfoodeng.2010.01.025

Ghosh, S., and Rousseau, D. (2011). Fat crystals and water-in-oil emulsion stability. *Curr. Opin. Colloid Interfaces Sci.* 16, 421–431. doi: 10.1016/j.cocis.2011.06.006

Glasgow, J. E., Capehart, S. L., Francis, M. B., and Tullman-Ercek, D. (2012). Osmolyte-mediated encapsulation of proteins inside MS2 viral capsids. *ACS Nano* 6, 8658–8664. doi: 10.1021/nn302183h

Han, F. Y., Thurecht, K. J., Whittaker, A. K., and Smith, M. T. (2016). Bioerodable PLGA-based microparticles for producing sustained-release drug formulations and strategies for improving drug loading. *Front. Pharmacol.* 7:185. doi: 10.3389/fphar.2016.00185

He, J., Niu, Z., Tangirala, R., Wang, J.-Y., Wei, X., Kaur, G., et al. (2009). Self-assembly of tobacco mosaic virus at oil/water interfaces. *Langmuir* 25, 4979–4987. doi: 10.1021/la803533n

Hitchcock, J. P., Tasker, A. L., Stark, K., Leeson, A., Baxter, E. A., Biggs, S., et al. (2018). Adsorption of catalytic nanoparticles onto polymer substrates for controlled deposition of microcapsule metal shells. *Langmuir* 34, 1473–1480. doi: 10.1021/acs.langmuir.7b02874

Hu, Y., Zandi, R., Anavitarte, A., Knobler, C. M., and Gelbart, W. M. (2008). Packaging of a polymer by a viral capsid: the interplay between polymer length and capsid size. *Biophys. J.* 94, 1428–1436. doi: 10.1529/biophysj.107.117473

Kaur, G., He, J., Xu, J., Pingali, S., Jutz, G., Böker, A., et al. (2009). Interfacial assembly of turnip yellow mosaic virus nanoparticles. *Langmuir* 25, 5168–5176. doi: 10.1021/la900167s

Kawano, M., Doi, K., Fukuda, H., Kita, Y., Imai, K., Inoue, T., et al. (2015). SV40 VP1 major capsid protein in its self-assembled form allows VP1 pentamers to coat various types of artificial beads *in vitro* regardless of their sizes and shapes. *Biotechnol. Rep.* 5, 105–111. doi: 10.1016/j.btre.2014.12.008

Kopecek, J. (2013). Polymer-drug conjugates: origins, progress to date and future directions. *Adv. Drug Deliv. Rev.* 65, 49–59. doi: 10.1016/j.addr.2012.10.014

Liu, X., Okada, M., Maeda, H., Fujii, S., and Furuzono, T. (2011). Hydroxyapatite/biodegradable poly(l-lactide–co-ε-caprolactone) composite microparticles as injectable scaffolds by a pickering emulsion route. *Acta Biomater.* 7, 821–828. doi: 10.1016/j.actbio.2010.08.023

Macierzanka, A., Szelag, H., Szumała, P., Pawłowicz, R., Mackie, A. R., and Ridout, M. J. (2009). Effect of crystalline emulsifier composition on structural transformations of water-in-oil emulsions: emulsification and quiescent conditions. *Colloids Surf. A Physicochem. Eng. Aspects* 334, 40–52. doi: 10.1016/j.colsurfa.2008.09.053

Manuela, C., De Souza, P. L., Aditya, R., and Stenzel, M. H. (2017). The effect of drug loading on micelle properties: solid-state NMR as a tool to gain structural insight. *Angew Chem.* 129, 8561–8565. doi: 10.1002/ange.201701471

Marchetti, M., Wuite, G. J. L., and Roos, W. H. (2016). Atomic force microscopy observation and characterization of single virions and virus-like particles by nano-indentation. *Curr. Opin. Virol.* 18, 82–88. doi: 10.1016/j.coviro.2016.05.002

Mukherjee, S., Kler, S., Oppenheim, A., and Zlotnick, A. (2010). Uncatalyzed assembly of spherical particles from SV40 VP1 pentamers and linear dsDNA

incorporates both low and high cooperativity elements. *Virology* 397, 199–204. doi: 10.1016/j.virol.2009.10.050

Ngai, T., Auweter, H., and Behrens, S. H. (2006). Environmental responsiveness of microgel particles and particle-stabilized emulsions. *Macromolecules* 39, 8171–8177. doi: 10.1021/ma061366k

Ramazani, F., Chen, W. L., Van Nostrum, C. F., Storm, G., Kiessling, F., Lammers, T., et al. (2016). Strategies for encapsulation of small hydrophilic and amphiphilic drugs in PLGA microspheres: state-of-the-art and challenges. *Int. J. Pharm.* 499, 358–367. doi: 10.1016/j.ijpharm.2016.01.020

Read, E. S., Fujii, S., Amalvy, J. I., Randall, D. P., and Armes, S. P. (2004). Effect of varying the oil phase on the behavior of pH-responsive latex-based emulsifiers: demulsification vs. transitional phase inversion. *Langmuir* 20, 7422–7429. doi: 10.1021/la049431b

Russell, J. T., Lin, Y., Böker, A., Su, L., Carl, P., Zettl, H., et al. (2005). Self-assembly and cross-linking of bionanoparticles at liquid–liquid interfaces. *Angew Chem. Int. Edn.* 44, 2420–2426. doi: 10.1002/anie.200462653

Speir, J. A., and Johnson, J. E. (2012). Nucleic acid packaging in viruses. *Curr. Opin. Struc. Biol.* 22, 65–71. doi: 10.1016/j.sbi.2011.11.002

Tasker, A. L., Hitchcock, J., Baxter, E. A., Cayre, D. O. J., and Biggs, S. (2017). Understanding the mechanisms of gold shell growth onto polymer microcapsules to control shell thickness. *Chem. Asian J.* 12, 1641–1648. doi: 10.1002/asia.201700536

Tasker, A. L., Hitchcock, J. P., He, L., Baxter, E. A., Biggs, S., and Cayre, O. J. (2016). The effect of surfactant chain length on the morphology of poly(methyl methacrylate) microcapsules for fragrance oil encapsulation. *J. Colloid Interfaces Sci.* 484, 10–16. doi: 10.1016/j.jcis.2016.08.058

Tasker, A. L., Puttick, S., Hitchcock, J., Cayre, O. J., Blakey, I., Whittaker, A. K., et al. (2018). A two-step synthesis for preparing metal microcapsules with a biodegradable polymer substrate. *J. Mater. Chem B* 6, 2151–2158. doi: 10.1039/C8TB00348C

Vaughan, R., Tragesser, B., Ni, P., Ma, X., Dragnea, B., and Kao, C. C. (2014). The tripartite virions of the brome mosaic virus have distinct physical properties that affect the timing of the infection process. *J. Virol.* 88, 6483–6491. doi: 10.1128/JVI.00377-14

Veverka, M., Dubaj, T., Veverková, E., and Šimon, P. (2018). Natural oil emulsions stabilized by β-glucan gel. *Colloids Surf. A Physicochem. Eng. Aspects* 537, 390–398. doi: 10.1016/j.colsurfa.2017.10.043

Wagdare, N. A., Marcelis, A. T. M., Boom, R. M., and Van Rijn, C. J. M. (2011). Microcapsules with a pH responsive polymer: influence of the encapsulated oil on the capsule morphology. *Colloids Surf. B Biointerfaces* 88, 175–180. doi: 10.1016/j.colsurfb.2011.06.028

Wang, Z., Qiu, T., Guo, L., Ye, J., He, L., and Li, X. (2018). Polymerization induced shaping of Pickering emulsion droplets: from simple hollow microspheres to molecularly imprinted multicore microrattles. *Chem. Eng. J.* 332, 409–418. doi: 10.1016/j.cej.2017.09.027

Wen, A. M., and Steinmetz, N. F. (2016). Design of virus-based nanomaterials for medicine, biotechnology, and energy. *Chem. Soc. Rev.* 45, 4074–4126. doi: 10.1039/C5CS00287G

**Conflict of Interest Statement:** The authors declare that the research was conducted in the absence of any commercial or financial relationships that could be construed as a potential conflict of interest.

frontiers in Chemistry

ORIGINAL RESEARCH
published: 01 June 2018
doi: 10.3389/fchem.2018.00196

# Metal Coated Colloidosomes as Carriers for an Antibiotic

*Qian Sun*[1], *Ziyan Zhao*[2], *Elizabeth A. H. Hall*[2] *and Alexander F. Routh*[1]*

[1] *Department of Chemical Engineering and Biotechnology, BP Institute, University of Cambridge, Cambridge, United Kingdom,* [2] *Department of Chemical Engineering and Biotechnology, University of Cambridge, Cambridge, United Kingdom*

Colloidosomes are polymer shell microcapsules. They are stable and easy to prepare and have been used to encapsulate drugs for release at specific areas in the body. Traditional polymer shell capsules cannot totally seal drugs, since they are porous, and small molecules diffuse through the polymer shell. In this paper, we report a method for encapsulating an antibiotic kanamycin using gold or silver coated colloidosomes. The colloidosomes are impermeable and can be triggered using ultrasound. To investigate the application of the capsules in a biological system, *Escherichia Coli* (*E. coli*) was chosen as a model organism. After triggering, the released antibiotic, as well as the metal shell fragments, kill *E. coli*. Both the silver and gold shells colloidosomes are toxic to this bacterial system and the gold coated colloidosomes can load a higher concentration of kanamycin.

**Keywords: encapsulating, impermeable, silver shells, gold shells, *E. coli***

OPEN ACCESS

***Edited by:***
*Erica Wanless,*
*University of Newcastle, Australia*

***Reviewed by:***
*Alison Tasker,*
*The University of Queensland, Australia*
*Syuji Fujii,*
*Osaka Institute of Technology, Japan*

***Correspondence:**
*Alexander F. Routh*
*afr10@cam.ac.uk*

***Specialty section:***
*This article was submitted to Chemical Engineering, a section of the journal Frontiers in Chemistry*

***Received:*** *20 November 2017*
***Accepted:*** *15 May 2018*
***Published:*** *01 June 2018*

***Citation:***
*Sun Q, Zhao Z, Hall EAH and Routh AF (2018) Metal Coated Colloidosomes as Carriers for an Antibiotic. Front. Chem. 6:196. doi: 10.3389/fchem.2018.00196*

## INTRODUCTION

Small molecular weight drugs are widely used in pharmaceutical applications. In order to deliver the encapsulant to targeted areas, drug delivery vehicles are developed and have attracted considerable interest. Many systems can be used as drug delivery vehicles, including micro-emulsions (Osborne et al., 1991; Kogan and Garti, 2006; Lawrence and Rees, 2012), nanotubes (Liu et al., 2008), metal organic frameworks (Horcajada et al., 2006, 2010), nanogels (Zha et al., 2011), polymers (Pillai and Panchagnula, 2001; Schmaljohann, 2006; Cho et al., 2008), and capsules (Delcea et al., 2001; Wang et al., 2008; Yang et al., 2008).

Optimally, the drug delivery vehicle should display a sufficient circulation lifetime to allow a successful delivery to the targeted region. Furthermore, for toxic drugs, encapsulation in drug carriers reduces the harmful side effects (Chertok et al., 2008; Ho et al., 2009). Among drug delivery vehicles, microcapsules have attracted considerable interest and development, since they are stable and easy to prepare. In addition, one can easily load the drug and achieve release at targeted areas (Qiu and Park, 2001; Zhao et al., 2007; Hu et al., 2008; Broaders et al., 2011). However, traditional polymer shell capsules cannot totally seal small molecule encapsulated drugs, since they are porous and diffusion occurs through the polymer shells (Shi and Caruso, 2001; Yow and Routh, 2006; Keen et al., 2014). One solution is to place a second impermeable layer around the microcapsules in order

to enhance the seal ability and stability (Mandal et al., 2010; Sander and Studart, 2011; Hitchcock et al., 2015; Gao et al., 2016).

In our previous studies, we made impermeable metal coated colloidosomes, which were polymer shell capsules coated with either gold or silver (Sun and Routh, 2016; Sun et al., 2017a,b). **Figure 1** shows a schematic representation of the encapsulation method and the release of small molecules. As shown, the polymer shells lose small molecules after washing. However, the metal shell blocks and strengthens the porous polymer. To release the encapsulated materials, ultrasound was used, breaking most of the capsules.

In this paper, to investigate the application of the metal coated colloidosomes in a biological system, *Escherichia Coli* (*E. coli*) bacteria were mixed with colloidosomes containing the antibiotic kanamycin. *E. coli* have been studied extensively and are an ideal model organism. Kanamycin is an aminoglycoside antibiotic that induces its bactericidal effect by introducing errors in protein synthesis through tRNA mismatch upon binding to the bacterial ribosome (Feldman et al., 2010). Here, we report the drug loading method using gold and silver coated colloidosomes. We then use ultrasound to break the capsules and release the drugs. After triggering, the released antibiotic, and broken shell fragments both kill *E. coli*.

# MATERIALS AND METHODS

## Materials

The base latex particles are poly (methyl methacrylate-co-butyl acrylate) with a diameter of 153 nm. They were synthesized via emulsion polymerization as reported elsewhere (Keen et al., 2014). The glass transition temperature of the latex was found using differential scanning calorimetry to be 35°C.

The deionized water in all experiments had a resistivity of 18.2 MΩ●cm and was produced by a Pure Lab Ultra apparatus. Sodium dodecyl sulfate (SDS, Fisher Scientific), buffer solution pH 10.0 (Sigma-Aldrich), 4,4′-dithiodibutyric acid (DDA, 95%, Sigma-Aldrich), and kanamycin monosulphate (Sigma-Aldrich) were all used as received without purification. The vortex mixer was a TopMix FB15024 (Fisher Scientific).

For cell viability studies, pET-24a (+) plasmid with a kanamycin resistant site (Novagen) was transferred into *E. Coli* BL21 (DE3) competent cells (Novagen). The cells were grown in kanamycin containing Luria Bertani (LB) Media. The LB media was prepared with 10 g/L tryptone (mirobiologically tested, Sigma-Aldrich), 5 g/L yeast extract (for use in microbial growth medium, Sigma-Aldrich), 10 g/L NaCl (Sigma-Aldrich), and 1.5% (w/v) Agar powder (ThermoFisher Scientific).

## Drug Encapsulation Using Gold Coated Colloidosomes

**Figure 2** shows the fabrication method for gold coated colloidosomes loading kanamycin monosulphate. A Silverson high shear mixer (model SL2) was used to mix 4 mL Span 80 with 200 mL sunflower oil in a 400 mL beaker. The latex particle suspension (11.2 wt% in pH 10 buffer solution) was mixed with 12.5 mg/mL kanamycin monosulphate, to get a mixture, which contained 5.6 wt% latex particles and 6.25 mg/mL kanamycin monosulphate in buffer solution. 2 mL of this mixture was then added into the sunflower oil. After emulsification, the mixture was heated in a water bath at 50 ± 0.5°C. This allows the latex particles to merge into a smooth shell.

After sintering, 20 mL of the emulsion mixture was centrifuged at 2,500 rpm for 10 min at 20°C. The oil was removed via pipetting and 20 mL of 1 wt % aqueous solution of $HAuCl_4$ and 2 mL of 1 wt% aqueous SDS solution were added and the microcapsules redispersed in the aqueous phase using a vortex mixer. Then 2 mL L-ascorbic acid solution (15 wt% in water) was added to the tube and rested for 1 h to allow the gold forming reaction. After the reduction reaction, the mixture was centrifuged at 1,500 rpm for 2 min at 20°C to recover the sediment and the supernatant was removed via pipetting. The resulting gold coated colloidosomes, loaded with kanamycin, were washed, and redispersed, using a 0.1 wt% SDS solution.

The SDS surfactant solution affects the cell viability. However, without the surfactant the capsules are heavily aggregated in water. Consequently we used 4,4′-dithiodibutyric acid (DDA) to modify the capsule surfaces, which allows the metal shell capsules to disperse in water. A known mass of gold coated colloidosomes were dispersed in 20 mL of 0.5 wt% 4,4′-dithiodibutyric acid (DDA) in ethanol using the vortex. The mixture was then mixed by a magnetic stirrer for 48 h at room temperature. After the reaction, the mixture was centrifuged at 1,500 rpm for 2 min. The supernatant was removed and the modified gold shell capsules were washed and redispersed using ultra-pure water.

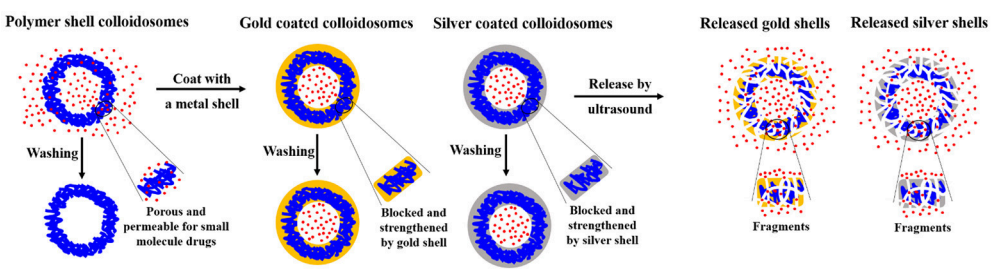


**FIGURE 1 |** Schematic representation of microcapsule encapsulation and release of small molecules. Blue lines represent latex particles, the red represents small molecule drugs, the orange represents the gold particles, and gray the silver particles.

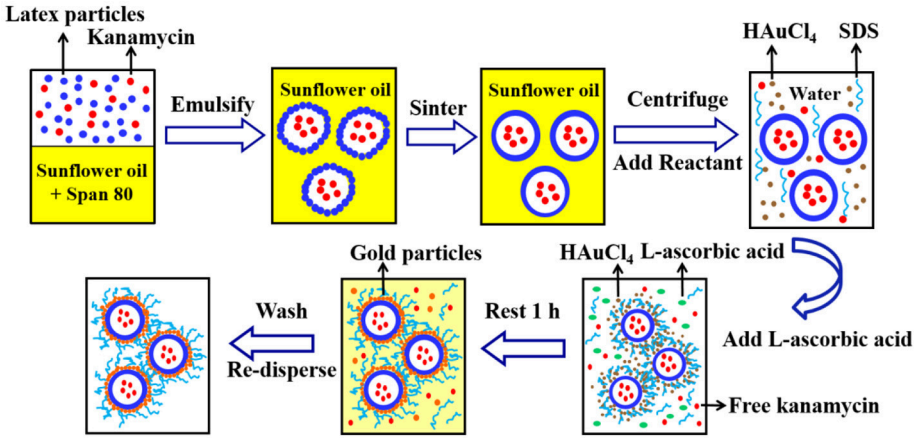


**FIGURE 2 |** A typical method for fabrication of the gold coated colloidosomes loading kanamycin monosulphate.

## Drug Encapsulation Using Silver Coated Colloidosomes

The method of silver shell fabrication is similar to that for the gold shell capsules. For silver shells, 24 mL $AgNO_3$ solution (0.1 wt% in water) and 2 mL SDS (1 wt% in water) were added in each tube. Then 2 mL L-ascorbic acid solution (15 wt% in water) was added and rested for 1 h allowing the silver forming reaction.

## Release by Ultrasonic Treatment

Remote activation of microcapsules was conducted using an ultrasonic probe operating at a frequency of 23 kHz and 50 W. The suspension of microcapsules was subjected to ultrasound sonication, performed using an ultrasonic processor (Sanyo soniprep 150). The probe was placed into a 5 mL capsule suspension in a 50 mL plastic tube. An ice bath was applied to ensure that the temperature change of the capsule suspension was less than 5°C.

## Cell Viability Test

The kanamycin resistant *E. coli* BL21 (DE3) cells were grown for 16 h in 10 mL LB medium supplemented with 50 μg/mL kanamycin. 100 μL of the overnight culture were then transferred to 50 mL falcon tubes containing the same LB medium for inoculation. The growth of cells was monitored by measuring the optical density at 600 nm ($OD_{600}$) of the cell culture using a UV-visible spectrophotometer (Infinite M200 Tecan). The treatments were added to the cells, when the culture $OD_{600}$ was approximately 0.7. For blank kanamycin measurements, 1 mL of kanamycin solution at various concentrations was added to the cells to obtain final concentrations between 50 and 5,000 μg/mL. For metal shell capsules, blank silver/gold shells and silver/gold shells loading kanamycin with intact shells were added to the cell culture, achieving a final concentration in the range of 7.1 $\times 10^5$ to 3.5 $\times 10^8$ capsules/mL. A hemocytometer (a counting chamber) was used for determining the number of microcapsules per unit volume of a suspension. For drug release experiments, the same concentrations of ultrasound-broken capsules were added to the cell culture. Treated cells were then grown for 24 h. All cultures were shaken at 37°C, 225 rpm in a multitron shaker (Infors HT). The resulting cell cultures were then diluted in LB media and spread evenly on a 90 mm LB Agar plate supplemented with 50 μg/mL kanamycin, to result in 30-300 CFU per agar plate. The plates were then grown at 37°C in an incubator (Heraeus Instruments) for 16 h before the CFU for each plate was counted.

## Sample Characterizations

The colloidosomes were imaged by scanning electron microscopy (SEM), using a Zeiss X-beam FIB SEM at an accelerating voltage of 5.0 kV. A drop of colloidosome suspension was air-dried on a stainless steel SEM stub overnight and the samples were imaged without any treatment.

The elemental analysis of colloidosome samples was detected by Energy-dispersive X-ray spectroscopy (EDX). The electron beam excitation used is from a Zeiss X-beam FIB scanning electron microscope with an accelerating voltage of 10.0 kV.

# RESULTS AND DISCUSSION

## Drug Encapsulation Using Metal Coated Colloidosomes

**Figure 3** shows SEM images of (a) a polymer shell colloidosome, (b) gold coated colloidosomes, (c) gold coated colloidosomes loading kanamycin, (d) silver coated colloidosomes, and (e) silver coated colloidosomes loading kanamycin. In our previous studies, we made smooth polymer shell capsules, with a diameter of between 0.7 and 2 μm and the gold or silver shell was then placed on the outside. The diameter of the gold coated colloidosomes are between 0.8 and 2.1 μm, whilst the silver capsules are between 0.9 and 3.2 μm. We used a fluorescent dye as a model to test the loading efficiency of the metal shells. For gold shells, the loading efficiency is around 15.8, and 22.7% for silver shells. (Sun and Routh, 2016; Sun et al., 2017a,b)

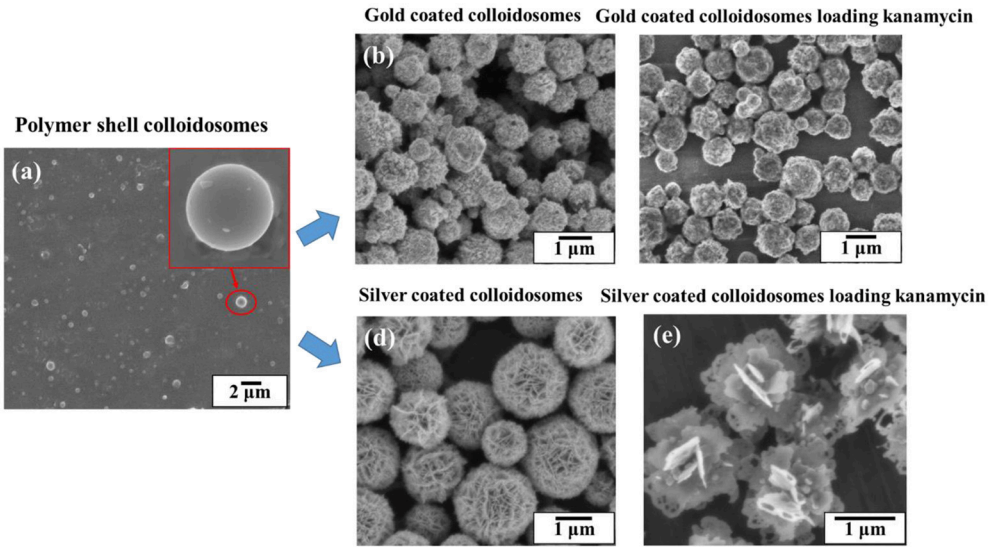


**FIGURE 3 |** SEM images of **(a)** a polymer shell colloidosome, **(b)** gold coated colloidosomes, **(c)** gold coated colloidosomes loading kanamycin, **(d)** silver coated colloidosomes, and **(e)** silver coated colloidosomes loading kanamycin.

Once made the metal coated colloidosomes are stable for at least many months. In this paper we report on the use of the metal coated colloidosomes for delivery of the antibiotic kanamycin into a biological system. There are some interested morphological changes to the capsules upon encapsulation of the antibiotic and we report on these first.

**Figure 4** shows the SEM and EDX images of the gold coated colloidosomes containing kanamycin. It can be seen that the polymer shells were fully covered by gold particles. After loading kanamycin, the morphology of the gold shells does not significantly change, and the capsules remain spherical. **Figure 4d** shows the corresponding EDX image which has high gold peaks, suggesting that the particles surrounding the surface of the colloidosomes are gold. There are also carbon and oxygen peaks, arising from the polymer shell. The aluminum and copper peaks were caused by the SEM stub. To release the encapsulated drug, ultrasound was used to trigger the capsules. As shown in **Figure 4e**, after 480 s sonication, only a few colloidosomes survived and there were a large number of small pieces of broken shell.

**Figure 5** shows the SEM and EDX images of the silver coated colloidosomes which contained kanamycin. As can be seen, the polymer shells were fully covered by lamellar silver particles. After loading kanamycin, the morphology of the silver shells change from the water core capsules shown in **Figure 3d**. The lamellar silver particles, surrounding the surface of the polymer shells, were thinner and some silver sheets became hollow at the edge. In the silver forming process, the kanamycin may affect the silver ions converting into metallic silver. This is likely because kanamycin might associate with the silver precursor, and prevent it from forming shell shaped capsules. (Xu et al., 2015).

**Figure 5d** shows the corresponding EDX image which has high silver peaks. The sodium and sulfur peaks were caused by the SDS surfactant. As shown in **Figure 5e**, after 240 s sonication, most of the silver coated colloidosomes are broken into fragments.

**Figure 6** shows SEM images of the silver coated colloidosomes encapsulating varying amounts of kanamycin. When the original kanamycin concentration was increased to 25.0 mg/mL, the silver particles became thinner. When the concentration increased to 50.0 mg/mL, there was no silver shell, just separate silver sheets. However, for gold shells, there was no effect of kanamycin concentration as shown in **Figure 6d**. For comparison, SEM images of gold and silver shell colloidosomes made without kanamycin are shown in **Figures 3b,d**.

## Cell Viability Studies

The application of the metal coated colloidosomes as small molecule drug carriers was investigated in a biological system. The CFU/mL data in **Figures 7–9** are calculated by counting the average number of the diluted cell colonies. Each experiment was repeated three times and the standard error of the results is shown by the error bars.

### Free Kanamycin

**Figure 7** shows the colony forming units results obtained after 24 h incubation of *E. coli* bacteria with different concentrations of free kanamycin. As can be seen, at a concentration of 50 and 100 μg/mL kanamycin, the bacteria grew to $1.2 \times 10^8$ CFU/mL. When the concentration increased to 150 μg/mL, the numbers of CFU dropped to was $5.7 \times 10^7$ CFU/mL.When the concentration increased to 200 μg/mL, the result was increased slightly to $6.6 \times 10^7$ CFU/mL, although within the error of the

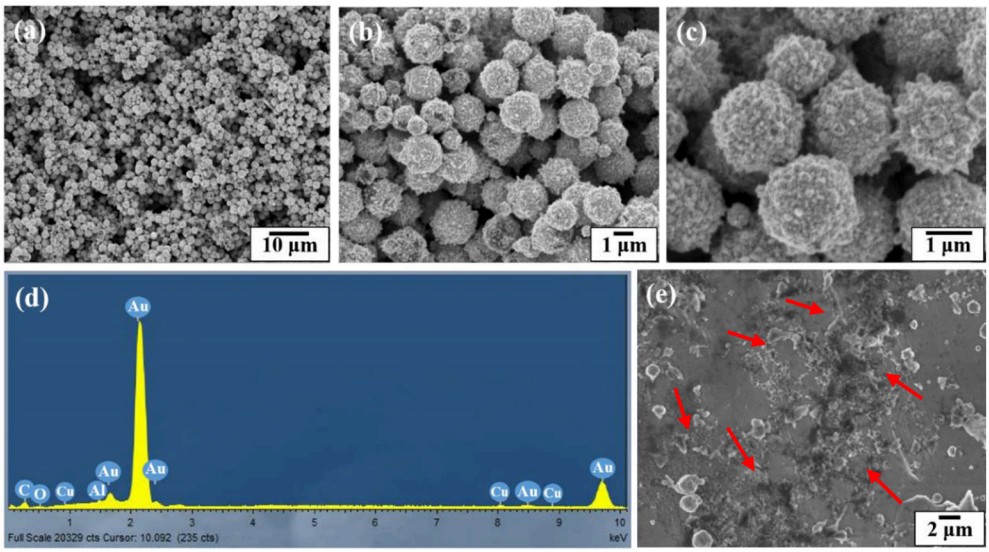


**FIGURE 4 |** SEM and EDX images of the gold coated colloidosomes which contained antibiotic kanamycin. **(a–c)** different magnification SEM images of gold coated colloidosomes loading kanamycin, **(d)** EDX image of gold coated colloidosomes loading kanamycin, and **(e)** SEM image of gold coated colloidosomes loading kanamycin after 480 s sonication.

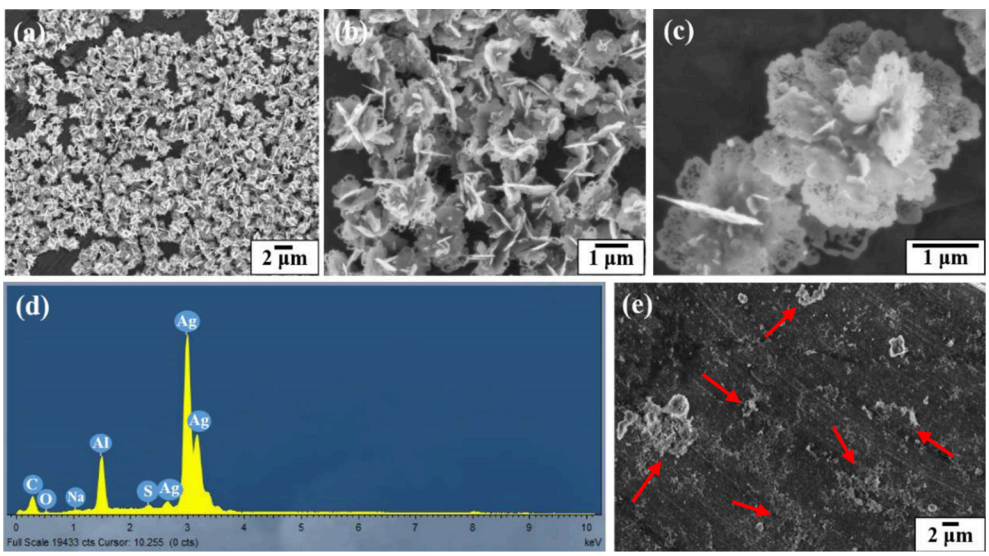


**FIGURE 5 |** SEM and EDX images of the silver coated colloidosomes which contained antibiotic kanamycin. **(a–c)** different magnification SEM images of silver coated colloidosomes loading kanamycin, **(d)** EDX image of silver coated colloidosomes loading kanamycin, and **(e)** SEM image of silver coated colloidosomes loading kanamycin after 240 s sonication.

experiment. The *E. coli* strain being investigated contains a pET-24a(+) plasmid with a kanamycin resistant gene, which produces aminoglycoside modifying enzymes. Such strains survive the kanamycin treated media at low drug concentrations. Therefore, by adding certain amount of kanamycin, we can control that the cells being grown are the kanamycin resistant cells, and are not contaminated by any environmental bacteria. A low concentration of kanamycin shows a beneficial effect for cell growth. With an increasing the amount of kanamycin, the inhibition of cells increased. There is a complete inhibition for *E. coli* at 5000 µg/mL kanamycin, when nearly all of the cells were killed.

## Gold Coated Colloidosomes Cell Viability Test

**Figure 8** shows the cell viability results obtained after 24 h incubation of *E. coli* bacteria with different number concentrations of blank gold coated colloidosomes, blank gold coated colloidosomes after ultrasound, gold

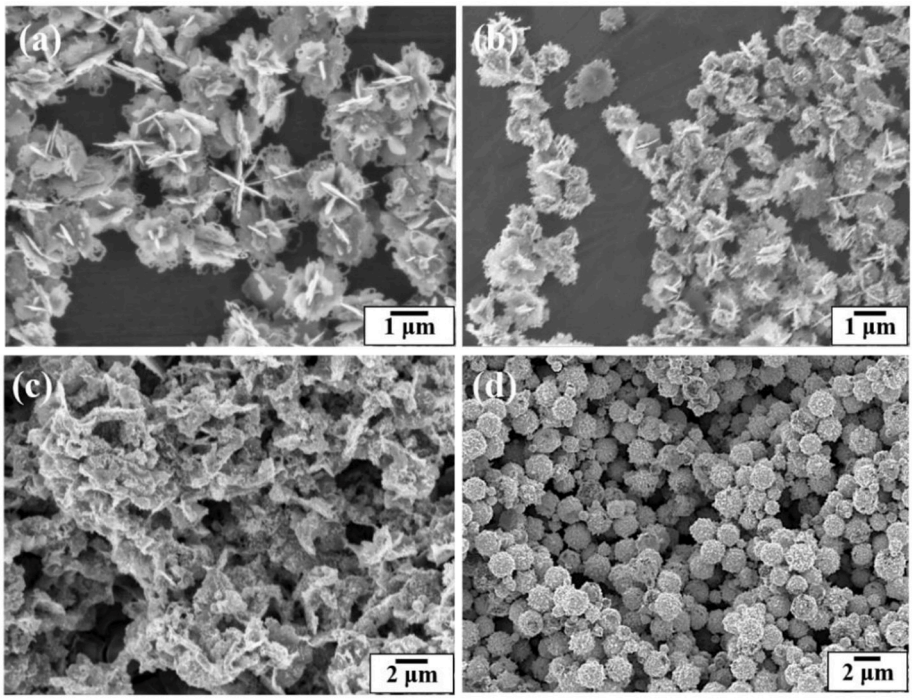


**FIGURE 6 |** SEM images of the silver coated colloidosomes loading various concentrations of kanamycin **(a)** 12.5 mg/mL, **(b)** 25.0 mg/mL, and **(c)** 50.0 mg/mL kanamycin. **(d)** SEM image of the gold coated colloidosomes loading 50.0 mg/mL of kanamycin.

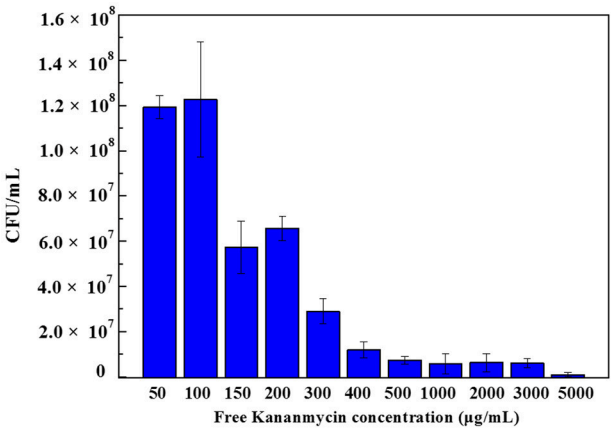


**FIGURE 7 |** Colony forming units of *E. coli* bacteria with different concentration of free kanamycin on agar plates. Each experiment was repeated three times and error bars show the standard error of the experimental results.

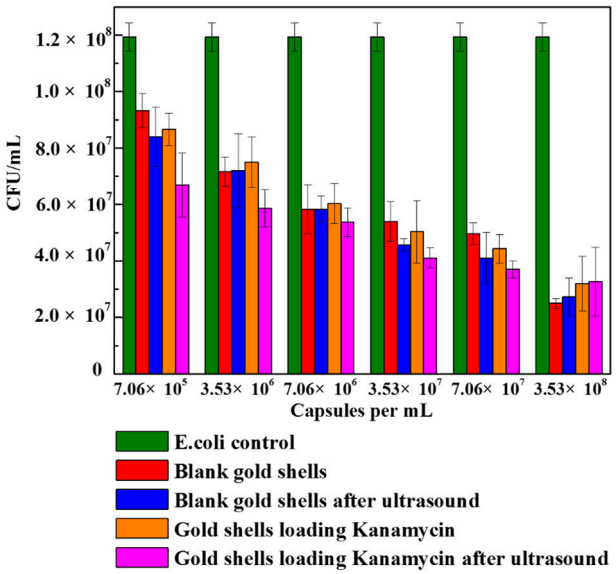


**FIGURE 8 |** Cell viability of control *E. coli* and the ones with different numbers of gold coated colloidosomes. Each experiment was repeated three times and error bars show the standard error of the experimental results.

coated colloidosomes loading kanamycin, and gold coated colloidosomes loading kanamycin after ultrasound. In order to break the gold shells, ultrasound was applied for 480 s, before adding the resulting solution to the bacteria.

As seen in **Figure 8**, there was a CFU decrease in all of the gold shell treated samples compared to the blank *E. coli* culture with 50 μg/mL kanamycin. This indicates the gold coated colloidosomes are toxic to the *E. coli* culture. The toxicity increases with increasing concentration of gold coated colloidosomes. With a concentration of $7.06 \times 10^5$ capsules/mL

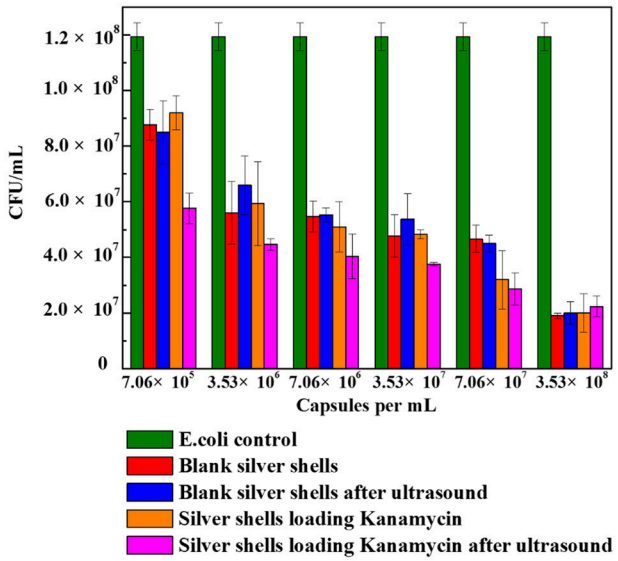


**FIGURE 9 |** Cell viability of control *E. coli* and the ones with different numbers of silver coated colloidosomes. Each experiment was repeated three times and error bars show the standard error of the experimental results.

the toxic effect from the colloidosomes after ultrasound results in a cell viability of approximately 6.7 × $10^7$ CFU/mL, a 25% drop from the case without ultrasound. Increasing the concentration of capsules, the toxicity becomes more obvious. When the number of the capsules reaches to 3.53 × $10^8$ capsules/mL, the encapsulation of kanamycin had minimal extra benefit, with the capsules themselves hindering the cell viability.

### Silver Coated Colloidosomes Cell Viability Test

**Figure 9** shows the cell viability results obtained after 24 h incubation of *E. coli* with different amounts of blank silver coated colloidosomes, blank silver coated colloidosomes after ultrasound, silver coated colloidosomes loading kanamycin, and silver coated colloidosomes loading kanamycin after ultrasound. Before rupture, there is minimal toxicity difference between the empty and kanamycin containing capsules. After ultrasound, the kanamycin has a significant effect on cell viability (Tsao and Hall, 2017).

In order to break silver shells, the ultrasound was applied for 240 s before adding the resulting solution into the bacteria. The effect of the silver coated colloidosomes on cell viability shows a similar trend to the gold capsules, with the cell viability decreasing, compared with the *E. coli* control. The effect on cell viability of silver coated colloidosomes loading kanamycin after ultrasound was most dramatic because of the released antibiotic. For the lowest concentration of silver shells, the cell viability after kanamycin was released dropped by 34% compared with other capsules. Increasing the concentration of capsules, the toxic effect becomes enhanced.

Both the silver and gold shells colloidosomes are toxic to this bacterial system. With a low concentration of 7.06 × $10^5$ capsules/mL, the difference of toxicity between gold and silver colloidosomes is not significant. Increasing the concentration of capsules, the cell viability is slightly different. For example, at a concentration of 3.53 × $10^8$ capsules/mL, for gold shells after ultrasound, there are around 3 × $10^7$ CFU remaining, and for silver shell capsules after ultrasound around 2 × $10^7$ CFU remain. This slight difference is likely to be because the silver shells, especially silver shell fragments in nano-size as well as any silver ions are toxic to biological systems and are leading to death of bacteria. (Zhou et al., 2008; Mu et al., 2014).

## CONCLUSION

This paper has demonstrated a method for encapsulating an antibiotic kanamycin using gold or silver coated colloidosomes. The colloidosomes are impermeable and can be triggered using ultrasound. To investigate the application of the capsules in a biological system, *E. coli* bacteria were chosen as a model organism. After triggering the metal shells by ultrasound, the released antibiotic, the broken fragments, and the antibiotic loading on the capsule surface all kill *E. coli*. Both the silver and gold shells colloidosomes are toxic to this bacteria system. Compared with silver coated colloidosomes, gold ones can load a higher concentration of kanamycin.

## AUTHOR CONTRIBUTIONS

QS made the capsules and characterized them. QS and ZZ performed the cell viability experiments together. QS wrote the manuscript with assistance from ZZ, EH, and AR. EH and AR supervised the research.

## FUNDING

QS and ZZ are grateful to the China Scholarship Council for funding their PhD studies. ZZ also thanks the Cambridge Trusts for financial support.

## ACKNOWLEDGMENTS

The authors thank Dr. Richard Langford and Eric Tapley (The Cavendish Laboratory, Department of Physics, University of Cambridge) for their assistance with use of the scanning electron microscopy.

## REFERENCES

Broaders, K. E., Pastine, S. J., Grandhe, S., and Fréchet, J. M. (2011). Acid-degradable solid-walled microcapsules for pH-responsive burst-release drug delivery. *Chem. Commun.* 47, 665–667. doi: 10.1039/C0CC04190D

Chertok, B., Moffat, B. A., David, A. E., Yu, F., Bergemann, C., Ross, B. D., et al. (2008). Iron oxide nanoparticles as a drug delivery vehicle for MRI monitored magnetic targeting of brain tumors. *Biomaterials* 29, 487–496. doi: 10.1016/j.biomaterials.2007.08.050

Cho, K., Wang, X. U., Nie, S., and Shin, D. M. (2008). Therapeutic nanoparticles for drug delivery in cancer. *Clin. Cancer Res.* 14, 1310–1316. doi: 10.1158/1078-0432.CCR-07-1441

Delcea, M., Möhwald, H., and Skirtach, A. G. (2001). Stimuli-responsive LbL capsules and nanoshells for drug delivery. *Adv. Drug Deliver. Rev.* 63, 730–747. doi: 10.1016/j.addr.2011.03.010

Feldman, M. B., Terry, D. S., Altman, R. B., and Blanchard, S. C. (2010). Aminoglycoside activity observed on single pre-translocation bibosome complexes. *Nat. Chem. Biol.* 6, 54–62. doi: 10.1038/nchembio.274

Gao, H., Goriacheva, O. A., Tarakina, N. V., and Sukhorukov, G. B. (2016). Intracellularly biodegradable polyelectrolyte/silica composite microcapsules as carriers for small molecules. *ACS Appl. Mat. Interfaces* 8, 9651–9661. doi: 10.1021/acsami.6b01921

Hitchcock, J. P., Tasker, A. L., Baxter, E. A., Biggs, S., and Cayre, O. J. (2015). Long-term retention of small, volatile molecular species within metallic microcapsules. *ACS Appl. Mat. Interfaces* 7, 14808–14815. doi: 10.1021/acsami.5b03116

Ho, K., Lapitsky, Y., Shi, M., and Shoichet, M. S. (2009). Tunable immunonanoparticle binding to cancer cells: thermodynamic analysis of targeted drug delivery vehicles. *Soft Matter* 5, 1074–1080. doi: 10.1039/b814204a

Horcajada, P., Chalati, T., Serre, C., Gillet, B., Sebrie, C., Baati, T., et al. (2010). Porous metal-organic-framework nanoscale carriers as a potential platform for drug delivery and imaging. *Nat. Mater.* 9, 172–178. doi: 10.1038/nmat2608

Horcajada, P., Serre, C., Vallet-Regí, M., Sebban, M., Taulelle, F., and Férey, G. (2006). Metal-organic frameworks as efficient materials for drug delivery. *Angew. Chem.* 118, 6120–6124. doi: 10.1002/ange.200601878

Hu, S. H., Tsai, C. H., Liao, C. F., Liu, D. M., and Chen, S. Y. (2008). Controlled rupture of magnetic polyelectrolyte microcapsules for drug delivery. *Langmuir* 24, 11811–11818. doi: 10.1021/la801138e

Keen, P. H., Slater, N. K., and Routh, A. F. (2014). Encapsulation of amylase in colloidosomes. *Langmuir* 30, 1939–1948. doi: 10.1021/la4047897

Kogan, A., and Garti, N. (2006). Microemulsions as transdermal drug delivery vehicles. *Adv. Colloid Interface Sci.* 123, 369–385. doi: 10.1016/j.cis.2006.05.014

Lawrence, M. J., and Rees, G. D. (2012). Microemulsion-based media as novel drug delivery systems. *Adv. Drug Deliver. Rev.* 64, 175–193. doi: 10.1016/j.addr.2012.09.018

Liu, Z., Chen, K., Davis, C., Sherlock, S., Cao, Q., Chen, X., et al. (2008). Drug delivery with carbon nanotubes for *in vivo* cancer treatment. *Cancer Res.* 68, 6652–6660. doi: 10.1158/0008-5472.CAN-08-1468

Mandal, S., Sathish, M., Saravanan, G., Datta, K., Ji, Q., Hill, J. P., et al. (2010). Open-mouthed metallic micro-capsules: exploring performance improvements at agglomeration-free interiors. *J. Am. Chem. Soc.* 132, 14415–14417. doi: 10.1021/ja107589m

Mu, Q., Jiang, G., Chen, L., Zhou, H., Fourches, D., Tropsha, A., et al. (2014). Chemical basis of interactions between engineered nanoparticles and biological systems. *Chem. Rev.* 114, 7740–7781. doi: 10.1021/cr400295a

Osborne, D. W., Ward, A. J. I., and O'Neill, K. J. (1991). Microemulsions as topical drug delivery vehicles: *in-vitro* transdermal studies of a model hydrophilic drug. *J. Pharm. Pharmacol.* 43, 451–454. doi: 10.1111/j.2042-7158.1991.tb03511.x

Pillai, O., and Panchagnula, R. (2001). Polymers in drug delivery. *Curr. Opin. Chem. Biol.* 5, 447–451. doi: 10.1016/S1367-5931(00)00227-1

Qiu, Y., and Park, K. (2001). Environment-sensitive hydrogels for drug delivery. *Adv. Drug Deliver. Rev.* 53, 321–339. doi: 10.1016/S0169-409X(01)00203-4

Sander, J. S., and Studart, A. R. (2011). Monodisperse functional colloidosomes with tailored nanoparticle shells. *Langmuir* 27, 3301–3307. doi: 10.1021/la1035344

Schmaljohann, D. (2006). Thermo-and pH-responsive polymers in drug delivery. *Adv. Drug Deliver. Rev.* 58, 1655–1670. doi: 10.1016/j.addr.2006.09.020

Shi, X., and Caruso, F. (2001). Release behavior of thin-walled microcapsules composed of polyelectrolyte multilayers. *Langmuir* 17, 2036–2042. doi: 10.1021/la001550d

Sun, Q., Du, Y., Zhao, Z., Hall, E. A. H., Gao, H., Sukhorukov, G. B., et al. (2017a). Functional silver coated colloidosomes as targeted carriers for small molecules. *Langmuir* 33, 3755–3764. doi: 10.1021/acs.langmuir.6b04594

Sun, Q., Gao, H., Sukhorukov, G. B., and Routh, A. F. (2017b). Silver-coated colloidosomes as carriers for an anticancer drug. *ACS Appl. Mat. Interfaces* 9, 32599–32606. doi: 10.1021/acsami.7b11128

Sun, Q., and Routh, A. F. (2016). Aqueous core colloidosomes with a metal shell. *Eur. Polym. J.* 77, 155–163. doi: 10.1016/j.eurpolymj.2016.01.044

Tsao, N. H., and Hall, E. A. H. (2017). Model for microcapsule drug release with ultrasound-activated enhancement. *Langmuir* 33, 12960–12972. doi: 10.1021/acs.langmuir.7b02954

Wang, Y., Bansal, V., Zelikin, A. N., and Caruso, F. (2008). Templated synthesis of single-component polymer capsules and their application in drug delivery. *Nano Lett.* 8, 1741–1745. doi: 10.1021/nl080877c

Xu, Y., Han, T., Li, X., Sun, L., Zhang, Y., and Zhang, Y. (2015). Colorimetric detection of kanamycin based on analyte-protected silver nanoparticles and aptamer-selective sensing mechanism. *Anal. Chim. Acta* 891, 298–303. doi: 10.1016/j.aca.2015.08.013

Yang, J., Lee, J., Kang, J., Lee, K., Suh, J. S., Yoon, H. G., et al. (2008). Hollow silica nanocontainers as drug delivery vehicles. *Langmuir* 24, 3417–3421. doi: 10.1021/la701688t

Yow, H. N., and Routh, A. F. (2006). Formation of liquid core-polymer shell microcapsules. *Soft Matter* 2, 940–949. doi: 10.1039/B606965G

Zha, L., Banik, B., and Alexis, F. (2011). Stimulus responsive nanogels for drug delivery. *Soft Matter* 7, 5908–5916. doi: 10.1039/c0sm01307b

Zhao, Q., Han, B., Wang, Z., Peng, C., and Shen, J. (2007). Hollow chitosan-alginate multilayer microcapsules as drug delivery vehicle: doxorubicin loading and *in vitro* and *in vivo* studies. *Nanomed. Nanotechnol.* 3, 63–74. doi: 10.1016/j.nano.2006.11.007

Zhou, H., Mu, Q., Gao, N., Liu, A., Xing, Y., Gao, S., et al. (2008). A nano-combinatorial library strategy for the discovery of nanotubes with reduced protein-binding, cytotoxicity, and immune response. *Nano Lett.* 8, 859–865. doi: 10.1021/nl0730155

**Conflict of Interest Statement:** The authors declare that the research was conducted in the absence of any commercial or financial relationships that could be construed as a potential conflict of interest.

The handling Editor and reviewer, SF, declared their involvement as co-editors in the Research Topic, and confirm the absence of any other collaboration.

frontiers in Chemistry

ORIGINAL RESEARCH
published: 12 June 2018
doi: 10.3389/fchem.2018.00213

# Droplet Fusion in Oil-in-Water Pickering Emulsions

*Catherine P. Whitby* and Floriane Bahuon*

*Institute of Fundamental Sciences, Massey University, Palmerston North, New Zealand*

We have formed compound droplets made of two or more drops of immiscible oils by temporarily destabilizing Pickering oil-in-water emulsions. The emulsions used are synergistically stabilized by mixtures of cationic surfactant and negatively-charged particles. They are highly sensitive to the concentration of surfactant present in the emulsions. We took advantage of transient droplet coalescence events that are triggered by reducing the surfactant concentration to fuse together drops of immiscible oils. This study provides guidelines for designing compound droplets by transient (or limited) coalescence in Pickering emulsions. We show that the possible geometries of particle-stabilized compound drops are determined by the interfacial tensions and relative volumes of the drops fused together. The implications of our results for designing strategies to fabricate multiphase drops are discussed.

**Keywords: particle-stabilized emulsion, limited coalescence, compound drop, Janus droplet, multiple emulsion**

OPEN ACCESS

***Edited by:***
*Grant Bruce Webber,*
*University of Newcastle, Australia*

***Reviewed by:***
*Roberto Pisano,*
*Politecnico di Torino, Italy*
*Omar Gonzalez-Ortega,*
*Universidad Autónoma de San Luis Potosí, Mexico*

****Correspondence:***
*Catherine P. Whitby*
*c.p.whitby@massey.ac.nz*

***Specialty section:***
*This article was submitted to Chemical Engineering, a section of the journal Frontiers in Chemistry*

***Received:*** *12 March 2018*
***Accepted:*** *25 May 2018*
***Published:*** *12 June 2018*

***Citation:***
*Whitby CP and Bahuon F (2018) Droplet Fusion in Oil-in-Water Pickering Emulsions. Front. Chem. 6:213. doi: 10.3389/fchem.2018.00213*

## INTRODUCTION

Compound droplets consist of drops of two (or more) immiscible fluids that have been fused together (Johnson and Sadhal, 1985; Neeson et al., 2012). Emulsions containing drops with multiple compartments have the potential to protect incompatible ingredients in foods (Muschiolik, 2007), pharmaceutics (Zhao, 2013), and cosmetics (Tadros, 1992). For example, multiple emulsions (Silva et al., 2016) have long been considered for use as vehicles for encapsulating sensitive ingredients in emulsion based food products (Pawlik et al., 2010; Sapei et al., 2012; McClements, 2015; Muschiolik and Dickinson, 2017). Yet the controlled production of large volumes of complex emulsions remains challenging. Advances in microfluidic emulsification techniques led to breakthroughs in the precise fabrication of small volumes of multiple emulsion droplets (Nisisako et al., 2005). They also enabled the assembly of compound droplets with morphologies that were previously unattainable. Novel configurations, such as Janus droplets, can form under the extreme flow conditions achieved in microfluidic channels (Choi et al., 2013). These developments have rejuvenated interest in designing robust and convenient routes for fusing drops of immiscible liquids together on a scale larger than that achieved in microfluidic channels (Hasinovic and Friberg, 2011; Fryd and Mason, 2014; Weyer et al., 2015; Ge et al., 2017; Wei et al., 2017). In this brief report, we describe a new approach that uses nanoparticles to control the fabrication of drops with multiple compartments.

Particles present during emulsion formation assemble at oil–water interfaces (of interfacial tension, $\gamma$) by becoming partially immersed in both liquids and forming a three phase oil-water-particle contact angle, $\theta$. This is energetically favorable because attached particles reduce the total interfacial area between the oil and water. For spherical particles (of radius $r_p$) with $\theta < 90°$, the free energy of attaching a particle to a drop (Levine et al., 1989; Binks and Lumsdon, 2000) is given by $\Delta G = \pi\gamma r_p^2 (1 - cos\theta)^2$. If the total number of particles present during emulsion

formation is not sufficient to fully coat the oil–water interface, the drops coalesce together until a critical degree of surface coverage by the particles is reached (Arditty et al., 2003). Surfactants are often mixed with particles to optimize the particle wettability at the oil–water interface (Binks et al., 2007; Eskandar et al., 2007; Wang et al., 2010; Reger et al., 2011; Hu et al., 2015; Wang and Wang, 2016). Synergistic stabilization of emulsions by mixtures of surfactant and particles makes them highly sensitive to changes in the concentration of surfactant present in the continuous phase (Binks and Whitby, 2005). We took advantage of the disruption to the interfacial particle layer caused by reducing the surfactant concentration to trigger fusion of droplets of immiscible oil in particle-stabilized (or Pickering) emulsions.

# MATERIALS AND METHODS

## Emulsion Formation and Fusion

Oil-in-water emulsions were stabilized by mixtures of hydrophilic fumed silica nanoparticles (Wacker Chemie N20) and hexadecyltrimethyl ammonium bromide (CTAB, 99% purity, Sigma Aldrich). The silica nanoparticles were obtained as a powder, with an average primary particle size of 10 nm. The powder dispersed in water as aggregates with an average size of 200 nm. The aggregates have a zeta potential of $-37 \pm 4$ mV (measured using a Malvern Zetasizer). For experiments involving drops of mutually immiscible oils we used olive oil (highly refined and of low acidity) and 5 cSt silicone oil. Both oils were obtained from Sigma Aldrich and passed through a column of chromatographic alumina prior to use.

To optimize particle wettability and hence emulsion stability, the silica nanoparticles were dispersed in aqueous solutions of 0.1 mM CTAB by sonication in an ultrasound bath (Soniclean 160 T, 70 W power, ∼44 kHz operating frequency) for 1 h. At these surfactant concentrations, the silica particles flocculated and the dispersions sedimented over time when left to stand. The pH of the dispersions was about 5.8.

Emulsions of each type of oil (at drop volume fractions $0.1 \leq \phi \leq 0.4$ and a total volume of 15 mL) were prepared by homogenizing appropriate volumes of the oil with the aqueous silica dispersions (0.5 wt.% in 0.1 mM CTAB) using a PowerGen 125 mechanical mixer with a 7 mm diameter shaft operated at 30,000 rpm for 2 min. The drops in the oil-in-water emulsions remain dispersed and do not coalesce for a few months under quiescent conditions. The emulsions release water over time due to the oil drops creaming, however there was no evidence of an excess of silica particles in the water, indicating that all the particles present in the emulsions were located at the droplet surfaces.

Destabilization was triggered by lowering the surfactant concentration in the emulsions. The emulsions were gently diluted in sufficient water to lower the CTAB concentration to ≤0.01 mM. To create multi-compartment emulsion droplets, samples of the emulsions of each type of oil were gently mixed by hand together with sufficient water to lower the CTAB concentration to 0.01 mM.

## Emulsion Characterization

To visualize the emulsion microstructure by optical microscopy we used a Zeiss Axiophot Microscope. To visualize the fused droplets by confocal microscopy we used a Leica SP5 DM6000B Scanning Confocal Microscope. Prior to emulsion formation the particles were stained with Nile Blue (0.1 mM in water). Nile Red (0.1 mM in oil) was used for staining the oil. Preliminary studies confirmed that the presence of the dyes did not alter emulsion structure or stability. The Nile Blue was excited at 633 nm and the Nile Red at 496 nm. Fluorescence intensity data for Nile Blue and Nile Red were collected in two separate channels corresponding to 520–570 and 653–750 nm, respectively. Each line of pixels in an image was scanned sequentially for Nile Red and Nile Blue fluorescence to avoid interference due to cross-fluorescence.

The drop size distributions in the emulsions were measured by static light scattering using Mastersizer 3000. The average of the volume-weighted mean diameter of three distributions measured on different samples of the same emulsion was calculated. The typical standard deviation of the mean drop diameters was 15 μm.

A glass cover slip was used as a planar substrate for wetting measurements. The glass cover slips were immersed in oil (olive oil or silicone oil) contained in a rectangular cell. A drop of surfactant solution was then placed onto the glass surface and left to equilibrate for 30 min. The advancing contact angle was measured through aqueous phase using a KSV CAM 200. The average of contact angle measurements on five drops was calculated. The typical standard deviation of the contact angle measurements was 8°.

Interfacial tensions were measured using an Attensiometer digital tensiometer with a platinum du Nouy ring. The average of three measurements of the interfacial tension was calculated. The typical standard deviation of the interfacial tension measurements was 3 mN $m^{-1}$.

# RESULTS AND DISCUSSION

We studied fusion in oil-in-water emulsions stabilized by mixtures of negatively charged silica nanoparticles and a cationic surfactant, hexadecyltrimethyl ammonium bromide. It should be noted that it was not possible to stabilize emulsions in the presence of the silica nanoparticles alone (the three phase oil-water-particle contact angle, θ, of silica particles is ∼0°). In the absence of particles, emulsions prepared from solutions of CTAB at the concentrations studied are also unstable to phase separation. Preliminary experiments established the criteria for forming dilute oil-in-water emulsions of each type of oil that were stable to coalescence. Emulsions of a single type of oil were typically stabilized by mixtures of 0.5 wt.% particles and CTAB at concentrations >0.01 mM. At this particle concentration there was no evidence of excess (unattached) particles in the emulsions. The emulsions were studied at drop volume fractions, $\phi$, ranging from 0.1 to 0.4, since the drops in more concentrated emulsions were unstable to coalescence. This is consistent with previous findings (Binks and Whitby, 2005) that adsorption of CTAB on silica nanoparticles alters the particle wettability and

stability to flocculation and hence improves emulsion stability to coalescence.

Destabilization was triggered by lowering the surfactant concentration in the emulsions to ≤0.01 mM. Diluting emulsions of a single type of oil in pure water to reduce the surfactant concentration caused the drops to undergo coalescence to a limited extent. For example, the average drop size measured by dynamic light scattering in emulsions (at a drop volume fraction of $\phi = 0.01$ after dilution) increased by 10% within 2 days of reducing the surfactant concentration. Further changes in the drop size distributions were not observed in very dilute emulsions. Larger increases in the average drop size were observed in emulsions at higher drop volume fractions. The average drop size in the emulsions at drop volume fractions, $\phi = 0.04$ increased by up to 50% within 2 days of reducing the surfactant concentration. A layer of oil was observed on top of the emulsions (at $\phi = 0.04$) after 7 days of standing at rest. A layer of emulsion did remain, however, indicating that destabilization was only temporary, as a fraction of the drop population had stopped undergoing coalescence.

The coalescence stability of Pickering emulsions is determined by the lifetime of the particle-stabilized thin films formed between drops that come into close contact. We propose that reducing the surfactant concentration in the emulsions alters the particle wettability and hence the position of the attached particles at the drop surfaces. This was tested by measuring the contact angle of aqueous surfactant solutions on planar glass surfaces (microscope slides) under oil. Under silicone oil, $\theta$ decreased from about 93° to 55° as the CTAB concentration was reduced from 0.1 to 0.01 mM. The contact angle under olive oil decreased from 108° to 67° over the same surfactant concentration range. The contact angle of the glass surfaces was about 90° at high surfactant concentrations due to the surfactant molecules adsorbing in conformations where the cationic head-group neutralizes an anionic site on the surface and the hydrocarbon tail is exposed, making the surface hydrophobic. This wettability is optimal for attaching particles to drop surfaces. Reducing the surfactant concentration caused desorption of surfactant molecules from the glass surface, reducing its hydrophobicity. A reduction in the wettability of the silica nanoparticles at the droplet surfaces would reduce the energy required to detach the particles from the drop surfaces, increasing the probability of thin film rupture and coalescence between drops that come into close contact. The disruption to the interfacial particle layer causes the drops to coalesce together until the density of the particles coating the surfaces of the merging drops is sufficient to inhibit further instability.

The proposed mechanism for the limited coalescence caused by reducing the surfactant concentration in the Pickering emulsions is illustrated in the schematic in **Figure 1A**. In the schematic, the orientation of the surfactant molecules adsorbed on particle surfaces in contact with oil is depicted as the same as the orientation of the surfactant molecules on particle surfaces in contact with water. This is because the mechanism by which emulsions prepared in the presence of mixtures of particles and surfactants are stabilized remains unclear. Although it is hypothesized that it is due to unique flocculation mechanisms between particles and surfactant, little is known about how particles and surfactant arrange at drop surfaces (Maestro et al., 2015). It is not known whether the orientation of the surfactant molecules changes on the part of the particle surfaces that become immersed in the oil.

It should be noted that lowering the surfactant concentration below 0.01 mM CTAB tended to cause uncontrolled coalescence. This led to phase separation of the emulsions during mixing (dilution). At very low surfactant concentrations there are insufficient surfactant molecules available to adsorb to the

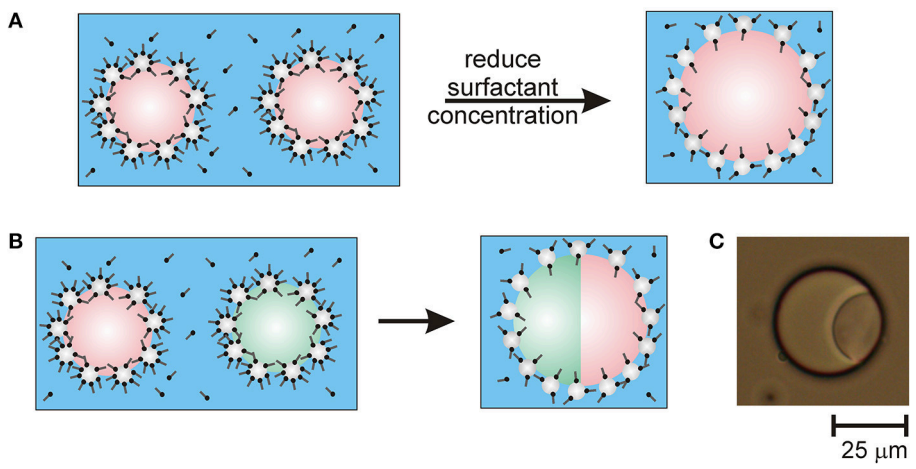


**FIGURE 1 |** Schematics of Pickering emulsion destabilization caused by reducing the surfactant concentration in emulsions stabilized by mixtures of particles and surfactant. **(A)** Destabilizing an emulsion containing drops of a single type of oil in water causes the drops to undergo limited coalescence. **(B)** Destabilizing an emulsion containing drops of two different immiscible types of oil causes the drops to fuse with multiple together into drops compartments. **(C)** Optical microscope image of a fused droplet containing compartments of olive oil and silicone oil.

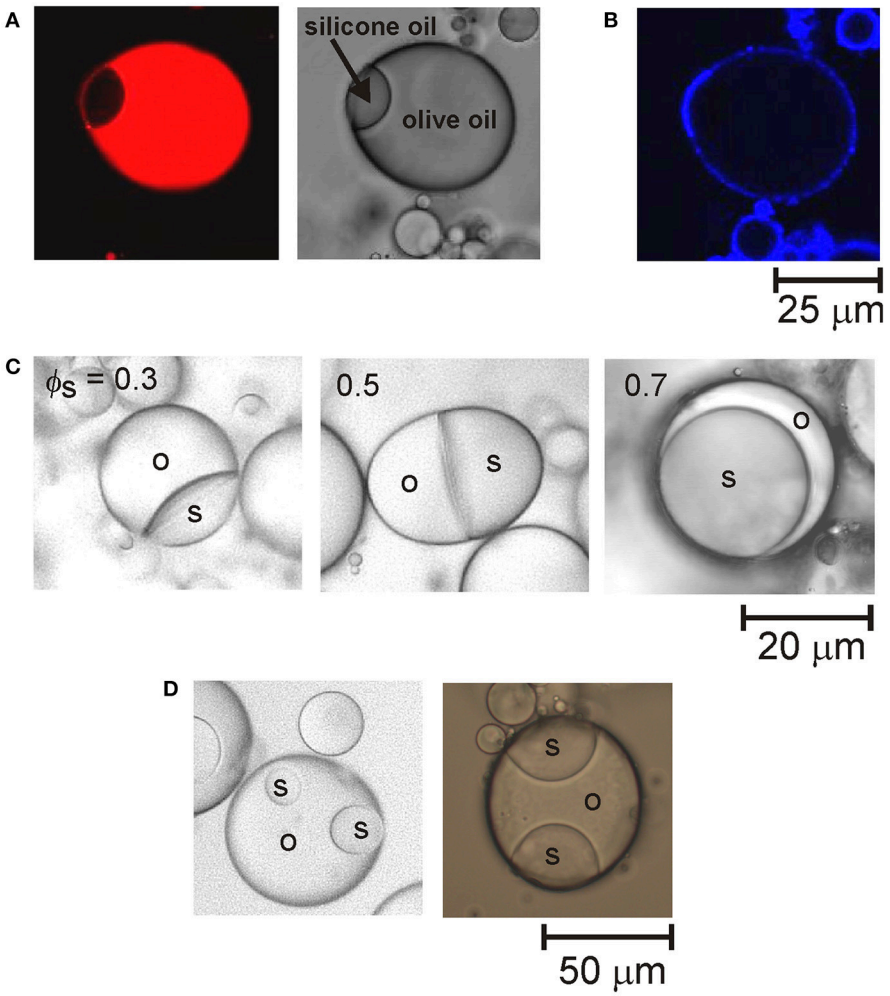


**FIGURE 2 | (A)** Confocal fluorescence image (left) and an optical microscope image (right) of a fused droplet of olive oil and silicone oil. The confocal image shows the fluorescence from the Nile Red staining the olive oil compartment. **(B)** Confocal fluorescence image of the particle shell encapsulating the fused droplet shown in **(A)**. **(C)** Optical microscope images of fused droplets of olive oil (o) and silicone oil (s) at different volume fractions of silicone oil ($\phi_S$) in the compound drops. The curvature of the interface between the two oil compartments changes from concave to planar to convex as the volume fraction of the silicone oil compartment increases. **(D)** Optical microscope images of fused droplets containing more than two compartments.

particle surfaces and increase the particle hydrophobicity for re-stabilization of the emulsion to occur. Thus, there is a range of surfactant concentrations over which coalescence (and fusion, as shown shortly) is limited and ceases after some time.

To create multi-compartment emulsion droplets, samples of the emulsions of each type of oil were gently mixed by hand together with sufficient water to lower the CTAB concentration to 0.01 mM. A schematic of the droplet fusion process expected to occur is shown in **Figure 1B**. After allowing the mixed emulsions to rest for 1 day, they were examined by optical microscopy. **Figure 1C** shows an example of the anisotropic droplet microstructures observed. The compound drops are composed of droplets of olive oil and silicone oil that have fused together due to the transient destabilization of the particle layers coating the drops caused by reducing the CTAB concentration. Since the oils used are not miscible, the drops fuse rather than completely merging their contents. This was confirmed by staining the oil phases in the emulsions with fluorescent dyes. To differentiate between the olive oil and PDMS compartments, the olive oil was stained with Nile Red or pyrene prior to emulsion formation. For example, **Figure 2A** shows fluorescence from Nile Red staining the olive oil compartment of the compound drop. Nile Red is a red phenoxazone dye that dissolves readily in olive oil (which is mainly composed of triglycerides) rather than polydimethylsiloxane (PDMS, or silicone oil).

The compound droplet microstructures are stabilized by layers of particles coating the perimeters of the fused drops. This was confirmed by staining the particles with Nile Blue prior to emulsion formation. **Figure 2B** shows that staining the particles rendered the external surfaces of the droplets visible. The internal interfaces between the droplet compartments are not coated by particles. This means that particles are displaced

from the olive oil–silicone oil interface that forms as the thin films between merging droplets rupture during droplet fusion. The displacement of the particles from the oil–oil interfaces can be accounted for by considering the interfacial tensions of the compound droplets. Interfacial tensions of $\gamma_{ow} = 16.4$ mN m$^{-1}$ and $\gamma_{sw} = 38.5$ mN m$^{-1}$ were measured for the olive oil–water and PDMS–water interfaces, respectively. The interfacial tension of the olive oil–PDMS interface was estimated to be much lower ($\gamma_{os} = 1$ mN m$^{-1}$). The lower interfacial energy trapping the particles at the oil–oil interfaces means that the particles tend to diffuse away from the area of contact between the droplets and increase the density of particles at the oil–water interfaces of fused drops.

The majority of fused drops formed in these experiments had only two compartments. They had partially engulfed, or Janus topologies, rather than completely engulfed configurations. This means that the two drops (or compartments) of immiscible oil have a common interface. The remaining portion of both drop surfaces are exposed to the water. A key factor that influences the shape of the two compartments is the relative volumes of the drops. **Figure 2C** shows examples of the morphology of Janus droplets formed by fusing drops of silicone oil and olive oil of different sizes. The curvature of the oil–oil interfaces changes as the volume fraction of the silicone oil compartment increases. The droplet configuration can be rationalized by considering the three interfacial tensions involved. If we consider a drop of olive oil placed at a silicone oil–water interface, the spreading coefficient is given by $S = \gamma_{sw} - (\gamma_{ow} + \gamma_{os})$. The coefficient must be a positive number for spreading to occur spontaneously. Due to the very low interfacial tension between the two oils, the spreading coefficient effectively depends on the difference between the olive oil–water and silicone oil–water interfacial tensions. The higher interfacial tension between silicone oil and water means that the olive oil will spontaneously spread over the silicone oil. Thus, fused droplets containing a relatively small compartment of silicone oil adopt a configuration where the silicone oil forms a small lens pinned on the surface of the olive oil compartment. Fused drops containing a small compartment of olive oil, on the other hand, adopt a configuration where the olive oil spreads around the surface of the silicone oil droplet. Thus, the transition between the different morphologies is consistent with theoretical predictions of the spreading behavior (Torza and Mason, 1969) of the two oils studied.

A small proportion of drops with several compartments was observed after mixing together emulsions containing relatively large oil volume fractions. This indicates that the fusion of three or four droplets is also possible during the transient destabilization. The more complex multiphase droplet structures that form consist of a number of small droplets of one type of oil located around the edge of a larger, central droplet of the other type of oil, as shown in **Figure 2D**.

The focus of this work was on demonstrating the formation of compound drops by using a well-known combination of particles and surfactant as synergistic stabilizers. CTAB is commonly used to modify the wettability of nanoparticles, however it is a toxic surfactant. A key step in the development of particle-stabilized compound drops for use in therapeutic or food formulations will involve using acceptable ingredients as stabilizers. The wide range of combinations of surfactants and particles used to synergistically stabilize emulsions (Dickinson, 2010) should make this a versatile and general route for preparing (kinetically) stable multi-compartment drops.

Compound drops stabilized by nanoparticles may have potential applications for the controlled release of sensitive ingredients. The formation of nanoparticle layers at fluid interfaces has been shown to be a highly effective strategy for protecting sensitive compounds encapsulated within simple oil drops and controlling their release (Eskandar et al., 2009; Kargar et al., 2011). Further experiments are required to investigate the encapsulation efficiency of particle-coated compound droplets.

## CONCLUSION

In conclusion we have established a straightforward process for generating compound drops from two or more immiscible oils with minimal agitation. Using the limited coalescence behavior of Pickering emulsions to fuse drops together opens up the possibility of creating large numbers of drops with multiphase structures. Applications of compound drops may benefit from the enhanced stability of particle-stabilized drops.

## AUTHOR CONTRIBUTIONS

CW guided the design of experiments. FB conducted the experiments. CW and FB analyzed the data and wrote the manuscript.

## FUNDING

This work was funded by Massey University and the MacDiarmid Institute for Advanced Materials and Nanotechnology.

## ACKNOWLEDGMENTS

CW acknowledges useful discussions with M. A. K. Williams and S. B. Hall at Massey University and G. R. Willmott at the University of Auckland.

## REFERENCES

Arditty, S., Whitby, C. P., Binks, B. P., Schmitt, V., and Leal-Calderon, F. (2003). Some general features of limited coalescence in solid-stabilized emulsions. *Eur. Phys. J. E* 11, 273–281. doi: 10.1140/epje/i2003-10018-6

Binks, B. P., and Lumsdon, S. O. (2000). Influence of particle wettability on the type and stability of surfactant-free emulsions. *Langmuir* 16, 8622–8631. doi: 10.1021/la000189s

Binks, B. P., Rodrigues, J. A., and Frith, W. J. (2007). Synergistic interaction in emulsions stabilized by a mixture of silica nanoparticles and cationic surfactant. *Langmuir* 23, 3626–3636. doi: 10.1021/la0634600

Binks, B. P., and Whitby, C. P. (2005). Nanoparticle silica-stabilised oil-in-water emulsions: improving emulsion stability. *Colloids Surf. A Physicochem. Eng. Aspects* 253, 105–115. doi: 10.1016/j.colsurfa.2004.10.116

Choi, C.-H., Weitz, D. A., and Lee, C.-S. (2013). One step formation of controllable complex emulsions: from functional particles to simultaneous encapsulation of hydrophilic and hydrophobic agents into desired position. *Adv. Mater. Weinheim.* 25, 2536–2541. doi: 10.1002/adma.201204657

Dickinson, E. (2010). Food emulsions and foams: stabilization by particles. *Curr. Opin. Colloid Interface Sci.* 15, 40–49. doi: 10.1016/j.cocis.2009.11.001

Eskandar, N. G., Simovic, S., and Prestidge, C. A. (2007). Synergistic effect of silica nanoparticles and charged surfactants in the formation and stability of submicron oil-in-water emulsions. *Phys. Chem. Chem. Phys.* 9, 6426–6434. doi: 10.1039/b710256a

Eskandar, N. G., Simovic, S., and Prestidge, C. A. (2009). Chemical stability and phase distribution of all-trans-retinol in nanoparticle-coated emulsions. *Int. J. Pharmaceut.* 376, 186–194. doi: 10.1016/j.ijpharm.2009.04.036

Fryd, M. M., and Mason, T. G. (2014). Self-limiting droplet fusion in ionic emulsions. *Soft Matter* 10, 4662–4673. doi: 10.1039/c4sm00453a

Ge, L., Li, J., Zhong, S., Sun, Y., Friberg, S. E., and Guo, R. (2017). Single, Janus, and Cerberus emulsions from the vibrational emulsification of oils with significant mutual solubility. *Soft Matter* 13, 1012–1019. doi: 10.1039/C6SM02690G

Hasinovic, H., and Friberg, S. E. (2011). One-step inversion process to a Janus emulsion with two mutually insoluble oils. *Langmuir* 27, 6584–6588. doi: 10.1021/la105118h

Hu, Z., Patten, T., Pelton, R., and Cranston, E. D. (2015). Synergistic stabilization of emulsions and emulsion gels with water-soluble polymers and cellulose nanocrystals. *ACS Sustain Chem. Eng.* 3, 1023–1031. doi: 10.1021/acssuschemeng.5b00194

Johnson, R. E., and Sadhal, S. S. (1985). Fluid mechanics of compound multiphase drops and bubbles. *Annu. Rev. Fluid Mech.* 17, 289–320. doi: 10.1146/annurev.fl.17.010185.001445

Kargar, M., Spyropoulos, F., and Norton, I. T. (2011). The effect of interfacial microstructure on the lipid oxidation stability of oil-in-water emulsions. *J. Colloid Interface Sci.* 357, 527–533. doi: 10.1016/j.jcis.2011.02.019

Levine, S., Bowen, B. D., and Partridge, S. J. (1989). Stabilisation of emulsions by fine particles.1. Partitioning of particles between continuous phase and oil-water interface. *Colloids Surf.* 38, 325–343. doi: 10.1016/0166-6622(89)80271-9

Maestro, A., Santini, E., Zabiegaj, D., Llamas, S., Ravera, F., Liggieri, L., et al. (2015). Particle and particle-surfactant mixtures at fluid interfaces: assembly, morphology, and rheological description. *Adv. Condens. Matter Phys.* 2015:917516. doi: 10.1155/2015/917516

McClements, D. J. (2015). Encapsulation, protection, and release of hydrophilic active components: potential and limitations of colloidal delivery systems. *Adv. Colloid Interface Sci.* 219, 27–53. doi: 10.1016/j.cis.2015.02.002

Muschiolik, G. (2007). Multiple emulsions for food use. *Curr. Opin. Colloid Interface Sci.* 12, 213–220. doi: 10.1016/j.cocis.2007.07.006

Muschiolik, G., and Dickinson, E. (2017). Double emulsions relevant to food systems: preparation, stability, and applications. *Compr. Rev. Food Sci. Food Saf.* 16, 532–555. doi: 10.1111/1541-4337.12261

Neeson, M. J., Tabor, R. F., Grieser, F., Dagastine, R. R., and Chan, D. Y. C. (2012). Compound sessile drops. *Soft Matter* 8, 11042–11050. doi: 10.1039/c2sm26637g

Nisisako, T., Okushima, S., and Torii, T. (2005). Controlled formulation of monodisperse double emulsions in a multiple-phase microfluidic system. *Soft Matter* 1, 23–27. doi: 10.1039/b501972a

Pawlik, A., Cox, P. W., and Norton, I. T. (2010). Food grade duplex emulsions designed and stabilised with different osmotic pressures. *J. Colloid Interface Sci.* 352, 59–67. doi: 10.1016/j.jcis.2010.08.049

Reger, M., Sekine, T., Okamoto, T., Watanabe, K., and Hoffmann, H. (2011). Pickering emulsions stabilized by novel clay–hydrophobin synergism. *Soft Matter* 7, 11021–11030. doi: 10.1039/c1sm06525d

Sapei, L., Naqvi, M. A., and Rousseau, D. (2012). Stability and release properties of double emulsions for food applications. *Food Hydrocoll.* 27, 316–323. doi: 10.1016/j.foodhyd.2011.10.008

Silva, B. F. B., Rodríguez-Abreu, C., and Vilanova, N. (2016). Recent advances in multiple emulsions and their application as templates. *Curr. Opin. Colloid Interface Sci.* 25, 98–108. doi: 10.1016/j.cocis.2016.07.006

Tadros, T. F. (1992). Future developments in cosmetic formulations. *Int. J. Cosm. Sci.* 14, 93–111. doi: 10.1111/j.1467-2494.1992.tb00045.x

Torza, S., and Mason, S. (1969). Coalescence of two immiscible liquid drops. *Science* 163, 813–814. doi: 10.1126/science.163.3869.813

Wang, J., Liu, G., Wang, L., Li, C., Xu, J., and Sun, D. (2010). Synergistic stabilization of emulsions by poly (oxypropylene) diamine and Laponite particles. *Colloids Surf. A Physicochem. Eng. Aspects* 353, 117–124. doi: 10.1016/j.colsurfa.2009.11.002

Wang, Z., and Wang, Y. (2016). Tuning amphiphilicity of particles for controllable pickering emulsion. *Materials* 9:903. doi: 10.3390/ma9110903

Wei, D., Ge, L., Lu, S., Li, J., and Guo, R. (2017). Janus particles templated by Janus emulsions and application as a pickering emulsifier. *Langmuir* 33, 5819–5828. doi: 10.1021/acs.langmuir.7b00939

Weyer, F., Lismont, M., Dreesen, L., and Vandewalle, N. (2015). Compound droplet manipulations on fiber arrays. *Soft Matter* 11, 7086–7091. doi: 10.1039/C5SM00364D

Zhao, C.-X. (2013). Multiphase flow microfluidics for the production of single or multiple emulsions for drug delivery. *Adv. Drug Deliv. Rev.* 65, 1420–1446. doi: 10.1016/j.addr.2013.05.009

**Conflict of Interest Statement:** The authors declare that the research was conducted in the absence of any commercial or financial relationships that could be construed as a potential conflict of interest.

frontiers in Chemistry

ORIGINAL RESEARCH
published: 19 June 2018
doi: 10.3389/fchem.2018.00220

# Ultrafine Particle Recovery Using Thin Permeable Films

*Daniel J. Borrow*, Kim van Netten and Kevin P. Galvin*

*Centre for Advanced Particle Processing, Newcastle Institute for Energy and Resources, University of Newcastle, Callaghan, NSW, Australia*

The selective recovery of ultrafine, $<10\,\mu m$, particles remains a significant challenge in the minerals industry. Indeed, these particles often report to tailings impoundments, resulting in under-utilization of mined resources and the need for tailings dams. Recently, a technique has been developed offering the potential to selectively recover particles down to $<1\,\mu m$ in size. This technique, originally inspired by oil agglomeration, uses a high internal-phase water in oil emulsion as a binder to selectively agglomerate hydrophobic particles. Due to the significant concentration of the dispersed aqueous phase, ~95%, the continuous organic phase forms a network of very thin, permeable films, estimated to be 60 nm thick. These are stabilized by an emulsifier. In the high shear field of the agglomeration process, the binder is fragmented into smaller hydrophobic portions, delivering its thin film coating to the adhering hydrophobic particles. Permeation of water across the thin films eliminates the viscous hydrodynamic resistance, permitting sub-micron particle recovery to occur at rates similar to those for particles considerably larger in size. This recovery occurs within seconds under intense mixing. In this study, a model system consisting of magnetite, with a Sauter mean diameter of $11.4\,\mu m$, was agglomerated using the water in oil emulsion binder. The binder, which contained the emulsifier sorbitan monooleate, appeared to also act as a collector for the magnetite, thus no separate particle conditioning step was required. Curiously, however, the binder requirements were higher than expected. Further investigations concerning the stability of the binder revealed that the magnetite particles were causing rapid binder degradation. Therefore, prior to agglomeration using the binder, the particles were conditioned with sorbitan monooleate to render them hydrophobic. This pre-conditioning led to significant reductions in the binder dosage required to achieve agglomeration. Moreover, the resulting dosage matched that predicted by a model silica system for the same specific hydrophobic surface area, thus allowing a model to be validated based on the required binder dosage for a known hydrophobic surface area. Examination of binder stability in the presence of conditioned magnetite revealed that the now hydrophobic particles stabilized the binder.

**Keywords: emulsion, hydrophobic, stabilization, permeable film, agglomeration, ultrafine particles**

OPEN ACCESS

***Edited by:***
*Syuji Fujii,*
*Osaka Institute of Technology, Japan*

***Reviewed by:***
*Roland Arthur Lee,*
*MacEwan University, Canada*
*Benoit Haut,*
*Free University of Brussels, Belgium*

****Correspondence:***
*Daniel J. Borrow*
*daniel.borrow@uon.edu.au*

***Specialty section:***
*This article was submitted to Chemical Engineering, a section of the journal Frontiers in Chemistry*

***Received:*** *15 February 2018*
***Accepted:*** *28 May 2018*
***Published:*** *19 June 2018*

***Citation:***
*Borrow DJ, van Netten K and Galvin KP (2018) Ultrafine Particle Recovery Using Thin Permeable Films. Front. Chem. 6:220. doi: 10.3389/fchem.2018.00220*

## INTRODUCTION

Froth flotation has been widely used in the selective recovery of fine hydrophobic particles for around 100 years. The process allows large scale and economic processing of crushed minerals and ores to produce many of the metals needed in the modern world. Challenges are emerging however due to falling ore grades, and increased demand for base and precious metals.

The flotation of ultrafine, $<10\,\mu m$, particles has been shown to be inefficient and beyond the hydrodynamic limits of flotation (Leja, 2012), resulting in these particles reporting to tailings impoundments, representing a loss in valuable resources, and an environmental legacy associated with toxic heavy metals. Economies of scale have led to the need for increasingly larger process systems up to 650 $m^3$ in volume (Wills and Finch, 2015). An alternative method for recovering and concentrating fine ($<100\,\mu m$) and ultrafine ($<1\,\mu m$) hydrophobic particles is oil agglomeration. The process, also called selective agglomeration, was originally developed for recovering fine coal from tailings, but has also been applied to tin, iron, and gold ores (Farnand et al., 1964, 1969; Sparks and Sirianni, 1974). Here, dispersed drops of oil are introduced, providing the hydrophobic interfaces in the same way air bubbles are used in flotation. Oil agglomeration offered many advantages, with higher recovery, improved kinetics, and the potential for dewatering using a mechanical screen (Mehrotra and Sastry, 1983). However, the process was never adopted across the industry due to the considerable cost of the oil (Miller, 1969).In an effort to economically recover ultrafine material, variations to both traditional froth flotation and oil agglomeration have been studied. Liu et al. (2002) developed the oily bubble flotation method, a process in which air bubbles are coated with thin oil films. By coating bubbles with an oil, flotation performance was improved as a result of the higher contact angle of the oil/particle surface. The stronger collecting power of the oil coated bubbles, over traditional air bubbles, resulted in lower processing times, however significant time was still required to achieve recoveries >95% (Wallwork et al., 2003). Gupta et al. (2016) have more recently developed the Hydrophobic-Hydrophilic Separation (HHS) process. Hydrophobic particles, such as coal, are transferred from a water phase to a hydrophobic liquid phase, generally a short chain alkane or oil. Coal agglomerates are formed in excess oil and then subsequently destabilized, such that entrapped water is released. The oil is then vaporized, condensed and recycled. Whilst being an efficient beneficiation process, multiple stages and significant energy input are required.

In other recent work, van Netten and co-workers have developed a novel hydrophobic binder for use in selective agglomeration. Originally developed with the aim of reducing the oil required in the selective agglomeration process, the hydrophobic binder has been shown to achieve rapid recovery across the full fine particle size range (van Netten et al., 2013, 2014, 2015, 2016). A high internal-phase (HIP) water in oil emulsion is used as the binder. This emulsion is characterized by a high internal phase volume fraction, i.e., >0.74. This is achieved by tightly packing water droplets within thin hydrophobic oil films. The tight packing, achieved through deformation of the drops, leads to internal phase volume fractions as high as 99% (Adamson, 1990).

Early work using the HIP water in oil emulsion binder showed a 2–3-fold (van Netten et al., 2013), followed by a 7-fold (van Netten et al., 2014) reduction in organic liquid requirements compared to conventional oil agglomeration in the recovery of coal particles. The most recent development however, resulted in a 10-fold reduction (van Netten et al., 2016). The hydrophobic emulsion binder consisted of a 95% dispersed aqueous phase and a 5% continuous organic phase. The aqueous phase consisted of a 3 wt% NaCl solution. The continuous organic phase contained equal mass portions of kerosene and emulsifier. The agglomeration process was remarkably complete within seconds, whilst traditional oil agglomeration needed residence times in the order of minutes.

To develop a clearer understanding of the hydrophobic emulsion binder functionality, further work was conducted using silica samples covering different particle size distributions (van Netten et al., 2017). A collector, CTAB, was added to the feed suspension to render the particles hydrophobic. The hydrophobic binder was then applied to the conditioned silica suspensions, achieving complete recovery of the particles in the form of agglomerates, using a mechanical screen to capture the solids. Silica particles ranging in size from $0.5\,\mu m$ to $>100\,\mu m$ were recovered. The hydrophobic binder achieved a 16-fold reduction in oil consumption over conventional oil agglomeration for this material.

**Figure 1** shows the oil consumption required to agglomerate the silica as a function of the specific surface area of the silica, for conventional oil agglomeration and for the hydrophobic binder. **Figure 1** provides a measure of the effective film thickness of the oil over the particles via the slope. The effective film thickness with respect to the silica particle surface is 1,040 and 66.1 nm for the conventional and hydrophobic emulsion binders respectively, representing a 16-fold reduction in oil requirements. The water drops within the binder had a Sauter mean diameter of 2.3 microns, hence the average oil thickness with respect to the drops was 29 nm, corresponding to 58 microns between opposing water drops.

The hydrophobic emulsion binder provides the ideal delivery system for efficiently presenting the hydrophobic oil interface to the hydrophobic particles. In the form of a concentrated water in oil emulsion, the oil is present as thin films of order 50 nm, while in conventional oil agglomeration the mixing might only disperse the oil to form drops of order 1,000 nm, delivering a completely new system in which oil can coat and agglomerate hydrophobic particles. Thus, for the same volume of oil, the thin films wet a much larger surface area of particles, resulting in the decreased oil requirements and subsequent cost.

In the same study, van Netten et al. (2017) discovered that when the hydrophobic binder was subjected to intense mixing in water, and hence fragmented into smaller portions, water permeated into the binder fragments. Driven by the osmotic pressure gradient between the suspending water and the aqueous phase within the binder, which contained 3 wt % NaCl, water permeates across the thin oil films surrounding the dispersed drops within the binder. The viscous hydrodynamic resistance between the hydrophobic particles impinging on the binder surface effectively disappears due to the permeability of the hydrophobic interface. Thus, complete recovery of the hydrophobic particles across the full size range is observed within a few seconds.

Water transport through permeable films between an internal aqueous phase of a W/O emulsion and an external aqueous phase,

i.e., a water-in-oil-in-water double emulsion, has previously been observed in the literature, with double emulsions used for drug release (Fukushima et al., 1983), cosmetics (Laugel et al., 1996), food (Garti, 1997), and agricultural fertilizers (Sela et al., 1994). However, in these applications it was desirable for the water (and water soluble material) to be transported from the internal aqueous phase to the external phase, i.e., the opposite direction to that which occurs in the agglomeration process using the hydrophobic binder (van Netten et al., 2017). Moreover, it appears that the work by van Netten et al. (2017) was the first to use the transport of water across a permeable hydrophobic interface for the simultaneous recovery of fine hydrophobic particles from suspension.

This study continues on from the previous work by van Netten and co-workers to examine the application of the hydrophobic binder to the recovery of magnetite from an aqueous suspension. This work represents the first successful attempt to recover a real mineral ore using the hydrophobic binder. Magnetite is naturally hydrophilic and thus requires a collector to render the surface hydrophobic. Typical aqueous collectors in magnetite flotation include fatty acids, hydroxamates and sulfates (Kulkarni and, 1980; Ma, 2012). Given that sorbitan monooleate (SMO) exists within the oil film as an emulsifier, the binder has the potential to simultaneously act as a collector for the magnetite. This means that hydrophilic particles of magnetite could literally attach to the hydrophobic binder due to the presence of the SMO at the interface. This mechanism is contrary to the so-called "hydrophobic interaction" acting to produce adhesion. Hence it is of interest to test this possible mechanism.

Impingement of the hydrophilic particles should damage the thin films while the hydrophobic particles should aid in the stability of the films. Ikem et al. (2008) have previously reported on the stabilization of HIP water in oil emulsions with silica particles hydrophobised by the adsorption of oleic acid, preparing stable emulsions with internal aqueous volume fractions of up to 95%. Moreover, Finkle et al. (1923) determined the relationship between a particle's hydrophobicity and its ability to stabilize either a water in oil (W/O) or oil in water (O/W) emulsion, with hydrophobic particles found to stabilize W/O emulsions. These findings are important here because it is of interest to maximize the recovery of hydrophobic particles while minimizing the extent to which the emulsion is degraded. Emulsion degradation is undesirable as it increases the effective organic liquid dosage required to achieve agglomeration.

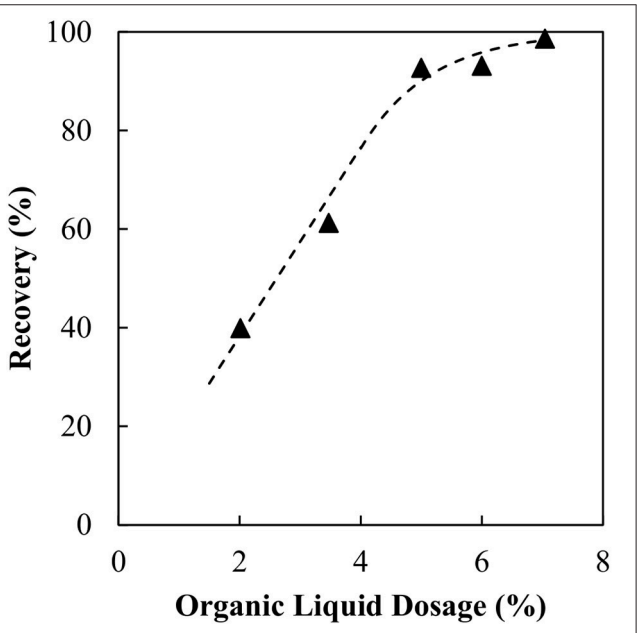


**FIGURE 2 |** Magnetite recovery as a function of organic liquid dosage.

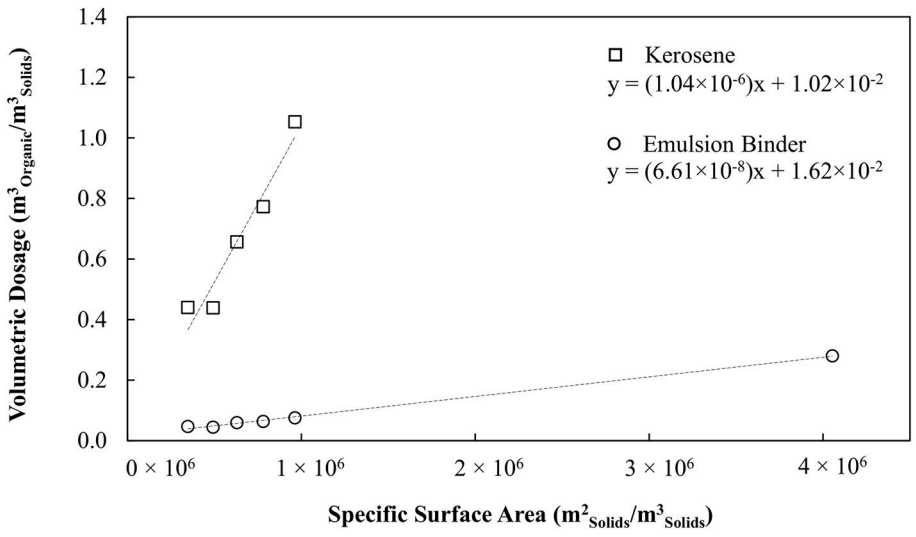


**FIGURE 1 |** Organic liquid dosage as a function of specific surface area of solid particles. Adapted with permission from van Netten et al. (2017). Copyright 2017 American Chemical Society.

The focus of the study is on how best to achieve full magnetite recovery, and to determine the minimum level of reagent and binder consumption. Ideally the magnetite can be recovered directly using the binder, with the SMO contained within the emulsion acting as a collector. This result will then be compared to the previous study, in which hydrophobic silica powder is agglomerated, to determine whether the binder addition is only dependent on the surface area of the particles. This will allow a model to be developed to determine the optimum binder requirements based on the specific surface area of the particles.

# MATERIALS AND METHODS

## Binder Preparation

The emulsion was prepared as previously described by van van Netten et al. (2017), consisting of a dispersed aqueous phase volume fraction of 95% and a continuous organic phase volume fraction of 5%. First, equal portions of kerosene (Recochem Inc.,) and industrial grade emulsifier (Vic Chem) were combined in a stainless steel mixing bowl. The industrial grade emulsifier comprised of 60 wt% sorbitan monooleate and 40 wt% glycerol monooleate. The aqueous phase, 3 wt% sodium chloride (Cerebos Ltd.,) solution, was then incrementally added to the kerosene and emulsifier solution under constant mixing using a Russell Hobbs Hand Mixer (RHMX1). The aqueous sodium chloride solution was added in increments less than that of the original organic phase volume to insure phase inversion of the emulsion did not occur. As the binder volume increased, so did the addition of the aqueous phase. A viscous, opaque, high internal phase emulsion then formed.

## Agglomeration Experiments

Agglomeration experiments were undertaken using a Waring high-speed blender (model LB20EG) operated at 22,000 rpm. Magnetite particles (Sibelco) with a Sauter mean diameter of 11.4 μm were added to 500 mL of tap water to produce an aqueous suspension. The aqueous suspension contained 60 g of solid particles in all experiments. The emulsion binder was then added in a single dose, with mixing occurring for 7 s. Since the emulsifier contained in the binder, sorbitan monooleate, acts as a collector for magnetite particles, no particle conditioning was used. At the conclusion of mixing, the contents of the blender were then poured over a 150 μm screen. The material retained on the screen was classified as the agglomerated product, whilst the material passing through was classified as the non-agglomerated reject. Both product and reject samples were dried in an oven (set at 110°C) and then weighed. The recovery value of an experiment was defined as the dry mass product as a percentage of the total dry feed. The binder dosage was progressively increased in order to determine the required organic liquid dosage to produce a fully agglomerated product.

## Emulsion Degradation

To investigate emulsion degradation, the conductivity of the suspending liquid was measured using a EUTECH conductivity meter (PCTesr 35). Intense mixing leads to gradual degradation of the binder due to the stresses applied to the thin oil films. Progressively, salt contained within the internal aqueous droplets is released into the outer suspending liquid. By measuring the conductivity, the extent of the salt released can be measured and used to quantify the degradation. The maximum theoretical mass of salt in the emulsion was added to 500 mL of water and the conductivity measured. This was done to normalize the conductivity measurements. Systems that contained no particles (i.e., only the emulsion binder) and hydrophobic particles that are believed to stabilize the binder were used. Mixing occurred between 1 and 30 s in the Waring variable speed blender, operated at 22,000 rpm. The contents of the blender were then filtered so that no binder fragments or solids passed through into the filtrate used for the conductivity measurements.

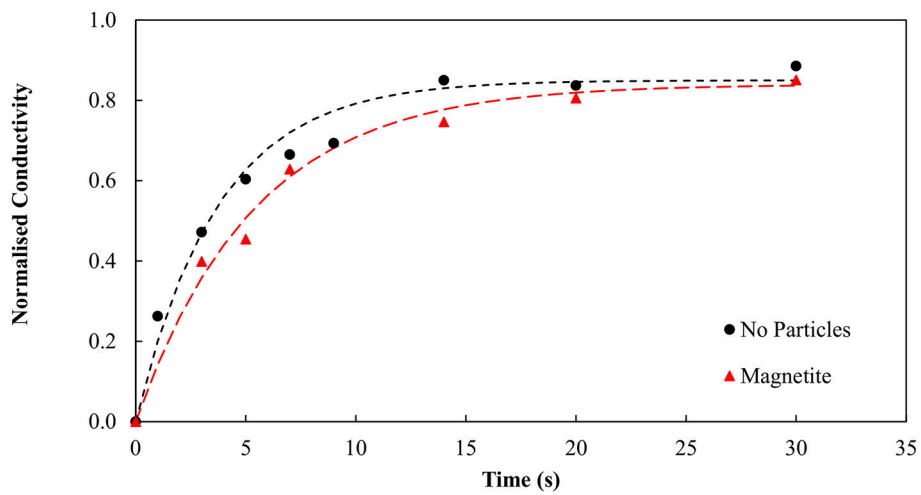


**FIGURE 3 |** Emulsion degradation over time for systems containing no particles and magnetite particles.

## RESULTS AND DISCUSSION

The recovery of magnetite as a function of the organic liquid dosage is shown in **Figure 2**. It is assumed in this case that the sorbitan monooleate within the binder acts as a collector, thus no pre-conditioning of the particles with a surfactant was required. A simple curve fit has been added to "guide the eye." The optimum organic liquid dosage was determined by fitting the values of (100% - recovery) to a simple exponential decay function. The dosage at 90% recovery was chosen as the optimum organic liquid dosage. For the magnetite particles the optimum dosage was determined to be 5.5 wt% organic liquid. This result appears to be remarkable, recovering hydrophilic particles using a hydrophobic binder. The Supplementary Material describes the method for determining the organic liquid dosage requirements in further detail.

It is evident that increasing the organic liquid dosage results in an increase in magnetite recovery as agglomerates. The trend is consistent with the findings in the previous coal and silica work. What is different here is that the magnetite is hydrophilic, hence there must be a mechanism that renders the particles hydrophobic. However, the organic liquid requirement needed to fully agglomerate the particles appears to be excessive. Comparing the results to our previous silica study, the dosage is 6 times higher for the same specific surface area.

It is now hypothesized that the magnetite particles, initially hydrophilic, act in two ways. Firstly, the hydrophilic magnetite particles collide with the emulsion, causing degradation of the binder, and hence release of the SMO. The released SMO then adsorbs at the magnetite surface, rendering the magnetite hydrophobic. Secondly, with the particles now hydrophobic, the excess emulsion then acts as the binder to form the agglomerated product. This mechanism helps to explain why the level of binder required was excessive.

Emulsion degradation experiments were therefore conducted in the presence of (a) no particles and (b) magnetite particles. It was initially believed that the impinging magnetite would stabilize the binder system. **Figure 3** shows very similar trends for systems containing both particles and no particles. This result is contrary to the initial hypothesis that the magnetite particles should become hydrophobic, and in turn stabilize the system. Clearly the binder appears to degrade over time when there are no particles present, and when the magnetite is present.

Thus, in subsequent experiments the magnetite particles were conditioned using SMO prior to the agglomeration with the binder. Here, the SMO acts as a collector, as in flotation, making the magnetite hydrophobic. In these new experiments, the particle conditioning occurred for 30 s at 22,000 rpm to disperse the SMO, followed by 30 min at 8,000 rpm. It is known that long conditioning periods are required to ensure the dispersed SMO adsorbs to the magnetite surface, making the particles hydrophobic (Kulkarni and, 1980), however, there was no optimisation here. The binder dosage was then reduced to the dosage predicted from previous work on a model silica system of the same specific surface area, i.e., ≈1 wt% organic liquid. In all experiments, the binder dosage remained constant. The SMO concentration in the magnetite solution was progressively increased from 0.5 wt% through to 2 wt% to find the optimum operating collector dosage. The influence of the SMO collector concentration can be seen in **Figure 4**.

As the SMO dosage increases, so too does the recovery of magnetite. Initially between 0.5 and 0.75 wt% the increase in

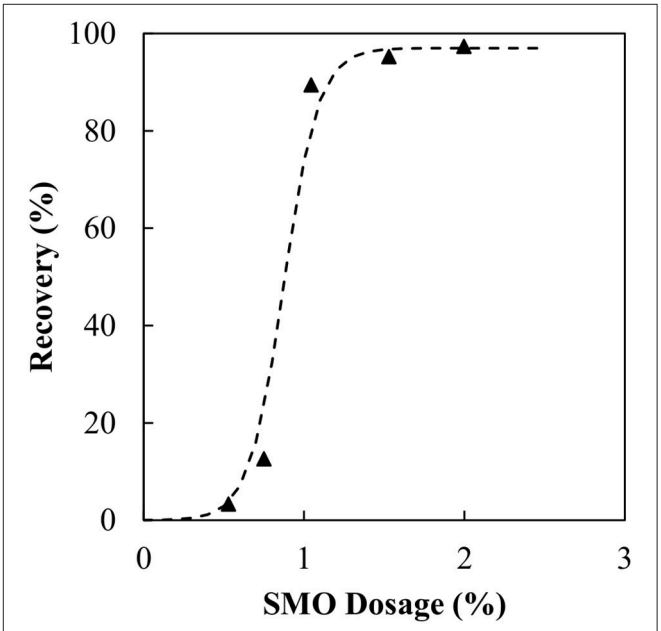


**FIGURE 4 |** Magnetite recovery as a function of SMO collector concentration at predicted organic liquid dosage.

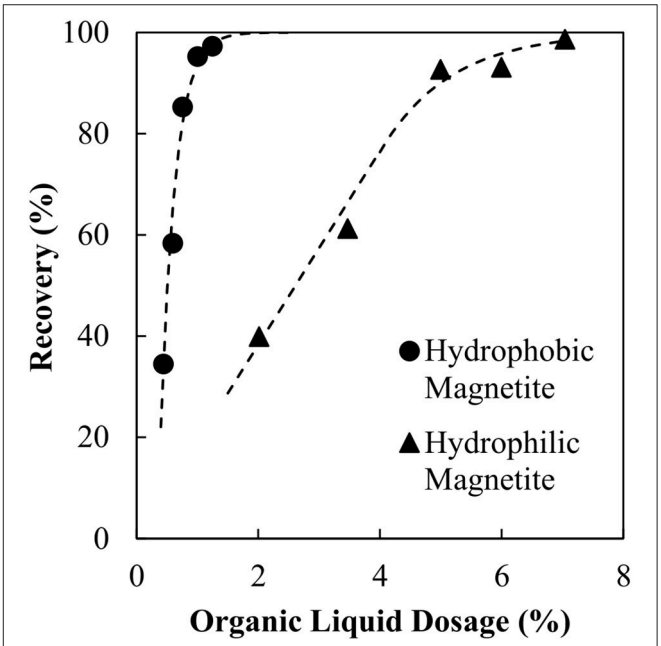


**FIGURE 5 |** Reduction in organic liquid requirement for conditioned magnetite particles.

recovery is quite small before a sudden increase at 1 wt%. Initially there is insufficient SMO to render all of the magnetite particles hydrophobic. Therefore, with some hydrophilic particles still present, the hydrophobic particles deliver improved binder stability while the hydrophilic particles contribute to the binder degradation. Beyond 1 wt% all particles are hydrophobic, resulting in almost full recovery. The agglomeration experiments were then repeated for particles conditioned with 1.5 wt% SMO in the manner described above. **Figure 5** presents the results from those experiments.

It is evident the organic liquid requirements are significantly reduced when the SMO is introduced directly as a collector and allowed to condition the particles prior to the agglomeration. By pre-dispersing the SMO as a collector, the binder functionality is preserved, resulting in the lower organic liquid dosage requirement. Emulsion degradation tests were conducted using the conditioned and thus hydrophobic magnetite particles and repeated for both no particles and the unconditioned, hydrophilic particles using the new optimum binder dosage of 0.98 wt% organic liquid to confirm the role of hydrophobic and hydrophilic particles in stabilizing and degrading the binder, respectively. **Figure 6** provides evidence that the hydrophobic magnetite particles stabilize the binder, producing much lower conductivity over time, whilst the unconditioned and effectively hydrophilic magnetite particles produce much higher conductivity over time.

The organic liquid requirements of the binder as a function of the specific surface area of the hydrophobic particles is shown in

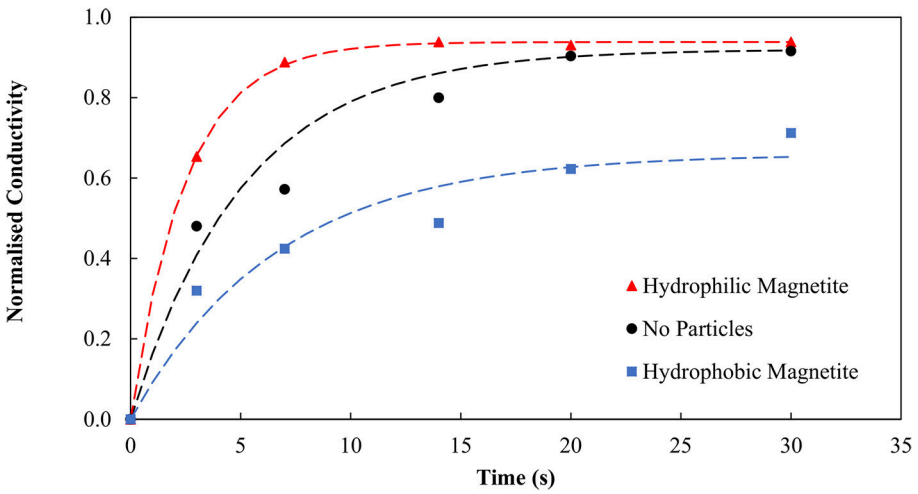


**FIGURE 6 |** Emulsion degradation over time for systems containing no particles, magnetite particles and conditioned magnetite particles. Here the magnetite particles produced the most degradation. Previously, in **Figure 3**, the binder was present in excess hence the magnetite had less impact.

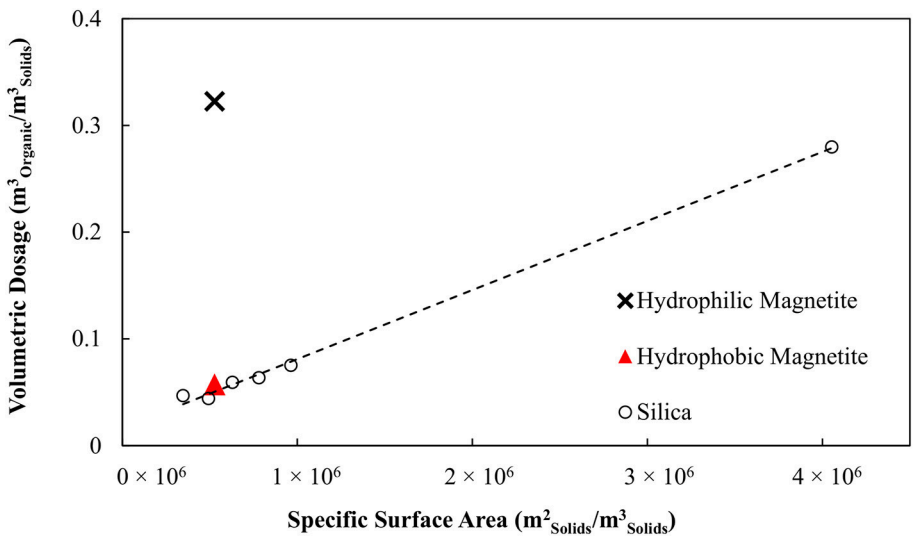


**FIGURE 7 |** Comparison of organic liquid requirements for magnetite, magnetite conditioned with SMO and silica powders.

**Figure 7** together with the earlier result obtained for no collector. These data are also compared with the results obtained in the previous work by van Netten et al. (2017) for silica. The organic liquid requirement of the binder is excessive when no collector stage is used, 6-fold higher than for silica. However, when the magnetite is made hydrophobic in advance of the agglomeration, the organic liquid dose is almost the same as for the silica.

These findings support clear conclusions concerning the application of the binder to the recovery and concentration of magnetite. Firstly, the collector cannot be introduced via the binder. Rather, the collector must be added to the suspension prior to the agglomeration to form hydrophobic particles. Moreover, these results indicate that the binder dosage required to achieve agglomeration can be predicted for particles of any known specific hydrophobic surface area using the model derived from the silica data. This information can also assist in the determination of the correct collector dosage for new materials to which the agglomeration process is applied.

## CONCLUSIONS

In this work, an aqueous suspension of magnetite particles with a Sauter mean diameter of 11.4 μm was agglomerated using a high internal-phase water in oil emulsion binder. Previous studies in which both coal (van Netten et al., 2013, 2015, 2016) and hydrophobic silica (van Netten et al., 2017) were agglomerated with the novel binder have shown a number of advantages over flotation and conventional oil agglomeration. These include ultrafast agglomeration, reduced oil requirements compared to conventional oil agglomeration and the ability to recover a wide range of particle sizes, including the recovery of material as fine as 500 nm. This study aimed to apply our previously found knowledge from the silica model to a new feed source with industrial applications.

Firstly, knowing that SMO can act as a magnetite collector, a study to determine whether the emulsion could double as a collector and binder was undertaken. Remarkably the particles were agglomerated with no conditioning, however the binder dosages were excessive and higher than expected. It was found that there was a 6-fold increase in binder requirements compared to a silica powder of the same specific surface area. Further experiments, which examined emulsion degradation, showed that the magnetite did not stabilize the binder. The introduction of SMO as a collector was found to significantly reduce the organic liquid requirements needed for agglomeration. By conditioning the particles the binder requirements were found to be equal to those of a silica powder with the same surface area. Re-examining binder stability in the presence of the conditioned, now hydrophobic, particles showed the particles stabilized the binder.

It was also shown that the organic liquid dosage required to agglomerate the pre-conditioned magnetite particles matched that predicted by work on a model silica system. It was therefore concluded that it may be possible to use the model derived from the silica system to predict the binder requirements of any hydrophobic material, given the specific hydrophobic surface area is known. The finding showing hydrophilic particles degrade the binder, whilst hydrophobic particles provide stability, is important as this has implications for real systems that contain both hydrophobic and hydrophilic particles.

## AUTHOR CONTRIBUTIONS

All authors listed have made a substantial, direct and intellectual contribution to the work, and approved it for publication.

## FUNDING

The authors acknowledge the support of the Australian Research Council, grant LP160100847, and the Australian Coal Association Research Program in funding this work.

## SUPPLEMENTARY MATERIAL

The Supplementary Material for this article can be found online at: https://www.frontiersin.org/articles/10.3389/fchem.2018.00220/full#supplementary-material

## REFERENCES

Adamson, A. W. (1990). *Physical Chemistry of* Surfaces. Los Angeles, CA: Wiley.

Farnand, J. R., Meadus, F. W., Goodhue, E. C., Puddington, I. E., and National Research Council Of Canada Ottawa Div Of C. (1969). *The Beneficiation of Gold Ore by Oil-Phase Agglomeration*. Fort Belvoir: Defense Technical Information Center.

Farnand, J. R., Meadus, F. W., Tymchuk, P., andPuddington, I. E. (1964). The application of spherical agglomeration to the fractionation of a tin-containing ore. *Can. Metall. Q.* 3, 123–135. doi: 10.1179/cmq.1964.3.2.123

Finkle, P., Draper, H. D., and Hildebrand, J. H. (1923). The theory of emulsification1. *J. Am. Chem. Soc.* 45, 2780–2788. doi: 10.1021/ja01665a002

Fukushima, S., Juni, K., and Nakano, M. (1983). Preparation of and drug release from W/O/W type double emulsions containing anticancer agents. *Chem. Pharm. Bull.* 31, 4048–4056. doi: 10.1248/cpb.31.4048

Garti, N. (1997). Progress in stabilization and transport phenomena of double emulsions in food applications. *LWT Food Sci. Technol.* 30, 222–235. doi: 10.1006/fstl.1996.0176

Gupta, N., Li, B., Luttrell, G., Yoon, R.-H., and Bratton, R. (2016). "Hydrophobic-hydrophilic separation (hhs) process for the recovery and dewatering of ultrafine coal," in *Paper Presented at the SME Annual Meeting* (Phoenix, AZ).

Ikem, V. O., Menner, A., and Bismarck, A. (2008). High internal phase emulsions stabilized solely by functionalized silica particles. *Angew. Chem. Int. Ed.* 47, 8277–8279. doi: 10.1002/anie.200990003

Kulkarni, R., and P. Somasundaran (1980). Flotation chemistry of hematite/oleate system. *Colloids Surf.* 1, 387–405.

Laugel, C., Chaminade, P., Baillet, A., Seiller, M., and Ferrier, D. (1996). Moisturizing substances entrapped in W/O/W emulsions: analytical methodology for formulation, stability and release studies. *J. Control. Release* 38, 59–67. doi: 10.1016/0168-3659(95)00103-4

Leja, J. (2012). *Surface Chemistry of Froth Flotation*. New York, NY: Springer. U. S.

Liu, J., Mak, T., Zhou, Z., and Xu, Z. (2002). Fundamental study of reactive oily-bubble flotation. *Miner. Eng.* 15, 667–676. doi: 10.1016/S0892-6875(02)00158-9

Ma, M. (2012). Froth flotation of iron ores. *Int. J. Min. Eng. Miner. Process.* 1, 56–61. doi: 10.5923/j.mining.20120102.06

Mehrotra, V. P., Sastry, K. V. S. and, Morey, B. W. (1983). Review of oil agglomeration techniques for processing of fine coals. *Int. J. Miner. Process.* 11, 175–201. doi: 10.1016/0301-7516(83)90025-X

Miller, J. D. (1969). Concentration. *Min. Eng.* 21, 94–96

Sela, Y., Magdassi, S., and Garti, N. (1994). Polymeric surfactants based on polysiloxanes—graft-poly (oxyethylene) for stabilization of multiple emulsions. *Colloids Surf. Physicochem. Eng. Asp*. 83, 143–150. doi: 10.1016/0927-7757(94)80097-9

Sparks, B. D., and Sirianni, A. F. (1974). Beneficiation of a phosphoriferous iron ore by agglomeration methods. *Int. J. Miner. Process*. 1, 231–241. doi: 10.1016/0301-7516(74)90017-9

van Netten, K., Borrow, D. J. and Galvin, K. P. (2017). Fast Agglomeration of ultrafine hydrophobic particles using a high-internal-phase emulsion binder comprising permeable hydrophobic films. *Ind. Eng. Chem. Res.* 56, 10658–10666. doi: 10.1021/acs.iecr.7b02215

van Netten, K., Moreno-Atanasio, R. and, Galvin, K. (2013). "Preparation of coal agglomerates using a water-in-oil emulsion,"in *Chemeca 2013, 41st: 2013* (Brisbane, QLD; Barton, ACT: Engineers Australia), 332–336.

van Netten, K., Moreno-Atanasio, R., and Galvin, K. P. (2014). Fine particle beneficiation through selective agglomeration with an emulsion binder. *Ind. Eng. Chem. Res.* 53, 15747–15754. doi: 10.1021/ie5027502

van Netten, K., Moreno-Atanasio, R. and Galvin, K. P. (2015). A kinetic study of a modified fine coal agglomeration process. *Procedia Eng.* 102, 508–516. doi: 10.1016/j.proeng.2015.01.201

van Netten, K., Moreno-Atanasio, R., and Galvin, K. P. (2016). Selective agglomeration of fine coal using a water-in-oil emulsion. *Chem. Eng. Res. Des*. 110, 54–61. doi: 10.1016/j.cherd.2016.02.029

Wallwork, V., Xu, Z., and Masliyah, J. (2003). Bitumen recovery with oily air bubbles. *Can. J. Chem. Eng.* 81, 993–997. doi: 10.1002/cjce.5450810510

Wills, B. A., and Finch, J. (2015). *Wills' Mineral Processing Technology: An Introduction to the Practical Aspects of Ore Treatment and Mineral Recovery*. Boston, MA: Elsevier Science.

**Conflict of Interest Statement:** The authors declare that the research was conducted in the absence of any commercial or financial relationships that could be construed as a potential conflict of interest.

frontiers in Chemistry

PERSPECTIVE
published: 10 July 2018
doi: 10.3389/fchem.2018.00280

# An Electrostatic Method for Manufacturing Liquid Marbles and Particle-Stabilized Aggregates

*Peter M. Ireland*[1]*, *Casey A. Thomas*[1], *Benjamin T. Lobel*[1], *Grant B. Webber*[1], *Syuji Fujii*[2,3] *and Erica J. Wanless*[1]

[1] *Priority Research Centre for Advanced Particle Processing and Transport, University of Newcastle, Callaghan, NSW, Australia,* [2] *Department of Applied Chemistry, Faculty of Engineering, Osaka Institute of Technology, Osaka, Japan,* [3] *Nanomaterials Microdevices Research Center, Osaka Institute of Technology, Osaka, Japan*

We have developed a method for transferring particles from a powder bed to a liquid droplet using an electric field. This process has been used to create liquid marbles with characteristics not normally found in those formed by direct contact methods such as rolling. It has also been used to manufacture hydrophilic particle-liquid aggregates and more complex layered aggregates incorporating both hydrophobic and hydrophilic particles. This article briefly outlines the electrostatic aggregation method itself, the materials used and structures formed thus far, and explores the rich fundamental physics and chemistry underpinning the process as they are understood at present.

**Keywords: liquid marble, electrostatics, air-water interface, adsorption, particle**

OPEN ACCESS

***Edited by:***
*Juha Salmela,*
*Spinnova, Finland*

***Reviewed by:***
*Anthony D. Stickland,*
*University of Melbourne, Australia*
*Timothy Nie Hunter,*
*University of Leeds, United Kingdom*

***Correspondence:**
*Peter M. Ireland*
*peter.ireland@newcastle.edu.au*

***Specialty section:***
*This article was submitted to Chemical Engineering, a section of the journal Frontiers in Chemistry*

***Received:*** *06 March 2018*
***Accepted:*** *20 June 2018*
***Published:*** *10 July 2018*

***Citation:***
*Ireland PM, Thomas CA, Lobel BT, Webber GB, Fujii S and Wanless EJ (2018) An Electrostatic Method for Manufacturing Liquid Marbles and Particle-Stabilized Aggregates. Front. Chem. 6:280. doi: 10.3389/fchem.2018.00280*

## INTRODUCTION

Drop-particle aggregates were first manufactured by our group using an electrostatic process in 2013 (Liyanaarachchi et al., 2013). In that early study, a bed of 100 μm diameter ballotini (glass spheres) was placed on a polytetrafluoroethylene (PTFE) coated glass slide, which had been negatively tribocharged (charged by rubbing). When the particle bed was brought near a water droplet suspended from a capillary, the glass spheres suddenly jumped to the drop in a vigorous "avalanche." Being hydrophilic, the particles were internalized by the drop, filling it like a "sack of marbles," and forming a pearl-like liquid-particle aggregate (**Figure 1**) on top of the particle bed. In subsequent studies, the tribocharged PTFE was replaced by a metal plate connected to a high voltage DC power supply, allowing a fully controllable driving potential.

A superficial resemblance was quickly noted between the liquid-particle aggregates formed in this early study, and the liquid marbles (LMs) first described nearly two decades ago (Aussillous and Quéré, 2001). The main difference was that our electrostatically-formed aggregate was a drop entirely filled with hydrophilic particles, whereas liquid marbles consist of a drop encased in hydrophobic particles. The resemblance was nonetheless of interest, since LMs display some remarkable properties, e.g., extreme recoverable deformability, low evaporation rate, and the ability to come into non-wetting contact with solid surfaces and to float on water (McHale and Newton, 2011, 2015; Janardan et al., 2015). These properties have in turn inspired a range of proposed applications for LMs, including gas sensors (Tian et al., 2010), bioreactors (Arbatan et al., 2012a,b), encapsulation media (Eshtiaghi et al., 2010; Ueno et al., 2014), pressure-sensitive adhesives (Fujii et al., 2016a) and materials delivery carriers (Paven et al., 2016; Kawashima et al., 2017).

LMs are conventionally formed by rolling a drop of liquid on a bed of hydrophobic particles, which adhere to the air-liquid interface. Clearly, the aggregates formed in our early experiments with hydrophilic particles cannot be formed by this method, as the liquid will simply soak into the particle bed. It was soon established that less hydrophilic particulate materials such as poly(methyl methacrylate) (PMMA) (Jarrett et al., 2014), coal, and sphalerite ((Zn,Fe)S) (Jarrett et al., 2016a) could be transferred to a drop by the electrostatic process, and that these remained at the air-water interface instead of being wetted and thus internalized, as the ballotini were in the initial experiment. This raised the prospect of electrostatically-formed "complex liquid marbles" (CLMs), consisting of a liquid-drop core with internalized hydrophilic particles, surrounded and stabilized by a shell of hydrophobic particles (**Figure 2A**). These were first produced with internalized silica particles and a shell of sphalerite particles (Jarrett et al., 2016b). The hypothesized core-shell structure was confirmed by capturing, resin-casting and sectioning individual marbles (Jarrett et al., 2016a). One can readily conceive of a variety of applications for a structure of this type, e.g., delivery and controlled release of pharmaceutical powders and water-efficient washing/collection of powder contaminants. The controlled manufacture of these sorts of structured aggregates has been a focussing goal of our subsequent research.

## THE ELECTROSTATIC TRANSFER PROCESS

During the electrostatic formation process, the capillary (and thus drop) were earthed via an electrometer, which recorded the flow of negative charge carried to the drop by the particles and thence to earth. Here, and in later experiments, it was not always clear whether the forces transferring particles from the bed to the drop were primarily due to their simply being imparted a net charge by the biased substrate via the bed, or primarily dielectrophoretic forces (where polarized particles are attracted to the region of stronger electric field where the field lines converge on the drop, as shown in **Figure 1**) (Jones, 2003). In the ballotini experiment already described, a substantial quantity of charge (over 200 $\mu C \cdot kg^{-1}$) was measured flowing from the drop to earth during particle transfer, confirming an initial net charge on the particles, despite the relatively low conductivity of soda-lime glass ($\sim 10^{-10}$ $S \cdot m^{-1}$) (Grayer, 1996). Our group is currently working on numerical models of the electric field geometry and forces on the particles, a task complicated by the deformation of the drop in the field, which may itself be complicated by the presence of particles at the air-water interface.

The influence of particle surface conductivity has been studied directly using polystyrene (PS) particles carrying a shell of polypyrrole (PPy), which can be doped to conduct electricity (**Figure 2B**). Since the core component (PS) remains the same for doped and de-doped particles, so do the density, dielectric constant, and other bulk properties. Comparison of doped and de-doped PS/PPy particles has shown that at larger values of the driving potential, the conductive particles are easier to extract from the bed than the non-conductive particles. It is not clear what mechanism is involved here—since conductivity determines the rate of charge transfer, it seems likely that it involves rearrangement of charge during ejection of the particle from the bed (Thomas et al., 2018). Surface conductivity is also thought to affect the rate at which particles discharge after being transferred to the drop, and via this, the rate at which particles jump to the drop once transfer has initiated.

In the meanwhile, however, some qualitative observations and hypotheses can be made about the mechanics of the system. It is apparent that the ability of particles to jump to the drop

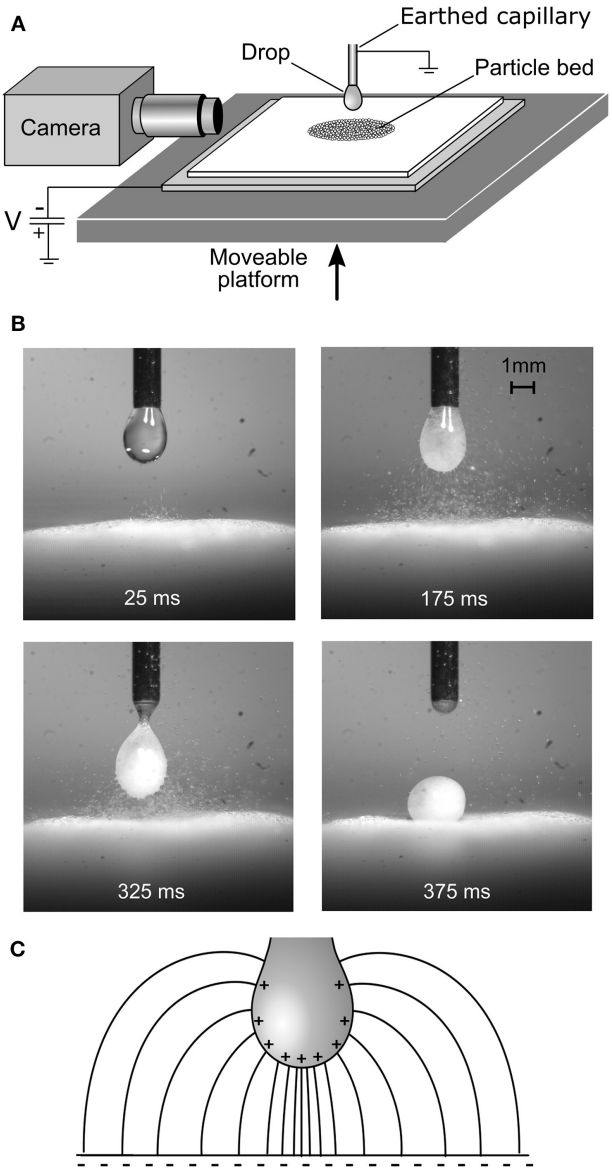


**FIGURE 1 | (A)** Schematic of the electrostatic aggregation method. **(B)** Formation of a metastable aggregate with hydrophilic ballotini. **(C)** Schematic of the converging shape of the electric field lines between the substrate and drop.

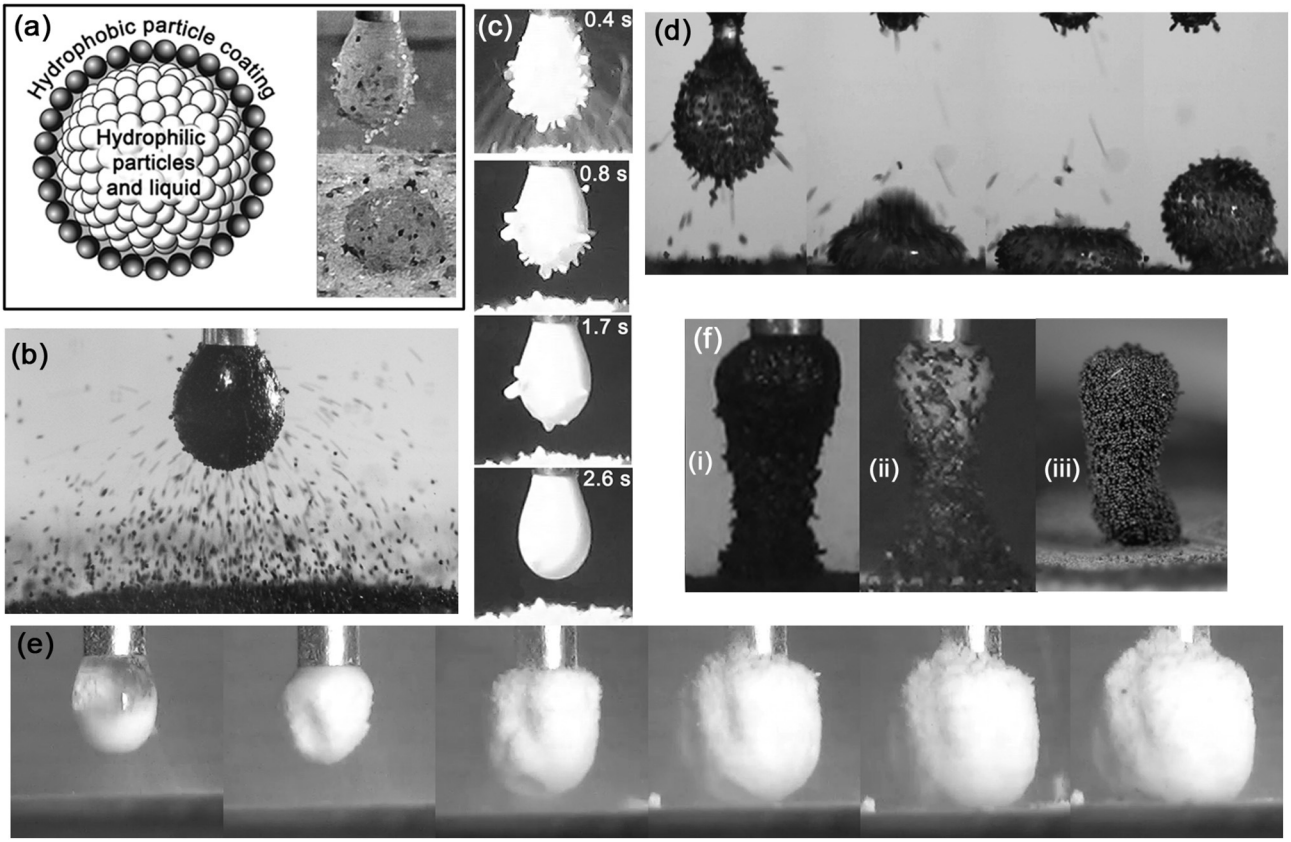


**FIGURE 2 | (A)** Schematic of a complex liquid marble, and CLM formed from silica and sphalerite particles (Jarrett et al., 2016b). **(B)** Aggregate being formed with 80 μm-sized PS/PPy (chloride ion doped) particles (Thomas et al., 2018). **(C)** Transfer to and internalization of PDEA-PS particles by a pH 5.6 droplet, with driving potential of 2.5 kV (Ireland et al., 2018). **(D)** Formation of a liquid marble with 90–125 μm diameter cinnamon particles. **(E)** Formation of large "fluffy" structure with edible $CaCO_3$ particles. **(F)** Tower structures formed with (i) Coal particles (ii) Coal and silica (iii) 80 μm-sized PS/PPy (chloride ion doped) particles.

from the particle bed is not merely a matter of the electrostatic lifting force overcoming their weight, and that interparticle cohesion and friction are also extremely important. Some of these cohesive effects, e.g., van der Waals attraction and mechanical entanglement/structural locking, are present in the absence of an external electric field. Others, such as dielectrophoretic cohesion (Moncada-Hernandez et al., 2014), come into play due to the electric field between the biased substrate and the drop. We have had little success transferring very fine powders (less than ∼5 μm), presumably due to cohesion. When these fine powders do jump to the drop, they tend to do so as grains composed of many particles, as observed for the PDEA-PS particles discussed later in this paper.

One curious attribute of the original ballotini experiments was the avalanche phenomenon (Liyanaarachchi et al., 2013). As the particle bed gradually approached the drop, one may have expected the particles to be gradually stripped from the top of the bed. Instead, apart from one or two individual precursors, the particles all leapt from the bed to the drop in an explosive cascade lasting less than half a second once some critical drop-bed separation was reached. The converging electric field geometry shown in **Figure 1** exerts a radially-inward force on the bed in the horizontal plane, in addition to the larger vertical force. The bed is essentially being squeezed horizontally inwards at the same time as it is being lifted vertically. This is in some ways analogous to the way a vertical load on an arch "locks" the structure together, except that the shape of an arch distributes a uniaxial vertical force horizontally, whereas in the present system the field itself has a horizontal component. In both cases, there is a limit to the vertical load the structure can bear without failing, and the avalanche occurs at this point. For a powder, in the simplest case, this point is given by the Mohr-Coulomb criterion (Labuz and Zang, 2012), according to which the shear and normal stress at yield have a positive linear relationship (i.e., for a greater compressive stress, a greater shear stress is required for yield). A quantitative mechanical model of the electrostatic stress in the bed, assuming a Mohr-Coulomb yield criterion, confirms this mechanism (Ireland et al., 2015).

## PARTICLE-DROP INTERACTIONS

It is worth noting that materials such as PMMA, sphalerite and coal are not "hydrophobic" in the sense of having a water contact angle greater than 90°. Thus, while they are not dispersible in the

liquid as silica is, and would be expected to stay at the interface, they should nonetheless reside more than half immersed in the liquid phase. One might therefore not expect to form genuine stable LMs with these particulate materials, since they do not properly encapsulate the liquid. This was observed with PMMA, which did not form stable marbles, but not with coal and sphalerite, which did. PMMA particles have reported contact angle values of ∼65°–85° (Briggs et al., 1990; Ma et al., 2007), compared to ∼75°–90° for sphalerite particles (Subrahmanyam et al., 1996) and ∼70°–90° for coal, depending on the carbon content (Keller, 1987). The difference appears to be that the PMMA particles were spherical, whereas the sphalerite and coal were more angular in shape, with sharp edges and points at which the air-water contact line could be pinned. These and other irregularly-shaped particles have demonstrated repeatedly that the ability to penetrate the air-water interface is dependent on much more than merely wettability. This applies particularly to this electrostatic formation process, which tends to be more "gentle" than direct mechanical drop-bed contact.

Experiments performed with PS particles provided further insight into these phenomena (Ireland et al., 2016). While these had a hydrophilic surface chemistry, their surface roughness and aggregation behavior tended to produce a metastable Cassie-Baxter wetting regime (Murakami and Bismarck, 2010), which allowed them to form stable liquid marbles. This can be seen almost as a microscale equivalent of the macroscopic morphological irregularity of the sphalerite and coal particles. Perhaps most interesting were the differences between these liquid marbles and those formed by direct mechanical contact such as rolling. It had previously been generally accepted that the maximum ratio of particle to drop diameter required to form stable liquid marbles by direct contact methods was ∼1:25 (Eshtiaghi and Hapgood, 2012). Using the electrostatic formation method, stable PS liquid marbles could be formed with particle to drop diameter ratios of up to ∼1:12. In addition, in some cases, a very thick, stable particle shell formed, quite unlike the thinner layer observed on rolled marbles. It is supposed that these unique properties of electrostatically-formed LMs are due to the relatively quiescent, shear-free character of the process, compared to direct-contact formation, which is more likely to detach large particles and disrupt thicker shell structures as they form.

## STIMULUS-RESPONSIVE PARTICLES

As already mentioned, the controlled manufacture of structured aggregates has been a focussing goal of our group's research effort. A potentially useful tool in controlling the process is the use of stimulus-responsive materials. A variety of studies have been carried out on the direct-contact formation of liquid marbles using materials whose wettability can be triggered by variation in pH, temperature, light, and other stimuli (Fujii et al., 2016b). Our group has begun to extend these studies to electrostatically-formed aggregates, using PS particles carrying a pH-responsive poly[2-(diethylamino)ethyl methacrylate] (PDEA) steric stabilizer on their surfaces (Ireland et al., 2018). PDEA displays hydrophilic behavior below pH ∼7 and hydrophobic behavior above pH ∼8 (Bütün et al., 2001; Kido et al., 2018). These protonated PDEA-PS particles, which were prepared by drying an acidic dispersion, tend to cohere into grains, in which form they jump from the bed to the drop, instead of being transferred as individual particles. These grains initially adhere to the air-water interface, since the interstices between the particles are full of air. They are then internalized by the drop as water infiltrates the interstices, as shown in **Figure 2C**. The aggregate formed in this way can thus be seen as a sort of "metastable liquid marble." Crucially, analysis of the kinetics of the particle transfer and internalization process indicated that it was much more rapid when the drop pH was below 7 than when it was above 8—thus achieving the desired result. Our group is currently extending this work on stimulus-responsive materials by studying electrostatic aggregation using particles coated with a temperature-sensitive polymer.

## EDIBLE PARTICLES, EXOTIC STRUCTURES

Even more remarkable phenomena occurred during attempts to form liquid marbles and other aggregates using edible particles. Food and pharmaceutical applications of simple and complex liquid marbles were prominent in our group's thinking since the beginning of this work, but many of them are complex and difficult to characterize physically and chemically. On the other hand, this complexity can result in rich behavior during electrostatic aggregation. For instance, experiments were performed with mildly hydrophobic cinnamon and hydrophilic edible calcium carbonate. The cinnamon consisted largely of elongated needle-like structures. These tended to align with the electric field and form end-to-end chains, often stretching unbroken from the drop to the cinnamon particle bed—an effect often observed in elongated dielectric particles, such as grass seeds (Jones, 2003). Since the electric field lines near the drop surface were normal to the air-water interface, the cinnamon particles tended to stick straight out once attached, like a pincushion. This had the further, unexpected result of producing extraordinarily stable liquid marbles for a very low interface coverage, as shown in **Figure 2D**. The outward-pointing needle-like particles maintained a substantial separation between the drop and the particle bed, even under extreme deformation, despite the air-water interface being clearly visible between the particles! Individual calcium carbonate particles were 20 μm spheres with rough surfaces, but these tended to break into more complex structures under moderate shear stress. **Figure 2E** shows the result of one experiment, in which an extraordinary "fluffy" structure, much larger than the original droplet, was formed. Literature values for the dielectric constant of calcium carbonate are 8.0–9.0 (CRC Handbook of Chemistry and Physics, 2005)—several times those for the other materials mentioned in this paper, which are all around 1.0–3.0. This relatively high dielectric constant may have contributed to the observed behavior by encouraging dielectrophoretic chaining (Jones, 2003). In any case, it is difficult to see how the observed

structures formed with cinnamon and calcium carbonate particles could have been produced by rolling of a drop on a particle bed.

We have already seen that irregularly-shaped particles can form stable liquid marbles even when their surface chemistry is hydrophilic. Another striking result of irregular shape is the formation of self-supporting tower-like structures during the particle transfer process (Jarrett et al., 2016b). **Figure 2F** shows several of these. In the case of coal and sphalerite, the particles are unable to penetrate the air-water interface and accumulate on the outside of the drop. This accumulation is most pronounced on the underside of the drop, where the electric field intensity is greatest and the particle transfer path the shortest, and a stalactite-like protrusion starts to form. The protrusion further concentrates the electric field and shortens the particle transfer path, meaning that subsequent particles preferentially jump to the end of the protrusion, which continues to lengthen until it meets the particle bed and forms a pillar of the sort shown in **Figure 2F(i)**. In many cases this structure continues to stand even when detached from the capillary. **Figure 2F(ii)** shows an even more complex structure which combines features of particle towers and complex liquid marbles as described above. It was produced by laying a particle bed consisting of a layer of hydrophilic silica on top of a layer of moderately hydrophobic coal. Initially, only silica jumped to the drop, filling it as in the initial ballotini experiments. Coal particles then jumped to the outside of the drop, accumulated on its underside, and formed a pillar as described above. The resulting tower structure resembled a coal wineglass holding a spherical aggregate of silica. These tower structures persisted even after being removed from the capillary and dried. This was not the case with all such particle towers. That shown in **Figure 2F(iii)** was composed of hydrophilic PS/PPy (chloride ion doped) particles. These were spherical, and thus without the interlocking structural stability of the coal and sphalerite. Unlike the coal and sphalerite structures, the PS/PPy towers collapsed upon being dried. It is hypothesized that the PS/PPy towers were held together by capillary forces due to the water from the droplet, which had infiltrated the whole structure.

## CONCLUSIONS

The experiments we have described are only a small sample of the wide range of particulate materials that can be aggregated in this way, and of physical behaviors and liquid-particle structures that one might create with them. For example, we have only just begun to explore the influence of the mechanical, electrical and chemical properties of the drop liquid on the process. A key lesson from this work has been that the results are *not* limited by the imagination—many of them have been spectacularly unexpected! With such rich possibilities on offer, a critical issue becomes control of the process. We are currently studying how the system geometry, bed composition and structure and stimulus-responsive materials can be used to produce a precise and readily replicable aggregate structure with a desired set of properties. These studies aim to refine a demonstrably powerful and flexible aggregate-manufacturing process into a practical and useful tool for a variety of industries.

## AUTHOR CONTRIBUTIONS

All authors contributed to writing the article. SF synthesized the particles unless otherwise noted. CT and BL performed experiments not published elsewhere.

## FUNDING

This work was supported by JSPS-OP (Australia) Bilateral Joint Research Projects (Grant No. 16039901-000541), and Electrostatic Formation of Liquid Marbles (Australian Research Council Discovery Project, DP170100578.). CT and BL each thank the Australian Government for a Research Training Program (RTP) Scholarship.

## ACKNOWLEDGMENTS

Mr. Eddie O'Reilly is thanked for his assistance with photography and contribution to **Figure 2**. Shiraishi Kogyo Kaisha Ltd. is thanked for the kind donation of $CaCO_3$ particles.

## REFERENCES

Arbatan, T., Al-Abboodi, A., Sarvi, F., Chan, P. P., and Shen, W. (2012a). Tumor inside a pearl drop. *Adv. Healthc. Mater.* 1, 467–469. doi: 10.1002/adhm.201200050

Arbatan, T., Li, L., Tian, J., and Shen, W. (2012b). Liquid marbles as micro-bioreactors for rapid blood typing. *Adv. Healthc. Mater.* 1, 80–83. doi: 10.1002/adhm.201100016

Aussillous, P., and Quéré, D. (2001). Liquid marbles. *Nature* 411, 924–927. doi: 10.1038/35082026

Briggs, D., Chan, H., Hearn, M. J., McBriar, D. I., and Munro, H. S. (1990). The contact-angle of poly(Methyl Methacrylate) cast against glass. *Langmuir* 6, 420–424. doi: 10.1021/la00092a023

Bütün, V., Armes, S. P., and Billingham, N. C. (2001). Synthesis and aqueous solution properties of near-monodisperse tertiary amine methacrylate homopolymers and diblock copolymers. *Polymer* 42, 5993–6008. doi: 10.1016/S0032-3861(01)00066-0

CRC Handbook of Chemistry and Physics (2005). *Internet Version 2005,* ed D. R. Lide (Boca Raton, FL: CRC Press).

Eshtiaghi, N., and Hapgood, K. P. (2012). A quantitative framework for the formation of liquid marbles and hollow granules from hydrophobic powders. *Powder Technol.* 223, 65–76. doi: 10.1016/j.powtec.2011.05.007

Eshtiaghi, N., Liu, J. J. S., and Hapgood, K. P. (2010). Formation of hollow granules from liquid marbles: small scale experiments. *Powder Technol.* 197, 184–195. doi: 10.1016/j.powtec.2009.09.013

Fujii, S., Sawada, S., Nakayama, S., Kappl, M., Ueno, K., Shitajima, K., et al. (2016a). Pressure-sensitive adhesive powder. *Mater. Horiz.* 3, 47–52. doi: 10.1039/C5MH00203F

Fujii, S., Yusa, S., and Nakamura, Y. (2016b). Stimuli-responsive liquid marbles: controlling structure, shape, stability and motion. *Adv. Funct. Mater.* 26, 7206–7223. doi: 10.1002/adfm.201603223

Grayer, G. H. (1996). "Resistivity Measurements on RPC Materials," in *Proceedings of the Third International Workshop on Resistive Plate Chambers and related detectors, Scientifica Acta Quaderni del dottorato XI* (Pavia), 285–295.

Ireland, P. M., Kido, K., Webber, G. B., Fujii, S., and Wanless, E. J. (2018). pH-responsive particle-liquid aggregates - electrostatic formation kinetics. *Front. Chem.* 6:215. doi: 10.3389/fchem.2018.00215

Ireland, P. M., Noda, M., Jarrett, E., Fujii, S., Nakamura, Y., Wanless, E. J., et al. (2016). Electrostatic formation of liquid marbles - influence of drop and particle size. *Powder Technol.* 303, 55–58. doi: 10.1016/j.powtec.2016.08.036

Ireland, P. M., Webber, G. B., Jarrett, E. D., and Galvin, K. P. (2015). Interaction of a particle bed with a droplet under an applied electric field. *J. Phys. Conf. Ser.* 646:012027. doi: 10.1088/1742-6596/646/1/012027

Janardan, N., Panchagnula, M. V., and Bormashenko, E. (2015). Liquid marbles: physics and applications. *Sadhana Acad. Proc. Eng. Sci.* 40, 653–671. doi: 10.1007/s12046-015-0365-7

Jarrett, E. D., Galvin, K. P., Ireland, P. M., and Webber, G. B. (2014). Collection of fine particles by a water droplet under an applied electric field. *Proc. of CHEMECA 2014, Sept 28- Oct 1 2014,* (Perth, WA).

Jarrett, E., Ireland, P. M., Webber, G. B., and Wanless, E. J. (2016a). "Electrostatic aggregation of mineral particles around a water droplet," in *Proceedings of CHEMECA 2016, Sept 25- 28 2016,* (Adelaide, SA).

Jarrett, E., Ireland, P. M., Webber, G. B., and Wanless, E. J. (2016b). Particle-liquid structures formed by electric fields. *Powder Technol.* 297, 1–7. doi: 10.1016/j.powtec.2016.04.021

Jones, T. B. (2003). Basic theory of dielectrophoresis and electrorotation. *IEEE Eng. Med. Biol. Mag.* 22, 33–42. doi: 10.1109/MEMB.2003.1304999

Kawashima, H., Paven, M., Mayama, H., Butt, H. J., Nakamura, Y., and Fujii, S. (2017). Transfer of materials from water to solid surfaces using liquid marbles. *ACS Appl. Mater. Interfaces* 9, 33351–33359. doi: 10.1021/acsami.7b11375

Keller, D. V. (1987). The contact-angle of water on coal. *Colloids Surf.* 22, 21–35. doi: 10.1016/0166-6622(87)80003-3

Kido, K., Ireland, P. M., Sekido, T., Wanless, E. J., Webber, G. B., Nakamura, Y., et al. (2018). Formation of liquid marbles using pH-responsive particles: rolling vs electrostatic methods. *Langmuir* 34, 4970–4979. doi: 10.1021/acs.langmuir.7b04204

Labuz, J. F., and Zang, A. (2012). Mohr-coulomb failure criterion. *Rock Mech. Rock Eng.* 45, 975–979. doi: 10.1007/s00603-012-0281-7

Liyanaarachchi, K. R., Ireland, P. M., Webber, G. B., and Galvin, K. P. (2013). Electrostatic formation of liquid marbles and agglomerates. *Appl. Phys. Lett.* 103:054105. doi: 10.1063/1.4817586

Ma, Y., Cao, X. Y., Feng, X. J., Ma, Y. M., and Zou, H. (2007). Fabrication of super-hydrophobic film from PMMA with intrinsic water contact angle below 90 degrees. *Polymer* 48, 7455–7460. doi: 10.1016/j.polymer.2007.10.038

McHale, G., and Newton, M. I. (2011). Liquid marbles: principles and applications. *Soft Matter* 7, 5473–5481. doi: 10.1039/c1sm05066d

McHale, G., and Newton, M. I. (2015). Liquid marbles: topical context within soft matter and recent progress. *Soft Matter* 11, 2530–2546. doi: 10.1039/C5SM00084J

Moncada-Hernandez, H., Nagler, E., and Minerick, A. R. (2014). Theoretical and experimental examination of particle-particle interaction effects on induced dipole moments and dielectrophoretic responses of multiple particle chains. *Electrophoresis* 35, 1803–1813. doi: 10.1002/elps.201300636

Murakami, R., and Bismarck, A. (2010). Particle-stabilized materials: dry oils and (Polymerized) non-aqueous foams. *Adv. Funct. Mater.* 20, 732–737. doi: 10.1002/adfm.200902007

Paven, M., Mayama, H., Sekido, T., Butt, H.-J., Nakamura, Y., and Fujii, S. (2016). Light-driven delivery and release of materials using liquid marbles. *Adv. Funct. Mater.* 26, 3199–3206. doi: 10.1002/adfm.201600034

Subrahmanyam, T. V., Prestidge, C. A., and Ralston, J. (1996). Contact angle and surface analysis studies of sphalerite particles. *Miner. Eng.* 9, 727–741.

Thomas, C. A., Kido, K., Kawashima, H., Fujii, S., Ireland, P. M., Webber, G. B., et al. (2018). Electrostatic formation of polymer particle stabilised liquid marbles and metastable droplets - effect of latex shell conductivity. *J. Colloid Interface Sci.* 529, 486–504. doi: 10.1016/j.jcis.2018.04.044

Tian, J., Arbatan, T., Li, X., and Shen, W. (2010). Liquid marble for gas sensing. *Chem. Commun.* 46, 4734–4736. doi: 10.1039/c001317j

Ueno, K., Hamasaki, S., Wanless, E. J., Nakamura, Y., and Fujii, S. (2014). Microcapsules fabricated from liquid marbles stabilized with latex particles. *Langmuir* 30, 3051–3059. doi: 10.1021/la5003435

**Conflict of Interest Statement:** The authors declare that the research was conducted in the absence of any commercial or financial relationships that could be construed as a potential conflict of interest.

frontiers in Chemistry

ORIGINAL RESEARCH
published: 14 June 2018
doi: 10.3389/fchem.2018.00215

# pH-Responsive Particle-Liquid Aggregates—Electrostatic Formation Kinetics

*Peter M. Ireland*[1]*, *Kohei Kido*[2], *Grant B. Webber*[1], *Syuji Fujii*[3,4] and *Erica J. Wanless*[1]

[1] Priority Research Centre for Advanced Particle Processing and Transport, University of Newcastle, Callaghan, NSW, Australia, [2] Division of Applied Chemistry, Graduate School of Engineering, Osaka Institute of Technology, Osaka, Japan, [3] Department of Applied Chemistry, Faculty of Engineering, Osaka Institute of Technology, Osaka, Japan, [4] Nanomaterials Microdevices Research Center, Osaka Institute of Technology, Osaka, Japan

Liquid-particle aggregates were formed electrostatically using pH-responsive poly[2-(diethylamino)ethyl methacrylate] (PDEA)-coated polystyrene particles. This novel non-contact electrostatic method has been used to assess the particle stimulus-responsive wettability in detail. Video footage and fractal analysis were used in conjunction with a two-stage model to characterize the kinetics of transfer of particles to a water droplet surface, and internalization of particles by the droplet. While no stable liquid marbles were formed, metastable marbles were manufactured, whose duration of stability depended strongly on drop pH. Both transfer and internalization were markedly faster for droplets at low pH, where the particles were expected to be hydrophilic, than at high pH where they were expected to be hydrophobic. Increasing the driving electrical potential produced greater transfer and internalization times. Possible reasons for this are discussed.

**Keywords: liquid marble, pH-responsive particle, electrostatics, air-water interface, adsorption**

OPEN ACCESS

***Edited by:***
*Florent Allais, AgroParisTech Institut des Sciences et Industries du Vivant et de L'environnement, France*

***Reviewed by:***
*Maria Graca Rasteiro, University of Coimbra, Portugal*
*Gil Garnier, Bioresource Processing Institute of Australia (BioPRIA), Australia*

***Correspondence:**
*Peter M. Ireland*
*peter.ireland@newcastle.edu.au*

***Specialty section:***
*This article was submitted to Chemical Engineering, a section of the journal Frontiers in Chemistry*

***Received:*** *12 February 2018*
***Accepted:*** *25 May 2018*
***Published:*** *14 June 2018*

***Citation:***
*Ireland PM, Kido K, Webber GB, Fujii S and Wanless EJ (2018) pH-Responsive Particle-Liquid Aggregates—Electrostatic Formation Kinetics. Front. Chem. 6:215. doi: 10.3389/fchem.2018.00215*

## INTRODUCTION

Our group first demonstrated the formation of liquid-particle agglomerates via an electrostatically-driven process in 2013 (Liyanaarachchi et al., 2013). A liquid droplet was produced at the end of an electrically grounded stainless steel capillary above a bed of particles, resting on a substrate to which a negative potential of several kilovolts was applied, causing the particles to jump from the bed to the pendent water droplet. These initial experiments produced metastable agglomerates consisting of a water drop filled with (hydrophilic) glass beads. The new electrostatic process was soon extended to hydrophobic particles (Ireland et al., 2016), which remained embedded at the air-liquid interface instead of entering the droplet. These were genuine "liquid marbles"—liquid drops encased in a shell of non-wetting particles—of the type first observed well over a decade ago (Aussillous and Quéré, 2001), whose remarkable physical properties (Aussillous and Quéré, 2006; McHale and Newton, 2015) rapidly recommended them for a variety of potential applications (Bormashenko, 2017; Oliveira et al., 2017), including gas sensors (Tian et al., 2010), bioreactors (Arbatan et al., 2012a,b), and encapsulation media (Eshtiaghi et al., 2010; Ueno et al., 2014), pressure-sensitive adhesives (Fujii et al., 2016a) and materials delivery carriers (Paven et al., 2016; Kawashima et al., 2017).

The conventional method of forming liquid marbles consists of rolling a droplet on a powder bed. This direct contact method cannot be used to form metastable hydrophilic particle-liquid aggregates, since the liquid would simply soak into a bed incorporating hydrophilic particles.

When applied to hydrophobic particles, the new electrostatic method, which did not involve direct contact, was able to circumvent some of the physical limitations of direct-contact formation—for example, larger ratios of particle to drop size were achieved than has previously been considered possible (Eshtiaghi and Hapgood, 2012; Ireland et al., 2016). The electrostatic method has in addition been used to manufacture a new class of liquid marble complexes that include both hydrophobic and hydrophilic particles, resulting in core-shell structures, for a variety of applications, e.g., delivery and controlled release of pharmaceutical powders and water-efficient washing/collection of powder contaminants (Jarrett et al., 2016). Manufacture of even more complex layered structures may also be feasible.

In this context, stimulus responsive materials, whose wettability can be "switched" by various external stimuli (pH, light, temperature, etc.) take on a special significance (Fujii et al., 2016b), as they have the potential to provide even more control over the formation of structured liquid marble complexes. One could envisage a pH-responsive powder being used to safely transfer a liquid through a given environment at high pH, to be released when it reaches a low-pH environment. The utility of these types of mechanisms in drug delivery, for example, is clear. A number of studies have investigated the formation and stability of liquid marbles incorporating stimulus-responsive materials (Fujii et al., 2011; Nakai et al., 2013; Yusa et al., 2014; Paven et al., 2016). In these cases, the marbles were formed by the conventional direct-contact method. Our group has recently attempted to transport stimulus-responsive particles to pendent water droplets by means of the electrostatic method described above in order to assess liquid marble or dispersion formation. The first stimulus-responsive material explored was polystyrene (PS) particles carrying pH-responsive poly[2-(diethylamino)ethyl methacrylate] (PDEA) colloidal stabilizer on their surfaces. PDEA is a weak polybase with a p$K_a$ of 7.3 that is soluble in aqueous media below pH ∼7 because of protonation of its tertiary amine groups (Bütün et al., 2001). At pH 8 or above, PDEA exhibits either very low or zero charge density, and hydrophobic character. It was confirmed that the powders obtained from pH 3.0 and pH 10.0 aqueous dispersions had hydrophilic and hydrophobic characters, respectively. The PDEA-PS powders prepared from pH 3.0 dispersions jumped to a pendent distilled water droplet to form an aqueous dispersion droplet. Conversely, the powders prepared from pH 10.0 did not transfer resulting in no liquid marble formation which was attributed to the cohesive PDEA colloidal stabilizer which resulted in larger grains. This technique may therefore immediately provide a means of preparatively sorting PDEA-PS powders obtained from aqueous dispersions at different pH. A more detailed account of these behaviors, and a comparison between direct-contact (rolling) and electrostatic formation of PDEA-PS marbles, is provided in a recent article by our group (Kido et al., 2018).

One key advantage of the electrostatic aggregate formation technique is the ability to control the final product by changing the kinetics of the formation process via adjustments to the driving potential, drop-bed separation, and bed shape and structure. A pH-responsive particle provides an additional tool for controlling the electrostatic formation kinetics, as it allows the rate at which the particles penetrate the air-water interface to be altered. This paper thus investigates the kinetics of particle transfer and internalization by the droplet of PDEA-coated polystyrene (PDEA-PS) particles during electrostatic formation. Here we focus on PDEA-PS particles that were dried from a solution at pH 3, as these were consistently transported to the pendent droplet.

# METHODOLOGY

## Particle Synthesis and Experimental Method

The PDEA-PS particles were synthesized by dispersion polymerization using PDEA homopolymer as a colloidal stabilizer in the same way reported previously (Sekido et al., 2017). The PDEA-PS particles were nearly monodisperse and had a number-average diameter of 2.20 μm and a coefficient of variation of 2%. PDEA loading was determined to be 2.66 wt% by elemental microanalysis and XPS studies on the PDEA-PS particles determined the surface coverage by PDEA to be approximately 47%. These results indicate that the PDEA is mainly located at the surface of the PS particles. Aqueous dispersion of PDEA-PS particles with a pH value of 3.0 (40 g, 10 wt%, adjusted using HCl aqueous solution) was dried at 21°C, 0.1 MPa and 42.8–87.4 RH% in air. The obtained dried cake-like white agglomerate was ground into powder using a pestle and mortar.

A schematic of the experimental apparatus is shown in **Figure 1**. A bed of dried PDEA-PS particle powder, depth ∼1 mm, was supported by a 1 mm thick glass slide, which in turn rested on a stainless steel plate connected to a high voltage power supply. The metal plate was held at a constant negative potential relative to earth of 1.5, 2.0, or 2.5 kV, and was gradually raised at a rate of 50 μm·s$^{-1}$ toward a pendent drop on the end of an earthed metal capillary syringe of 1.2 mm outer diameter. The drop liquid was either MilliQ water (pH 5.6), or an aqueous buffer at pH 3.0 (0.1 M potassium hydrogen phthalate/HCl) or 10 ($NaHCO_3$/NaOH) (De Lloyd, 2000). The nominal drop volume was 5 μL, as dispensed by a syringe pump (Harvard Apparatus 11Plus), before the application of the electric field and loading with particles. When the separation between the particle bed and drop became sufficiently small (between ∼0.7 mm for 1.5 kV and ∼2.0 mm for 2.5 kV), the powder was transferred across the gap to the drop, before becoming internalized within the drop. A video camera was used to record the entire process from the start of particle transfer to the completion of particle internalization.

## Preliminary Observations and Hypotheses

Preliminary electrostatic aggregation experiments with PDEA-PS particles revealed several interesting behaviors. The powder tended to jump to the drop not as individual particles, but as grains of substantial size containing many individual particles (**Figure 2**). For more information on the granular properties of this material, please refer to Kido et al. (2018). These initially attached to the air-water interface, before gradually being internalized by the droplet. Thus, the initially-smooth drop

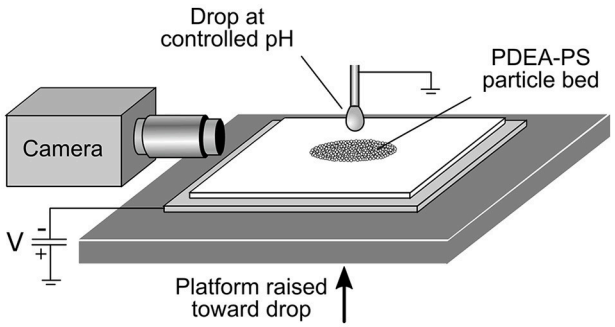


**FIGURE 1 |** Schematic of the apparatus used for electrostatic formation of liquid marbles.

surface (a) took on a "jagged" appearance as it was encrusted with PDEA-PS grains (b), then gradually became smooth again once particle/grain transfer ceased (c–e). This cessation normally corresponded to depletion of that part of the particle bed that was subject to transfer to the drop, i.e., the section of the bed where the electrostatic force was sufficient to counterbalance gravity and cohesive or static friction forces (Ireland et al., 2015). Since the particles were all eventually internalized by the drop, no stable liquid marbles were formed. It can be argued, however, that metastable liquid marbles were manufactured. These might be viewed as exhibiting "delayed instability"—starting as fully-stable liquid marbles, but losing that stability at a rate that can in principle be controlled by pH. This property may be useful in applications where the rate of release of a liquid into the surrounding environment needs to depend on the pH.

Given these observations, the process is conceptualized in terms of two main kinetic parameters—the time-scales for transfer of grains from the bed to the surface of the drop, and for internalization of grains attached to the air-water interface. The precise mechanism of internalization is not known, and may have included wicking of water into the interstices of the multiparticle PDEA-PS grains, as well as engulfment of the entire grain. The rate of both processes was expected to depend on the wettability of the particle surface. Since the PDEA surface of the particles was hydrophilic at pH values below the p$K_a$ of 7.3 and hydrophobic at higher pH values, it was hypothesized that the internalization process would be more rapid at low pH values of the drop liquid than at high values. A long internalization time would presumably promote an accumulation of grains at the drop surface, and it was hypothesized that this would suppress transfer and attachment of additional grains to the drop surface. Lower drop pH values were therefore expected to result in more rapid transfer as well as more rapid internalization.

Given the evolution of the droplet silhouette shown in **Figure 2**, the characteristic internalization and transfer times were estimated from video footage of the process using a two-stage transfer-internalization model and a fractal-based analysis technique. These characteristic times were compared for different values of the driving potential and drop pH, to test the above hypotheses.

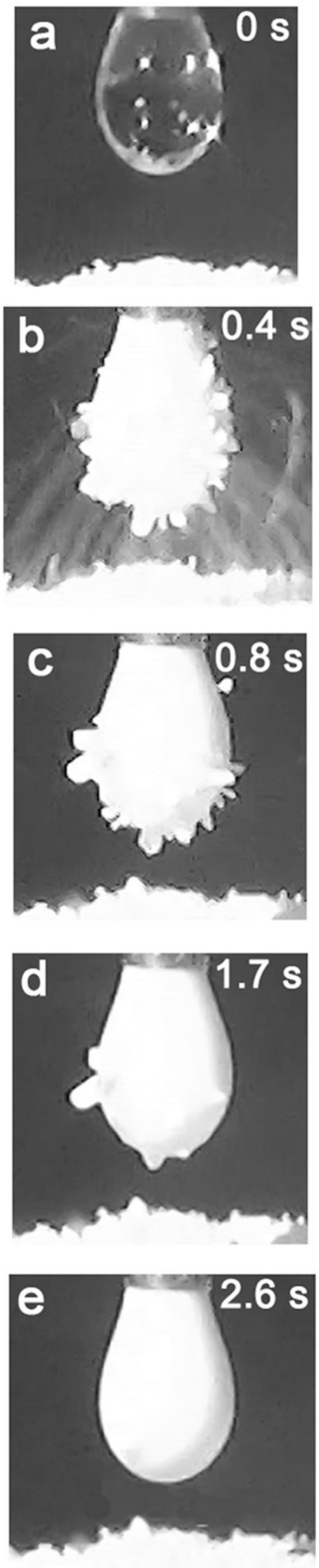


**FIGURE 2 |** Electrostatic transfer, followed by internalization, of PDEA-PS powder (dried from a solution at pH 3) into a water droplet, for a pH 5.6 droplet and a driving potential of 2.5 kV.

## Data Analysis

The fractal dimension of each aggregate's silhouette outline, as it evolved over time, was used to characterize the transfer and internalization kinetics. It was selected as an appropriate measure because of its robustness and scale-independence (Rasband, 1990). The fractal dimension gives a measure of the degree of "convolutedness" of the aggregate outline (Falconer, 1990). A drop outline without particles, or with entirely internalized particles, was smooth, with fractal dimension close to 1. The PDEA-PS powder tended to transfer to the drop surface in the form of multiparticle grains rather than individual particles, and there was thus a substantial increase in the fractal dimension of the drop outline when non-wetted grains were present at its surface. The scale-independence of the fractal dimension was considered to more than compensate for the fact that there was no obvious exact correlation between the fractal dimension and the number of particles at the bubble surface. Since we were chiefly interested in the rate constants for the process, not the actual numbers of particles, this was a secondary consideration. The fractal dimension was calculated using a standard box-counting algorithm, details of which are provided in the Supporting Information.

## Model

To assist in interpretation of kinetic data, a simple model of the transfer to and internalization of particles by the drop was developed. The drop surface is conceptualized as possessing a number of sites, $N_d$, to which particles (or in this case, grains) can attach. These sites can either be directly on the air-liquid interface, or may represent adhesion of incoming particles/grains to other particles/grains. The section of the particle bed beneath the drop possesses $N_b$ such sites. We let $n_d$ and $n_b$ be respectively the number of occupied sites on the drop surface and bed. It is assumed that the rate of change of the number of particles or grains in the bed is equal and opposite to the rate at which they jump to the drop, and that this is proportional to $n_b$. It is further assumed that only those particles/grains that jump to an unoccupied site on the drop surface are able to attach. The probability of this is proportional to the fraction of sites on the drop surface that are unoccupied, i.e., $1 - n_d/N_d$ . Thus

$$\frac{dn_b}{dt} = -\left(Transfer\ rate\right) = -\frac{1}{\tau_t} n_b \left(1 - \frac{n_d}{N_d}\right) \tag{1}$$

where $\tau_t$ is a time constant for particle transfer. In addition to this transfer process, which fills sites on the drop surface, particles/grains enter the interior of the drop, resulting in formerly occupied sites at the drop surface becoming unoccupied. The internalization rate is assumed to be proportional to the number of occupied states at the drop. Thus, the rate of change of the number of occupied sites on the drop surface is given by

$$\begin{aligned} \frac{dn_d}{dt} &= \left(Transfer\ rate\right) - \left(Internalisation\ rate\right) \\ &= \frac{1}{\tau_t} n_b \left(1 - \frac{n_d}{N_d}\right) - \frac{1}{\tau_i} n_d \end{aligned} \tag{2}$$

where $\tau_i$ is the time constant for the internalization process. Since we are not able to measure absolute values of $n_b$, $n_d$, $N_b$, or $N_d$, but only relative values, we can reduce the number of model variables by introducing the following ratios:

$$\nu = \frac{n_b}{N_b} \tag{3}$$

$$\mu = \frac{n_d}{N_d} \tag{4}$$

$$\eta = \frac{N_b}{N_d} \tag{5}$$

in terms of which Equations (1) and (2) take the simpler forms

$$\frac{d\nu}{dt} = -\frac{1}{\tau_t} \nu \left(1 - \mu\right) \tag{6}$$

$$\frac{d\mu}{dt} = \frac{1}{\tau_t} \eta \nu \left(1 - \mu\right) - \frac{1}{\tau_i} \mu \tag{7}$$

with only three instead of four parameters. All of the sites on the bed are initially occupied, and those on the drop surface are initially unoccupied, so

$$\nu\left(t = 0\right) = 1;\ \mu\left(t = 0\right) = 0 \tag{8}$$

When $\nu$ is reduced to zero, the region of the bed from which particles are able to jump is depleted (we see this physically as a region of bare substrate underneath the drop or aggregate).

# RESULTS AND DISCUSSION

**Figure 3** shows a plot of fractal dimension of the aggregate outline as a function of time for the transfer-internalization process of PDEA-PS particles to a droplet of pH 5.6 water under a 2.5 kV applied voltage. The increase in the fractal dimension during particle transfer and subsequent decrease with internalization is clearly apparent. Note that the fractal dimension is between 1.1 and 1.3, as we would expect for an outline that is somewhat convoluted in two dimensions, but is not near being space-filling.

## Extraction of Parameters

The fractal dimension vs. time data (**Figure 3**) were now fitted to Equations (6) and (7). Since, as already mentioned, there was no clear correlation between $\mu$ and the fractal dimension $d$, a linear correlation of the form

$$d\left(\mu\right) = A\mu + B \tag{9}$$

was used, where $A$ and $B$ are auxiliary constants corresponding to the proportionality of $\mu$ and $d$ and the fractal dimension of

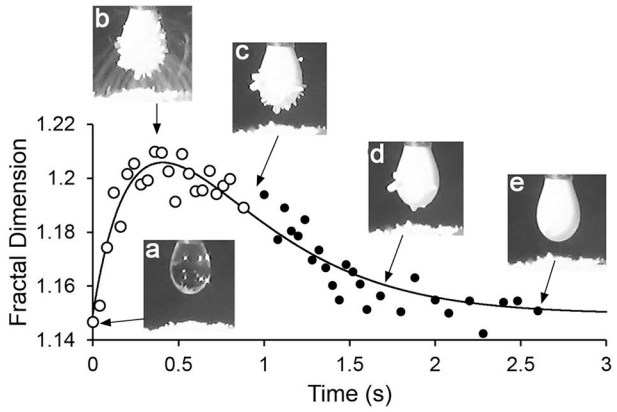


**FIGURE 3 |** Plot of fractal dimension of the aggregate outline during particle transfer and internalization, with drop pH 5.6 and driving potential 2.5 kV.

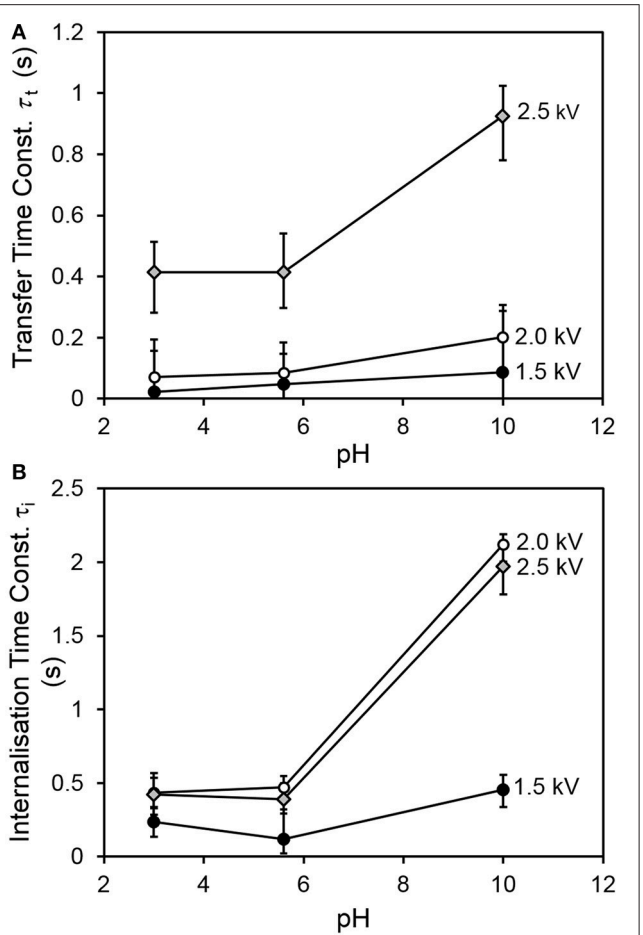


**FIGURE 4 | (A)** Characteristic transfer time and **(B)** characteristic internalization time vs. pH for all values of driving potential.

the smooth drop outline, respectively. It was discovered that a fit in which $\tau_t$, $\tau_i$, $\eta$ and the two auxiliary constants were adjusted simultaneously could produce one or more spurious solutions. This was prevented by first determining $\tau_i$, $A$ and $B$. The time at which grains ceased jumping from the bed to the drop was estimated by inspecting the video footage. With no particle transfer, both sides of Equation (6) and the first term on the right-hand side of Equation (7) become zero, and the solution of (7) is simply an exponential decay with time constant $\tau_i$. A curve of this form was fitted to the data after cessation of transfer (the section of the data in **Figure 3** after c, ∼0.9 s) using total least squares regression, with $\tau_i$, $A$ and $B$ as adjustable parameters, weighted equally for variation along the time and fractal dimension axes. Once $\tau_i$ was determined, $\tau_t$ and $\eta$ were found using a total least-squares fit of a numerical solution of Equations (6) and (7) to all the data. Uncertainties in the parameters were determined at a confidence level of 95% using 400 Monte Carlo simulations per fit, as in the method of Hu et al. (Hu et al., 2015). The uncertainty in both time constants was of the order of 0.1 s, and that of the parameter η was also ∼0.1. The parameter $A$ ranged from 0.03–0.037 for 1.5 kV experiments, 0.03–0.046 for 2.0 kV experiments, and 0.06–0.1 for 2.5 kV experiments, reflecting the different coverage patterns observed at different driving potentials. $B$, the 'baseline' fractal dimension for a bare drop, varied slightly from ∼1.135 at 1.5 kV to 1.15 at 2.5 kV, probably due to greater electrostatic elongation of the drop at higher driving potentials.

## Kinetics

**Figure 4** shows the transfer and internalization time constants respectively as a function of the driving potential and the drop pH. It is clear from **Figure 4A** that the transfer process is slower for a drop pH of 10, compared to drops at lower pH values. **Figure 4B** indicates that the internalization time follows a similar trend with drop pH. The latter trend is consistent with our expectations—since the p$K_a$ of PDEA is 7.3, we would expect the particles to be wettable at pH 3 and 5.6, and non-wettable at pH 10. The increase in transfer time with drop pH was also expected, as slower internalization means that transferred particles vacate drop surface states more slowly, and it was hypothesized that the rate of transfer would have an inverse relationship to the extent of occupation of the drop surface (recall Equations 6 and 7). Two different mechanisms are proposed for this hypothesized relationship. The first involves physical obstruction: a grain jumps from the bed but encounters a part of the drop surface already occupied by a non-wetted grain, and simply bounces off rather than attaching to the air-water interface. The second proposed mechanism involves an accumulation of net negative charge at the drop surface due to the presence of non-wetted charged grains, which have made only partial contact with the water and thus have not been fully neutralized. This accumulation of net negative charge at the drop surface would be expected in turn to decrease the electric field between the drop and the bed.

The increase of internalization time with driving potential initially seems counter-intuitive. It is hypothesized that at larger driving potentials, multiple layers of grains are able to adhere to the drop. Only a fraction of the adherent grains (the innermost) is in direct contact with the liquid at any given time. In our

simple model, the internalization rate is proportional to the number of occupied sites at the drop surface. No distinction is made between the time taken for grains in contact with the liquid to be internalized, and the time spent by adherent grains in the outer parts of the multilayer, waiting for inner grains to be internalized by the drop before making contact with the liquid themselves. The modeled internalization time is actually the sum of these two distinct processes, and will thus tend to be longer for multilayer coverage (as at higher driving potentials).

**Figure 5** shows the relationship between the transfer and internalization time constants, for all driving potentials and pH values. The 2.5 kV experiments exhibit a larger transfer time constant for the same internalization time constant than those at lower driving potentials. The reasons for this are not yet clear. A clue may be provided by **Figure 6**, which shows the parameter $\eta$ (recall Equation 5), representing the ratio of the total number of available sites for grains in the bed to that on the drop surface, as a function of pH. This suggests that in the 2.5 kV case, the number of available sites on the drop surface was relatively large for the number of grains able to jump to them, compared to the lower-potential cases, between which there is no significant difference. It seems reasonable that an increasing driving potential would increase the total number of available sites in both the bed and at the drop, but it is not clear why it would preferentially increase the number at the drop compared to those in the bed. This may be related to the shape of the electric field. For a larger driving potential, the electrostatic force is able to overcome cohesive forces in the bed and the particle/grain weight at a greater drop-bed separation. Thus, the geometry of the system is different during transfer at different driving potentials. On the other hand, pH appears to have only a weak effect, if any, on $\eta$. This is consistent with our model, which assumes that pH influences the rate at which occupied sites become vacant by internalization, not the actual number of those sites.

**Figure 7** shows a schematic of the electric field lines, and photographs of the corresponding stage of particle transfer, for a droplet at pH 5.6 and all three driving potentials (note that due to inertia and gravity, the particle trajectories differ somewhat from the field lines). For aggregate formation at lower driving potential values, the field lines and particle trajectories are concentrated under the lower part of the droplet, and originate from a much smaller area of the bed, with relatively direct particle trajectories. At higher driving potential values, the grains come from a much larger area of the bed and are transferred to the entire surface of the droplet, often via long, curving trajectories. It is hypothesized that this change in the morphology of the grain trajectories results in a larger relative increase in the number of available sites on the drop surface than it does the number of grains in the bed able to jump. Assessment of this hypothesis will require numerical modeling of the field shape and particle trajectories. We plan to explore the relationship between field morphology and the transfer kinetics in more detail in subsequent studies, using the COMSOL Multiphysics finite-element modeling environment (COMSOL Inc., Burlington, MA).

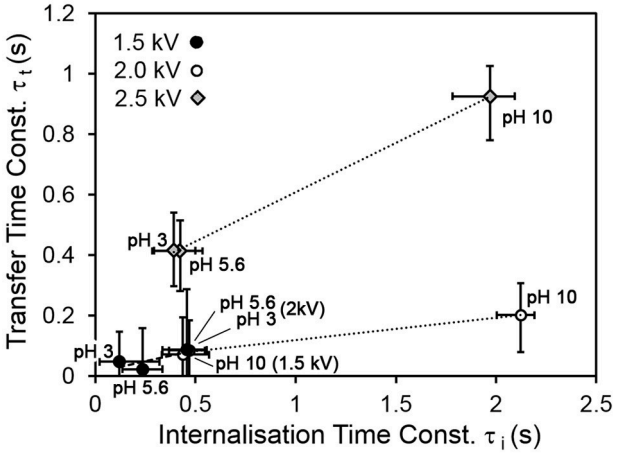


**FIGURE 5 |** Transfer time vs. internalization time for all pH and driving potential values.

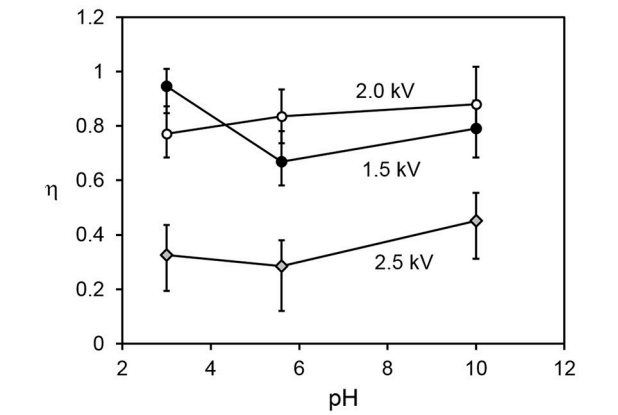


**FIGURE 6 |** Ratio of total number of available sites in the particle bed to those at the drop surface vs. pH, for all driving potential values.

## CONCLUSIONS

Our group's novel electrostatic method for manufacturing liquid marbles and other types of liquid-particle agglomerates was applied to a stimulus-responsive material, polystyrene particles coated in pH-responsive poly[2-(diethylamino)ethyl methacrylate] (PDEA), whose surface was hydrophilic at low pH and hydrophobic at high pH. The formation of aggregates with these PDEA-PS particles was modeled as two coupled processes, namely transfer of particles from the bed to the droplet surface, and internalization of the particles into the droplet. Since all particles in these experiments were eventually internalized, stable liquid marbles were not formed—instead, metastable liquid marbles were created. The kinetics of the transfer/internalization process were characterized using fractal analysis of video footage to track the "roughening" and "smoothing" of the droplet silhouette as grains were transferred to it and then internalized. Consistent with expectations, the characteristic time

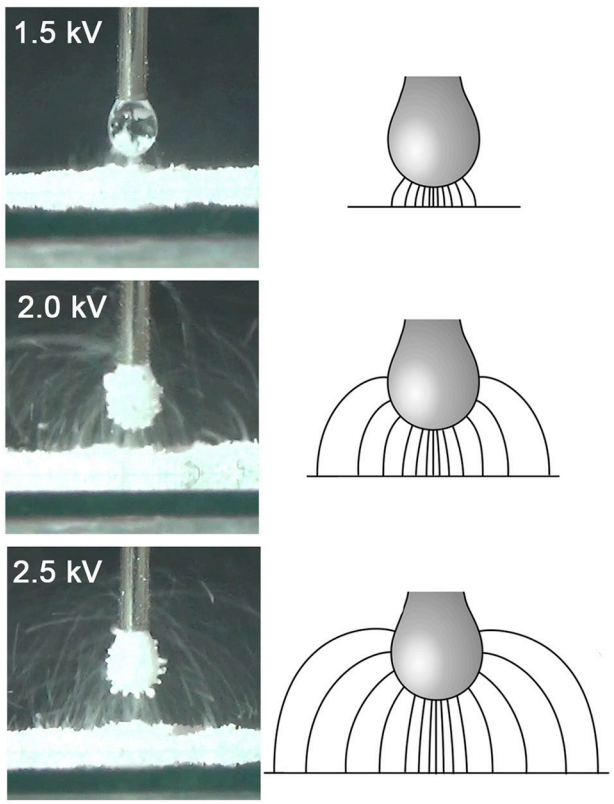


**FIGURE 7 |** Schematic of electric field lines and photographs of particle trajectories for equivalent stages in the particle transfer process (at approximately the time of the peak fractal dimension) at different values of the driving potential (and hence drop-bed separation). The photographs are all for a drop at pH 5.6.

for internalization was found to be markedly more rapid when the pH of the drop was below the p$K_a$ of PDEA (i.e., when the particle surface was expected to be hydrophilic) than when it was above the p$K_a$ (when it was hydrophobic). Grain transfer was also found to be more rapid at low pH, since more rapid internalization made more surface sites available for grains to jump to. The variation of transfer and internalization times with driving potential was broadly as expected, although full explanation of some aspects will require detailed modeling of the field morphology.

## AUTHOR CONTRIBUTIONS

KK performed the experiments under supervision of the other authors. PI developed the model and performed the analyses. SF synthesized and characterized the particles. PI, SF, GW, and EW wrote the article.

## FUNDING

This work was supported by JSPS-OP (Australia) Bilateral Joint Research Projects, and by Grant-in-Aid for Scientific Research (B) (JSPS KAKENHI Grant Number JP16H04207) and Scientific Research on Innovative Areas Engineering Neo-Biomimetics (No. 4402) (JSPS KAKENHI Grant Numbers JP15H01602 and JP25120511), New Polymeric Materials Based on Element-Blocks (No.2401) (JSPS KAKENHI Grant Numbers JP15H00767 and JP25102542), Molecular Soft Interface Science (No. 2005) (JSPS KAKENHI Grant Numbers 23106720) and Electrostatic Formation of Liquid Marbles (Australian Research Council Discovery Project, DP170100578.).

## ACKNOWLEDGMENTS

Mr. Edmund Jarrett is thanked for his assistance with the electrostatic LM formation experiments.

## SUPPLEMENTARY MATERIAL

The Supplementary Material for this article can be found online at: https://www.frontiersin.org/articles/10.3389/fchem.2018.00215/full#supplementary-material

## REFERENCES

Arbatan, T., Al-Abboodi, A., Sarvi, F., Chan, P. P., and Shen, W. (2012a). Tumor inside a pearl drop. *Adv. Healthcare Mater.* 1, 467–469. doi: 10.1002/adhm.201200050

Arbatan, T., Li, L., Tian, J., and Shen, W. (2012b). Liquid Marbles as Micro-bioreactors for Rapid Blood Typing. *Adv. Healthcare Mater.* 1, 80–83. doi: 10.1002/adhm.201100016

Aussillous, P., and Quéré, D. (2001). Liquid marbles. *Nature* 411, 924–927. doi: 10.1038/35082026

Aussillous, P., and Quéré, D. (2006). Properties of liquid marbles. *Proc. Roy. Soc. Math. Phys. Eng. Sci.* 462, 973–999. doi: 10.1098/rspa.2005.1581

Bormashenko, E. (2017). Liquid marbles, elastic nonstick droplets: from minireactors to self-propulsion. *Langmuir* 33, 663–669. doi: 10.1021/acs.langmuir.6b03231

Bütün, V., Armes, S. P., and Billingham, N. C. (2001). Synthesis and aqueous solution properties of near-monodisperse tertiary amine methacrylate homopolymers and diblock copolymers. *Polymer* 42, 5993–6008. doi: 10.1016/S0032-3861(01)00066-0

De Lloyd, D. (2000). *Preparation of pH Buffer Solutions* [Online]. Available online at: http://delloyd.50megs.com/moreinfo/buffers2.html

Eshtiaghi, N., and Hapgood, K. P. (2012). A quantitative framework for the formation of liquid marbles and hollow granules from hydrophobic powders. *Powder Technol.* 223, 65–76. doi: 10.1016/j.powtec.2011.05.007

Eshtiaghi, N., Liu, J. J. S., and Hapgood, K. P. (2010). Formation of hollow granules from liquid marbles: small scale experiments. *Powder Technol.* 197, 184–195. doi: 10.1016/j.powtec.2009.09.013

Falconer, K. (1990). *Fractal Geometry: Mathematical Foundations and Applications*. Chichester: John Wiley.

Fujii, S., Sawada, S., Nakayama, S., Kappl, M., Ueno, K., Shitajima, K., et al. (2016a). Pressure-sensitive adhesive powder. *Mater. Horizons* 3, 47–52. doi: 10.1039/C5MH00203F

Fujii, S., Suzaki, M., Armes, S. P., Dupin, D., Hamasaki, S., Aono, K., et al. (2011). Liquid Marbles Prepared from pH-Responsive Sterically Stabilized Latex Particles. *Langmuir* 27, 8067–8074. doi: 10.1021/la201317b

Fujii, S., Yusa, S., and Nakamura, Y. (2016b). Stimuli-responsive liquid marbles: controlling structure, shape, stability and motion. *Adv. Funct. Mater.* 26, 7206–7223. doi: 10.1002/adfm.201603223

Hu, W., Xie, J., Chau, H. W., and Si, B. C. (2015). Evaluation of parameter uncertainties in nonlinear regression using Microsoft Excel Spreadsheet. *Environ. Syst. Res.* 4:4. doi: 10.1186/s40068-015-0031-4

Ireland, P. M., Noda, M., Jarrett, E., Fujii, S., Nakamura, Y., Wanless, E. J., et al. (2016). Electrostatic formation of liquid marbles - Influence of drop and particle size. *Powder Technol.* 303, 55–58. doi: 10.1016/j.powtec.2016.08.036

Ireland, P. M., Webber, G. B., Jarrett, E. D., and Galvin, K. P. (2015). Interaction of a particle bed with a droplet under an applied electric field. *J. Phys. Conf. Ser.* 646:012027. doi: 10.1088/1742-6596/646/1/012027

Jarrett, E., Ireland, P. M., Webber, G. B., and Wanless, E. J. (2016). Particle-liquid structures formed by electric fields. *Powder Technol.* 297, 1–7. doi: 10.1016/j.powtec.2016.04.021

Kawashima, H., Paven, M., Mayama, H., Butt, H. J., Nakamura, Y., and Fujii, S. (2017). Transfer of materials from water to solid surfaces using liquid marbles. *ACS Appl. Mater. Interf* 9, 33351–33359. doi: 10.1021/acsami.7b11375

Kido, K., Ireland, P. M., Sekido, T., Wanless, E. J., Webber, G. B., Nakamura, Y., et al. (2018). Formation of liquid marbles using ph-responsive particles: rolling vs electrostatic methods. *Langmuir* 34, 4970–4979. doi: 10.1021/acs.langmuir.7b04204

Liyanaarachchi, K. R., Ireland, P. M., Webber, G. B., and Galvin, K. P. (2013). Electrostatic formation of liquid marbles and agglomerates. *Appl. Phys. Lett.* 103:054105. doi: 10.1063/1.4817586

McHale, G., and Newton, M. I. (2015). Liquid marbles: topical context within soft matter and recent progress. *Soft Matter* 11, 2530–2546. doi: 10.1039/C5SM00084J

Nakai, K., Fujii, S., Nakamura, Y., and Yusa, S. (2013). Ultraviolet-light-responsive Liquid Marbles. *Chem. Lett.* 42, 586–588. doi: 10.1246/cl.130119

Oliveira, N. M., Reis, R. L., and Mano, J. F. (2017). The potential of liquid marbles for biomedical applications: a critical review. *Adv. Healthcare Mater.* 6:1700192. doi: 10.1002/adhm.201700192

Paven, M., Mayama, H., Sekido, T., Butt, H.-J., Nakamura, Y., and Fujii, S. (2016). Light-driven delivery and release of materials using liquid marbles. *Adv. Funct. Mater.* 26, 3199–3206. doi: 10.1002/adfm.201600034

Rasband, S. N. (1990). *Chaotic Dynamics of Nonlinear Systems*. New York, NY: Wiley.

Sekido, T., Kappl, M., Butt, H. J., Yusa, S., Nakamura, Y., and Fujii, S. (2017). Effects of pH on the structure and mechanical properties of dried pH-responsive latex particles. *Soft Matter* 13, 7562–7570. doi: 10.1039/C7SM01625E

Tian, J. F., Arbatan, T., Li, X., and Shen, W. (2010). Liquid marble for gas sensing. *Chem. Commun.* 46, 4734–4736. doi: 10.1039/c001317j

Ueno, K., Hamasaki, S., Wanless, E. J., Nakamura, Y., and Fujii, S. (2014). Microcapsules fabricated from liquid marbles stabilized with latex particles. *Langmuir* 30, 3051–3059. doi: 10.1021/la5003435

Yusa, S., Morihara, M., Nakai, K., Fujii, S., Nakamura, Y., Maruyama, A., et al. (2014). Thermo-responsive liquid marbles. *Polym. J.* 46, 145–148. doi: 10.1038/pj.2013.84

**Conflict of Interest Statement:** The authors declare that the research was conducted in the absence of any commercial or financial relationships that could be construed as a potential conflict of interest.

# Advantages of publishing in Frontiers

**OPEN ACCESS**
Articles are free to read for greatest visibility and readership

**FAST PUBLICATION**
Around 90 days from submission to decision

**HIGH QUALITY PEER-REVIEW**
Rigorous, collaborative, and constructive peer-review

**TRANSPARENT PEER-REVIEW**
Editors and reviewers acknowledged by name on published articles

**Frontiers**
Avenue du Tribunal-Fédéral 34
1005 Lausanne | Switzerland

**Visit us:** www.frontiersin.org
**Contact us:** info@frontiersin.org | +41 21 510 17 00

**REPRODUCIBILITY OF RESEARCH**
Support open data and methods to enhance research reproducibility

**DIGITAL PUBLISHING**
Articles designed for optimal readership across devices

**FOLLOW US**
@frontiersin

**IMPACT METRICS**
Advanced article metrics track visibility across digital media

**EXTENSIVE PROMOTION**
Marketing and promotion of impactful research

**LOOP RESEARCH NETWORK**
Our network increases your article's readership